Author:
Peschke, Patrick M

Title:
Design and applications of enzyme powered motile hybrid organic/inorganic-microcapsules

Author:
Peschke, Patrick M

Title:
Design and applications of enzyme powered motile hybrid organic/inorganic-microcapsules

Design and applications of enzyme powered motile hybrid organic/inorganic-microcapsules

By

Patrick M. Peschke

Department of Chemistry

University of Bristol

A dissertation submitted to the University of Bristol in accordance with the requirements of the degree of *Doctor of Philosophy* in the Faculty of Science.

Word Count: 90588

January 2022

Abstract of the thesis

Protocells have been established as an important platform in the understanding of contemporary naturally occurring, cellular phenomena or in the study of the origin of life. By designing protocells from the bottom up, the cell complexity can be reduced to the bare minimum, which allows the research of very specific functionalities, which often mimic naturally occurring properties of cells or microcompartments. The previously published work by Kumar *et* al. from the group of Prof. Stephen Mann found inspiration in gas vesicles of *Halobacterium salinarium*, which allowed the organism to move vertically via the manipulation of the buoyant force the organism experiences. In a similar manner, Kumar *et al*. designed giant buoyant microcapsules which maintained their vertical motility through enzymatic control of an O_2-microbubble inside the capsule.

The first experimental chapter of this thesis presents a novel protocell-system in protamine/DNA-microcapsules and compares it to the previously presented AMP/DNA-microcapsules from Kumar *et al*.. The cells are demonstrated as very robust and easy to fabricate with high stability in various chemical environments and under physical stress. What makes the capsules so valuable for the further experiments of this thesis though is their capability of entrapping various functional components like enzymes, or micro- or nano particles within them. The second half of this chapter then investigates the entrapment capabilities, by assessing the capsule's membrane thickness, permeability and its structure microscopically to establish a thorough hypothesis on the localisation of the entrapped enzymes, their stability, how they are entrapped and what the capsule-membrane looks like.

The following chapter then establishes the core functions of microcapsule motility. Entrapment of catalase and glucose oxidase enables the nucleation and consumption of an O_2-microbubble which in return causes the capsule to ascend or descend, facilitated by buoyancy. The first half of this chapter focuses on showcasing both the catalase mediated ascent and the glucose oxidase-mediated descent before combining both concepts into an oscillatory motion. Furthermore, the effect of the growing O_2-bubble on the capsule and its structural integrity is studied, which finally establishes protamine/DNA-microcapsules as superior to their predecessors. The second half of this chapter then focuses on the concept of microcapsule oscillations. Due to the complexity of the experimental design and since diffusion of spatially separated substrates plays a big role in them, the experimental devices will be explained and assessed both through computational simulation and practical diffusion studies with dyes. Stable oscillations and the novel concept of damped oscillations are presented in context to their experimental setups and are analysed through computer-assisted tracking of the microcapsule. Since the understanding of the growth- and depletion rate of the O_2-microbubble are so important, the last part of this chapter focuses on analysing the microbubble dynamics in relation to the substrate concentrations. Furthermore, enzyme leakage appeared as a reoccurring phenomenon throughout this thesis, which will be discussed regarding microcapsule oscillations and whether it causes any issues for the general legitimacy of the concept.

Lastly, the third experimental chapter utilises the previously established tools to exploit microcapsule oscillations to perform a rudimentary uptake, transport and release of functional cargo. This work introduces polyoxometalate coacervate vesicles (PCVs) as secondary cargo containers, which can retain molecular cargo via sequestration, and which are subsequently loaded onto protamine/DNA-microcapsule through electrostatic- and other non-defined surface-surface interactions. Next, the uptake conditions for protamine/DNA-capsules and PCVs and the release of the cargo, which is conceptualised around disintegration of the PCVs in response to a rising pH to ~9 will be discussed. To initiate the PCV-disintegration internally, urease was entrapped and used as the trigger for PCV-disintegration through the reaction with urea. Finally, multiple full and successive uptake, transport and release cycles are presented and discussed with several different cargo species.

Dedication and Acknowledgements

First and foremost, I want to dedicate this work to the memory of my father, who recently passed away in 2020. My father himself was a chemist holding the honours of a PhD and he was the reason I started following a similar path. From him I inherited my interest and curiosity about our world and in science. He not only taught me how to be a good and kind person, but also the importance of asking questions, forming my own opinion based on facts but also admitting being wrong and learning from my mistakes, which are pillars of our current scientific method. His final years were plagued by his struggle against cancer but even then, he remained positive, hopeful and supportive for both myself and my family, which I will keep as an inspiration for the rest of my life.

I want to acknowledge Prof. Stephen Mann, who was so kind to give me the opportunity to participate in his research and work alongside so many smart and helpful colleagues. He supported me both professionally, with advice, constructive commentary and discussion, but also personally during my most complicated hours over the last 1-2 years, for what I am very grateful. Next, I want to thank Dr. Avinash Patil, who served as my assessor and supervisor during the time of my PhD, but which frankly undersells his work and commitment. He was always there whenever I had a professional or personal issue, he supported me through various projects, some of which could not be finished due to the ongoing pandemic, and he was a great mentor, who is full of ideas and emits a general fascination and professional aptitude for science, which motivated me a lot during the more difficult times and made me into a better and more independent scientist. I also want to thank Dr. Pavan Kumar Bosukonda, who was not only a colleague and mentor for my PhD, but also a good friend and source of inspiration for protocellular science and for science in general.

Like many students starting their PhD, I was aware of the emotional and physical stress so many of my predecessors had to endure, but I dismissed it as something that I would overcome by simply being smarter or better. It is humbling in a way, that all the preparation in the world does not protect you from the ups and downs of a PhD-studentship, but it also shaped me into the scientist I am today. For that I am grateful, but I am also aware that none of this would have been possible without the personal support of so many of my colleagues, some of which I would also call my good friends. So, I want to dedicate my gratitude to them, for being there over the years, for the time we spent together and the hardship we endured as a group.

I want to thank my girlfriend and partner Carmen, who has been by my side every step of the way. I want to thank my family, my mother, my two brothers Frédéric and André and my sister Nicole, who I missed every day since I moved to the UK but who were always there whenever I needed them. And I want to say thanks to my friends back home in Germany, who have not forgotten about me and who made some periods of time over the past 2 years manageable either through video call, video games or just by plain text. Thanks to all of you for being a part of my life.

And finally, I want to finish these dedications with a quote of one of my favourite authors H. P. Lovecraft.

,,*The oldest and strongest emotion of mankind is fear, and the oldest and strongest kind of fear is fear of the unknown."*

- H. P. Lovecraft -

As scientists, the unknown is something we're all accustomed to and our work is proof, that the only way to conquer fear, is by shining light into the darkness. Through curiosity, knowledge, courage and

kindness, we can overcome our fears, we can fight stigmata, prejudice and hate and only then we can grow as an individual or as a community.

Author's Declaration

I declare that the work in this dissertation was carried out in accordance with the requirements of the University's Regulations and Code of Practice for Research Degree Programmes and that it has not been submitted for any other academic award. Except where indicated by specific reference in the text, the work is the candidate's own work. Work done in collaboration with, or with the assistance of others is indicated as such. Any views expressed in the dissertation are those of the author.

SIGNED:…  …. DATE:……10.05.2022……

Table of Contents

List of Abbreviations

2D:	two-dimensional
3D:	3-dimensional
ABTS:	(2,2'-azino-bis(3-ethylbenzothiazoline-6-sulfonic acid))
AFM:	Atomic force microscopy
ALP:	Alkaline phosphatase
AMP:	Aminopropyl-functionalised
Aq:	Aqueous
APTES:	(3-aminopropy)triethoxysilane
ATP:	Adenosine-triphosphate
ATR:	Attenuated total reflection
A.U.:	Arbitrary units
BSA:	Bovine serum albumin
Cat:	Catalase
CD:	Circular dichroism
CM-Dextran:	Carboxymethyl-dextran
CNT:	Carbon nanotube
COOH-:	Carboxylate
CSTR:	Continuous stirred tank reactor
DADMAC:	Diallydimethylammonium chloride
DLS:	Dynamic light scanning
DM:	Dialysis membrane
DMSO:	Dimethyl sulfoxide
DNA:	Deoxyribonucleic acid
DSC:	Differential scanning calorimetry
E. Coli:	Escherichia coli
EDC:	1-Ethyl-3-(3-dimethylaminopropyl)carbodiimide
EDX:	Energy-dispersive X-ray spectroscopy
EM:	Electron microscopy
Em.:	Emission

et al.:	Translated from Latin: “and others”
Exc.:	Excitation
Fig.:	Figure
FITC:	Fluorescin-isothiocyanate
FTIR:	Fourier-transform infrared spectroscopy
GOx:	Glucose oxidase
HCl:	Hydrochloric acid
HOMO:	Highest occupied molecular orbital
HRP:	Horseradish peroxidase
IR:	Infrared
LUMO:	Lowest unoccupied molecular orbital
M:	Moles per dm^3
MC:	Merocyanine
mM:	millimoles per dm^3
MNM:	Micro/Nanomachines
MW:	Molecular weight
MWCNT:	Multi-walled carbon nanotubes
NHS:	N-hydroxysuccinimide
NIR:	Near-infrared
NMR:	Nuclear magnetic resonance spectroscopy
PAH:	Poly(allylamine hydrochloride)
PCV:	Polyoxometalate coacervate vesicles
PEG:	poly(ethylene glycol)
PDMS:	polymethyl methacrylate
PDDA:	Poly(diallydimethylammonium chloride)
PI:	Isoelectric point
PMMA:	polymethylmethacrylate
PNIPAAm:	Poly(N-isopropylacrylamide)
POM:	Polyoxometalate
ppm:	Parts per million
Protamine:	short for protamine-sulfate

PTA:	Phosphotungstate
PTFE:	Polytetrafluorethylene
Re:	Reynolds number
RITC:	Rhodamine-B-isothiocyanate
SE:	Secondary electrons
SEM:	Scanning electron microscope
SP:	Spiropyran
TEM:	Transmission electron microscope
TWEEN20®	Polysorbate 20
T_x:	Time-period of X
UoB:	University of Bristol
UV:	Ultraviolet
VIS:	Visible
wt%:	Weight percentage
XRD:	X-ray powder diffraction
“z”:	Vertical dimension in microscopy or oscillation experiments

Introduction

1.1 The origin of life

The origin of life is a large term, seemingly brimming with philosophical and scientific meaning, yet it is a question that has never been more relevant or important than now. We live in a time of emerging space travel, we have decoded the genetic code and have understood many of the most fundamental processes in nature, yet we simply still don't know how life emerged. This question gains even more importance under the label of astrobiology, which not only discusses the origin of life in relation to earth, but also in context of the whole universe. Which leaves us with another question: How can we study the universe and its potential life forms, if we don't even properly understand where and how we humans and all our fellow life forms from the planet earth have emerged?

One of the most popular theories on the emergence of life is the one of the Russian biochemist Alexander Oparin, who claimed that life successively developed from non-living assemblies of simple chemical components into more and more complex arrangements which can ultimately be called life. [1] What this suggests, is that the beginning of life is difficult to pin down. There most likely is not a simple answer to the question of a common ancestor, as we are all derived from a primordial soup of molecules, which gradually increased in complexity. What we can do though, is to describe a primordial organism, which contained some of the most basic functions, from which many if not all future organisms developed from, which is called the "Last Universal Common Ancestor" or LUCA. [2,3] Considering this definition, it seems very much understandable that the origin of life is not only of interest for biologists and historians but also for chemists. While biologists can only approach the question from a mere theoretical point of view, chemists possess the tools to rearrange matter and therefore design and recreate potential candidates that might resemble the earliest cells or molecular complexes that were found on our planet. Nonetheless, one issue that science has always struggled with is to gain the necessary funding for its research, and the origin of life is no exception. [4]

There are several theories on when the LUCA existed, one of them coming from the University of Bristol, which dated the LUCA about 4.5 billion years ago within the Hadean period. [5] Structurally, the LUCA was most likely a simple single celled organisms with DNA as its main information storage, which was already comprised of the current 4 nucleotides: deoxycytidine, deoxythymidine, deoxyadenosine and deoxyguanosine. It is furthermore assumed that the LUCA contained enzymes like DNA polymerase, repair enzymes, RNA-polymerase and a full expression (translation and transcription) system for the production of proteins. [6-8]

This leaves the question what the chemical environment actually looked like on a prebiotic earth. Miller and Urey conducted one of the first experiments, that tried to simulate the actual physical conditions of an early earth to see what molecular species could have evolved from it and whether

Oparin's and Haldane's [9] theories were feasible. They built a closed system, which contained a heated flask filled with water and a mixture of gasses which were assumed to be present in the atmosphere during this period like H_2O, NH_3, CH_4 and H_2, which would primarily describe reducing conditions. To start chemical reactions, the necessary energy was applied in form of sparks, which were supposed to represent lightnings on the prebiotic earth. They were able to characterise various components like amino acids, sugars, lipids and even more organic molecules, even though DNA or RNA was not found in the experiment. [10,11] This was an amazing find, as it would prove a direct pathway for the synthesis of many prebiotic pre-cursors which are common in contemporary biology. Nonetheless, the success of the experiment did not come without criticism. Many scientists questioned the core assumption of a mainly reducing atmosphere and that a prebiotic earth must have contained a lot more oxygen than Miller and Urey expected. [12,13] What the experiment shows nonetheless, is that simple building blocks, which play a big role in the biochemistry of organisms, can be synthesised under primitive chemical and physical conditions. While these molecules on their own would not form a living entity, their organisation does. The spontaneous self-organisation of small molecules in form of compartmentalisation is a very specific and relevant phenomenon, which most likely laid the foundation for most living organisms of today.

1.2 Compartmentalisation

In the context of the origin of life compartmentalisation describes the emergence of a permeable, or semi-permeable membrane around discrete water-droplets. [14] While this description appears a lot simpler in comparison to modern cells, which contain a highly complex network of proteins and polymers within a functional semi-permeable membrane, it already describes the core principle of almost every cell in existence. Semi-permeability allows the cell to control the in- and outflux of nutrients or molecules, as only components of a specific size, polarity or charge are able to traverse the membrane. These molecules, which are capable of moving through the membrane are enriched within the compartment, which creates a concentration hotspot and enables new forms of chemistry which have not been possible before. One way to facilitate such chemical reactions is by building up electrochemical gradients along the membrane, which can then be used to synthesise energy-rich molecules used to power internal processes of the cell. And indeed, some complex molecular structures like the ones of polypeptides can only be synthesised within an enclosed environment. This has been shown for polymerases [15], while at the same time, the membrane also keeps polymers or polypeptides entrapped within the cell. One of the most fascinating aspects of the emergence of life is not just the increase in complexity, but also the shift towards a completely self-referential entity, which means, that the system creates the products which it needs for its own existence. [16] As a chemist and experimenter, this is a daunting task considering that chemistry, as we know it, is based on a simple mathematical model: We add A to B and we get C, or described in an example, we add surfactants to water droplets and observe the self-assembly of a simple membrane. What this does not include is the concept of creating something with the primary goal of maintaining its own viability, what Mann *et al*. proposed to call "*self-determining chemistry".* [16]

In order to recreate primitive cells or cells with primitive functions, the pathways one can take can vary, but are usually described in form of two different methods: the so called "*top-down*-"and the "bottom-up"-approach. The former focuses on contemporary cells and approaches the primordial cell through successive reduction or manipulation of the hosts genome complexity. The method generally utilises common techniques from synthetic biology like metabolic and genetic engineering to alter the genome until all but the most minimal functions have been removed, that are necessary to maintain the basic conditions of reproduction, metabolism etc. [17]

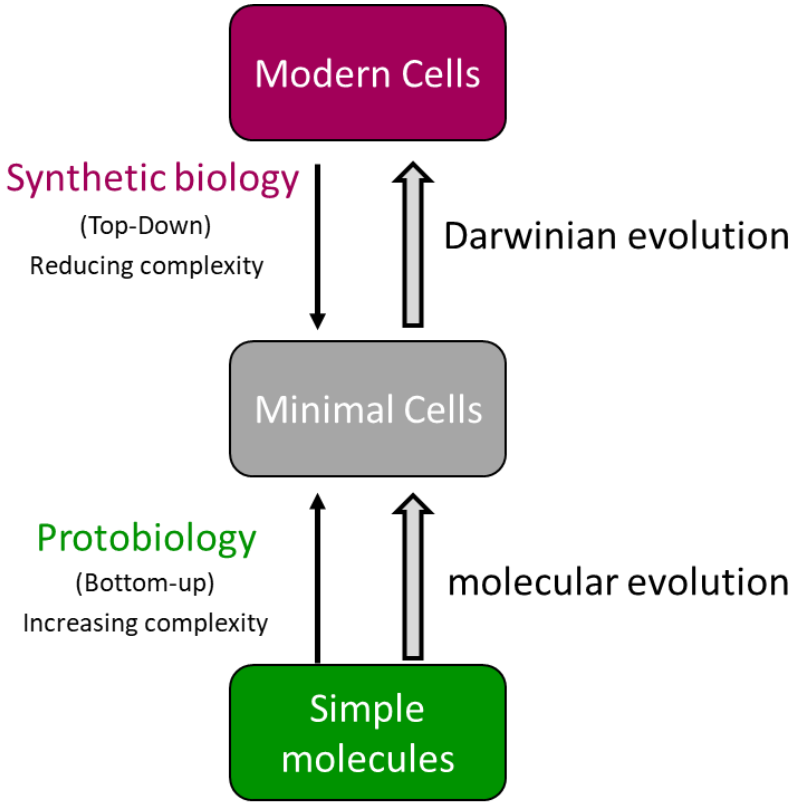

Figure 1.2-1: *Design of primitive cells from either the top down or the bottom up.* [16]

On the other hand, the bottom-up-approach aims to design cells from an origin of life-perspective by mainly utilising smaller molecular components by increasing the complexity of the cell gradually. In contrast to top-down, the bottom-up method demands a different set of techniques and knowledge, which usually revolves around physiochemical phenomena like self-organisation or self-assembly, complexation, polymerisation and many more, which makes the outcome of the experiments often easier to predict. It not only offers a more realistic approach, as it considers the conditions of a primordial earth under which it tries to fabricate the primitive cell, but furthermore makes use of a vast repertoire of building blocks and established techniques from fields like organic- or macromolecular synthesis, which opens a sheer infinite space of possibilities and creativity. [16,18]

When working on primitive cell-structures, the word "*protocell*" is most likely going to be used at some stage. Its definition is not set in stone and is often used rather loosely for any kind of primitive cell [19], which means that it can relate to replications of primordial cells in the context of the origin of life or simply to cells with a highly reduced content of molecular machinery and function. This also explains, that protocellular research does not necessarily need to revolve around the origin of life but could also focus on mimicking cellular functions of interest of contemporary cells or engineering protocells according to an application-based approach. The latter could serve as a novel platform for the design of artificial cells that could drive the progress in pharmacology, nanomedicine, drug delivery, bio-sensing, catalysis or vaccine research. [20]

But what minimal requirements does a protocell need to fulfil the conditions of life? While there is no consensus on what life is, there are a few definitions which are commonly found in all live beings and without which life would usually be impossible. [21] Compartmentalisation, usually in form of a semi-permeable membrane has already been described above and is one of the core principles of life on earth, as it not only protects the organism and its internal components, but also creates the conditions to facilitate chemical reactions and to conserve energy. But the cell on its own would not be able to

form complex organisms If it wasn't capable of reproduction. In modern cells, reproduction is based on the interactions between many different proteins and DNA, which serves as the blueprint of the cell. To reproduce, the cell not only needs to multiply its own genetic information (DNA-replication) but it also needs to be able to read (Transcription) and produce (Translation) the building blocks to maintain or create a new generation of cells. In natural cells, reproduction usually means the growth and division of a single cellular entity into two, while reproducing the exact cellular contents inside the daughter cell. This would not suffice though, as the cell requires a constant influx of energy and chemical components to be able to reproduce, which is described as the metabolism or the "regenerative" property of the cell. The necessary molecules for the metabolism are usually sequestered from the environment and sometimes stored within the cell. The process of self-regulation, which a cell undergoes in response to a changing chemical environment to keep the internal conditions in a steady state is called homeostasis and is highly important, considering many of the chemical processes are conducted by enzymes which are sensitive to a changing pH, temperature and chemical environment. Another important factor, which is often included in the definition of life is that the cell is subject to Darwinian evolution, which means that the change of the genetic code due to mutations during reproduction or environmental effects and its phenotypic expression result in a change of fitness in the organism and in a natural selection. Luisi *et al*. described the importance of compartmentalisation regarding evolution as followed: Considering a population of free RNA-replicases in solution, better replicases would perform their work at a faster rate, but due to the dilution, would not increase over a relevant threshold, which means that these replicases could not evolve to a higher and better adapted species. On the other hand, when keeping these enzymes within a compartment which is undergoing replication, the new generations with a faster mutant of the replicase will be able to replicate quicker than the ones with the original replicase. [15]

1.3 Molecular interactions

In both the fabrication of synthetic cells and the research of the origin of life, self-assembly is a very important process. Especially when considering the former, it would be highly tedious, time intensive and most likely expensive to fabricate cells by assembling molecular building blocks one by one. Over the past decades, molecular self-assembly has been used in various fields to fabricate objects from the nano- to the micro scale, which ranges from organic [22,23] and inorganic [24,25] crystals to organic polymers and macromolecules [26,27] over to higher order structures like self-assembled monolayers [28-30], nanoparticles [31,32], -tubes [33] or -rods [34] and up to complex microscopic architectures like self-assembling fluidic machines [35], micromixers [36], or self-assembling electronic circuits. [37] Peptides, for example, have emerged as an interesting platform for self-assembly in biomedicine or biotechnology, bringing advantages like structural programmability, good biocompatibility, biodegradability, low immunogenicity and versatility. [38] In their 2009 publication, Grzybowski *et al*. defined self-assembly "as the spontaneous formation of organized structures from many discrete components that interact with one another directly (e.g. by electrostatic repulsions [39]) and/or indirectly, through their environment (e.g., magnetohydrodynamic self-assembly [40])", which also separates self-assembly from other molecular aggregations like precipitation. [41,42] While the concept of molecular self-assembly seems intuitive and easy to understand on the surface, it is necessary to come up with a definition, as even simple molecular reactions could be considered self-assembly.

Thermodynamically, the process of self-assembly is defined by minimising the Gibbs free energy, at constant temperature T, pressure P and number of molecules N within the system. With the entropy S and the enthalpy H, the Gibbs free energy G is defined as followed:

$$\Delta G = \Delta H - T\Delta S \qquad \textit{(Equation 1.3.-1)}$$

Alternatively, at constant temperature T and volume V, the process would be described by a minimum of the Helmholtz free energy F, which is described by the entropy S and the internal energy U as followed:

$$\Delta F = \Delta U - T\Delta S \qquad \textit{(Equation 1.3.-2)}$$

So, from a thermodynamic perspective, what drives the process of self-assembly is either entropic, enthalpic, or both. [42] When looking at the interactions of the molecules specifically though, it needs to be addressed what types of interactions are responsible for self-assembly. While covalent forces can play a role in some forms of self-assembly like for polyoxometalates [43], the predominant form of interactions are non-covalent weak interactions like electrostatic-, hydrophobic-, π–π–, Van der Waals-interactions and hydrogen-bonds. These effects can lead to self-organisation both intramolecularly, like it is the case for the secondary structure of proteins [38], and intermolecularly. Electrostatic interactions are probably one of the more relevant interactions in case of self-assembly and many other phenomena described within this thesis. They happen between charged molecules and can be either attracting when the charges are opposing or repulsing when they are the same. The strength of an ionic bond can vary but usually lies around 170 – 1500 kJ/mol [38,44,45] (e.g. NaCl has a lattice energy of -756 kJ/mol). [46] In contrast to the ion-ion-interactions, Van der Waals-forces, which temporarily create electric dipoles by the randomly fluctuating electrons of the atoms, and hydrogen bonds are much weaker with only 5 kJ/mol and 10-40 kJ/mol respectively. [38] By changing the pH, temperature or the concentration of the electrolyte within the solution, the interactions can be altered and tuned to optimise the self-assembly process.

1.4 Motility of artificial micro/nano-motors

Over the course of the following chapters, a variety of micro- and nanomotors will be introduced which have been showcased in literature over the past decades and which feature many different means to facilitate motion. While the rest of this thesis will focus on case studies revolving around specific micro/nanomachines (MNMs), this paragraph will instead look at the different motility concepts and their physical fundamentals.

Based on the fact that most artificial MNMs are made from synthetic materials, either inorganic or organic, the repertoire of possible materials to fabricate micro/nano-motors is sheer endless. Nonetheless, the motility concepts behind the motors are a lot more limited to a few physical effects which can be applied to MNMs to drive them forward. From the best of my knowledge, these involve bubble propulsion, diffusiophoresis, chemotaxis, self-electrophoresis, buoyancy, thermophoresis, enhanced diffusion, motion induced via surface tension gradients (Marangoni-effects), and motion facilitated through interaction with a magnetic-, acoustic, electromagnetic or electric field. It needs to be addressed, that all these motility concepts go hand in hand with the design of the motor and are usually not interchangeable, ergo a motor that is propelled by buoyancy most likely will not be able to facilitate diffusiophoretic properties without extensive re-design of the micromotor.

The latter are most likely the easiest to explain, as the motility is not facilitated by the motor itself, but rather by the interaction of the motor with an external force field. Suspended particles generally have a surface charge through which they interact with other charged molecules in solution, thus forming a so called "*double layer*". [47] When applying a homogenous electric field to these suspended particles, the ions in the double layer experience a coulomb force, which drags the particle with them,

thus creating motion. The most popular description of electrophoretic motion is described by the Smoluchovski equation, with ε_r as the dielectric constant of the dispersion medium, ε_0 as the permittivity of free space, ζ as the zeta potential and η as the dynamic viscosity of the dispersion medium (Equation 1.4-1). [48]

$$\mu_e = \frac{\varepsilon_r \varepsilon_0 \zeta}{\eta} \qquad \textit{(Equation 1.4-1)}$$

Alternatively, electric fields can induce polarisation within symmetrical (e.g. spherical) particles, which can trigger opposing redox reactions on each hemisphere of the particle and thus driving the particle forward through a secondary mode of motility like bubble propulsion. [49] On the other hand acoustic waves in the low megahertz range can interact with the particle directly thus causing an effect termed acoustophoresis. The forces that drive the motion are based on the scattering of the acoustic wave on the surface of the particle, which can cause linear or even rotational motion. The latter is often realised through asymmetrical designs of the micro/nanomotor. [50-52] Electromagnetic radiation is another important means to induce motion, even though one has to distinguish between different interactions once more, as light can interact in several different ways. The classic photophoresis, ergo motion induced by light, is not as straight forward as the acoustic counterpart, and one has to distinguish between two different kinds as followed: Direct photophoresis terms the motion of particles via direct energy transfer of the photons through refraction and reflection. [53] Indirect photophoresis on the other hand describes motion through thermal gradients, which are induced through uneven absorption of light throughout the particle surface. The particle then experiences an asymmetrical force due to the collisions of the solvent molecules of higher energy along the temperature gradient, which is called thermophoresis. [54,55] A model which utilises the concept of radiation pressure to perfection is the optical tweezer, which can suspend and fixate microscopic and sub-microscopic particles. [56]

One of the most popular and widely applied motility strategies is bubble propulsion via generation and ejection of small gas-bubbles through chemical reactions on one side of the surface of the MNM. While there are different approaches to this concept like tubular jets, wires or spherical Janus-particles, the physical explanation to the motion is usually the same. Nucleation and growth of a gas bubble creates a flow of liquid as it is displaced until the bubble detaches. This displacement creates a net-force in the opposite direction to the bubble-growth site, thus moving the object forward. [57-59] Due to the complexity of interactions that can affect micro- and especially nanoscale objects, it is not always clear what forces effectively drive the motion and there has been a lot of debate with no clear consensus up to this date. Chapter 4 discusses the case of Au/Pt- and Ni/Pt-nanowires, which showcase opposite directionality, once through bubble-propulsion and once without, even though their chemical compositions are not too different. But changing nickel to gold promotes a completely different physical phenomenon which is called self-electrophoresis, during which the object, instead of generating O_2-bubbles on the Pt-end through decomposition of H_2O_2, generates an electric field which drives the motion of the nanowire. [60,61]

Another very important motility concept is diffusiophoresis, and which is often discussed in contrast to motion via bubble-propulsion. Here, instead of using the displacement of the liquid phase through a gas-phase, the motion is induced through creation of local concentration gradients. The enrichment of a molecular species, either charged or non-charged, gives rise to a migration of molecules due to the chemical potential of the gradient, which then facilitates a net-force based on the imbalanced transfer of kinetic energy of the solute molecules to the particle. In case of charged particles, this explanation has to be extended though, as the enrichment not only creates a local concentration gradient within the bulk around the particle, but also a concentration- and charge gradient within the

particle's double layer. This uneven distribution of charge then creates a polarisation and thus an electric driving force as well. [62,63] Concentration gradients are highly important in nature, as they serve as a signal and guidance for organisms to find their way to food sources or other important nutrients. This guided motion is called chemotaxis and could be seen as one of the highest and most complex forms of motion for an artificial system. A very common form of chemotaxis is enhanced diffusion in which enzymes diffuse faster along a concentration gradient of their own substrate. [64] The group around Prof. Ayusman Sen have a long history of chemotaxis-research and have shown this behaviour of induced motion of catalysts in response to substrate turnover and many other examples of chemotaxis. [65,66] Finally, gradients of surface tension can be used as another source to induce mass-flows and therefore motion of micro/nanoscopic objects. L. Rodriguez-Arco *et al.* from the group of Stephen Mann have shown self-propulsion of microdroplets via Marangoni-convective flows along the interface of the droplet and under non-equilibrium conditions. [67]

While these are the most popular candidates for induced motility of MNMs, there are likely many more possible pathways, some of which have not been discovered as of today. Nonetheless, they offer a large set of tools to design the appropriate engine for many different applications of MNMs.

1.5 Motivation for this thesis

The previous paragraph depicted the various ways the experimenter can establish motility in MNMs, yet the work of this thesis will focus solely on one of them, more specifically buoyancy. While the physics behind it will be elucidated at a later point in chapter 4, the advantages of buoyancy can be easily described in relation to other, previously mentioned motility concepts: It is highly linear, whereas other concepts like bubble propulsion or diffusiophoresis are more prone to divergence from a straight line due to fluctuations of the forces applied to the motor. Buoyancy on the other hand is solely governed by two, directly counteracting forces which are the buoyant force and gravity. This makes buoyancy a very predictable type of motion, which is ideal for laboratory experiments and application based designs. It also offers motion in the vertical dimension, which is a lot more difficult to realise with other motility concepts, especially in the microscopic realm, where objects are still very much susceptible to gravity via sedimentation. Using buoyancy in micromotors is not a novel concept, even though it showed less popularity in contrast to e.g. bubble-propelled systems, most likely since it poses less relevancy regarding medicinal or therapeutic applications. Nonetheless, there have been many interesting designs for buoyancy-propelled micromotors in recent years, some of which simply used buoyant motion as a next level of complexity for their previously established design [68], whereas others utilised buoyancy to study catalytic micromotors at the air/liquid interface [69], or implemented buoyancy as part of their application based design for degradation of pollutants via catalytic micromotors. [70] The latter reference, which was published by J. Wu *et al.* is representative for one of the most interesting ideas when it comes to buoyant micromotors, which is environmental remediation of water bodies. Buoyant MNMs possess a variety of benefits over other motility designs, namely that their vertical motion enables interaction with various depths of the liquid body, depending on where the toxic pollutant is residing, whereas other MNMs would simply sediment to the ground and become redundant. Furthermore, removal of the remediating-agent is necessary as to not further pollute the water body. Buoyancy offers a very comfortable approach to this, as MNMs can simply float up to the surface, from where they can be removed.

So what drives the motivation for work of this thesis? While it follows a strictly chronological bottom-up approach, it is not starting from square one. Probably the most important reference, and the platform from which this thesis expands its ideas, is the publication of Kumar *et al.* from 2018, which showcased enzyme-powered buoyancy of microcapsules via an internally nucleated O_2-microbubble.

[71] Based on this, it would be easy to simply use bioremediation as the overarching motivator for this thesis, but it is not that easy. While scientific progress surely is one of the core foundations of this research, it still lacks the influence from a more creatively oriented field, which is art. From a scientific point of view, the following chapters will show various novelties, which have not been described to that extent in recent literature. Most motile micro/nanomotors lack the complexity for multiple modes of motility, ergo moving back and forth or adjusting their directionality. Here, a new micromotor in enzyme powered protamine/DNA-microcapsules is described, which can oscillate in a controlled fashion and in response to its environment. So far and to the best of my knowledge, buoyant micromotors did not maintain any kind of oscillation for longer periods of time or over more than a few oscillations, which stands in stark contrast to the long-lasting oscillations of this thesis. [70,72] Furthermore, complex oscillation patterns in form of damped oscillations were achieved through meticulous control of the chemical environment and the experimental design. Finally, microcapsule oscillations were utilised to perform a repetitive uptake, transport and release of secondary cargo containers, loaded with a molecular payload.

While all of these points stand true as novel concepts in relation to buoyant microcarriers, it is not simply an application based design, nor is it merely a case of biomimicry, even though the motivation stems from buoyant microorganisms. [73] The design principles shown for every step of this thesis are very much human and follow a more curiosity-based approach. What started out as simply mimicking the idea of buoyancy with the toolset of protocellular design, quickly strayed further and further away from the biological origin. Microcapsules were designed by repurposing naturally occurring biopolymers like DNA or protamine as structural components. Buoyant oscillations, in respect to the natural origin which only moves over scales of less than a few millimetres, were taken to the extreme by making the micromotor oscillate over multiple centimetres and at velocities which exceed any biological process. Furthermore, oscillations were designed in a very visually pleasing way, which can be showcased, tuned and tracked depending on the interest of the experimenter, but not according to a functional purpose. Damped oscillations did not serve to answer the question whether it is reasonable, but rather if it is possible and to what extent. Finally, the transportation-concept presented in chapter 5 takes another step further away from nature, as it is not simply portraying uptake and release on a molecular scale, but rather a very human-influenced idea of the process, like moving a ball from the floor to the table. It is almost game-like, to impose this redundant task of uptake/release on these microcarriers, just to see through how many cycles they can carry their cargo and release the payload before breaking down.

Science and art are not mutually exclusive, rather the opposite as art can be found in many scientific projects, it usually depends on the perspective of the viewer. Instead, by embracing the latter, projects can gain relevancy and a certain creative spirit, which is sadly lacking in some work these days, even though the people behind it put years of effort into it.

1.6 Literature for the introduction

1. Oparin, A. I. & Morgulis, S. *The Origin of Life*. (Dover Publications, 2003).
2. Woese, C. The universal ancestor. *Proceedings of the National Academy of Sciences* **95**, 6854-6859, doi:10.1073/pnas.95.12.6854 (1998).
3. Woese, C. R. & Fox, G. E. The concept of cellular evolution. *Journal of Molecular Evolution* **10**, 1-6, doi:10.1007/BF01796132 (1977).
4. Mann, S. The Origins of Life: Old Problems, New Chemistries. *Angewandte Chemie International Edition* **52**, 155-162, doi:https://doi.org/10.1002/anie.201204968 (2013).
5. Betts, H. C. *et al.* Integrated genomic and fossil evidence illuminates life's early evolution and eukaryote origin. *Nature Ecology & Evolution* **2**, 1556-1562, doi:10.1038/s41559-018-0644-x (2018).
6. Delaye, L. & Becerra, A. Cenancestor, the Last Universal Common Ancestor. *Evolution: Education and Outreach* **5**, 382-388, doi:10.1007/s12052-012-0444-8 (2012).
7. Glansdorff, N., Xu, Y. & Labedan, B. The Last Universal Common Ancestor: emergence, constitution and genetic legacy of an elusive forerunner. *Biology Direct* **3**, 29, doi:10.1186/1745-6150-3-29 (2008).
8. Weiss, M. C., Preiner, M., Xavier, J. C., Zimorski, V. & Martin, W. F. The last universal common ancestor between ancient Earth chemistry and the onset of genetics. *PLoS genetics* **14**, e1007518-e1007518, doi:10.1371/journal.pgen.1007518 (2018).
9. Tirard, S. J. B. S. Haldane and the origin of life. *J Genet* **96**, 735-739, doi:10.1007/s12041-017-0831-6 (2017).
10. Ferus, M. *et al.* Formation of nucleobases in a Miller–Urey reducing atmosphere. *Proceedings of the National Academy of Sciences* **114**, 4306-4311, doi:10.1073/pnas.1700010114 (2017).
11. MILLER, S. L. & UREY, H. C. Origin of Life. *Science* **130**, 1622-1624, doi:10.1126/science.130.3389.1622-a (1959).
12. Cronin, J., Pizzarello, S. & Cruikshank, D. Meteorites and the early Solar System. *University of Arizona Press, Tucson*, 819-857 (1988).
13. Kasting, J. F. Earth's early atmosphere. *Science* **259**, 920-926 (1993).
14. Chen, I. A. & Walde, P. From self-assembled vesicles to protocells. *Cold Spring Harbor Perspectives in Biology* **2**, a002170 (2010).
15. Szostak, J. W., Bartel, D. P. & Luisi, P. L. Synthesizing life. *Nature* **409**, 387-390 (2001).
16. Dzieciol, A. J. & Mann, S. Designs for life: protocell models in the laboratory. *Chem Soc Rev* **41**, 79-85, doi:10.1039/c1cs15211d (2012).
17. Luisi, P. L., Walde, P. & Oberholzer, T. Lipid vesicles as possible intermediates in the origin of life. *Current Opinion in Colloid & Interface Science* **4**, 33-39, doi:https://doi.org/10.1016/S1359-0294(99)00012-6 (1999).
18. Luisi, P. L. *The Emergence of Life: From Chemical Origins to Synthetic Biology*. (Cambridge University Press, 2016).
19. Schrum, J. P., Zhu, T. F. & Szostak, J. W. The origins of cellular life. *Cold Spring Harbor perspectives in biology* **2**, a002212 (2010).
20. Brea, R. J., Hardy, M. D. & Devaraj, N. K. Towards self-assembled hybrid artificial cells: novel bottom-up approaches to functional synthetic membranes. *Chemistry (Weinheim an der Bergstrasse, Germany)* **21**, 12564 (2015).
21. Alberts, B. & Information, N. C. f. B. *Molecular Biology of the Cell*. (Garland, 2004).
22. Desiraju, G. R. Supramolecular synthons in crystal engineering—a new organic synthesis. *Angewandte Chemie International Edition in English* **34**, 2311-2327 (1995).
23. Moulton, B. & Zaworotko, M. J. From molecules to crystal engineering: supramolecular isomerism and polymorphism in network solids. *Chemical reviews* **101**, 1629-1658 (2001).
24. Aizenberg, J., Muller, D. A., Grazul, J. L. & Hamann, D. Direct fabrication of large micropatterned single crystals. *Science* **299**, 1205-1208 (2003).
25. Blake, A. *et al.* (1999).

26. Lehn, J. M. Perspectives in supramolecular chemistry—from molecular recognition towards molecular information processing and self-organization. *Angewandte Chemie International Edition in English* **29**, 1304-1319 (1990).
27. Philp, D. & Stoddart, J. F. Self-assembly in natural and unnatural systems. *Angewandte Chemie International Edition in English* **35**, 1154-1196 (1996).
28. Bain, C. D. *et al.* Formation of monolayer films by the spontaneous assembly of organic thiols from solution onto gold. *Journal of the American Chemical Society* **111**, 321-335 (1989).
29. Love, J. C., Estroff, L. A., Kriebel, J. K., Nuzzo, R. G. & Whitesides, G. M. Self-assembled monolayers of thiolates on metals as a form of nanotechnology. *Chemical reviews* **105**, 1103-1170 (2005).
30. Witt, D., Klajn, R., Barski, P. & Grzybowski, B. A. Applications, properties and synthesis of ω-functionalized n-alkanethiols and disulfides-the building blocks of self-assembled monolayers. *Current Organic Chemistry* **8**, 1763-1797 (2004).
31. Li, M., Schnablegger, H. & Mann, S. Coupled synthesis and self-assembly of nanoparticles to give structures with controlled organization. *Nature* **402**, 393-395 (1999).
32. Mirkin, C. A., Letsinger, R. L., Mucic, R. C. & Storhoff, J. J. A DNA-based method for rationally assembling nanoparticles into macroscopic materials. *Nature* **382**, 607-609 (1996).
33. Fan, S. *et al.* Self-oriented regular arrays of carbon nanotubes and their field emission properties. *Science* **283**, 512-514 (1999).
34. Yan, M., Zhang, H., Widjaja, E. & Chang, R. Self-assembly of well-aligned gallium-doped zinc oxide nanorods. *Journal of applied physics* **94**, 5240-5246 (2003).
35. Grzybowski, B. A., Radkowski, M., Campbell, C. J., Lee, J. N. & Whitesides, G. M. Self-assembling fluidic machines. *Applied physics letters* **84**, 1798-1800 (2004).
36. Campbell, C. J. & Grzybowski, B. A. Microfluidic mixers: from microfabricated to self-assembling devices. *Philosophical Transactions of the Royal Society of London. Series A: Mathematical, Physical and Engineering Sciences* **362**, 1069-1086 (2004).
37. Gracias, D. H., Tien, J., Breen, T. L., Hsu, C. & Whitesides, G. M. Forming electrical networks in three dimensions by self-assembly. *science* **289**, 1170-1172 (2000).
38. Wang, J., Liu, K., Xing, R. & Yan, X. Peptide self-assembly: thermodynamics and kinetics. *Chemical Society Reviews* **45**, 5589-5604, doi:10.1039/C6CS00176A (2016).
39. Grzybowski, B. A., Wiles, J. A. & Whitesides, G. M. Dynamic self-assembly of rings of charged metallic spheres. *Physical review letters* **90**, 083903 (2003).
40. Grzybowski, B. A., Stone, H. A. & Whitesides, G. M. Dynamic self-assembly of magnetized, millimetre-sized objects rotating at a liquid–air interface. *Nature* **405**, 1033-1036 (2000).
41. Petrucci, R. H. *General Chemistry: An Integrated Approach*. (Prentice Hall PTR, 1998).
42. Grzybowski, B. A., Wilmer, C. E., Kim, J., Browne, K. P. & Bishop, K. J. M. Self-assembly: from crystals to cells. *Soft Matter* **5**, 1110-1128, doi:10.1039/B819321P (2009).
43. Schreiber, R. E., Avram, L. & Neumann, R. Self-Assembly through Noncovalent Preorganization of Reactants: Explaining the Formation of a Polyfluoroxometalate. *Chemistry – A European Journal* **24**, 369-379, doi:https://doi.org/10.1002/chem.201704287 (2018).
44. Askeland, D. R. & Wright, W. J. *The Science and Engineering of Materials, Enhanced, SI Edition*. (Cengage Learning, 2015).
45. Soboyejo, W. *Mechanical Properties of Engineered Materials*. (Taylor & Francis Group, 2019).
46. Atkins, P. & Overton, T. *Shriver and Atkins' Inorganic Chemistry*. (OUP Oxford, 2010).
47. Lyklema, J. *Fundamentals of Interface and Colloid Science: Solid-Liquid Interfaces*. (Elsevier Science, 1995).
48. von Smoluchowski, M. Contribution à la théorie de l'endosmose électrique et de quelques phénomènes corrélatifs. *Bull. Akad. Sci. Cracovie.* **8**, 182-200 (1903).
49. Loget, G. & Kuhn, A. Electric field-induced chemical locomotion of conducting objects. *Nature Communications* **2**, 535, doi:10.1038/ncomms1550 (2011).

50. Gupta, S. & Bit, A. in *Bioelectronics and Medical Devices* (eds Kunal Pal *et al.*) 123-144 (Woodhead Publishing, 2019).
51. Wang, W., Castro, L. A., Hoyos, M. & Mallouk, T. E. Autonomous Motion of Metallic Microrods Propelled by Ultrasound. *ACS Nano* **6**, 6122-6132, doi:10.1021/nn301312z (2012).
52. Voß, J. & Wittkowski, R. Propulsion of bullet- and cup-shaped nano- and microparticles by traveling ultrasound waves. *Physics of Fluids* **0**, null, doi:10.1063/5.0089367.
53. Gerlach, M., Rakovich, Y. P. & Donegan, J. F. Radiation-pressure-induced mode splitting in a spherical microcavity with an elastic shell. *Opt. Express* **15**, 3597-3606, doi:10.1364/OE.15.003597 (2007).
54. Rong, Q., Zhou, Y., Yin, X., Shao, Z. & Qiao, X. Higher-order micro-fiber modes for Escherichia coli manipulation using a tapered seven-core fiber. *Biomed Opt Express* **8**, 4096-4107, doi:10.1364/BOE.8.004096 (2017).
55. Yalamov, Y. I., Kutukov, V. B. & Shchukin, E. R. Theory of the photophoretic motion of the large-size volatile aerosol particle. *Journal of Colloid and Interface Science* **57**, 564-571, doi:https://doi.org/10.1016/0021-9797(76)90234-4 (1976).
56. Ashkin, A. Acceleration and Trapping of Particles by Radiation Pressure. *Physical Review Letters* **24**, 156-159, doi:10.1103/PhysRevLett.24.156 (1970).
57. Gallino, G., Gallaire, F., Lauga, E. & Michelin, S. Physics of Bubble-Propelled Microrockets. *Advanced Functional Materials* **28**, 1800686, doi:https://doi.org/10.1002/adfm.201800686 (2018).
58. Gibbs, J. G. & Zhao, Y.-P. Autonomously motile catalytic nanomotors by bubble propulsion. *Applied Physics Letters* **94**, 163104, doi:10.1063/1.3122346 (2009).
59. Gao, W., Sattayasamitsathit, S., Orozco, J. & Wang, J. Efficient bubble propulsion of polymer-based microengines in real-life environments. *Nanoscale* **5**, 8909-8914, doi:10.1039/C3NR03254J (2013).
60. Mirkovic, T., Zacharia, N. S., Scholes, G. D. & Ozin, G. A. Nanolocomotion—Catalytic Nanomotors and Nanorotors. *Small* **6**, 159-167, doi:https://doi.org/10.1002/smll.200901340 (2010).
61. Paxton, W. F., Sundararajan, S., Mallouk, T. E. & Sen, A. Chemical Locomotion. *Angewandte Chemie International Edition* **45**, 5420-5429, doi:https://doi.org/10.1002/anie.200600060 (2006).
62. Lee, E. in *Interface Science and Technology* Vol. 26 (ed Eric Lee) 323-358 (Elsevier, 2019).
63. Shim, S. Diffusiophoresis, Diffusioosmosis, and Microfluidics: Surface-Flow-Driven Phenomena in the Presence of Flow. *Chemical Reviews* **122**, 6986-7009 (2022).
64. Feng, M. & Gilson, M. K. Enhanced Diffusion and Chemotaxis of Enzymes. *Annual Review of Biophysics* **49**, 87-105, doi:10.1146/annurev-biophys-121219-081535 (2020).
65. Gentile, K., Somasundar, A., Bhide, A. & Sen, A. Chemically powered synthetic "living" systems. *Chem* **6**, 2174-2185 (2020).
66. Mohajerani, F., Zhao, X., Somasundar, A., Velegol, D. & Sen, A. A Theory of Enzyme Chemotaxis: From Experiments to Modeling. *Biochemistry* **57**, 6256-6263, doi:10.1021/acs.biochem.8b00801 (2018).
67. Rodríguez-Arco, L., Li, M. & Mann, S. Phagocytosis-inspired behaviour in synthetic protocell communities of compartmentalized colloidal objects. *Nature Materials* **16**, 857-863, doi:10.1038/nmat4916 (2017).
68. Rodríguez-Arco, L., Kumar, B. V. V. S. P., Li, M., Patil, A. J. & Mann, S. Modulation of Higher-order Behaviour in Model Protocell Communities by Artificial Phagocytosis. *Angewandte Chemie International Edition* **58**, 6333-6337, doi:https://doi.org/10.1002/anie.201901469 (2019).
69. Adams, L. L. A., Lee, D., Mei, Y., Weitz, D. A. & Solovev, A. A. Nanoparticle-Shelled Catalytic Bubble Micromotor. *Advanced Materials Interfaces* **7**, 1901583, doi:https://doi.org/10.1002/admi.201901583 (2020).

70. Wu, J. *et al.* Enhanced degradation of organic pollutant by bimetallic catalysts decorated micromotor in advanced oxidation processes. *Journal of Environmental Chemical Engineering* **10**, 107034, doi:https://doi.org/10.1016/j.jece.2021.107034 (2022).
71. Kumar, B. V. V. S. P., Patil, A. J. & Mann, S. Enzyme-powered motility in buoyant organoclay/DNA protocells. *Nature Chemistry* **10**, 1154-1163, doi:10.1038/s41557-018-0119-3 (2018).
72. Varshney, R., Gill, A. K., Alam, M., Agashe, C. & Patra, D. Fluid actuation and buoyancy driven oscillation by enzyme-immobilized microfluidic microcapsules. *Lab on a Chip* **21**, 4352-4356 (2021).
73. Pfeifer, F. Distribution, formation and regulation of gas vesicles. *Nature Reviews Microbiology* **10**, 705-715, doi:10.1038/nrmicro2834 (2012).

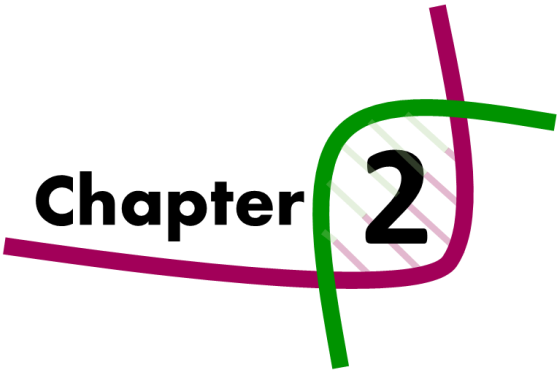

General Materials and Methods

This chapter describes the materials used throughout this thesis and highlights relevant experimental methods and analytical techniques and the theories behind them. If not described otherwise, all experiments in this thesis have been performed at ambient temperature and pressure and deionised water was supplied from a Merck Milli-Q water purification system.

2.1 Materials

For the synthesis of aminopropyl-functionalised magnesium phyllosilicate-clay (AMP) 3-aminopropyltriethoxysilane (APTES, Sigma Aldrich) and Magnesium Chloride ($MgCl_2$, Sigma Aldrich) were purchased. Ethanol (absolute >99.5%) was distributed from university chemical stores.

For the synthesis of microcapsule-protocells, a wide array of materials was tested and used throughout the experiments. AMP-clay was used as synthesised and protamine sulfate (from salmon as amorphous powder, Sigma Aldrich), DNA (from Salmon, D1626, Sigma Aldrich), Polydiallyldimethylammonium chloride (PDDA, 100-200 kDa as 20 wt%-solution, Sigma Aldrich), Protease (from *Bacillus Lichenformis*, 2.5 U/g, Sigma Aldrich) and Polyallylamine hydrochloride (PAH, 15 kDA, Sigma Aldrich) were acquired commercially. The inventory of enzymes consisted of catalase ("Cat", from bovine liver, filtered solution, 39.61 kU/mL, 0.67 mg/mL, purchased from Worthington biochemical Corp.), Glucose Oxidase ("GOx", from *Aspergillus Niger*, 145200 U/g, Sigma Aldrich), Bovine serum albumin (BSA, lyophilised powder, Sigma Aldrich), Urease (from *Canavalia ensiformis*, Type III, powder, 40150 U/g, Sigma Aldrich) and Peroxidase (from horseradish, "HRP", 150 U/mg, Sigma Aldrich) and the respective substrates α–D-glucose, urea, hydrogen peroxide (H_2O_2, 30 wt% solution, Sigma Aldrich), and 2,2'-Azino-bis(3-ethylbenzthiazoline-6-sulfonic acid (ABTS, Sigma Aldrich) and Ampliflu^{TM} Red (10-Acetyl-3,7-dihydroxyphenoxazine, Sigma Aldrich) as a substrate for HRP. Sucrose (Sigma Aldrich) was also purchased to create density gradients within multi-substrate environments.

Dyes were purchased to tag enzymes but also used as indicators for membrane permeability studies, which included: Fluorescein isothiocyanate (FITC, Sigma Aldrich), Rhodamine-B-isothiocyanate (RITC, Sigma Aldrich), pyranine, FITC-Dextran of various sizes (4 kDa, 10 kDa, 40 kDa, 70 kDa, 150 kDa, 2000 kDa, Sigma Aldrich), acridine orange and methylene blue.

Particles used in this thesis came from multiple sources: Silica microparticles (from Cospheric, P2011SL: 2.5-3.5 μm in diameter), green fluorescent (from Cospheric, Fluorescent green polymer microspheres, 1.3-1.5 μm, Excitation λ_{Exc}= 515 nm, Emission λ_{Em}= 414 nm) blue fluorescent particles

(from *Cospheric*, Fluorescent blue polymer microspheres, 1.3-1.5 µm, Excitation λ_{Exc}= 445 nm, Emission λ_{Em}= 407 nm), magnetic microparticles (1: from Bangs Laboratories Inc., COMPEL^{TM} magnetic polymer beads, COOH-surface modified, $\varnothing_{Average}$ = 2.6 µm. 2: from GE Healthcare-Lifesciences, Sera-Mag Carboxylate-modified magnetic Speedbeads, COOH-surface modified, 0.871 µm in diameter). Furthermore, buffers and general lab chemicals were acquired: NaH_2PO_4 (Sigma Aldrich) for enzyme dialysis, NaCl (Sigma Aldrich), MES (Sigma Aldrich).

2.2 General Techniques

2.2.1 Microscopy Methods

2.2.1.1 Brightfield and fluorescence microscopy

Most analysis in this thesis was done via microscopy, or more specifically brightfield and fluorescence microscopy. Throughout this thesis, two readily available microscopes, one Olympus BX53 and one Leica DMI3000B, were used. The Olympus BX53 is a more conventional upright microscope with a halogen lamp as a brightfield light source and 5 different objective lenses (4X, 10X, 20X and 40X), which was mainly used for quick analysis or for instances where a conventional top-down microscope is more suitable. The microscope also had a camera equipped which, in combination with the Olympus Cell-sense-standard software, made it possible to take photos and use image processing techniques like vertical z-stacking. Figure 2.2-1-a describes the general setup of this type of microscope. One important feature, which was used to increase the quality of images, is the phase-contrast filter. In a normal brightfield setup, the light is focused onto the specimen, from which some is being scattered, diffracted and shifted in phase by the structures of the specimen material (highlighted in red in Figure 2.2-1-a) and some light is unaffected (Figure 2.2-1-a yellow), which is called the surround wave. Both, surround and diffracted waves then enter the objective front-lens element and are focused at the intermediate image plane where it comes to interference between the two. [1]

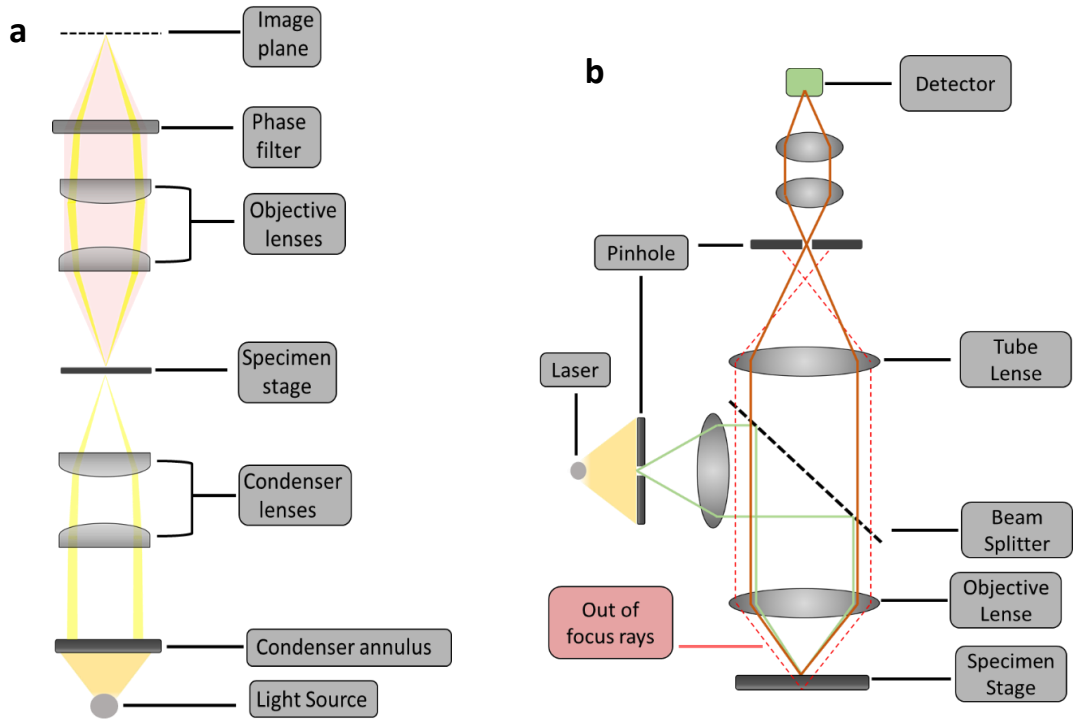

Figure 2.2-1: *Illustration of the internal setup of a brightfield microscope (**a**) [1] and a confocal microscope (**b**). [2,3]*

The diffracted light is usually phase shifted by $\phi \approx 90°$ within biological samples due to the similar optical path and the diffractive index difference between the specimen and the surrounding medium. [1,4] In order to achieve maximum interference and therefore a strong contrast between the diffracted and the surround wave-front, the surround's phase is advanced or retarded by around 90° while, at the same time, reducing its amplitude to gain contrast in the resulting image. The microcapsule system presented in this thesis shows very nice and strong contrasts when working with phase-contrast microscopy, which improved the imaging immensely.

The second microscope system (Leica DMI3000B) has an inversed setup, with the lenses being underneath the sample holder and the brightfield light being channelled onto the sample from the top. Additional to the brightfield-lamp, this microscope also has a Leica EL6000 light source attached to it for fluorescence microscopy. The microscope is furthermore equipped with 5 different filters, covering the analysis of all popular fluorophores like FITC, RITC, Dylight™ and so on. When irradiated with a specific wavelength, fluorophores can absorb the light, exciting electrons from their ground state S_0 into an excited state S_1. Relaxation of the electron back to the ground state then releases the remaining absorbed energy in form of electromagnetic radiation of a different wavelength, which can be instrumentally detected or even seen with the bare eye. [5,6] The whole process can be described in a so called Jablonski diagram (Figure 2.2-2). [7]

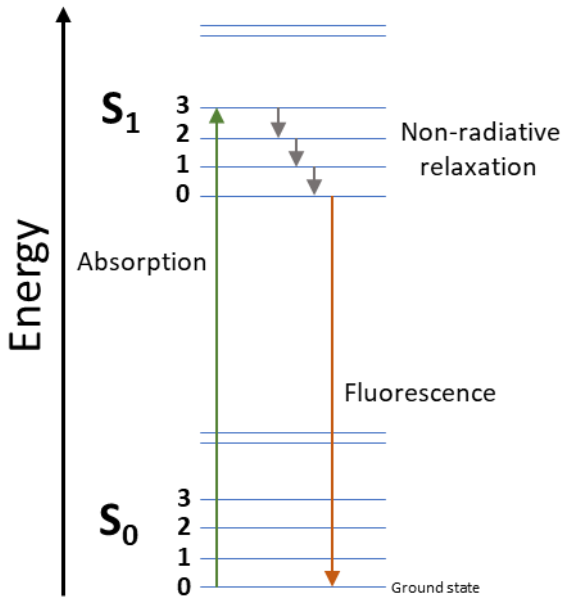

Figure 2.2-2: *Illustration of the change of electronic states of electrons during fluorescence.* [5-7]

Table 2.2-1: *Fluorescence filters used for the Leica DMI3000B. Each filter was defined by the excitation and emission wavelengths for the corresponding fluorophores.*

Fluorescence	*Excitation wavelength* $\lambda_{Excitation}$	*Emission wavelength* $\lambda_{Emission}$
Green	515 - 560	580
Brightfield	---	---
Blue	450 - 490	510
UV	340 - 380	400
Violet	355 - 435	455

To acquire even higher resolutions under fluorescence conditions confocal laser scanning microscopy was applied as well. Confocal microscopes, in contrast to conventional brightfield microscopes, do not illuminate the whole sample but use point-illumination to visualise the sample via scanning techniques. Instead of a brightfield lamp, a laser is directed through a pinhole, thus creating a point illumination which is then projected onto the sample via a mirror and an objective lens. The reflected light then passes through the dichroic mirror before being focused through another pinhole, behind which the detector is located (Figure 2.2-1-b). This pinhole specifically filters out light that does not originate from the same plane as the sample, which leads to a much higher resolution and depth, while sacrificing some the signal's intensity. Due to the scanning nature of the confocal microscope, it can create cross sections of the sample of various sizes which can then be used to model 3D-images of the observed object for analysis. By applying multiple lasers of different wavelengths which are coupled to variable detectors, confocal microscopes are also capable of exciting multiple fluorophores in a sample in a very short amount of time. [2] These signals can then be superimposed into one image to visualise different fluorescent colours inside the sample. The confocal images of this thesis were captured with a Leica SP5 or Leica SP5II, which was equipped with several lasers which offer 405, 458, 476, 488, 496, 514, 561, 594 and 633 nm laser lines and 10X and 20X dry lenses and 40X and 63X immersion oil lenses. The images were then processed with the *LEICA LAS X* software

2.2.1.2 Scanning electron microscopy

One of the major setbacks of conventional optical microscopy is its limit in resolution. Due to the diffraction limit defined by Ernst Karl Abbe, an object can only be visualised if it is larger than half the wavelength of the light used to observe it, which limits most applications to sizes of about 250 nm if not more. [8]

$$d = \frac{\lambda}{2d\ sin\ (\Theta)} \qquad \textit{(Equation 2.2-1)}$$

In contrast to optical microscopy, electron microscopy uses electrons to interact with matter and create a measurable visual signal. Electrons behave both as particles and as waves according to the wave-particle duality, so considering their low mass, their relativistic wavelength is only a few picometers long. Looking back at the diffraction limit defined above, it is now possible to achieve much higher resolutions than with any electromagnetic radiation produced by a conventional lamp. An electron beam is usually generated by thermic emission from a tungsten filament cathode. Anode elements inside the electron microscope tube with voltages at around 40 – 100 keV then accelerate the electrons towards the sample stage and serve as electromagnetic lenses to focus the electron beam. Once the primary electrons interact with the sample, there's a variety of secondary information that can be detected (Figure 2.2-3). Secondary electrons are probably the most common signal from SEM-scans and return a very plastic and detailed image of the sample-topography. Other important signals like backscattered electrons or characteristic X-rays (EDX) yield important information about the atomic numbers and atomic composition of the sample and originate from deeper within the sample structure. Should the electrons penetrate the sample completely, electrons can be read as transmitted electrons instead of reflected or scattered electrons, which offers even more information about the internal structure of the material. [9,10]

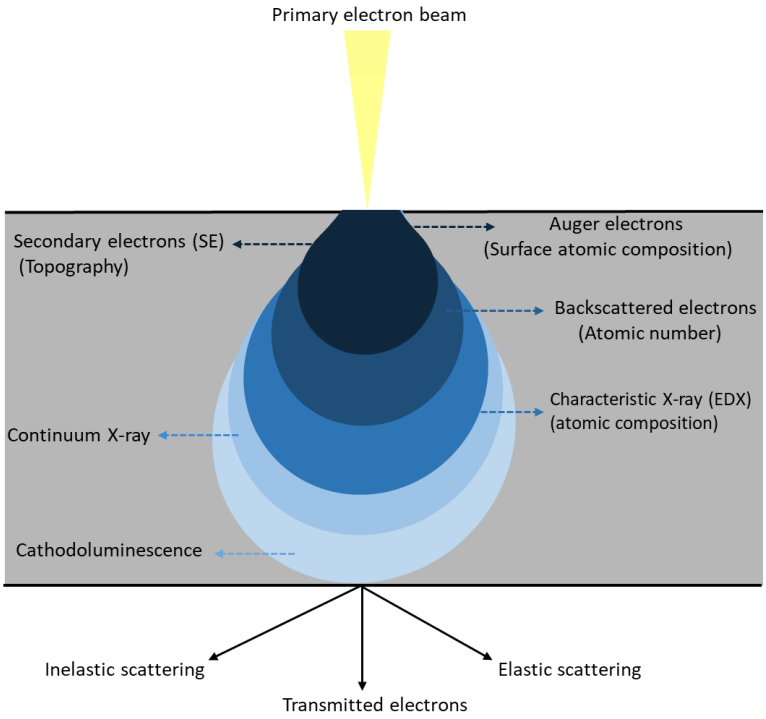

Figure 2.2-3: *Illustration of the Interaction volume of a primary electron beam with matter and the resulting electromagnetic signals.* [9,10]

In this thesis, SEM-measurements are generally used to achieve a better understanding of protocell-structures made from biological synthetic-organic materials. The major difficulty here is to retain the integrity of the cell material while also working in vacuum within the SEM. For this purpose, all samples were freeze dried after pre-treatment with liquid N_2.

2.2.2 Other analytical methods

2.2.2.1 Dynamic light scattering and Zeta-potential scans

Dynamic light scattering is a technique used to determine the size of small particles or polymers in the nanometre scale and is based on Brownian motion. When dispersed and not influenced by external forces, particles move randomly in all direction because the particles are colliding with solvent molecules. These collisions and the transferred energy have a greater effect on smaller particles, thus making them move faster compared to larger ones. Mathematically this can be summed up in the Stokes-Einstein equation (Equation 2.2-2) [11-13]:

$$D = \frac{k_B T}{6\pi\eta R_H} \qquad \textit{(Equation 2.2-2)}$$

Knowing the speed of the particles as the translational diffusion coefficient and the viscosity of the dispersant, we can calculate the hydrodynamic radius of the particles. The only condition for this calculation is that all particle-motion is based on Brownian motion, which means that the size at which sedimentation happens is the crucial limit for this technique.

A second important technique to analyse colloidal dispersions and polymers is the zeta-potential scan, or electrokinetic potential. The zeta potential gives important information about the stability of colloidal dispersions and can predict aggregation or electric stabilisation. While it is not directly corresponding to the electric surface charge of the particle, it can be used as an indicator to support further discussions. Dispersed colloids are surrounded by a double layer of ions due to the interaction

of the particle's own charge with molecules of the surrounding medium. The inner layer is the so called "Stern layer", which is mostly static and defined by a strong interaction of ions with the particle surface charge. The outer layer, or "slipping plane", is a much more diffuse phase where ions are free to exchange. The zeta-potential, or ζ-potential, is the electric potential between the slipping plane and a point in the bulk medium, thus not directly referring to the surface charge of the particle. By applying an external electric field, it is possible to measure the electrophoretic mobility of the particles and calculate the ζ-potential using Henry's equation, with u_e as the electrophoretic mobility, η as the viscosity and ε as the dielectric constant (Equation 2.2-3 [14-16], Figure 2.2-4 [17]):

$$u_e = \frac{2\,\varepsilon_{rs}\varepsilon_0}{3\eta}\,\zeta f_1(ka) \qquad \textit{(Equation 2.2-3)}$$

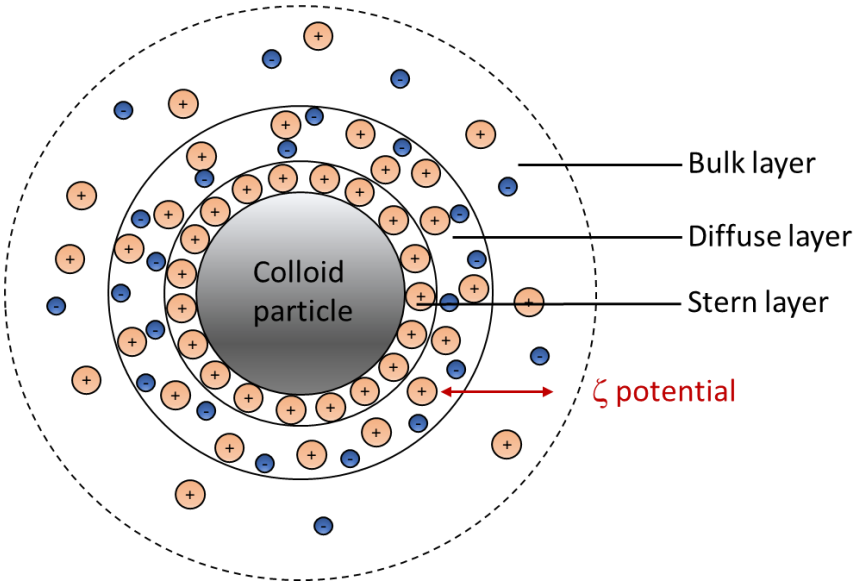

Figure 2.2-4: *Illustration of a particle which is suspended in a dispersion medium and its ionic layers.* [17]

This means for both techniques, the zeta-potential and the dynamic light scattering, that the cells in this thesis and other super-micrometre dispersions are too large for the measurement, or that it would otherwise exhibit very large errors. For this reason, the techniques are mainly used to analyse the basic materials used to fabricate the cells but not the protocells themselves.

For all measurements, a Malvern Instruments Zetasizer Nano ZS was used.

2.2.2.2 Digital Camera analysis and tracking

A large part of the work in this thesis revolves around the motion and oscillation of protocell-microcapsules. Due to their size (~400 μm), they are in an uncomfortable spot when it comes to choosing a technique for their visualisation. Microscopes are great for observing the cell and its structural details, but the magnification is too high to monitor motion. Cameras on the other hand are very useful to observe the motion of microcapsules but cannot capture any of their features. Nonetheless and since capsule oscillation is the main interest here, a static camera setup with a Nikon 6D Mark II was used, with a Canon Macro lens (EF 100 mm 1:2.8L). The images were taken in short intervals and due to the lengthiness of the experiments, it was necessary to come up with different ways to process the image-sets. One method simply transformed the image-set into a video, which is a great way to present the experimental results, but sadly cannot be used for a written report, paper or thesis and furthermore does not supply any numerical information about the oscillation. Instead, a tracking software was used to capture the capsule's location in each frame of the image-set ("Modular

Image Analysis" was provided and written by Stephen Cross from *Wolfson Bioimaging Facility* of the University of Bristol). The software is a plugin, which utilises a bundle of different addons within the *Fiji-ImageJ*-software suite, which includes: "Auto Threshold", "bUnwarpJ", "BioFormats", "Colour Deconvolution", "Correct Bleach", "MPICBG", "TrackMate" [18], "Weka Trainable Segmentation", "Ridge Detection", and "MorphoLibJ".

2.2.2.3 Ultraviolet-visible spectroscopy (UV/VIS)

UV/VIS spectroscopy is a type of absorption-spectroscopy, which utilises electromagnetic radiation in the UV to IR-regions (~200 – 800 nm). Molecules with bonding and non-bonding electrons are capable of absorbing light of a specific wavelength to excite electrons from the highest occupied- (HOMO) to the lowest unoccupied molecular orbital (LUMO). The higher the energy-gap between those two, the lower the wavelength of the light that is necessary to excite the electron. Generally there are 4 possible transitions: π-π*, σ-σ*, n-π* and n-σ* (Figure 2.2-5). [19,20]

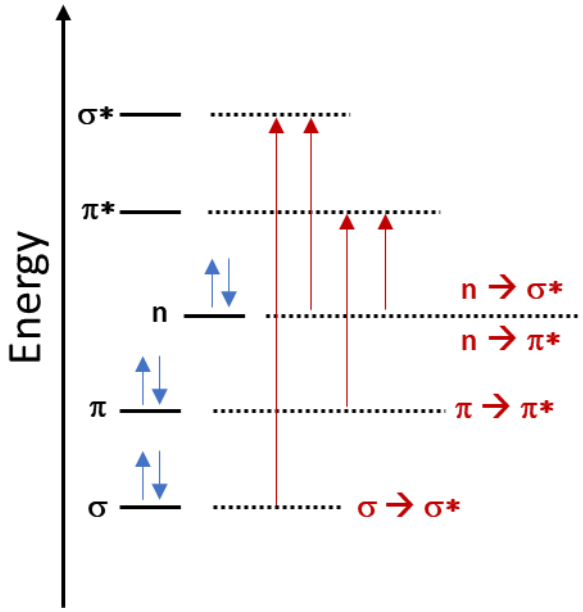

Figure 2.2-5: *Illustration of possible transitions of electrons after excitation with appropriate electromagnetic radiation.* [19,20]

Mathematically the absorption of light can be described via the Lamber-Beer-law (Equation 2.2-4) [19]:

$$A = log_{10}\left(\frac{I_0}{I}\right) = \varepsilon C l \qquad \textit{(Equation 2.2-4)}$$

The absorption A is defined by the intensity of the incident light and the transmitted light after penetrating the sample. This can be simplified for the experimental setup by using the extinction coefficient ε (L mol^{-1} cm^{-1}), the path length of the sample or cuvette l (cm) and the concentration of the sample C (mol/L). [19]

A Perkin Elmer Lambda 750 UV/VIS/NIR-spectrophotometer was used for all experiments in this thesis.

2.2.2.4 Circular Dichroism Spectroscopy

Most optical techniques use linearly polarised light and are therefore not able to distinguish between optically active chiral compounds. In circular dichroism spectroscopy light is being circularly polarised. An electromagnetic wave consists of two perpendicular vectors, the electric- and the magnetic field. In linearly polarised light, the electric field vector only oscillates in a fixed plane, when polarised

circularly, this vector starts rotating around its propagation direction, which enables two different polarisations, a left-handed and a right-handed one.

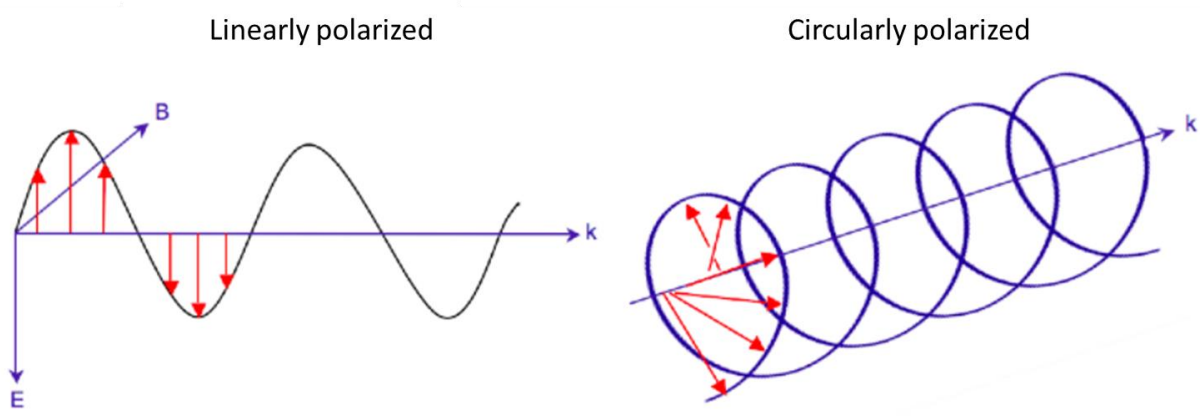

Figure 2.2-6: *Illustration of the difference between linearly- and circularly polarized light.* [21]

When working with chiral compounds or larger molecules that contain helical structures like proteins or DNA, circularly polarised light can lead to different absorptions, depending on the polarisation. Generally, the circular dichroism can be defined as followed, with A as the absorption difference between the left handed and the right handed polarisation (Equation 2.2-5): [21]

$$CD = \Delta A = A_{left} - A_{right} \qquad \textit{(Equation 2.2-5)}$$

This can give crucial information about secondary structures of proteins, or the helical structure of DNA molecules. Since all of the capsule-systems in this thesis are based on DNA as a structural component, CD-spectroscopy can serve as an important tool to understand the structure of the DNA strands before and after implementation as cell material. The device was kindly provided and maintained by the Woolfson group of the University of Bristol.

2.2.2.5 X-ray powder diffraction (XRD)

XRD is a very useful technique for the analysis of powdered, crystalline samples to gather information about the crystal-cell arrangement and to identify materials. In contrast to other light-based spectroscopy techniques mentioned above, XRD looks at diffraction patterns of X-rays. The instrument usually consists of a cathode-ray tube to generate the X-radiation, a sample holder on a flexible axis and a detector to measure the diffracted radiation. The technique is based on the constructive interference of the X-rays once they interact with the sample according to Bragg's law (Equation 2.2-6) [22,23]:

$$n\lambda = 2d\ sin(\Theta) \qquad \textit{(Equation 2.2-6)}$$

The wavelength of the incident X-ray needs to be comparable to the distance between atoms. This way, two x-rays being scattered at different planes of the crystal lattice will interfere constructively, since they stay in phase as the wavelength and the pathlength difference are the same or multiples of each other. By tilting the sample in all 2θ angles, the instrument can detect all possible diffraction orientations of the lattice within the random orientation of the powder and average the signal to get a consistent diffraction pattern.

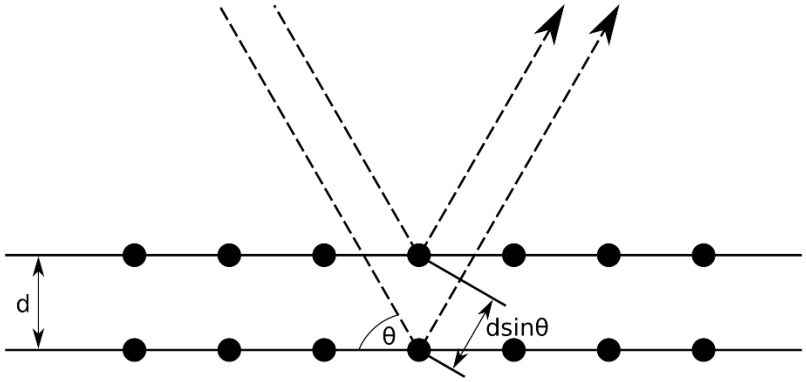

Figure 2.2-7: *Illustration of Bragg diffraction on a crystalline solid. The lower beam moves the extra distance of* $2d\sin\theta$. [22,23]

In this thesis, XRD will be used to analyse and characterise the synthesised aminopropyl-functionalised magnesium phyllosilicate clay. The devices used were provided and maintained by the X-ray-facility of the University of Bristol.

2.2.2.6 IR-spectroscopy

Infrared spectroscopy is a technique that uses electromagnetic radiation in the infrared-domain from 4000-500 cm^{-1} to analyse substances and give feedback on their chemical composition. The technique is widely used in both inorganic and organic chemistry and can generally be used for gaseous, liquid and solid samples. The spectrum itself commonly visualises either the absorbance or the transmittance of the infrared light after interaction with the sample. In contrast to ultraviolet or visible light, infrared radiation does not interact with the state of the electrons of the molecules but excites overtones or harmonic molecular vibrations. The frequency of the absorbed radiation needs to match the intrinsic vibration of the molecule or of the molecular bond and are characteristic for the atom-composition of the molecule. There are several ways, or "vibrational modes", the molecule can vibrate in and it is important to distinguish between them to understand and read IR-spectra. Generally, linear molecules with N number of atoms will have 3N-5 degrees of vibrational modes, whereas non-linear molecules will have 3N-6 degrees. R_2-CH_2-groups for example have 9 degrees of vibrational freedom, which usually get descriptive names to distinguish them from each other. Just in case of the -CH_2-group, there are three directions a bond can vibrate in: Longitudinal, Latitudinal and radial with each having a symmetrical and an asymmetrical case. This variety of vibrational modes leads to the complexity of IR-spectra, which can be overwhelming when analysing larger molecules. Nonetheless, each vibration between two specific atoms can be categorised and found at identical locations within different spectra. [24]

In all experiments of this thesis, a Perkin Elmer Spectrum One FT-IR spectrometer was used. Attenuated total reflectance (ATR) is a specific IR-technique, which measures the reflectance of the IR-beam at the interface of a diamond crystal and the solid sample. This technique enables very quick measurements as samples do not have to go through any sort of sample preparation as long as they are solid or liquid. Fourier-transform-Infrared spectroscopy on the other hand describes the general method on how the sample is being irradiated with light and how the data is being processed. Instead of using monochromatic light, a broad spectrum of different wavelengths is used. Via an interferometer, some wavelengths of the spectrum are periodically blocked, making the sample experience a different spectrum at each point in time. A detector is then measuring the absorbance/reflectance of each spectrum, after which the raw data is being processed via fourier-transformation to change it from cm (the displacement of the interferometer-mirror) to cm^{-1} (wavenumbers).

2.2.2.7 Size Exclusion chromatography

Size exclusion chromatography is a technique, most commonly used to analyse and separate large molecules from smaller components in solution. The technique is usually performed in columns and consists of a stationary phase and a mobile phase. The stationary phase can be made from different materials like dextran polymers (Sephadex), polyacrylamide gels (Sephacryl, BioGel P) or agarose gels (Sepharose). The analyte in the mobile phase must not interact with the surface of the stationary phase in any electrostatic or chemical fashion. Instead, the different elution times stem from trapping of the analyte inside the pores of the stationary phase. Each material is comprised of differently sized pores in the size range of the contaminants to be separated. As the mobile phase moves through the column, smaller molecules wander through the pores of the gel-beads, and therefore have to traverse a much larger volume of the stationary phase than larger molecules which only pass by the beads and elute faster. This way, molecules are progressively being separated merely by their size. The upper limit of a size exclusion material can be defined as the size where molecules become too large to enter any of the pores of the material, whereas the lower limit is the size where molecules are small enough to enter all the pores of the stationary phase. The lower limit is usually defined by a single elution band. [25]

In this thesis PD10-desalting columns were used for the purification of tagged and modified enzymes. The protocol for these columns is standardised and has been applied throughout this thesis. The PD-10-column was washed 5 times with 5 mL of di-water and then equilibrated 5 times with 5 mL of the buffer of choice. Then, the buffer was eluted until the supernatant was on level with the stationary phase, after which 2.5 mL of the protein sample were added on top of the column. Once the sample has fully penetrated the column and the supernatant was on level with the stationary phase, 3.5 mL of elution-buffer were added to elute the protein. 3.5 mL of the elute were captured underneath and then used for further experiments.

2.3 Literature for General Techniques

1. Di Gianfrancesco, A. in *Materials for Ultra-Supercritical and Advanced Ultra-Supercritical Power Plants* (ed Augusto Di Gianfrancesco) 197-245 (Woodhead Publishing, 2017).
2. Pawley, J. *Handbook of Biological Confocal Microscopy*. (Springer US, 2010).
3. Olympus - Thomas J. Fellers, M. W. D. *Introduction to Confocal Microscopy*, <https://www.olympus-lifescience.com/en/microscope-resource/primer/techniques/confocal/confocalintro/> (
4. Contributing Authors: D. B. Murphy, R. O., S. Schwartz, M. W. Davidson. *Introduction to phase contrast microscopy*, <https://www.microscopyu.com/techniques/phase-contrast/introduction-to-phase-contrast-microscopy> (
5. Harris, D. C. & Bertolucci, M. D. *Symmetry and Spectroscopy: An Introduction to Vibrational and Electronic Spectroscopy*. (Dover Publications, 1989).
6. Skoog, D. A., Holler, F. J. & Crouch, S. R. *Principles of Instrumental Analysis*. (Thomson Brooks/Cole, 2007).
7. Jaffé, H. H. & Miller, A. L. The fates of electronic excitation energy. *Journal of chemical education* **43**, 469 (1966).
8. Lipson, S. G., Lipson, H. & Tannhauser, D. S. *Optical Physics*. (Cambridge University Press, 1995).
9. Goldstein, J. I. *et al.* in *Scanning Electron Microscopy and X-Ray Microanalysis* 1-14 (Springer New York, 2018).
10. Vernon-Parry, K. D. Scanning electron microscopy: an introduction. *III-Vs Review* **13**, 40-44, doi:https://doi.org/10.1016/S0961-1290(00)80006-X (2000).
11. Chandrasekhar, S. Stochastic problems in physics and astronomy. *Reviews of modern physics* **15**, 1 (1943).
12. Einstein, A. On the movement of small particles suspended in stationary liquids required by the molecularkinetic theory of heat. *Ann. d. Phys* **17**, 1 (1905).
13. Sutherland, W. LXXV. A dynamical theory of diffusion for non-electrolytes and the molecular mass of albumin. *The London, Edinburgh, and Dublin Philosophical Magazine and Journal of Science* **9**, 781-785 (1905).
14. Delgado, A. V., González-Caballero, F., Hunter, R. J., Koopal, L. K. & Lyklema, J. Measurement and Interpretation of Electrokinetic Phenomena (IUPAC Technical Report). *Pure and Applied Chemistry* **77**, 1753-1805, doi:doi:10.1351/pac200577101753 (2005).
15. Makino, K. & Ohshima, H. Electrophoretic mobility of a colloidal particle with constant surface charge density. *Langmuir* **26**, 18016-18019 (2010).
16. O'Brien, R. W. & White, L. R. Electrophoretic mobility of a spherical colloidal particle. *Journal of the Chemical Society, Faraday Transactions 2: Molecular and Chemical Physics* **74**, 1607-1626 (1978).
17. Shnoudeh, A. J. *et al.* in *Biomaterials and Bionanotechnology* (ed Rakesh K. Tekade) 527-612 (Academic Press, 2019).
18. Tinevez, J.-Y. *et al.* TrackMate: An open and extensible platform for single-particle tracking. *Methods* **115**, 80-90, doi:https://doi.org/10.1016/j.ymeth.2016.09.016 (2017).
19. Kaflé, B. P. *Chemical Analysis and Material Characterization by Spectrophotometry*. (Elsevier Science, 2019).
20. Perkampus, H. H., Grinter, H. C. & Threlfall, T. L. *UV-VIS Spectroscopy and Its Applications*. (Springer Berlin Heidelberg, 2013).
21. Kobayashi, N., Muranaka, A., Mack, J. & Chemistry, R. S. o. *Circular Dichroism and Magnetic Circular Dichroism Spectroscopy for Organic Chemists*. (Royal Society of Chemistry, 2012).
22. Waseda, Y., Matsubara, E. & Shinoda, K. *X-Ray Diffraction Crystallography: Introduction, Examples and Solved Problems*. (Springer Berlin Heidelberg, 2011).

23. Bragg, W. H. & Bragg, W. L. The reflection of X-rays by crystals. *Proceedings of the Royal Society of London. Series A, Containing Papers of a Mathematical and Physical Character* **88**, 428-438, doi:doi:10.1098/rspa.1913.0040 (1913).
24. Stuart, B. H. *Infrared Spectroscopy: Fundamentals and Applications*. (Wiley, 2004).
25. Mori, S. & Barth, H. G. *Size Exclusion Chromatography*. (Springer Berlin Heidelberg, 2013).

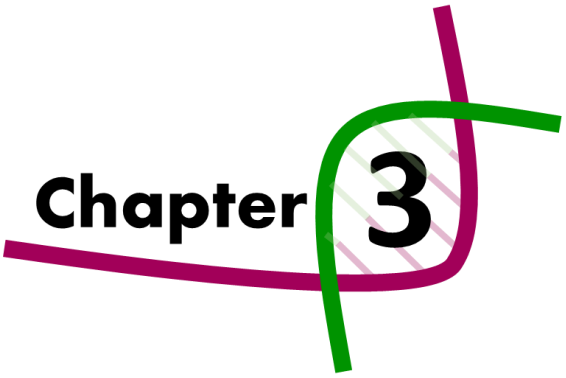

Inorganic/organic DNA-hybrid microcapsules

3.1 Abstract

In this chapter, a novel protocell system based on complexation of double stranded DNA with cationic polymers was introduced, described and studied. Aminopropyl-functionalised magnesium phyllosilicate clay was the first example as a material to interact with DNA to form this very specific type of protocell, which has already been published by Kumar *et al.* in 2018. [1] The first parts of this chapter will focus on the synthesis and analysis of aminopropyl-clay (AMP) and the fabrication of complex inorganic/organic DNA-hybrid microcapsules via a custom-made extrusion device. As a next step towards even more robust and reliable cells, protamine was introduced as an alternative to AMP-clay to create novel protamine/DNA-microcapsules. Both capsule types were analysed by a variety of methods and compared to assess their structure, size, membranes, permeability behaviour and uptake of functional components like enzymes and particles via encapsulation or adsorption. Furthermore, much smaller microcapsules were fabricated by making small changes to the extrusion device, which enabled the creation of more complex, hierarchical structures of AMP/DNA or protamine/DNA microcapsules. Finally, further synthetic- or bio-organic materials were assessed as possible candidates to form dsDNA-complex microcapsules.

3.2 Introduction

3.2.1 Synthetic cellularity

The drive of science to create and research artificial cells can come from different perspectives. There is of course the everlasting question for the origin of life, which is continuously pushing current research to its limits as we still struggle to understand where the first cells come from and what they looked like. Oparin proposed in "*The Origin Of Life*" in the year 1938 his theory, that life could only come from simple non-living molecular building blocks, which progressively formed a more extensive library of complex molecular structures. He specifically took the environment of our early earth into account, which most likely consisted of smaller and simpler molecules, which then started to undertake subsequent chemical reactions. [2] Following the bottom-up principle, as it is described in the introduction to this thesis, this leaves only reasonable number of pathways for the creation of protocells. One molecular species which is still being used a lot by contemporary science as a representation for small water filled compartments which could resemble the very first cells on our planet are lipids and fatty acids. Both can be described by the term amphiphile, which means that they both contain a hydrophobic tail and a bulky hydrophilic head-group (Figure 3.2-1). Lipids, and more specifically phospholipids are capable of forming stable bi-layer membranes that enclose an aqueous interior based on the self-assembly of the hydrophobic and the hydrophilic moieties of the

amphiphiles. Driven by the entropic hydrophobic effect, the contact surface of the water-molecules with the hydrophobic domains is minimised by aggregation into a bi-layered membrane, with the hydrophilic head groups reaching out of, and into the vesicle. [3]

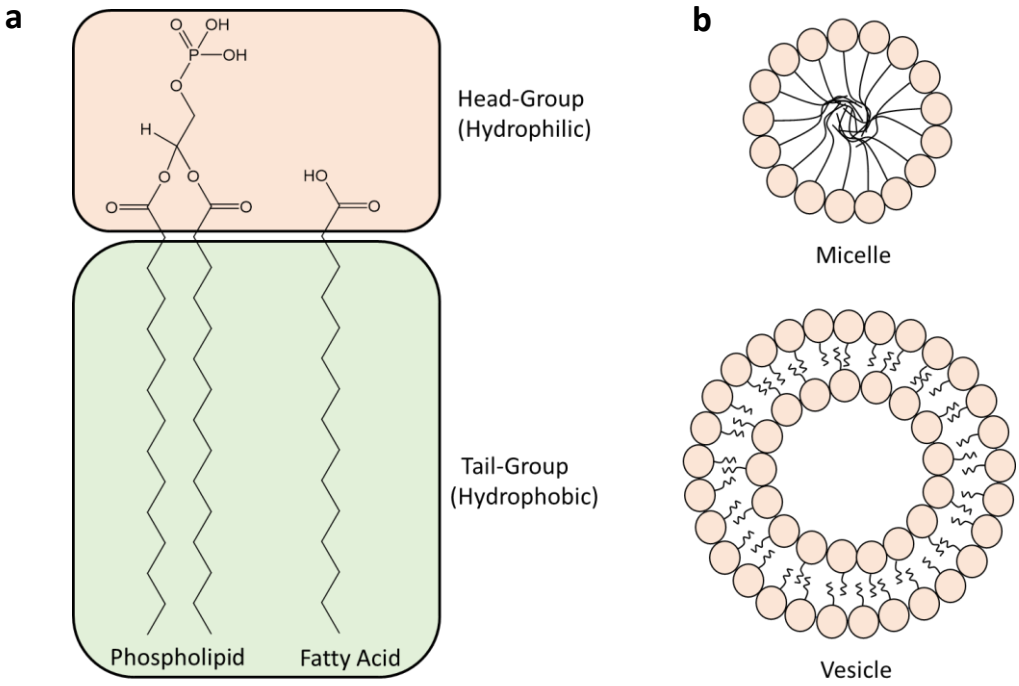

Figure 3.2-1: *Illustration of the structures of* ***a*** *phospholipids and fatty acids with their distinct hydrophobic tail- and hydrophilic head-groups, and* ***b*** *the self-assembled structure of micelles in comparison to larger, double-layered vesicles.*

In regard to the origin of life, phospholipids most likely did not play a larger role, as it seems unlikely that complex structures like this existed under early earth conditions. Furthermore, bi-layer vesicle structures prevent the diffusion of most nutrients or ions into and out of the vesicle, which would need further channel-proteins to facilitate the uptake. Nonetheless, lipid-vesicles are of great interest for protocellular research, not only due to their resemblance to modern cells because of their bi-layer membrane, [4,5] but also because of their stability to pH- and temperature changes. [6] They are furthermore rather easy to fabricate [7,8], and can even undergo changes in shape which resemble the fission of living cells during reproduction. [9-11] This makes lipid based vesicles an interesting platform for the design of mimics of living cells or to carry out rudimentary chemical and biochemical reactions inside. In recent years, there has been a huge array of publications, which investigated the implementation of biochemical processes, which are normally found in biological cells, into lipid vesicles, which included enzymatic synthesis of nucleic acids [12,13], polymerase chain reaction of DNA [14], protein expression inside vesicles, and more specifically the expression of a protein which directly influences the membrane permeability [15-23], replication of genetic information [24] and the synthesis of sugars inside the vesicles via autocatalytic reaction. [5,25]

Vesicles based on fatty acids have much more relevancy, as their structure is a lot less complex, has been proven to form under very natural conditions and was isolated under simulated pre-biotic conditions like thermal vents [5] or spark discharges [4]. Like lipids, fatty acid vesicles were used to encapsulate and perform basic chemical reactions with biological relevancy. P. Walde *et al.* encapsulated the enzyme polynucleotide phosphorylase, which catalysed the polycondensation of

ADP into the polyribonucleotide Poly(A), which served as a mimic for the synthesis of RNA. [26] In a different study, synthesis of double stranded DNA was showcased by encapsulation of a single stranded poly cytosine-template which had a DNA-primer attached to it, from where the double stranded product is being formed via guanosine polymerisation. [27] Another important concept for protocells is cell-division for self-reproduction, which was mimicked by fatty acid vesicles through extrusion of the vesicles through a porous membrane, which forced the cells to divide [28], or through the addition of an amphiphile feedstock, ergo more monomeric fatty acids, which promoted cell-growth and self-reproduction. [29-32]

While all these concepts serve as potential candidates for mimics of primordial cells, the perspective of the origin of life leaves very little room for improvement of cells from a synthetic or a technological standpoint. Amphiphile-based lipid- or fatty acid vesicles are often limited by the retention of encapsulated compounds and especially fatty-acid vesicles have a strong tendency to break under increased stress due to changes in pH, ionic strength and temperature, and because of a lack of internal structuration, which makes them unsuitable for various chemical environments. [3,33] In order to design promising mimics which feature important biological processes, it is necessary to take a step away from the concept of the origin of life, and rather design primitive protocells from the bottom-up and with a focus on chemical and physical stability, biocompatibility, functionalisation capabilities and the control of permeability and membrane functions. As the following approaches present a wide spectrum of different techniques and materials which strive far away from potential early earth materials, these types of cells can rather be described under the term “synthetic cellularity”.

For the past years, the group under Professor Steven Mann has embraced this concept of synthetic cell-designs and participated in the development of many different cell types and applications. The portfolio contains the work on alternative cell-systems based on the self-assembly of membranes comprised of proteins (proteinosomes), inorganic nanoparticles (colloidosomes) and polymers (polymerosomes). Furthermore, membrane-less liquid microdroplets based on phase separation were investigated and used as a platform for higher order hybrid cells. The cell systems named above will be explained in the following section with an emphasis on the current research.

Polymerosomes are made via self-assembly of amphiphilic block copolymers into stable vesicles with a bilayer-membrane, which resembles the structure of liposomes. [33-36] Polymerosomes generally utilise building blocks with larger molecular weights than common lipids in liposomes, while exhibiting a higher stability. At the same time, block copolymer chemistry provides a wide array of tools to design highly specific building blocks for polymer-vesicles. To use polymer-vesicles as nano-reactors, it is fundamental to establish a way to induce a controllable permeability. The choice of copolymer, for one, can directly introduce and tweak membrane permeability through the formation of pores. [33-38] A different approach was introduced by Meier *et al.* where semi-permeable behaviour was established through the implementation of membrane-channel proteins into the polymer-membrane assembly. [35] Another way proposed by Sumerlin *et al.* and later continued by the van Hest-group, utilises a stimulus-responsive block copolymer, which disassembles in response to pH-changes or increases in concentration of D-glucose. [36,39] Encapsulation of functional components or sub-compartmentalisation are another important concept when looking at protocell-designs. Like many other cell types described in this introduction, polymerosomes are capable of co-encapsulating larger sized components like enzymes [40] or even smaller polymerosomes. This enables the fabrication of highly functional nanoreactors and even the fabrication of cell-like organelles which resemble natural compartmentalisation. [41-45]

One very important aspect for the fabrication of many synthetic protocells is the stabilisation of bi-phasic liquid/liquid environments. Colloidosomes are derived from what is called a Pickering emulsion,

which has first been described in 1907 by S.U. Pickering. [46] In a water/oil emulsion, small particles with sizes of less than 100 nm assemble around the liquid/liquid interface. The general driving force for this behaviour is the loss of the total free energy when the particles assemble around the interface of the oil-, or water droplets, which are either immersed in a water, or oil continuous phase. [47] Since the particles would only be loosely attached to the interface, a second step is necessary to crosslink and stabilise them. Common strategies can range from electrostatic binding with polyelectrolytes [48,49], Van-der-Waals-interactions [48,49], sintering [49,50], gelation [51,52], chemical crosslinking [53,54] and polymerisation. [55]

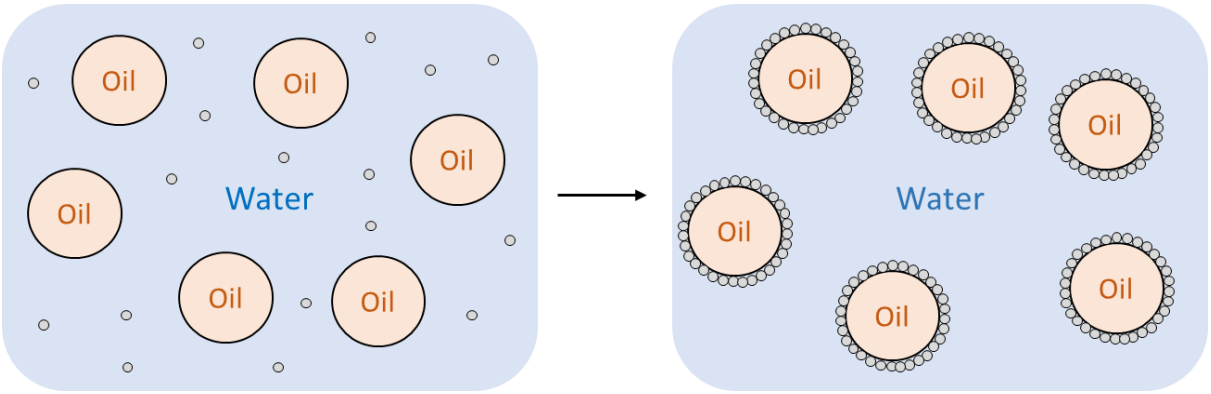

***Figure 3.2-2**: Illustration of an oil-in-water Pickering emulsion. The small, dispersed particles (**grey spheres**) self-assemble around the oil/water-interface and form consistent, tightly packed inorganic shells.*

Recent studies have investigated a variety of materials with the goal to fabricate colloidosomes like silica [56,57], clays [58], $CaCO_3$ [59] , gold particles [60], polyoxometalate-organic hybrid particles [61] and various oxides [62-66]. The Mann-group and others focused a lot of their work on colloidosomes based on silica-nanoparticles, which were subsequently crosslinked with tetramethyl orthosilicate (TMOS). They showcased the encapsulation capabilities of water filled colloidosomes by entrapping biomolecules for enzymatic catalysis or implemented a cell-free gene-expression system within the colloidosomes. [57] The semi-permeable inorganic membrane is another focus of many studies and was modified by grafting with a pH-responsive copolymer which enabled a pH-controlled gating. [67] Other methods to alter the membrane's permeability include temperature responsive polymer particles [50,68], pH-responsive crosslinkers [69] or using nanoparticles of varying sizes and shapes. [70] Furthermore, and despite the rigid shell of crosslinked particles, Li *et al.* proposed a creative model as a mimic for the natural process of growth and cell-division or self-reproduction. [71]

The fact that colloidosomes are made from inorganic or organic nanoparticles makes them a very versatile cell-type, as it offers a broad range of options for functionalisation and modification. A downside of it surely is the practical side of the fabrication, as stabilised and crosslinked Pickering emulsions usually need to be dialysed over longer periods of time to transfer the cells into a purely aqueous medium. Another issue, which has been addressed in many studies is the leakage of smaller molecular species, as the membrane permeability often only retains larger molecules. [71,72]

A much more recent concept for membrane-bound organic protocells are proteinosomes. Instead of inorganic particles, proteins are conjugated with a polymer to form an amphiphilic protein-polymer-nanoconjugate. A popular nanoconjugate-example is the thermo-responsive polymer poly(N-isopropylacrylamide) (PNIPAAm) and BSA. [73] Like with colloidosomes, the self-assembled protein-nanoconjugates need to be crosslinked to enable the formation of a stable semi-permeable membrane. Proteinosomes usually measure sizes of 10-30 μm and can be used to encapsulate and retain biomolecules like enzymes, DNA, or even small molecular dyes to perform membrane-gated

enzyme catalysis or gene-directed protein synthesis. [73] As the building blocks of the cell themselves can be functional proteins, it is furthermore possible to build microcompartments with highly functional membranes. Studies by Huang *et al.* prepared proteinosomes from nanoconjugates of the enzymatic triad of glucose oxidase, glucose amylase and horseradish peroxidase, which retained their enzymatic function after crosslinking and were capable of a membrane mediated catalytic cascade reaction. [74] Similar to colloidosomes, proteinosomes offer many options for modification pre- and post-fabrication. Huang *et al.* showcased this in the design of a higher order functionality by altering the membrane's permeability through controlled disassembly with protease. [75]

All the examples above share a common structural feature, which is a membrane around a predominantly aqueous interior. From a technological point of view, all the cell models described contributed to a broader understanding of synthetic cellularity and pushed cells further into a direction, which could one day serve as precursors for drug delivery, as micro- or nanoreactors, and to advance cytomimetic engineering, synthetic biology and biomaterials research. [73] And indeed, liposomes for example have already proven to be industrially relevant for applications in creams and cosmetics or drug delivery. [76,77] When used as a platform to approach the primordial cell from an early earth perspective though, many of these cell-concepts seem to struggle as they are way too complex, or do not exhibit the necessary functionality to explain the origin of life.

Coacervation is another physical concept which can be utilised for the fabrication of cell-like entities, but which do not contain any form of membrane whatsoever. First described in the year 1949 [78] coacervation is described as the demixing of two macromolecules in a single solvent. One of the core driving forces for this behaviour is thermodynamics, or more specifically, a change of entropy. Coacervation forms two distinct phases of the two polymers, which in return causes a change in entropic energy. [79,80] While neutral polymers can cause coacervation [81] a more popular form of coacervation is the complex coacervation, which is the demixing of two macro-polyions with opposing charges in a single solvent. Here, it is necessary to expand the explanation from a purely thermodynamic approach to the electrostatic interactions between the polyions. Coacervation happens at the point when both charges are equalised within the coacervate phase, even though both poly-ions are completely miscible within the solvent. By reaching the electrostatic equilibrium, the solution starts to demix and form a highly enriched coacervate phase and a deprived bulk-phase around it. [82] What makes this concept so interesting, is that complex coacervation can lead to the formation of small cell-like enriched liquid microdroplets, which are very easy and quick to fabricate as they form almost readily once the macro-ion concentrations have been matched correctly. The variety of coacervate-compositions is sheer endless, as many different poly-ions, polymers and even smaller cations or anions can be used for the fabrication of coacervate microdroplets. A popular example, which has been studied by the Mann group are coacervates made from oligomeric lysine and adenosine-phosphates. What makes this specific model so interesting, is the comparably small size of the ions while being stable within a broad range of pH and temperature. [83] Coacervates are furthermore capable of sequestration of small and larger molecules, which enables them to take up and retain functional species like enzymes or even particles, even though they do not contain a membrane. The studies from Koga *et al*. [83] and Crosby *et al*. [84] not only showed the sequestration of enzymes, but also proved that it increased the reaction rate of the enzymes inside the droplets. They furthermore stated the reason for sequestration as a change in the dielectric constant between the coacervate phase and the bulk phase around the droplets. While coacervates exhibit a lot of benefits, especially due to the simplicity in their fabrication, maintaining them as separate droplets and handling them can be much more complicated, as they tend to coalesce into larger droplets or a continuous coacervate phase. Recent publications have shown the assembly of secondary components onto the coacervate microdroplets. With the restrictions mentioned above, these

approaches offered another layer of support for the liquid microdroplets, which in return made them a lot more stable and provided even more cell-like properties. Many of those studies originated from the Mann group and focused on different auxiliary structures in interaction with coacervates like 8-anilionaphthalene [84], fatty acids [85] or phosphotungstic acid. [86] The latter was especially interesting as it turned out to form a very distinct 3-layered structure with an outer membrane-layer made from phosphotungstic acid and the polyelectrolyte PDDA, an ATP/PDDA coacervate-layer underneath and an aqueous cell interior. This cell-type was eventually given the name phosphotungstic acid-coacervate vesicle, or PCV. [86]

All the systems described above have advanced our understanding of cells and more specifically synthetic cellularity from a bottom-up approach and they all come with their own benefits and disadvantages. Some of the most important aspects of a synthetic cell are a fast and easy fabrication, capabilities for functionalisation of the membrane or the interior, stability over varying temperature, pH and different chemical environments, a controllable uptake and release via a semi-permeable membrane and probably many more. While none of the cells seems to combine all benefits, there has been another recent publication, which focused on a simple, easy-to-make cell, with some very unique qualities.

3.2.2 Aminopropyl-functionalised magnesium phyllosilicate-clay/DNA-microcapsules

Kumar *et al.,* published their work in 2018 and gave the inspiration for many experiments which will be presented in this chapter and thesis. In their work, they presented cells made from a complex precipitate from DNA, and an inorganic clay-material with the name “aminoproyl-functionalised magnesium phyllosilicate clay” , or in other words aminoclay, organocaly or simply AMP-clay. [1]

Clay minerals possess an interesting array of properties, ranging from good electrical, mechanical, ion-exchange and catalytic properties, to the ability of intercalating guest molecules into their layered structures. [87-89] Phyllosilicate clays follow a basic structural concept with minor changes depending on the incorporation of different cations. The clay used in the previous report by Kumar *et al.* consists of alternating tetrahedral silicate-oxide sheets and octahedral aluminium- or magnesium-(hydr)oxide sheets. Phyllosilicates can be categorized into different groups depending on the combination of stacked tetrahedral and octahedral layers. The work of this thesis though solely focuses on talc-like structures with a 2:1 combination of one octahedral MgO_4-layer, sandwiched between two tetrahedral SiO_4-layers, which adds up to an overall cell formula of $Si_8Mg_6O_{16}(OH)_4$. [88,89] To design a highly cationic clay-material, 3-aminopropyl-triethoxysilane was used during the condensation-reaction, to form an organic phyllosilicate-network with the approximate formula $[H_2N(CH_2)_3]_8[Si_8Mg_6O_{16}(OH)_4]$. [87] Due to the layered structure of the clay, the amine groups exist in close proximity to each other and cause repulsion once they become protonated in water, which forces the packed clay sheets to exfoliate. Furthermore, the protonation of the amine-groups leads to an overall positive charge of the phyllosilicate-clay, which can be exploited for the self-assembly of microcompartments by letting them interact with poly-anions like DNA.

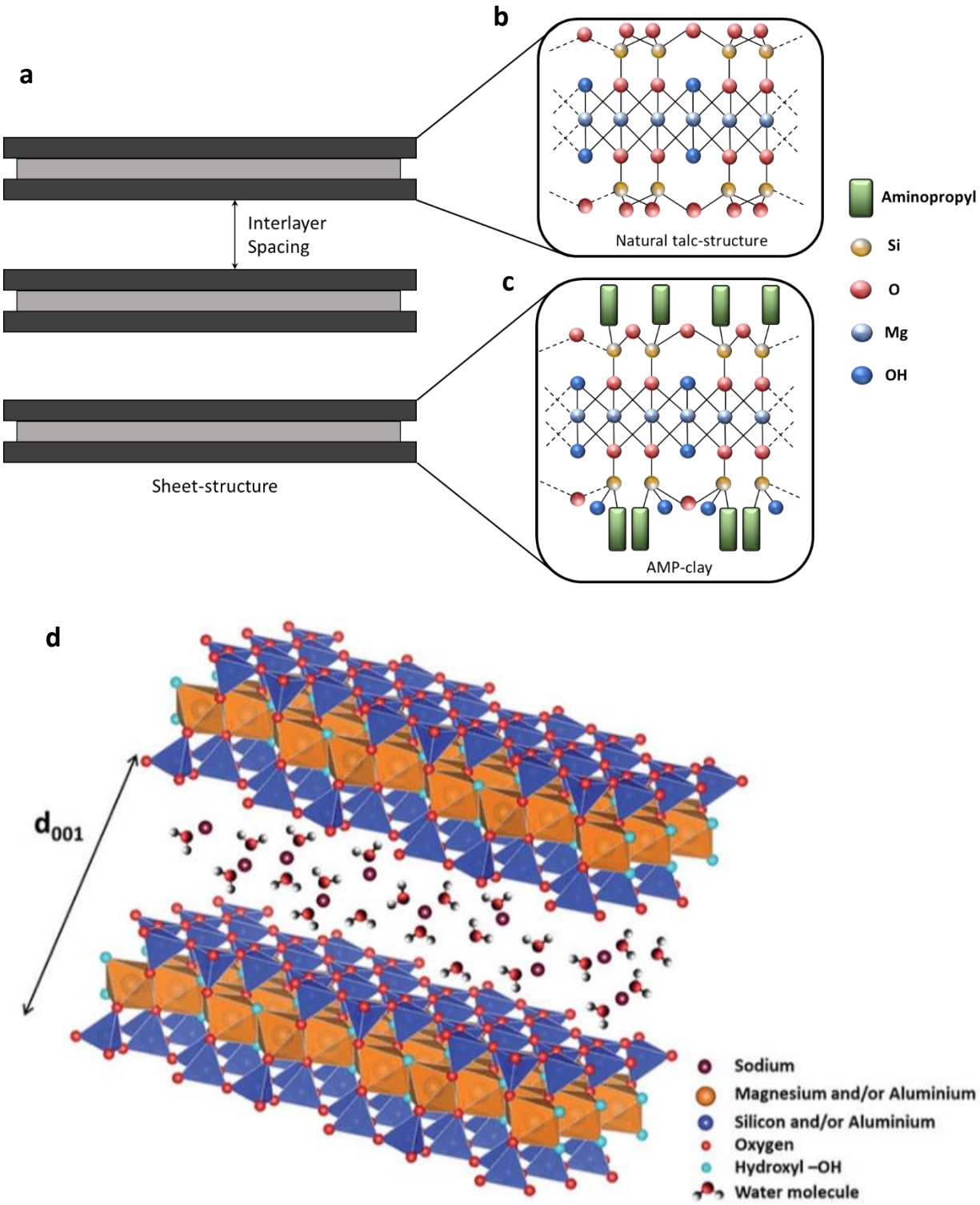

Figure 3.2-3: a *Schematic representation of the layered structure of a 2:1 trioctahedral-phyllosilicate (talc),* ***b*** *molecular composition of natural talc [$Si_8Mg_6O_{20}(OH)_4$],* ***c*** *aminopropyl-functionalised magnesium phyllosilicate clay [$Si_8R_8Mg_6O_{16-X/2}(OH)_{4+x}$]; x = 2, with the assumption that not all of the organosiloxane-groups are fully condensed* [18] ***, d*** *schematic of the 2:1 coordination of tetrahedral- and octahedral layers.* [90]

In order to explain and understand aminoclay/DNA-capsules they can be compared to the coacervate vesicles, which were discussed above. Both cell-types are made from the interaction of two different ionic components, yet the paper clearly shows, that the aminoclay/DNA-capsules contain a solid membrane, whereas coacervate vesicles are mere separated liquid phases in form of droplets, which

can coalesce and do not exhibit any longevity. [1] This is an important distinction to be made, as both liquid-liquid- (Coacervation) and liquid-solid-phase separations (Precipitation) come from similar interactions but have different underlying kinetics. Liquid-liquid-phase transitions like coacervations exist under reversible equilibriums, whereas precipitation is kinetically controlled and therefore more or less irreversible. Polyelectrolytes and proteins are interacting so strongly that it comes to water expulsion which irreversibly forms a solid precipitate. A key factor, which decides whether two polyelectrolytes form a coacervate or a precipitate is the pH. Depending on the pH, polyelectrolytes and proteins contain different surface charges and therefore exhibit different electrostatic interactions to each other. Finding the right pH can decide over coacervate-formation, dissolution or precipitation. [91,92] Furthermore comparing the organoclay-capsules from Kumar *et al*. [1] and the coacervates made from ATP and PDDA [86] it becomes apparent that the length of the polyions also influences the result, with longer polyions tending to exhibit stronger interactions and forming precipitates more likely.

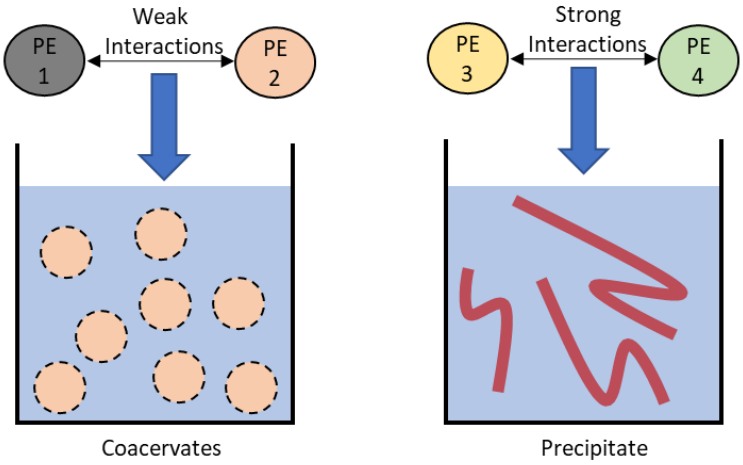

Figure 3.2-4: *Schematic representation of the formation of liquid-liquid- (coacervation) and liquid-solid-phase separations (precipitation), depending on the strength of the oppositely charged polyelectrolytes.*

The second component next to the aminoclay, and probably one of the most important components of this thesis is double stranded DNA. Considering the relevancy of DNA as an information storage medium in living organisms, it seems highly counterintuitive to use it as a structural component in protocells. What makes DNA so interesting regarding self-assembly of cells is the high negative surface charge it gains from its phosphate backbone. The DNA which was used for this thesis has been determined to have a length of about 2000 base-pairs and a weight of ~ 1300 kDa. [93] On the other hand, shorter dsDNA-oligomers were previously used for the formation of coacervate droplets by N. Martin *et al.* [94], which highlights the importance of the net charge and the length of the polymers for the formation of precipitates and coacervates.

The core part of this thesis discussed the development and application of motile protocells via self-induced buoyancy. Kumar *et al.* [1] have already presented a feasible model with organoclay/DNA-microcapsules, which lacks the structural stability to facilitate long-lasting motility in aqueous media. For this reason, the work in chapter 3 will present a novel microcapsule system based on the interaction of protamine with DNA, which not only improved the cell stability, but also the overall convenience and versatility when working on microcapsule buoyancy.

Protamines are naturally occurring nuclear proteins and come from a diverse family which are being synthesised during the late stages of the spermatogenesis within many mammals and plants. Even though there is no consensual protamine structure between all the different organisms, they usually

exhibit very characteristic arginine-rich domains with cysteine groups around them. Protamine functions similar to nuclear histones and are capable of compressing DNA into a much tighter packed and inaccessible form via condensation. The condensed DNA must then be decompressed first before it can be read for protein-synthesis. The two most studied protamines are the species P1 and P2, even though this thesis will only focus on P1 from salmon testes. Generally, P1-protamines are 49-50 amino acids long and contain a central arginine-rich domain which is mostly responsible for the interaction with the DNA. More specifically, protamine P1 wraps around the DNA double-helix along the major groove with one protamine-molecule per turn. [95,96] As it is expected, the main form of interaction between protamine and DNA is of electrostatic nature between the cationic arginine-groups and the phosphate-backbone of the DNA but hydrogen-bonds also play a role. The result is a highly stable DNA-condensate, which contorts into much smaller toroidal-shaped chromatin subunits, which are about 50-75 nm in diameter, 25 nm thick and contain 50000 base pairs. [95-99]

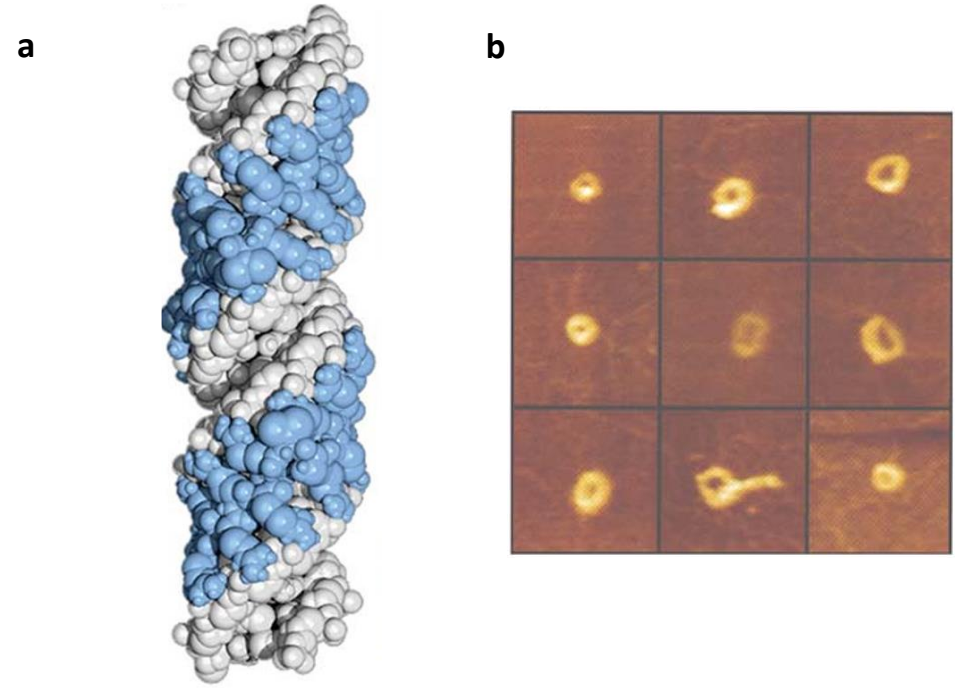

Figure 3.2-5: *DNA-condensation with protamine.* ***a*** *Protamine-molecules (**blue atoms**) attach to the phosphate-backbone of the DNA double helix (**white atoms**) along the major groove via electrostatic interactions* ***b*** *Scanning-probe (AFM) images of protamine/DNA-condensates which were prepared on a graphite surface. The interaction between the DNA and protamine coils the complex into a toroidal structure. The images were taken from the studies of Balhorn et al. [96,99]*

Protamine, or more specifically protamine-sulfate, which was used for the projects of this thesis, is not only used by nature but also in man-made drugs. Protamine can be used as a counteragent to neutralise the anti-clotting effects of heparin, [100] it was used as an additive to insulin, which in return prolonged insulin's blood-glucose lowering effects [101] and has also found application as a drug to fight obesity as protamine causes lipase inhibition, which in return reduces the absorption of fats into the body. [102]

Salmine is a protamine which is being produced in salmon sperm and is the molecular species which has been used all throughout this thesis. The amino acid sequence of salmine has been determined in a variety of studies and while the actual amino-acid composition can vary between species, the sequence below should give a close representation of the peptides used in this work.

AS-sequence: Protamine

PRRRRSSSRPVRRRRRPRVSRRRRRRGGRRRR

Figure 3.2-6: *Amino acid sequence of protamine from salmon sperm.* [103]

3.3 Methods

Important note regarding concentration statements and nomenclature in this thesis

Throughout the discussion and the results of this thesis, there will be references and information about the concentration of components, which were added during the fabrication of microcapsules. These concentrations are, if not declared otherwise, always referring to the concentration of the compound inside the dsDNA-solution which was used to fabricate the capsules, and not the concentration inside a single capsule. Furthermore, protamine/DNA- and aminoclay/DNA-microcompartments are generally referred to as "microcapsules", "capsules", "cells" or "microcompartments" and should not be misunderstood with biological cells or other protocell-systems. The term protamine/DNA- or aminoclay/DNA is also often abbreviated by removing "DNA", since all microcapsule systems, which will be discussed within this thesis, are using DNA as an anionic complexing agent.

3.3.1 Synthesis of aminopropyl-functionalised magnesium phyllosilicate (AMP-clay, $[H_2N(CH_2)_3]_8[Si_8Mg_6O_{16}(OH)_4]$)

For the synthesis of the AMP-organoclay, the experimental methods of A. Patil *et al.* [88,89] were used. First, a solution of magnesium chloride (8.4g, 36.2 mmol) in 157.8 mL ethanol was prepared and stirred inside a beaker for 10 minutes until the $MgCl_2$ was fully dissolved. Then, 3-aminopropyltriethoxysilane (13 mL, 58.5 mmol) was added dropwise to the solution over a time span of 15 minutes to prevent rapid hydrolysation. Halfway through the addition of the silane a colourless precipitate started to form until the once clear solution turned into a cloudy suspension. The white slurry was stirred overnight (16h) and the beaker was covered to prevent the ethanol from evaporating. The next day, the suspension was transferred into 50 mL centrifuge tubes and centrifuged at 7000 rpm for 10 minutes. The supernatant was removed, and the colourless precipitate was washed with 40 mL ethanol. The suspension was centrifuged again, and the washing step repeated two times. The colourless substance was then combined on a petri dish and dried over night at 40°C in a convection oven. The synthesis yielded 5.12g of a colourless crystalline substance.

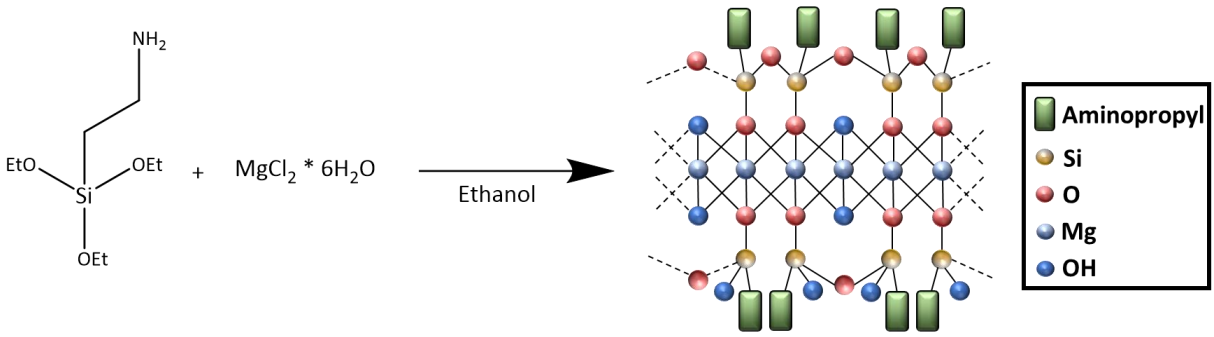

Figure 3.3-1: *Synthesis of aminopropyl-functionalised magnesium phyllosilicate-clay from aminopropyltriethoxysilane and magnesium chloride.*

3.3.2 AMP-clay exfoliation

AMP-clay was generally dissolved in di-water with a final concentration of 5 mg/mL. In order to ensure that the clay was properly exfoliated, the vial with the clay-dispersion was sonicated in a sonicator (*VWR – Ultrasonic cleaner*) for 15 minutes. During the sonication, the cloudy dispersion started to turn clear. The solution was then mixed with a small stir bar on a magnetic stirrer and eventually filtered through a syringe-filter with a 5 µm membrane, to make sure that other smaller particles are removed.

3.3.3 Fabrication of microcapsules via air-jet supported microdroplet formation

All microcapsules in this thesis were fabricated the same way. The device which was used for microcapsule-formation is custom-made and combined several necessary functions: the formation of DNA-microdroplets, the acceleration of the droplet towards an AMP/Protamine-interface and the control over the output of the DNA-solution. To control the size of the microcapsules it is important to control the size of the dsDNA-droplets. For this purpose, a setup was prepared which combined a syringe (*BD Plastipak™* 1 mL syringe, with *BD PrecisionGlide™* Needles: Gauge 30, 0.3mm x 25mm), loaded with an aqueous solution of dsDNA (4 mg/mL) and mounted to a syringe pump (*KD Scientific*: KDS 200, Extrusion volume: 20 µL, Flowrate: 10 µL/min) and a custom made nozzle with a 1.93 mm diameter outlet, which can be applied to the tip of the syringe and through which a coaxial airstream (2.1 L/min) was funnelled. The syringe pump enabled exact control over the amount of dsDNA-solution extruded through the syringe. Small droplets formed at the tip of the needle and the shearing forces induced by the coaxial airstream detached the 200-500 µm microdroplets from the needle. The droplets were then accelerated into the vial underneath the needle, containing the cationic poly-ion solution.

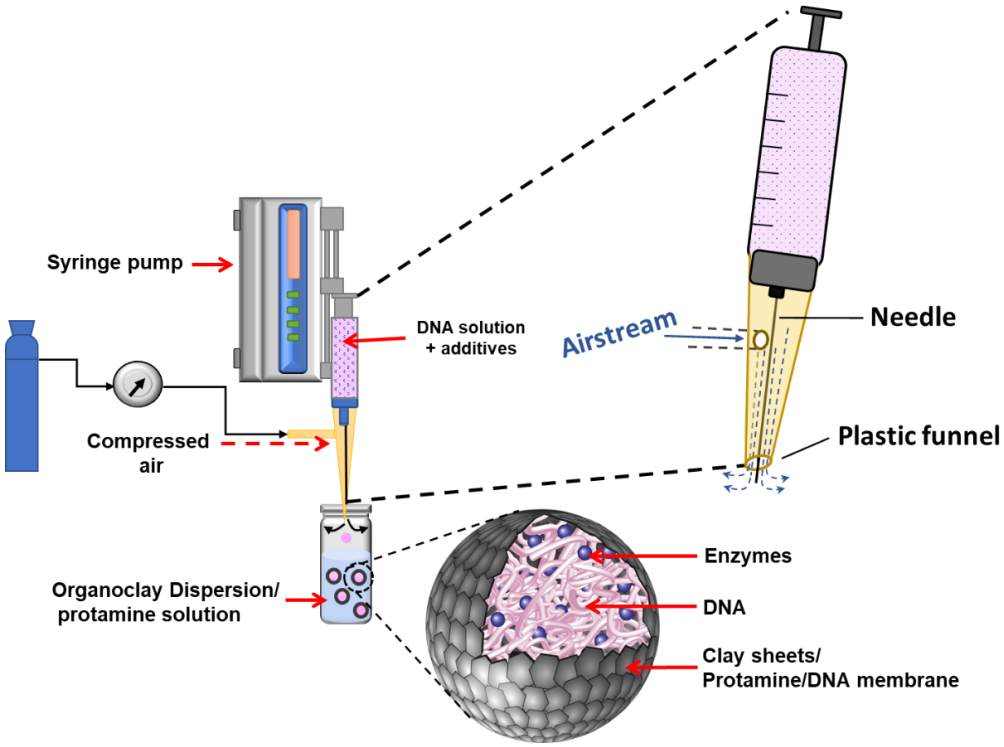

Figure 3.3-2: *Experimental setup for DNA/organoclay and DNA/Protamine-microcapsule formation. A syringe, loaded with an aqueous solution of ds-DNA is mounted to a syringe pump. A nozzle is applied to the tip of the syringe, which channelled a coaxial airstream, so that it shears the extruded ds-DNA microdroplets and accelerates them towards the AMP dispersion or Protamine-solution underneath. Electrostatically induced self-assembly then leads to the formation of a semi-permeable membrane of complex dsDNA and AMP-sheets or Protamine with entrapped enzymes like Catalase or Glucose Oxidase, or particles like magnetic polymer-microspheres, fluorescent particles or silica particles.* [1]

For the fabrication of AMP/DNA microcapsules, aminopropyl-functionalised magnesium phyllosilicate clay was first exfoliated in water. For this purpose, 5 mg/mL of AMP was sonicated for about 15 minutes or until the white suspension had fully turned into a clear exfoliated AMP-dispersion. In case of protamine/DNA-microcapsules, a 0.5 mg/mL protamine solution was prepared. In either case, 1 mL of the solution was filled into a small 1.7 mL glass vial and positioned underneath the nozzle of the syringe. To increase microcapsule viability, 3 µL of 53 µg/mL Tween®20-solution were added to the mixture. After the extrusion, the microcapsules were washed 3 times with either a 0.5 mg/mL organoclay-solution (for AMP-capsules) or with water (for Protamine-capsules) and kept for further experiments. Furthermore, enzymes like catalase and glucose Oxidase, or particles like silica particles, fluorescent particles or magnetic polymer microspheres were encapsulated by simply adding them to the dsDNA-solution before microcapsule formation. Here, the following final concentrations in a 500 µL volume of DNA-solution were commonly used: 19.8 kU/mL catalase, 2.9 kU/mL glucose oxidase, 20 mg/mL silica particles or any other particle.

To produce "small microcapsules" the nozzle described above is the limiting factor. By decreasing the nozzle diameter, higher airstream-pressures were realised which led to higher shearing forces and therefore smaller droplets. With this smaller nozzle-system, microdroplets were produced with sizes of 50 – 200 µm.

3.3.4 Analysis of microcapsule shrinkage during formation

To understand the shrinkage of microcapsules during their formation it is necessary to measure the size of the dsDNA-droplets once they have been ejected from the needle tip. For this purpose, the droplets were accelerated onto a PTFE-membrane, which served two purposes: serve as a planar surface and barrier, on which the accelerated droplets can rest against, and retain the droplets' spherical structure due to PTFE's high contact angle and low wettability, in order to measure the droplet diameter.

The PTFE-membrane was wrapped around the opening of a small 1.7 mL glass vial, creating a smooth and planar surface. Afterwards, the vial was positioned right underneath the needle, ejecting the droplets onto the PTFE-barrier. Once a droplet was visible on the membrane, they were observed and measured via a horizontally lying optical brightfield microscope.

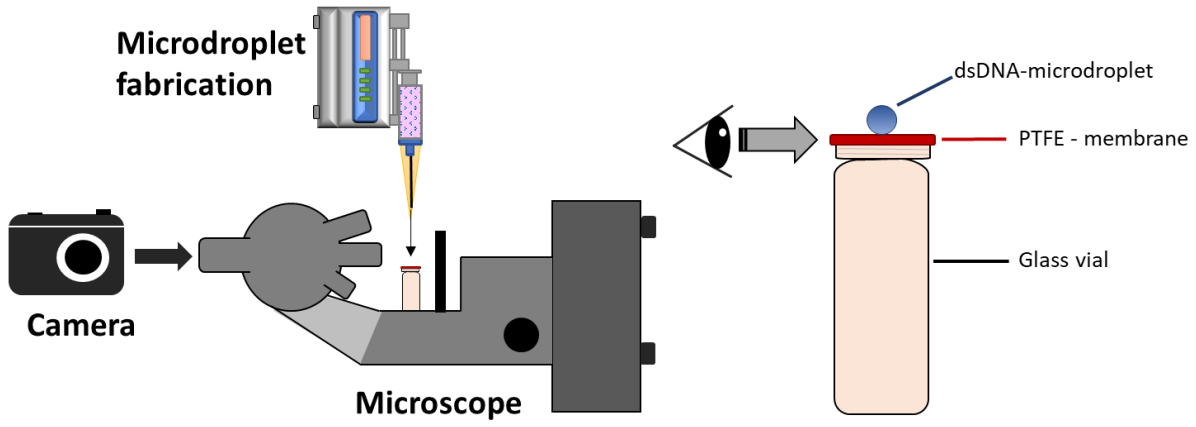

Figure 3.3-3: *Experimental setup to analyse the size of dsDNA-microdroplets after they've been ejected from the syringe. The dsDNA-droplets were captured on the PTFE-surface via a digital camera, which was attached to the microscope.*

3.3.5 Microcapsule stability screening

Protamine/DNA- and AMP/DNA-microcapsules were fabricated as described in part 3.3.3 with 4 mg/mL DNA and with 4 mg/mL silica particles in case of aminoclay-capsules, to make them easier to see. The microcapsules were then immersed in either di-water, 50 mM sodium phosphate or 0.5 mg/mL aminoclay and observed with an optical microscope.

3.3.6 Acridine orange staining of microcapsules

For several different experiments, microcapsules were stained with the DNA-intercalating dye acridine orange, and the staining process was performed as followed: Protamine/DNA- and AMP/DNA-microcapsules were fabricated as described in 3.3.3 with 4 mg/mL DNA. The capsules were then stained by immersing them in a 10 mM acridine orange solution for 10 minutes before washing them several times with di-water to remove any excess dye.

3.3.7 Temperature stability of microcapsules

Acridine orange-stained microcapsules were fabricated as described in 3.3.6. The microcapsules were then transferred onto a heating stage which was connected to the specimen stage of the fluorescence microscope. The heating stage was set to ramp up to 95°C with a ramp-speed of 1°C/min. Meanwhile, the microcapsules where observed under the fluorescence microscope by detecting the absorption of acridine orange at $\lambda_{Abs,\ acridine\ orange}$ = 468-490. [104]

3.3.8 Enzyme-tagging with FITC, RITC or Dylight-405

The protocol used to tag enzymes with fluorescent dyes was kept the same throughout this thesis. 4 mg/mL of the enzyme of choice was dissolved in 10 mL sodium carbonate buffer (0.1 M, pH 8). Parallelly, a 2 mg/mL solution of the respective dye (e.g. FITC or RITC) was prepared in DMSO after which 200 µL were added to the enzyme-solution. The mixture was stirred over night at 4°C inside a fridge. The following day, the sample was filled into dialysis bags (*Medicell Membranes*: Dialysis tubing, Size 9, Dia. 36/32" – 28.6 mm, molecular cut-off: 12-14 kDa) and dialysed against sodium-phosphate buffer (1L, 50 mM, pH 7.5). The solution was refreshed 3 times a day over 3 days. Afterwards, the tagged enzyme was freeze dried for 1 day and stored at -20 °C.

The protocol for the tagging with Dylight-405 was taken from Thermo Fisher-Scientific. [105] 10 mg/mL of the enzyme of choice was dissolved in 0.1 M sodium phosphate-buffer (pH 8.5) and mixed with 5.46 µL of Dylight-405-solution (1 mg/mL in DMSO). The mixture was stirred well and incubated at room temperature for 1 hour. Once the reaction was done, the sample was purified via size exclusion chromatography and eluted in 3.5 mL of di-water or buffer.

3.3.9 Synthesis of citrate-capped platinum nanoparticles

Platinum nanoparticles were fabricated according to the protocol of Wu *et al.,* [106] which is based on a simple reduction of platinum salts with citrate. Here, aqueous solutions of K_2PtCl_6 (Sigma-Aldrich, 1 mL, 16 mM, 7.78 mg/mL) and trisodium citrate (1 mL, 40 mM, 10.3 mg/mL) were mixed in a small Erlenmeyer flask and stirred for 30 minutes. Afterwards an $NaBH_4$-solution (200 µL, 50 mM, 1.89 mg/mL) was added dropwise during which the solution changed its colour from slightly yellow, to dark brown. After the addition was completed, the mixture was stirred for another 60 minutes before the citrate-capped Pt-nanoparticles were used for the experiments as synthesised.

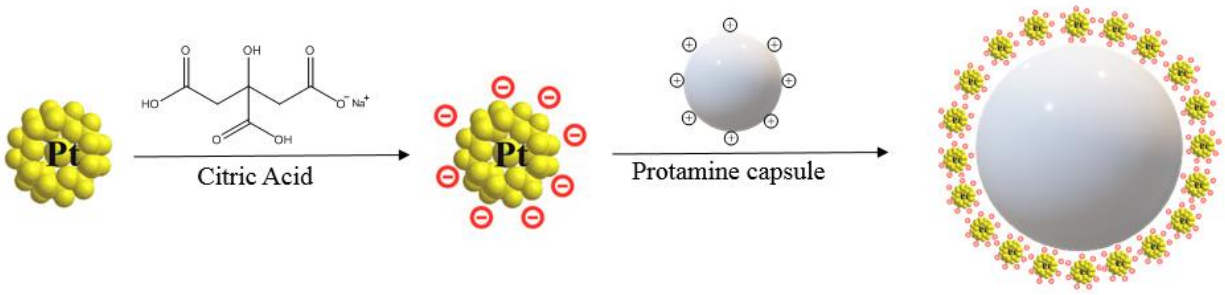

Figure 3.3-4: *Synthesis of citrate-capped platinum nanoparticles.* [106]

3.3.10 Adsorption of functional components onto protamine-microcapsules

Protamine microcapsules were fabricated as described above in 3.3.3. The capsules were then incubated in the following mixtures for 1.5 hours: 1 mL of citrate-capped platinum nanoparticles (as synthesised in 3.3.9) or FITC-Catalase (2.5 mg/mL). In case of COOH-functionalised magnetic microparticles, the capsules were either mixed or sedimented onto a bed of particles in order to bind them to the membrane. Once the adsorption-process was done, all capsules were washed 5 times with di-water to remove any excess material from the dispersion.

3.3.11 Fabrication of alternative microcapsule-systems

For the fabrication of microcapsules based on alternative complex-materials, Polydiallyldimethylammonium-chloride (PDDA, 100-200 kDa, 10 mM), Polyallylamine-hydrochloride (15 kDa, 10 mg/mL) and protease (from *Bacillus Lichenformis*, 0.75 U/g) were used as cationic polymers. The microcapsules were then fabricated as described in 3.3.3 with 4 mg/mL DNA.

3.3.12 Determination of the capsule-count per batch

To understand how many capsules are produced in one "batch", microcapsules were fabricated under the standardised fabrication conditions in 3.3.3 with 4 mg/mL DNA, 19.8 kU/mL catalase, 2.9 kU/mL glucose oxidase, 20 mg/mL silica particles, an extrusion volume of 20 µL at 10 µL/min and with a coaxial airflow of 2.1 L/min. Since the capsule count is independent from the cationic material used, protamine was used as the material of choice. Once the fabrication was finished, 100 µL of the capsule dispersion was transferred onto a microscope-glass slide and examined with a brightfield microscope. The amount of capsules was counted and then extrapolated to the amount of capsules in the whole batch. This value was then used to calculate internal concentrations of functional components inside the microcapsules.

3.3.13 Determination of enzyme leakage after fabrication

Protamine/DNA-microcapsules were fabricated according to the established protocol (3.3.3) with 4 mg/mL DNA and varying amounts of FITC-GOx (16, 10, 5, 2 mg/mL), which was previously tagged according to (3.3.8). 20 µL of the dsDNA/FITC-GOx-solution were extruded for each batch of microcapsules. The microcompartments were then disposed of and the supernatant was used to assess the FITC-GOx leakage with a UV/VIS spectrometer at $\lambda_{Excitation}$ (FITC) = 495 nm. To correlate the absorbance to the concentration, a calibration curve was prepared by measuring the UV/VIS-absorbance of different FITC-GOx concentrations (0.5, 0.25, 0.1, 0.05, 0.01, 0.005, 0.001 mg/mL) at $\lambda_{Excitation}$ (FITC) = 495 nm.

3.3.14 Determination of enzyme leakage after washing with di-water via fluorescence microscopy

Protamine/DNA and AMP/DNA-microcapsules were fabricated as stated above in 3.3.3 with 4 mg/mL dsDNA and 2 mg/mL FITC-GOx in case of protamine/DNA-capsules and 2 mg/mL RITC-GOx in case of aminoclay-capsules. To test whether the tagged enzymes are leaking out in di-water, the capsules were washed 1X, 3X, 5X and 10X and then examined with the fluorescence microscope. To ensure that the fluorescence-conditions are identical for all samples, all images were taken with 2.5X-magnifiation and under identical exposure times. The fluorescence intensity was then averaged and plotted over 30 different microcapsules per sample via the software *Fiji-ImageJ*.

3.3.15 Coupled enzyme assay to assess enzyme leakage from protamine/DNA-microcapsules

Protamine/DNA-microcapsules were fabricated as stated in 3.3.3 with 2.9 kU/mL glucose oxidase and 20 mg/mL silica particles. The capsules were washed 5 times after fabrication and then transferred into a 96-well plate which contained 200 μL of 50 mM sodium phosphate (pH 7.0), where they were incubated for 1h. The capsules were then transferred back into water and washed 5 times to remove any excess buffer.

To assess the activity of the remaining entrapped enzymes, a coupled assay with glucose oxidase, horseradish peroxidase (HRP) and the chromophore 2,2'-azino-bis(3-ethylbenzothiazoline-6-sulfonic acid (ABTS) was chosen. For the colorimetric assay, the following solution was prepared inside an optical cuvette: ABTS (8.19 mM), HRP (8.3 U/mL), Glucose (25 mM). The reaction was started by adding 2 protamine/DNA-capsules per measurement into prepared cuvette. The absorbance of ABTS was observed at 420 nm with measurements taken every minute for 5 minutes altogether inside the UV/VIS-spectrometer (*Perkin Elmer* - Lambda 750 UV/VIS spectrometer). Protamine-capsules, which have not been incubated in sodium phosphate-buffer were taken as a reference.

Parallelly, the supernatant from the buffer/capsule-dispersion was assessed as well. 100 μL of the supernatant were mixed with 100 μL of the assay-solution (ABTS (8.19 mM), HRP (8.3 U/mL), Glucose (25 mM)) inside a 96-well-plate and then left until the reaction changed the colour to a dark green, which usually took about 1-5 minutes.

3.3.16 Determination of enzyme-leakage from protamine/DNA-microcapsules via fluorescence microscopy

The capsules were fabricated according to 3.3.3 with 2 mg/mL RITC-glucose oxidase (see 3.3.8 for the tagging protocol) and 20 mg/mL silica particles. The capsules were washed 5 times and then transferred into a 96-well-plate, which was positioned under the fluorescence microscope to take a picture at t=0 with an excitation wavelength of λ_{RITC} = 560 nm. The solution was then exchanged with 50 mM sodium phosphate buffer (pH 7.0) and again placed under the fluorescence microscope. To prevent any unnecessary photo-bleaching, images were taken in 30 minute intervals during which the lamp was turned off.

3.3.17 SEM-analysis of protamine/DNA- and AMP/DNA-microcapsules

Protamine/DNA- and aminoclay/DNA-capsules were prepared as described in 3.3.3 with 4 mg/mL. To prepare the microcapsules for the scanning electron microscope, they were lyophilised in liquid nitrogen. For this purpose, a small disposable vial was filled with liquid nitrogen. Once the liquid nitrogen stopped bubbling and the vial has reached the minimum temperature, the microcapsule dispersion was added to the liquid nitrogen. To prevent aggregation, the microcapsules were added

dropwise with a pipette (10-100 μL) until the hole dispersion was immersed in liquid nitrogen, after which the sample was freeze dried overnight (*LABCONCO* – Freeze Zone 1 L bench top freeze dryer). The next day, the samples were used for the electron microscopy. All images were taken without sputter deposition to retain any nanoscopic structures.

3.3.18 Design of hierarchical microcapsule structures

Hierarchical microcapsule structures were prepared by encapsulation of smaller microcapsule entities within larger species. These experiments were performed with different permutations of large microcapsule hosts and small microcapsule guests made from AMP/DNA- and protamine/DNA-complexes, which is why these methods will present a generalised approach.

Small microcapsules were prepared according to 3.3.3, with 4 mg/mL DNA to fabricate sizes of ~50-100 μm in diameter. Next, the small microcapsules were slowly immersed in 4 mg/mL DNA-solution. To ensure that they would disperse in the viscous medium, they were added dropwise, while the DNA-solution was “vortexed” inside a disposable *Eppendorf*-vial. Once all capsules were dispersed, large microcapsules were formed according to 3.3.3 using the prepared DNA/capsule dispersion. The host compartments were aimed to be around 400 μm and were washed 4-5 times after fabrication.

3.4 Results and Discussion

3.4.1 Characterisation of aminopropyl-functionalised magnesium phyllosilicate, protamine and dsDNA

Aminopropyl-functionalised magnesium phyllosilicate-clay was synthesised as previously described by precipitating the clay in an ethanolic solution of magnesium chloride after addition of 3-aminopropyltriethoxysilane. To assess the structure of the synthesised clay, X-ray diffraction and FT-infrared spectroscopy were used. The identification of the XRD-signals was done in reference to several publications. [107,108]

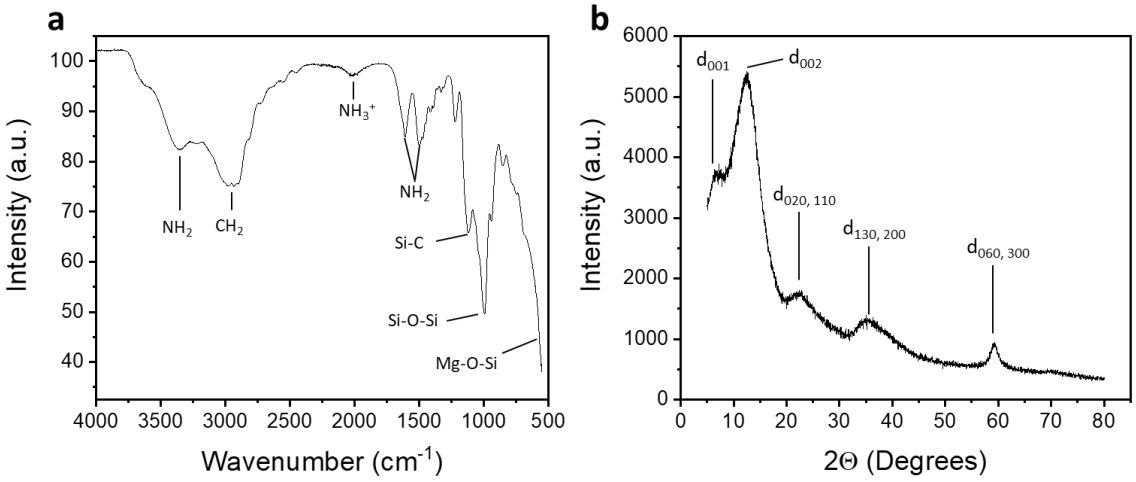

Figure 3.4-1: *FT-IR-spectrum (**a**) and XRD-diffraction pattern (**b**) of aminopropyl-functionalised magnesium phyllosilicate clay.*

In its natural form, talc exhibits a characteristic reflection of d_{001} = 9.4° (2θ). Using the bragg-equation, the diffraction angle can be translated into the interplane-distance d with wavelength λ:

$$d = \frac{\lambda}{2\,sin(\theta)} \qquad \textit{(Equation 3.4-1)}$$

This results in a value of ~ 9.4 Å between each sheet of naturally occurring talc. The as prepared AMP-clay exhibited the characteristic d_{001}-reflection at a slightly lower diffraction angle of $2\theta = 6.3°$, which correlates to an interlayer spacing of 14.1 Å. In comparison to natural talc, the interlayer spacing of AMP-clay was 4.7 Å larger, which is consistent with reported literature. [109,110] The larger distance between the talc sheets can be explained by looking at the aminopropyl-groups, which are now attached to each side. As these groups occupy more space between the sheets than the native talc, they force the sheets away from each other, thus increasing the interlayer distance. Due to the larger distance between the sheets seen in the XRD-diffraction-pattern, it is plausible that the aminopropyl-groups are located around each side of talc-sheet structure and therefore reach into the interlayer-volume between the sheets, which in return forces the sheets further away from each other. Further distinctive signals that were found for the characterisation of AMP-clay are the d_{002} -diffraction at $\theta_{d002} = 10.5°$, the $d_{020,110}$ – diffraction at $\theta_{d020,110} = 21.5°$, and $d_{130,200}$ at $\theta_{d130,200} = 36°$. [111] Another important diffraction $d_{060,300}$ was found at $\theta_{d060,300} = 60°$, which is a characteristic signal in smectites, and which highlights the 2:1 trioctahedral phyllosilicate structure.

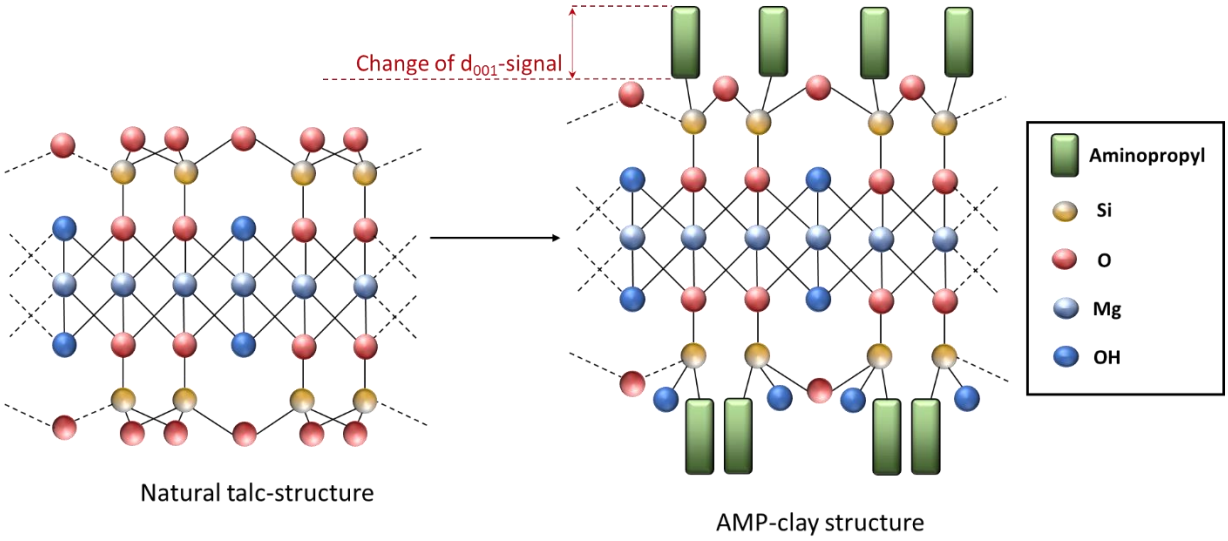

Figure 3.4-2: *Schematic representation of the molecular composition of natural talc [$Si_8Mg_6O_{20}(OH)_4$] and aminopropyl functionalised magnesium phyllosilicate clay [$Si_8R_8Mg_6O_{16-x/2}(OH)_{4+x}$]; x = 2, with the assumption that not all of the organosiloxane-groups are fully condensed.* [112]

Alternatively, the organoclay-structure was confirmed using FT-IR-measurements (Figure 3.4-1-b). The covalently linked aminopropyl-groups were characterised by the following signals: NH_2-Stretching (3380 cm^1), NH_3^+ (1990 cm^1), CH_2-stretching (2935 cm^1) and NH_2-bending (1621 cm^1 and 1496 cm^1). The phyllosilicate framework was furthermore identified by Si-O-Si-stretching (1020 cm^1) and the Si-C signal at 1176 cm^1. Theoretically there should also be a visible signal for the Mg-O-Si-bending around 670 cm^1, which was obscured though, since the samples were analysed with an ATR-FTIR, which cannot resolve signals past 680 cm^{-1}. [109,110] Nonetheless the data presented was enough to confirm the structure and presence of AMP-clay.

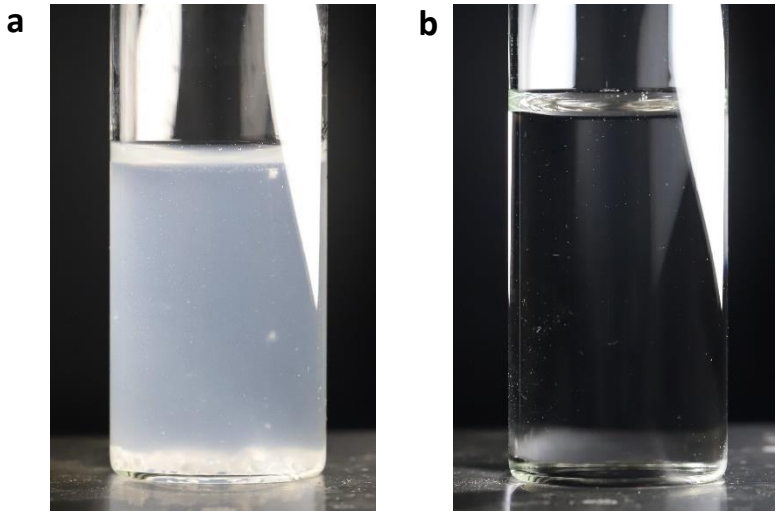

Figure 3.4-3: *AMP-clay exfoliation-process.* ***a*** *AMP-clay in water right after addition and* ***b*** *after 5 minutes of sonication.*

Before the clay was used for microcapsule fabrication it was necessary to confirm its viability in an aqueous dispersion. 5 mg/mL suspensions of AMP-clay in di-water were sonicated for 10 minutes and it was observed if the clay-sheets exfoliated. If they stayed as a cloudy suspension, the clay was discarded and the synthesis repeated, as this confirmed that the functionalisation was not successful. Figure 3.4-3 shows an example of how the exfoliation process is supposed to look like. Furthermore,

sonication of the clay-dispersion was necessary, as the clay-sheets would otherwise not exfoliate properly, or the process would take substantially longer.

Zeta-potential scans served as an important source of information for many parts of this thesis and can be applied here as well to get a better understanding of the surface charge of the materials. What needs to be discussed before though, is the utilisation of DLS zeta-scans for polyelectrolytes and proteins. Like it was described in chapter 2.2.2.1, the zeta-potential is being measured at the electrical double layer of a colloidal particle which forms between the surface charge of the particle and the counterions in solution. The zeta potential is measured between the so called "slipping plane" and the bulk dispersant. What stands out in this definition is that the zeta potential generally revolves around colloid particles, which usually refers to a solid phase in a liquid dispersant with a defined charge-distribution around its surface. [113] This raises the question, whether polyelectrolytes or proteins fall into this category or can be used for zeta scans at all. Many proteins form globular structures, where hydrophobic amino acids are closely packed and buried inside the protein globule in order to minimize the active surface which is in contact with the aqueous dispersant. [114,115] While not being identical to an inorganic colloid like for example a nanoparticle, proteins could be approximated as one, which would give more legitimacy for the measurement of the zeta potential. Polymers, or more specifically polyelectrolytes on the other hand, are often comprised of long linear chains with a very homogenous distribution of charged groups or side chains, which does not allow for a globular packing. Considering polymers like DNA, AMP-clay, FITC-dextran and CM-dextran, which will be used later in this chapter and potentially even protamine, one would expect a rather linear and flexible structure, due to the hydrophilic interactions of the side-chains with the water molecules. Moreover, due to the flexibility of the structure, it would enable the aqueous dispersant to flow through the polymer. This would contradict the theoretical assumption of a rigid spherical particle and therefore the applied mathematical foundations of Henry's equation. [116] Nonetheless, since the zeta potential ζ is derived from the electrophoretic motility of a charged species within an electric field, it should still be possible use the data qualitatively to understand the general charge of the molecules. Organoclay, dsDNA but also protamine, which was used as an alternative material to AMP throughout this thesis to fabricate novel protocells were analysed by DLS zeta-scans. The results can be seen in Figure 3.4-4.

As expected from theory, both organoclay and protamine exhibit a positive surface charge. For AMP-clay we measured a zeta potential of about 24 mV (Figure 3.4-4-dark red), whereas protamine was found much higher at around 117 mV (Figure 3.4-4-pink). While the numbers of zeta-potential measurements can only be used as indicators to describe and compare the behaviour of materials in this thesis, they can be used to predict the interactions between the cationic materials and dsDNA. Due to the higher positive zeta-potential of protamine, we would expect a stronger interaction with DNA. This could be explained due to the fact that protamine contains arginine-rich regions, which most likely contribute to the large positive surface charge, whereas AMP-clay gains its positive charge from the ATES ((3-aminopropyl)-triethoxysilane), which could be less densely distributed. In foresight to later studies within this thesis, the zeta-potential scans can also be used to explain stability issues and differences between AMP/DNA- and protamine/DNA-microcapsules. Lastly, the zeta-potential of dsDNA was also examined and measured at around -41 mV (Figure 3.4-4-orange). Again, this confirms the negative charge of dsDNA due to its phosphate backbone and the potential to interact with the positively charged materials protamine and the aminoclay.

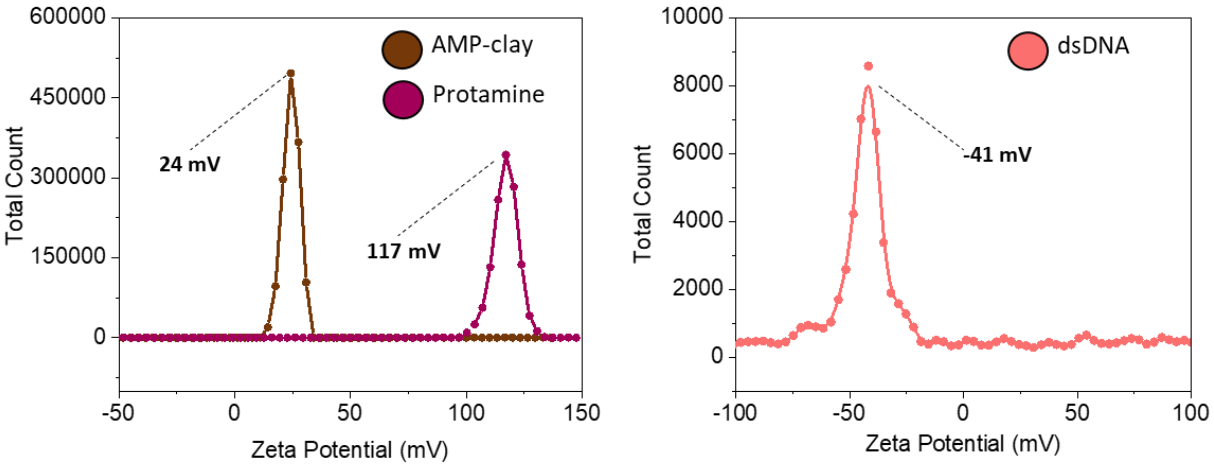

Figure 3.4-4: *DLS-zeta scans of AMP-clay (**brown**), protamine (**purple**) and dsDNA (**pink**). All samples were measured at concentrations of 1 mg/mL.*

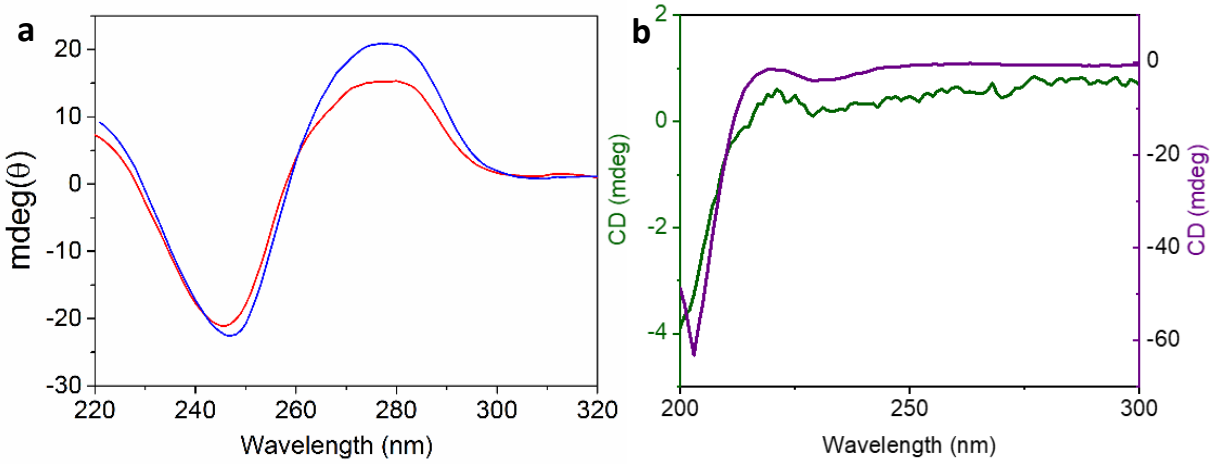

Figure 3.4-5: a *Circular dichroism spectrum of free dsDNA (**blue**) and organoclay/DNA-microcapsules (**red**). **b** CD-spectrum of protamine (**purple**) and* protamine/DNA-microcapsules (**green**).

While the supplied DNA used for microcapsule fabrication is double stranded, it is important to understand whether the double strands are retained within the microcapsules. Figure 3.4-5-a (blue plot) confirms the double stranded structure of DNA in solution but also as a complex within AMP-capsules (Figure 3.4-5-a, red-plot). The CD-spectrum of protamine-capsules on the other hand has shown to be much more difficult to analyse, since protamine produces a signal within the CD-spectrum as well due to its chiral nature, whereas the AMP-clay does not. The protamine signal overlaps with the signal of the DNA in the protamine/DNA-complex while also showing a much higher intensity, which makes it impossible to assess the dsDNA-signal underneath (Figure 3.4-5-b). Furthermore, the signal yielded from protamine/DNA-microcapsules is very low and exhibited a lot of noise, but mainly showed the characteristics of native protamine. For this reason, the analysis of protamine/DNA-capsules via CD-spectroscopy was found to be impractical.

3.4.2 Characterisation of AMP/DNA- and protamine/DNA-microcapsules

As the protamine/DNA-capsules were developed parallelly to working with the AMP/DNA-system, both systems will be discussed side by side from this point onwards, in order to highlight important differences and to establish a superior microcapsule type for further experiments in this thesis.

The exact fabrication of any type of microcapsule in this thesis was done with a custom-built microdroplet extrusion device, which was described in the methods (3.3.3). A syringe pump extruded a dsDNA-solution through a needle and the small droplets were shorn of the tip by a co-axial airstream. To funnel that air-stream and to direct it towards the cationic solution underneath, a plastic *Eppendorf* pipette tip (10-200 μL, yellow tip) was attached to the syringe, with the needle barely reaching out of it. Although the device appears complex, the fabricated capsules were notably defined by only two different parameters: The diameter of the needle (gauge) and the resulting air-velocities at the exit of the plastic funnel. By either reducing the exit-diameter of the funnel or increasing the air-pressure externally, the formed droplets were shorn off much quicker, resulting in much smaller microdroplets and, therefore, smaller microcompartments. Generally, needles with a diameter of 0.31 mm (Gauge 30) and an air-stream of ~2.1 L/min were used throughout the experiments to produce highly uniform capsules, whereas the diameter at the exit of the plastic nozzle was kept at 1.93mm. Nonetheless, as the device contained self-made parts and was manually re-assembled for every experiment, there was a certain persistent error that decreased the reproducibility even when following the protocol pedantically (See Figure 3.3-2). Realistically, there were several factors that could change the outcome of the microcapsule formation like the turbulence of the airstream inside the plastic funnel and the resulting direction of it when it leaves the tip, the air-pressure, the distance how far the needle protrudes out of the nozzle, the distance and the positioning of the nozzle to the cationic solution underneath, the viscosity of the dsDNA-solution and probably even more. All of these details could have a crucial effect on the droplets and decide over the size of the capsules, if they are monodisperse or polydisperse, if they are deformed or spherical and sometimes if they form at all or rather accumulate around the sides of the vial or at the air/water interface, or even stick to each other.

When fabricating microcapsules, the DNA-concentration was one of the first core parameters to optimise, as it not only decided over the amount of anionic material, but also over the general viscosity of the solution, which in return influenced the size of the droplets formed and the general viability of the procedure. If the viscosity was too high, the droplets generally became too big and would often not shear off the needle properly, whereas if the viscosity went below a certain threshold, the accelerated droplets lacked a certain stability when getting in contact with the solution underneath, thus forming complex debris or highly deformed membranes. Generally, microcapsules were able to form at a dsDNA-concentration of 1 mg/mL and higher, but studies revealed optimal viscosity and cell forming properties at a DNA-concentration of 4 mg/mL, which was used all throughout this thesis. Next, microcapsule compartments with distinct concentrations of cationic materials were fabricated. Figure 3.4-6 shows microscopic images of AMP- and protamine-microcapsules, produced from 5 mg/mL organoclay and 0.5 mg/mL protamine in di-water respectively.

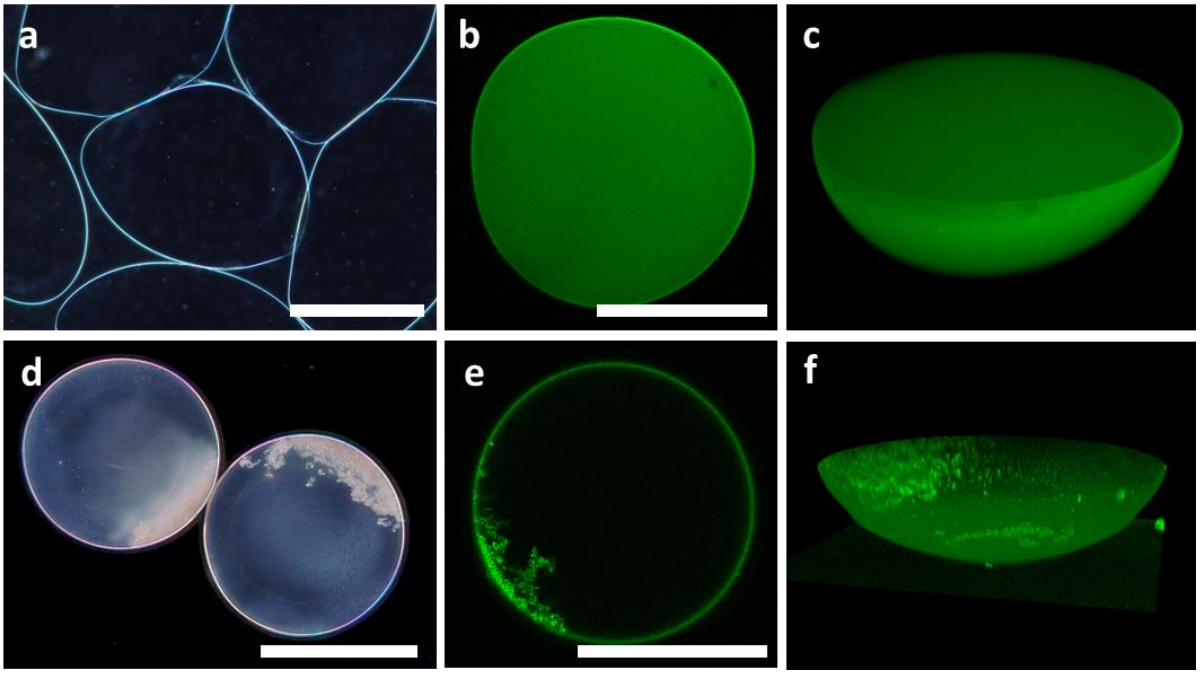

Figure 3.4-6: *AMP/DNA and protamine/DNA microcapsules.* ***a*** *Optical micrographs of AMP/DNA-microcapsules in a 0.5 mg/mL AMP-clay solution (with phase contrast to further highlight the membrane),* ***b*** *Confocal-micrographs of a single AMP/DNA-microcapsule after staining it with 10 mM acridine orange,* ***c*** *3D-representation of a z-stack of confocal images of an acridine orange-stained AMP/DNA microcapsule,* ***d*** *optical micrograph of protamine/DNA-microcapsules in di-water,* ***e*** *Confocal image of an acridine orange-stained protamine/DNA-microcapsule,* ***f*** *3D-representation of the a z-stack of confocal images of an acridine orange stained protamine/DNA-microcapsule. Scale bars: 300 µm.*

In both cases the produced microcapsules exhibited consistent and stable membranes (Figure 3.4-6-a,d). AMP/DNA-microcapsules generally appeared to be very translucent (Figure 3.4-6-a) and with a more pronounced and visible membrane, whereas the inside of the microcompartment seemed to be empty. This was specifically bothersome when working with these capsules, as they were hardly visible to the bare eye, even though their large size should make them convenient to see when they are dispersed in solution. Using the fabrication-conditions outlined in the methods (3.3.3), the microcapsules reliably formed at sizes of about 400-500 µm and their shape was rarely uniform. Instead of spheres, most cells rather resembled oval shapes or deformed in several other ways. The reason for this behaviour most likely stems from the way they are fabricated. Since the dsDNA-droplets were launched into the AMP-solution at high speeds, it only seems likely that the collision with the AMP-solution interface would have caused deformation. Once the droplets were immersed in the solution, the complexation of DNA and the organoclay captured this deformed state of the droplet rather than turning into a spherical shape. An interesting aspect of the membrane of these capsules can also be seen in Figure 3.4-6-a, where multiple AMP/DNA-capsules were placed in direct contact to each other. Instead of holding their initial shape, the capsules deformed in response to the contact to their neighbours, which resulted in a close packing of these capsules. This means that the membrane is not stiff but rather soft and deformable. Since the cell is comprised of AMP/dsDNA-complexes, the small intercalating dye acridine orange (10 mM) was used to stain the DNA-strands. This enabled the localisation of the AMP/DNA-complexes via fluorescence microscopy (Figure 3.4-6-b). Surprisingly, the cell not only exhibited fluorescence around the membrane but also inside the cell, which means that DNA can also be found in the cell interior from where it apparently wasn't able to diffuse out through the membrane anymore. In contrast to initial believes that the cells might be

empty, these studies showed a highly crowded molecular environment inside the cell instead. The 3D-image from Figure 3.4-6-c is another representation of this observation.

A core issue of the novel protamine-capsules arose during their formation. When fabricated in a 0.5 mg/mL protamine solution, the capsules had a tendency to accumulate and aggregate on the air/water interface of the solution or on the wall of the glass vial, thus becoming defective and unusable (Figure 3.4-7-b). After adding 3 µL of a 53 µg/mL TWEEN®20 solution, the capsules started to form normally with no loss on neither the meniscus nor the glass wall (Figure 3.4-7-c). TWEEN®20 is a polysorbate-type non-ionic surfactant and is being applied in many different areas as emulsifier or detergent, but also in the food and cosmetic industry due to its low toxicity. [117-119]

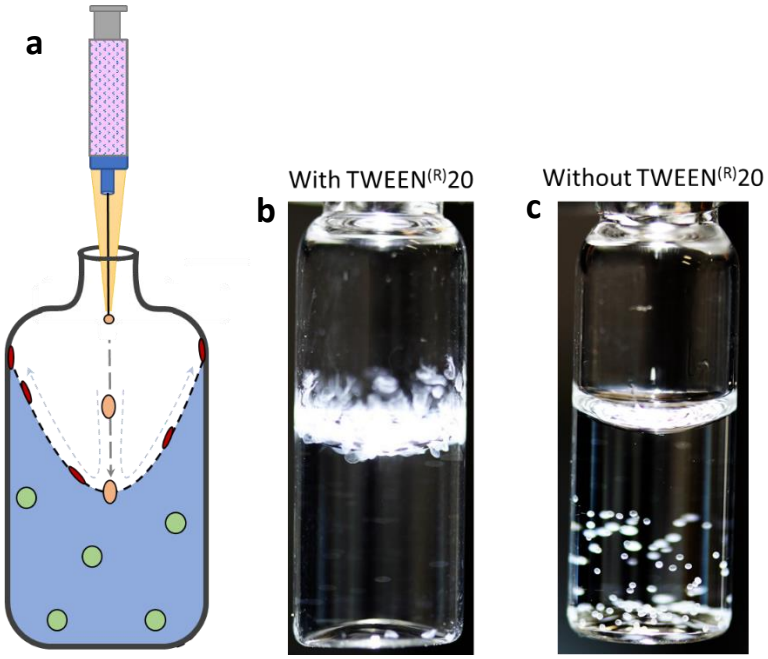

Figure 3.4-7: a *Illustration of protamine-capsule formation and meniscus effect due to the co-axial airstream.* ***Orange****: dsDNA-microdroplets after being ejected from the needle,* ***red****: defective protamine-microcapsules which did not breach through the surface of the protamine solution and settled on the glass wall or meniscus,* ***green****: Viable protamine-microcapsules.* ***b*** *Camera image of microcapsule fabrication using protamine without any additives, capsules do not breach the meniscus and settle on the surface,* ***c*** *when adding a surfactant like TWEEN®20, the capsules are able to breach through the meniscus and become viable.*

Surfactants like TWEEN®20 are known to reduce the surface tension of water, which enables the capsules to traverse through the meniscus much easier, thus explaining the higher viability. [120] Studies furthermore showed, that the addition of TWEEN®20 had no undesired side-effects on the capsule structure, stability or on any encapsulated functional component, especially enzymes and their activity, when used at sufficiently low concentrations.

AMP-capsules were generally stable for long periods of time when kept in 0.5 mg/mL AMP-dispersions but showed decreased stability when kept in water or even buffers, where they started to bloat and fall apart after mere days or even hours. In these experiments, silica particles were used to enhance the contrast of the cell under the microscope, but also to highlight the damages that occurred on the membrane during the experiment. Repetition without silica particles lead to identical results.

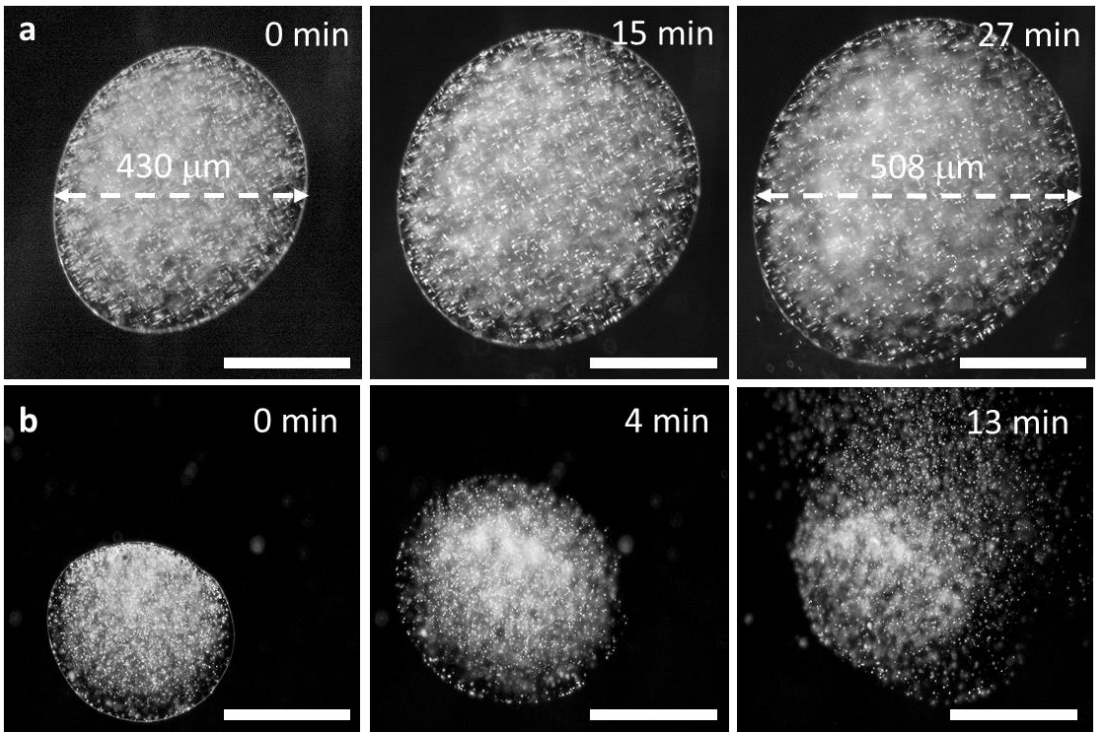

Figure 3.4-8: *Disintegration of AMP/DNA-microcapsules in di-water (**a**) and 50 mM sodium phosphate buffer (**b**). Images were taken with a brightfield microscope and a phase-contrast filter. To enhance the contrast of the capsule to the background, the capsules were fabricated with 4 mg/mL silica microparticles. All scale Bars: 200 μm.*

Figure 3.4-8-a shows an AMP/DNA-capsule after being transferred from a 0.5 mg/mL AMP-clay dispersion into di-water. Even though the cell is not falling apart straight away, it only took about 30 minutes for the cell to bloat up substantially. The membrane became thinner, and the equatorial cell diameter increased from 430 μm to 508 μm. This effect is especially detrimental if it occurs within a population of AMP/DNA-microcapsules like after their fabrication, as they started to stick to one another, and it would soon become impossible to handle them with a pipette without breaking them due to their thin membranes. Changing the solution from water to a 50 mM sodium-phosphate buffer accelerated this process even further (Figure 3.4-8-b). After mere 4 minutes the cell had expanded to a point that the membrane was barely visible anymore and after 6 minutes the membrane started to rupture, which caused the silica particles inside the cell to flow out until the cell structure was completely gone.

Although there are no studies present on the exact mechanism of AMP-capsule disassembly, it can be discussed, nonetheless. The interaction of the AMP-sheets with the DNA-molecules but also between the sheets themselves relies heavily on the pH. Like it was discussed above, protonation of the amino-groups of the clay is necessary to make them repel each other and therefore exfoliate the clay in water. A 0.5 mg/mL dispersion of AMP-clay sheets in water exhibited a pH of 10.35, which kept the cells stable over longer periods of time. Reducing it on the other hand, by exchanging the exterior solution with water for example, changed the pH back to pH 6.9 which in return could cause more protonation and therefore increase the repulsion between the clay sheets or even between the aminoclay and the DNA. Looking at the results of Figure 3.4-8 though, and what seems even more likely, are osmotic effects. It was already shown that AMP/DNA-capsules are containing DNA and therefore most likely also aminoclay-sheets inside their lumen. By changing the exterior solution from an AMP-dispersion to water the osmotic pressure began to rise and water started to diffuse into the

cell to dilute the internal- and equilibrate the overall concentrations. Furthermore, the addition of salt-ions in form of sodium phosphate buffer seemed to accelerate this process drastically, probably also due to interference from the electrostatic interactions of DNA with the AMP-clay sheets.

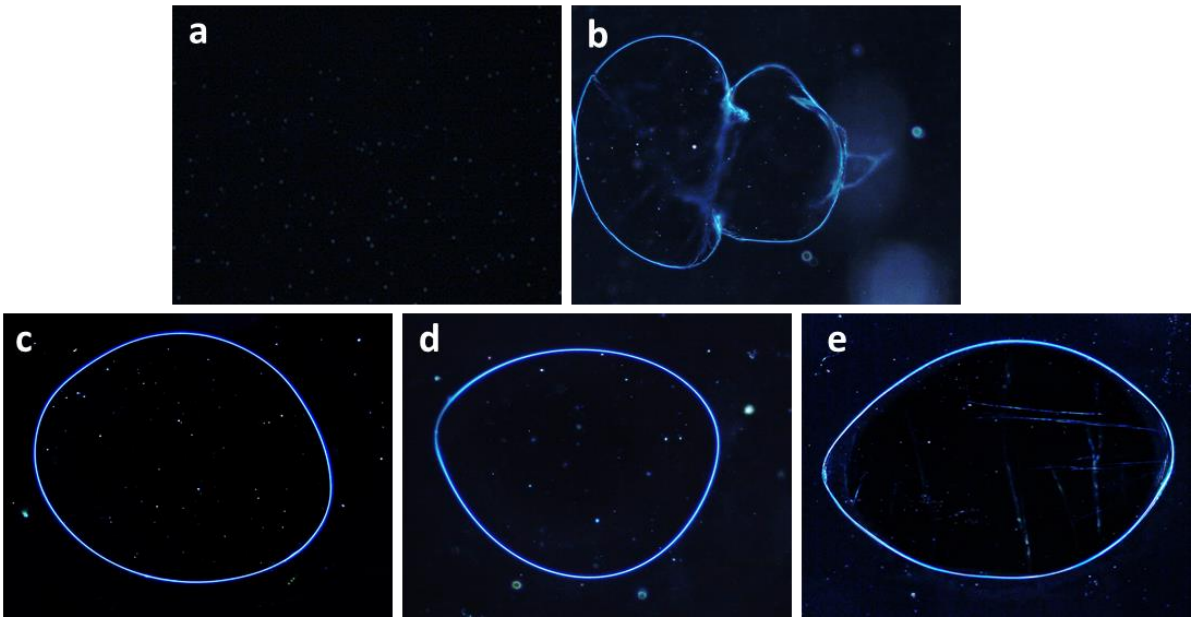

Figure 3.4-9: *Aminoclay-capsules fabricated from 4 mg/mL DNA and various AMP-concentrations: 0.1 mg/mL (a), 1 mg/mL (b), 5 mg/mL (c), 10 mg/mL (d) and 20 mg/mL (e).*

Another important question to ask is the influence of the AMP- and the DNA-concentration during the fabrication of the cells. Here, the aminoclay-concentration was varied between 0.1, 1, 5, 10 and 20 mg/mL and the resulting cells were examined via optical microscope (Figure 3.4-9). Aminoclay-concentrations of 0.1 mg/mL and lower (Figure 3.4-9-a) did not lead to any microcapsule formation, but only a cloudy dispersion. With such a low concentration of the AMP-clay, it most likely takes too long to stabilise the dsDNA-droplet, which causes the droplet to disperse in the solution before the complex can form. A concentration of 1 mg/mL (Figure 3.4-9-b) lead to the formation of cells but with very noticeable deformations and defects, which can be explained similarly to the case before. 5 mg/mL (Figure 3.4-9-c) appeared to be the first concentration under which consistent AMP/DNA-microcapsules were fabricated without any defects. On the other hand, increasing the aminoclay-concentration even further to 10 mg/mL (Figure 3.4-9-d) or even 20 mg/mL (Figure 3.4-9-e) did not change the quality of the capsules or even their appearance.

Protamine/DNA-microcapsules on the other hand showed a much different set of properties. The capsules appeared much duller than the AMP/DNA-microcapsules, which can be seen by the blue tint of the cell interior in Figure 3.4-6-d. The cells were a lot easier to see with the bare eye and appeared to be heavier as well, as they tended to take less time to sediment. What was most surprising, is the fact that protamine/DNA-microcapsules were almost uniformly spherical and much more monodisperse than AMP/DNA capsules, when using a protamine-concentration of 0.5 mg/mL for their fabrication. Another interesting feature of these cells is a debris like cluster which could be found inside every protamine/DNA-capsule. Most of the time this debris was found accumulated on one side of the cell like it is shown in Figure 3.4-6-d. Again, acridine orange (10 mM) was used to localise the DNA inside the microcapsules, which were then analysed via confocal microscopy. Here, important information was found which confirmed the origin of the debris-like structures inside the cells. As it can be seen in Figure 3.4-6-e, the stained DNA is not only visible all along the cell membrane, but also

inside the debris clusters, which proves that the debris is just an aggregation of protamine/DNA-condensate. When the cells are formed inside the protamine-solution, the first DNA-molecules to be condensed by protamine are the ones at the very interface of the microdroplet, which could lead to the following hypothesis: As the membrane starts forming, more and more DNA is being drained from the droplet-interior and accumulated into the membrane, whereas the DNA-molecules from the centre of the droplet are the last ones to be condensed. At this point, the membrane has almost finished forming and protamine molecules are also penetrating the newly formed cell. Finally, the last DNA-molecules will form protamine/DNA-condensates but instead of being incorporated into the membrane, they condense and accumulate inside the cell. The forces from the vortex-like current inside the vial during the fabrication of the cells could then lead to the debris being accumulated on one side of the capsule. This goes hand in hand with another interesting result, which is that protamine/DNA-capsules appear to be hollow. The acridine orange staining experiments only showed a bright fluorescent membrane, but no fluorescence inside the cell (Figure 3.4-6-e,f), which proves that there is no excess DNA inside the cell like it was the case for the aminoclay-capsules. Again, this can be explained by the fact that all DNA inside the cell has already been condensed, leaving no or only very little free macromolecules.

Parallelly the stability of protamine/DNA capsules in different solutions was investigated. Di-water was chosen as the first solvent to test and the capsules appeared to be very stable. Even after several washing steps not one of the protamine/DNA-capsules seemed to be deformed or expanded. Figure 3.4-10-a shows protamine capsules in di-water after a 60 minute incubation period after which no deformations were registered, neither at the start, nor during the 60 minute incubation. And indeed, even when left for several days, the capsules retained their structure. When changing the medium to a 50 mM sodium phosphate buffer, the capsules showed some deformation along the membrane, which usually came in form of little dents. In most cases, the capsules would revert back to their original spherical structure over time. In some other cases, like the one in Figure 3.4-10-b, the capsule slowly but not completely recovered from the deformation. Assuming the deformation stems from a change of osmotic pressure due to the environmental change from di-water into the buffered medium, it can be assumed that the pressure decreased over time, as the small buffer molecules should most likely penetrate the cell-membrane and eventually equilibrate the concentration gradient between the inside and outside the capsule. Since the introduction of sodium phosphate also drastically changed the ionic strength, it might furthermore alter the interaction between DNA and protamine, which in return could lead to structural changes that cannot be reverted over time. This is only an assumption though and would need more studies to validate. The quintessence from this experiment, especially regarding the further work in this thesis, is that protamine/DNA-capsules appear to be far superior when it comes to structural stability in different media. The mere fact, that protamine/DNA-capsules are stable in water and do not need any stabilising agents like AMP/DNA-capsules do, makes them far more convenient to work with.

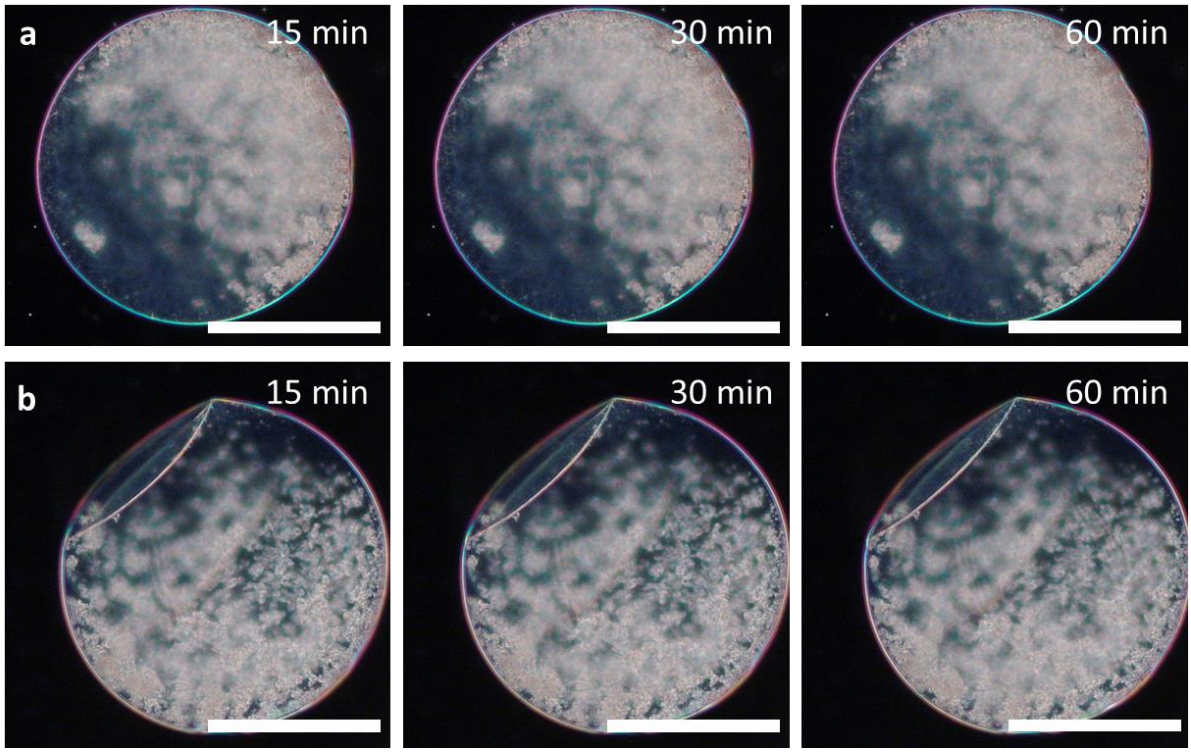

Figure 3.4-10: *Optical micrographs of protamine/DNA-microcapsules in di-water (**a**) and sodium phosphate buffer (50 mM) (**b**). Images were taken over a time of 60 minutes to observe structural changes of the microcapsules. All scale bars: 300 µm*

One issue of the fabrication method used for these microcapsules is that it is very hard if not impossible to observe the actual formation process because of the speed of the ejected microdroplets, the turbulence of the protamine solution due to the applied airflow and the constant motion of the newly formed cells. For the same reason it was also impossible to follow the formation of the white precipitate-aggregate inside the capsules, but it is not impossible to draw conclusions from alternative experiments. Here, a different approach will be pursued by investigating different protamine concentrations during the formation of the microcapsules. If the precipitate originated from condensed DNA, then a change should become observable when changing the protamine concentration, as this should alter the speed of DNA-condensation altogether. Figure 3.4-11 shows the results of microcapsules formed from 4 mg/mL DNA and 0.1, 0.5, 1, 2, 5 and 10 mg/mL protamine-solutions. All cells in the coming chapters of this thesis were fabricated under 0.5 mg/mL conditions, as this appeared to be the lowest protamine concentration to form consistent and stable protamine/DNA-capsules (Figure 3.4-11-e). Going below this concentration, microcapsules were still forming on the interface, but they tended to aggregate into large cell clusters while becoming very unstable (Figure 3.4-11-f). Reducing the protamine concentration led to slower condensation speeds and therefore weaker membranes. Since the membranes did not fully develop, they not only tended to exhibit defects or break, but the capsules also started to stick to each other and even the glass walls of the vials, where they formed large clusters. This can be explained either by the excess non-condensed DNA, which could leak out of the cells due to the slow condensation speeds and cause the capsules to crosslink or because of the soft labile membranes, which stick to each other because of non-specific soft matter interactions. Increasing the protamine concentration to 1 mg/mL (Figure 3.4-11-d) showed little to no difference in comparison to 0.5 mg/mL. Once it was increased further though, some very interesting structures inside cells became apparent. Instead of a scattered precipitate, at 2 mg/mL (Figure 3.4-11-c) a second, sub-compartment-like structure inside the outer

membrane was found. At this point it can only be assumed if this truly is another membrane or maybe some form of “coacervate-like” phase separation. Another interesting observation is the opacity of the outer membrane. At lower concentrations, the membrane of protamine capsules always exhibited a certain dullness, whereas AMP/DNA-capsules in comparison almost looked completely translucent. At 2 mg/mL protamine on the other hand, the outer membrane looked much clearer and less cloudy. In fact, it almost looked like the dull part of the outer membrane has been condensed into a secondary compartment-entity inside the cell, whereas the white protamine/DNA-precipitate was now located in this second substructure. Increasing the protamine-concentration to 5 mg/mL (Figure 3.4-11-b) now showed another layer. Instead of 2 structural compartments there were now 3. The outer membrane was still existing, but there was now a third, membrane like structure, almost detaching and separating from the outer membrane. Again, the opacity from the outer membrane became lower, whereas the second membrane exhibited a dull blue tint. The third sub-structure, which was already visible for 2 mg/mL, still existed with the white protamine/DNA-precipitate inside. Finally, in case of 10 mg/mL there were now 3 clearly separated compartments which were hierarchically encapsulated inside each other.

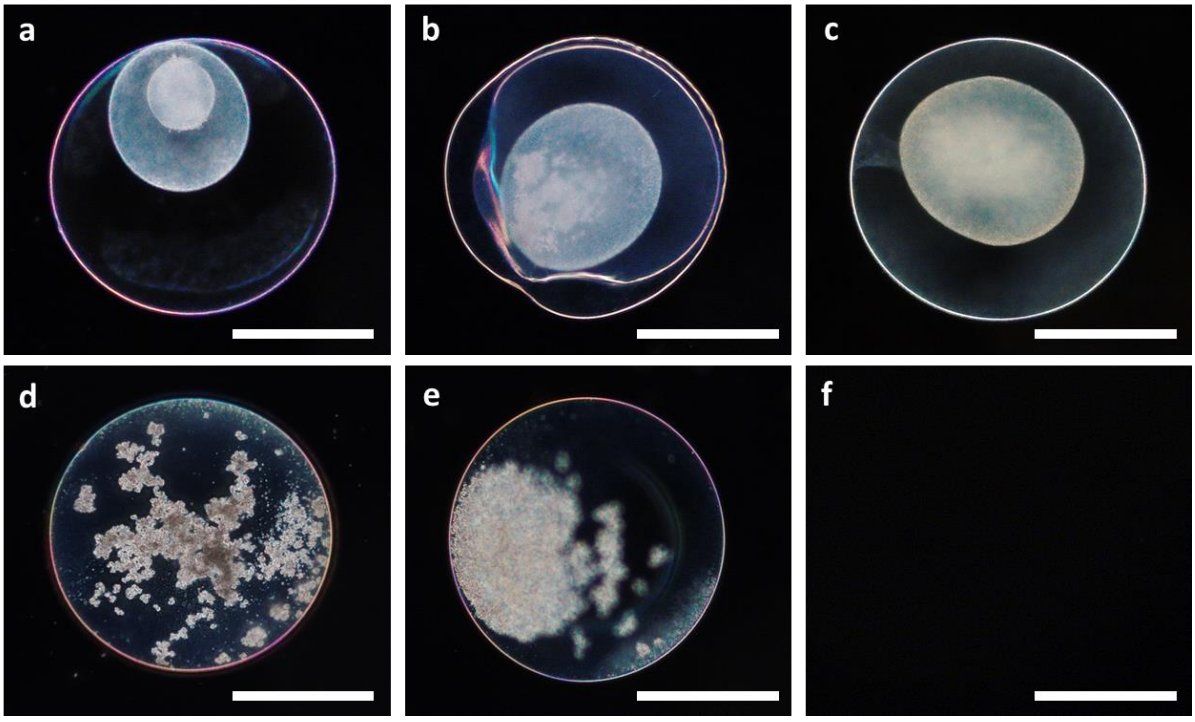

Figure 3.4-11: *Optical micrographs of protamine/DNA-microcapsule formation* ***a*** *10 mg/mL,* ***b*** *5 mg/mL,* ***c*** *2 mg/mL,* ***d*** *1 mg/mL,* ***e*** *0.5 mg/mL and* ***f*** *0.1 mg/mL protamine solution and 4 mg/mL DNA. All scale bars: 200 µm.*

This experiment poses some interesting questions but also answers a few. As it was assumed, the capsule formation is highly dependent on the protamine concentration. Since the fabrication of the protamine/DNA-microcapsules was already done at the lowest possible protamine concentration (0.5 mg/mL), it can be assumed that it is impossible to prevent the formation of the protamine/DNA-clusters inside the cells. Furthermore, it can only be hypothesised how the structures at higher protamine-concentrations formed, but it seems logical to look at the condensation speed as the primary cause. The higher the protamine-concentration, the faster the DNA inside the droplet condenses, which then forms the membrane and the substructures described above. What is important, and given enough time, is that once a structure has formed it cannot be reversed or converted into a different one. For example, transferring a capsule made from 0.5 mg/mL protamine

into a 10 mg/mL protamine solution did not cause the formation of the respective substructures anymore, instead the capsules stayed the same. This means, that the formation of said substructures happened in the very first moments of the cell fabrication and is very much relying on the condensation speeds. This also gives a strong implication, that the material which is used to form the sub-compartments at higher concentrations is still very much embedded in the membrane at lower concentrations (0.5 mg/mL, 1 mg/mL). One reason, why different layers of condensation were observed could be the composition of the DNA. The DNA used for the fabrication of the cells contains a range of different sizes with a predominant size of 2000 base pairs or 1.3 million Da, which in return lead to different condensation speeds in contact with protamine, even though the exact weight-distribution was not given by the distributor. At higher protamine concentrations, the larger molecules condensed slower than the smaller ones, but fast enough to separate from the other compartments. At the same time, it seems questionable though why a diffuse mixture of different lengths of DNA strands would form such distinct condensate structures. Either way, it is an interesting model of DNA-condensation, as it not only forms cell membranes but also, almost nucleus-like sub-structures which very much resembled real eukaryotic cells.

Increasing the protamine concentration even higher still led to the formation of protamine/DNA-capsules but without any further distinction or new features (Figure 3.4-12). Instead, the surrounding solution was found to turn cloudy while the DNA-droplets entered the protamine solution. The turbidity lasted for 3-5 minutes before turning clear once more. Under the microscope little spherical droplets were observed next to the large capsule, which started to vanish or coalesce after a short amount of time. Compared with other systems, these small droplets resembled those of liquid-liquid phase separations, or "*coacervates".* Even though there was no direct interest for the further work of this thesis, it would be an interesting find, nonetheless. The phase separation of coacervates normally relies on electrostatic interactions of oppositely charged molecules like ATP and PDDA. In this case though, while satisfying the condition of being of opposite charges, DNA and protamine exhibit much stronger interactions than most cations and anions, which should normally lead to precipitation instead of coacervation.

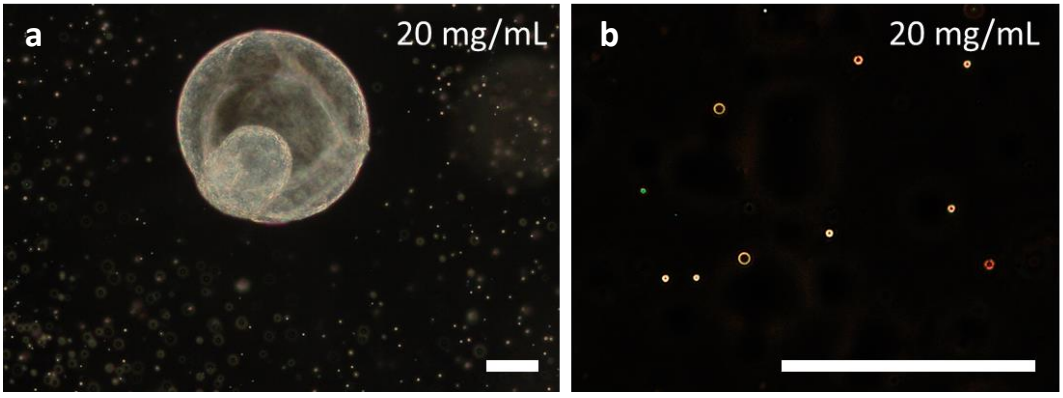

Figure 3.4-12: *Optical micrographs of protamine/DNA-microcapsule formation with 20 mg/mL protamine and 4 mg/mL DNA.* ***a*** *Protamine/DNA-microcapsule and* ***b*** *coacervate-like droplets. Scale Bars: 100 µm.*

While the chemical stability of the capsules has been assessed above, the physical, or more specifically the thermal stability, has not been investigated yet. Figure 3.4-13 shows image sequences of both AMP/DNA- (taken with consent from Kumar *et al*. [1]) and protamine/DNA-microcapsules, which were fabricated and stained with 10 mM acridine orange.

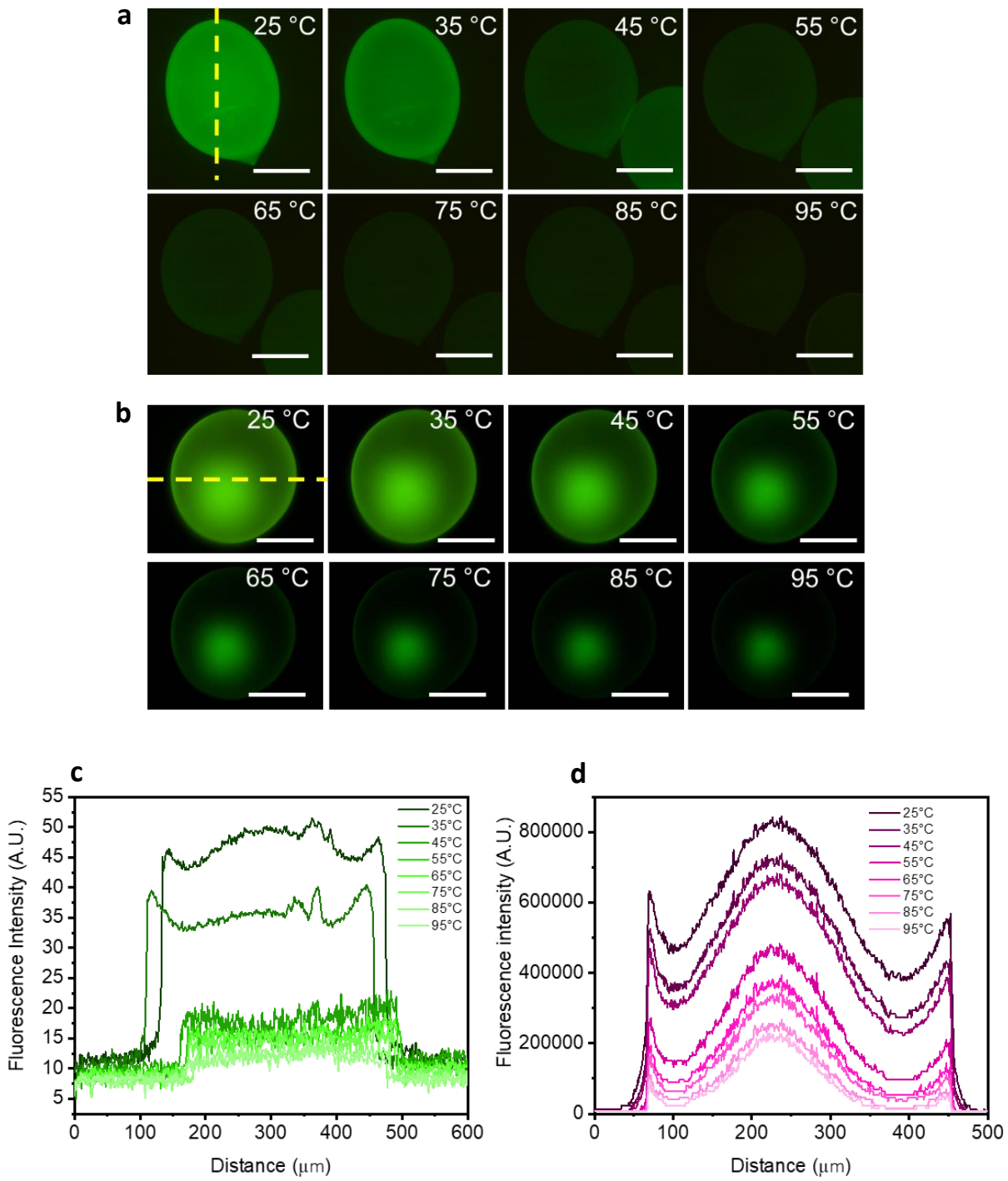

Figure 3.4-13: *Temperature-stability tests of microcapsules. Fluorescence micrographs of acridine orange-stained AMP/DNA- (**a**) and protamine/DNA-microcapsules (**b**) were taken on a heat-stage which slowly ramped up the temperature from 25°C to 95°C. Images were taken in 10°C intervals after a 5 minute incubation, each time a new temperature mark was reached. All scale bars are 200 µm. A linear cross section (yellow line) was used to plot the fluorescence intensity for each frame. The results of the fluorescence intensity plots are displayed for AMP/DNA-(**c**) (taken with consent from Kumar* et al. *[1]) and protamine/DNA-capsules (**d**).*

The capsules were examined under the fluorescence microscope and attached to a heat-stage, which enabled temperature control from 25 to 100°C. To visualise the stability of the capsules, the fluorescence intensity was plotted via line-profile and superimposed over 8 different temperatures (Figure 3.4-13-c and d). AMP/DNA-microcapsules (Figure 3.4-13-a) showed only a minor decrease in fluorescence from 25°C to 35°C but then exhibited a maximum decrease from 35°C to 45°C. After that,

the fluorescence intensity decreased further but only minorly. The capsules themselves did not appear to change structurally at all, even at hight temperatures of 95°C. This shows that the capsule structure seemed to be quite resilient to thermal changes. Nonetheless the loss of fluorescence intensity needs to be addressed and most likely stemmed from melting of dsDNA to single stranded DNA. Acridine orange is an intercalating dye, which means it is able to bind electrostatically in-between the nucleotide base-pairs of double stranded DNA. So, once the double strands of the DNA are starting to break, acridine orange is leaking out as it cannot intercalate between the base pairs anymore. This would also put the dsDNA melting temperature somewhere in between 35°C and 45°C. In case of protamine/DNA-microcapsules the results were slightly different. Between 35°C and 45°C, the fluorescence intensity appeared mostly stable and only deteriorated a little. After that, the intensity dropped by a larger amount and then steadily decreased from 65°C to 95°C. Although both capsule-systems utilise the same dsDNA as a structural component, the melting-points of the DNA seemed to be slightly shifted. The most likely explanation for this behaviour is the fact, that protamine is not only binding but condensing and packing the DNA into a tighter form. This makes it even more difficult to discuss the experiment, since a second physical effect needs to be addressed as well. Due to the condensation, the double stranded DNA appeared to need more thermal energy to break into single strands. Once this happened, acridine orange is released, although the release did not happen suddenly after a certain temperature, but steadily. Another possible explanation for the progressive decrease in fluorescence could be that there are multiple stable states of condensed DNA. Depending on the stability of the DNA/protamine condensate, the DNA then exhibited different melting temperatures which lead to a progressive release of the fluorophore along the temperature ramp. Another noticeable feature to point out is the little circle in the centre of the capsule which exhibited a much higher fluorescence intensity and which also stayed fluorescent much longer compared to the membrane. This spot is the same dsDNA/protamine-aggregate which was described in Figure 3.4-6. Due to the aggregated nature, it became and stayed much brighter through the fluorescence microscope, whereas the rest of the capsule started to fade.

While DNA can easily be stained by intercalating agents like acridine orange, it is a bit more difficult to highlight the cationic materials AMP and protamine. Here it was attempted to tag them with the blue-fluorescent dye Dylight-405. For the organoclay, the attempts failed as the clay started to precipitate after the tagging-reaction and was not able to exfoliate anymore, which made it useless for capsule formation. In case of protamine, the protein was stable after the tagging and was still capable of forming capsules, nonetheless the resulting capsules appeared much different than usual. As seen in Figure 3.4-14 the resulting capsule showed an almost cell-nucleus like phase inside, which resembled the results from Figure 3.4-11. Dylight-405 is an NHS-ester based structure, which means it reacts primarily with free amine groups on protamine. Looking back at the amino acid sequence of protamine, all amino-groups stem from arginine residues, which also play an important role in the DNA-condensation. Even though NHS-chemistry works best for primary amines, it should also work in case of arginine, which contains secondary amine residues. [121] Assuming the coupling reaction of the fluorophore to arginine groups is successful and the fluorescence is not merely originating from adsorbed fluorophores on the cell-membrane, this should drastically reduce the interaction of the tagged protamine with the DNA as the active arginine groups are blocked by the Dylight-405-moelcules. What was seen though, is a nucleus-like condensate, which was originally only found in cases where the protamine concentration was increased, which means the activity was higher. This could mean that the mechanisms at play in this experiment are different to the ones from Figure 3.4-11, or that the explanation above is lacking after all. Either way, it has been shown that an alteration of the active protamine concentration has a big impact on the structure of protamine/DNA-microcapsules, so it is not surprising that a similar change was found in this experiment.

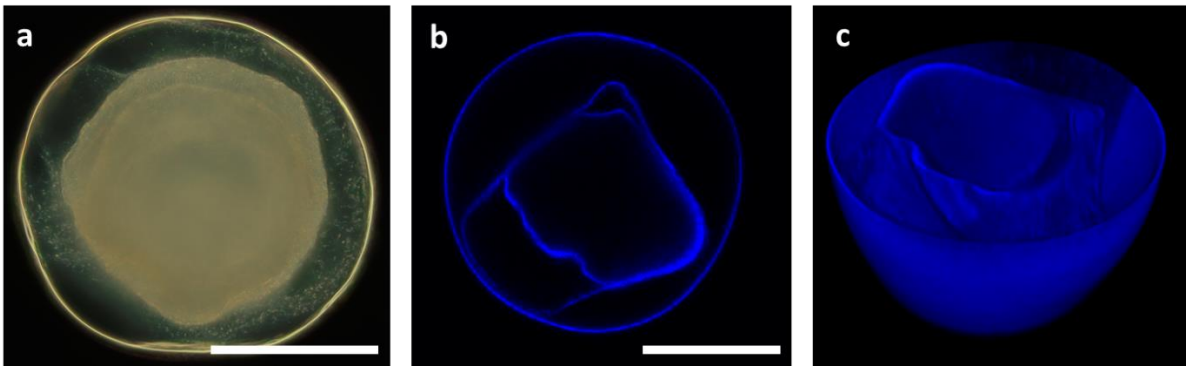

Figure 3.4-14: *Confocal-microscopy of Dylight-405-tagged protamine used for the formation of protamine/DNA-capsules.* ***a*** *brightfield image,* ***b*** *fluorescent microscopy image and* ***c*** *3D-Z-stack of Dylight-405-protamine/DNA-capsule. All Scale Bars: 200 µm.*

Next, the size of the microcapsules was investigated, which was primarily defined by the size of the microdroplets. When fabricated under the conditions described in the methods (3.3.3) the size distribution from a sample size of 300 capsules looked as described in Figure 3.4-15. Although both capsule systems were fabricated under the same conditions, the results exhibited drastically different sizes. By average, AMP capsules were roughly 134% larger in diameter than the corresponding protamine capsules. Furthermore, the size distribution per batch is rarely monodisperse, instead standard deviation of 53 µm was calculated for protamine- and 55 µm for AMP-capsules. While it is interesting that both exhibit almost identical deviations, it makes sense considering the capsule size is purely reliant on the size of the ejected microdroplets, which are similar in both cases.

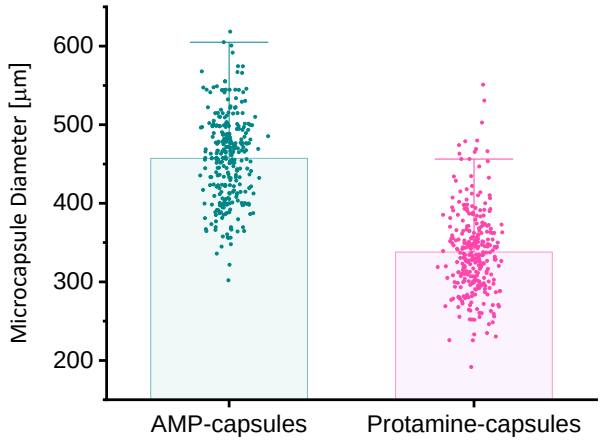

Figure 3.4-15: *Size distribution of AMP- and protamine microcapsules under standard fabrication parameters: 2.1 L/min airstream, extrusion of 20 µL at 10 µL/min, with 4 mg/mL DNA and 0.5 mg/mL protamine-solution or 5 mg/mL AMP-dispersion.*

Even though this experiment explains the size distributions, it is not sufficient to understand why protamine/DNA-capsules appear to be smaller. To discuss this phenomenon more properly, another experiment was conducted, in order to understand the change in size, not only between AMP- and protamine capsules but also between the droplet diameters before and after they reach the cationic solution. The problem when trying to understand the size of the microdroplets though is, that they only exist in the brief moment between being ejected from the syringe and traversing the air-liquid interface. One could capture them with a high-speed camera, but even then, their geometries would

be deformed due to the forces applied to them and the friction they experience mid-air. So instead of capturing them while they are being accelerated, the experimental setup was adjusted by modifying the vial which originally contained the cationic solution underneath. Here, the vial opening was covered with a thin PTFE-membrane, which formed a smooth and even surface. Polytetrafluoroethylene, or PTFE, is a compound which is known for its low wettability in case of water or aqueous solutions, which means that small droplets exhibit very large contact angles and ultimately maintain a highly spherical geometry (Figure 3.4-16-b). Literature has determined the contact angle of water on a PTFE-surface to be about 106.94°, which is still far away from the purely theoretical maximum contact angle of an ultra-hydrophobic surface of 180°. Nonetheless, it suffices as an approximation to compare the droplet structure and diameters to the ones of the microcapsules. The droplets were formed under the conditions described in the methods (3.3.3) and ejected right onto the PTFE-membrane, which was placed in front of a horizontally-positioned optical microscope. (Figure 3.4-16-c).

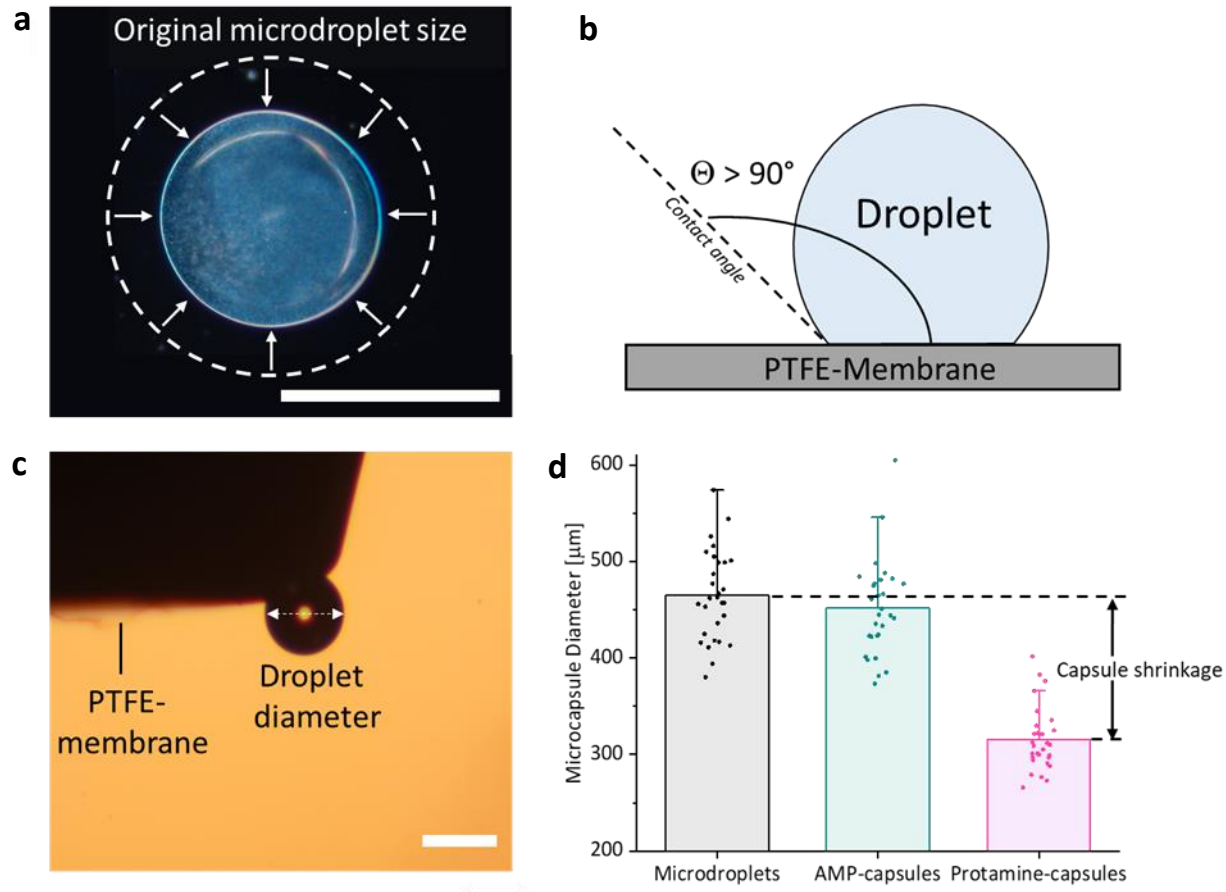

***Figure 3.4-16: a** Optical microscopy image of a protamine capsule and schematic illustration of capsule shrinkage during formation, **b** Illustration of the contact angle of a water-droplet on PTFE-membrane. **c** Optical microscopy image of a PTFE-film, wrapped around the neck of a 1.7 mL glass vial with a dsDNA-microdroplet on top. **c** Size distribution of dsDNA-microdroplets, AMP- and protamine capsules. Scale bars: 400 µm.*

AMP- and protamine capsules were fabricated under identical conditions to compare their sizes to the DNA-droplets. Figure 3.4-16-d shows the results in form of a bar-plot which summarizes the diameters of 30 different droplets and capsules. AMP-capsules shrank by about 3% on average, which is fairly little and can easily be explained by the fact that the complexation of AMP and DNA leads to a tighter packing of the materials due to the attractive electrostatic forces of the aminoclay and DNA, which in return yields slightly smaller capsules. In case of protamine-capsules though, a roughly 32% decrease

in diameter was observed, which is most likely the result of the DNA-condensation. Again, DNA-condensation leads to a much tighter packing of dsDNA, which therefore occupies a much smaller space and contracts the membrane so that the diameter during the formation of the microcapsule progressively shrinks until all DNA-material has been condensed.

Both protamine/DNA and AMP/DNA-microcapsules show many differences when compared to other protocell-systems, even though one stands out the most, which is their large size. With diameters of about 300-500 μm, these capsules are often 10 times larger than most other cell systems, which usually are in the size-ranges of 25 μm (e.g. Coacervates [83] and proteinosomes [73]) – 100 μm (e.g. Colloidosomes [122]). This enormous size difference also prevents them from being used in many aspects of protocellular research and applications, which often rely on much smaller cell-sizes. So, in order to reduce the capsule size, the plastic nozzle from the microcapsule-fabrication device was redesigned, effectively reducing its diameter from 1.93 mm to about 0.1 mm. This way, the air-flow is funnelled even more to achieve a higher air-pressure and larger shearing forces at the tip of the needle to make smaller droplets. Figure 3.4-17 shows the results for both protamine- and AMP-capsules in form of a bar-plot that summarizes the diameters of 100 AMP/DNA and protamine/DNA microcapsules.

The resulting capsules were found to be much smaller than their large counterparts described in previous experiments, with sizes all the way down to 20 μm in diameter (Figure 3.4-17-d). Small AMP/DNA-capsules had an average size of about 70 μm and were about 22% larger than the average protamine capsule. While the size difference between the two cell systems is not as large as in Figure 3.4-16, the fact that protamine capsule turned out to be smaller goes hand in hand with the explanation given above for large microcapsules.

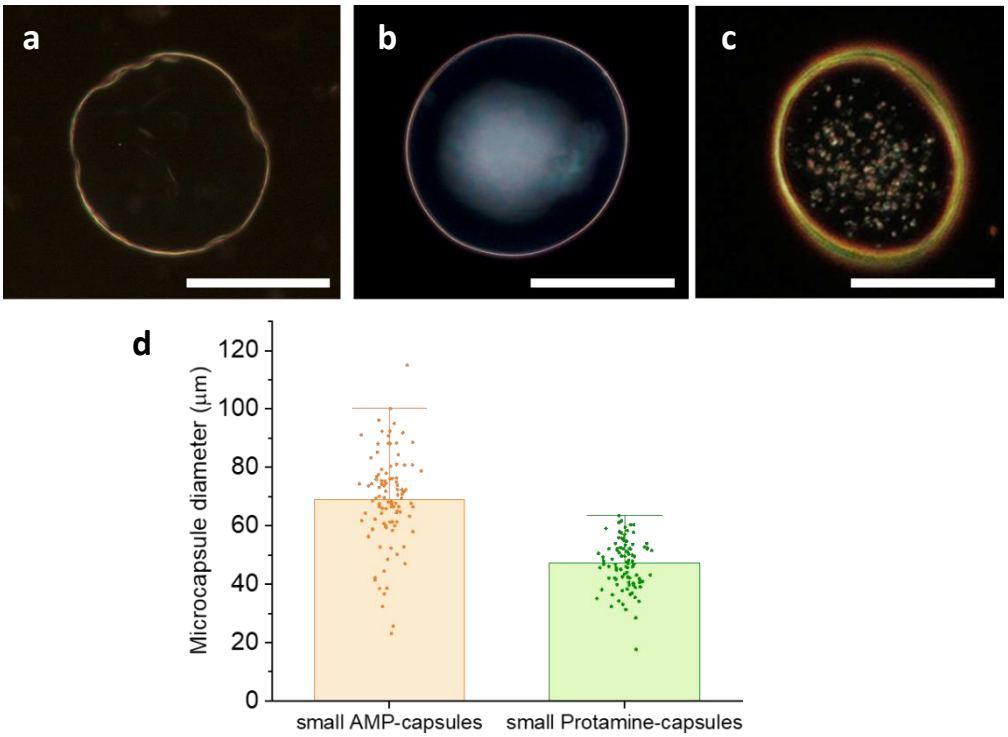

Figure 3.4-17: ***a*** *small AMP-microcapsule,* ***b*** *small protamine microcapsule with DNA-condensate aggregate,* ***c*** *small protamine microcapsule without DNA-condensate aggregate but small, randomly diffusing particles,* ***d*** *size-distribution of small protamine/DNA and AMP/DNA microcapsules: sample size: 100 small microcapsules. 5 mg/mL silica particles were added for the fabrication of each capsule system. Scale bars: 50 μm*

Visually, small AMP/DNA-capsules appeared very similar to the large capsules, even though some of them exhibited a rougher surface. Their membrane was very translucent, and the cells are hardly visible to the bare eye. Small protamine/DNA-microcapsules on the other hand appeared a lot smoother and very similar to their large counterparts. Interestingly, some cells contained the typical DNA-condensate aggregate, whereas others did not. Instead, small particles were observed, which were randomly diffusing inside the cell interior. These particles are most likely the same DNA-condensate which was normally aggregated on one side of the capsule but were now freely moving through its interior (Figure 3.4-17-c). Since the capsule size was now much smaller, it was not possible anymore to distinguish between the capsules with the bare eye. What was found instead is best described by a turbid dispersion, which resembled a snow globe. Unfortunately, this also decreased the convenience of the fabrication, as it now took substantially longer for the capsules to sediment before they could be washed. Another problem that came to light was an increase in microcapsule stickiness, which was specifically apparent for protamine/DNA-capsules. These capsules have always been stickier towards other capsules or materials than AMP/DNA-capsules and making them smaller only increased this effect. Due to the higher air-pressure at the location where the droplets are ejected, it seems likely that they experienced much higher speeds before reaching the air-liquid interface. Droplets might even be sheared multiple times or break upon impact with the liquid-interface, as there was a large amount of debris in form of small floaters after both AMP/DNA- and protamine/DNA microcapsule fabrication. On top of that, the higher air-pressure caused much larger turbulences inside the cationic solution, which in return could cause more defects on the capsules as they traverse the interface. These defects, the debris, along with what looked like a rougher surface (Figure 3.4-17-a) compared to the large capsules, could lead to more unspecific interaction between the capsules and therefore stickiness. In order to somehow circumvent this issue, a small amount of silica particles (5 mg/mL) was incorporated into the capsules by mixing them with the DNA-solution, which can be seen as small dark dots inside the capsules (Figure 3.4-17-a,b). The particles mainly served as additional weight to help the capsules sediment faster and to make them easier to see without a microscope, but it also appeared to improve the issues with the stickiness, as capsules formed less aggregates than before.

In combination with the general flaws of the fabrication device mentioned above, this way of producing small aminoclay- or protamine-microcapsules is far from perfect and it needs a lot of time to assemble the device and align it properly. Nonetheless, it proves that it is possible to scale the microcapsule system down to much smaller sizes which could enable a larger repertoire of applications.

3.4.3 Entrapment of functional components into AMP/protamine microcapsules

One of the core functions of the microcapsule systems is the ability to encapsulate or entrap functional components. The membranes of both capsule types are semi-permeable and will be further investigated in the next part of this chapter. This means, that once the capsules have been formed, it seems unlikely that functional components like enzymes or particles can traverse into or out of the capsule. For this reason, it is necessary to add these components during the fabrication, so they will be enclosed and encapsulated into the capsule while it is forming. Here, enzymes and particles were simply mixed with the DNA-solution to form functional microdroplets the same way it was described above, which offered an easy and fast way to produce functional microcapsules.

To prove the flexibility of this system, a variety of different materials was tested, which are highlighted in Figure 3.4-18.

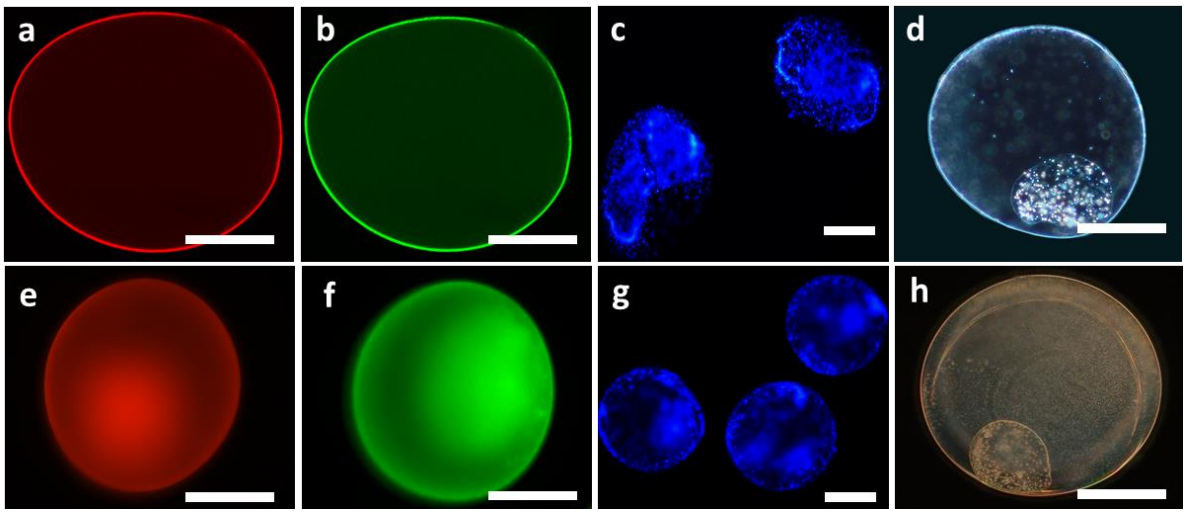

Figure 3.4-18: *Fluorescence micrographs of entrapment of different components into protamine and AMP-microcapsules. (**a-d**): AMP-microcapsules, (**e-h**): protamine microcapsules: **a** RITC-tagged glucose oxidase, **b** FITC-tagged catalase, **c** blue-fluorescent microparticles **d** AMP-microcapsules **e** RITC-tagged glucose oxidase **f** FITC-tagged catalase, **g** blue-fluorescent microparticles **h** AMP-microcapsules. All scale-bars: 200 μm*

First, it was attempted to encapsulate a large variety of different enzymes which find wide usage in most labs, ranging from BSA, catalase over glucose oxidase, urease to horseradish peroxidase. The images from Figure 3.4-18 show the encapsulation of enzymes with the examples of RITC-glucose oxidase (Figure 3.4-18-a,e) and FITC-catalase (Figure 3.4-18-b,f). Encapsulation of enzymes is especially important for the studies in the next chapter, as this enabled the functionalisation and establishment of enzyme cascade reactions within the microcapsule-compartments. Larger components were encapsulated in form of fluorescent polymer-microparticles (Figure 3.4-18-c,g) or silica microparticles, like it was already mentioned previously. Silica particles were generally encapsulated to increase the weight of the capsule and to accelerate the sedimentation which, in return, drastically improved the convenience in working with the cells, but other particles like functional nanoparticles, magnetic particles or fluorescent particles for imaging were successfully entrapped as well. Interestingly, it was also possible to entrap smaller capsules within larger capsule hosts. Figure 3.4-18-d and Figure 3.4-18-h show two cases of small AMP-capsules within larger AMP/DNA- and protamine/DNA-hosts, which presents a second level of compartmentalisation within this capsule system. These hierarchical structures of microcapsules will be studied at a later point within this thesis (see part 3.4.6).

Another important information, when looking at the entrapment of functional components is the actual estimated concentration per cell. One way to calculate an approximation for this value is by counting the number of cells which are fabricated per batch. As a reference, most cell studies in this thesis were done under very similar conditions. The cells were consistently fabricated in batches by ejecting 20 μL of dsDNA-solution and to create cell-sizes of 400 μm in diameter. With these parameters being constant, it was possible to calculate the overall number of cells per batch by simply counting the number of cells in an evenly mixed fraction of the whole cell dispersion and then averaging the overall number. Figure 3.4-19 summarizes the averaged cell-count of 10 different batches. Since the overall cell-count per batch is solely depending on the number of ejected DNA-droplets, the number can account for both protamine/DNA- and aminoclay/DNA-microcapsules.

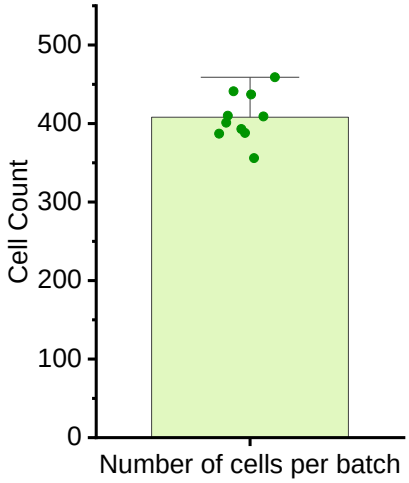

***Figure 3.4-19**: Statistical analysis of the number of capsules per batch. Each batch was fabricated from 4 mg/mL dsDNA which was ejected with 20 μL per batch and to fabricate cell sizes of 400 μm in diameter.*

So, by average, each batch is comprised of about 408 cells. With this number, it is possible to approximate the concentration of encapsulated components per cell. Again, most experiments in this thesis have been performed under similar conditions, which is why we can assume the following fabrication-conditions for these exemplary components: 20 mg/mL silica particles, 2.9 kU/mL glucose oxidase and 19.8 kU/mL catalase. This leads to an average concentration per cell of 0.98 μg silica particles, 0.14 U GOx and 0.97 U catalase per protamine- or aminoclay capsule. These calculations are all under the assumption that all functional components are indeed incorporated into the cells and do not leak out during the formation or afterwards.

It seems unlikely though, that all enzymes would be incorporated into the cells and leakage is a phenomenon, which will be discussed at many points within this thesis. So, to get a better understanding of enzyme-leakage during the fabrication of the cells, glucose oxidase was tagged with FITC and encapsulated into protamine capsules. Since protamine-capsules played a much more important role for the coming chapters, and also due to a lack of time to repeat this experiment, AMP-capsules have not yet been investigated under the following experimental protocol to assess the enzyme leakage during the fabrication. All capsules were generally prepared as described in 3.3.3 and by adding a varying amount of FITC-GOx to the dsDNA-solution (2, 5, 10, 16 mg/mL). After injecting 20 μL into the protamine-solution, the capsules were removed, and the fluorescent FITC-tag was used to determine the amount of enzyme which leaked from the droplets or the cells into the supernatant with a UV/VIS-spectrometer ($\lambda_{Excitation,FITC}$ = 495 nm). To be able to calculate the actual amount of enzyme per cell, a calibration-curve was prepared by screening a variety of FITC-GOx-concentrations at $\lambda_{Excitation,FITC}$ = 495 nm (Figure 3.4-20). The leakage was then calculated for every FITC-concentration, which further enabled the derivation of the amount of enzyme per capsule and the percentage of leaked enzyme, which is summarised in Table 3.4-1. Since it was necessary to know the number of cells which were produced in each batch, the capsule count from Figure 3.4-19 was implemented into the calculations. And indeed, in all cases it was possible to measure a noticeable amount of FITC-GOx which leaked into the surrounding solution during and/or post fabrication. The amount of the entrapped FITC-GOx increased with the concentration almost linearly, which shows, that protamine-capsules can most likely retain much more enzyme than the established protocols in this thesis have used so far. What is interesting though, is that the amount of leakage seemed to be fairly similar between 16-5 mg/mL FITC-GOx. Over three experiments and for each concentration, an average of ~33% of the original FITC-GOx leaked off the cells. On the one hand, the amount of leakage seemed

to increase with higher FITC-GOx concentrations, which makes sense as the capsules will have a limit to how much they can bind, and the more enzyme is being added, the more likely it will become that not all of it will be adsorbed. On the other hand, the leakage also seemed to increase with lower FITC-GOx-concentrations. This observation did most likely stem from an increasing error though, as it can be seen in the FITC-GOx leakage absorbance plot (Figure 3.4-20). The spectrometer is already working at its very limits measuring the small amounts of the fluorophore leaked at 2 mg/mL FITC-GOx, which increased the error, and which lead to a misrepresentation of the calculated amount of leaked FITC-GOx. Since this method required an absorbing fluorophore, it is very unlikely that it can be used to gather information about other encapsulated materials which were used in this thesis like GOx, catalase or HRP. Nonetheless, it is a very useful set of data which can be used as a representation for the enzyme lost during the fabrication of protamine/DNA-capsules, and which could even be used to approximate the leakage of other enzyme-additives.

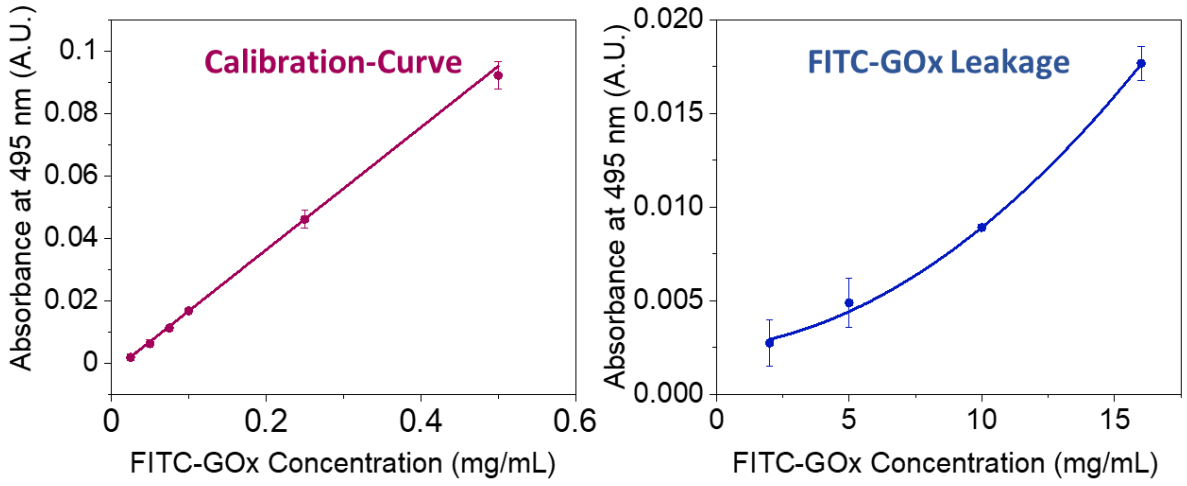

Figure 3.4-20: *Entrapment and leakage of FITC-GOx during the fabrication of protamine/DNA-microcapsules. A calibration curve was fitted by measuring various FITC-GOx concentrations at $\lambda_{Excitation}$ (FITC) = 495 nm. To measure the leaked FITC-GOx from the fabricated cells, all capsules were removed after extrusion of 20 µL of the dsDNA/FITC-GOx-solution, and the supernatant was used to measure the absorbance at $\lambda_{Excitation}$ (FITC) = 495 nm.*

Table 3.4-1: *Calculated FITC-GOx content within cells after fabrication for ideal and real conditions under the assumption of leakage*

FITC-GOx concentration [mg/mL]	*Original amount in 20 µL [mg]*	*Expected amount per capsule [ng]*	*Real amount per capsule [ng]*	*Leakaged during fabrication [%]*
16	320	784.31	528.42 ± 11.18	32.62 ± 1.42
10	200	490.19	343.86 ± 2.32	29.85 ± 0.47
5	100	245.09	149.04 ± 16.34	39.18 ± 6.66
2	40	98.03	28.87 ± 17.61	70.54 ± 17.96

Although it is not possible to get larger particles or molecules to move through the membrane once the cell is formed, the membrane can still be functionalised externally via adsorption. Both capsule-types, but especially the protamine/DNA-system, turned out to be very sticky towards larger objects like particles or the glass-wall of a vial and readily adsorbed a variety of components onto their

membrane. Protamine/DNA-capsules furthermore appeared to be much more reliable and stable for this kind of experiment. AMP-capsules on the other hand tended to break apart or deformed in enzyme- or nanoparticle environments due to osmotic shrinkage or expansion, which is why AMP-capsules will not be compared in this section (Figure 3.4-21).

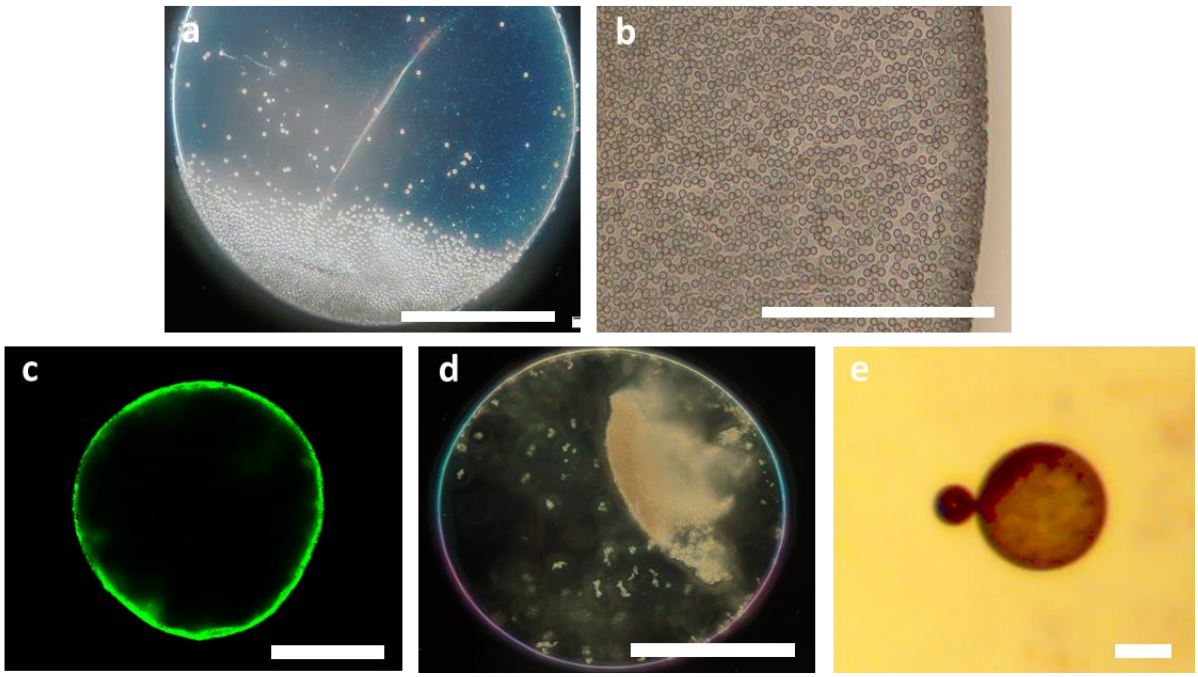

Figure 3.4-21: *Optical and fluorescent micrographs of different components adsorbed onto the membrane of protamine/DNA-microcapsules. All capsules were washed 5 times with di-water after adsorption was complete.* ***a,b*** *COOH-functionalised magnetic microspheres* ***c*** *FITC-catalase* ***d*** *Platinum nanoparticles* ***e*** *Catalytic activity of adsorbed Pt-nanoparticles after addition of 160 mM H_2O_2: a small oxygen-bubble was produced on the side of the capsule. All scale bars: 200 μm.*

Protamine/DNA-capsules are formed by charge-interaction of anionic and cationic materials, but this does not mean that all charge has been successfully quenched via complexation. Since protamine came in excess compared to DNA, it seems much more likely, that the fabricated capsules would exhibit an overall positive charge on their surface due to the remaining amine-groups from the protamine-molecules. Due to the large size of the cells though, it is nearly impossible to gather reliable data about the surface-charge via for example DLS-zeta-potential scans, as this method is designed for much smaller cell- or particle-systems, which range from about 3.8 nanometers to 100 μm according to the manufacturers website (*Malvern Panalytical* – Zetasizer-Nano). [123]

All components used in the adsorption experiments possessed a negative charge: magnetic microspheres were surface functionalised with carboxylate-groups (*GE Healthcare-Lifesciences*, Sera-Mag Carboxylate-modified magnetic Speedbeads, COOH-surface modified) and platinum nanoparticles were stabilised by capping them with citrate groups and to add a negative surface charge. FITC-catalase is a more complicated case due to a lack of literature on that matter. Instead, it was assumed that the isoelectric point of catalase and FITC-catalase would not differ too much, so it can be used to predict the surface charge of the enzyme. According to literature catalase has an isoelectric point of $PI_{Catalase} = 5.4$ [124], which means that its surface charge would turn negative in di-water (pH 6.9). To validate these statements, catalase was analysed via zeta potential scan (Figure 3.4-22), which indeed showed a slightly negative zeta potential at about -5 mV. This is also in accordance with literature which found the zeta potential of catalase at -4.2 mV. [125] With this data in

mind, one could at least assume that catalase exhibits a negative surface charge, but it is necessary to keep the previous discussion in mind, that zeta-potential data must be analysed carefully, especially when it comes to polyelectrolytes and proteins.

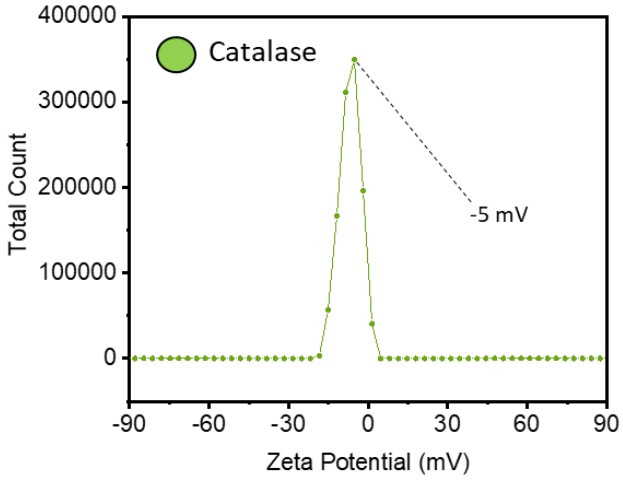

Figure 3.4-22: *Zeta potential-measurement of 0.1 mg/mL catalase in di-water (pH 6.9).*

As seen in Figure 3.4-21, COOH-functionalised magnetic microparticles are readily adsorbed onto the microcapsule at pH 7 (di-water) (Figure 3.4-21-b). What is even more interesting, it is possible to fabricate "Janus-like" magnetic microcapsules just by settling the capsule onto a bed of magnetic particles, thus adsorbing them onto only one hemisphere (Figure 3.4-21-a). Asymmetric systems like this are highly interesting for biological, electrical or medicinal applications, and regarding the later chapters of this thesis, for motility concepts. [125-129] It was furthermore possible to adsorb smaller enzymes or nanoparticles onto the membrane by simply mixing them with the capsules, like FITC-catalase (Figure 3.4-21-c) and citrate-capped platinum nanoparticles (Figure 3.4-21-d). FITC-catalase could easily be imaged via fluorescence microscopy. In case of citrate capped platinum nanoparticles though, the catalytic reaction of platinum with hydrogen peroxide was exploited to understand if they successfully adsorbed onto the membrane. For this purpose, ~10 µL of 160 mM hydrogen peroxide was added to the capsules after which small bubbles were nucleating around the membrane. [130] Elemental platinum can react with hydrogen peroxide and catalytically convert it to oxygen. Once formed, the oxygen is nucleating in form of little bubbles around or even inside the cell, which can be seen on Figure 3.4-21-e. Since all capsules were washed several times after the adsorption process, it left no doubt that these adsorbed compounds are bound to the membrane and stable even after mixing.

Another important question that arose when working on encapsulation of functional components is if the compounds are retained within the cell or if they leak out over time after the cell has been fabricated. Here, FITC-glucose oxidase was encapsulated into protamine/DNA- and RITC-GOx into aminoclay/DNA-capsules, which were then washed 1, 3, 5 and 10 times to assess if the fluorescent signal of the entrapped enzyme will progressively weaken due to a potential leakage during the washing steps (Figure 3.4-23). The mean fluorescence was determined via the software *FIJI-ImageJ* for each cell and then plotted over a sample size of 30 capsules for each washing protocol. Protamine/DNA-microcapsules showed no decrease in fluorescence, even after 10 consecutive washing steps. On the contrary, the plots from Figure 3.4-23-a even gave the impression that the fluorescence is slightly increasing. This seemed very unrealistic though and was most likely caused by a small error of the measurement, since not all capsules showed an identical fluorescence. The large

error for the 10X-dataset further supported this theory. Nonetheless, the dataset showed that FITC-tagged GOx was not leaking from the cells when mixed and washed with di-water. The same results were found when using AMP/DNA-microcapsules. The mean fluorescence intensity plots showed barely any change, and the capsules looked the same under the fluorescence microscope, which is why it was assumed, that the enzyme did not leak from the cells. So in summary, it can be expected that entrapped enzymes indeed stay entrapped on the cells, even when washing them a large number of times with di-water.

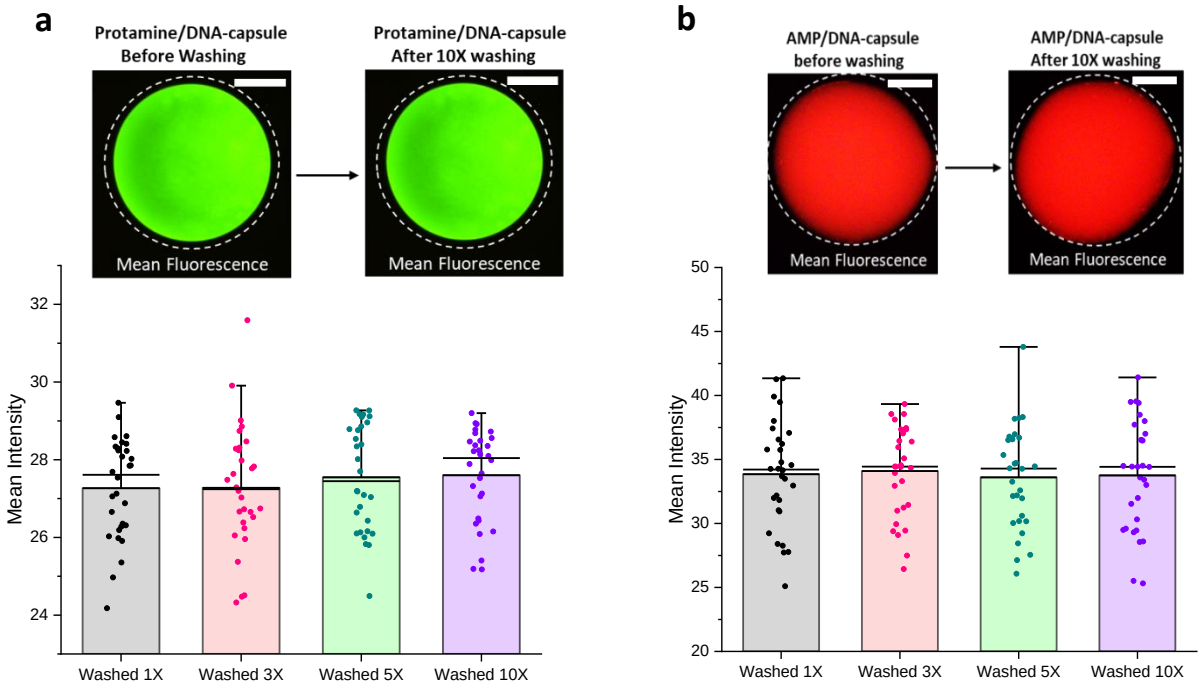

Figure 3.4-23: *Enzyme-retention assay for AMP/DNA and protamine/DNA-microcapsules. FITC-GOx was encapsulated into protamine/DNA-microcapsules (**a**) and RITC-GOx into AMP/DNA-microcapsules (**b**). Both cell-types were then washed 1, 3, 5 and 10 times and the mean fluorescence intensity was measured over the cell and compared. Scale bars: 100 µm.*

3.4.4 Membrane characterisations

The studies presented above provide a good foundation to understand the concept of entrapment of components into AMP- or protamine microcapsules, but it lacks a proper understanding of the localisation of the encapsulated compounds and a characterisation of the membrane, as these play a crucial role in the retention and uptake of compounds into the cell interior. Figure 3.4-18 gave a first impression on the localisation of encapsulated compounds, but it did not contain enough information in order to distinguish between the inside of the cell and the cell membrane. The reason for this lies in the method used to observe the cells. In the previous chapter, a fluorescence microscope was used which lacks the resolution to image small cross sections of the cell, which are necessary to understand whether the enzymes are encapsulated in the cell lumen, on the membrane or both. In order to gather a higher resolution for the following membrane studies, all images were taken by a scanning confocal microscope.

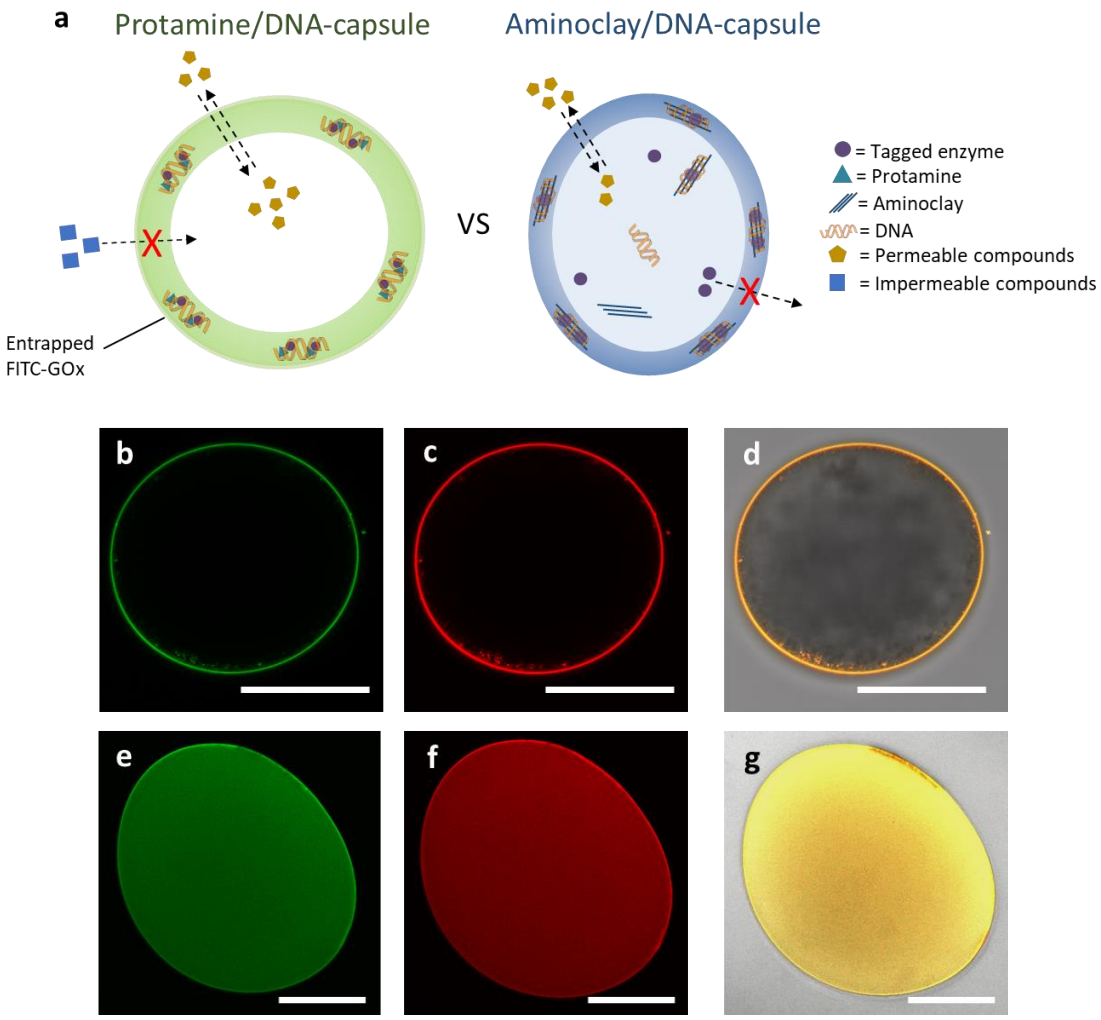

Figure 3.4-24: *Figures to depict the localisation of entrapped enzymes inside protamine/DNA- and AMP/DNA-microcapsules.* ***a*** *Illustration of the assumed cell-structure, with the tagged enzyme being entrapped inside the protamine/DNA- or AMP/DNA-microcapsules.* ***b*** *Confocal fluorescence microscopy images of FITC-cat and* ***c*** *RITC-GOx encapsulated into a protamine/DNA-microcapsule.* ***d*** *Overlay of the fluorescent signals onto a brightfield image of the capsule.* ***e*** *Confocal fluorescence microscopy images of FITC-cat and* ***f*** *RITC-GOx encapsulated into an AMP/DNA-microcapsule.* ***g*** *Overlay of the fluorescent signals onto a brightfield image of the capsule. All scale bars: 200 µm.*

To answer the question of where the encapsulated compounds are localised, tagged enzymes were again entrapped in AMP/DNA and protamine/DNA-microcapsules and examined under the confocal microscope. AMP/DNA-microcapsules appeared fluorescent all the way throughout the cell interior with a slightly more pronounced membrane (Figure 3.4-24 e-g). This is not only in accordance with the previous results from Figure 3.4-18 but also proves, that the enzymes are indeed entrapped within the cell and cannot permeate, or leak, through the membrane. Here, one can also assume that a large portion of excess dsDNA, aminoclay sheets and aminoclay/DNA-complexes were entrapped inside the capsules as well, as their size would not allow them to permeate through the membrane either. It is furthermore assumed, that the majority of the encapsulated tagged enzymes are most likely not free but rather attached to the aminoclay-sheets due to electrostatic interactions. The membrane on the other hand appeared slightly more fluorescent than the rest of the cell, which lead to the conclusion, that a large fraction of the enzymes is either entrapped or physically bound to the complex network of the membrane. Due to the compact structure of the membrane, the concentration of the fluorophores per volume is higher which makes the membrane appear brighter than the rest of the

cell. Nonetheless it is complicated to discuss whether the membrane accommodates more enzymes than the cell interior or not.

In case of protamine/DNA-microcapsules, the main source of fluorescence is the membrane of the capsules although the images also show fluorescence of the protamine/DNA-condensate aggregate inside (Figure 3.4-24-b-d). No fluorescence was found inside the capsule lumen, which enabled some important characterisations about “co-encapsulation”. In case of protamine/DNA-capsules, enzymes are therefore not literally encapsulated but rather incorporated into the protamine/DNA-condensate. This is especially easy to explain by looking at the confocal-Z-stack of a protamine/DNA-capsule from Figure 3.4-25, as the DNA-condensate aggregate turned out to be fluorescent as well.

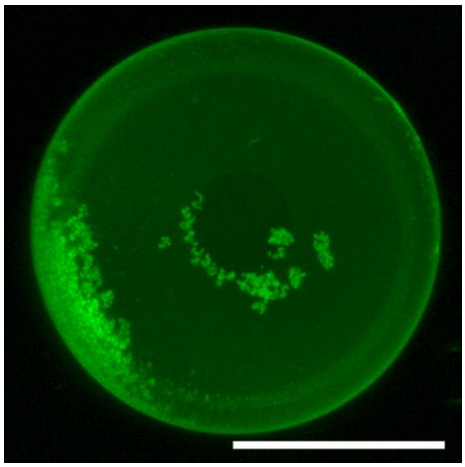

Figure 3.4-25: *Confocal micrograph of a protamine/DNA-microcapsule with encapsulated FITC-catalase. The image was processed as a Z-stack from 270 separate images with 2 μm between each slice. Scale Bar: 200 μm*

This leads to the following distinction between the two capsule systems: AMP/DNA-microcapsules can retain enzymes and larger molecular compounds within the capsule interior, whereas protamine/DNA-microcapsules can only entrap them within the protamine/DNA-condensate, while the capsule interior appeared to be almost exclusively aqueous.

This brings up a very important question: Are the enzymes sterically entrapped within the protamine/DNA-condensate or are they merely bound to the membrane via electrostatic interactions. To understand the latter, glucose oxidase was incorporated into protamine/DNA-capsules. If the enzymes were retained on the membrane by electrostatics, a change of ionic strength in the surrounding solution should alter the interactions and most likely make the enzymes desorb from the membrane. For this purpose, GOx-containing protamine/DNA-capsules were fabricated and incubated in 50 mM sodium phosphate buffer (pH 7.0). Since there was no visual feedback whether the enzymes are still adsorbed on the membrane, it was necessary to alter the approach so that a chemical signal could be recorded. Here, the GOx-mediated catalytic conversion of glucose to hydrogen peroxide and gluconic acid was exploited to create a visual stimulus, which could be measured by UV/VIS spectroscopy. Hydrogen peroxide served as a substrate for a second enzyme horseradish peroxidase, which used it as a substrate for the oxidation of the chromophore 2,2'-azino-bis(3-ethylbenzothiazoline-6-sulfonic acid), or ATBS. ABTS forms a colourless or slightly green solution in di-water when it is in its reduced form and turns dark green when oxidised by HRP, which was then measured spectroscopically through its absorbance at $\lambda_{Excitation,ABTS}$ = 420 nm. The following reaction equations will summarize all the important catalytic steps (Figure 3.4-26):

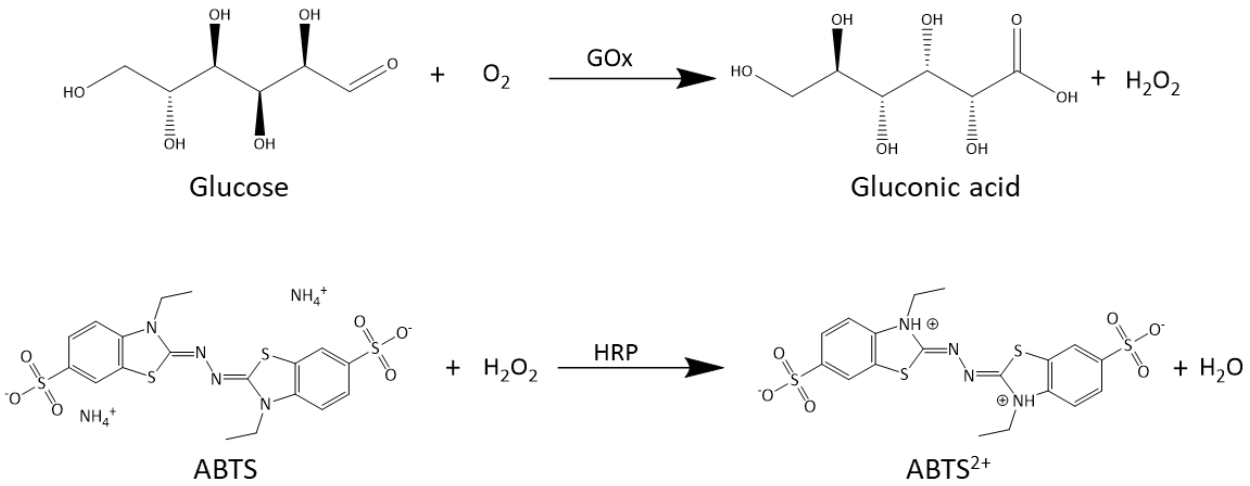

Figure 3.4-26: *Catalytic conversion of glucose by GOx and ABTS by HRP.*

The complete experimental setup is described in chapter 3.3.15 and each measurement was performed in a disposable optical cuvette with two GOx-containing protamine capsules. The results are presented in Figure 3.4-27. Again, this experiment confirms the previous experimental results that the enzymes would stay attached to the cells even after multiple successive washing steps with di-water and that there was no leaking to be observed. After incubating the GOx-containing protamine/DNA-microcapsules in 50 mM sodium phosphate buffer (pH 7.0) however, the capsules showed a severely reduced activity (Figure 3.4-27), which can only mean one of two things: the higher ionic strength of the buffer caused the enzymes to desorb from the membrane, or the enzyme became somehow inactive while still remaining on the cell surface. To understand whether the enzymes detach, a second experiment was designed. Instead of assessing the GOx-activity spectroscopically, the supernatant was simply removed after the incubation step in 50 mM sodium phosphate and exposed to the same colorimetric assay with HRP and ABTS. So, assuming the enzyme is leaking from the cells, it should be found in the supernatant. The experiments were performed in a 96-well plate and with 100 µL of the supernatant from the GOx-containing protamine capsules in either water or 50 mM sodium phosphate.

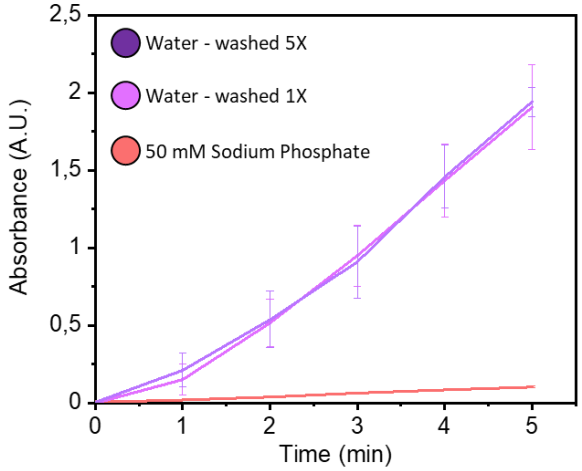

Figure 3.4-27: *Glucose-oxidase activity of 2 protamine/DNA-microcapsules after incubation in either water (purple graph) or 50 mM sodium phosphate (red graph). The activity was measured in form of a coupled enzymatic assay with HRP and the chromophore ABTS. As ABTS was oxidised by HRP, its absorbance was measured at* $\lambda_{Excitation}$ *(ABTS) = 420 nm.*

Figure 3.4-28 shows, that the supernatant of the water/capsule-dispersion does not show any colorimetric signal, which means that there was very little or no GOx in solution. The sodium phosphate buffer on the other hand showed a very strong coloration after mere minutes. This proves that the enzyme has indeed leaked from the cells into the solution and that a loss of enzyme activity can most likely be ruled out.

Lastly, these leakage studies can also be used to gather clues to the question, whether all enzymes are loosely bound to the membrane via electrostatic interactions or if they are sterically entrapped. The studies above clearly indicated that most of the enzyme can be desorbed from the surface if the external conditions are changed. But even capsules which have been incubated in a sodium phosphate solution for longer than 1 hour still showed a diminished but measurable GOx activity.

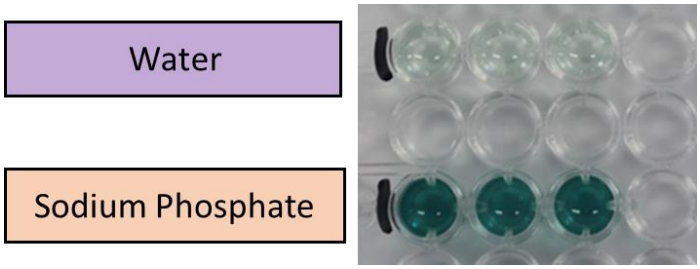

Figure 3.4-28: *Photo of the results of the supernatant-test to understand whether GOx can leak from protamine/DNA-microcapsules. The cells were either kept in water or in sodium phosphate buffer (50 mM, pH 7.0). Each condition was tested in triplets with 1 capsule per well. The images were taken 5 minutes after the addition of the colorimetric assay solution (0.05 mg/mL HRP, 9.1 mM ABTS, 25 mM Glucose)*

To get a qualitative understanding of how much GOx is still bound to the capsule membrane after the transfer into 50 mM sodium phosphate, glucose oxidase was tagged with the fluorophore RITC. The capsule was fabricated with 2 mg/mL of the tagged RITC-GOx, and the fluorescence was imaged under a fluorescence microscope right before the capsule was transferred into the buffered solution and in successive 60 minute intervals.

The micrographs of Figure 3.4-29 show how the fluorescence is deteriorating over the 120 minutes the capsule is residing in the sodium phosphate solution until it is ultimately about 50% weaker than the original intensity. Even though it is difficult to directly correlate these fluorescence intensity measurements to the GOx-activity-screening from Figure 3.4-27 and Figure 3.4-28 , it can still be used as a part of the discussion. It can be assumed that about 50% of the fluorescent enzymes have been lost due to the interactions in the buffered solution, but this should not lead to the same reduction in enzymatic activity like it was shown in Figure 3.4-27, where the activity was estimated to be reduce by almost 10 to 20 times. So, it seems increasingly unlikely, that all enzymes were and can be detached from the cells through mere electrostatic interactions. One explanation could be that it just takes a lot longer to detach all the enzymes from the cells or that some are just bound much stronger to the protamine/DNA-condensate. Some of these enzymes might not exhibit the same activity as others due to their local environment, which could explain why the experiments showed a very deteriorated activity but a much less decreased fluorescence. Furthermore, it could be misleading to compare the fluorescence-signal directly to the GOx-activity, as they most likely are not correlating linearly. This means, that the fluorescent signal could be much stronger and implicate a higher load of enzymes, even though most of the GOx has already been washed off the cell.

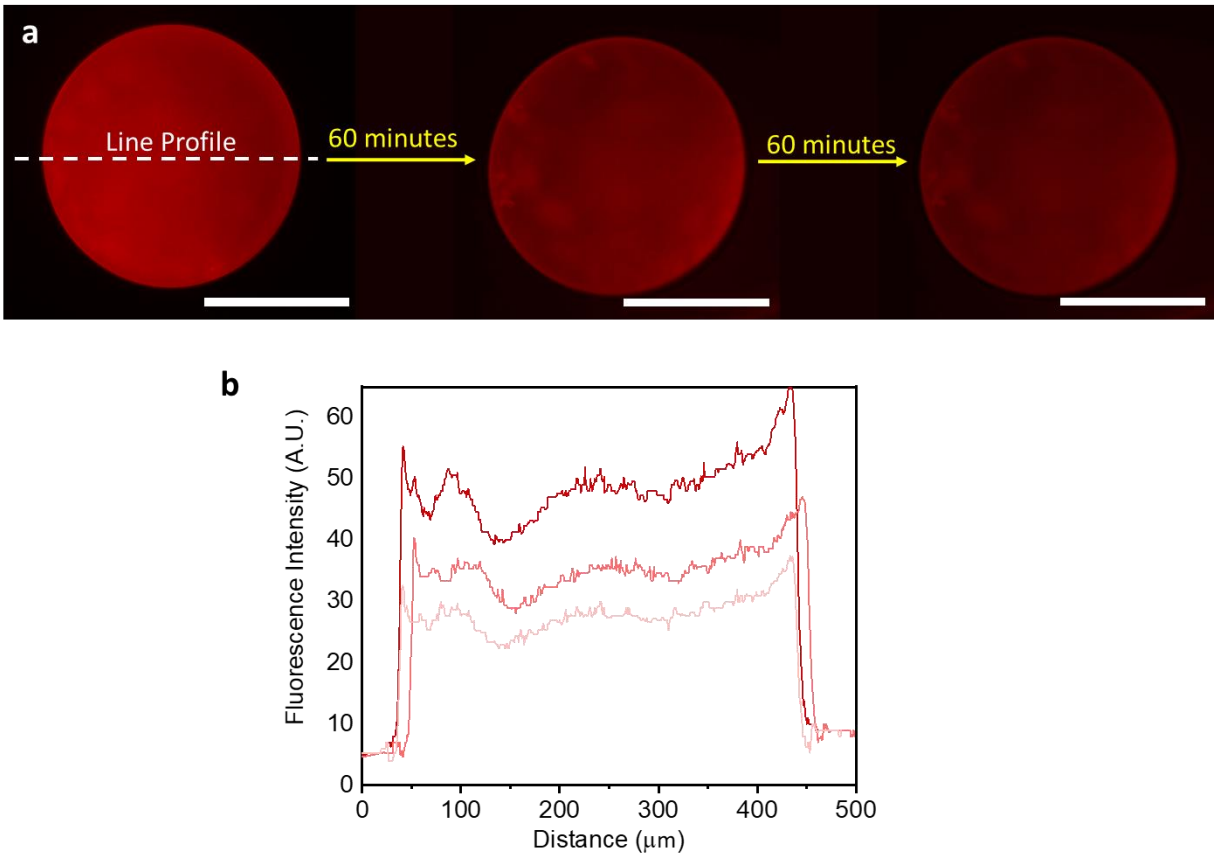

Figure 3.4-29: a *Fluorescence micrographs of RITC-GOx leakage from protamine/DNA-microcapsules in a 50 mM sodium phosphate solution. Images were taken at time t = 0, 60, and 120 minutes. All scale bars: 200 μm.* ***b*** *Superimposed fluorescence line profiles (Indicated by dotted line in* ***a*** *from t = 0, 60 and 120 minutes.*

It is now established that it is possible to immobilise enzymes on microcapsules and that the enzymes can also be desorbed from the surface again by exposing the capsules to a higher ionic strength. What is still not known though, is whether the enzymes can move at all once they are adsorbed to the surface or if the electrostatic interactions prevent any form of molecular exchange. An easy method to understand lateral diffusion of the tagged enzyme within the membrane is FRAP or "*fluorescent recovery after photobleaching*". This time FITC-BSA (2 mg/mL) was encapsulated into both AMP- and protamine/DNA capsules and irradiated with several short pulses of a 495 nm laser to induce photobleaching. In case of protamine/DNA-microcapsules, and as expected, a bright green fluorescent ring was found where the membrane was supposed to be (Figure 3.4-30). The capsules were furthermore washed to remove any excess FITC-BSA-protein, so there was no other fluorescent signal neither inside, nor outside the capsule. After bleaching a small 40 μm^2 large area on the membrane for ~10 seconds, a dark spot appeared where the fluorophores have been irradiated. After waiting 20 seconds and longer, the bleached area did not recover, and indeed, even when looking at the measured mean fluorescence, there was no increase to be observed (Figure 3.4-30-d). Now this gives some very important insight into the molecular dynamics within the membrane of protamine/DNA-microcapsules. Since there is no recovery after photobleaching, it can be assumed, that there is no exchange of protein-molecules inside the membrane, which goes hand in hand with the previous assumption that most enzymes are bound to the protamine/DNA-condensate via electrostatic interactions, which prevent any form of lateral diffusion.

Aminoclay/DNA-microcapsules were prepared the same way, and again, both the cell membrane and the interior were found to be fluorescent, whereas the exterior of the cell appeared black (Figure 3.4-30-c). After photo-bleaching of the membrane for 5 seconds, a dark bleached spot appeared both on the membrane and inside the AMP-microcapsule. Surprisingly though, the bleached area seemed to recover almost completely. A general bleaching of the cell segment was observed due to the confocal-laser every time a picture was taken, but the small, bleached area was almost indistinguishable from the surrounding area after ~60 seconds. So, in contrast to the membrane of protamine-microcapsules, AMP-microcapsules did recover after photobleaching which could imply an exchange of molecules. Why this is happening can only be assumed at this point. On the one hand, one could assume that FITC-BSA is indeed able to diffuse freely within the membrane, which then enables the recovery after photobleaching. On the other hand, considering there is still plenty of FITC-BSA within the capsule lumen, it is also plausible that the free FITC-BSA diffused from the cell interior towards the bleached spot on the membrane which recovered the bleaching even though the membrane-bound FITC-BSA is still entrapped. Previous publications by Patil *et al.* [108] furthermore discussed the capabilities of AMP-clay to intercalate biomolecules and showed that the sheet-like structure of the phyllosilicate clay enabled the molecules to move freely to a certain degree. At the same time this could pose the question why the enzymes are not leaking out of the cells, which has already been refuted by the previous leakage-experiments in Figure 3.4-23.

Either way, the membrane seems to be one of the most important differences between these two cell-types, especially as it defines the molecular environment inside the cells. To understand the molecular dynamics in the cell interior, FITC-BSA was encapsulated inside the microcapsules before washing them to remove any excess protein. After that, a small area inside the cell (40 μm^2) was photobleached. In case of AMP/DNA-capsules, the small, bleached spot recovered after mere 40 seconds (Figure 3.4-30-b, 88% recovery). Again, a general bleaching has to be accounted for due to the images that were taken during the process, but it can be assumed that the fluorescence would have recovered to a very high degree. This means, that even though the AMP-capsules exhibited a highly crowded molecular environment of DNA, aminoclay sheets and enzymes inside the microcompartment, which cannot permeate through the membrane, these molecules are not physically or chemically entrapped and were still able to diffuse within the microcapsule interior.

Since encapsulation of enzymes into protamine/DNA-capsule has already proven to be rather difficult, and in order to simulate a similar experiment like it was done for AMP/DNA-microcapsules, a smaller fluorophore in pyranine was used instead of FITC-BSA. Here, pyranine was added after fabricating the capsules and was not washed away, so it could freely permeate into the cell interior. Figure 3.4-30-a shows a protamine/DNA-capsule in a pyranine solution after photo-bleaching and, instead of only a small spot, the whole cell-interior was chosen as the bleaching area. Once the bleaching stopped, pyranine permeated from the outside of the microcapsule through the membrane and exchanged the bleached molecules, almost recovering the fluorescence completely after 20 seconds (98% recovery). What can be taken from this experiment is that the general recovery time is pretty quick, which is not surprising given the fact that pyranine is a fairly small molecule. But it also points towards the same assumptions which were already made above, that protamine/DNA-capsules were predominantly aqueous inside and did not contain any other macromolecules which could inhibit the diffusion inside the cell.

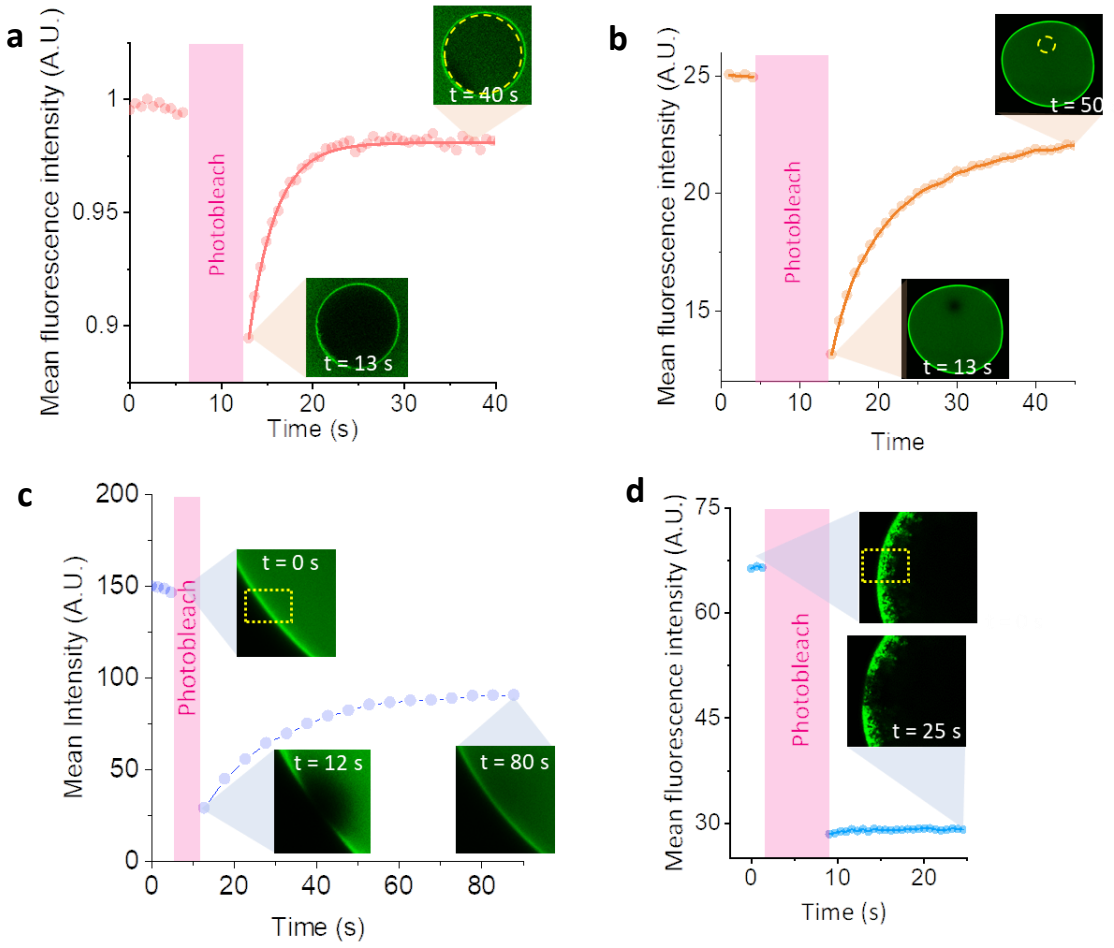

Figure 3.4-30: *Fluorescence recovery after photobleaching (FRAP)-experiments with AMP- and protamine microcapsules.* ***a-b*** *Molecular diffusion was assessed within the microcompartments with pyranine in protamine/DNA-microcapsules (**a**) and FITC-BSA in AMP/DNA-microcapsules (**b**).* ***c-d*** *Furthermore, molecular diffusion was analysed within the membrane of protamine/DNA- (**c**) and AMP/DNA-microcapsules (**d**) with entrapped FITC-BSA. The irradiated area was highlighted with a* ***yellow dotted circle or rectangle****.*

The previous studies mainly tried to understand the entrapment of enzymes in or on the capsules, even though they still did not gather much information about the membrane itself. In this next step, confocal microscopy was used to measure the membrane thickness by staining it with acridine orange. All capsules were stained in a 10 mM acridine orange solution and consecutively washed to remove any excess dye. The membrane thickness was then assessed and plotted from 8 different microcapsules of each type (Figure 3.4-31). The membrane of protamine capsules generally measured around 4-6 µm (Figure 3.4-31-b), whereas AMP-capsules had membranes which appeared a lot thinner with 1-2 µm (Figure 3.4-31-a). This is interesting, especially from the aspect of DNA-condensation. As it was already shown above, protamine/DNA-capsules are generally smaller than AMP/DNA-microcapsules, which was primarily attributed to the fact that condensed DNA is more compact and takes less space than a DNA-complex with a cationic polymer like AMP. Instead, the membrane was 2-3 times thicker, which seems counterintuitive, but it can be explained, nonetheless. As it can be seen in Figure 3.4-31-a and in many images above, AMP-capsules retained many large molecules in their interior, including DNA. This means, that not all DNA has been incorporated into the membrane but rather floats around inside the capsule. In case of protamine/DNA-capsules, all DNA has been condensed and can only be found along the membrane. So, in other words, the membrane of protamine/DNA-capsules is most likely thicker, because more of the material has been incorporated than in case of AMP-capsules. Of course, it is also possible that excess DNA has just

diffused out or got condensed outside of the cell during the fabrication of the protamine capsule, but it seems like a valid assumption to explain the difference in membrane thickness, nonetheless.

While this method leads to reproducible sets of data, it needs to be discussed to allow for error. In order to gather a proper cross-section, the microscope needs to be aligned around the centre of the capsule. Especially for AMP-capsules, which are rarely properly spherical, this can lead to errors when measuring the thickness of the fluorescent membrane. Another issue is the fluorescence itself, since the microscope always captures additional signals from below and above the cross-section as well and therefore makes the membrane-thickness look larger than it is. To really get a proper understanding about the membrane, a combination of methods would be necessary. In other cell studies, SEM turned out to be very helpful, as cells tend to break under the stress of lyophilisation, which in return enabled the study of the membrane at these cracks. [86] SEM-experiments with the capsule systems of this thesis though turned out to be much more difficult than expected, as the capsules often merely deformed but did not break during the lyophilisation-process. So far, no SEM-analysis of the membrane was possible and for now, the membrane-thickness will be defined by the acridine-orange staining experiments below.

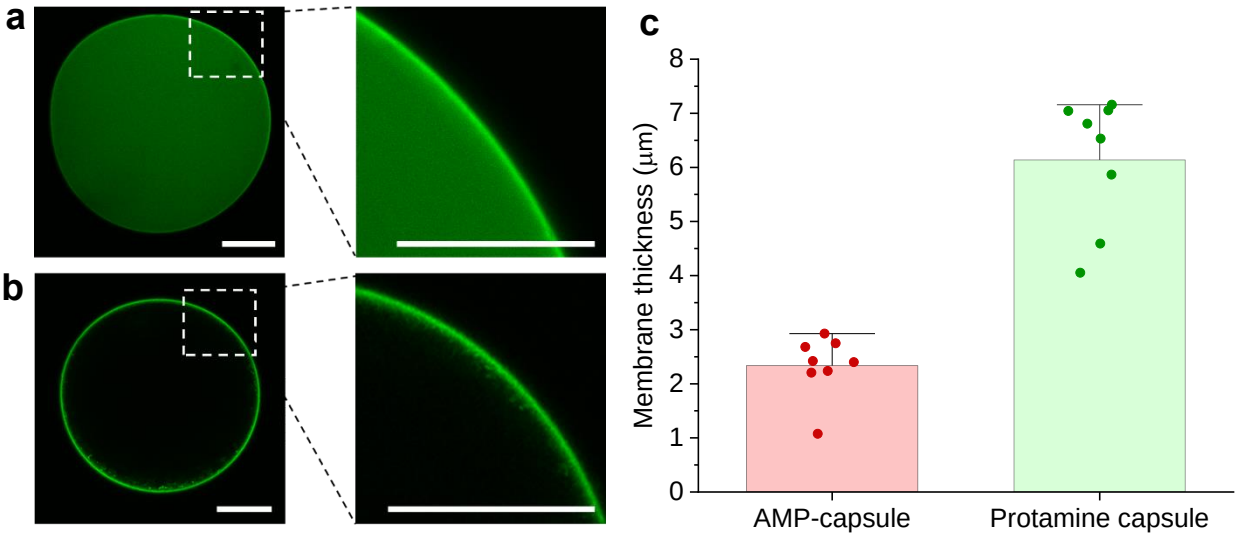

Figure 3.4-31: *Confocal micrographs of acridine orange stained AMP/DNA (**a**) and protamine/DNA-microcapsules (**b**). The membrane thickness of the cells was assessed digitally and over a dataset of 8 different cells. Figure **c** shows the bar-scatter-plot of measured membrane thickness of both capsule systems. The **white rectangle** highlights the magnified area.*

With all the information that has been accumulated up until this point, it is unavoidable to focus this next part of the investigation on the membrane permeability. Before looking at the results, it is necessary to discuss the setup of the experiment. Whether a chemical compound is able to traverse a semi-permeable membrane is depending on a lot of different factors like the molecular weight, the surface-charge of the permeating compounds but also of the membrane, the pore geometry of the membrane and molecular geometry of the compound (for example globular proteins vs long linear polymers), the pH, temperature and probably even more. [131-133] Combining all these factors would make an experimental design almost impossible, so it will be necessary to focus on a single molecular parameter, that is easy to follow. Since the molecular size and more specifically the weight is probably the most important one to understand, this will be the focus in the following experiment. FITC-dextrans are long-chain dextran molecules which are available in various sizes and which contain side-chains of the fluorophore fluorescein isothiocyanate, which makes it easy to study the permeation via

fluorescence microscopy. FITC-dextrans have been used extensively in studies revolving around cell-processes but also to understand permeability. [134] Dextran furthermore possesses no charged groups and the only charge that could interact with the membrane stems from the coupled fluorescein-side chains. To understand the permeability of the microcapsule membrane, the following FITC-dextran lengths were investigated: 4 kDa, 10 kDa, 20 kDa, 40 kDa, 70 kDa, 250 kDa and 2000 kDa. The capsules were prepared without any additives and washed 5 times with either di-water (protamine/DNA-capsules) or 0.5 mg/mL aminoclay in water (AMP/DNA-capsules) to ensure their stability. The permeability of the compounds was then assessed via confocal microscopy and by calculating the ratio of the mean fluorescence intensity inside and outside of the capsule. Each datapoint was averaged from 10 individual capsules and then plotted against the size of FITC-dextran (Figure 3.4-33).

AMP/DNA capsules were mostly permeable for FITC-dextran sizes between 4-20 kDa. With increasing size though, the compounds were progressively less able to permeate through the membrane, which led to a decrease in the mean intensity ratio. Ultimately, the fluorescence-ratio minimum was reached for any FITC-dextran with sizes of 70 kDa and higher. For an ideal membrane and permeating compound, there should be a clear size-limit or cut-off, after which nothing should be able to permeate anymore. But as described above, there are many different factors that can influence the permeation of a molecule. Another possible factor is the molecular composition of the FITC-dextran-samples. Even though advertised for a specific size, it is questionable if all molecules are indeed of one single molecular weight, or rather exhibit a size distribution.

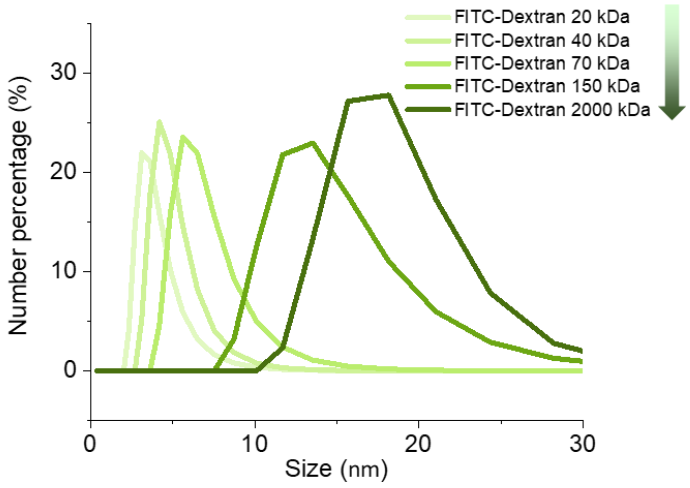

Figure 3.4-32: *DLS-size analysis of FITC-dextran (Molecular weights of 20, 40, 70, 150 and 2000).*

To get a better understanding of this, the sizes of FITC-dextrans were analysed via DLS (Figure 3.4-32). Here, the sizes for FITC-dextran 20, 40, 70, 150 and 2000 kDa were identified as 3.12, 4.18, 5.61, 13.54 and 15.68 nm respectively. In comparison, the commercial data available described sizes of 3.3, 4.5, 6.0 and 8.5 nm for 20, 40, 70 and 150 kDa FITC-dextran respectively [135], whereas the size of FITC-dextran 2000 kDa could only be referenced from literature with a size of about 15 nm. [136] So, this shows that there is a small difference between the measured and the expected size-values for FITC-dextran 150 kDa of about 5 nm, even though the other samples appeared to be very close to the literature. Regarding the size-distribution, a clear trend was apparent when comparing the lower molecular weights to the higher ones. The distribution seemed to become wider the larger the molecules are, with FITC-dextran 2000 kDa exhibiting the largest distribution which spanned from 10 to over 30 nm in size. This would explain why, even though the fluorescence ratio is going down, there

were still molecules permeating into the cell. Another factor could be the membrane of the capsules itself. While there is no clear footage of the exact porosity of the membrane, it could be assumed that not all pores exhibit the same size, which would allow larger molecules to permeate but at a much smaller rate. Either way, it is not trivial to define a clear permeability-limit, but it can be assumed that it has to lie somewhere between 20 and 70 kDa.

Next, protamine/DNA-capsules were investigated (Figure 3.4-33-b). The capsules were highly permeable for any FITC-dextran up until 250 kDa, while only showing a slight decrease in the fluorescence ratio at 250 kDa. In fact, the calculated intensity ratio was found to be above 1 for most of these cases, which means that the fluorescence intensity inside these cells was higher than outside. It seems unlikely that these cells would sequester small FITC-dextrans inside the cell interior, as the membrane is permeable for the molecules to diffuse through and with no other molecules inside the cells, there should be nothing that could prevent an equilibration between the FITC-dextran concentration outside and inside the cell. Instead, it seems more plausible that the cell appeared brighter due to adsorption effects. The protamine/DNA-membrane has shown to be capable of adsorbing a wide array of compounds very easily and even though the confocal microscope has a very high spatial resolution, it will pick up signals from other planes above and below as well. In other words, since a lot of the FITC-dextran might be adsorbed on the membrane, the fluorescence might appear more intense on the capsule than around it. Considering that the capsules appeared to be permeable even for large 250 kDa FITC-dextran, the experiment was already running close to the limit of the commercial spectrum of FITC-dextran compounds. 2000 kDa FITC-dextran was the largest available species and ultimately the first one to show a significant drop in permeability. Figure 3.4-33-b shows a low fluorescence inside the cell with the ratio falling to about 0.38, but which implies nonetheless that some FITC-dextran molecules are still diffusing through the membrane. Here, one can apply the same discussion that was already used for AMP-capsules to explain their diffuse permeability-limit, only this time it weighs in even heavier due to the larger size distribution of FITC-dextran 2000 kDa.

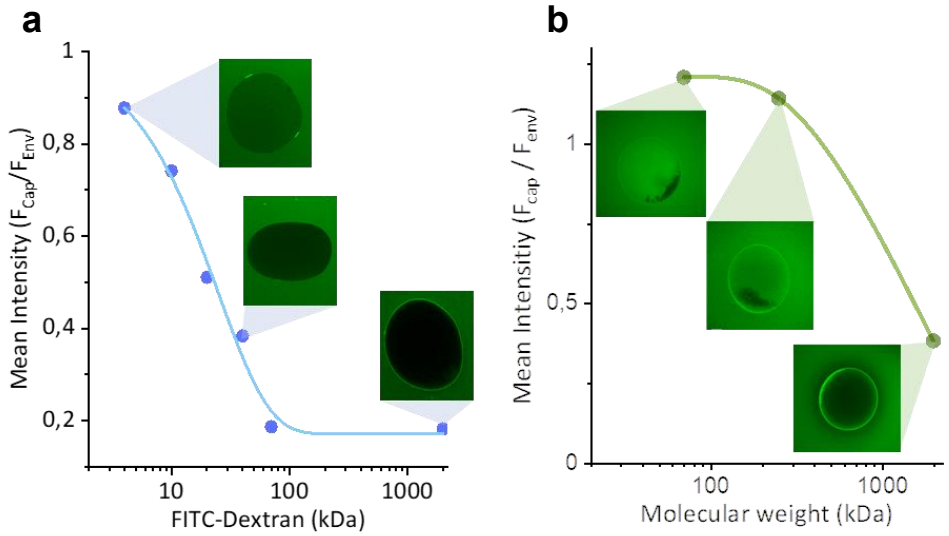

Figure 3.4-33: *Permeability screening for AMP/DNA-(**a**) and protamine/DNA-microcapsules (**b**). The following FITC-dextran-sizes were investigated: 4 kDa, 10 kDa, 20 kDa, 40 kDa, 70 kDa, 150 kDa, 250 kDa and 2000 kDa. The capsules were immersed in 0.1 mg/mL of the respective solution and examined under the confocal microscope. Confocal fluorescence micrographs can be seen in **a** and **b** as representations of the respective FITC-dextran molecular size.*

With this in mind, the permeability limit of protamine-capsules can be assumed to lie somewhere between 250-2000 kDa. This is highly interesting though, as it explains a lot of the experimental results discussed above. In contrast to the membrane of AMP-capsules, this one appeared to be highly permeable, which would also facilitate the diffusion of protamine and large enzymes like catalase through the pores of the capsules. DNA is a more complicated case, as the DNA used in this thesis has an approximate weight of 1300 kDa, which could very well exceed the permeability of the capsules. Assuming excess DNA would stay inside, it is now pretty much confirmed that it would get condensed and probably incorporated into the membrane either way. So, this serves as an explanation to why protamine/DNA-capsules contained neither enzymes nor DNA inside and it furthermore suggests, that even if enzymes are initially entrapped inside the capsules during the formation, they will ultimately diffuse out during the fabrication or become entrapped within the protamine/DNA-condensate.

Another observation that can be found with all types of capsules and cells alike is the deformation of the membrane due to osmotic pressure. Adding new solutes to a cell-dispersion which is in an isotonic state, causes a concentration gradient between the cell interior and the exterior. This is normally answered by the solvent, in most cases water, to flow through the membrane and out of the cell, which causes the cell to collapse (Hypertonicity). Having a higher concentration inside the cell on the other hand, causes the opposite effect which makes the cell swell up (Hypotonicity). The latter has most likely already been observed in Figure 3.4-8, where AMP/DNA-capsules swelled up and broke in di-water. Even though the deformation due to osmotic stress usually is more of an inconvenience for the experiment, it can also be used to understand more aspects about the cell membrane. Here, a small molecule in glucose and a large molecule in carboxymethyl-dextran (CM-dextran, 10-20 kDa) were added to the cell dispersion, to understand more about membrane permeability, but also whether the cell membrane can be deformed and reverted back to its native form. For this purpose, cells were fabricated without any additives and then transferred into either 0.5 M glucose or 3 mg/mL CM-dextran (10-20 kDa) solutions.

In case of glucose, the capsule membrane collapsed as soon as the capsule entered the hypertonic environment. The micrographs from Figure 3.4-34 show how both, the originally spheric protamine- and aminoclay-capsules become deformed and shrivelled. In case of the aminoclay-capsules (Figure 3.4-34-a), as soon as the capsules entered the glucose solution, the membrane deformed by protruding inwards, which proves, that water is permeating from the cell interior through the membrane to dilute the higher glucose concentration outside. After only a few seconds though, it became apparent that the membrane had already started to revert back to its original shape. After 3 minutes, most of the cell was already reformed and after 4 minutes, the cell looked like before the transfer into the glucose solution. Glucose is a small molecule and should therefore be able to permeate freely through the membrane of the capsule. Once the glucose-concentration gradient between the inside of the cell and the outside equilibrated, water permeated back into the cell and therefore reverted the osmotic deformation. While this was to be expected, it is nonetheless interesting to see that the membrane is flexible enough to withstand such major deformations and is able to take back its original shape in such a short amount of time. The protamine-capsules showed a very similar behaviour, even though the deformations were generally less pronounced. In Figure 3.4-34-b this process can be seen for a single protamine/DNA-capsule and with only a small concave gouge on one side of the cell. Like it was already discussed at the beginning of this chapter, the protamine/DNA-condensate forms a very strong and stable complex which also leads to much thicker membranes. Looking at the images of Figure 3.4-34-b one can assume that the membrane is much more rigid and would need to experience much higher osmotic pressures to deform. Another likely explanation is that the cell overall experienced a much smaller osmotic pressure than the AMP-capsule due to the much larger porosity and permeability of the protamine/DNA membrane. Glucose and

other molecules could diffuse quicker and at a much higher rate, which would reduce the pressure in return. And indeed, protamine/DNA-capsules generally took less time for the membrane to stabilise and revert to its original structure, even if it was just by 1 minute.

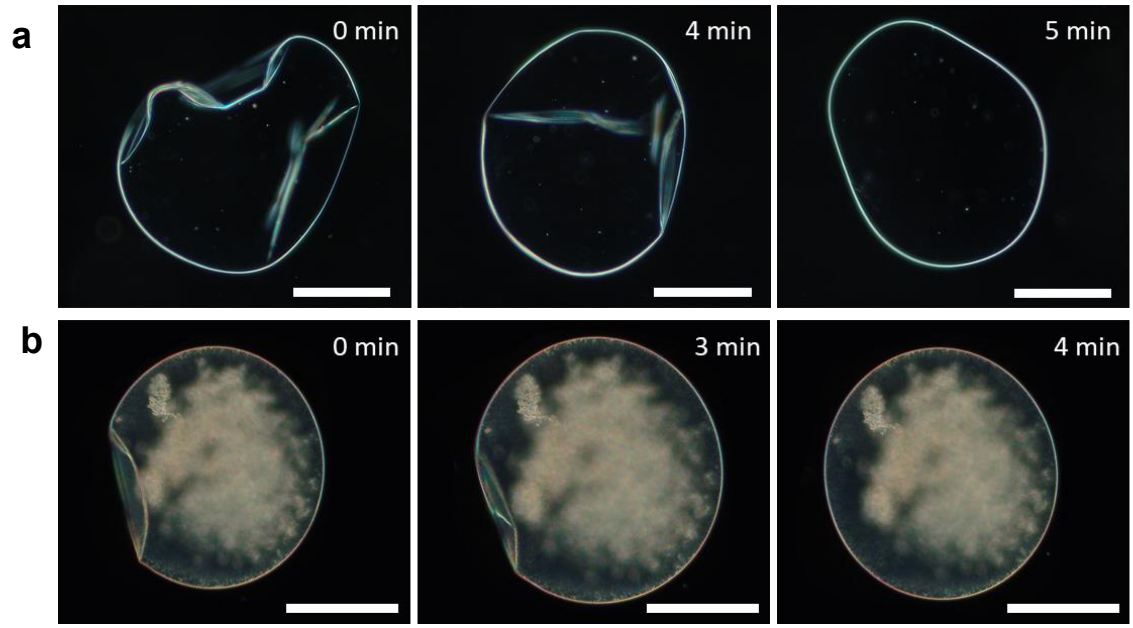

Figure 3.4-34: *Membrane-deformation due to osmotic pressure from transferring AMP/DNA-(**a**) and protamine/DNA-microcapsules (**b**) into a 0.5M glucose solution. All Scale bars: 200 µm.*

In case of CM-Dextran on the other hand, the capsules equally deformed once they entered the solution. AMP/DNA-capsules from Figure 3.4-35-a looked rather similar to the cells in a glucose solution, whereas protamine-capsules seemed to deform much more this time. Instead of only a small dent, almost all of the top half of the cell appeared collapsed. What was especially surprising though, is that neither AMP- nor protamine capsules would turn back to their original shape, even after leaving the capsules over night for 14 hours. In regard to the size of the CM-dextran-polymers (10-20 kDa) used for this experiment, these results could have been expected for AMP-capsules, as their membrane permeability was limited to sizes around 20 kDa. In case of protamine/DNA-capsules though, it seemed rather puzzling why a cell which exhibited such a vast permeability, would still be influenced by osmotic pressure from a much smaller polymer.

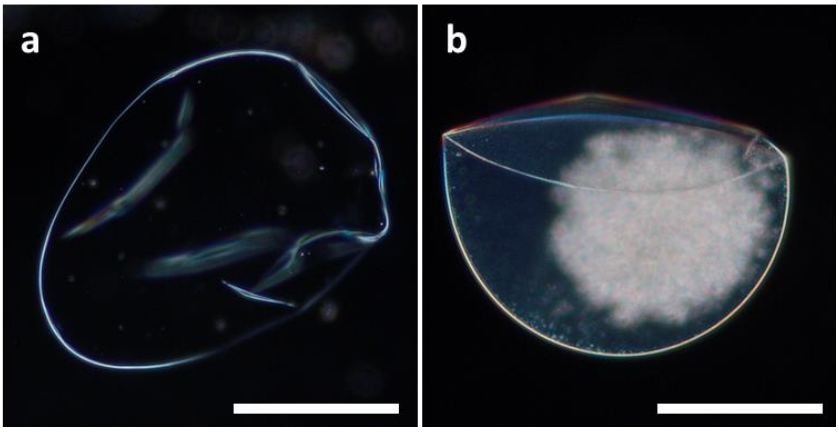

Figure 3.4-35: *AMP/DNA-(**a**) and protamine/DNA-microcapsule (**b**) after transfer into a 3 mg/mL CM-dextran-solution (Image taken after 14 hours). All scale bars: 200 µm.*

Another questionable point is the fact, that the previous diffusion studies just utilised a very similar compound in FITC-dextran, where no deformation or collapse was observed, with the only difference being the FITC-moieties compared to the carboxymethyl-residues. So, to understand this issue, it is necessary to focus on another important difference between CM-dextran and other compounds like glucose or FITC-dextran, which is the charge. Carboxy-methyl groups are negatively charged and should realistically provide the polymer with an overall negative net-charge. FITC on the other hand also contains a COOH-group, but it takes part in a molecular equilibrium between a closed-ring and an open-ring structure, which ultimately delocalises the negative charge. [137] Neither the FITC- nor the carboxymethyl-content of both polymers have been determined or could be found on the published certificates, so the following explanation can only rely on assumptions. Based on the size of FITC, it seems likely that CM-dextran will contain a much larger number of COOH-groups than there are FITC-groups on FITC-dextran, which should provide the molecule with a much higher negative net charge. In another attempt to gather further evidence for the previous assumption, both FITC-dextran and CM-dextran were analysed via DLS-zeta scans. Figure 3.4-36 shows a zeta potential of about -7.8 mV for CM-dextran and a surprisingly high potential of +76 mV for FITC-dextran. While the zeta-potential for CM-dextran was expected to be more negative, the potential of FITC-dextran appeared outright questionable, as the molecule does not contain any positively charged moieties.

Again, as it was discussed above, DLS-zeta potential scans can be used to gather some very valuable data which can be used to refer to the surface charge of a species, but it needs to be taken with a grain of salt and discussed properly. As there is no simple pathway to understand the charges of molecules, it is necessary to gather as much information as possible in order to create a bigger picture and even if the information provided with the DLS-zeta potential scans seems flawed, it can add to the understanding of the system. All in all, the explanation to understand the osmotic behaviour of microcapsules in CM-dextran-solutions can only be assumed. Since the membrane of the capsules most likely exhibited a positive charge, it can interact with a variety of negatively charged species and therefore also with CM-dextran. While proteins like catalase, BSA or GOx readily adsorb onto the cells, they do not cause any sort of osmotic deformation. Instead, only CM-dextran caused irreversible deformations, which leads to the hypothesis, that CM-dextran potentially interacts much stronger with the protamine/DNA-condensate or the AMP/DNA-complex than any of the other components due to the higher concentration of COOH-groups, or maybe even blocks the pores of the cell membrane completely.

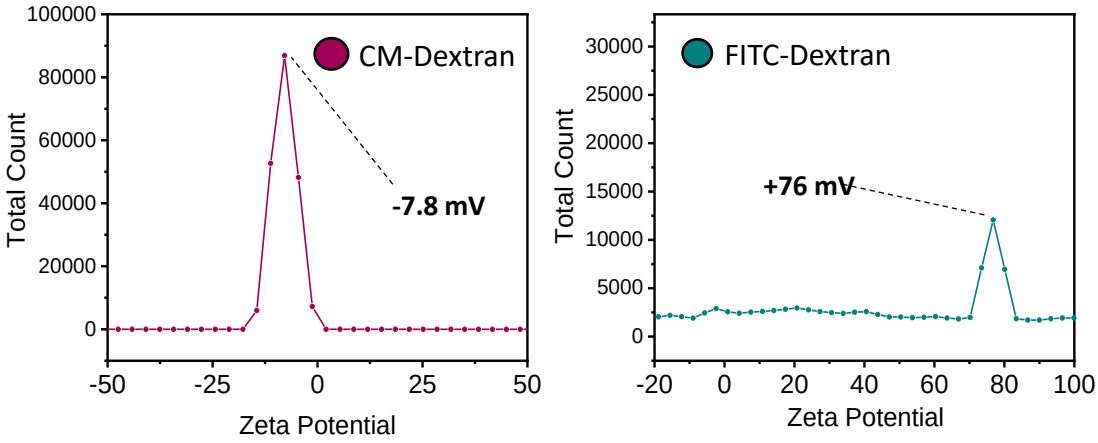

Figure 3.4-36: *DLS-zeta scans of CM-dextran (**dark red**, 10 mg/mL) and FITC-Dextran (**dark green**, 10 mg/mL) in di-water.*

Finally, the capsules were visualised with a scanning electron microscope. SEM-imaging can present some unique features, which goes beyond the capabilities of common microscopy. The physical limitation of optical microscopy only allows the resolution of microscopic structures. The membrane of microcapsules on the other hand are not only comprised of micro- but also nanopores, which most likely explain many of the observations from the previous studies. For the preparation, it is essential that SEM-samples are dried and do not contain any water. The lyophilisation, which is usually performed in liquid nitrogen and is used to dry the sample, is a very invasive method for most organic samples and can have severe effects on the appearance and structure of cells. So, SEM-images need to be discussed carefully, as they can contain misleading information which is not present in the cell before the lyophilisation.

Protamine/DNA and AMP/DNA-microcapsules were fabricated without any additives and then prepared for the lyophilisation by immersing them in liquid nitrogen. Here, it was very important to reduce the amount of water which is coming in contact with the liquid nitrogen as much as possible. Previous attempts of freezing capsules in bulk by simply adding the liquid nitrogen on top showed no success, since capsules started to aggregate and stick together. Instead, the capsule dispersion was added dropwise into a small volume of liquid nitrogen, which seemed to support the native structure and kept them separate. After freeze-drying overnight, the cells were examined under the scanning electron microscope (Figure 3.4-37).

The protamine capsules seemed to be mostly intact as they did not to appear collapsed and the membrane did not show any major damages except some smaller holes, which can be seen on the surface of the membrane (Figure 3.4-37-a,b). Figure 3.4-37-a presents a very nice specimen, where the protamine/DNA-capsule structure was mostly intact and it even retained its spherical structure which was visible in all of the previous microscopic images. The size of the capsule measured 343 μm in diameter, which is a little smaller than the cells before the freeze-drying process (400 μm in diameter), but which can easily be explained by the shrinkage due to the lyophilisation. Most other capsules looked rather shrivelled nonetheless and exhibited little dents or even more prominent deformations. Figure 3.4-37-b shows a very predominant shape, which could be found with a lot of capsules under the SEM and where the capsule looked more oval than spherical. The membrane furthermore exhibited a structural feature which looked like it is merging into a single point or like it was pinched together, which can be seen at the top left of the capsule in Figure 3.4-37-b, whereas the rest of the capsule appeared much smoother. In retrospect, this could be an artefact which came from the formation of the capsule and which was not visible when the capsules were examined with the optical- or fluorescence microscope in an aqueous environment. Then again, a more likely reason for these observations is the lyophilisation in liquid nitrogen, which puts the small capsules under large amounts of stress. As water crystallises and the materials contract, it could happen that the membrane breaks around a weak point. And indeed, these little rupture-points can be found in several locations of Figure 3.4-37-a, which either looks like little incisions or holes. When magnifying the surface, it becomes evident that it is not smooth, but highly porous. Indeed, it was expected to be a porous material to facilitate semi-permeability, but the pores here in case of protamine/DNA-microcapsules were in size ranges of 1 μm in diameter. The pores were very evenly scattered all over the capsule and had a very uniform size-distribution. Looking back at the results of the permeability experiments from Figure 3.4-33, the size exclusion was determined to be between 250 – 2000 kDa. While the SEM-images could serve as another part of the evidence to explain the high permeability of protamine capsules, they appear to be unlikely big.

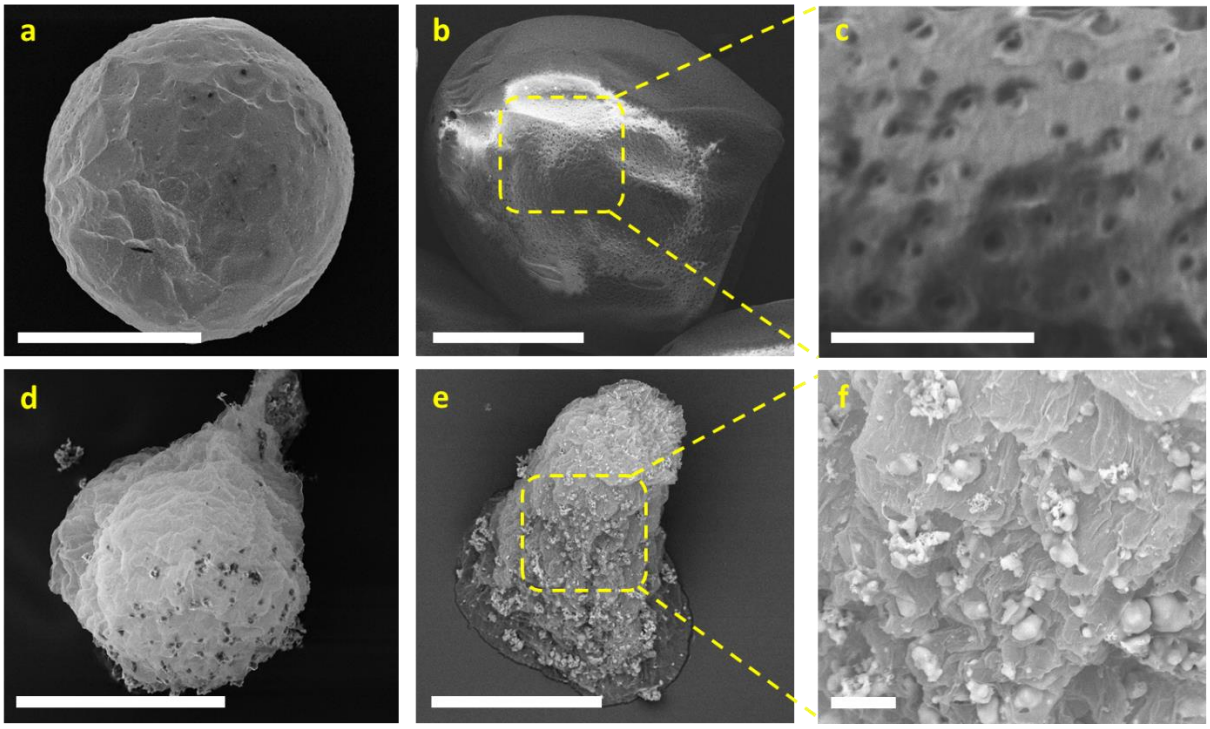

Figure 3.4-37: *Scanning electron microscope images of protamine and AMP-microcapsules.* ***a*** *and* ***b*** *show two different protamine/DNA-capsules and* ***c*** *showing a magnification of a porous membrane structure.* ***d*** *and* ***e*** *represent two different aminoclay/DNA-microcapsules with* ***f*** *magnifying the membrane structure of* ***e****. Scale bars:* ***a,b,d,e:*** *200 µm,* ***c,f****: 10 µm.*

And indeed, with pores of this size, it would basically be permeable for everything below 1 µm, whereas the hydrodynamic radius of FITC-dextran (2000 kDa) was calculated to be around 15.68 nm. As this is much smaller than the size of the pores seen in the SEM-images, it seems unlikely that this is realistic. What seems more plausible though, is that the pores stem from the lyophilisation process. As ice-crystals form and grow along and inside the membrane they expand further than the liquid water due to the lower density of solid H_2O, which could ultimately cause large pores to form. Another possibility is, that these pores narrow as they go deeper into the capsule, thus forming small tunnels which can be used by molecules to enter the capsule, while keeping larger ones out. Nonetheless there is little evidence to support any of the assumptions further, and even worse, it is very hard to image the membrane in a hydrated state.

AMP/DNA-microcapsules on the other hand proved to be much more difficult to visualise under the SEM. Several different attempts were made to lyophilise the cells, but no matter the approach, the cells collapsed badly under the stress of the liquid nitrogen (Figure 3.4-37-d-e). The once spherical structure was deformed into pillar-like structures which did not resemble the original cell anymore. Magnifying the former membrane even further also did not yield any interesting substructures like it was the case for protamine-capsules, but only showed small precipitations sticking to the material. As the cells were kept in a 0.5 mg/mL aminoclay-dispersion to ensure their stability it is easy to understand that excess clay would precipitate during the freeze-drying process, which most likely can be seen as the residues or precipitate in Figure 3.4-37-f.

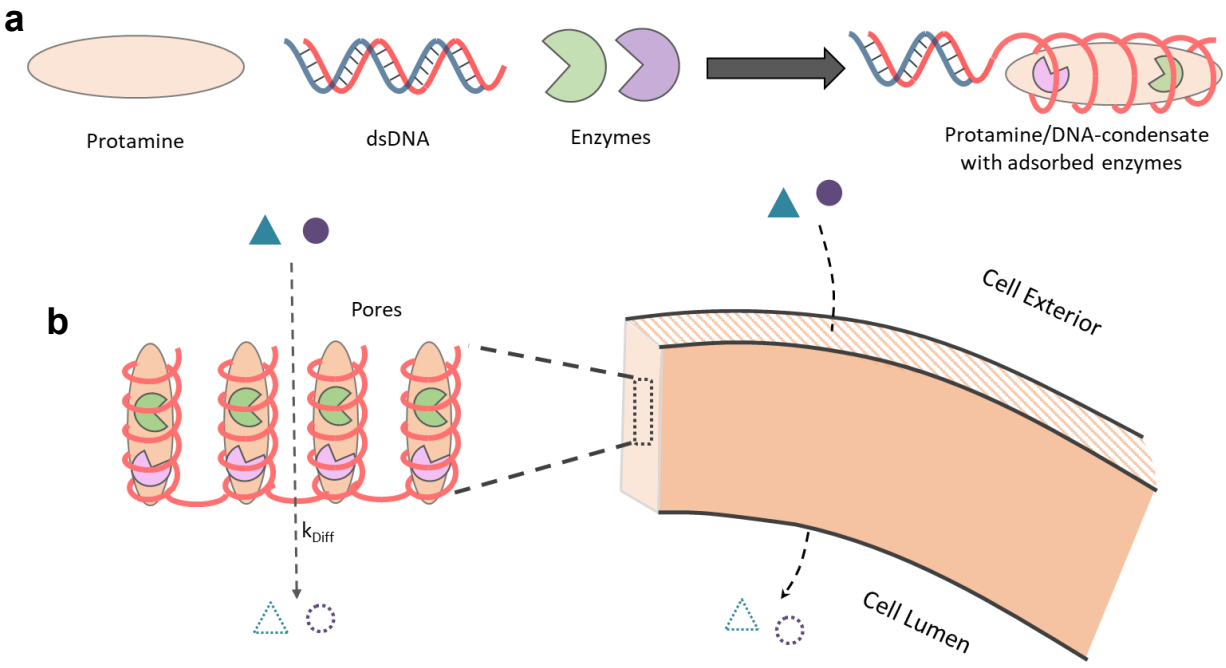

Figure 3.4-38: *Illustration of the assumed membrane-structure of protamine/DNA-microcapsules.* ***a*** *Protamine forms a condensate with dsDNA and is capable of either interacting with enzymes electrostatically or potentially entrapping them sterically during the formation of the condensate, thus forming a very stable complex of DNA, protamine and functional components.* ***b*** *The membrane is comprised of a porous mesh of protamine/DNA-condensate. Smaller molecules and larger species up to molecular weights of 100-200 kDa can pass through these pores, whereas larger molecules and particles will be retained within the cell.*

So, all in all the observations made for protamine/DNA-capsules can be summarised in the following schematic (Figure 3.4-38). The membrane is a highly porous mesh made from a protamine/DNA condensate with permeability cut-offs in the ranges of 100-200 kDa (in reference to FITC-dextran). While SEM-images suggest even larger pores, it seems unlikely that this is the case, nonetheless, the porosity makes the capsule unable to retain smaller molecular species in its interior. In fact, the only two possible mechanisms for protamine/DNA-microcapsules to keep enzymes from leaking out are electrostatic interactions between the enzyme and the condensate and a potential steric entrapment inside the protamine/DNA mesh during the formation of the cell.

3.4.5 Microcapsule types based on dsDNA-complexes with alternative macro-cations

Since the formation of microdroplets with help of the fabrication-device described above (3.3.3) has proven to be an easy way to form microcapsules from oppositely charged macromolecules, this part will demonstrate the general applicability of the air-jet flow method to produce microcompartments with alternative materials. Since DNA has proven to be a reliable anionic material, the cationic counterpart was changed instead. The materials tested for this purpose were Polydiallyldimethylammonium-chloride (PDDA, 100-200 kDa), Polyallylamine-hydrochloride (15 kDa) and protease (from *Bacillus Lichenformis*, 2.5 U/g). The capsules were formed as described in the methods in 3.3.3.

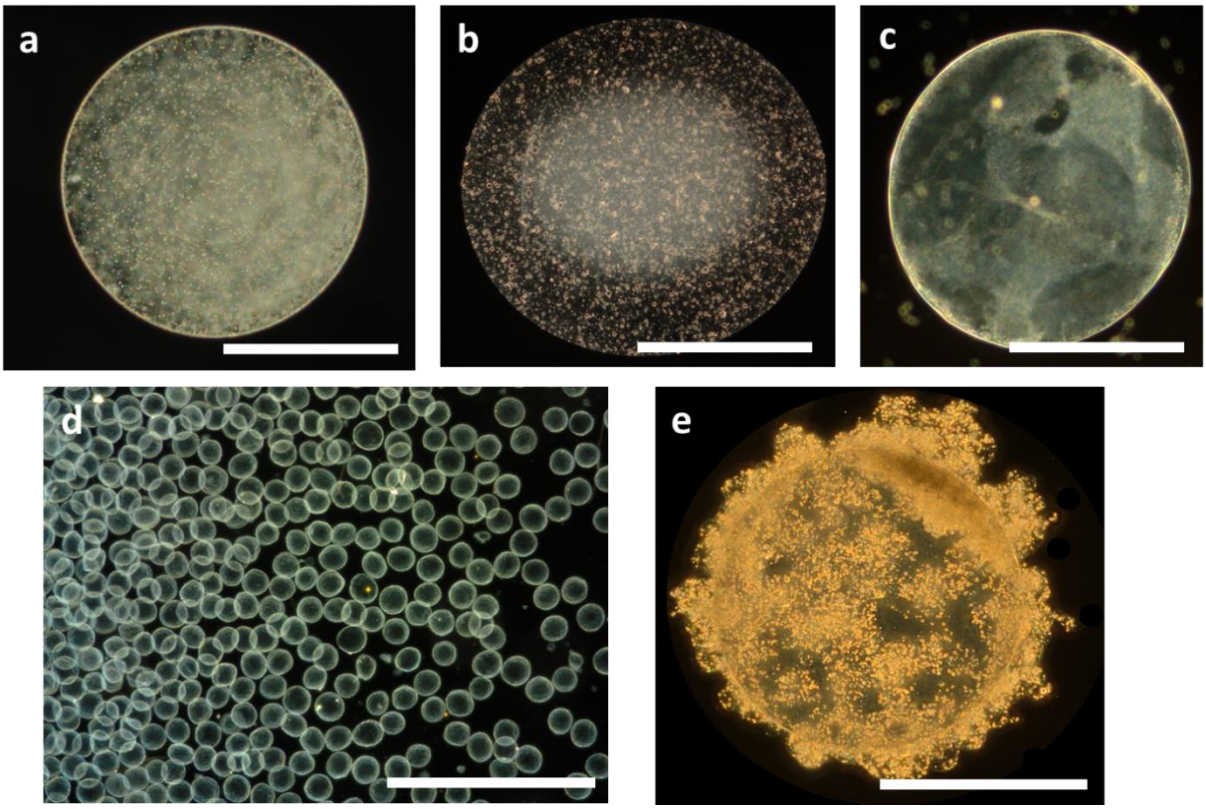

Figure 3.4-39: *Microcapsules made from dsDNA and alternative cationic materials:* ***a*** *Polyallylamine-hydrochloride (15 kDa),* ***b*** *protease (from Bacillus Lichenformis 2.4 U/g) and* ***c*** *Polydiallyldimethylammonium-chloride (PDDA, 100-200 kDa). Furthermore, small PDDA/DNA-microcapsules were fabricated (****d****) which readily adsorbed onto the surface of large protamine/DNA-microcapsules. All scale bars: 300 µm.*

In contrast to AMP- and protamine capsules, PDDA-, protease- and PAH-capsules had a tendency to shrivel right after formation, most likely due to the osmotic pressure between the cell and the exterior solution. Once the capsules were washed with di-water, they started inflating again and were observed as shown in Figure 3.4-39. These capsules stayed stable for several days when kept in 0.5 mg/mL of the respective cationic solution, after which they seemed to disintegrate. Similar to AMP-capsules, they started expending when incubated in water until the membrane would break when it became too thin. Furthermore, these capsule-systems were also capable of encapsulation or adsorption of functional materials or the formation of much smaller capsules which, especially in the case of PDDA/DNA-microcapsules, lead to very monodisperse populations of small PDDA/DNA-microcapsules (Figure 3.4-39-d). Interestingly, most capsules showed very little stickiness or adsorption towards other cell-systems. In the case of the small PDDA-microcapsules though, they appeared highly sticky towards protamine microcapsules. After mixing them together, they were readily adsorbed on the protamine/DNA-surface after mere seconds and could not be removed even with rigid mixing, what resulted in satellite-like structures of small PDDA/DNA-capsules on protamine/DNA-capsules. PDDA is a highly cationic polymer, and it would seem counterintuitive to assume that the stickiness is based on electrostatic interactions, regarding the assumptions made above about the adsorption of anionic particles and proteins. Instead, it seemed more likely, that PDDA/DNA-microcapsules were generally more sticky, due to their soft material and other non-specific surface-interactions.

3.4.6 Hierarchical microcapsule structures

The experiments in chapter 3 have shown that microcapsules are a great host system for the encapsulation of numerous functional components. Nonetheless, an important concept in nature is compartmentalisation of functionalities into cellular subunits. Here, the co-encapsulation capabilities of AMP/DNA and protamine/DNA microcapsules were exploited to produce hierarchical host/guest structures, with either large AMP/DNA or protamine/DNA hosts which contain small guest capsules of the other or even the same species, which provides an excellent opportunity to construct nested micro-compartmentalised systems for protocell research.

As a first experiment the different possible variants of host/guest capsule systems were investigated and analysed via brightfield-microscope. Figure 3.4-40 shows all 4 different possible permutations. Small AMP/DNA-guest capsules were easily encapsulated into AMP-host capsules (Figure 3.4-40-a-b). When trying to encapsulate AMP/DNA-guests into protamine/DNA-hosts though, they often formed amalgamates of the small guests and the host's membrane (Figure 3.4-40-c). As discussed above, protamine/DNA-capsules experience a certain amount of shrinkage during their formation. As the capsule forms from the dsDNA-droplet, the membrane starts to shrink, which could get the membrane in contact with the AMP/DNA guests, and while the membrane is not fully stabilised yet, the small capsules become stuck in between. While this is not what the experiment was designed for, this is an interesting result, as the AMP/DNA-guests could now serve as an interface between the in- and the exterior.

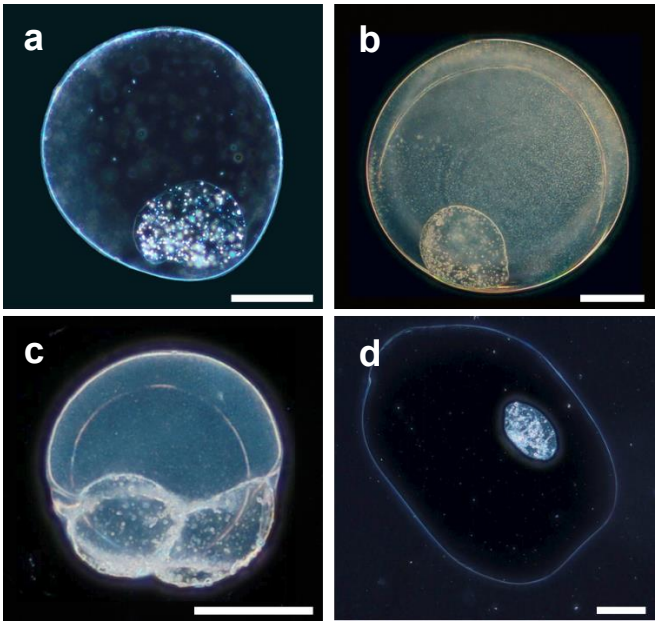

Figure 3.4-40: *Optical micrographs of hierarchical co-encapsulation of small "guest"-capsules into large "host" capsules.* ***a****: encapsulation of a small AMP-capsule into a large AMP-capsule.* ***b****: encapsulation of a small AMP-capsule into a large protamine capsule.* ***c****: semi-encapsulation of two small AMP-capsule into a large protamine capsule.* ***d****: encapsulation of a small protamine-capsule into a large AMP capsule. All scale bars: 100 µm.*

In order to avoid these protamine/DNA and AMP/DNA amalgamates, larger microdroplets were formed during the formation of the cells, which provided more volume for the guest-cells and in return yielded stable protamine/DNA hosts with AMP/DNA-guests inside (Figure 3.4-40-b). The encapsulation of small protamine/DNA-guest capsules on the other hand appeared to be much more complicated and was rarely successful. When using AMP/DNA capsules as hosts, most of them appeared to be empty and even in the few cases small protamine/DNA-capsules were found inside the host, they seemed deformed and collapsed (Figure 3.4-40-d). As it was shown above, AMP/DNA-

capsules are much more molecularly crowded inside, which would apply a larger osmotic pressure on the guests, which in return could explain the deformation. Lastly, using protamine/DNA-hosts for the encapsulation of protamine/DNA-guests failed completely, mostly because both protamine/DNA guests and hosts adhered strongly to each other and rather formed large aggregations instead of separate cell dispersions. Therefore, the work on small protamine/DNA-guests wasn't followed any further.

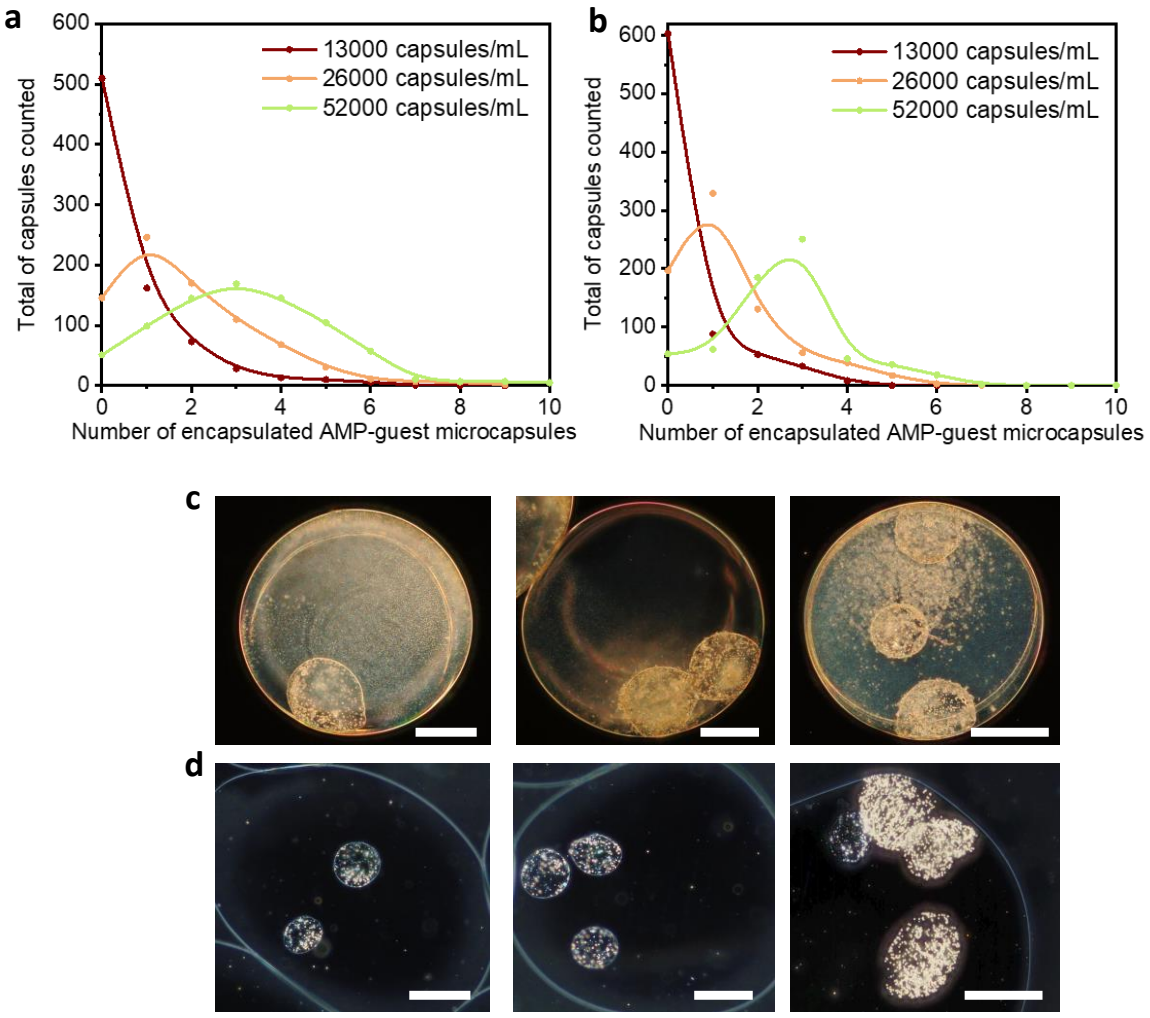

Figure 3.4-41: *Distribution of small AMP/DNA-microcapsule-guests inside* ***(a)*** *AMP/DNA- and* ***(b)*** *protamine/DNA-hosts. The concentration of guests was varied from 13000, 26000 to 52000 guest-capsules/mL. For each concentration, 800 host/guest-capsules were examined via light microscopy and the encapsulated guests counted.* ***(c)*** *micrographs of protamine/DNA- and* ***(d)*** *AMP/DNA-hosts with varying number of guests inside. All scale bars: 100 μm.*

The capsules presented above show merely one or two encapsulated guests. When looking at a whole batch of capsules though, the distribution of guests varies much more and is highly dependable on the amount of guest capsules added to the dsDNA-solution during the formation. To get a better understanding about the stochastics of guest-distribution, 3 different guest-concentrations were investigated and microscopically analysed. Both Host-systems exhibited similar gaussian distributions with average maxima at 0, 1 and 3 encapsulated guests for 13000, 26000 and 52000 guest-capsules/mL respectively. AMP-hosts appeared to have much broader distributions (Figure 3.4-41-a), whereas in case of protamine/DNA-hosts the average peaks were much sharper and more defined (Figure 3.4-41-b). One thing that clearly stood out is that protamine/DNA-microcapsules appeared a

little less likely to encapsulate small AMP/DNA-guests, most likely due to the shrinkage the host-capsule experiences during its formation, which was already discussed for Figure 3.4-40. Altogether, there did not seem to be a limit to how many guest capsules can be encapsulated inside the larger hosts, even though the exact number of guests could not be defined on demand as it is nearly impossible to know how many guests will be found within the droplet.

While encapsulation has been shown many times throughout this chapter, and even though the capsule-structure has been analysed thoroughly, there's still no information available whether small particles or cell-sub compartments are able to move within the host. To gain more insight into the cell-interior, small magnetic particles were encapsulated into AMP/DNA-guest capsules, which were then introduced into AMP/DNA-hosts. The images in Figure 3.4-42 show the motion of one AMP/DNA-guest inside the host-lumen. The moving capsule was digitally highlighted with a purple colour, so it is easier to follow it for the reader.

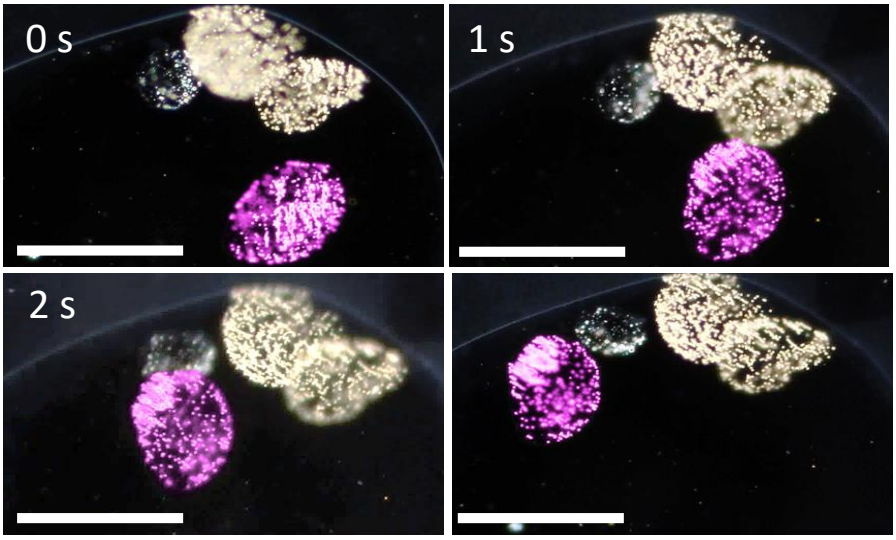

Figure 3.4-42: *Magnetic field-induced movement of a small AMP/DNA guest inside a large AMP/DNA host towards a magnetic field originating from the top- left side of the picture. The moving capsule was digitally highlighted in pink. All scale bars: 100 µm.*

The observed specimen contained 4 guest capsules altogether and motility was induced by placing a magnet next the specimen stage of the microscope (magnet was placed at the top-left corner of the images). The images confirm that the AMP/DNA-guest capsule can move through the host. The capsule traversed a distance of almost 200 µm through the AMP/DNA-host, guided by the external magnetic field, until it got stuck close to the cell-wall. But looking at the specific timeframes, even more useful information can be extracted from this experiment. Moving from 0s to 1s, the magnetic field has not only started moving the capsule, but also the magnetic particles inside the guests which started to accumulate in one corner, which means that even smaller particles are able to move through the microcapsule, or more specifically, the microcapsule guest-compartments. Nonetheless, the majority of the particles seemed to be immobile or stuck on the inner side of the membrane. This could be explained by the fact that the magnetic particles used for this experiment contained negatively charged carboxylate residues on their surface, which might interact with the cell-membrane. Another possible explanation is that the microparticles have been incorporated into the membrane during the formation of the capsule or that they are physically stuck in the soft material of the protamine/DNA-condensate.

3.5 Summary and Outlook

Synthetic cellularity offers a sheer infinite number of possibilities when looking at the number of established techniques and building blocks for the fabrication of micro- or nano compartments. In this chapter, the work from Kumar *et al.* from 2018 [1] was carried on by taking the aminoclay/DNA-microcapsule system and expanding the experimental knowledge about the cells, while developing a promising novel microcapsule-concept in protamine/DNA-capsules. The general leitmotif of this chapter was a direct comparison between both cell-systems, not just to further elucidate and confirm past results, but also to provide a thorough discussion to support the benefits of the new protamine/DNA-capsule system for the coming chapters of this thesis. To make it easier for the reader to get a proper understanding of the capsule-design choices and the consecutive analysis, this chapter followed a similar structure like the chronology of the experiments.

First, the basic structural components dsDNA, aminoclay and protamine were analysed and discussed in the context of microcapsule-fabrication. The cost effective, custom made air-jet extrusion device was introduced and critically discussed, which worked exceptionally well and produced reliable and reproducible microdroplets for the microcapsule formation. Aminoclay/DNA- and protamine/DNA-microcapsules were then compared microscopically and based on their physical and chemical integrity. The latter was of particular interest, as protamine-capsules appeared to be much more stable, both in water and in 50 mM sodium phosphate, whereas AMP-capsules tended to break and fall apart after short amounts of time. The reason for this, and probably the biggest difference between the two cell types, was most likely the condensation of DNA. This could be directly addressed when examining the capsule sizes, as protamine/DNA-capsules tended to be generally smaller than aminoclay-capsules due to the tighter packing of the protamine/DNA condensate.

The most important feature of either microcapsule system though, was the capability of encapsulating functional components like enzymes (catalase, glucose oxidase, horseradish peroxidase, urease), particles (silica particles, polymer particles, magnetic particles) and polymers (FITC-dextran). At the same time, the capsules were also able to adsorb many functional molecules and even particles on their membrane through mere electrostatic interactions, which was shown for enzymes like catalase, platinum particles or even larger magnetic particles. While the encapsulation of molecules inside the cells appeared straight forward for aminoclay/DNA-capsules, it posed more questions for protamine-capsules and started an array of experiments to elucidate this process even further. The results showed that protamine-capsules were only able to retain enzymes on the membrane but not inside the cell, whereas AMP-capsules were capable of doing both. Neither system was prone to enzyme leakage in water but exposing the capsules to 50 mM sodium phosphate led to a substantial decrease of active enzyme on the protamine-capsules. This form of enzyme leakage as a response to the ionic strength of the solution was then further assessed via enzymatic assays with glucose oxidase, horseradish peroxidase and the chromophore ABTS, which confirmed the previous assumption.

As the membranes of the two cell systems appeared to be substantially different, they were thoroughly examined via fluorescence confocal microscopy. The membranes of protamine-capsules appeared to be thicker (4-6 μm) than AMP-capsules (1-2 μm) and exhibited an interesting behaviour when analysed via FRAPS-measurement. Here, no exchange of molecules and therefore no recovery was observed within the membrane after photobleaching, whereas AMP-capsules on the other hand recovered after the optical stimulus. The incapability of retaining anything smaller than particles inside the cell appeared to be one of the most interesting aspects of protamine/DNA-capsules and was further investigated by assessing the membrane permeability with large FITC-dextran oligomers. In line with the previous studies [1], AMP-capsules exhibited a membrane cut-off at around 20-40 kDa but protamine-capsules were permeable up to 200 kDa and more, with 2000 kDa FITC-dextran being

the only molecule to not readily diffuse through the membrane. Finally, both cell types were analysed via scanning electron microscope, which again proved that protamine-capsules were more stable than AMP-capsules, as the latter collapsed under the stresses of lyophilisation.

There are still several open questions which would need to be addressed specifically to properly understand the dynamics and composition of the capsule-membranes. Assumptions were made on the correlation between the ionic strength and the desorption of enzymes from protamine/DNA-microcapsules, but it is still not clear whether the sodium-phosphate buffers used for these experiments are not damaging the cells more than it was seen through the microscope, which in return could release the enzymes from the membrane. More experiments would be necessary to gather data about how exactly enzymes are bound to protamine/DNA-capsules, if they are simply attached via electrostatic interactions or if there are other interactions or even steric entrapment involved, which play a part in the binding and detachment of components. Especially the membrane permeability appeared to be a very important and at the same time questionable subject, which needs to be addressed further to understand the exact permeability cut-off for both cell types. It would furthermore be interesting to find a proper way to prepare aminoclay-capsules for the analysis with the SEM, without them collapsing beforehand. One option could be to use a substance with an even lower temperature like liquid helium, which could potentially accelerate the freezing process and retain the capsule's structure.

Due to the simplicity of the cell-fabrication and to expand the repertoire of different cell-types, other novel DNA-cell-compositions were investigated. Every material offers different properties and changes how the cells behave, even if just by a small margin. For future experiments it is necessary to have a broad understanding of the DNA-microcapsule system and what materials can be used for microcapsule fabrication, to design the most fitting capsules for the purpose of the experiment. Next to the already discussed protamine and aminoclay-capsules, the following materials were investigated in combination with dsDNA: Polydiallyldimethylammonium-chloride, polyallylamine-hydrochloride and protease. All cells formed successfully and exhibited very similar properties regarding encapsulation and adsorption of functional components. Another interesting concept to investigate would be the design of composite materials of different cationic polymers within one cell. Since protamine/DNA-capsules are incapable of retaining functional components inside, it could potentially be possible to prevent enzyme leakage by stabilising AMP/DNA-capsules with protamine after their fabrication or even mix the two components together during the fabrication of the cell, to form an AMP/Protamine/DNA-composite complex. Nonetheless, regarding the work of the next chapters, all other capsule systems were inferior to the structural stability of protamine/DNA-capsules.

Lastly, this chapter investigated the fabrication of nested microcompartments. To enable this, small AMP- or protamine microcapsule were made by manipulating the fabrication-device, which were then co-encapsulated into larger AMP/DNA- or protamine/DNA-hosts. The boundaries of this concept were analysed by using both capsule-types as either hosts or guests and the number of encapsulated guests was assessed statistically. By encapsulating magnetic particles into guest-compartments, the small guest objects were moved through the host, thus proving that the cell interior of the microcapsules does not prevent the motion of macroscopic objects like particles or even small cells. The design of hierarchical substructures and sub-compartments offers some interesting opportunities for future experiments. This chapter has established the encapsulation of functional components into microcapsules, which works for both large and small species. With this in mind, it should be possible to design functional sub-compartments instead of plainly entrapping one or more enzymes in the host. This way, the cells would take another step closer to biological systems which rely on the separation of functionality within different cell-organelles.

The purpose of chapter 3 is to provide enough information for the reader to establish a broad foundation, which further investigation can be based on towards a much more interesting topic and application for inorganic/organic hybrid microcapsules. In this next step, the enzymes catalase and glucose oxidase will be encapsulated to design a controllable, reliable and versatile mechanism for microcapsule motility via buoyancy. Kumar *et al.* [1] have established the concept of microcapsule buoyancy in their paper for AMP/DNA-microcapsules but the general convenience and, most importantly, stability of the capsules would soon set the limits for further, more complex motility concepts. With the novel protamine/DNA-capsules though, not only microcapsule buoyancy but also long lasting oscillations between separate chemical environments will be investigated, followed by a thorough analysis of the dynamics between the enzymes inside the capsules and the substrate environment around them.

3.6 Literature for chapter 3

1. Kumar, B. V. V. S. P., Patil, A. J. & Mann, S. Enzyme-powered motility in buoyant organoclay/DNA protocells. *Nature Chemistry* **10**, 1154-1163, doi:10.1038/s41557-018-0119-3 (2018).
2. Oparin, A. I. The origin of life. *Nord Med* **65**, 693-697 (1961).
3. Dzieciol, A. J. & Mann, S. Designs for life: protocell models in the laboratory. *Chem Soc Rev* **41**, 79-85, doi:10.1039/c1cs15211d (2012).
4. Reeves, J. P. & Dowben, R. M. Formation and properties of thin-walled phospholipid vesicles. *J Cell Physiol* **73**, 49-60, doi:10.1002/jcp.1040730108 (1969).
5. Walde, P. Building artificial cells and protocell models: experimental approaches with lipid vesicles. *Bioessays* **32**, 296-303, doi:10.1002/bies.200900141 (2010).
6. Monnard, P. A. & Deamer, D. W. Membrane self-assembly processes: steps toward the first cellular life. *Anat Rec* **268**, 196-207, doi:10.1002/ar.10154 (2002).
7. Akashi, K., Miyata, H., Itoh, H. & Kinosita, K., Jr. Preparation of giant liposomes in physiological conditions and their characterization under an optical microscope. *Biophys J* **71**, 3242-3250, doi:10.1016/S0006-3495(96)79517-6 (1996).
8. Angelova, M. I. & Dimitrov, D. S. Liposome electroformation. *Faraday Discussions of the Chemical Society* **81**, 303-311, doi:10.1039/DC9868100303 (1986).
9. Menger, F. M. & Angelova, M. I. Giant Vesicles: Imitating the Cytological Processes of Cell Membranes. *Accounts of Chemical Research* **31**, 789-797, doi:10.1021/ar970103v (1998).
10. S. Svetina, B., Zeks. Shape behavior of lipid vesicles as the basis of some cellular processes. *Anatomical Record, The* **268**, 215-225 (2002).
11. Svetina, S. Vesicle Budding and the Origin of Cellular Life. *ChemPhysChem* **10**, 2769-2776, doi:https://doi.org/10.1002/cphc.200900577 (2009).
12. Chakrabarti, A. C., Breaker, R. R., Joyce, G. F. & Deamer, D. W. Production of RNA by a polymerase protein encapsulated within phospholipid vesicles. *Journal of Molecular Evolution* **39**, 555-559, doi:10.1007/BF00160400 (1994).
13. Shohda, K. I. & Sugawara, T. DNA polymerization on the inner surface of a giant liposome for synthesizing an artificial cell model. *Soft Matter* **2**, 402-408, doi:10.1039/b516834a (2006).
14. Oberholzer, T., Albrizio, M. & Luisi, P. L. Polymerase chain reaction in liposomes. *Chem Biol* **2**, 677-682, doi:10.1016/1074-5521(95)90031-4 (1995).
15. Yu, W. *et al.* Synthesis of functional protein in liposome. *J Biosci Bioeng* **92**, 590-593, doi:10.1263/jbb.92.590 (2001).
16. Oberholzer, T. & Luisi, P. L. The use of liposomes for constructing cell models. *J Biol Phys* **28**, 733-744, doi:10.1023/A:1021267512805 (2002).
17. Nomura, S.-i. M. *et al.* Gene Expression within Cell-Sized Lipid Vesicles. *ChemBioChem* **4**, 1172-1175, doi:https://doi.org/10.1002/cbic.200300630 (2003).
18. Noireaux, V. & Libchaber, A. A vesicle bioreactor as a step toward an artificial cell assembly. *Proc Natl Acad Sci U S A* **101**, 17669-17674, doi:10.1073/pnas.0408236101 (2004).
19. Deamer, D. A giant step towards artificial life? *Trends Biotechnol* **23**, 336-338, doi:10.1016/j.tibtech.2005.05.008 (2005).
20. Murtas, G., Kuruma, Y., Bianchini, P., Diaspro, A. & Luisi, P. L. Protein synthesis in liposomes with a minimal set of enzymes. *Biochem Biophys Res Commun* **363**, 12-17, doi:10.1016/j.bbrc.2007.07.201 (2007).
21. Kuruma, Y., Stano, P., Ueda, T. & Luisi, P. L. A synthetic biology approach to the construction of membrane proteins in semi-synthetic minimal cells. *Biochim Biophys Acta* **1788**, 567-574, doi:10.1016/j.bbamem.2008.10.017 (2009).
22. Pereira de Souza, T., Stano, P. & Luisi, P. L. The Minimal Size of Liposome-Based Model Cells Brings about a Remarkably Enhanced Entrapment and Protein Synthesis. *ChemBioChem* **10**, 1056-1063, doi:https://doi.org/10.1002/cbic.200800810 (2009).

23. Saito, H. *et al.* Time-Resolved Tracking of a Minimum Gene Expression System Reconstituted in Giant Liposomes. *ChemBioChem* **10**, 1640-1643, doi:https://doi.org/10.1002/cbic.200900205 (2009).
24. Kita, H. *et al.* Replication of Genetic Information with Self-Encoded Replicase in Liposomes. *ChemBioChem* **9**, 2403-2410, doi:https://doi.org/10.1002/cbic.200800360 (2008).
25. Gardner, P. M., Winzer, K. & Davis, B. G. Sugar synthesis in a protocellular model leads to a cell signalling response in bacteria. *Nature Chemistry* **1**, 377-383, doi:10.1038/nchem.296 (2009).
26. Walde, P., Wick, R., Fresta, M., Mangone, A. & Luisi, P. L. Autopoietic Self-Reproduction of Fatty Acid Vesicles. *Journal of the American Chemical Society* **116**, 11649-11654, doi:10.1021/ja00105a004 (1994).
27. Mansy, S. S. *et al.* Template-directed synthesis of a genetic polymer in a model protocell. *Nature* **454**, 122-125, doi:10.1038/nature07018 (2008).
28. Hanczyc, M. M., Fujikawa, S. M. & Szostak, J. W. Experimental Models of Primitive Cellular Compartments: Encapsulation, Growth, and Division. *Science* **302**, 618-622, doi:10.1126/science.1089904 (2003).
29. Berclaz, N., Müller, M., Walde, P. & Luisi, P. L. Growth and Transformation of Vesicles Studied by Ferritin Labeling and Cryotransmission Electron Microscopy. *The Journal of Physical Chemistry B* **105**, 1056-1064, doi:10.1021/jp001298i (2001).
30. Chen, I. A. & Szostak, J. W. A kinetic study of the growth of fatty acid vesicles. *Biophys J* **87**, 988-998, doi:10.1529/biophysj.104.039875 (2004).
31. Zhu, T. F. & Szostak, J. W. Coupled Growth and Division of Model Protocell Membranes. *Journal of the American Chemical Society* **131**, 5705-5713, doi:10.1021/ja900919c (2009).
32. Stano, P. & Luisi, P. L. Achievements and open questions in the self-reproduction of vesicles and synthetic minimal cells. *Chemical Communications* **46**, 3639-3653, doi:10.1039/B913997D (2010).
33. Discher, D. E. & Eisenberg, A. Polymer Vesicles. *Science* **297**, 967-973, doi:10.1126/science.1074972 (2002).
34. Broz, P. *et al.* Toward Intelligent Nanosize Bioreactors: A pH-Switchable, Channel-Equipped, Functional Polymer Nanocontainer. *Nano Letters* **6**, 2349-2353, doi:10.1021/nl0619305 (2006).
35. Kumar, M., Grzelakowski, M., Zilles, J., Clark, M. & Meier, W. Highly permeable polymeric membranes based on the incorporation of the functional water channel protein Aquaporin Z. *Proceedings of the National Academy of Sciences* **104**, 20719-20724, doi:10.1073/pnas.0708762104 (2007).
36. Kim, K. T., Cornelissen, J. J. L. M., Nolte, R. J. M. & van Hest, J. C. M. A Polymersome Nanoreactor with Controllable Permeability Induced by Stimuli-Responsive Block Copolymers. *Advanced Materials* **21**, 2787-2791, doi:https://doi.org/10.1002/adma.200900300 (2009).
37. Gaitzsch, J., Appelhans, D., Wang, L., Battaglia, G. & Voit, B. Synthetic Bio-nanoreactor: Mechanical and Chemical Control of Polymersome Membrane Permeability. *Angewandte Chemie International Edition* **51**, 4448-4451, doi:https://doi.org/10.1002/anie.201108814 (2012).
38. Huang, X., Appelhans, D., Formanek, P., Simon, F. & Voit, B. Tailored Synthesis of Intelligent Polymer Nanocapsules: An Investigation of Controlled Permeability and pH-Dependent Degradability. *ACS Nano* **6**, 9718-9726, doi:10.1021/nn3031723 (2012).
39. Roy, D., Cambre, J. N. & Sumerlin, B. S. Sugar-responsive block copolymers by direct RAFT polymerization of unprotected boronic acid monomers. *Chemical Communications*, 2477-2479, doi:10.1039/B802293C (2008).
40. Axthelm, F. *et al.* Antioxidant Nanoreactor Based on Superoxide Dismutase Encapsulated in Superoxide-Permeable Vesicles. *The Journal of Physical Chemistry B* **112**, 8211-8217, doi:10.1021/jp803032w (2008).

41. Shum, H. C., Zhao, Y.-j., Kim, S.-H. & Weitz, D. A. Multicompartment Polymersomes from Double Emulsions. *Angewandte Chemie International Edition* **50**, 1648-1651, doi:https://doi.org/10.1002/anie.201006023 (2011).
42. Thompson, K. L., Chambon, P., Verber, R. & Armes, S. P. Can Polymersomes Form Colloidosomes? *Journal of the American Chemical Society* **134**, 12450-12453, doi:10.1021/ja305789e (2012).
43. Huang, X. & Voit, B. Progress on multi-compartment polymeric capsules. *Polymer Chemistry* **4**, 435-443, doi:10.1039/C2PY20636F (2013).
44. Marguet, M., Bonduelle, C. & Lecommandoux, S. Multicompartmentalized polymeric systems: towards biomimetic cellular structure and function. *Chemical Society Reviews* **42**, 512-529, doi:10.1039/C2CS35312A (2013).
45. Peters, R. J. R. W. *et al.* Cascade Reactions in Multicompartmentalized Polymersomes. *Angewandte Chemie International Edition* **53**, 146-150, doi:https://doi.org/10.1002/anie.201308141 (2014).
46. Pickering, S. U. CXCV.—The chemistry of bordeaux mixture. *Journal of the Chemical Society, Transactions* **91**, 1988-2001, doi:10.1039/CT9079101988 (1907).
47. Wang, H., Zhu, X., Tsarkova, L., Pich, A. & Möller, M. All-Silica Colloidosomes with a Particle-Bilayer Shell. *ACS Nano* **5**, 3937-3942, doi:10.1021/nn200436s (2011).
48. Velev, O. D., Furusawa, K. & Nagayama, K. Assembly of Latex Particles by Using Emulsion Droplets as Templates. 1. Microstructured Hollow Spheres. *Langmuir* **12**, 2374-2384, doi:10.1021/la9506786 (1996).
49. Dinsmore, A. D. *et al.* Colloidosomes: Selectively Permeable Capsules Composed of Colloidal Particles. *Science* **298**, 1006-1009, doi:10.1126/science.1074868 (2002).
50. Yow, H. N. & Routh, A. F. Release Profiles of Encapsulated Actives from Colloidosomes Sintered for Various Durations. *Langmuir* **25**, 159-166, doi:10.1021/la802711y (2009).
51. Noble, P. F., Cayre, O. J., Alargova, R. G., Velev, O. D. & Paunov, V. N. Fabrication of "Hairy" Colloidosomes with Shells of Polymeric Microrods. *Journal of the American Chemical Society* **126**, 8092-8093, doi:10.1021/ja047808u (2004).
52. Duan, H. *et al.* Magnetic Colloidosomes Derived from Nanoparticle Interfacial Self-Assembly. *Nano Letters* **5**, 949-952, doi:10.1021/nl0505391 (2005).
53. Croll, L. M. & Stöver, H. D. H. Formation of Tectocapsules by Assembly and Cross-linking of Poly(divinylbenzene-alt-maleic anhydride) Spheres at the Oil−Water Interface. *Langmuir* **19**, 5918-5922, doi:10.1021/la026485h (2003).
54. Thompson, K. L. *et al.* Covalently Cross-Linked Colloidosomes. *Macromolecules* **43**, 10466-10474, doi:10.1021/ma102499k (2010).
55. Chen, T., Colver, P. J. & Bon, S. A. F. Organic–Inorganic Hybrid Hollow Spheres Prepared from TiO2-Stabilized Pickering Emulsion Polymerization. *Advanced Materials* **19**, 2286-2289, doi:https://doi.org/10.1002/adma.200602447 (2007).
56. Binks, B. P. & Murakami, R. Phase inversion of particle-stabilized materials from foams to dry water. *Nat Mater* **5**, 865-869, doi:10.1038/nmat1757 (2006).
57. Li, M., Green, D. C., Anderson, J. L. R., Binks, B. P. & Mann, S. In vitro gene expression and enzyme catalysis in bio-inorganic protocells. *Chemical Science* **2**, 1739-1745, doi:10.1039/C1SC00183C (2011).
58. Subramaniam, A. B., Wan, J., Gopinath, A. & Stone, H. A. Semi-permeable vesicles composed of natural clay. *Soft Matter* **7**, 2600-2612, doi:10.1039/C0SM01354D (2011).
59. Wang, C., Liu, H., Gao, Q., Liu, X. & Tong, Z. Facile Fabrication of Hybrid Colloidosomes with Alginate Gel Cores and Shells of Porous CaCO3 Microparticles. *ChemPhysChem* **8**, 1157-1160, doi:https://doi.org/10.1002/cphc.200700147 (2007).
60. He, J., Liu, Y., Babu, T., Wei, Z. & Nie, Z. Self-Assembly of Inorganic Nanoparticle Vesicles and Tubules Driven by Tethered Linear Block Copolymers. *Journal of the American Chemical Society* **134**, 11342-11345, doi:10.1021/ja3032295 (2012).

61. Zhang, J., Song, Y.-F., Cronin, L. & Liu, T. Reverse-Vesicle Formation of Organic–Inorganic Polyoxometalate-Containing Hybrid Surfactants with Tunable Sizes. *Chemistry – A European Journal* **16**, 11320-11324, doi:https://doi.org/10.1002/chem.201000794 (2010).
62. Bachinger, A. & Kickelbick, G. Pickering emulsions stabilized by anatase nanoparticles. *Monatshefte für Chemie - Chemical Monthly* **141**, 685-690, doi:10.1007/s00706-010-0273-9 (2010).
63. Zgheib, N. *et al.* Stabilization of Miniemulsion Droplets by Cerium Oxide Nanoparticles: A Step toward the Elaboration of Armored Composite Latexes. *Langmuir* **28**, 6163-6174, doi:10.1021/la300494g (2012).
64. Zhou, J., Wang, L., Qiao, X., Binks, B. P. & Sun, K. Pickering emulsions stabilized by surface-modified Fe3O4 nanoparticles. *J Colloid Interface Sci* **367**, 213-224, doi:10.1016/j.jcis.2011.11.001 (2012).
65. He, Y. *et al.* Factors that Affect Pickering Emulsions Stabilized by Graphene Oxide. *ACS Applied Materials & Interfaces* **5**, 4843-4855, doi:10.1021/am400582n (2013).
66. Pang, M. *et al.* Synthesis and Integration of Fe-soc-MOF Cubes into Colloidosomes via a Single-Step Emulsion-Based Approach. *Journal of the American Chemical Society* **135**, 10234-10237, doi:10.1021/ja403994u (2013).
67. Li, M., Harbron, R. L., Weaver, J. V. M., Binks, B. P. & Mann, S. Electrostatically gated membrane permeability in inorganic protocells. *Nature Chemistry* **5**, 529-536, doi:10.1038/nchem.1644 (2013).
68. Shah, R. K., Kim, J.-W. & Weitz, D. A. Monodisperse Stimuli-Responsive Colloidosomes by Self-Assembly of Microgels in Droplets. *Langmuir* **26**, 1561-1565, doi:10.1021/la9041327 (2010).
69. Cayre, O. J. *et al.* pH-responsive colloidosomes and their use for controlling release. *Soft Matter* **8**, 4717-4724, doi:10.1039/C2SM00002D (2012).
70. Bollhorst, T. *et al.* Synthesis Route for the Self-Assembly of Submicrometer-Sized Colloidosomes with Tailorable Nanopores. *Chemistry of Materials* **25**, 3464-3471, doi:10.1021/cm401610a (2013).
71. Li, M., Huang, X. & Mann, S. Spontaneous Growth and Division in Self-Reproducing Inorganic Colloidosomes. *Small* **10**, 3291-3298, doi:https://doi.org/10.1002/smll.201400639 (2014).
72. Rosenberg, R. T. & Dan, N. Designing Nanoparticle Colloidal Shells for Selective Transport. *Soft Materials* **11**, 143-148, doi:10.1080/1539445X.2011.591867 (2013).
73. Huang, X. *et al.* Interfacial assembly of protein–polymer nano-conjugates into stimulus-responsive biomimetic protocells. *Nature Communications* **4**, 2239, doi:10.1038/ncomms3239 (2013).
74. Huang, X., Li, M. & Mann, S. Membrane-mediated cascade reactions by enzyme–polymer proteinosomes. *Chemical Communications* **50**, 6278-6280, doi:10.1039/C4CC02256D (2014).
75. Huang, X., Patil, A. J., Li, M. & Mann, S. Design and Construction of Higher-Order Structure and Function in Proteinosome-Based Protocells. *Journal of the American Chemical Society* **136**, 9225-9234, doi:10.1021/ja504213m (2014).
76. Lopez-Berestein, G. *et al.* Liposomal amphotericin B for the treatment of systemic fungal infections in patients with cancer: a preliminary study. *J Infect Dis* **151**, 704-710, doi:10.1093/infdis/151.4.704 (1985).
77. Lasic, D. Liposomes. *American Scientist* **80**, 20-31 (1992).
78. Kruyt, H. R. *Colloid Science, Volume II: Reversible Systems*. (Elsevier Publishing Company, 1949).
79. Flory, P. J. *Principles of polymer chemistry*. (1953).
80. Albertsson, P.-Å. in *Advances in Protein Chemistry* Vol. 24 (eds C. B. Anfinsen, John T. Edsall, & Frederic M. Richards) 309-341 (Academic Press, 1970).
81. Mace, C. R. *et al.* Aqueous Multiphase Systems of Polymers and Surfactants Provide Self-Assembling Step-Gradients in Density. *Journal of the American Chemical Society* **134**, 9094-9097, doi:10.1021/ja303183z (2012).

82. Veis, A. A review of the early development of the thermodynamics of the complex coacervation phase separation. *Adv Colloid Interface Sci* **167**, 2-11, doi:10.1016/j.cis.2011.01.007 (2011).
83. Koga, S., Williams, D. S., Perriman, A. W. & Mann, S. Peptide–nucleotide microdroplets as a step towards a membrane-free protocell model. *Nature Chemistry* **3**, 720-724, doi:10.1038/nchem.1110 (2011).
84. Tang, T. Y. D., Antognozzi, M., Vicary, J. A., Perriman, A. W. & Mann, S. Small-molecule uptake in membrane-free peptide/nucleotide protocells. *Soft Matter* **9**, 7647-7656, doi:10.1039/C3SM50726B (2013).
85. Dora Tang, T. Y. *et al.* Fatty acid membrane assembly on coacervate microdroplets as a step towards a hybrid protocell model. *Nature Chemistry* **6**, 527-533, doi:10.1038/nchem.1921 (2014).
86. Williams, D. S., Patil, A. J. & Mann, S. Spontaneous Structuration in Coacervate-Based Protocells by Polyoxometalate-Mediated Membrane Assembly. *Small* **10**, 1830-1840, doi:https://doi.org/10.1002/smll.201303654 (2014).
87. Burkett, S. L., Press, A. & Mann, S. Synthesis, Characterization, and Reactivity of Layered Inorganic−Organic Nanocomposites Based on 2:1 Trioctahedral Phyllosilicates. *Chemistry of Materials* **9**, 1071-1073, doi:10.1021/cm9700615 (1997).
88. Holmström, S. *Self-assembled bioinorganic hybrid materials*, (2008).
89. Patil, A. J. & Mann, S. Self-assembly of bio–inorganic nanohybrids using organoclay building blocks. *Journal of Materials Chemistry* **18**, 4605-4615, doi:10.1039/B805653F (2008).
90. Lainé, M. *et al.* Reaction mechanisms in swelling clays under ionizing radiation: influence of the water amount and of the nature of the clay mineral. *RSC Adv.* **7**, 526-534, doi:10.1039/C6RA24861F (2017).
91. Comert, F. & Dubin, P. L. Liquid-liquid and liquid-solid phase separation in protein-polyelectrolyte systems. *Advances in Colloid and Interface Science* **239**, 213-217, doi:https://doi.org/10.1016/j.cis.2016.08.005 (2017).
92. Comert, F. *et al.* Precipitate–Coacervate Transformation in Polyelectrolyte–Mixed Micelle Systems. *The Journal of Physical Chemistry B* **121**, 4466-4473, doi:10.1021/acs.jpcb.6b12895 (2017).
93. Tanaka, K. & Okahata, Y. A DNA−Lipid Complex in Organic Media and Formation of an Aligned Cast Film1. *Journal of the American Chemical Society* **118**, 10679-10683, doi:10.1021/ja9617855 (1996).
94. Martin, N. *et al.* Photoswitchable Phase Separation and Oligonucleotide Trafficking in DNA Coacervate Microdroplets. *Angewandte Chemie International Edition* **58**, 14594-14598, doi:https://doi.org/10.1002/anie.201909228 (2019).
95. Bench, G. S., Friz, A. M., Corzett, M. H., Morse, D. H. & Balhorn, R. DNA and total protamine masses in individual sperm from fertile mammalian subjects. *Cytometry* **23**, 263-271, doi:https://doi.org/10.1002/(SICI)1097-0320(19960401)23:4<263::AID-CYTO1>3.0.CO;2-I (1996).
96. Gagnon, C. *The male gamete: from basic science to clinical applications*. (Cache River Press, 1999).
97. Brewer, L. R., Corzett, M. & Balhorn, R. Protamine-Induced Condensation and Decondensation of the Same DNA Molecule. *Science* **286**, 120-123, doi:10.1126/science.286.5437.120 (1999).
98. Vilfan, I. D., Conwell, C. C. & Hud, N. V. Formation of native-like mammalian sperm cell chromatin with folded bull protamine. *J Biol Chem* **279**, 20088-20095, doi:10.1074/jbc.M312777200 (2004).
99. Balhorn, R. The protamine family of sperm nuclear proteins. *Genome Biology* **8**, 227, doi:10.1186/gb-2007-8-9-227 (2007).
100. Carr, J. & Silverman, N. The heparin-protamine interaction: a review. *Journal of cardiovascular surgery* **40**, 659 (1999).

101. Owens, D. R. Insulin Preparations with Prolonged Effect. *Diabetes Technology & Therapeutics* **13**, S-5-S-14, doi:10.1089/dia.2011.0068 (2011).
102. Duarte-Vázquez, M. *et al.* Effect of protamine in obesity induced by high-fat diets in rats. *International Journal of Obesity* **33**, 687-692, doi:10.1038/ijo.2009.78 (2009).
103. SAUTIÈRE, P., BRIAND, G., GUSSE, M. & CHEVAILLIER, P. Primary Structure of a Protamine Isolated from the Sperm Nuclei of the Dog-Fish Scylliorhinus caniculus. *European Journal of Biochemistry* **119**, 251-255, doi:https://doi.org/10.1111/j.1432-1033.1981.tb05601.x (1981).
104. Markarian, S. A. & Shahinyan, G. A. The effect of dimethylsulfoxide on absorption and fluorescence spectra of aqueous solutions of acridine orange base. *Spectrochimica Acta Part A: Molecular and Biomolecular Spectroscopy* **151**, 662-666, doi:https://doi.org/10.1016/j.saa.2015.06.126 (2015).
105. Scientific, T. *DyLight® Amine-Reactive Dyes*, <https://www.thermofisher.com/document-connect/document-connect.html?url=https%3A%2F%2Fassets.thermofisher.com%2FTFS-Assets%2FLSG%2Fmanuals%2FMAN0011595_DyLight_AmineReactive_Dye_UG.pdf&title=VXNlciBHdWlkZTogIER5TGlnaHQgQW1pbmUtUmVhY3RpdmUgRHllcw==> (2021).
106. Wu, G.-W. *et al.* Citrate-Capped Platinum Nanoparticle as a Smart Probe for Ultrasensitive Mercury Sensing. *Analytical Chemistry* **86**, 10955-10960, doi:10.1021/ac503544w (2014).
107. Mann, S. *et al.* Sol−Gel Synthesis of Organized Matter. *Chemistry of Materials* **9**, 2300-2310, doi:10.1021/cm970274u (1997).
108. Patil, A. J., Muthusamy, E. & Mann, S. Fabrication of functional protein–organoclay lamellar nanocomposites by biomolecule-induced assembly of exfoliated aminopropyl-functionalized magnesium phyllosilicates. *Journal of Materials Chemistry* **15**, 3838-3843, doi:10.1039/B504288G (2005).
109. Chandrasekaran, G., Han, H.-K., Kim, G.-J. & Shin, H.-J. Antimicrobial activity of delaminated aminopropyl functionalized magnesium phyllosilicates. *Applied Clay Science* **53**, 729-736, doi:https://doi.org/10.1016/j.clay.2011.07.001 (2011).
110. Yang, L., Choi, S.-K., Shin, H.-J. & Han, H.-K. 3-aminopropyl functionalized magnesium phyllosilicate as an organoclay based drug carrier for improving the bioavailability of flurbiprofen. *International journal of nanomedicine* **8**, 4147-4155, doi:10.2147/IJN.S51756 (2013).
111. Ferreira, R. B., da Silva, C. R. & Pastore, H. O. Aminopropyl-Modified Magnesium−Phyllosilicates: Layered Solids with Tailored Interlayer Access and Reactivity. *Langmuir* **24**, 14215-14221, doi:10.1021/la802142s (2008).
112. T. Whilton, N., L. Burkett, S. & Mann, S. Hybrid lamellar nanocomposites based on organically functionalized magnesium phyllosilicate clays with interlayer reactivity. *Journal of Materials Chemistry* **8**, 1927-1932, doi:10.1039/A802120A (1998).
113. Jalil, A. H. & Pyell, U. Quantification of Zeta-Potential and Electrokinetic Surface Charge Density for Colloidal Silica Nanoparticles Dependent on Type and Concentration of the Counterion: Probing the Outer Helmholtz Plane. *The Journal of Physical Chemistry C* **122**, 4437-4453, doi:10.1021/acs.jpcc.7b12525 (2018).
114. Misra, A. Ch. Chapter 8 – Proteomics, 387-427 (Elsevier, 2010).
115. Shen, C.-H. in *Diagnostic Molecular Biology 1st Edition* Ch. Chapter 4 – Gene Expression: Translation of the Genetic Code, 87-116 (Academic Press, 2019).
116. Delgado, A. V., González-Caballero, F., Hunter, R. J., Koopal, L. K. & Lyklema, J. Measurement and Interpretation of Electrokinetic Phenomena (IUPAC Technical Report). *Pure and Applied Chemistry* **77**, 1753-1805, doi:https://doi.org/10.1351/pac200577101753 (2005).
117. Ayorinde, F. O., Gelain, S. V., Johnson Jr., J. H. & Wan, L. W. Analysis of some commercial polysorbate formulations using matrix-assisted laser desorption/ionization time-of-flight mass spectrometry. *Rapid Communications in Mass Spectrometry* **14**, 2116-2124, doi:https://doi.org/10.1002/1097-0231(20001130)14:22<2116::AID-RCM142>3.0.CO;2-1 (2000).

118. Kim, C. & Hsieh, Y.-L. Wetting and absorbency of nonionic surfactant solutions on cotton fabrics. *Colloids and Surfaces A: Physicochemical and Engineering Aspects* **187-188**, 385-397, doi:https://doi.org/10.1016/S0927-7757(01)00653-7 (2001).
119. Adamantini, P. & Vassilis, K. Use of polysorbate 80 to reduce cholesterol in dehydrated egg yolk. *International Journal of Food Science & Technology* **30**, 57-63, doi:https://doi.org/10.1111/j.1365-2621.1995.tb01946.x (1995).
120. Bąk, A. & Podgórska, W. Interfacial and surface tensions of toluene/water and air/water systems with nonionic surfactants Tween 20 and Tween 80. *Colloids and Surfaces A: Physicochemical and Engineering Aspects* **504**, 414-425, doi:https://doi.org/10.1016/j.colsurfa.2016.05.091 (2016).
121. Wang, M., Guo, Y., Ma, P. X. & Lei, B. Photoluminescent arginine-functionalized polycitrate with enhanced cell activity and hemocompatibility for live cell bioimaging. *Journal of Biomedical Materials Research Part A* **106**, 3175-3184, doi:https://doi.org/10.1002/jbm.a.36512 (2018).
122. Lv, K., Perriman, A. W. & Mann, S. Photocatalytic multiphase micro-droplet reactors based on complex coacervation. *Chemical Communications* **51**, 8600-8602, doi:10.1039/C5CC01914A (2015).
123. Panalytical, M. <https://www.malvernpanalytical.com/en/support/product-support/zetasizer-range/zetasizer-nano-range/zetasizer-nano-zs> (2021).
124. Samejima, T., Kamata, M. & Shibata, K. Dissociation of Bovine Liver Catalase at Low pH. *The Journal of Biochemistry* **51**, 181-187 (1962).
125. Liu, D. *et al.* Catalase-linked immunosorbent pressure assay for portable quantitative analysis. *Analyst* **144**, 4188-4193, doi:10.1039/C9AN00499H (2019).
126. Ma, X. *et al.* Enzyme-Powered Hollow Mesoporous Janus Nanomotors. *Nano Letters* **15**, 7043-7050, doi:10.1021/acs.nanolett.5b03100 (2015).
127. Sánchez, S., Soler, L. & Katuri, J. Chemically Powered Micro- and Nanomotors. *Angewandte Chemie International Edition* **54**, 1414-1444, doi:https://doi.org/10.1002/anie.201406096 (2015).
128. van den Heuvel, M. G. L. & Dekker, C. Motor Proteins at Work for Nanotechnology. *Science* **317**, 333-336, doi:10.1126/science.1139570 (2007).
129. Wu, Y., Si, T., Shao, J., Wu, Z. & He, Q. Near-infrared light-driven Janus capsule motors: Fabrication, propulsion, and simulation. *Nano Research* **9**, 3747-3756, doi:10.1007/s12274-016-1245-0 (2016).
130. Katsounaros, I. *et al.* Hydrogen peroxide electrochemistry on platinum: towards understanding the oxygen reduction reaction mechanism. *Physical Chemistry Chemical Physics* **14**, 7384-7391, doi:10.1039/C2CP40616K (2012).
131. Pashley, D. H. & Livingston, M. J. Effect of molecular size on permeability coefficients in human dentine. *Archives of Oral Biology* **23**, 391-395, doi:https://doi.org/10.1016/0003-9969(78)90098-5 (1978).
132. Shinoda, W. Permeability across lipid membranes. *Biochimica et Biophysica Acta (BBA) - Biomembranes* **1858**, 2254-2265, doi:https://doi.org/10.1016/j.bbamem.2016.03.032 (2016).
133. Wolkers, W. F. *et al.* Factors Affecting the Membrane Permeability Barrier Function of Cells during Preservation Technologies. *Langmuir* **35**, 7520-7528, doi:10.1021/acs.langmuir.8b02852 (2019).
134. Miyazaki, K. *et al.* Establishment of a method for evaluating endothelial cell injury by TNF-α in vitro for clarifying the pathophysiology of virus-associated acute encephalopathy. *Pediatric Research* **81**, 942-947, doi:10.1038/pr.2017.28 (2017).
135. SigmaAldrich. *FLUORESCEIN ISOTHIOCYANATE-DEXTRAN* <https://www.sigmaaldrich.com/content/dam/sigma-aldrich/docs/Sigma/Product_Information_Sheet/1/fd250spis.pdf> (

136. Nagaraja, T. N., Keenan, K. A., Brown, S. L., Fenstermacher, J. D. & Knight, R. A. Relative distribution of plasma flow markers and red blood cells across BBB openings in acute cerebral ischemia. *Neurological Research* **29**, 78-80, doi:10.1179/174313206X153815 (2007).
137. Li, T. *et al.* A novel fluorescein derivative as a colorimetric chemosensor for detecting copper(II) ion. *Dyes and Pigments* **88**, 103-108, doi:https://doi.org/10.1016/j.dyepig.2010.05.008 (2011).

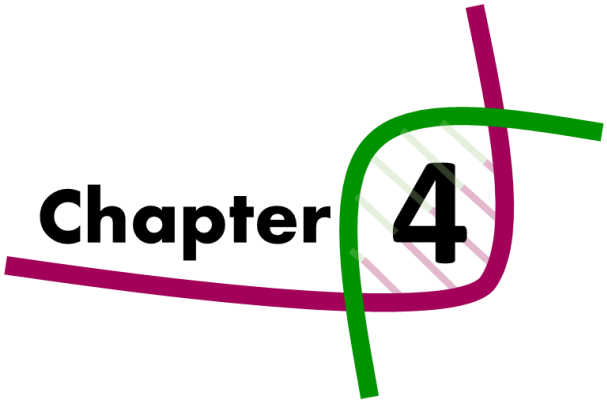

Buoyancy mediated motility of inorganic/organic DNA-hybrid microcapsules

4.1 Abstract

After presenting AMP/DNA and protamine/DNA microcapsules as a promising new protocell system, this chapter introduces a novel approach, which was designed to enable motility through antagonistic enzymatic interactions inside microcapsules. Co-entrapment of the enzymes catalase and glucose oxidase into the microcapsules enabled the nucleation of small oxygen-bubbles inside the capsule interior as a response to a hydrogen-peroxide-rich environment. The growth of the O_2-bubble facilitated a buoyancy effect which forced the capsules to rise upwards. Successive change of the environment to a glucose-enriched phase activated glucose oxidase and oxygen-consumption which, in return, lead to a decrease of the buoyant force until the capsule descended downwards again. Here, a thorough study on oxygen-bubble nucleation will be presented to understand the necessary enzyme- and substrate concentrations, the bubble growth rates, the stability of the membrane and the velocities of the capsule during the negative and positive geotaxis. As a next step, the microcapsule motility will be channelled into autonomous oscillations by creating a controlled chemical environment with spatially separated glucose and hydrogen-peroxide gradients. Long lasting, stable oscillations were achieved by keeping the gradient static through a flow-based design, whereas a diffusing gradient introduced damping into the oscillation. Thorough studies will be presented in order to discuss the conditions under which stable and damped oscillations can be influenced and to understand the underlying mechanisms that change the oscillation patterns. Finally, the deterioration of GOx-enzyme activity during the oscillations will be discussed in reference to the enzyme leakage experiments from chapter 3.

4.2 Introduction

4.2.1 Motility of micro- and nanoscopic entities

As humans, we are used to move by simply using our legs to buy groceries, going to work or exercise, but we rarely think about the fundamental importance of being motile, or changing the location due to a certain need. In fact, most organisms developed some means to move around: birds fly, fish swim, snakes crawl and so on. And it is of utmost importance for these organisms to be able to move, since without it, they would starve or lack purpose altogether. While these macroscopic forms of motility are common knowledge for most people, it gets more interesting the smaller the organism or the object becomes, as not only the size, but also the mechanics of movement change. Many organisms utilise nanomotors to move and change their direction or facilitate biochemical processes, which are

commonly based on the reaction of small energy rich molecules like adenosine triphosphate (ATP). One of the most well studied and fascinating forms of motility are the flagella, which can be found in sperm cells or bacteria like *E. coli*. [1]

The flagellum is a unique nanomotor which can easily be compared with the structure of a ship's propellor. The "engine" is grounded in between the inner and outer membrane of the cell and connected to the tail via a hook. The motor-proteins Mot-A and Mot-B which generate the torsional force are located within the inner membrane, powered by either ATP (like in archaea [2]) or by a transmembrane electrochemical gradient via flow of H^+ or Na^+, which in return starts rotating the MS-ring, thereby transmitting the force onto the hook and the tail (Figure 4.2-1-a). [3] As a result the tail starts rotating and the asymmetric motion generates a force that drives the cell-body forward. Another closely related system is the cilium, which can be found in eukaryotic cells. The cilium is comprised of an almost identical apparatus but showcases a wavelike motion pattern instead of a rotation and, in contrast to the flagellum, is used to move cargo rather than the whole cell. What makes this apparatus even more fascinating, is the fact that it not only enables the bacteria to move but also to stir their direction chemotactically. The cells can change between linear motion and random tumbling, while sensing the chemical attractant they are after. [3,4]

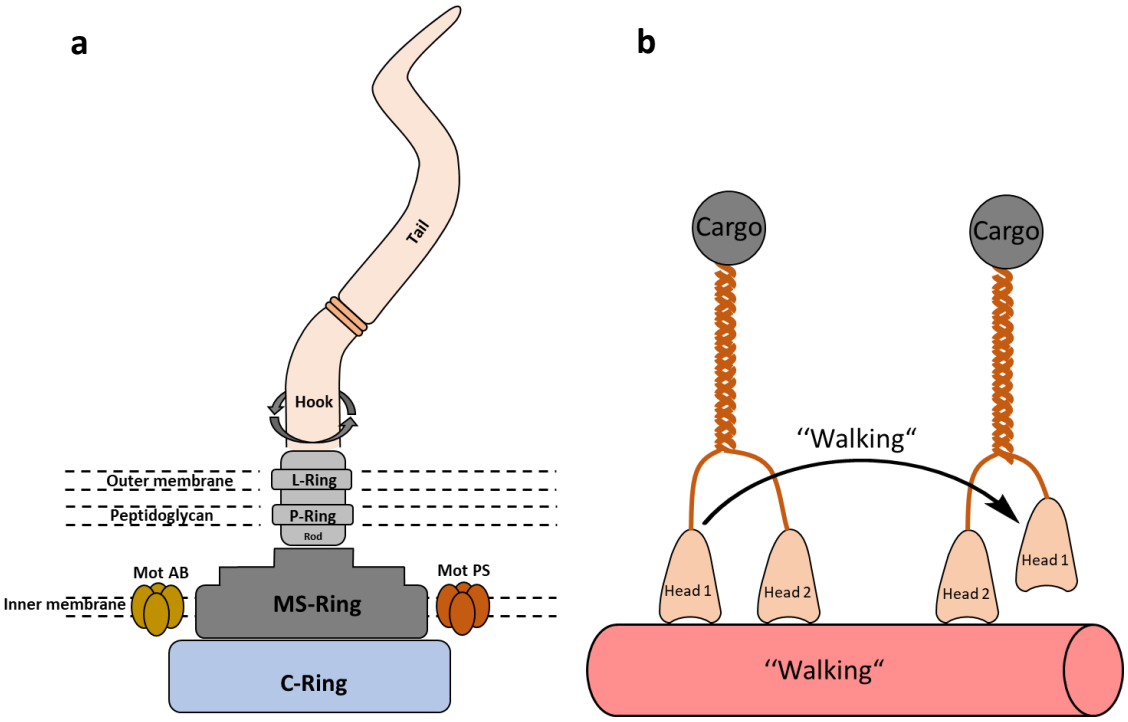

Figure 4.2-1: *Illustration of important biological nanomotors:* ***a*** *The prokaryotic flagellum is comprised of a multi-layered structure, found within the inner and outer membrane. The stationary C-ring is rooting the motor within the cell, MotAB utilises an ion-gradient or ATP to induce rotation of the MS ring which transfers the force over the rod onto the hook, which is attached to the tail. The rotational motion of the tail then generates enough force to move the organism the flagellum is attached to.* ***b*** *Kinesin walking along microtubules, comprised out of two head-structures that can bind to the microtubule and walk powered by ATP-consumption. The heads are connected to a stem with a large cargo on top.*

Another interesting design-concept are motor proteins like kinesins (Figure 4.2-1-b) and myosins. Kinesin has two head-moieties which are able to bind to microtubules inside the organism. Powered by ATP-consumption, the head-groups detach and re-attach further down the microtubule, thus exhibiting an almost walk-like pattern. On the opposite site, kinesins are capable of binding to large cargos, which enables them to transport these payloads linearly and unidirectionally on the

microtubules of the cellular cytoskeleton. [1] Although these are only two examples, they already showcase some very important functions of motility of nanomotors: the ability to generate motion, to steer the motion towards a location of preference or necessity and the uptake, transport and release of payloads and even speed variations in response to external stimuli. [5]

Biological nanomotors exhibit a very high complexity and even though we are capable of building large machines and engines, on the small scale we're still very much behind nature's ingenuity. Most synthetic systems that have been developed so far, were either reduced to one of the functions named above or were based on repurposing the biological nanomotors without designing a new system from scratch. Generally, most synthetic systems can therefore be categorised as followed: (1) synthetic motors that exhibit controlled motility, which is usually directed by an external force field. So far, there have been studies on electrical [6], acoustic [7,8] and magnetic [9,10] force fields but also motility-control via light. [11,12] (2) Motors driven by chemical reactions around interfaces which results in random motion without any directionality. [13-18] (3) Hybrid motors, combining the two approaches before to enable both motility and control over orientation and direction.

Many of these motors are based on simple inorganic nano or microstructures, mostly rod- or sphere-like particles. With regard to the concepts from point (1), stainless steel microparticles were used to facilitate motility within an electric field [6], gold microrods were moved via ultrasonic standing waves [7,8], AgCl microparticles showed aggregation behaviour under light [11,12] and flexible chains of magnetic microparticles were attached to red blood vessels to mimic the swimming motion of a flagellum. [9] Micromotor-propulsion via chemical reactions has mainly been put in the spotlight by the studies of Whitesides *et al*. in 2002 where they presented micrometre sized and platinum covered objects that were able to propel themselves via oxygen bubble-generation. [15] This concept was then carried on towards asymmetric systems like Pt/Au nanorods [19] or Janus-particles where one hemisphere of polystyrene beads was coated with platinum. [13] In order to introduce biochemical reactions into these inorganic systems, Schattling *et al.* and Pantarotto *et al.* attached catalase and glucose oxidase to microparticles [17] and multi-walled carbon nanotubes (MWCNTs) [15] and showed propulsion by oxygen-generation over a GOx/catalase-cascade reaction. In contrast to nano-wires, nano- and microtubes offer a hollow interior, which can serve as a nucleation site for gas-bubbles and thus turn the small motor into a jet-like engine. Y. Mei *et. al.* from the group of G. Schmidt, pioneered this concept in 2008 [20], after which new methods were developed to further decrease the size of the microjets into the nano-realm [21,22] and to increase the repertoire of different material compositions to fabricate micro and nanojets. [23-27] While all these systems rely on bubble propulsion, the eventual direction the object is moving to is not easily predicted. Figure 4.2-2 shows two almost identical examples of asymmetric Ni/Pt [28-30] and Au/Pt [16] nanowires. In contact with H_2O_2 the Ni/Pt-nanowires produce O_2-bubbles on the Pt-side and propel themselves along their long axis towards the Ni-side, when observing Au/Pt-nanowires though, they would move in the exact opposite direction. The reasons for this behaviour are two completely different mechanisms, which move the nanowires. In case of the Ni/Pt-nanowires (Figure 4.2-2-a), bubble propulsion is causing the object to move, whereas in case of Au/Pt self-electrophoresis is the reason for the motion and the wires move in a self-generated electric field due to asymmetrically generated ions (Figure 4.2-2-b). [30-32] The mechanisms are still heavily discussed and several different models were proposed that can explain the motion of these small nanowires like a change of interfacial tension due to decomposition of chemical components [16], or self-diffusiophoresis due to a self-generated concentration gradient, that drives the motion. [13] Another model discussed by Dhar *et. al.* discusses a phenomenon based on the Brownian ratchet concept [33,34], where the production of oxygen-bubbles decreases the viscosity in the vicinity of the Pt-side of the rod, which in return enables thermal motion to propel the object forward. [35]

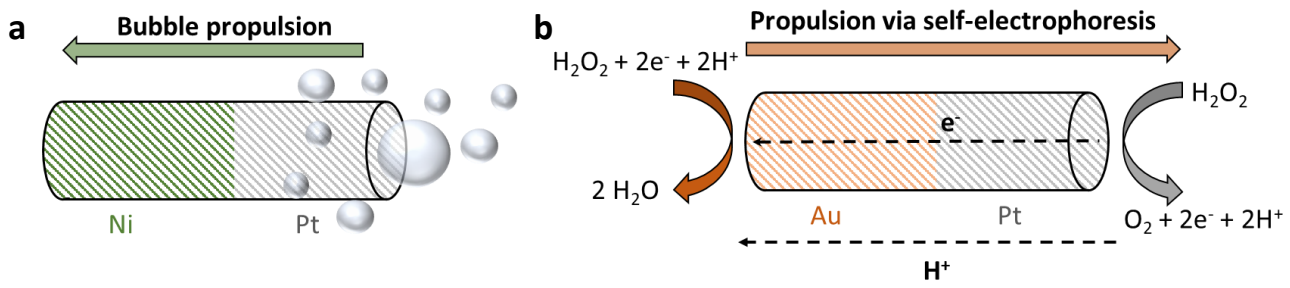

Figure 4.2-2: *Illustration of mechanisms of chemical and physical propulsion of micro rods.* ***a*** *Propulsion via bubble formation on the Pt-end of a Ni/Pt-rod.* [28,29] ***b*** *Propulsion via self-electrophoresis of a Au/Pt-rod.* [16]

Another important factor that arises when looking at motion of micro- and sub-microscopic objects is the so called Reynolds-number, which is defined by the density of the fluid ρ, the velocity of the particle V, the length of the particle l and the dynamic viscosity μ and describes the context between inertial and viscous forces. Practically, we are moving from the macroscopic world, which is predominantly defined by inertial forces, to the microscopic and sub-microscopic plane, which is progressively more influenced by viscous drag and Brownian motion and less by inertia. [30,36]

$$Re = \frac{\rho V l}{\mu} = \frac{inertial\ forces}{viscous\ forces} \qquad \textit{(Equation 4.2-1)}$$

To get a better understanding about the dimension of Reynolds numbers, the review by Sanchéz *et al.* compares a Re number of 10^4 to a person swimming in water whereas 10^{-4} refers to a swimming bacterium. [30] All fluid's behaviour can be explained by the Navier-Stokes equations:

$$\nabla \cdot \underline{u} = 0 \qquad \textit{(Equation 4.2-2)}$$

$$\rho\left(\frac{D\underline{u}}{Dt}\right) = -\nabla p + \mu\nabla^2\underline{u} + p\underline{F} \qquad \textit{(Equation 4.2-3)}$$

While looking complex, these two equations are mere representations of the conservation of mass (Equation 4.2-2) and the conservation of momentum (Equation 4.2-3) with $\underline{u}$ as a velocity vector, ρ as the density, $\rho\left(\frac{D\underline{u}}{Dt}\right)$ as the mass, $-\nabla p + \mu\nabla^2\underline{u}$ as the internal forces of the fluid particles and $p\underline{F}$ as the external forces like gravity. [37] Another way to express the Navier-Stokes equation utilises the Reynolds-number as followed, with R_T as the oscillatory Reynolds number:

$$Re_T = \frac{\rho L^2}{\mu T_0} \qquad \textit{(Equation 4.2-4)}$$

$$Re_T \frac{du'}{dt'} + Re(u' \cdot \nabla)u' = \nabla^2 u' - \nabla p' + f' \qquad \textit{(Equation 4.2-5)}$$

For flows primarily determined by viscous forces, the inertial term of the equation and therefore the Reynolds-number is approximating 0, which can then be neglected. So, for low Re-domains with dominant viscous forces, Equation 4.26 can be rearranged to the so called Stoke equation:

$$\nabla^2 u' - \nabla p' = f \qquad \textit{(Equation 4.2-6)}$$

The Stokes-equation is strictly time-independent which describes the unique environment that microscopic swimmers are existing in. Since time and therefore inertia does not play any role in the equation, the motion of microscopic objects is heavily reliant on both constant and asymmetric actuation. Since symmetrical movement is time-reversible, it only leads to mere back and forth motion

in a non-inertia environment. [36] This is also described as the *Scallop Theorem*, which takes its name from the scallop, which moves by opening and closing its shell which in return propels it forward. Since this is a symmetrical form of actuation, based on the inertial forces of the water, it would not be possible for the scallop to move at low Re-numbers. This design was also presented experimentally in 2014 by fabrication of polydimethoxysiloxan (PDMS) micro-scallops, which were actuated by a magnetic field. As long as the shell opened and closed symmetrically, which means at similar speeds, the micro-scallop was not able to move in a Newtonian fluid, but if closed quickly and opened slowly, it started to move forward. [38]

A lot of the work in the past 20 years was focused on solid inorganic systems like the ones described above, but there has not been a similarly large amount research on motility of droplets, micro- and nano-compartmentalised systems such as cells or vesicles. Microdroplets are a popular system which have been investigated as a primitive mimic of biological cells. B. Grzybowski *et al.* have written a thorough review and added their own share of interesting experiments, especially in regard to protocell motility. Here they presented chemotactic, non-equilibrium microdroplets, that autonomously moved through a complex maze, merely directed by a pH-gradient and facilitated by surface tension effects. [39,40] Other surface tension based systems were presented by Sugarawa *et al.* who experimented on oleic anhydride oil droplets in a surfactant medium, where hydrolysis of the surfactant ultimately lead to surface tension gradients and motion of the microdroplets [41], or by W. Francy *et al.* who formed droplets from the ionic liquid trihexyl(tetradecyl)phosphonium chloride ($[P_{6,6,6,14}][Cl]$), which released the $[P_{6,6,6,14}]^+$-cation in an aqueous environment and in return reduces the surface tension. Since the release was coupled to Cl^- association, the droplets could be moved directionally by placing them into a Cl^- gradient, with the droplets moving towards the side of higher Cl^- concentration. [42] Another interesting concept is the actuation of droplets by light. Many experiments were based on molecules that readily react with light and change their chemical properties or structure in return. Azobenzene photo switches have been used by Ichimura *et al.* to fabricate O-carboxymethylated calix[4]resorcinarene bearing p-octylazobenzene surfaces, which change their wettability according to the wavelength of the light It is exposed to, which in return actuates oil-droplets on the surface towards the light -beam. [43] Obviously and similarly to the inorganic systems above, phototactic systems can also be combined with chemotactic systems in order to make them more versatile and respondent. [44,45] All in all microdroplets pose as a versatile platform, not only for protocellular research but also for the means of motility. Nonetheless, the fact that they do not contain a membrane causes many problems regarding stability, uptake-capabilities, longevity, convenience and more due to their biphasic nature.

While the field of membrane-bound protocells is vast and the amount of research is even larger, there are several groups that have done and published outstanding work in recent years regarding micro swimmers and protocell motility. The van Hest group has presented an extensive portfolio of work about synthetic polymeric vesicles, or polymerosomes, and also delved into motility concepts in recent years. Here they utilised nanoscopic, bowl-shaped polymerosomes, so called stomatocytes, and showcased motility via bubble propulsion facilitated through entrapped Pt-nanoparticles [46,47], or by magnetic control with magnetic nickel in combination with Pt-nanoparticles. [48] In other studies a combination of bubble propulsion and magnetic steering was used by implementing Fe-Pt-nanoparticles into polymer microcapsules, which were then able to take up microcapsule-cargo and deliver it to a new location. [49] Janus-style, hollow silica microcapsules [50], and polyelectrolyte microcapsules [51] were fabricated and chemotactically motorised by enzymatic reactions. More recent studies of the van Hest group saw the development of motile cucurbit-shaped polymerosome with aggregation induced emission moieties [52]The group around Samuel Sánchez has also committed

a large portion of their work towards the development and understanding of more and more complex motility designs on the micro and nanoscale. Recent publications especially are now more focused on applying the knowledge which has been gathered over the past decades in order to utilise micro/nanomachine motility towards higher applications. Especially life sciences and biomedical approaches have always been a major motivation and are showcased in many of their publications. Here, recent studies have investigated micro/nanomotors as candidates for the treatment of bacterial infections [53,54] or as carriers of drug-molecules [55-57] for therapeutic purposes. At the same time, Sánchez *et al.* published various studies on more advanced micro/nano-motor concepts like swarming behaviour [58], biohybrid-motors [59-61] and investigated the effect of stochastic distribution of enzymes on the directionality of the motion of micro/nanomotors. [62]

The relevancy of these studies can be increased when one changes the perspective from a single entity towards the interaction between multiple microcompartments or even a whole community, as this enables the establishment of communication. In 2017, the Mann group published an interesting concept that combined cell-motility and cell-interaction by designing predatory behaviour within magnetic Pickering emulsion droplets towards small silica-colloidosomes. Surfactant mediated destabilisation of the magnetic particle shell led to holes, through which the droplets were capable to perform a rudimentary form of phagocytosis. At the same time, engulfment of silica colloidosomes lead to lateral movement due to Marangoni convective flows along the droplet interface, which effectively made the predator-droplets move and rotate. [63] The van Hest group showcased another interesting motion-less project based on cell-to-cell communication of giant vesicles through diffusing chemical gradients, which led to long-distance signalling within cell consortia. [64]

All the cells and swimmers discussed above already cover a large array of physical and chemical means of motility, even though some of them are not necessarily represented in any living organism. Nonetheless, there are even more motility concepts found in nature, some of which might still be undiscovered. Another very interesting mechanism, which is also the core of this thesis, can be found within strains of bacteria, including phyla or archaea, but most frequently in cyano bacteria, anoxygenic photosynthetic bacteria, cold-loving heterotrophic bacteria and mesophilic haloarchaea living in brine pools. [65] These cells contain gas vacuoles, which are comprised of little gas vesicles which enable the cell to stay afloat or move upwards via buoyancy. The vesicles are built from a small 7-8 kDa gas vesicle protein (GvpA and GvpC) which forms a 2 nm thin, gas permeable membrane. These gas-vesicles change their shape as they grow, as seen in case of *Halobacterium salinarum*. The shape develops from a spindle-like shape (Figure 4.2-3-a) to cylindrical vesicles, depending on the state of their development (Figure 4.2-3-b). To control the buoyancy and to ensure that the cell is not aimlessly drifting to the surface, the cells developed different means to steer their vertical motion. For one, they are generally highly sensitive to changes in pressure. Once the pressure reaches a critical value, the vesicles collapse, thus forcing the cell to descend. Photosynthetic cyanobacteria use their buoyancy to move towards higher intensities of light to engage in photosynthesis or move away from harmful UV-radiation during daytime. The carbohydrates produced during photosynthesis are then used as ballast due to their higher density, thus shifting the equilibrium towards descent. Even though these cells only move a couple of centimetres per day, it suffices to regulate their photosynthetic functions. Other cell types regulate the buoyancy according to the surrounding conditions, depending on the temperature, anoxic or aerobic conditions (*Halobacterium salinarium*) and even the salt concentration (*Haloferax mediterranei*). [45.46]

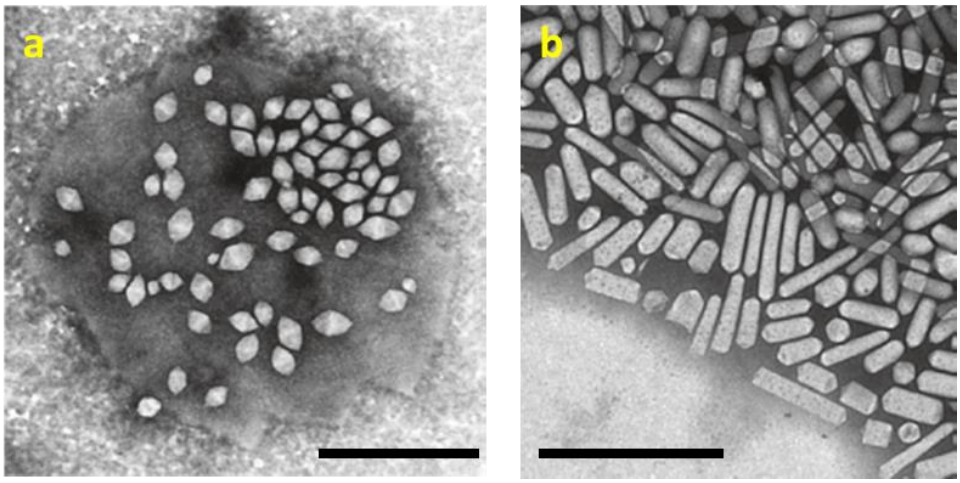

***Figure 4.2-3**: Electron micrograph of gas-vesicle formation within a lysed Halobacterium salinarium cell. **a** Bicone- and spindle-shaped gas vesicles at the early stages of development, **b** Cylinder-shaped gas-vesicles at the final stage of development.* [65,66]

Utilising buoyancy as a means of motility is interesting for multiple reasons. For one, it is strictly one-directional and highly predictable compared to other systems previously described which often either exhibit chaotic or barely linear trajectories. There have not been many publications regarding protocell-buoyancy. One exception also came from the Mann group in form of buoyant, magnetic, Pickering emulsion droplets, similar to those described above. [63] Small, catalase containing silica colloidosomes were engulfed within magnetic Pickering emulsion droplets, which produced oxygen when getting in contact with H_2O_2 and which accumulated within the droplet and ultimately propelled it upwards via buoyancy. [67] This is highly interesting as it proves that bubble-induced buoyancy within cells is possible and chemically controllable, but it still remains with some issues that makes working with them rather inconvenient. As the magnetic Pickering emulsion droplets are aqueous, they can only exist within an organic environment, more specifically in a dodecane solution. While this is manageable by using colloidosomes as enzyme-carriers, it is far-fetched when it comes to mimicking biological systems or even origin of life-related cells, as the harsh environment of aliphatic solvents would denature or break most cells and proteins.

To get a physical understanding of buoyancy, one can go way back to 250 BC when Archimedes of Syracuse suggested the theorem on floating bodies, that said that any object immersed in a fluid is buoyed up by a force equal to the weight of the fluid displaced by the object. [68] This simple expression can be described as followed, with $F_{Buoyant}$ as the upward force and W_f as the weight of the fluid displaced by the object:

$$F_{Buoyancy} = W_f \qquad \textit{(Equation 4.2-7)}$$

Although Archimedes already understood the relations between buoyant forces and objects of different materials, we can now express the physical reasons behind buoyancy and why some objects float, while others will not. Figure 4.2-4 illustrates the basic forces coming into play when a capsule is immersed in water. [68,69]

Since fluid pressure only changes with the depth of the fluid-column, any object with a volume experiences a smaller fluid pressure on its topside and a higher on its bottom side. The relation between the two forces can be expressed as the buoyancy force $F_{Buoancy}$ as followed:

$$F_{Buoyancy} = F_{up} - F_{down} \qquad \textit{(Equation 4.2-8)}$$

$$P = \frac{F}{A}, hA = V \text{ and } P_{fluid} = \rho g h \qquad \textit{(Equation 4.2-9)}$$

$$F_{Buoyancy} = (\rho g h_{bottom}) * A - (\rho g h_{top}) * A \qquad \textit{(Equation 4.2-10)}$$

$$F_{Buoyancy} = \rho g A * h_{capsule} \qquad \textit{(Equation 4.2-11)}$$

$$F_{Buoyancy} = \rho g V_{capsule} = W_f \qquad \textit{(Equation 4.2-12)}$$

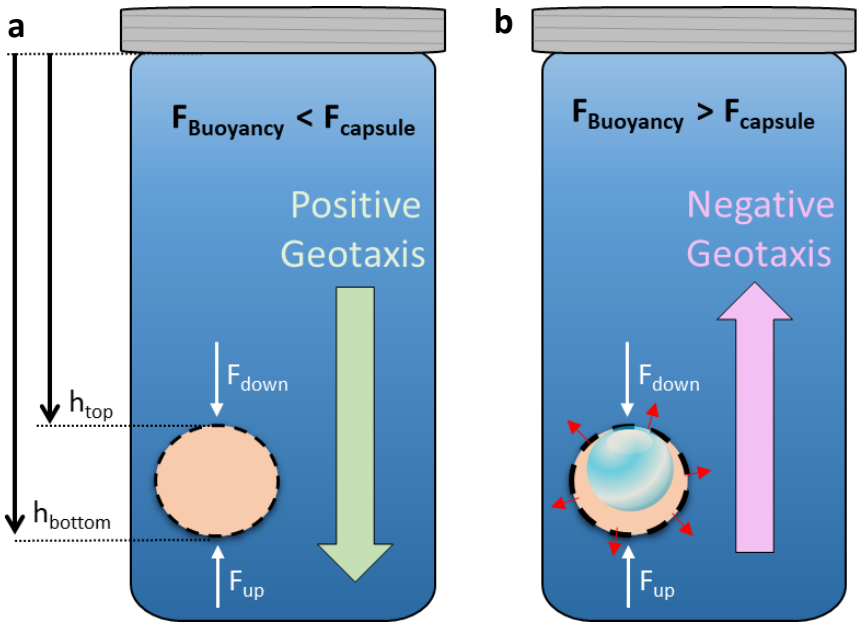

***Figure 4.2-4**: Explanation of forces experienced by microcapsules in an aqueous solution before (**a**) and after oxygen-bubble production (**b**).*

Finally, to understand when an object sinks or floats, a net force is defined from the buoyancy $F_{Buoyancy}$ and the opposing weight of the capsule $F_{Capsule}$, and it can be seen that the only deciding factors are the fluid's and the object's density (Equation 4.2-14).

$$F_{net} = F_{Buoyancy} - F_{Capsule} \qquad \textit{(Equation 4.2-13)}$$

$$F_{net} = Vg(\rho_{fluid} - \rho_{capsule}) \qquad \textit{(Equation 4.2-14)}$$

This way, we are now able to understand the physics behind the buoyancy, induced by oxygen bubble-production inside a cell. In the absence of the bubble, the density of the capsule is higher than the one of water, making it sink to the bottom (Figure 4.2-4-a), but as an oxygen-bubble has been nucleated within, it forces water and other small molecules out of the cell through the semi-permeable membrane, ultimately reducing the internal density until $F_{Buoyancy} > F_{Capsule}$ which gives the capsule an upward momentum (Figure 4.2-4-b).

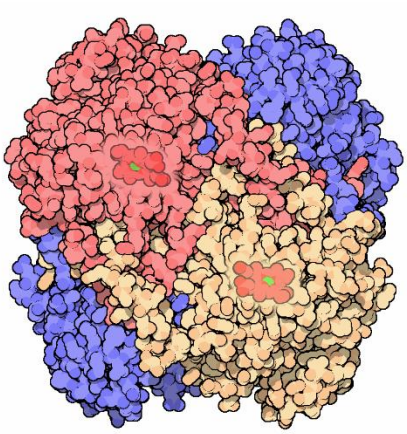

Figure 4.2-5: *Protein structure of catalase: The tetrameric subunits are highlighted in red, blue, and orange with the heme-iron-clusters shown in green.* [70]

To produce oxygen or a gas that makes the cells become buoyant, there are only a limited number of pathways to go. Using catalytic particles like Pt-nanoparticles would be one possibility, another would be enzymatic via catalase. Either system has been used in previous research, but since this work aims for a more biologically relevant approach, an enzymatic mechanism seemed more appropriate. Catalase is an important enzyme and can be found in almost all living beings from plants over bacteria to animals. It belongs to the class of hyperoxidases and serves as an antioxidant within our cells to prevent oxidative damage. Catalase is a very well researched enzyme due to its biological relevancy, but also because it is one of the most efficient enzymes with one of the highest turnover-numbers we have so far found on our planet. Each catalase enzyme can convert millions of H_2O_2-molecules per minute and convert them to water and oxygen. Bovine catalase as it was used in the studies of this thesis is tetrameric, which means it is comprised of 4 identical 60 kDa subunits which adds up to an overall molecular weight of ~232 kDa (Figure 4.2-5). Each unit of the tetramer has its own active site with a heme-group and an iron-ion which catalyses the decomposition of hydrogen peroxide. Catalase is also an unusually stable enzyme, especially considering it exists at locations with very reactive radicals and molecules around. [71,72]

While the exact mechanism of how H_2O_2 is converted to H_2O and O_2 is still not completely solved, the key reactions can be divided in two steps. In the first reaction, the hydrogen peroxide oxidises Fe(III) of heme to an oxyferryl species. The necessary electrons come from both the heme-iron and the porphyrin. In a second step, another H_2O_2 is then being reduced by the same components, thus restoring the Por-Fe^{III}-structure and producing water and oxygen. The reactions can be seen as followed:

$$(Por - Fe^{III}) + H_2O_2 \rightarrow (Por^{+\cdot} - Fe^{IV} = O) + H_2O \qquad \textit{(Equation 4.2-15)}$$

$$(Por^{+\cdot} - Fe^{IV} = O) + H_2O_2 \rightarrow (Por - Fe^{III}) + H_2O + O_2 \qquad \textit{(Equation 4.2-16)}$$

Since the motility of the cells of this thesis is strictly based on the production of oxygen by catalase, another enzyme will be introduced to counteract and reduce the oxygen-concentration: glucose oxidase, which originally went by the name notatin, or, for the simplicity within this thesis just GOx. Glucose oxidase belongs to the class of oxido-reductase enzymes and chemically catalyses the oxidation of β-D-glucose to D-glucono-1,5-lactone and hydrogen peroxide. In an aqueous solution, D-glucono-1,5-lactone then hydrolyses further to gluconic acid, which in return lowers the pH of the environment. Glucose oxidase is found in several species of insects and on the surface of fungi and serves as an antibacterial agent to prevent infection from bacteria through the formation of hydrogen

peroxide. One popular example is the honeybee-worker which can produce glucose oxidase within its hypopharyngeal glands and add it to the honey as a natural preservative. [73] Historically, GOx was first discovered from *Penicillium notatum*, the same organism from which the first penicillin was extracted. Nonetheless, the GOx used in this work came from the common black mold species *Aspergillus niger*. [74,75]

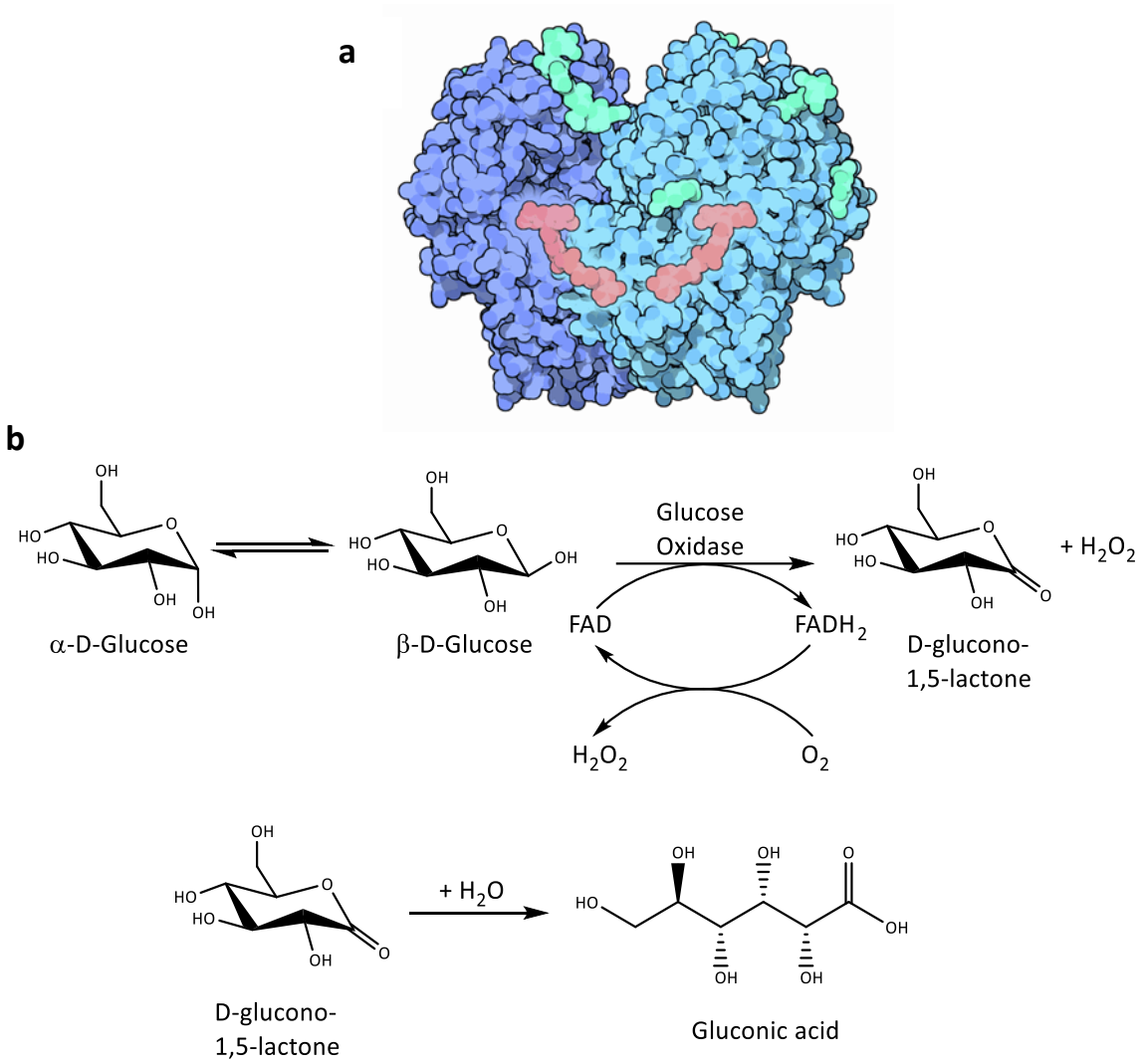

Figure 4.2-6: a *Protein structure of glucose oxidase from Aspergillus niger. The dimeric subunits are highlighted in dark- and light blue, the FAD-cofactors in red and carbohydrate chains in green.* [76]. ***b*** *Chemical mechanism of oxidation of β-D-Glucose to D-glucono-1,5-lactone and spontaneous hydrolysis to gluconic acid catalysed by glucose oxidase.* [77]

The enzyme consists of two identical 80 kDa-subunits and thus has a combined weight of 160 kDa (Figure 4.2-6-a). Each subunit contains an active site within a deep pocket, but which can only react with glucose in combination with the cofactor flavin adenine dinucleotide or FAD. FAD serves as an electron acceptor and selectively catalyses the oxidation of β-D-Glucose, thus forming $FADH_2$ and D-glucono-1,5-lactone. $FADH_2$ then serves as an electron donor to oxidise elemental oxygen in return, which restores FAD and forms H_2O_2 (Figure 4.2-6-b). [78-80]

While relevant for organisms in nature, glucose oxidase has also become an important industrial asset in biotechnology and research. Since glucose plays such a large part in our own bodies and other organisms but is hard to measure as a molecule by analytical instruments, glucose oxidase comes into

play in form of biosensors. Generally, GOx oxidises glucose and produces H_2O_2, which is much easier to trace and measure spectroscopically via addition of chromogens that react with the peroxide. This method can be used to determine glucose concentrations in blood-serum or plasma. Furthermore, glucose oxidase finds application as a marker for antigens and antibodies in enzyme immunoassays, as an agent to remove oxygen in food products or glucose from drinks for diabetics and was also applied in cancer research due to its anti-cancer properties from the produced H_2O_2. [75]

Another enzyme that needs to be discussed, as it will be used in one experiment of this chapter is alkaline phosphatase or simple ALP. The enzyme can be found throughout multiple organisms, even though its structure exhibits minor differences depending on the organism and the environment it was found in. ALP is a dimeric enzyme with a combined molecular weight of 140 – 160 kDa. [81,82] The enzymes contain four Zn^{2+} and two Mg^{2+} ions which can be found at the active sites and which are involved in the catalytic reaction. The enzyme's function is to dephosphorylate compounds and it can be found almost everywhere inside the human body.

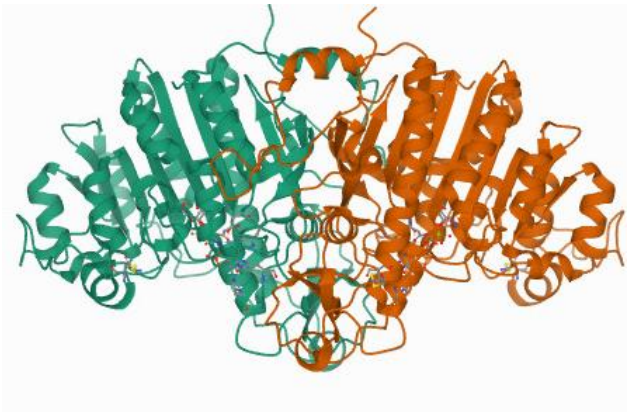

Figure 4.2-7: *Protein structure of alkaline phosphatase. The two dimers are highlighted in green and orange.* [83]

Some named functions are its role in intestinal homeostasis or during inflammation [84,85], or the regulation of lipid absorption in the duodenal mucosa and the growth of bones. [86,87] ALP is found predominantly inside the liver, the bile duct, kidney, the bones, placenta and the intestinal mucosa [84-88] and can be used for the diagnosis of a variety of diseases or dysfunctions of the organs above.

Since enzymes play such a vital role in these studies, it is necessary to find the proper tools and theory to describe their conversion-rates. One of the most fundamental and best known models for enzyme kinetics is the one from the German biochemist Leonor Michaelis and the Canadian physician Maud Menden, also called Michaels-Menten-kinetics. The mathematical model was first presented in 1913 and was then looking at the hydrolysis of sucrose into glucose and fructose by the enzyme invertase. The enzymatic reaction and the kinetics were first simplified, with k_f as the rate constant for the forward-reaction and k_r for the reversed reaction, E as the Enzyme, S as the binding substrate, ES as the enzyme-substrate complex, k_{cat} as the catalytic rate constant and P as the product:

$$E + S \underset{K_r}{\overset{K_f}{\rightleftharpoons}} ES \xrightarrow[K_{cat}]{} E + P \qquad \textit{(Equation 4.2-17)}$$

One assumption, that must be made in order to establish a mathematical expression, is that the enzyme-concentration is much smaller than the substrate-concentration. With that in mind, the enzymatic rate ν, or the product formation-rate, can be described as followed:

$$\nu = \frac{d[P]}{dt} = V_{max}\ \frac{[S]}{K_M + [S]} = k_{cat}[E]_0\ \frac{[S]}{K_M + [S]} \qquad \textit{(Equation 4.2-18)}$$

Here, it is now possible to define the two important constants that define the Michaelis-Menten-kinetics: V_{max}, which describes the maximum reaction rate and K_M, the concentration of substrate at which the reaction rate is exactly $\frac{1}{2}\ V_{max}$. The concentration of the substrate will then further decide about the structure of Equation 4.2-18. With [S] << K_M, the term from Equation 4.2-18 becomes $\nu = k_{cat}[E]_0 \frac{[S]}{K_M}$, so that the enzymatic rate depends linearly on the substrate concentration [S], which can be described as "*first order kinetics".* On the other hand, when [S] >> K_M, the term $\frac{[S]}{K_M+[S]}$ becomes effectively 1 and independent of [S], which turns the initial enzymatic velocity to $\nu = k_{cat}[E]_0$, which approximates V_{max} asymptotically and resembles "*zero-order kinetics"*.

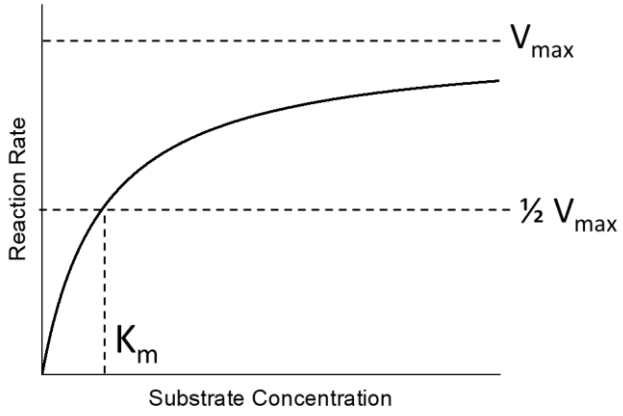

***Figure 4.2-8*:** Michaelis-Menten plot, showing the enzymatic reaction rate in relation to the substrate concentration. Due to the zero-order kinetics, the reaction rate approximates V_{max} asymptotically. K_M is defined as the substrate concentration where half the maximum velocity V_{max} is reached. [89,90]

$[E]_0$ is the initial enzyme concentration and V_{max} is reached when all enzymes are bound to a substrate molecule and k_{cat} is the turnover number, so the maximum amount of molecules of substrate, that one molecule of enzyme can convert per second. K_M furthermore serves as a number to measure the affinity of an enzyme towards its substrate. The lower K_M, the higher the affinity is of the enzyme, ergo, the lower is the concentration of enzyme needed to reach half the maximum velocity V_{max}. [89,90] For the work in this thesis, this means that enzymatic reaction rates can be calculated experimentally to mathematically approximate the Michaelis-Menten-constants V_{mx} and K_M.

As a step towards a more biocompatible cell-buoyancy system, chapter 3 has laid the foundation for AMP/DNA and protamine/DNA microcapsules by showing their entrapment capabilities of multiple functional components, specifically enzymes. In this chapter, the oxygen-production and consumption of catalase and glucose oxidase was used by entrapping them within the capsule-membrane, to establish chemically triggered buoyancy and "reversed buoyancy", ergo gravitational descent due to oxygen consumption by GOx. This way, and by separating glucose to the top- and hydrogen peroxide to the bottom side of a vial, the enzyme powered oscillation of the microcapsules was investigated (Figure 4.2-9). An important question arises though when looking at the products of both enzymes. While glucose oxidase is consuming oxygen, it also produces hydrogen-peroxide which in return fuels catalase and the oxygen production, so one could assume that both enzymes cancel each other out.

$$2\ H_2O_2 \rightarrow 2\ H_2O + O_2 \qquad \textit{(Equation 4.2-19)}$$

$$Glucose + O_2 \rightarrow D\text{-}Glucono\text{-}1,5\text{-}lactone + H_2O_2 \qquad \textit{(Equation 4.2-20)}$$

Equation 4.2-19 and Equation 4.2-20 show the chemical reactions of both enzymes and here it becomes obvious that catalase always consumes 2 molecules of H_2O_2, while GOx only produces one, which ultimately means that, during GOx activity, O_2-concentration will decrease.

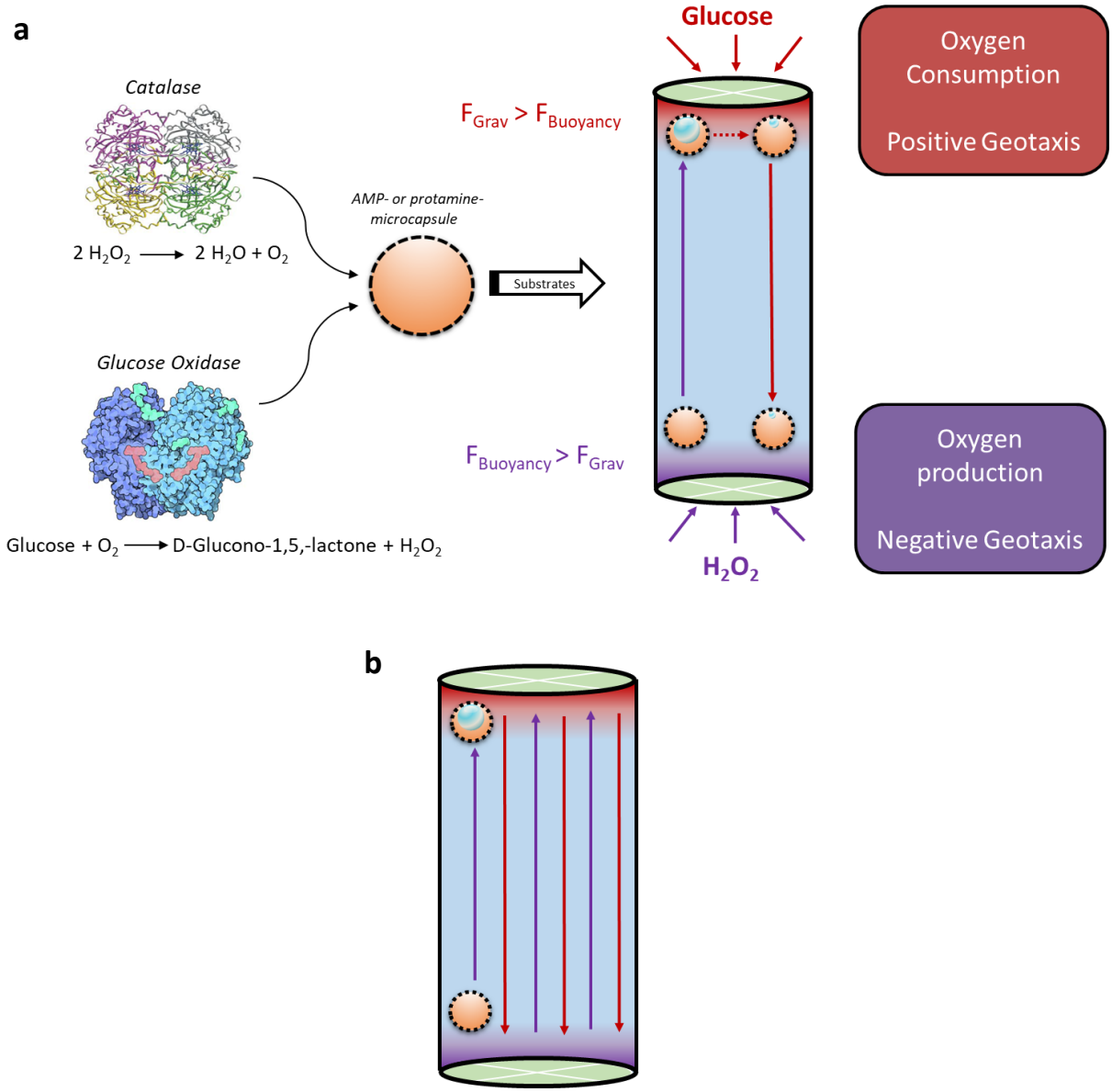

Figure 4.2-9: a *Buoyancy-based motility concept for AMP/DNA and protamine/DNA microcapsules: catalase and glucose oxidase will be encapsulated into the cells. Separation of hydrogen peroxide and glucose leads to oxygen production at the bottom- and oxygen-consumption at the top side, which will make the capsule move up and down according to the chemical stimulus.* ***b*** *Simplified illustration of stable microcapsule oscillation between a glucose- and a H_2O_2 rich phase.*

In this work, the control of the antagonistic interaction between the two enzymes catalase and glucose oxidase will be utilised to perform multiple successive repeats of buoyancy and reversed buoyancy, which will be shown in the form of long lasting oscillations, guided by spatially segregated glucose and H_2O_2-phases within a vertical oscillation column. To understand oscillations on the other hand, it is necessary to go back and look at the physics behind it. The simplest example for harmonic oscillation is an object, connected to a spring (Figure 4.2-10).

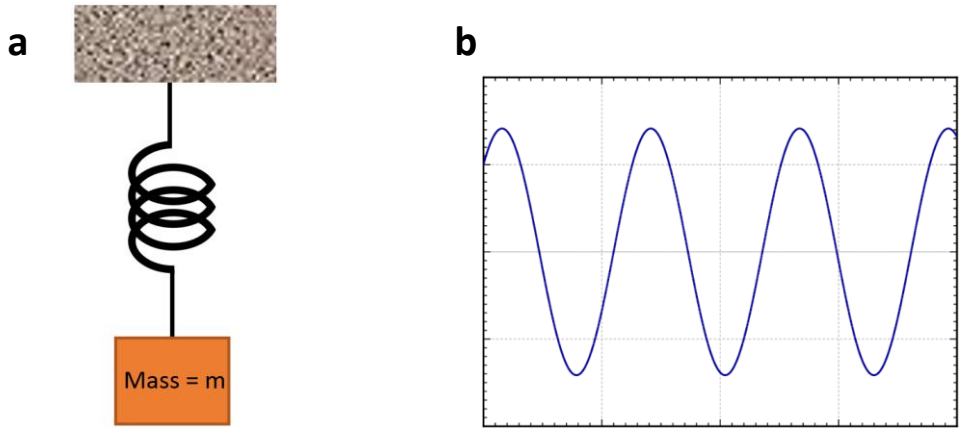

Figure 4.2-10: *Harmonic oscillator: a) object with mass m attached to a spring. b) Generic plot of harmonic oscillation after displacement of the object.*

If the mass of the object is m and the object is experiencing both the gravitational force and the opposing force of the spring, the balance of forces according to Newton's second law of mechanics can be described as:

$$F = ma = m * \frac{d^2x}{dt^2} = -kx \qquad \textit{(Equation 4.2-21)}$$

By displacing the object, it will start oscillating. Here we have to describe two different possible scenarios: one with and one without friction. In a case without friction, the object will keep oscillating harmonically without losing any of its energy to the system or the environment. Although this is an ideal scenario, which is unlikely to be found in nature, it can still be of value for a wide range of different experiments. To derive a function which describes the harmonic oscillation of an object, it is necessary to solve Equation 4.2-21. One solution is described in Equation 4.2-22.

$$x(t) = A * cos(\omega t + \varphi) \qquad \textit{(Equation 4.2-22)}$$

With ω as the angular frequency, described as $\omega = \sqrt{\frac{k}{m}} = \frac{2\pi}{T}$, T as the period, and φ as the phase of the oscillation. [69,91]

Perfect harmonic oscillations only exist under ideal theoretical conditions, ergo do not exist under real world conditions. To adjust this model, it is necessary to introduce further counteracting forces like friction, which define the much more realistic damped harmonic oscillations. Here the, the system is still oscillating harmonically but loses its velocity gradually because of frictional forces. Again, the balance of forces is described, which depends on the damping force F_D (F_D = -bv, with v = velocity and b = proportionality Constant), the restoring force created by the spring F_K and the gravitational force experienced by the object F_G.

$$-bv + (-kx) = ma \qquad \textit{(Equation 4.2-23)}$$

$$0 = m\frac{d^2x}{dt^2} + b\frac{dx}{dt} + kx \qquad \textit{(Equation 4.2-24)}$$

Equation 4.2-24 describes the equation of motion for objects experiencing damped harmonic oscillation. With $\omega_0 \equiv \sqrt{\frac{k}{m}}$ and $\gamma \equiv \frac{b}{m}$ an exponential solution (Equation 4.2-25) is used to solve the differential equation above.

$$x(t) = C * e^{\alpha t} \qquad \textit{(Equation 4.2-25)}$$

Division by m and substituting x in Equation 4.2-24 with Equation 4.2-25 then leads to:

$$\alpha^2 C e^{\alpha t} + \gamma \alpha C e^{\alpha t} + \omega_0^2 C e^{\alpha t} = 0 \qquad \textit{(Equation 4.2-26)}$$

$$\alpha = \frac{-\gamma \pm \sqrt{\gamma^2 - 4\omega_0^2}}{2} \qquad \textit{(Equation 4.2-27)}$$

Depending on the sign of $\sqrt{\gamma^2 - 4\omega_0^2}$, there are now three different scenarios to consider, with each case having a different damping effect on the oscillation:

$$Overdamped: \gamma > 2\omega_0 \qquad \textit{(Equation 4.2-28)}$$

$$Underdamped: \gamma < 2\omega_0 \qquad \textit{(Equation 4.2-29)}$$

$$Critically\ damped: \gamma = 2\omega_0 \qquad \textit{(Equation 4.2-30)}$$

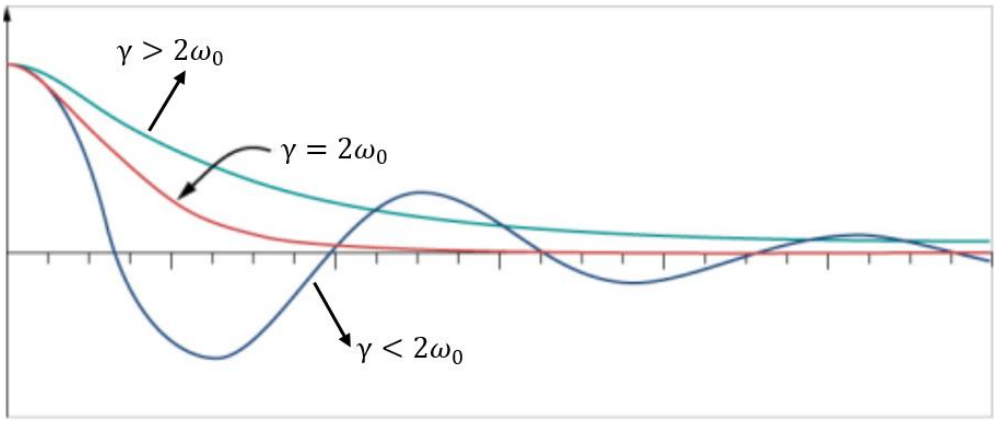

Figure 4.2-11: *Three different cases of damped harmonic oscillation. Overdamped ($\gamma > 2\omega_0$): the system returns to equilibrium without oscillating, critically damped ($\gamma = 2\omega_0$): the system returns to equilibrium as quickly as possible without oscillating, underdamped ($\gamma < 2\omega_0$): the system oscillates with the amplitude gradually decreasing to zero.*

Since this work solely focuses on underdamped oscillation, the other two scenarios will be ignored. A function x(t) is now needed for the motion of an underdamped system. First, ω_U will be defined as the angular frequency of an underdamped system:

$$\omega_U \equiv \frac{1}{2}\sqrt{4\omega_0^2 - \gamma^2} \Rightarrow \omega_U = \sqrt{1 - (\frac{\gamma}{2\omega_0})^2} \qquad \textit{(Equation 4.2-31)}$$

Because $\gamma < 2\omega_0$ for an underdamped system, α will have a complex part when Equation 4.2-31 is applied and inserted it into Equation 4.2-27, which leads to the following two solutions (Equation 4.2-33):

$$\alpha = -\frac{\gamma}{2} \pm i\omega_U \qquad \textit{(Equation 4.2-32)}$$

$$x_1(t) = C_1 e^{\left(-\frac{\gamma}{2}+i\omega_U\right)t} \quad and \quad x_2(t) = C_2 e^{\left(-\frac{\gamma}{2}-i\omega_U\right)t} \qquad \textit{(Equation 4.2-33)}$$

Equation 4.2-33 are two second-order differential equations with at most two linearly independent solutions, the most general solution is the sum of the two:

$$x(t) = e^{\frac{-\gamma t}{2}}(C_1 e^{i\omega_U t} + C_2 e^{-i\omega_U t}) \qquad \textit{(Equation 4.2-34)}$$

Considering x(t) must be real, it can be assumed that the two terms in Equation 4.2-34 are complex conjugates of each other, which implies that $C_2 = C_1^*$ and $C_1 = Ce^{i\phi}$. This way the imaginary parts cancel each other out which results in:

$$x(t) = e^{\frac{-\gamma t}{2}} C(e^{i(\omega_U t+\varphi)} + e^{-i(\omega_U t+\varphi)}) \qquad \textit{(Equation 4.2-35)}$$

$$x(t) = e^{\frac{-\gamma t}{2}} C * 2\cos(\omega_U t + \varphi) \qquad \textit{(Equation 4.2-36)}$$

$$x(t) = Ae^{\frac{-\gamma t}{2}} \cos(\omega_U t + \varphi); \textit{with } A \equiv 2C \qquad \textit{(Equation 4.2-37)}$$

The function of Equation 4.2-37 consists of two distinct terms describing the damped harmonic oscillation. $Ae^{-\frac{\gamma t}{2}} = Ae^{-\frac{b}{2m}t}$ stands for the exponential decay of the amplitude and can be approximated by the exponential envelope functions as seen in Figure 4.2-12, whereas $\cos(\omega_U t + \varphi)$ characterises the oscillatory motion of the object. [69,91]

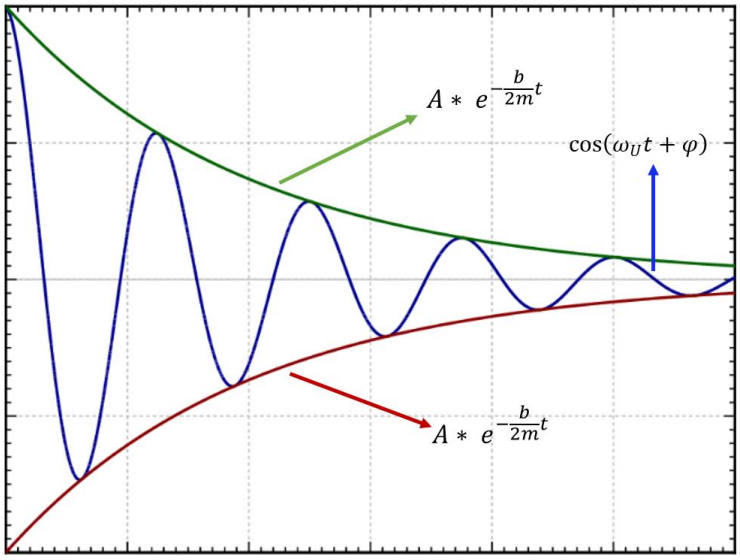

Figure 4.2-12: *Envelope functions of an underdamped harmonic oscillator.*

With $\sigma = -\frac{b}{2m}$ it is possible to calculate the so called damping coefficient σ, an important value for the description of damped harmonic oscillation.

Furthermore, to distinguish between the 3 types of damping and to characterise their shape the so called damping ratio ζ can be defined. Since we're only looking at underdamped systems, the damping ratio can be derived from logarithmic decrementation, which calculates the logarithmic decrement δ of two successive amplitude peaks and ζ as followed:

$$\delta = \frac{1}{n} * \frac{x(t)}{x(t+nT)} \qquad \textit{(Equation 4.2-38)}$$

$$\zeta = \frac{1}{\sqrt{1+(\frac{2\pi}{\delta})^2}} \qquad \textit{(Equation 4.2-39)}$$

where x(t) is the amplitude at time t and *x(t+nT)* is the amplitude of the peak, n periods away. While this method works good for $\zeta \leq 0.5$, it becomes less and less accurate the closer it gets to 1, the point the system becomes overdamped. [91-94]

4.3 Methods

4.3.1 Microcapsule buoyancy

This experiment is a mere proof of concept to showcase buoyancy and oxygen-bubble nucleation within AMP/DNA- and protamine/DNA microcapsules. To both observe and gather image-data, a microscope was set up horizontally, through which the observer was able to see the vertical motion of a small microcapsule inside an optical cuvette.

Catalase containing microcapsules were fabricated as described in 3.3.3 with 4 mg/mL DNA, 19.8 kU/mL catalase and 8 mg/mL silica particles. First, the cuvette was filled with di-water in case of protamine/DNA microcapsules or 0.5 mg/mL AMP-clay solution in case of AMP-capsules. Then, a small PDMS cube was prepared and inserted into the column, just leaving a small gap on the side, through which the capsule was added next. Once the capsules have sedimented to the bottom, the cuvette was fixated in front of the 1.25X microscope lens via a stage and a metal clamp, so that the ~8 mm field of view of view of the microscope just covered the distance between the bottom of the cuvette to the PDMS cube. Once everything was set up, 10 µL hydrogen peroxide (160 mM) was added with a 10 µL pipette, after which an oxygen-bubble nucleated within the capsule.

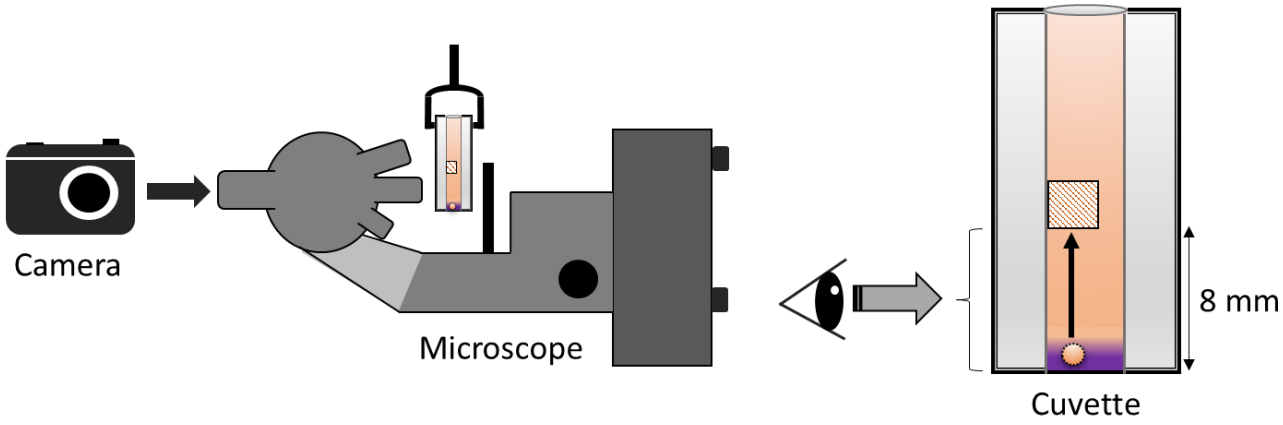

Figure 4.3-1: *Experimental setup for the observation of microcapsule buoyancy. An optical microscope was turned around by 90° and an optical cuvette was fixated with a metal clamp, so that the microscope was focused onto the bottom of the cuvette. The cuvette (External dimensions: Length: 7.5 mm, width: 12.5 mm, height: 48 mm. Internal dimensions: Length: 5 mm, width: 4 mm, height: 46 mm, Internal volume: 0.7 mL) contained a small PDMS-cube which served as a non-sticking barrier to limit the capsule's movement to the field of view of the microscope.*

4.3.2 Buoyancy screening for microcapsules with different dsDNA-concentrations

To assess the influence of the dsDNA-concentration during the fabrication of AMP/DNA- and protamine/DNA microcapsules, this experiment will prepare two different populations with either 4 mg/mL and 1 mg/mL dsDNA solution. The capsules were prepared as described in 3.3.3 with 19.8 kU/mL catalase and with sizes of around 400 µm in diameter. 100 µL and 50 capsules of each

population were then transferred into separate wells of a 96-well pate and left to sediment. Once the capsules were found on the bottom of the well, they were mixed with 100 μL H_2O_2-solution (160 mM or 80 mM) and the number of buoyant microcapsules was counted through an optical microscope.

4.3.3 Buoyancy probability screening

In this experiment, AMP/DNA and protamine/DNA capsules were prepared as described in 3.3.3 with varying concentrations of catalase (31.1, 15.5, 7.8 and 3.9 kU/mL) and washed 5 times with di-water. The average size of the capsules was 350-400 μm. 100 μL with 25-30 microcapsules each were then transferred into a well of a 96-wellplate. The capsules were left to sediment before adding 100 μL hydrogen-peroxide solution of varying concentrations (60, 120, 180, 240 mM). The buoyant microcapsules were examined and counted under a brightfield microscope.

4.3.4 Bubble growth screening inside AMP/DNA and protamine/DNA-microcapsules

Here, the growth of the oxygen-bubble inside AMP/DNA- and protamine/DNA-microcapsules was examined in a constant concentration of hydrogen peroxide.

AMP/DNA- and protamine/DNA-microcapsules were fabricated the same way as described in 3.3.3 and with 4 mg/mL silica particles and 19.8 kU/mL catalase. Both capsules had an average size of 350-400 μm in diameter to make them comparable. The experiment was conducted under the Olympus BX 53 brightfield microscope, and the bubble growth was tracked via video recording. The capsule along with 200 μL di-water was transferred onto a microscope-glass slide so that the liquid forms a firm droplet. The glass slide was then positioned underneath the microscope before adding 10 μL hydrogen peroxide (160 mM) directly into the droplet. Once the bubble nucleates, the capsule rises to the top of the droplet, where it can be easily tracked by the camera.

For the viability screenings, 20 AMP/DNA- or protamine/DNA-microcapsules were similarly prepared one after another and the bubble growth tracked until the membrane ruptured.

4.3.5 Collective transport of a dialysis bag with AMP/DNA-microcapsules

The experimental protocol was taken from Kumar *et al.* [95] with consent from the authors.

AMP/DNA microcapsules were fabricated as described in 3.3.3 with 39 kU/mL catalase. 200 capsules, together with ~ 10 mL di-water, were then transferred and sealed into a dialysis bag (*Medicell Membranes – Dialysis tubing: 12-14 kDa cutoff, 28.6 mm x 30 mm*), and the dialysis bag was placed on the bottom of a measuring cylinder (100 mL, 25 cm in height). The cylinder was filled with 100 mL di-water before adding 500 μL hydrogen peroxide solution (160 mM, 3 wt% sucrose) right on top of the dialysis bag with a pipette. The sucrose increased the density, which helped the H_2O_2-solution to settle on the bottom, rather than diffusing upwards right away. Oxygen bubbles nucleated inside the capsules and, once a certain threshold was reached, the bag started to become buoyant as well and slowly ascended to the surface.

4.3.6 Collective motion and catalytic conversion of phenolphthalein bisphosphate (PPBP) via encapsulated alkaline phosphatase (ALP) inside AMP/DNA-microcapsules

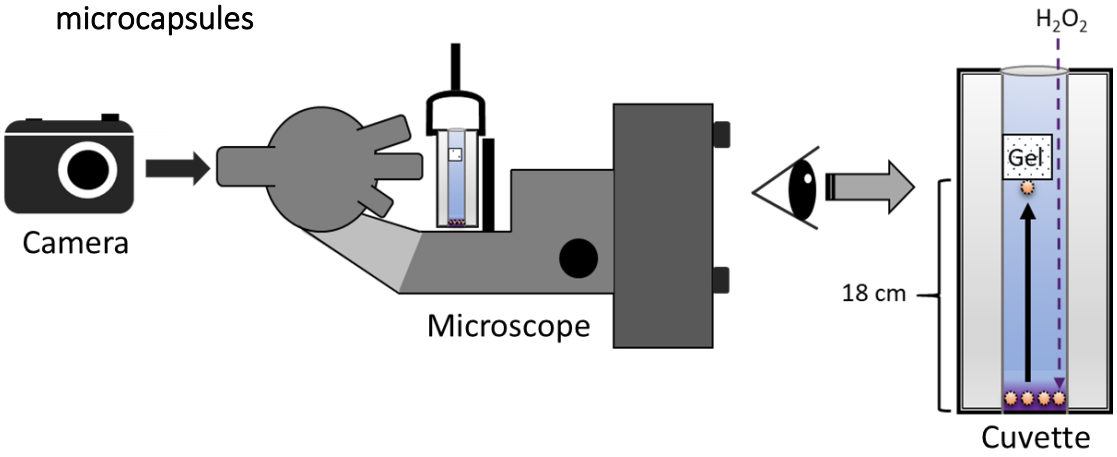

Figure 4.3-2: *Illustration of the experimental setup. A small optical cuvette (External dimensions: Length: 7.5 mm, width: 12.5 mm, height: 48 mm. Internal dimensions: Length: 5 mm, width: 4 mm, height: 46 mm, Internal volume: 0.7 mL) was fitted with a small phenolphthalein bisphosphate-containing agarose cube, so that one side of the cuvette was left open. Through this gap, small AMP/DNA-microcapsules and hydrogen peroxide (160 mM) were added to the cuvette. The cuvette was mounted into the beam-path of a horizontally positioned optical microscope to observe the capsules and the dephosphorylation of PPBP.*

The experimental protocol was taken from Kumar *et al.* [95] with consent from the authors.

AMP/DNA-microcapsules were fabricated as described above in 3.3.3 with 39 kU/mL catalase. To set up the experiment, a small optical cuvette was filled with 0.5 mg/mL AMP-clay solution and about 30 AMP/DNA-microcapsules were added into the column. Once the capsules have settled on the bottom, a small agarose gel was fitted about 18 mm from the bottom of the cuvette and so, that a small gap exists between the wall and the gel. The gel was fabricated from 2 wt% agarose-mixture with 50 mM phenolphthalein bisphosphate. The cuvette was then placed into the beam-path of a horizontally positioned brightfield microscope, so that the vertical displacement of the capsules could be observed Microcapsule buoyancy was then initiated by addition of 15 µL H_2O_2 (160 mM) close to the capsules via a pipette. Once the capsules started ascending, they were stopped by the gel. The production of the pink phenolphthalein was observed through the microscope and recorded by a digital camera.

4.3.7 Reversed buoyancy via magnetic polymer microparticles inside AMP/DNA-microcapsules

The experimental protocol was taken from Kumar *et al.* [95] with consent from the authors.

AMP/DNA-microcapsules were fabricated as described above in 3.3.3 and with 6 mg/mL magnetic polymer microparticles and 19.8 kU/mL catalase. The experiment was performed in an optical cuvette identical to the device described in Figure 4.3-6. The cuvette was filled with 0.5 mg/mL AMP-clay solution and a small PDMS-cube was fitted into the column about 8 mm from the bottom of the cuvette which left a little gap between the cube and the wall of the cuvette to enable the addition of the capsule and the substrate. One AMP/DNA-microcapsule was then added and left to sediment. Once the capsule has settled on the ground of the cuvette, hydrogen peroxide (160 mM) was added via a pipette. The substrate was added slowly and right above the capsule, so that the addition could

be stopped, the second the capsule nucleated a small oxygen bubble inside. Once the capsule rose to the surface it was blocked by the PDMS-cube. To induce the reversed buoyancy, a magnet was placed underneath the cuvette, which pulled the capsule back to the ground. The movement of the capsule was observed and tracked via a digital camera, which was applied to the microscope.

4.3.8 Pre-nucleation of an internal oxygen-bubble within microcapsules

To pre-nucleate an oxygen bubble inside protamine/DNA- or AMP/DNA-microcapsules, a single fabricated microcapsule was transferred into a separate vial with 1 mL di-water. There, the capsule was left to sediment and then gently immersed in 5-10 µL H_2O_2 (160 mM), which was slowly ejected above the capsule with a pipette. Once the O_2-bubble nucleated and the capsule started to rise to the surface, it was transferred out of the vial and into the experimental device for observation. Alternatively, and for experiments which utilise entrapped glucose oxidase to promote O_2-bubble consumption, the capsule was transferred into a second vial, filled with a 0.1 M glucose solution. There, the capsule was left until it started to sediment, at which point it was transferred out of the glucose solution and into the experimental contraption.

4.3.9 Reversed buoyancy via encapsulated glucose oxidase (GOx) inside AMP/DNA and protamine/DNA-microcapsules

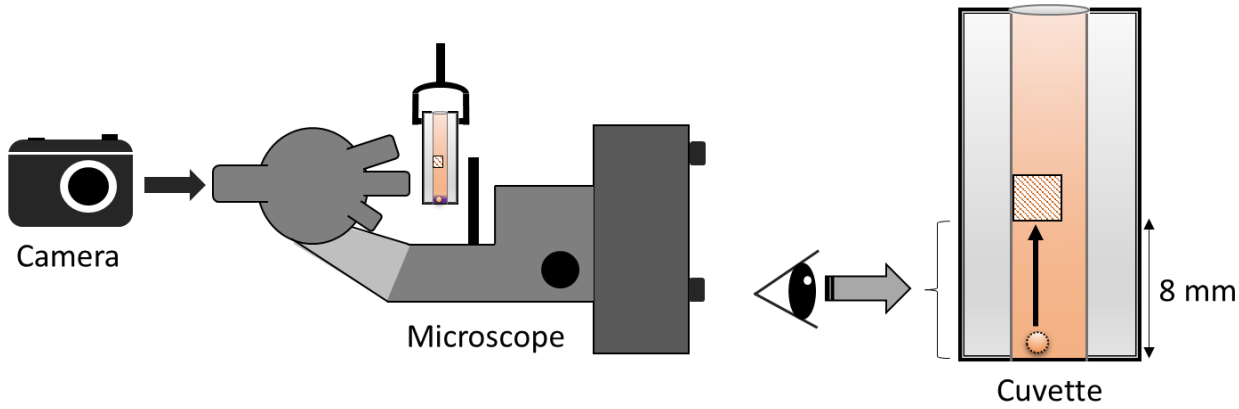

Figure 4.3-3: *Illustration of the experimental setup. A small optical cuvette (External dimensions: Length: 7.5 mm, width: 12.5 mm, height: 48 mm. Internal dimensions: Length: 5 mm, width: 4 mm, height: 46 mm, Internal volume: 0.7 mL) was fitted with a small PDMS cube, which served as a physical barrier. A small AMP/DNA- and protamine/DNA microcapsules were added to the cuvette. The capsules were generally added with a pre-nucleated oxygen-bubble. The cuvette was mounted into the beam-path of a horizontally positioned optical microscope in order to observe the capsules and the shrinkage of the oxygen bubble.*

Protamine/DNA- and AMP/DNA-microcapsules were fabricated according to the established method in 3.3.3 with 4 mg/mL DNA, 19.8 kU/mL catalase, 20 mg/mL silica particles, 2904 U/mL glucose oxidase and with sizes of 400 µm in diameter. For protamine/DNA-microcapsules, the cuvette was filled with di-water, in case of AMP/DNA-microcapsules the cuvette was filled with 0.5 mg/mL AMP-clay to ensure capsule-stability over longer periods of time. The cuvette was furthermore fitted with a small PDMS-cube, which served as a physical barrier for the capsule to ascend against, while leaving enough room on the side for the addition of the capsule or other components. A capsule with a pre-nucleated O_2-bubble (4.3.8) was then transferred into the optical cuvette. Once the capsule was added and has settled against the PDMS-barrier, 300 µL glucose solution (0.1 M) was added through the small cavity next to the cube. Due to the higher density, the glucose settled on the bottom and displaced the water/clay-solution until the capsule got in contact with the glucose. The experiment was monitored via an optical microscope with a 1.25X lens. The microscope was turned horizontally, and the cuvette

mounted onto a clamp, so that it reached into the beam-path of the microscope. A digital camera was attached to the microscope and recorded the shrinkage of the bubble with a frame height of 8 mm.

4.3.10 Glucose oxidase kinetic assay inside protamine/DNA-microcapsules

The kinetics of glucose oxidase inside protamine/DNA-microcapsules were assessed with a coupled enzyme-assay with glucose oxidase, horseradish peroxidase (HRP) and ABTS as a detectable chromophore. First, protamine/DNA-microcapsules were fabricated according to the established protocol with 2904 U/mL glucose oxidase.

Before screening GOx inside the capsules, ABTS concentrations needed to be calibrated in reference to the signal inside the UV/VIS-spectrometer. For this, the following ABTS-concentrations were prepared inside disposable optical cuvettes: 0, 0.91, 9.1, 18.2, 45.5 and 91 μM. The final volume of each sample was 1 mL, and the experiment was started after the addition of HRP (8.3 U/mL) and hydrogen peroxide (50 mM). Each sample was mixed via glass pipette and left for 10 minutes, or until the absorbance inside the spectrometer was stable, to ensure all ABTS has reacted with HRP. The results were plotted and approximated linearly, in order to refer to the actual ABTS-concentrations later on.

Next, the activity of GOx inside the capsules was screened over a range of different glucose concentrations: 0, 5, 10, 25, 50, 75, 100, 200 and 500 mM. The solutions were prepared inside disposable optical cuvettes with ABTS (8.19 mM) and HRP (8.3 U/mL) and the corresponding glucose concentration, with a final volume of 1 mL. To start the experiment, 2 GOx-containing protamine/DNA-capsules were added into the cuvette, and the first measurement inside the spectrometer was taken (absorbance of $ABTS^{OX}$ detected at $\lambda_{Abs,ABTS}$ = 420 nm). As soon as the absorbance was detected, the cuvette was removed from the device and the solution gently mixed with a pipette. Here it was important not to break the capsules due to heavy mixing or stirring. The absorbance was then measured every minute for 5 minutes altogether.

Eventually the results of all samples were plotted and fitted to a Michaelis-Menten-plot in order to extract the kinetic constants.

4.3.11 O_2-bubble: Auto-depletion vs GOx-mediated consumption

Protamine/DNA capsules with a diameter of 400 μm were fabricated with 4 mg/mL DNA, 19.8 kU/mL catalase, 20 mg/mL silica particles and 2904 U/mL GOx according to the established protocol in 3.3.3. The capsules were then washed 5 times before pre-nucleating an oxygen bubble inside the capsules (4.3.8). The capsules were then transferred into either di-water or 0.1 M glucose inside a 96-well plate. The oxygen bubble volume of the capsules was tracked microscopically until the bubble was totally depleted. As a negative sample, capsules without GOx but with a pre-nucleated O_2-bubble were also investigated after adding them into di-water. The tracked bubble volume was then plotted.

4.3.12 Combination of catalase-induced buoyancy and GOx-induced reversed buoyancy

Protamine/DNA capsules with a diameter of 400 μm were fabricated with 4 mg/mL DNA, 19.8 kU/mL catalase, 20 mg/mL silica particles and 2904 U/mL GOx according to the established protocol in 3.3.3. The cuvette was prepared by adding 1 mL glucose solution (0.1 M) and the PDMS-block as an upper barrier. The cuvette was then placed in front of a horizontal microscope as it has been already shown in previous experiments (see for example Figure 4.3-3) and the capsule, with a pre-nucleated O_2-bubble was added into the device, so that the capsule rested against the PDMS-block. 10 μL H_2O_2 (160 mM, 3 wt% sucrose) were gently added with a pipette, so that it formed a separate layer on the

bottom of the device without causing any mixing between the glucose and the H_2O_2. The oscillation was then observed via a digital camera which was attached to the microscope.

4.3.13 Fabrication of oscillation devices

All devices used for microcapsule oscillation in this thesis have been designed with the help of the mechanical workshop and the glass workshop of the school of chemistry at Bristol University.

4.3.14 Fabrication and assembly of the device for stable oscillations

The first concept was prepared for long-term oscillations with direct control over the input of the substrates glucose and hydrogen peroxide by using a flow based design. The device was made out of borosilicate glass and consisted of 3 parts: a large cuboid central column (Dimensions in Table 4.3-1) with round necks on each side and with each neck having flat ring-shaped surface to seal off the device and two hat-shaped compartments, which can be attached to the central column with clamps and the help of rubber-O-rings around the necks of the column. Both compartments furthermore have two glass-tubes fitted to enable the application of flow systems via syringe pumps, connected to the device via tubes. The same was done for the central column, although here the input and output do not align linearly but on top of each other, which is used to refresh the solution of the central column during the oscillation experiments.

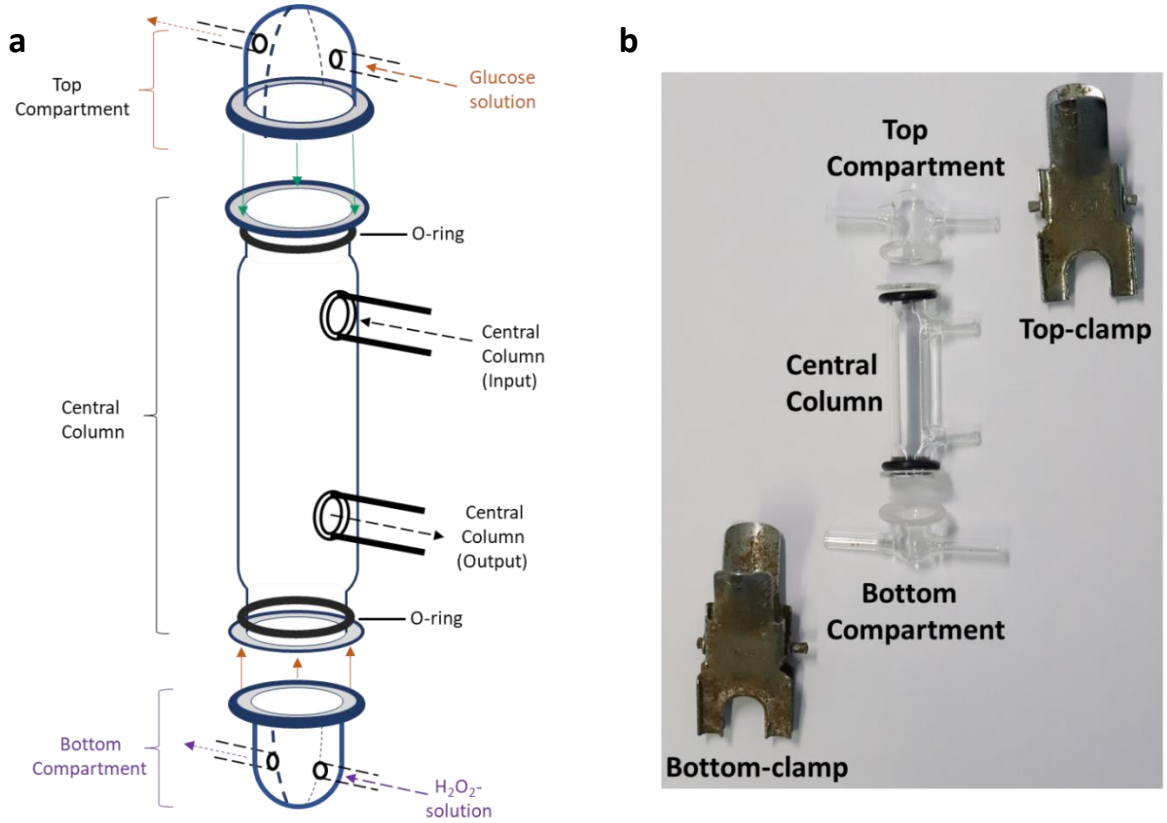

***Figure 4.3-4**: Schematic (**a**) and camera-image (**b**) of the glass device used for long-term oscillation experiments. The device consists of 3 units, one central column fitted with O-rings on each side and two glass tubes (inlet and outlet) on the column to enable flow and solution exchange and two hat-shaped compartments which can be fitted to each side of the central column via clamps. Both compartments also have glass tubes fitted to enable flows.*

***Table 4.3-1**: Measurements of the oscillation device from Figure 4.3-4.*

Part	Measurement
Central Column Volume	4.2 mL
Central Column external dimensions	12.94 x 8.5 x 61.66 mm
Central Column internal dimensions	6.5 x 10.5 mm x 61.7 mm
Central column internal geometry	Cuboid
Supply pipes-dimensions	Ø = 3 mm , 0.1 mL
Top compartment volume	1.2 mL, Ø ~ 8.78 mm
Bottom compartment volume	1.2 mL, Ø ~ 8.78 mm

Besides holding the central column and the top/bottom compartment together, the clamps are also used to mount the device onto a scaffold. This way the column can be aligned upright and in a proper position for a camera to observe the capsule inside the device.

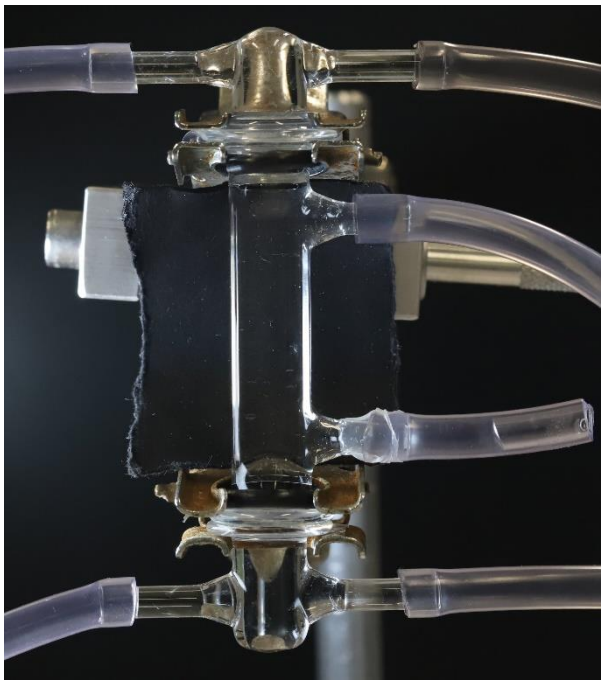

***Figure 4.3-5:** Stable oscillation device: set up for experimental procedures. The central oscillation-column is connected to the top and the bottom compartments via metal clamps. The top clamp is furthermore connected to a metal scaffold, which holds the device in place. All compartments are connected to tubing, which enables the flow of substrates through the device. The bottom-tube from the central column is usually left open, to be used as an entry point for cells.*

The device was generally assembled the same way throughout all experiments in this thesis. Before use, all three pieces were thoroughly cleaned in a basebath (1.2 M NaOH in isopropanol/water 4:1) over night and then washed extensively with di-ionised water. Once the device was clean, the O-rings were assembled around each side of the column and all tubing was attached to both the central column and the bottom/top compartments. To reduce the risk of evaporation of water, PORTEX™-tubing (8H, 4mm ID 7mm OD) was used. Aa single sheet of pre-soaked dialysis membrane (*Medicell Membranes – Dialysis tubing: 12-14 kDa cutoff, 28.6 mm x 60 mm*) was placed on each opening and the bottom- and top compartments were successively placed onto the dialysis membrane and

carefully fixated with a clamp. Once both sides were attached, the central column was filed by using the top-port as "Input" and the bottom-port as "output", after which the top- and bottom compartments were filled. Depending on the experiment, the respective solutions were either added to the device by hand with a syringe or with the aid of a syringe pump.

In all oscillation experiments, a Nikon 6D Mark II was used, with a Canon Macro lens (EF 100 mm 1:2.8L) and positioned in front of the oscillation device in order to capture the central column with the capsule in it. Due to the curved nature of the necks on each side of the oscillation column, the camera wasn't able to follow the capsule right before the dialysis membrane. As these last 1-2 mm were generally cut off, the capsule could not be tracked all the way, although this did not affect the tracking plots in any meaningful way.

4.3.15 Diffusion studies inside the stable oscillation device

The oscillation device was prepared as described in 4.3.14 and filled with 3 wt% sucrose for the bottom-phase, 2wt % sucrose in the central column and 0 wt% sucrose in the top phase through the syringe pump system. Depending on the side of interest, either the top- or the bottom side was mixed with 5 mM methylene blue, to ensure a strong contrast and to enable a visual representation of the diffusion and the flows within the device. Once the experiment started, all flows were set to 20 μL/min and the diffusion of the dye was recorded through images taken in 30s intervals. To compare the flow-induced- to the diffusion induced effects, all flows were turned off after 10h after which images were taken for another 10h.

To enable a quantitative analysis of the diffusing methylene blue and its concentration, a calibration curve was prepared. The oscillation device was filled with methylene blue solutions of varying concentrations (50 mM, 5 mM, 1 mM, 0.5 mM, 0.1 mM, 0.05 mM, 0.01 mM, 0.005 mM, 0.001 mM) and then analysed via digital camera images. Here, the mean intensity of the blue colour was calculated via ImageJ and then plotted as a calibration curve.

4.3.16 Stable oscillations

The stable oscillation device was assembled as described in 4.3.14 and the following substrate concentrations were investigated: 1) 0.1 M glucose/9 mM H_2O_2, 2) 0.1 M glucose/30 mM H_2O_2, 3) 0.03 M glucose/9 mM H_2O_2, 4) 0.03 M glucose/30 mM H_2O_2. A density-gradient was established by mixing 3 wt% sucrose to the H_2O_2-bottom phase, 2 wt% sucrose to the aqueous central phase and 0 wt% sucrose in the glucose-top phase. Once the device was prepared, glucose- and H_2O_2-solution were pumped through the top- and bottom compartment respectively at 20 μL/min. The central column was merely flushed with a 2 wt% sucrose solution, leading into the top-inlet and leaving through the lower outlet at 20 μL/min. The flows were turned ON for 1 hour in order to get the device to reach the steady state before the oscillation experiment with the protamine/DNA-microcapsule was started. Protamine/DNA capsules with a diameter of 400 μm were fabricated with 4 mg/mL DNA, 19.8 kU/mL catalase, 20 mg/mL silica particles, and 2904 U/mL GOx according to the established protocol in 3.3.3. The microcapsule with a pre-nucleated O_2-bubble (4.3.8) was then transferred into the oscillation column through the lower inlet, from where it would rise to the top membrane and eventually start its oscillations.

4.3.17 Fabrication and assembly of device for damped oscillations

The device used for dampened microcapsule oscillations was based on an optical cuvette (purchased from Starna Scientific LTD.) with the following dimensions: Length: 7.5mm, Width: 12.5mm, Height: 48mm. The cuvette was made from *special optical glass* and looked as followed (Figure 4.3-6).

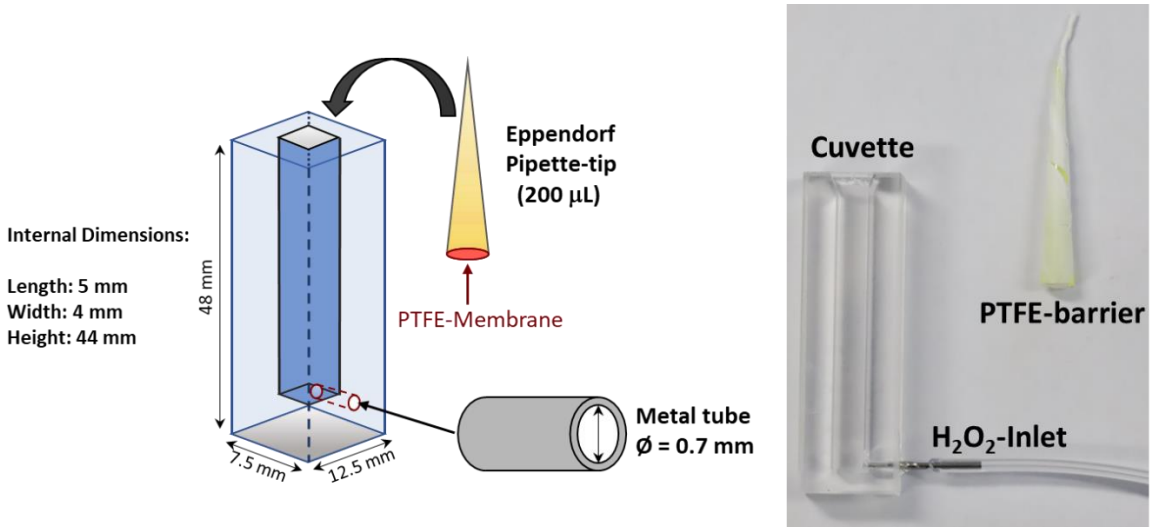

Figure 4.3-6: *Schematic (a) and camera image of device for dampened oscillation. The device consists of an optical cuvette with a whole drilled to the bottom side of the internal cavity. A tube was fitted into the hole to enable the application of syringe pump systems to add substrates or other compounds right at the bottom without disturbing the surrounding environment.*

Table 4.3-2: *Dimensions of damped oscillation device and inlets from Figure 4.3-6.*

Part	***Measurement***
Cuvette external dimensions	7.5 x 12.5 x 48.0 mm
Cuvette internal dimensions	5.0 x 4.0 x 44.0 mm
Pipette-tip/PTFE-membrane diameter	*Eppendorf* pipette-tip (yellow), Ø = 4 mm
Metal-tube inlet-diameter	Ø = 0.7 mm

To customise the device for the purpose of inducing dampened oscillations, a small hole has been drilled, just so it aligns with the bottom of the internal compartment of the cuvette. The hole was ~ 0.9 mm in diameter and fit with a hollow metal tube with an internal diameter of 0.7 mm. Once the tube was in place, the hole was sealed with an optical glue (Norland Product Inc., NOA 61) and cured under UV light (365 nm). In order to restrict the volume in which the capsule is allowed to oscillate, a PTFE-membrane was wrapped around the broad end of an *Eppendorf* pipette tip (200 µL, yellow), which served as a non-sticking barrier. To assemble the device, the cuvette was first cleaned thoroughly with base bath (1.2 M NaOH in isopropanol/water 4:1) over night and then washed extensively with di-ionised water. To make sure that even fine contaminations are removed, the device was then briefly cleaned with piranha solution (by mixing 300 µL of concentrated sulfuric acid (H_2SO_4) with 100 µL H_2O_2 (30 wt%) inside the cuvette and, again, washing it thoroughly with di-water.

Similar to the long-term oscillation experiments, the cuvette was then mounted onto a scaffold via a clamp and positioned in front of a camera. The cuvette was filled with the respective solution and the PTFE-membrane was inserted up to 8 mm above the bottom of the cuvette, which eventually spans the oscillation distance for the capsule. To prevent any form of evaporation of the liquids inside the column, the top of the cuvette was usually blocked with a PDMS-cap (Figure 4.3-7).

Figure 4.3-7: *Dampened oscillation device. An optical cuvette was used as the oscillation-column and a small hole was drilled right at the bottom which was fitted with a small metal tube (ø = 0.7 mm) that was connected to a syringe mounted to a syringe pump. From there, hydrogen-peroxide solution was fed into the cuvette system. To reduce the oscillation-length, a PTFE-membrane was wrapped around a yellow Eppendorf-pipette tip (200 µL) and inserted into the cuvette, eventually leaving a 8 mm gap between the bottom and the membrane.*

4.3.18 Damped oscillations within the stable oscillation device

The stable oscillation device was prepared as described in 4.3.14. The top compartment and the central column were filled with 0.03 M glucose whereas the bottom compartment was filled with either 16 mM or 32 mM H_2O_2. In this experimental setup, no flows were applied and H_2O_2 was merely moving by diffusion. The protamine/DNA-microcapsule was prepared according to the established protocol (3.3.3) with 4 mg/mL DNA, 19.8 kU/mL catalase, 2904 U/mL GOx, 20 mg/mL silica particles and with a general diameter of 400 µm. The capsule was then added into the device with a pre-nucleated O_2-bubble (4.3.8) through the lower inlet, from where the capsule would rise to the top membrane and start its oscillations.

4.3.19 Damped oscillations within the damped oscillation device.

Protamine/DNA-capsules were fabricated according to the established protocol (3.3.3) with 4 mg/mL DNA, 19.8 kU/mL Catalase, 2904 U/mL GOx and 12 mg/mL silica particles and with a general diameter of 400 µm. For each experiment, an O_2-bubble was pre-nucleated inside the protamine/DNA-microcapsule before it was added to the oscillation-device (4.3.8). In the meantime, the damped oscillation device was prepared as described in 4.3.17. It was filled with the glucose solution before adding the PTFE-membrane-scaffold. The capsule with the pre-nucleated O_2-bubble was added to the device, so that the capsule was blocked by the PTFE-membrane. Once the capsule started to descend from the membrane, the H_2O_2-solution with 3 wt% sucrose was added via the syringe pump (7 µL at 5 µL/min). The concentrations of glucose (100 mM, 80 mM, 60 mM) and H_2O_2 (210 mM, 150 mM, 90 mM) were varied over the course of this experiment, which lead to 3X3 combinations to be investigated. The oscillation was then observed and tracked via digital camera images in 5s intervals.

4.3.20 Bubble-growth tracking during damped and stable oscillations

In order to be able to track the size of the oxygen-bubble within protamine-microcapsules, the oscillations were again performed in a cuvette as described in 4.3.17 but in front of a horizontally placed microscope like it was done before in e.g. 4.3.1. The device was assembled as described before

by adding the glucose solution first, followed by the PTFE-inlet. Protamine/DNA-microcapsules were fabricated with 4 mg/mL DNA, 19.8 kU/mL catalase, 2.9 kU/mL GOx and 12 mg/mL silica particles (3.3.3). A single protamine capsule with a pre-nucleated O_2-bubble was then added into the device so that its ascent was blocked by the PTFE-membrane. Once the capsule started to descend, the H_2O_2-solution was injected at 5 µL/min. The concentrations were set to 0.1 M glucose and 5 µL of 90 mM H_2O_2 for the damped oscillation and 0.08 M glucose and 5 µL of 210 mM H_2O_2 for the stable oscillation. The Oscillation was tracked via a digital camera attached to the microscope.

4.3.21 Setup of the interface oscillations device

First, the device for the interface oscillations was prepared. The bottom phase consisted of a H_2O_2-solution, mixed with 0.1 mM methylene blue and 3 wt% sucrose, which was loaded into a syringe and mounted to a syringe pump. The bottom phase was added into the device until it almost reached the second upper inlet. Through a second syringe on a syringe pump, glucose solution (with 2 wt% sucrose) was then added into the column through the upper inlet at 100 µL/min until the column was filled almost to the top (Figure 4.3-8-b). The protamine-capsule was prepared according to the established protocol (3.3.3) with 4 mg/mL DNA, 19.8 kU/mL catalase, 2.9 kU/mL GOx and 20 mg/mL silica particles and with a pre-nucleated oxygen bubble (4.3.8). The capsule was then transferred into an external vial with a 0.1 M glucose solution until the capsule started to descend, after which it was transferred into the oscillation device. The oscillations were recorded via digital camera.

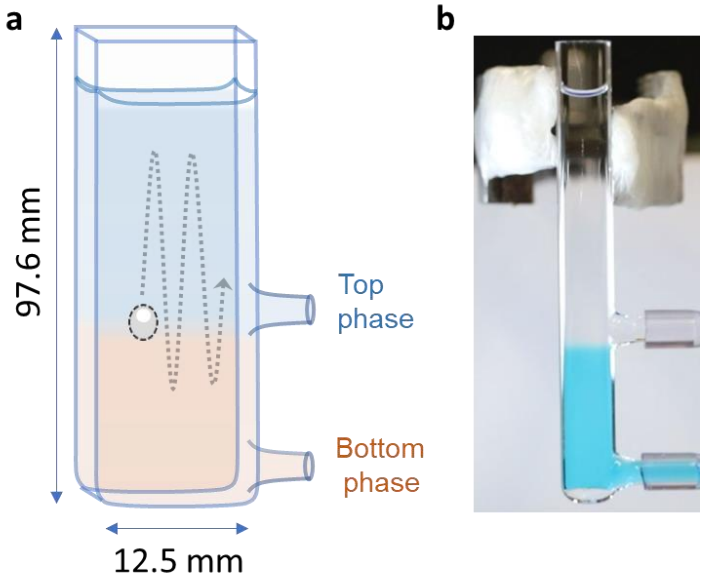

Figure 4.3-8: a *Illustration of a microcapsule oscillating between the glucose- (top) and H_2O_2 (bottom)-interface inside the interface oscillation device.* ***b*** *Camera-image of the interface oscillation device. Methylene blue was added to the bottom-phase to increase the contrast between the two phases.*

4.3.22 Bubble growth studies

Protamine/DNA-microcapsules were fabricated according to the established protocol (3.3.3) with 4 mg/mL DNA, 19.8 kU/mL catalase, 2.9 kU/mL GOx and 20 mg/mL silica particles. Before each experiment, the capsule was treated to pre-nucleate an internal oxygen bubble (4.3.8) and then transferred into a 0.1 M glucose solution. Once the capsule started to sediment, the capsule was transferred into a well of a 96-well plate. The solution was drained from the well without removing the capsule and the capsule was washed with 100 µL of the respective substrate mixture. This was repeated 2 times after which the capsule and the bubble volume was tracked through an optical

microscope (Olympus BX53). For each experiment, the capsule was immersed in a distinct mixture of glucose (0, 20, 40, 60, 80, 100 mM) and H_2O_2 (0, 6, 12, 18, 24, 30 mM), thus leading to 36 different concentration combinations.

4.3.23 Analysis of glucose oxidase fatigue via CSTR-activity studies

To study the temporal variation in activity of glucose oxidase within the protamine/DNA microcapsules, a continuous stirred tank reactor (CSTR) was used to 'house' the microcapsules while the reagents were flowed into the reactor and the formation of products was monitored at the outlet. The CSTR was fabricated from acrylic and made in the workshop of the school of chemistry (10:1 monomer/crosslinker ratio; 70 °C curing for 6 h) and the top of the reactor was sealed with an acrylic lid, that was fixated via screws onto the CSTR. A rubber O-ring prevented the CSTR from leaking once the lid was attached (Figure 4.3-9). 30 protamine-microcapsules, which were fabricated from DNA (4 mg/mL), catalase (19.8 kU/mL), silica particles (20 mg/mL) and glucose oxidase (2.9 kU/mL) were loaded into the reactor and the inlet was connected via a Y-shaped connector to two syringes containing aqueous solutions of ABTS (0.64 mM) and glucose (0.2 M), and HRP (2 U/mL) respectively. The syringes were operated using a syringe pump with the flow rate set to 0.25 mL/min each which led to a refresh rate of the reactor of 0.58/min. Catalase was also entrapped inside the capsules to simulate identical conditions to the oscillation-experiments. The HRP- and ABTS/glucose-solutions were separated into different syringes to avoid any interference from potential cross reactions between ABTS and HRP before the experiment was started. The outlet of the CSTR was attached to a flow cell (Hellma Analytics, special optical glass (1787118510-20), 10 mm light path, Height: 35 mm, Width 12.5 mm, Depth 12.5 mm) inside a UV/VIS spectrometer to monitor the oxidised ABTS at $\lambda_{Exc.,ABTS\text{-}ox}$ = 420 nm.

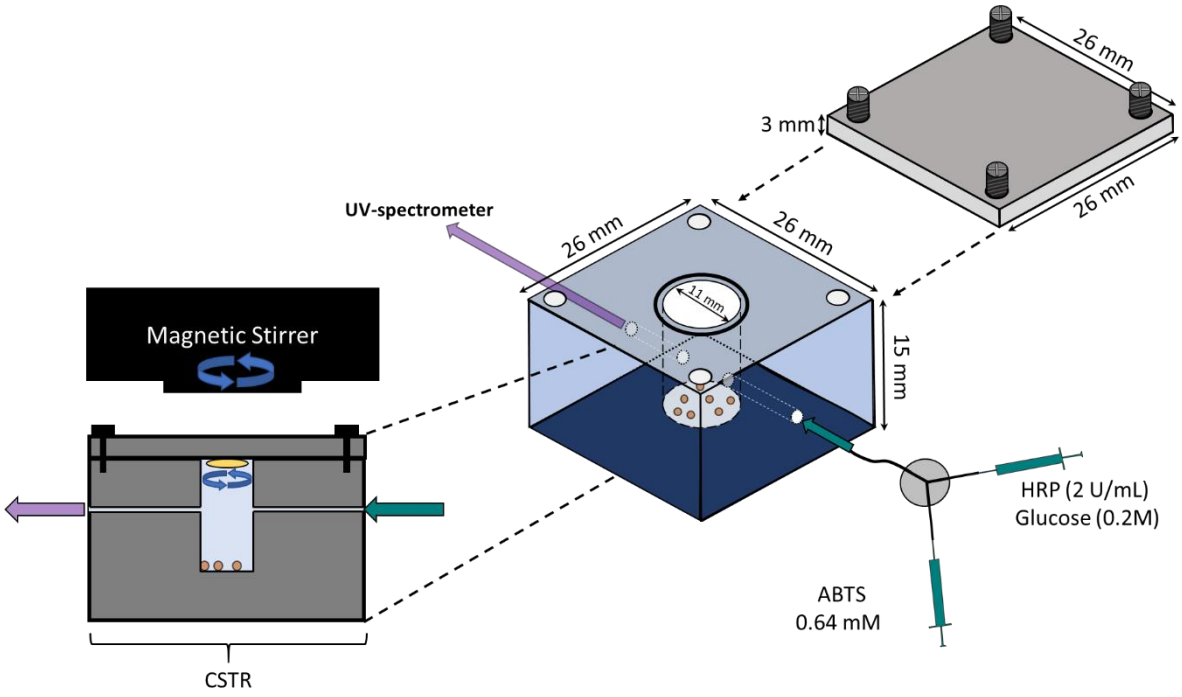

Figure 4.3-9: *Illustration of the CST-reactor. 30 capsules were loaded into the device and a steady flow of substrates (0.25 mL/min, 0.64 mM ABTS, 0.2 M glucose) and HRP (2 U/mL) was applied. The capsules were stirred through a small magnetic stir bar, which was spun at the top of the device through an upside down magnetic stirrer. The activity of glucose was indirectly determined via UV/VIS spectroscopy through the oxidised ABTS at* $\lambda_{Exc.,ABTS\text{-}ox}$ *= 420 nm.*

4.3.24 Enzyme leakage and oxidative damage of enzymes in protamine/DNA-microcapsules

This is a general protocol for the experiments done to assess enzyme leakage and oxidative damage. Protamine/DNA-capsules were fabricated according to the established protocol with either 19.8 kU/mL catalase, 2.9 kU/mL GOx, 2 mg/mL FITC-catalase and 2 mg/mL RITC-GOx, depending on the aim of the experiment. The capsules were then incubated in a substrate solution of choice (glucose, H_2O_2, or a mixture of glucose and H_2O_2) for up to 3 hours, after which the enzyme leakage or damage were either analysed through fluorescence microscopy or via a colorimetric assay. The latter was done in form of a coupled colorimetric assay with ABTS and HRP. An optical cuvette was prepared by mixing ABTS (8.19 mM), HRP (8.3 U/mL) and glucose (25 mM). After washing the protamine capsules 5 times with di-water, 2 capsules were isolated and used for the colorimetric assay. The capsules were transferred into the cuvette, which presented the value at time 0, after which the measurements were repeated every minute for up to 5 minutes. The capsules and the solution were mixed gently with a pipette between each measurement and without breaking them.

4.4 Results and discussions

4.4.1 Microcapsule Buoyancy

The beginning of this chapter aims to introduce and describe enzyme mediated microcapsule buoyancy. Kumar *et al.* [95] recently published the foundation for the work on buoyant microcapsules, which will serve as a motivation and reference for the more fundamental experiments in this introduction into buoyancy induced motility. Since the previous [95] and the current work on microcapsule motility is an ongoing cooperative project and due to the introduction of the novel protamine/DNA-microcapsule system, some experiments will be repeated and also updated, as not only the capsule type was changed, but also the catalase used in the upcoming experiments, which was purchased from a different supplier. It is furthermore necessary to establish the fundamentals of microcapsule motility via buoyancy, as these basic experiments lay the foundation to understand the more complex oscillation phenomena reported later in this chapter. Like in the previous chapter, the comparison between the two capsule-types (AMP/DNA- and protamine/DNA-microcapsules) will be continued and concluded within the first half of this chapter, to determine and confirm the benefits of protamine/DNA-capsules.

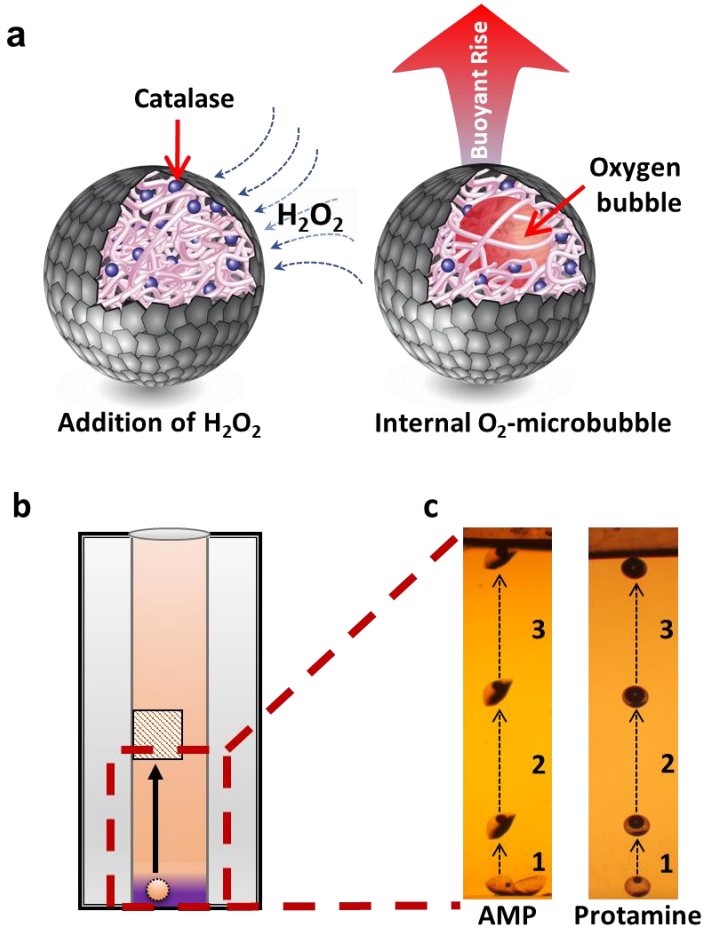

Figure 4.4-1: *Buoyancy of AMP/DNA and protamine/DNA-microcapsules.* ***a*** *Illustration of the interaction of encapsulated catalase with hydrogen peroxide. The enzyme produces oxygen which nucleates in form of a micro-bubble inside the capsule interior. Once the bubble has reached a certain volume, the buoyant force will carry the capsule upwards.* ***b*** *Illustration of an optical cuvette with a fitted PDMS-cube, which was used to study microcapsule buoyancy.* ***c*** *optical micrographs of the different steps of microcapsule buoyancy: 1) Oxygen-bubble nucleation, 2) microcapsule buoyancy and reaching of terminal velocity, 3) stop of buoyancy due to barrier. The buoyancy is shown for both AMP/DNA- (****c-left****) and protamine/DNA-microcapsules (****c-right****).*

First, it was necessary to get a good understanding whether enzyme mediated microcapsule buoyancy is feasible at all, or in other words, if the entrapped catalase is active, if it produces oxygen in form of microbubbles and if these bubbles actually nucleate inside the capsule or rather on the outer side of the membrane.

The buoyancy of a catalase-containing microcapsule was observed inside a cuvette, which was placed in front of a horizontally positioned optical microscope, which was equipped with a digital camera (See Figure 4.3-1). The micrographs of Figure 4.4-1 show the buoyancy of AMP/DNA (Figure 4.4-1-c-left) and protamine/DNA-microcapsules (Figure 4.4-1-c-right) after addition of 10 μL H_2O_2 (160 mM). First, the oxygen bubble nucleated inside the capsule (**1**), slowly growing until it reached its critical volume after which the capsule started to become buoyant and accelerated up to a terminal velocity (**2**). Eventually, the capsule would either reach the surface of the volume, or as in this case, stop as it collided with the PDMS-block (**3**). So, this simple experiment proved that oxygen, produced by entrapped catalase can indeed nucleate in form of oxygen bubbles inside the both capsule-types, which in return makes them rise to the top. By using tracking-software like *Fiji-ImageJ's Trackmate*, the upward-velocities of buoyant capsules were calculated from capsule tracking data. To measure the velocity, 10 buoyant capsules were observed for about 3 seconds inside a glass cuvette after addition of hydrogen peroxide (3 μL, 160 mM) until they reached the surface of the liquid phase inside a glass cuvette with a height of 48 mm. Comparing the two different datasets, protamine capsules exhibited faster travelling times (~ 8 mm/s) in comparison to AMP/DNA-microcapsules, which only reached a maximum velocity of ~ 5 mm/s, even though the latter showed less diversion from the average velocity profile. Overall, the average maximum speeds achieved by both capsules were slightly different with 5.79 mm/s for protamine/DNA- and 4.03 mm/s for AMP/DNA capsules. One factor that might contribute to the observations is the shape of the capsules. Since AMP/DNA-microcapsules are generally more deformed and less uniform in comparison to the very spherical protamine/DNA-microcapsules, it could affect the O_2-microbubble nucleation or growth or even the hydrodynamics of the capsules. The velocity profiles generally followed a sigmoidal shape, where the capsule would accelerate and eventually reach a terminal velocity. Some capsules reached the surface though before they reached this plateau and all capsules continued to accelerate as their O_2-bubbles kept growing after they left the H_2O_2-enriched phase. This can be explained by excess H_2O_2 inside the cell, which sustained the O_2-production during the ascent, or by H_2O_2-diffusion into the water column.

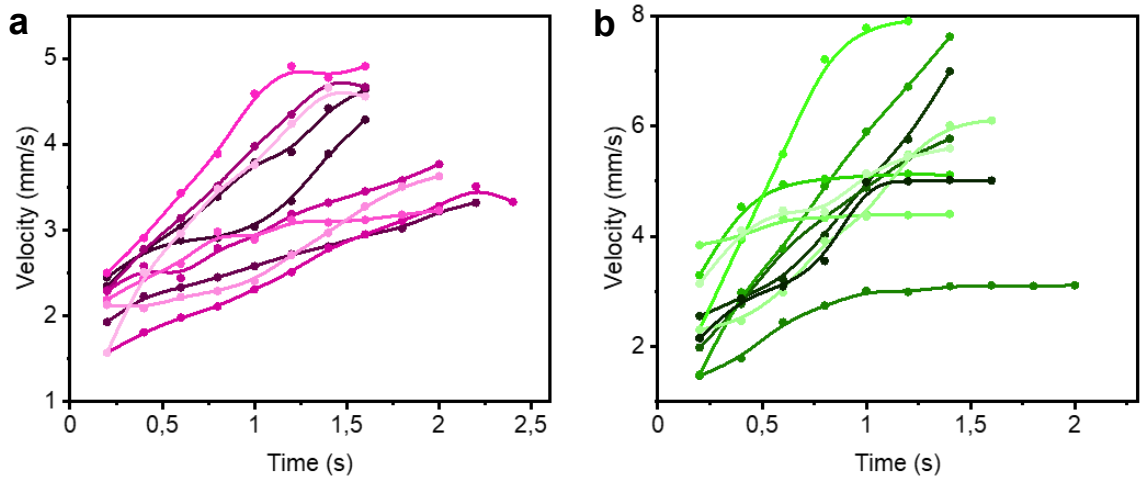

Figure 4.4-2: *Velocity profiles of 10 buoyant AMP/DNA- (**a**) and protamine/DNA microcapsules (**b**). Each capsule was placed in a 48 mm high glass cuvette, filled with water, after which buoyancy was induced by addition of 3 μL of H_2O_2 (160 mM). The velocities were tracked by taking video footage via digital camera and analysing it with the Fiji-ImageJ tracking-plugin TrackMate.*

The first important aspect that needs to be discussed is the probability of O_2-bubble nucleation when changing the concentration of entrapped catalase or added H_2O_2. Here, 100 µL di-water with 25 to 30 microcapsules of varying catalase-concentrations (3.9, 7.8, 15.5 and 31.1 kU/mL) were transferred into a well of a 96-well plate. The collective buoyancy was then induced by addition of 100 µL hydrogen-peroxide (60, 120, 180 and 240 mM) solution and the buoyant capsules were counted with a microscope. The results of the experiments can be seen in Figure 4.4-3.

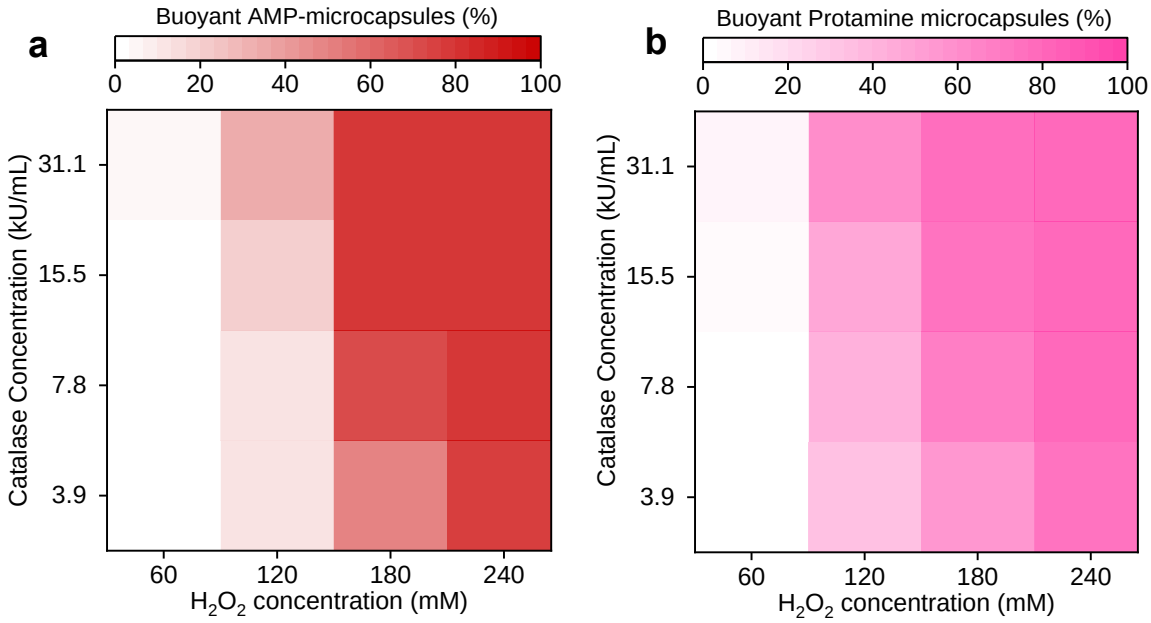

Figure 4.4-3: *Heatmaps, describing the buoyancy responsiveness studies for AMP/DNA- (**a, red**) and protamine/DNA-microcapsules (**b, pink**). 25-30 microcapsules were immersed in 100 µL di-water inside a 96-well plate and mixed with 100 µL H_2O_2-solution. The catalase-(3.9, 7.8, 15.5 and 31.1 kU/mL) and the concentration of the added H_2O_2-solution (60, 120, 180, 240 mM) were varied throughout the experiment.*

Generally, 180 mM and higher H_2O_2-concentrations resulted in almost 100% buoyant capsules in both systems. Reducing the H_2O_2-concentration to 60 mM and below on the other hand proved to be too little for the cells to produce O_2-bubbles inside, except for only a few positive examples at high catalase concentrations (31.1 kU/mL). Instead, the bubble nucleated outside the cell on either the cell-membrane or the walls of the well-plate, which prevented the cell from becoming buoyant. Generally, changing the catalase concentration did not have a large impact on the buoyancy of the capsules, only increasing the number of buoyant microcapsules by less than 10% when increasing the catalase content during the fabrication of the capsules from 3.9 to 31.1 kU/mL. The amount of H_2O_2 on the other hand increased the buoyancy-probability almost exponentially when doubling the H_2O_2-concentration. Protamine/DNA-capsules appeared to be slightly more responsive than AMP/DNA-capsules, especially around 120 mM H_2O_2, although AMP-capsules exhibited 100% buoyancy at high catalase concentrations for 180 mM H_2O_2, whereas protamine-capsules did not. Eventually, 160 mM H_2O_2 and 19.8 kU/mL catalase were established as a reliable standard for future experiments, which represents the optimum between uncontrollable O_2-overproduction, underproduction or external O_2-nucleation.

The buoyancy experiments above showed that bubble nucleation happened at a preferential location, depending on the concentration of substrate. At very low H_2O_2-concentrations, O_2-bubbles would rather nucleate externally (Figure 4.4-4-b)., whereas once a certain concentration threshold was reached, the bubbles were found inside the cells (Figure 4.4-4-a,c).

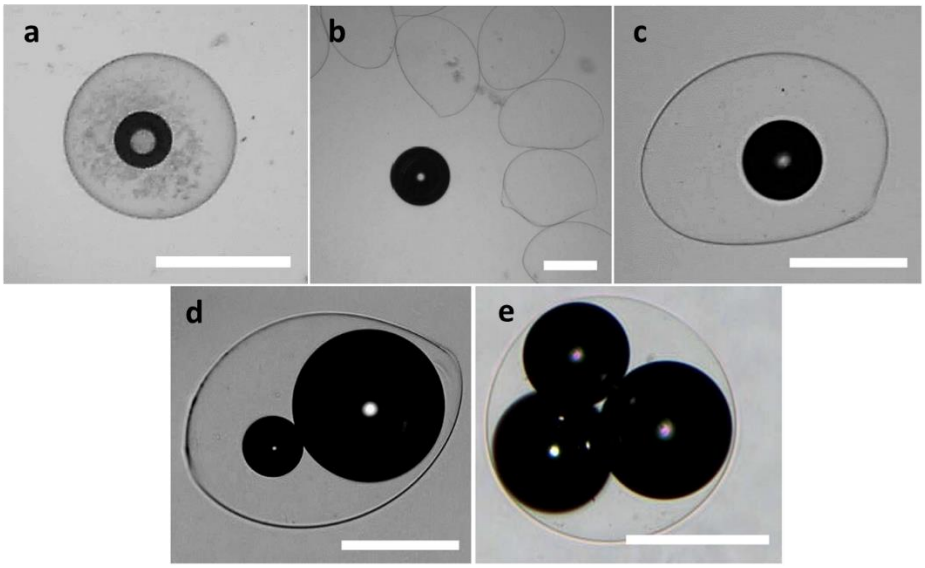

Figure 4.4-4: *Optical micrographs of O_2-microbubble nucleation.* ***a*** *Protamine microcapsule with O_2-bubble nucleated insider the microcapsule. AMP-microcapsules with:* ***b*** *external bubble nucleation,* ***c*** *internal bubble nucleation,* ***d-e*** *multiple internal bubble nucleation.*

This led to the hypothesis, that the capsule-interior is preferential for the bubble to nucleate and stabilises its growth, possibly due to DNA and entrapped enzymes adsorbing to the surface of the O_2-bubble. This seemed logical for AMP/DNA-capsules as their membrane could retain enzymes and free DNA. Figure 4.4-5-a tried to investigate this theory by observing the buoyancy behaviour of two different populations of AMP-microcapsules, one fabricated with 1 mg/mL DNA and the other with 4 mg/mL. These two populations showed a clear trend that the one made from 4 mg/mL DNA-solution had a ~20% higher chance of becoming buoyant than the one with 1 mg/mL. Interestingly, protamine/DNA-microcapsules showed a similar behaviour, as the active population was decreased by about 10% when lowering the DNA-concentration to 1 mg/mL (Figure 4.4-5-a). This is surprising, since it was established that protamine/DNA-capsules do not contain any free DNA or other macromolecules inside, which means that the stabilisation of the oxygen bubble can only come from the condensed DNA-material from the cell walls. A more likely explanation for this behaviour could be found with the amount of enzyme that can be entrapped inside the membrane. With a higher DNA-concentration, more protamine/DNA-condensate can be formed, which can, in return, accommodate more catalase and lead to a higher activity. Then again, the same explanation would apply for AMP/DNA-microcapsules.

External bubble nucleation on the other hand was a phenomenon mainly seen in cases of very low H_2O_2- or catalase concentrations (Figure 4.4-4-b). Here, one could hypothesise that the peroxide-molecules are not able to penetrate the cell interior and instead only react with the catalase molecules closer to the surface, which in return forms oxygen bubbles either on the exterior membrane or close to the capsule. Another interesting observation was made for AMP/DNA-capsules at higher H_2O_2 and catalase concentrations. When going beyond 200 mM H_2O_2, single, double and even multiple bubble-nucleation could be observed within the capsule (Figure 4.4-4-d-e), which would later merge to a single, larger O_2-bubble. Figure 4.4-5 shows a descriptive diagram that outlines the conditions for multi-, single- and extracellular bubble-growth in AMP-capsules and in relation to the concentrations from Figure 4.4-3. Kumar *et al*. [75] presented similar bubble nucleation studies, even though their work reported much lower H_2O_2-concentrations to achieve similar results. This can be explained by the fact that the catalase which was used for the previous experiment had been discontinued by the

manufacturer and supplier, and a new catalase supply had been established (purchased from Worthington biochemical Corp), which showed a decreased activity.

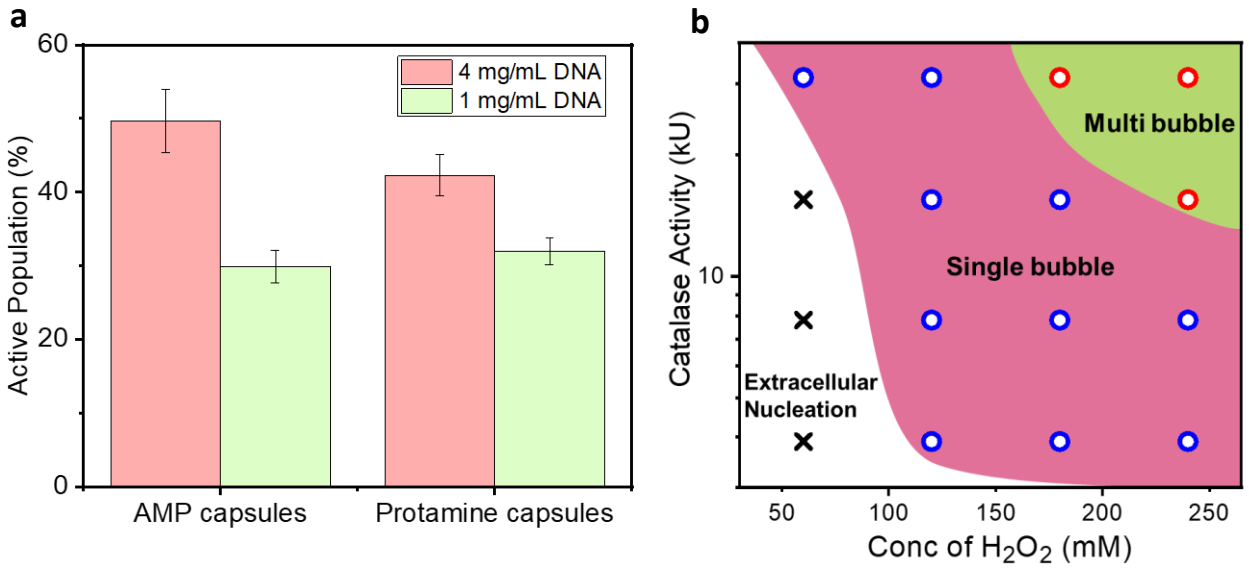

Figure 4.4-5: *Bubble-nucleation dynamics.* ***a*** *Bar-plot of buoyant populations of 50 AMP/DNA- or protamine/DNA-microcapsules, which were fabricated with either 4 mg/mL or 1 mg/mL dsDNA.* ***b*** *Diagram depicting the amount and location of O_2-microbubble nucleation in- or outside AMP/DNA-microcapsules depending on the H_2O_2- and catalase-concentration.*

Protamine/DNA-capsules on the other hand showed no such behaviour and consistently produced single bubbles instead. AMP/DNA-microcapsules generally exhibit more deformations while also having a molecularly crowded interior, which could support the nucleation of multiple O_2-bubbles inside the microcapsule. Nonetheless, more studies would be necessary to understand this very specific nucleation behaviour.

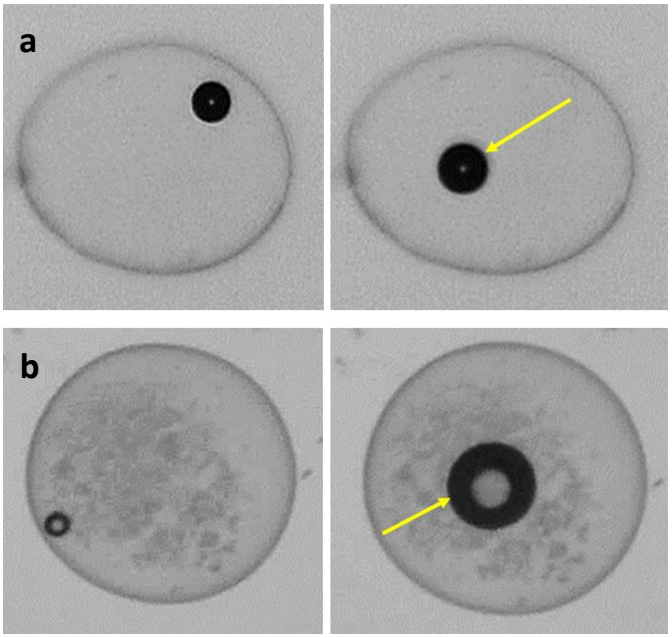

Figure 4.4-6**:** Micrographs of oxygen-bubbles moving within **a** AMP/DNA and **b** protamine/DNA-microcapsules right after their nucleation.

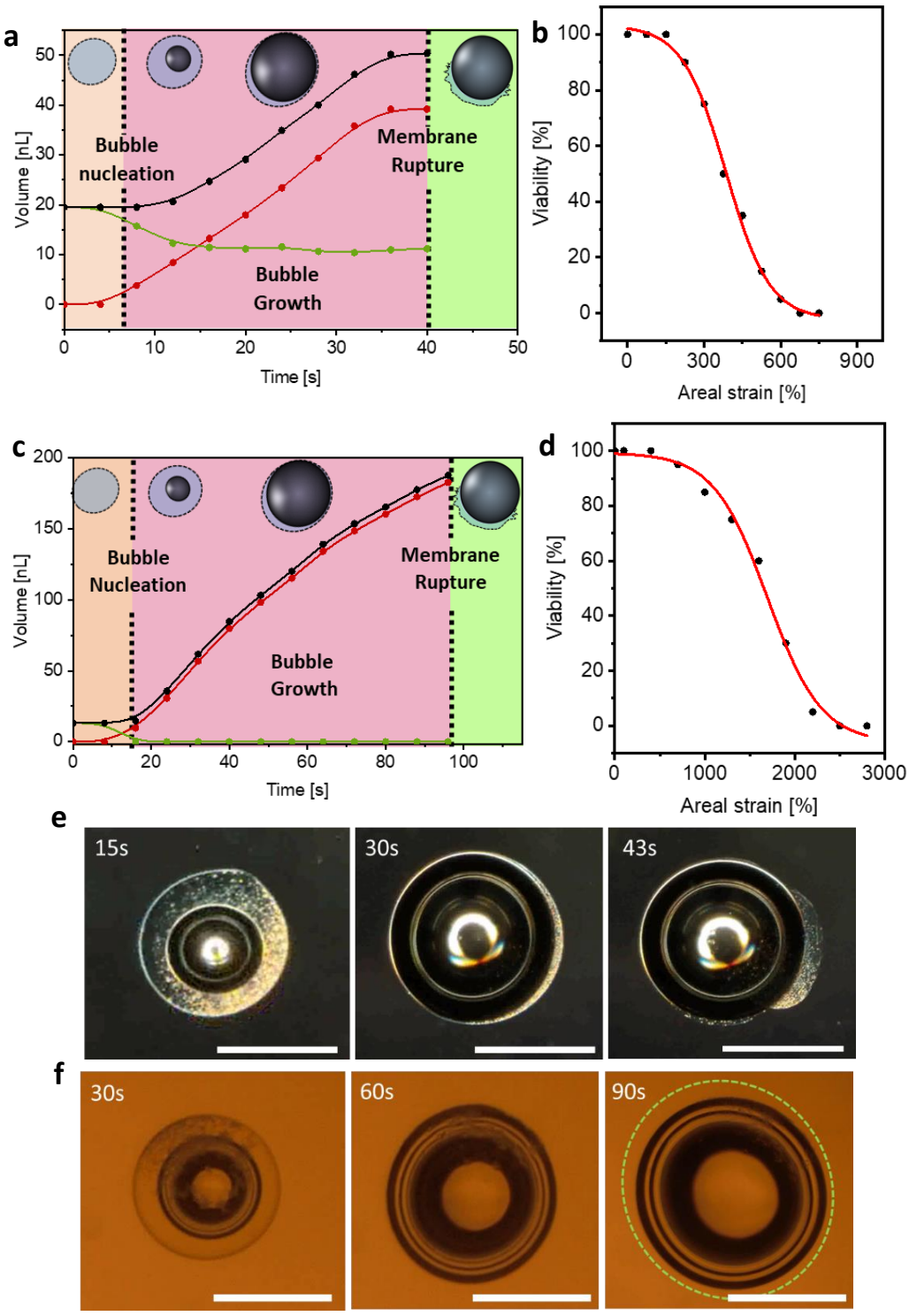

Figure 4.4-7: *Bubble growth studies within AMP/DNA- and protamine/DNA-microcapsules.* ***a*** *The capsule and the growing bubble were tracked by a brightfield microscope and the bubble volume (**red**), the volume of the entrapped aqueous phase (**green**) and the capsule volume (**black**) were plotted.* ***b*** *The strain of the membrane was plotted against the viability of a population of 20 AMP/DNA-microcapsules and the loss of viability was determined as the point of membrane rupture.* ***c-d*** *Show the same plots as in **a+b** for protamine/DNA-microcapsules.* ***e-f*** *Optical micrographs of catalase containing (19.8 kU/mL) AMP/DNA-microcapsules (**e**) and protamine/DNA-microcapsules (**f**) with entrapped silica particles (4 mg/mL). The images were taken with a phase-contrast filter to improve image quality for AMP/DNA-microcapsules. The deformation from a spherical- to an oval-shaped protamine/DNA-microcapsule was indicated through a green dotted line (**f**). All Scale bars: 300 µm*

Figure 4.4-6 furthermore confirms the assumptions made in chapter 3 (Figure 3.4-42), as the nucleated O_2-microbubbles were able to move within the microcapsules once they started growing and eventually settled at the top of the inside of the capsule.

The previous studies mainly focused on the oxygen-bubble nucleation, so the next step is to investigate the bubble growth and how it affects the capsule interior, its membrane and the overall structural integrity. Here, catalase-containing AMP/DNA- and protamine/DNA-microcapsules were simply immersed in a small di-water droplet, which was mixed with 10 μL H_2O_2 (160 mM), after which the O_2-microbubble-volume was observed and tracked microscopically. The bubble growth was divided into three characteristic phases, the bubble nucleation (Figure 4.4-7-a,c-orange phase), growth (Figure 4.4-7-a,c-pink phase) and the rupture point of the membrane (Figure 4.4-7-a,c-green phase), once the bubble became too big. The growth phase was divided into a general growth phase until the bubble reached the capsule's volume, and the membrane-expansion phase during which the bubble expanded beyond the capsule's volume and applied an increasing strain on the membrane. It was expected, that the capsule- and the bubble volume would eventually become identical but Figure 4.4-7-a,e show, that the volume of AMP/DNA-capsules was always a little larger due to a little "pouch"-like compartment, which the bubble couldn't fill. The reason for this were most likely encapsulated components like DNA and enzymes which couldn't permeate through the membrane, even under the increasing pressure of the growing O_2-bubble.This also explained why the volume of the aqueous phase of the capsule in Figure 4.4-7-a (green) never reached 0 but remained around 10 nL until the capsule broke apart and the oxygen-bubble was able to leave through the rupture, leaving only the husk of the capsule behind (Figure 4.4-7-e-43s). For AMP/DNA-microcapsules of sizes of around 400 μm, the capsule volume generally increased from ~20 nL up to 50 nL. To get a better understanding of how much internal pressure the membrane can endure, the viability of 20 AMP-microcapsules was plotted against the areal strain it took for them to break. Figure 4.4-7-b shows, that even after a 4-fold increase of the surface area, 50% of the capsules were still intact, which is a strong argument for the flexibility of the membrane. Some capsules even expanded as much as 6 times their original surface-area and volume. As to be expected from previous results, protamine/DNA-microcapsules exhibited slightly different properties and behaviour. Figure 4.4-7-c,f show the internal volume of a growing O_2-bubble inside a protamine-capsule and, in contrast to the AMP-capsules, the O_2-bubble grew until it filled the whole capsule volume. Since protamine-capsules lack the encapsulated macromolecules due to their high permeability and DNA-condensation, the O_2-bubble ultimately displaced all smaller aqueous components and forced them out of the capsule until it reached a similar volume to its host (Figure 4.4-7-f-90s). Another interesting difference can be found in the eventual shape of the capsules. While AMP/DNA-capsules were spherical before they burst under the pressure of the bubble, protamine/DNA-capsules were rather ellipsoid. The reason for this could be due to asymmetrical condensation which lead to slightly different thicknesses along the membrane. The condensate-aggregate, which has been discussed in chapter 3 could also contribute to this phenomenon. As expected from the discussion, the aqueous phase within protamine-capsules eventually approximated zero, as the bubble filled out the whole cell.

The capsule-volume in Figure 4.4-7-c grew from an initial ~13 nL to eventually 182 nL right before the capsule burst. The slight difference between the bubble- (Figure 4.4-7-c-red) and the capsule-volume (Figure 4.4-7-c-black) can be attributed to experimental difficulties to measure the actual volume from the images and due to the fact that the DNA-condensate-aggregate took up a small portion of the internal volume as well. Compared to AMP/DNA-capsules though, protamine/DNA-capsules were able to withstand a surprising amount of strain. Capsules were able to expand their surface area by 16 times before even half the population broke under the pressure and some capsules expanded even

up to 20 times (Figure 4.4-7-d). This proves that protamine/DNA-capsules are much more stable under mechanical stress while also being able to stretch almost 3.5 times more than AMP/DNA capsules can.

Microcapsule buoyancy can be used to perform simple and even more chemically demanding tasks, which will be discussed over the next pages. In 2018, Kumar *et al.* [95] presented three interesting examples for the utilisation of buoyant AMP/DNA-microcapsules, which will be discussed over the coming pages (with consent of the authors) for the sake of the following work within this thesis and for future applications of buoyant microcapsules. Since protamine/DNA-microcapsules behaved exactly the same, the experiments will only be discussed in reference to previously published results with AMP/DNA-capsules. [95] In the first experiment, AMP/DNA-microcapsule collectively carried a small object from the bottom of a water-column to the top. Here, a dialysis bag was used as the payload and filled with 200 catalase containing AMP/DNA-microcapsules. The ~ 3 cm long dialysis bag (Figure 4.4-8-b) was placed at the bottom of a water-column and 500 µL hydrogen peroxide (160 mM, 3 wt% Sucrose) were added close to the bottom. The sucrose prevented H_2O_2 from diffusing upwards too quickly and ensured that there was enough time for it to permeate through the dialysis bag into the capsules. Once enough microcapsules became buoyant, the dialysis bag slowly ascended to the surface. It took the bag ~7 minutes to reach the top of the water column and it accelerated up to a terminal velocity of 30 mm/min.

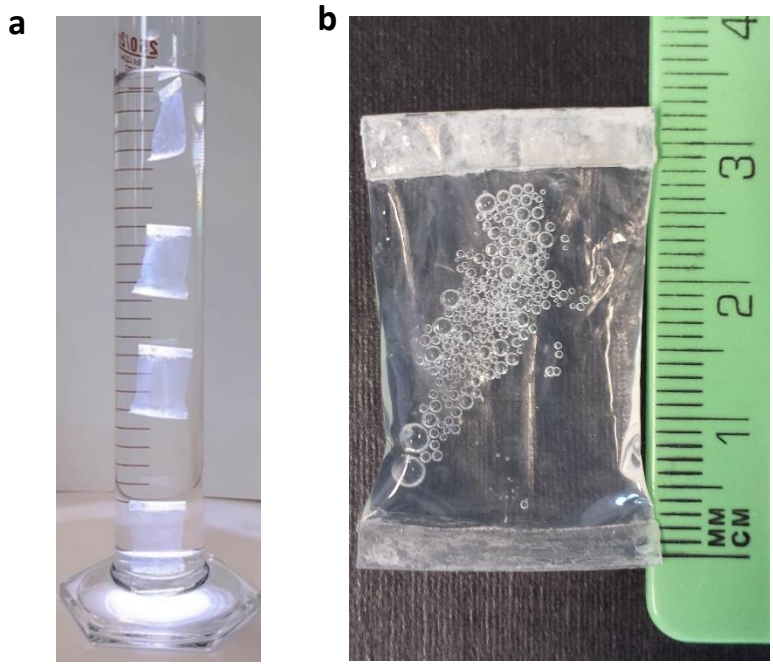

Figure 4.4-8: *Transport of a dialysis-bag via collective buoyancy of AMP/DNA-microcapsules.* ***a*** *In this experiment, ~200 catalase containing AMP/DNA-microcapsules were entrapped inside a 3x3 cm dialysis bag. The dialysis bag with the capsules was transferred into a 100 mL water inside a 100 mL measuring cylinder (25 cm in height) and the buoyancy was induced by addition of 500 µL H_2O_2 (160 mM).* ***b*** *Photographic image of the dialysis bag with the microcapsules after the experiment. Nucleated oxygen bubbles accumulated on the top side of the dialysis bag (Images from Kumar et al. [95]).*

In another experiment, buoyant AMP-microcapsules were used to perform a simple chemical reaction after making them ascend into a chemically enriched environment. Alkaline phosphatase (ALP, 300 U/mL) was co-encapsulated next to catalase (19.8 kU/mL) (Figure 4.4-9-a) to drive the de-phosphorylation of phenolphthalein bisphosphate (PPBP), which resulted in the release of phenolphthalein, a pink dye which was easy to observe with the bare eye or a microscope (Figure

4.4-9-b). Phenolphthalein bisphosphate was entrapped inside an agarose gel (2%), which was also used as the top barrier for the buoyant capsules. Since a single capsule did not result in a very strong signal, a collective of 30 buoyant microcapsules was used instead. Within only a few minutes from reaching the gel-interface, a pink colour was observed, which was emanating from the capsules and diffusing into the surrounding solution (Figure 4.4-9-c).

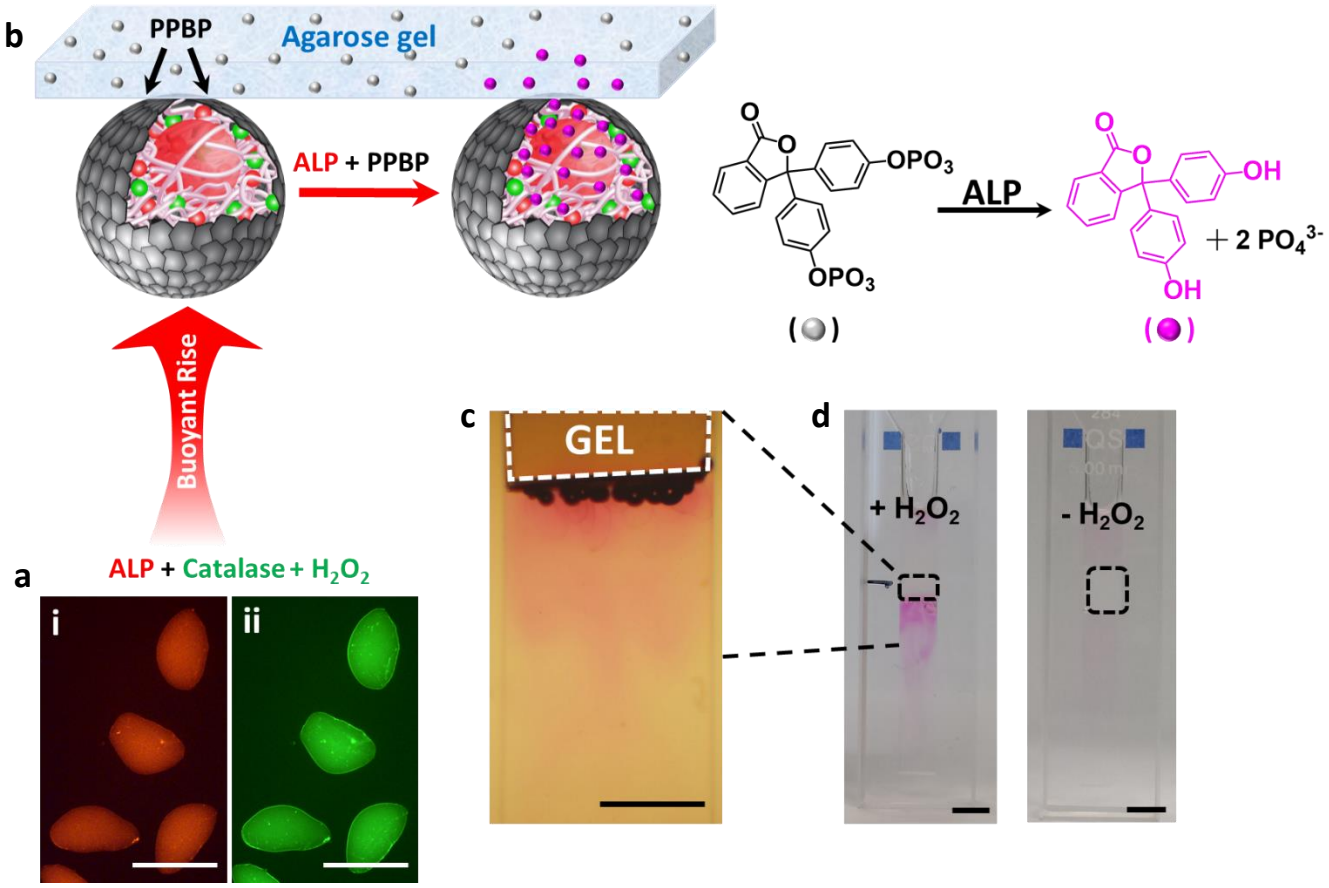

Figure 4.4-9: *Figures and illustrations that depict the utility of motile organoclay/DNA-microcapsule-populations by dephosphorylating phenolphthalein bisphophosphate (PPBP) via alkaline phosphatase.* ***a*** *Fluorescence microscopy micrographs of the parallel co-entrapment of RITC-ALP and FITC-catalase inside AMP/DNA-microcapsules.* ***b*** *Illustration of the catalase-induced buoyancy and migration of ALP-containing AMP/DNA-microcapsules towards a chemically active environment. An agarose gel (2%) served both as a barrier for the capsules and as a container for phenolphthalein bisphophosphate (PPBP), which was entrapped inside the gel and slowly diffused out. Once the capsule reached the gel-barrier, ALP started to react with PPBP, which cleaved the phosphate group and thus produced phenolphthalein, which shown as a deep pink colour due to the high pH of the surrounding solution (0.5 mg/mL AMP-clay solution, pH 10.35).* ***c*** *Vertical micrographs of buoyant AMP/DNA-capsules which are suspended against a PPBP-containing agarose gel. ALP-activity can be seen in form of a pink colour emanating from the capsules due to the produced phenolphthalein.* ***d*** *Digital photo of the devices used for the experiment. An optical cuvette was filled with a 0.5 mg/mL AMP-clay solution and the agarose-gel was fitted about 18 mm from the bottom (see dotted circles). Only when H_2O_2 was added, AMP/DNA-capsules were able to ascend and convert PPBP to phenolphthalein. (*Images from Kumar *et al.* [95]*)*

This not only proves that ALP is active within the capsules, but also that both enzymes, catalase and ALP, can coexist next to each other inside a cell without inhibiting each other. To make sure, that phenolphthalein-production exclusively happened around the capsules, the experiment was repeated without the addition of H_2O_2 which kept the cells at the bottom of the cuvette and prevented the dephosphorylation-reaction. While this experiment is still fairly one-dimensional, as the capsules are merely able to ascend once and the signal is only coming from the phosphorylation of a dye, it is still

a first step towards the design of concepts for communication between different chemical environments via microcapsules.

4.4.2 Glucose oxidase mediated reversed buoyancy of microcapsules

Catalase mediated ascent of AMP/DNA and protamine/DNA microcapsules has proven to work reliably and reproducibly under the optimal concentrations that have been developed in the previous part. To further advance the system towards a more biologically relevant approach, it will be necessary to add another level of control, so the capsules can also descend again after becoming buoyant.

As a first approach towards microcapsule descent, small magnetic polymer micro-particles were encapsulated into AMP/DNA-capsules to counteract the buoyant forces with a magnet (for reference, see Kumar *et al.* [95]). As in previous experiments, the capsule was first left to sediment inside an optical cuvette with a PDMS-block fitted into the column to serve as a barrier for the capsule. Addition of hydrogen peroxide induced buoyancy and the capsule ascended to the PDMS-block (Figure 4.4-10-b). Without any further interaction, the capsule would stay forced against the PDMS-cube, but by applying a magnetic field underneath the device, the buoyant forces were counteracted, and the capsule started to descend. Obviously, this process could be repeated almost indefinitely, or as long as the oxygen-bubble maintained the buoyancy. This way, buoyancy and the so called "reversed buoyancy" could be switched on and off by the magnetic field.

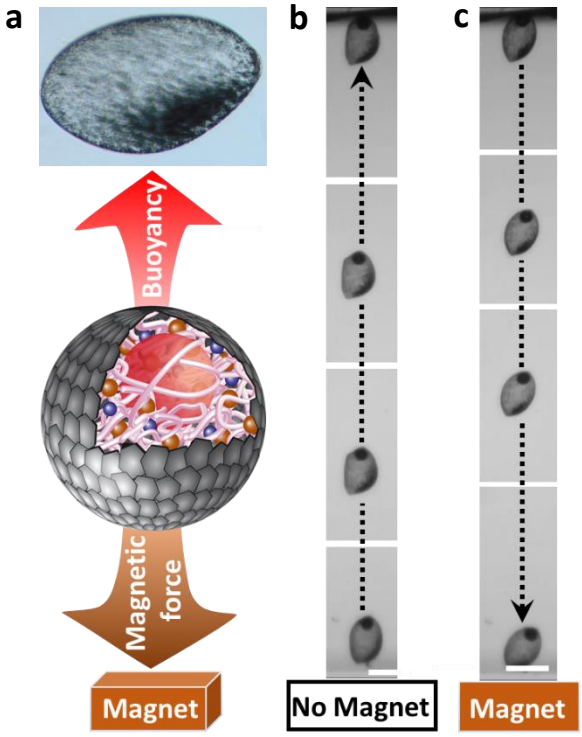

Figure 4.4-10: Reversed buoyancy via encapsulated magnetic polymer microparticles inside AMP/DNA-microcapsules. [95] **a** Illustration of the antagonistic interactions between catalase induced buoyancy and magnetic force inside AMP/DNA-microcapsules and optical micrograph of organoclay/DNA-microcapsule with 6 mg/mL magnetic polymer microparticles. **b** Time sequence of cropped optical micrographs, showing the catalase mediated ascent of a AMP/DNA-microcapsule via buoyancy up to a PDMS-barrier at the top of the images inside an optical cuvette. From bottom to top, the images were taken at 0, 0.6, 1.3 and 2 seconds. **c** Time sequence of cropped optical micrographs, showing the descent of an AMP/DNA-microcapsule with a magnetic field underneath the cuvette-device. From top to bottom, the images were taken at 0, 1.7, 2 and 2.3 seconds *(*Images from Kumar *et al.* [95]*)*

Using magnetic particles inside a cell is a very easy and responsive way to facilitate motion, as the magnetic field can be operated externally without interfering with the environment of the cell, and it can be done on demand and within very short time-periods. While this sounds very convenient from an experimental point of view, and it is most certainly useful as a proof of concept, it serves rather little to mimic the motility apparatus of biological systems like the cyanobacteria which were mentioned in the introduction. Instead of an externally controlled system, the motility should originate from an interaction with the environment. Catalase does so by using hydrogen peroxide as a substrate, which is why another enzyme was introduced into the cells. Glucose oxidase (GOx) is a direct antagonist to catalase as it consumes oxygen together with glucose, which will eventually trigger the capsule's descent.

A simple cuvette experiment was used to determine whether GOx can deplete the oxygen bubble and make the capsule descend. The capsule was inserted into the device with a pre-nucleated oxygen bubble, which means that it was mixed with H_2O_2 externally to form a bubble inside the capsule before transferring the capsule into the cuvette. This way, no hydrogen peroxide was present during the experiment, which could interfere with the oxygen consumption. The column was filled with 0.1 M glucose for protamine/DNA-capsules and 0.1 M glucose and 0.5 mg/mL aminoclay, to increase the AMP-capsule stability.

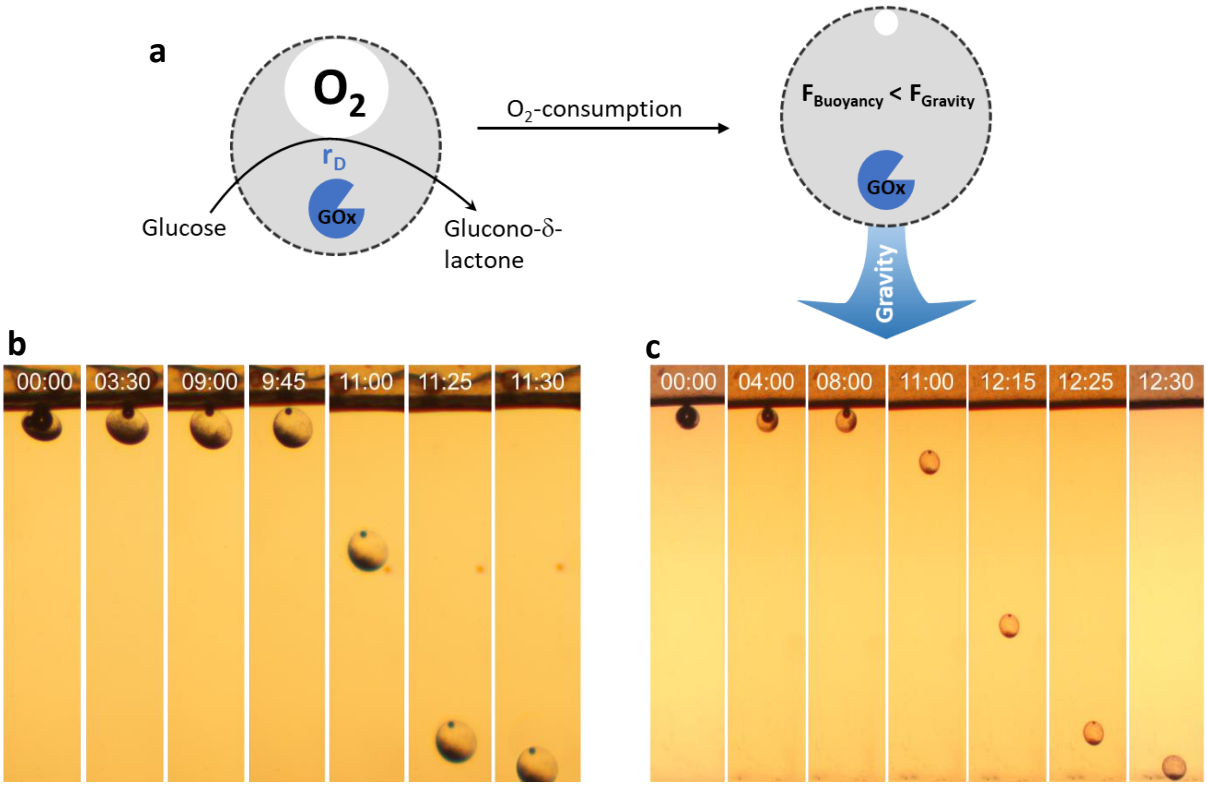

Figure 4.4-11: *Reversed buoyancy experiment to showcase oxygen-bubble depletion via encapsulated glucose oxidase.* ***a*** *Illustration of the interaction of entrapped glucose oxidase within a glucose environment and with an internal oxygen bubble. O_2-bubbles were pre-nucleated before an AMP/DNA- (**b**) or protamine/DNA (**c**)-microcapsule was added into an optical cuvette, fitted with a PDMS-barrier (top of the device). The columns were filled with 0.1 M glucose + 0.5 mg/mL aminoclay (**b**) or 0.1 M glucose (**c**). The optical micrographs are showing the O_2-bubble-depletion after the capsule settled against the top barrier.*

The image sequences of Figure 4.4-11 show the oxygen-bubble depletion in a protamine/DNA (Figure 4.4-11-c) and an AMP/DNA-capsule (Figure 4.4-11-b). Within 8-12 minutes, the oxygen bubble shrank substantially up to the point where the capsule's gravitational force became larger than the buoyant

force, thus, the capsule detached from the PDMS-barrier and descended to the bottom of the cuvette. Generally, AMP/DNA-capsules appeared to be marginally less responsive than protamine/DNA-capsules, taking slightly more time for the bubble to be consumed. This could be explained by the fact that the experiment was conducted in a 0.5 mg/mL AMP-clay dispersion mixed with glucose, whereas the protamine/DNA-capsules were observed in a mere glucose solution. 0.5 mg/mL AMP clay dispersions exhibited a pH of ~10.35, which is really high for many enzymes. Glucose oxidase exhibits optimal activity at pH ~ 5.5 and has a broad range from pH 4 – 7. [96,97] This means that the enzyme must have experienced some inhibition due to the high pH of the clay-solution. In fact, the pH is so much higher than the reported pH-ranges of GOx, that it seems almost surprising, that the enzyme is still active enough to deplete the oxygen bubble for the capsule to descend in just 15 minutes. A. Patil *et al.* showed in a previous publication, that intercalation of enzymes into the organoclay sheet-structure can be beneficial for the enzymatic activity and even stabilise the enzyme at higher pH, which could serve as an explanation for this behaviour. [98,99]

To further discuss the issues arising with AMP/DNA-microcapsules, the same experiment was repeated in 0.1 M glucose without the addition of amino-clay. The results can be seen in Figure 4.4-12.

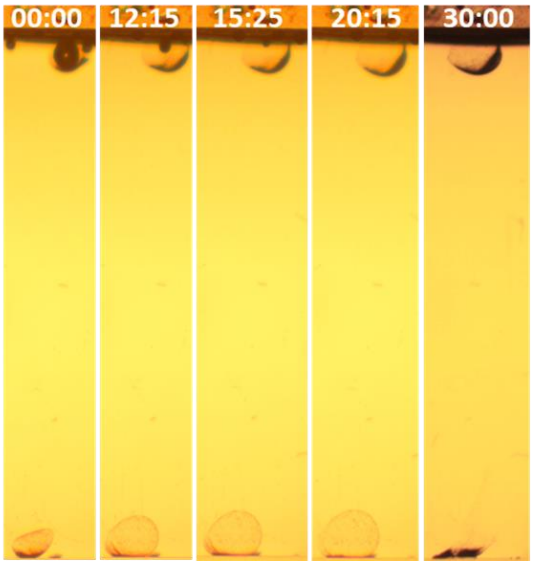

Figure 4.4-12: *Vertical optical micrographs showcasing the deterioration of AMP/DNA-microcapsules within a glucose phase. Two capsules were added, one with a pre-nucleated O_2-bubble and nested GOx and catalase, and a second capsule without any entrapped enzymes. The image sequence shows the depletion of the oxygen-bubble and the swelling of the capsule over a time-span of 30 minutes.*

Furthermore, in order understand whether glucose oxidase has any effect on the stability of the capsule, two different capsules were investigated: one with a pre-nucleated O_2-bubble and entrapped catalase and GOx (Figure 4.4-12-top capsule), and another capsule without any enzymes (Figure 4.4-12-bottom capsule). Just like the in the stability studies in chapter 3, the capsules started to swell after 10 minutes until they lost their shape and started to disintegrate. The GOx-containing capsule lasted a little longer but started to swell as well and adhered to the PDMS-surface, from which it could not detach without breaking. This further supports the argument against the usage of AMP/DNA-capsules for any further projects. All experiments in this chapter rely heavily on the activity and viability of enzymes, which would deteriorate quickly in a high pH-medium like the aminoclay. Furthermore, the experiments demand the capsules to remain stable over long periods of time, which cannot be guaranteed with AMP/DNA-capsules, as the experiment above and the ones from chapter 3 have already proven. For this reason and from here on out, the comparison between the two

microcapsule systems will be concluded and all further experiments will be conducted with protamine/DNA-capsules, as they have proven to be much more reliable and stable.

Before exploring the possibilities of GOx-mediated reversed buoyancy even further, it is important to gain a better insight into the kinetics of glucose oxidase within the protamine/DNA-microcapsules. One way to investigate the activity of GOx would be the direct measurement of the oxygen concentration of the solution with an oxygen-detecting probe. While this is a feasible solution, the measurement of oxygen concentrations is complicated, as oxygen can be exchanged at the air-liquid interface, which makes the experimental setup a lot more demanding. Instead, the produced hydrogen peroxide can be used indirectly to measure the activity and kinetics of the enzyme. Horseradish peroxidase (HRP) was used as a second enzyme to assess the production of H_2O_2 in combination with the chromophore ABTS. Its oxidised species $ABTS^{OX}$ can be easily detected via UV/VIS spectroscopy at 420 nm and at very low concentrations (Figure 4.4-13-a). The experiment was conducted under fixed concentrations of ABTS (8.19 mM) and HRP (8.3 U/mL) while varying the glucose concentration from 0, 5, 10, 25, 50, 75, 100, 200 to 500 mM. To calibrate the absorbance of the spectrometer to the ABTS-concentration, different ABTS-concentrations (0, 0.91, 9.1, 18.2, 45.5 and 91 µM) were mixed with HRP (8.3 U/mL) and hydrogen peroxide (50 mM) before letting them react until the absorbance was stable, ergo, no more ABTS was oxidised. Linear approximation of the results then served as a calibration curve for the GOx-activity assay.

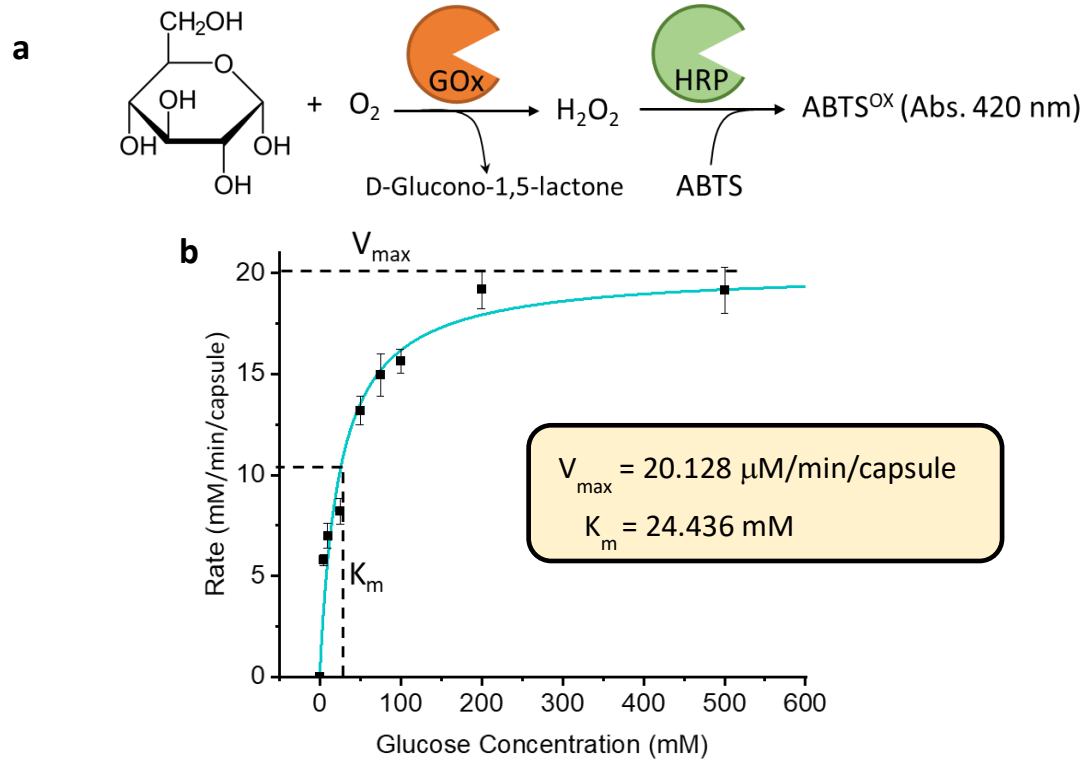

Figure 4.4-13: *Glucose oxidase kinetics assay.* ***a*** *Illustration of the enzymatic reaction-cascade of GOx and HRP.* ***b*** *Results of the kinetic assay of glucose oxidase according to Michaelis-Menten. GOx-activity was measured at the following glucose concentrations: 0, 5, 10, 25, 50, 75, 100, 200 and 500 mM. The activity for each concentration was calculated via linear approximation and then plotted against the glucose concentration.*

The results in Figure 4.4-13-b show a classic Michaelis-Menten kinetics-plot. The enzymatic rate rose almost linearly between glucose concentration of 0 and 25 mM but then decreases exponentially. Michaelis-Menten parameters were calculated from the plot with V_{max} = 20.128 µM/min/capsule and K_m= 24.436 mM. In contrast to normal kinetic-plots though, the enzymatic rate was calculated per

capsule instead of using the enzymatic concentration, since this project focused on the enzymatic activity within the protamine/DNA-microcapsules.

While the activity of glucose oxidase within the capsules has been proven in the experiments above, it still needs to be assessed whether the enzyme is the sole reason for the depletion of the O_2-bubble. Oxygen-gas is soluble in water, even though the solubility might be fairly low. At normal conditions with a temperature of 25 °C and a pressure of 1 atm, oxygen exhibits a solubility of $1.22 * 10^{-3}$ mol/dm^3 in pure and fresh water. [100] While this value on its own does not stand for much in the context of GOx-mediated oxygen depletion, it supports the concern that GOx is not the only reason for the O_2-bubble depletion. This "auto-depletion" needs to be addressed, since it directly interferes with the intention of the GOx-entrapment. The following experiment investigates the difference between GOx-mediated- and auto-depletion of the oxygen-bubble inside protamine/DNA-microcapsules. The microcapsules were fabricated with catalase and GOx and with a pre-nucleated O_2-bubble before being transferred into either 200 µL of 0.1 M glucose or di-water inside a 96-well plate.

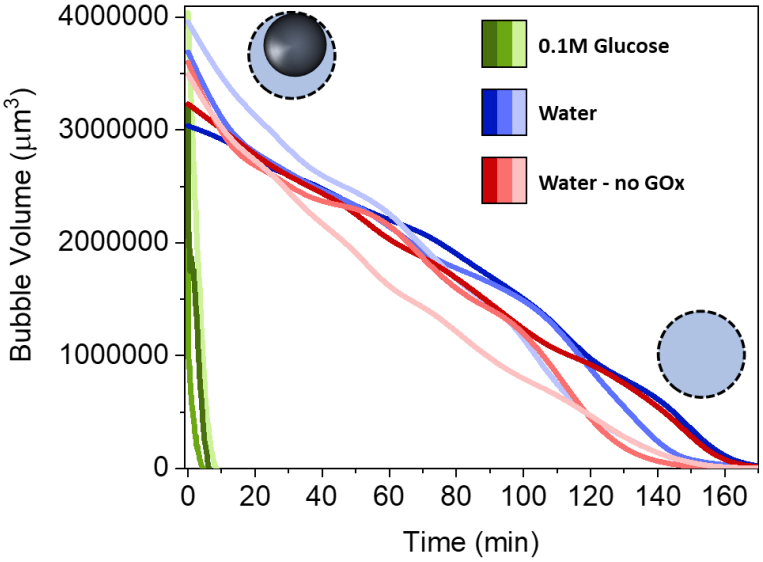

Figure 4.4-14: *Oxygen-bubble depletion plotted over time. Oxygen bubble depletion was screened inside protamine/DNA-microcapsules during incubation in 0.1 M glucose (**green**), in water (**blue**) and in water without encapsulated GOx (**red**). All experiments were done in triplets.*

Figure 4.4-14 shows the bubble volume plotted over time until the O_2-bubble was fully depleted. In case of 0.1 M glucose, it took the enzyme inside the capsules mere 5-10 minutes before the bubble was completely consumed (Figure 4.4-14-green). Without the substrate, the enzyme stayed inactive and the oxygen-bubble could only deplete from dissolution into the surrounding solution. Here, the oxygen bubbles were much more stable and only depleted after 2-3 hours (Figure 4.4-14-blue). Plain protamine/DNA-capsules without any encapsulated GOx served as a control, which showed that GOx does not exhibit any background activity when the substrate is missing, since both the capsules with, and the ones without GOx, took the same time for the bubble to be dissolve (Figure 4.4-14-red). In summary, glucose oxidase is the driving factor for a quick bubble depletion once the substrate is present. Without it, the bubble will dissolve slowly and in a matter of hours, which goes far beyond the time spectrum of most experiments of this thesis.

The next logical step now is the combination of enzyme mediated ascent and descent into a fluent and uninterrupted oscillation. The following experiment served as a proof-of-concept and shows the oscillation of a protamine/DNA-microcapsule inside an optical cuvette.

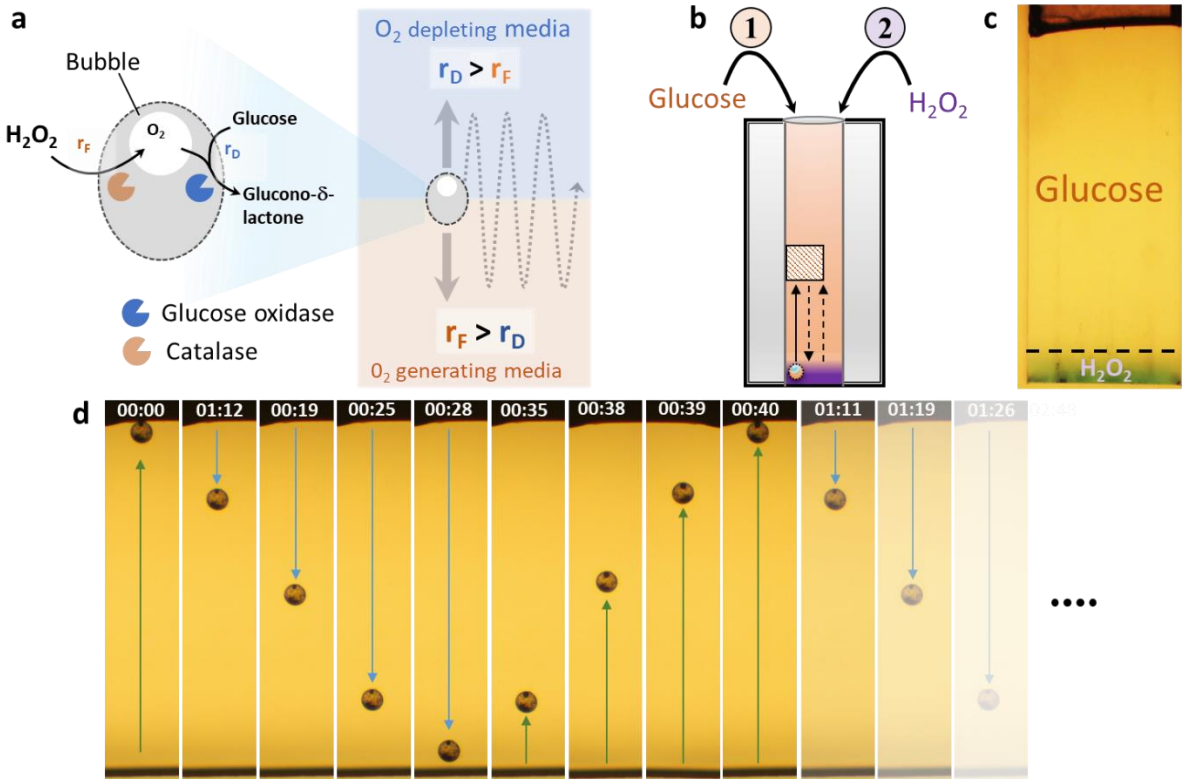

Figure 4.4-15: *protamine/DNA-microcapsule oscillation inside an optical cuvette between a hydrogen-peroxide-(bottom) and a glucose-rich phase (top).* ***a*** *Illustration of microcapsule oscillation between an O_2-generating and an O_2-depleting medium. The encapsulated enzymes glucose oxidase and catalase serve as the engine of the capsule, generating oxygen in form of an oxygen-bubble and depleting it, depending on the medium the capsule is located at. Consecutive depletion and production of the oxygen-bubble then leads to oscillatory motion of the capsule.* ***b*** *Illustration of the experimental setup. Glucose-solution (0.1 M) served as the bulk phase inside a quartz glass cuvette. The capsule was added with a pre-nucleated oxygen-bubble and the H_2O_2-phase was added via pipette (10 µL, 160 mM with 3 wt% Sucrose) right before the capsule detached from the PDMS-block and started to descend.* ***c*** *Optical micrograph of the H_2O_2/Glucose-interface inside the cuvette. H_2O_2 and sucrose were mixed with 10 mM methylene blue before adding 10 µL right above the bottom of the cuvette.* ***d*** *Optical brightfield micrographs of the oscillation of a protamine/DNA-microcapsule inside the cuvette-device after addition of hydrogen peroxide.*

Before the experimental results can be discussed, it is necessary to focus on the experimental setup, as this is and will be an important task throughout all oscillation experiments in this thesis. Oscillation can only be achieved if the oxygen-generation and depletion is spatially separated. This way, only one of the two enzymes is either switched ON or OFF, which in return causes the capsule to go up or down. Since hydrogen-peroxide is the oxygen-generating medium, it will always be at the bottom, whereas the glucose-phase needs to be above it. A 0.1 M glucose solution has a higher density than H_2O_2 though and will therefore always settle on the bottom. To circumvent this issue, the hydrogen peroxide solution was mixed with 3 wt% sucrose, which has an even higher density than the one of glucose ($\rho_{Glucose}$ = 1.56 g/cm^3 , $\rho_{Sucrose}$ = 1.59 g/cm^3) [101,102] and which drags the hydrogen-peroxide down to the bottom of the cuvette. Due to diffusion, H_2O_2 would slowly disperse into the bulk medium over time, which would eventually stop the oscillation. Since this process took substantially longer though it was ignored for the sake of this experiment.

The brightfield image-sequence in Figure 4.4-15-d shows the oscillation of a single protamine/DNA-microcapsule after adding it to the device. As the capsule contained a pre-nucleated oxygen-bubble, it went straight up against the PDMS-barrier. External pre-nucleation of the oxygen bubble is an important step for all oscillation-experiments in this thesis. On the one hand, it is more convenient to immerse the capsule in H_2O_2 outside the oscillation-device. On the other, and what is much more important, the oxygen-bubble nucleation itself demands much higher concentrations of hydrogen peroxide (> 60 mM H_2O_2) then it takes to sustain the bubble inside the capsule. Once it has formed, catalase can sustain the oxygen bubble even at very low H_2O_2-concentrations, considering it is not being outworked by glucose oxidase at the same time. This is very important, as the control of the concentration of the bottom-phase has a big impact on the success or the shape of the oscillation. A high H_2O_2-concentration would automatically cause an O_2-overproduction, which will extend the time it takes for GOx to consume it, whereas a very low H_2O_2-concentration might cause the oscillation to stop, as not enough O_2 is being produced to counteract the O_2-consumption. When done right though, the microcapsule will only spend a limited amount of time on either side, while continuously oscillating back and forth and without losing its velocity or showing a decreasing amplitude. The first image of Figure 4.4-15-d shows the first frame of an oscillation-loop, where glucose oxidase has consumed enough oxygen from the oxygen-bubble so that the gravitational force exceeded the buoyant force and the capsule started to descend. As the capsule moved downwards, the bubble shrank further and the capsule accelerated until it reached the H_2O_2/Glucose interface. The localisation of the interface was determined in a separate experiment, in which H_2O_2 was mixed with the dye methylene blue (Figure 4.4-15-c), which gave a visual representation of the H_2O_2/Glucose interface. Once the capsule was getting in contact with the hydrogen-peroxide layer after about 25 seconds, the bubble volume started to increase, which in return made the capsule ascend again until it reached the PTFE-barrier (Figure 4.4-15-40s). Here it resided until GOx depleted the oxygen bubble once more for the capsule to descend again and the cycle to repeat anew.

With this experiment, the foundation for microcapsule oscillation has been established. In the coming part of this chapter, protamine/DNA-microcapsule oscillations will be advanced and improved to establish long lasting and even damped oscillation patterns.

4.4.3 Continuous stable oscillations

The first oscillation concept to investigate is a stable and ongoing oscillation with no or only very little changes in the oscillation pattern like the amplitude and/or frequency. Before discussing the experimental results though, it is necessary to explain and discuss the design of the device used for stable oscillations (Figure 4.4-16). The device consists of 3 different glass-parts with a long central column and two identical top/bottom compartments. Each piece furthermore has two glass pipes, one inlet and one outlet, which will be connected to syringe pumps to establish a 6 point-flow system. Like it was mentioned in the previous experiment, repetitive oscillations require the system to have distinct H_2O_2- and glucose-regimes with defined interfaces. By default, this sets the O_2-producing H_2O_2-phase at the bottom and the glucose phase at the top. The central column on the other hand was used as a non-reactive phase for the capsule to oscillate in. To enable the layering of semi-stable substrate-phases, a density gradient was used by mixing different sucrose concentrations to the substrate solutions. A standard setup for stable oscillations aimed for 3 wt% sucrose in the H_2O_2-bottom-phase, 2 wt% sucrose in the central water column and 0 wt% sucrose in the glucose top phase. Nonetheless over long periods of time, the density gradient would not prevent the substrates from mixing completely. Instead, external flows (20 μL/min) constantly refreshed each phase through the inlet and outlet-tubes, which formed stable substrate-phases once the setup reached its steady state. The central column was flushed with di-water (2 wt% sucrose) from the top inlet to the bottom outlet,

whereas the top compartment was flushed with glucose- (0 wt% sucrose) and the bottom compartment with H_2O_2-solution (3 wt% sucrose), which usually went from left (inlet) to right (outlet).

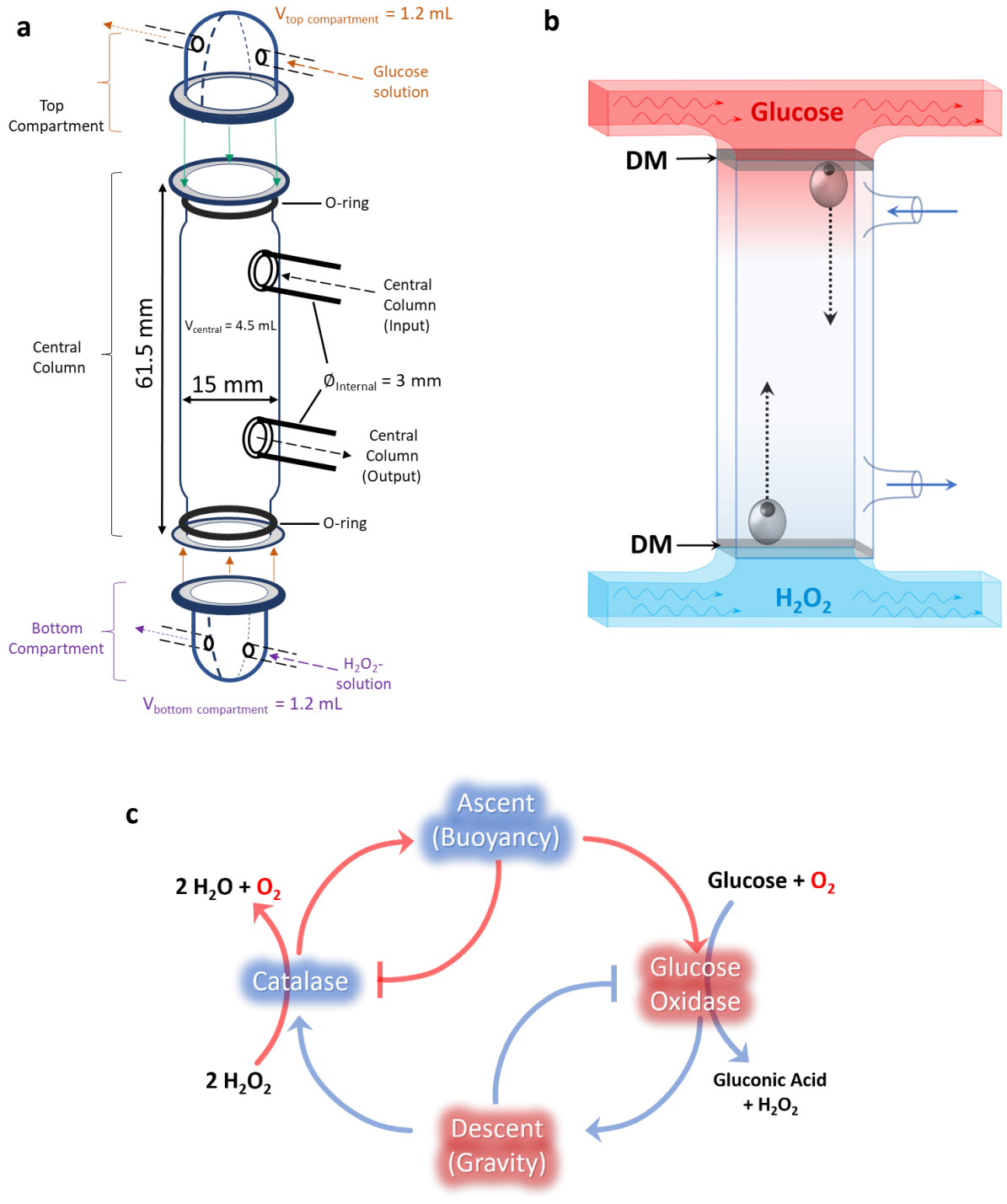

Figure 4.4-16: a *Blueprint for a stable-oscillation device. The device consists of 3 units, one central column fitted with O-rings on each side and two glass tubes on the column to enable flow and solution exchange, and two hat-shaped compartments which can be fitted to each side of the central column via clamps. Both compartments also have glass tubes fitted to enable flows.* ***b*** *Illustration of the working device. Glucose and hydrogen-peroxide are segregated into the top- and the bottom-compartment and constantly flowed through the device at a static rate. The central column is filled with water and horizontal flows at the top and the bottom of the column prevent*

the accumulation of the substrate in the central column. ***c*** *Illustration of the antagonistic oxygen production and consumption of catalase and glucose oxidase during the oscillation.*

Furthermore, dialysis membranes (12-14 kDa cut-off) were applied between the compartments and the central column, to limit the influx of substrate from the compartments to diffusion and prevent any unwanted flows or mixing, while also serving as a physical, non-sticking barrier for the capsule to oscillate against. Whereas the substrate flows in the top/bottom compartment merely ensured a consistent concentration profile, the flow of the central column was probably the most important aspect of the device, as it truly enabled long lasting oscillations. By being aligned vertically, the flow dragged diffusing glucose from the top-phase and H_2O_2 from the bottom phase towards the outlet of the column. While this drag caused some mixing, the substrate concentrations would be severely diluted while maintaining a concentration-peak along the respective membranes. This way, the oscillation of the capsule would not become influenced drastically until the capsule reached the proximity of the membrane. So, the most important factors, which will define the oscillation-pattern of the capsule inside the central column, are the glucose, H_2O_2, catalase, GOx concentrations and the weight of the capsule, which was usually defined by the amount of encapsulated silica particles. Finding the optimum between all these variables is necessary to prevent one of the two enzymatic antagonists to become overly active, which would either overproduce or overdeplete the bubble and therefore bring the oscillation to a halt.

To ensure stable and reproducible oscillations, it is necessary to understand how the substrate-interfaces behave in a flow- and diffusion-based environment. This is specifically difficult, as all three phases are colourless and do not give any distinguishable visual feedback. For this reason, methylene blue was used as a visual indicator, which will represent the respective substrate in the following flow/diffusion studies. Experimentally, the column was prepared with a density gradient as described above. To ease the analysis, each dataset would only focus on either the glucose- or the H_2O_2-phase by adding 5 mM methylene blue to the respective side. The experiment began by starting the flow-system. The flows were then cut off after 10 hours, after which the experiment continued for another 10 hours during which the interfaces were observed in a purely diffusion based environment. The results are summarised in (Figure 4.4-17) in form of camera-images and kymograph line-profiles which spanned from the top to the bottom-membrane.

Figure 4.4-17-a+b show that the interfaces did not develop symmetrically, which is mainly attributed to the internal flow of the column, which went from the upper to the lower outlet. In the bottom-phase, the substrate would slowly diffuse upwards up until it reached the lower outlet. Here, the interface became slightly warped due to the flow, which pushed the substrate further into the column around the left wall, whereas it was being pushed down around the lower outlet. Nonetheless, the interface stayed stable over long periods of time and showed only minor penetration into the column, which can be seen by a slight blue tint, which developed over time. Once the flows were turned off, the interface became levelled and started to penetrate deeper into the central column, which can be seen as an abrupt increase in the kymograph (Figure 4.4-17-c). In case of the top-phase though, the substrate-diffusion profile would look completely different. As expected, the flows dragged the diffusing compounds further into and out of the column through the lower outlet. Interestingly, this formed multiple interfaces, with a highly concentrated phase around the top membrane, a second interface right in the middle of the column and a third interface just above the lower outlet. While there is no direct indicator to why this happened, it could be hypothesised that the interfaces develop as a response to the density gradient between the bottom, central and top-phase, which started to mix due to the flow. Again, once the flows were turned off, the concentrated substrate-phase started to penetrate deeper into the oscillation column, thus proving the benefit of the flow.

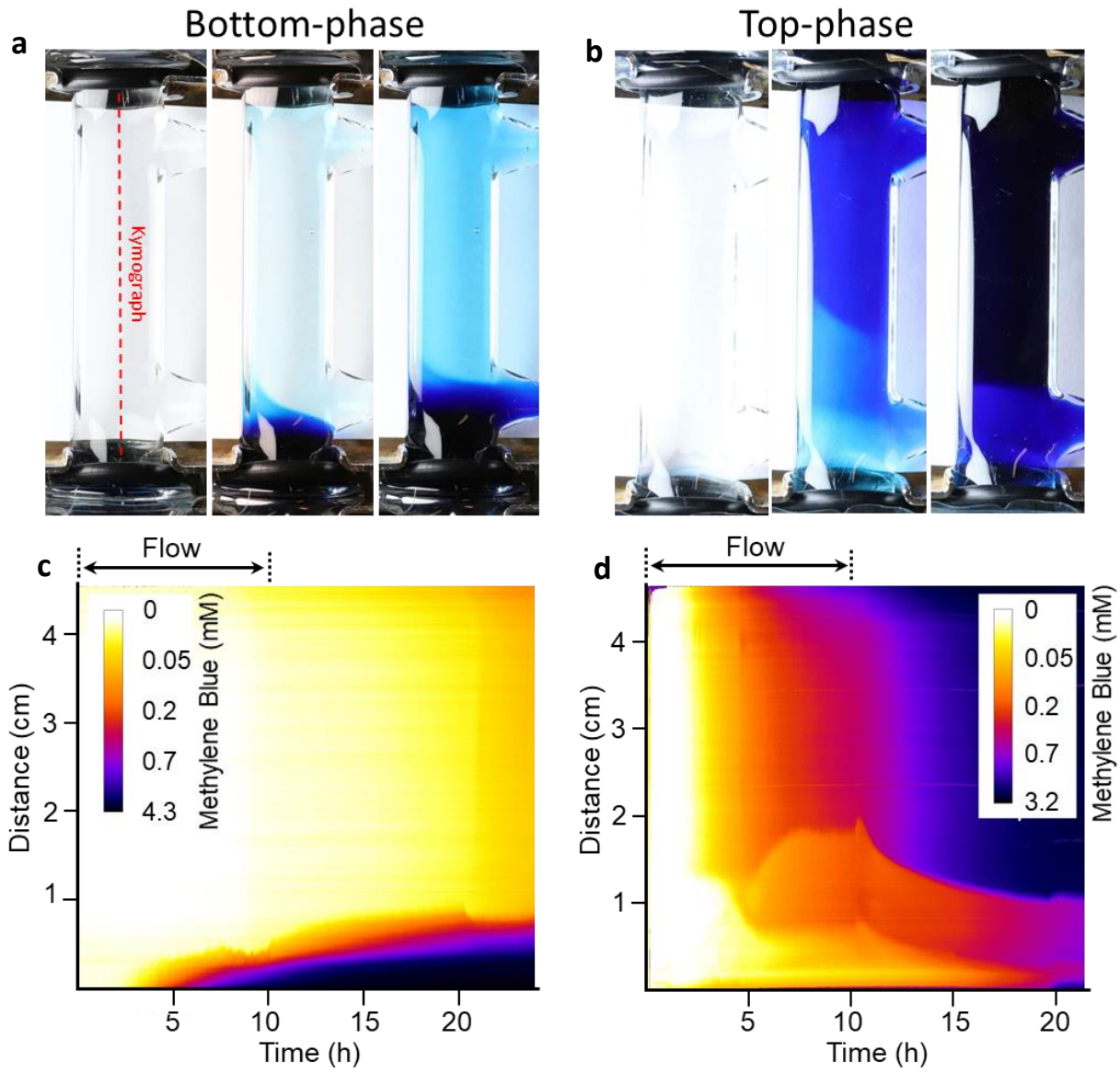

Figure 4.4-17: *Development of the glucose- and H_2O_2-interfaces inside the oscillation column.* ***a+b*** *Camera images of the substrate-profile of the bottom- and top phase. The images show the beginning of the experiment (0h) the cut-off point of the flows (10h) and the state at the end of the experiment (20h).* ***c+d*** *Kymographs (line profiles) of the flow- and diffusion-based interface development. The axis of the kymograph is depicted as a reline in* ***a****.*

When merely observing the intensity of the dye, one could assume that there would be a substantial amount of dye penetrating the column, even when the flows are turned on. What needs to be kept in mind is, that the visual colour density is not correlating linearly with the concentration, but rather exponentially (Figure 4.4-18). Using these results as a calibration for the diffusion-data from Figure 4.4-17, it shows that even the very visible coloration from Figure 4.4-17-b (middle image), which could imply a heavy mixing of the substrate with the central column, has in fact a much lower concentration (~ 0.2 mM). So, while a certain amount of mixing cannot be prevented inside the column due to the

applied flows, it is fairly minimal, which should guarantee a long term stability of the substrate interfaces.

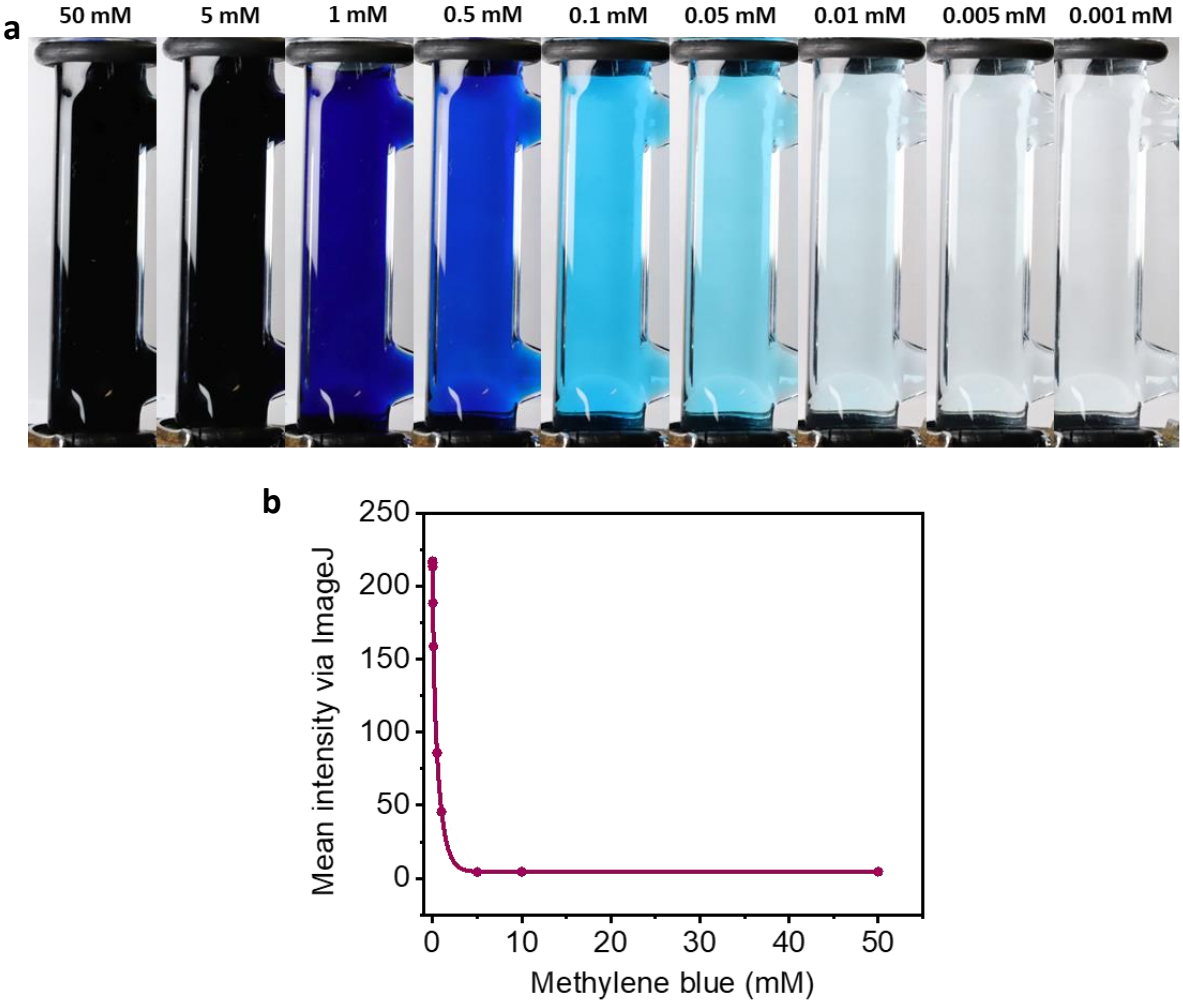

Figure 4.4-18: *Correlation of the colour-density of methylene blue with its concentration.* ***a*** *Camera images of the oscillation column filled with methylene-blue of various concentrations.* ***b*** *Plotted mean colour intensity vs the concentration of the dye.*

To support and maybe even confirm the experimentally determined diffusion profiles, the diffusion was furthermore calculated through computational simulation. This work was done in two steps and with two different software packages.

In the first step, the oscillation device was turned into a 3D-model with the help of the *Autodesk-Inventor* software. The dimensions of the 3D-model are shown below in Figure 4.4-19. While designed according to the real device, the 3D-model does not represent the external, but the internal dimensions. The reason for this is a simplification made for the sake of the simulation, in which the whole volume of the model will be treated as a liquid. This makes it easier to design and export the model for the second software, *Autodesk-Computational fluid dynamics (CFD)*. Before the simulation can be run though, it is necessary to understand all the parameters and simplifications made in order to enable the simulation of substrate diffusion within the device. As described before, all three main compartments were assigned as a liquid material and its standard physical parameters were the ones of water. Since the software would not allow different adjacent materials, it was necessary to define a different variable to distinguish between for example the bottom compartment with H_2O_2, and the

central column. So instead of defining materials, the density of the material was assigned to a scalar variable, which was defined as a piecewise linear function with multiple values. Since sucrose played an important role in the oscillation experiments, the density was defined along the density-values for 1-3% sucrose solutions, which were taken from literature. [103,104]

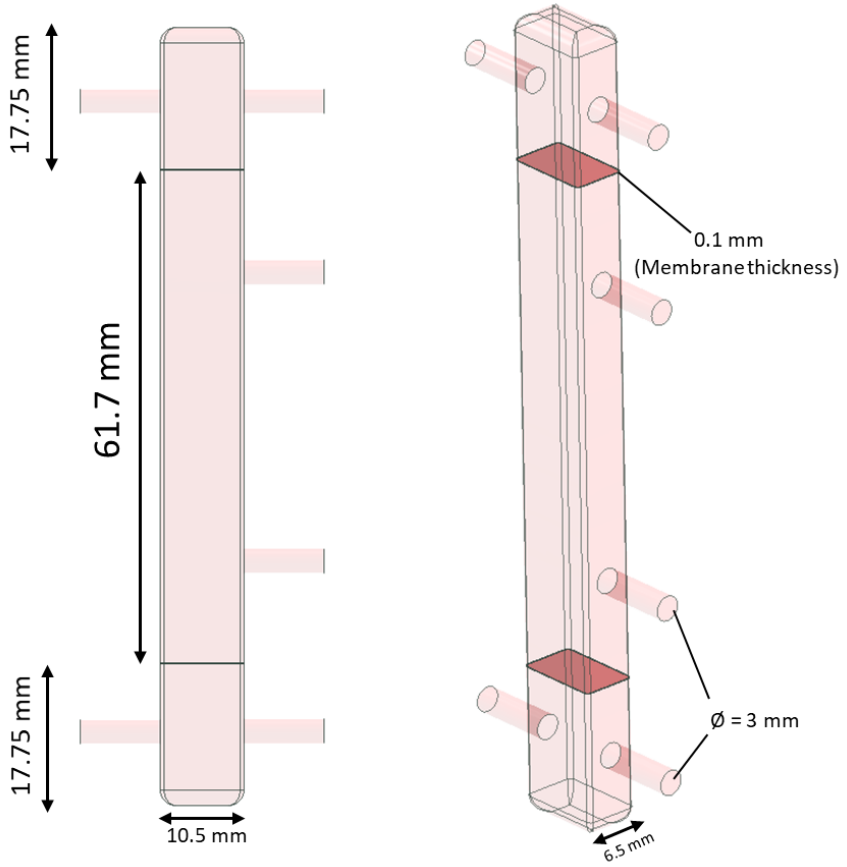

Figure 4.4-19: *3D-model of the stable-oscillation device. The model was designed with the Autodesk-Inventor software and the dimensions represent the internal measurements of the glass compartments.*

Next, the so called "initial conditions" were defined for all three compartments by setting the scalar variable to either 0 or 1. This effectively makes the software simulate a bi-phasic system, with all of compound A concentrated in the compartments with a scalar-value of 0 and compound B accumulated in the volumes with scalar = 1. This also highlights the next restriction of the software, as only one side of the device (e.g. the diffusion of glucose out of the bottom compartment) can be simulated at a time but never both simultaneously. Up to this point, the software only knows where the compound of interest is accumulated and what its density is, but it still has no connection to glucose or H_2O_2. To do this, the "general scalar" was defined through a diffusion coefficient of either H_2O_2 (when simulating the bottom compartment) or glucose (when simulating the top compartment). Furthermore, the membranes were defined as hydrodynamic resistances with a Darcy-permeability coefficient of $3.7*10^{-11}$ m^2 [105] and the flows were directed from the left to the right for the top/bottom compartments and from the top to the bottom within the central compartment at 20 µL/min. The diffusion within the device was then simulated for a timespan of 25h with 300 datapoints, each iterated 5 times.

Since the transient simulation video footage cannot be displayed within this thesis, the following images are representations of the steady state, which the system reached after ~25 hours (Figure 4.4-20)

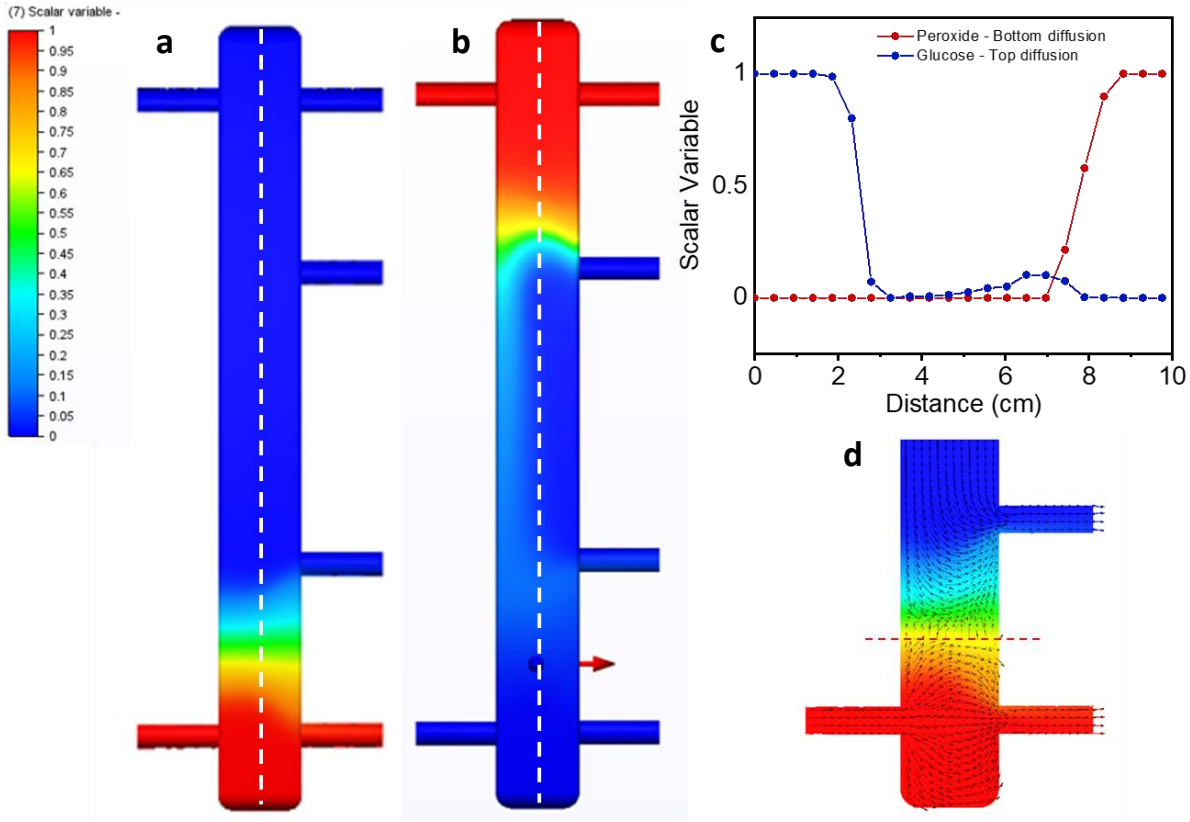

Figure 4.4-20: *Steady-state of the simulated diffusion of H_2O_2 (**a**) from the top-compartment and glucose (**b**) from the bottom compartment. **c** The diffusion line-profile is described as the value of the scalar variable over the distance from the top to the bottom of the device. **d** Vector field representing the flow velocities within the bottom compartment and around the membrane within the steady state.*

The scalar variable, or in other words the diffusing compound, can be seen as a red phase which is slowly penetrating the blue volume. Figure 4.4-20-d shows the flow-induced velocities as a vector field, which nicely illustrates the role of the dialysis membrane between the bottom/top-compartment and the central column. Even though the system is under constant flow, the membrane serves as a barrier and prevents mixing and a strong influx of substrate into the oscillation-column. Right above the indicated membrane (dotted red line), the vectors align parallelly and in orthogonal orientation to the membrane, which indicates that the flows are only experienced within the compartment and the membrane is only permeable via passive diffusion.

Both diffusion profiles (Figure 4.4-20-a+b) showed a strong resemblance to the experimental diffusion studies (Figure 4.4-17). The diffusion profiles are defined by the asymmetry of the flow within the central column. Whereas the H_2O_2-phase only diffused a few centimetres until it reached the lower outlet pipe, the glucose phase was carried all the way from the top to the bottom outlet-pipe, once it got in contact with the flow. The scalar-values for the top-phase could imply that less substrate is penetrating the column compared to the methylene-blue experiments, but it needs to be addressed that the scalar variable is indeed scaling linearly, whereas the methylene blue concentration correlated exponentially with its intensity. This means that the simulated data could give a more realistic impression of the real substrate diffusion. At the end of the day though, neither the

experimental, nor the simulated diffusion data will represent the actual experimental conditions but it is necessary to gather enough data in order to understand a complex experimental setup like this.

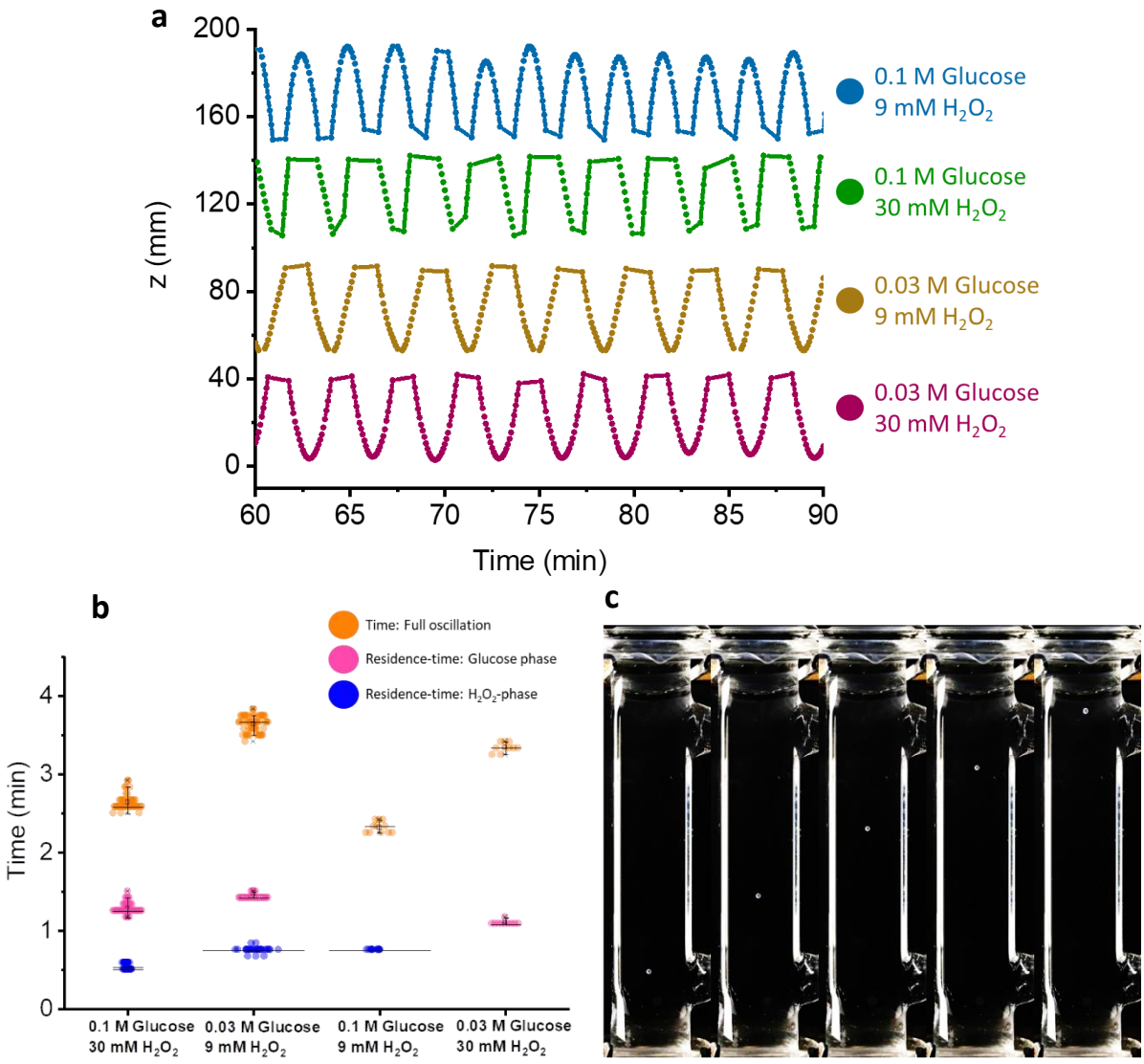

Figure 4.4-21: a *Oscillation profiles of protamine/DNA-microcapsules. The respective glucose and H_2O_2-concentration of the top- and bottom compartments were varied between 0.1-0.03 M glucose and 30 – 9 mM H_2O_2. The flows of the device were all set to 20 µL/min and the motion of the capsule was tracked digitally. Each graph shows the vertical displacement of a single protamine/DNA-microcapsule. Furthermore, each plot is only a short segment of a much longer oscillation, with oscillation periods between 2 – 10 hours. All oscillation-plots were superimposed with a single y-axis and an offset of 60 mm to simplify the presentation.* ***b*** *Each oscillation was divided into a bottom-phase- (**blue**), top-phase- (**pink**) and free-oscillation-residence time (**orange**). The dataset represents the respective residence times for each segment of the column and for each condition in **a**.* ***c*** *Consecutive camera images of a protamine/DNA-microcapsule ascending in the oscillation-column after entering the H_2O_2-bottom-phase.*

Next, the gathered information from previous experiments was applied to perform a fully functioning microcapsule oscillation. For the following experiments, the oscillation device from Figure 4.4-16 was used and merely the concentrations of glucose and H_2O_2 in the top and bottom compartments were

changed. The flows of the device were all set to 20 μL/min and the capsule was fabricated with 19.8 kU/mL catalase, 2.9 kU/mL GOx and 20 mg/mL silica particles as weight. Again, adding the capsule with a pre-nucleated O_2-bubble was crucial, due to the low H_2O_2-concentrations in the bottom compartment. Figure 4.4-21 shows the superimposition of 4 oscillation-profiles of protamine/DNA-microcapsules, to understand how the substrate concentration can change the capsule's trajectory. The glucose feed to the top compartment was altered between 0.1 M and 0.03 M whereas the H_2O_2 was changed from 30 mM to 9 mM. As the capsule often spent a prolonged time on either the top or the bottom side, it is useful to analyse the residence times in each phase. Figure 4.4-21-b shows the calculated residence times in the top- and the bottom-phase and the time it took for each full oscillation. Figure 4.4-22 furthermore provides a magnified view of a single oscillation at the bottom interface for each of the concentrations to highlight the impact of the concentration on the oscillation pattern.

High glucose- and H_2O_2-concentrations (0.1 M glucose, 30 mM H_2O_2, green), exhibited the shortest residence times in the H_2O_2-phase with just ~0.5 min, but very long times in the top phase (~1.2 min). The top-side of the oscillation curve appeared to be shaved off, which stems from the way the oscillation-device was build. Since the membranes lie a few millimetres above and below the camera's view, it kept losing track of the capsule whenever it got close to the oscillation boundaries. At the bottom-side on the other hand, the capsule would only briefly enter the H_2O_2-phase before ascending again, leading to a very sharp oscillation-curve (Figure 4.4-22). The generally short residence times in the H_2O_2-phase all over the 4 different concentration combinations shows that the oxygen-producing side was much more responsive compared to the, over a minute long, residence times in the glucose phase. The residence time of a full oscillation, which was comprised of both the residence times in the bottom- and top-phase plus the travelling period between them, was found to be at ~2.65 min.

Next, both the H_2O_2- and the glucose-concentration (0.03M glucose, 9 mM H_2O_2, yellow) were lowered, which essentially extended both the oscillation-length and the residence-times in all three phases. The residence times reached the highest values out of all the conditions with ~1.35 min in the top phase and ~0.7 min in the bottom phase, while simultaneously changing the bottom trajectory to a much rounder curve (Figure 4.4-22). When reducing the H_2O_2-concentration to 9 mM while keeping glucose at 0.1 M (Figure 4.4-21-blue), the capsule penetrated the glucose-phase, but did not reach the top membrane anymore, as it can be seen from the much smoother curves. This not only shortened the residence-times in both phases, but made the capsule oscillate freely without ever touching either boundary, which was the closest case to an actual oscillator. This experiment also demonstrated the flow induced transport of glucose from the top membrane into the device, which exposed the capsule to substrate before it even reached the top-membrane. Due to the low H_2O_2-concentration at the bottom, the glucose dragged by the flow sufficed to induce enough O_2-consumption to make the capsule descend. Lastly, the H_2O_2-concentration was increased to 30 mM while leaving the glucose-concentration at 0.03M (Figure 4.4-21-a-pink). Here, the capsule did not penetrate the bottom phase at all but reinitiated the buoyancy by merely getting into contact with upwards diffusing H_2O_2, while instead increasing the residence times at the top phase (~ 3.35 min). The first example (Figure 4.4-21-green) did not show this behaviour even though it was run under identical H_2O_2-concentrations. This can be explained by the lower glucose concentrations in the pink plot of Figure 4.4-21, which caused the oxygen-bubble to deplete slower during the descent, which in return needed less oxygen production to reinitiate the buoyancy.

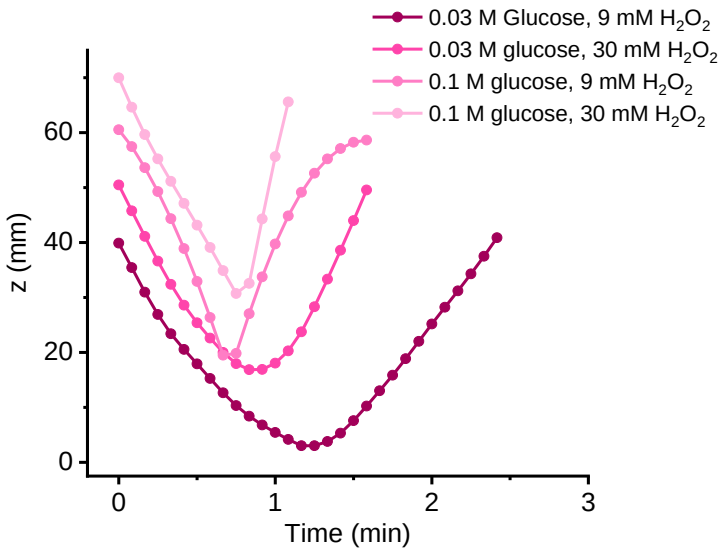

Figure 4.4-22: *Superimposition of single oscillation trajectories from each condition discussed in Figure 4.4-21. Each plot shows the vertical displacement of one protamine/DNA-microcapsule oscillating between a glucose top-phase and a H_2O_2-botom-phase.*

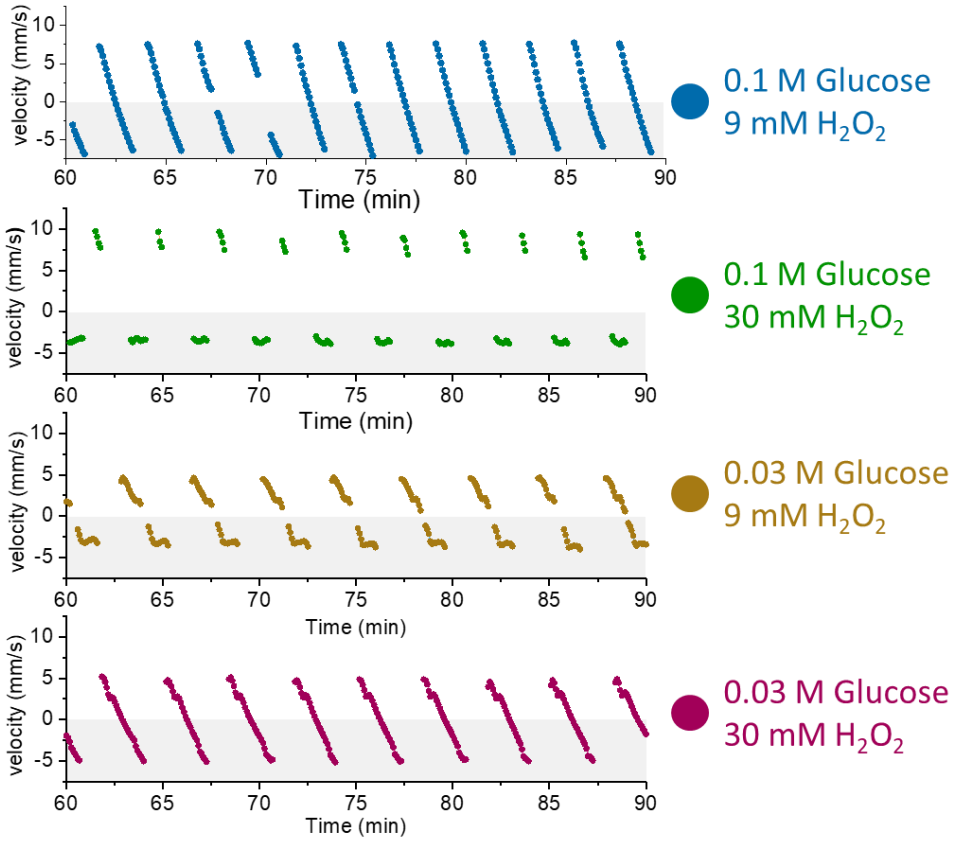

Figure 4.4-23: *Velocity-profiles of protamine/DNA-microcapsule oscillations. The respective glucose and H_2O_2-concentration of the top- and bottom compartments were varied between 0.1-0.03 M glucose and 30 – 9 mM H_2O_2. The flows of the device were all set to 20 μL/min and the motion of the capsule was tracked digitally and transformed into the plots of the figure. Each graph shows the velocity-profile of one protamine/DNA-microcapsule during its oscillation.*

To look at the plots from Figure 4.4-21 from a different perspective, the velocity profiles for each condition were calculated and plotted (Figure 4.4-23). As expected, there was a general increase in both velocities when increasing the substrate concentrations from 0.03 M glucose and 9 mM H_2O_2 (Figure 4.4-23 yellow) to 0.1 M glucose and 30 mM H_2O_2 (Figure 4.4-23 green) and the capsules accelerated much quicker, which means that the oxygen bubble growth and depletion was happening at a much quicker rate. On the other hand, changing the concentrations from 0.03 M glucose/9 mM H_2O_2 (Figure 4.4-23 yellow) to 0.03 M glucose/30 mM H_2O_2 (Figure 4.4-23 pink), exhibited a rather small increase in the upward velocity, whereas changing the glucose concentration to 0.1 M as well (Figure 4.4-23 green), the upward velocity increased much more. This can be explained similarly to the previous discussion, since the increased oxygen-consumption directly fed into how far the capsule penetrated into the bottom-phase and, therefore, how much and how fast it produced oxygen.

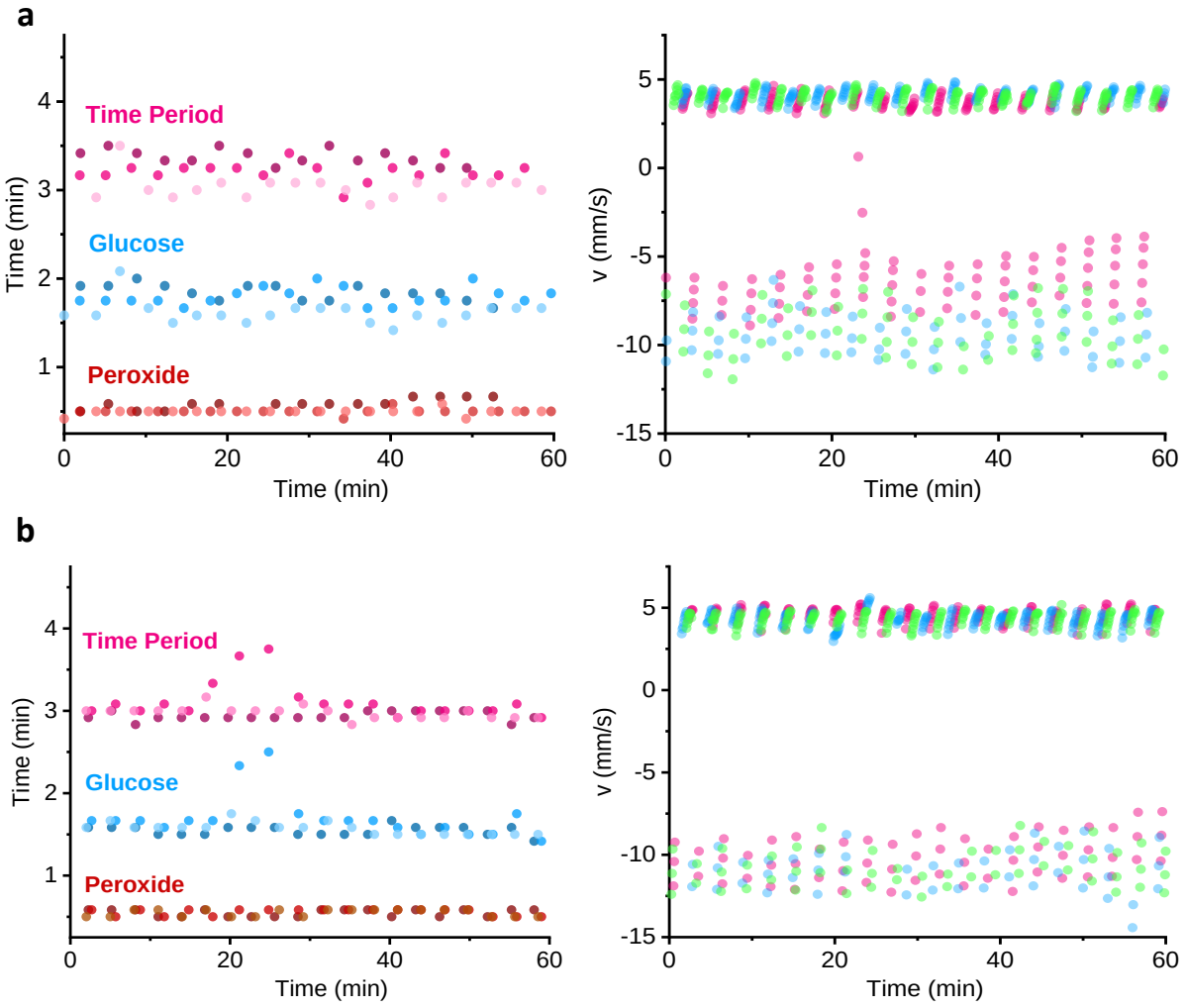

Figure 4.4-24: *Time-dependent plots of the tracked residence times and velocities of oscillating protamine/DNA-microcapsules.* ***a*** *All flows of the device were set to 20 µL/min with 0.1 M glucose and 30 mM H_2O_2.* ***b*** *The flow of the central column was set to 50 µL/min, while keeping all other flows at 20 µL/min and concentrations at 0.1 M glucose and 30 mM H_2O_2.*

Figure 4.4-24 furthermore analysed the general stability of the oscillations at 0.1 M glucose and 30 mM H_2O_2 by plotting the oscillation period, residence-periods and the velocity against the time. The glucose-phase showed the largest variance between the datapoints, which is not surprising, considering the capsule resided in the top phase the longest. While the variance increased slightly for

the residence in the H_2O_2-phase after 40 minutes, the residence times over 3 datasets appeared to be very similar. This furthermore means that the overall variance for oscillations is mainly attributed to the residence time in the top phase. The velocities paint a similar picture, as the positive upward motion is overall consistent and shows very little deviation. The GOx-mediated descent of the capsule on the other hand shows a lot more spread of the datapoints within one set with values between -12.5 to –2.25 mm/s. Changing the flows of the top and the bottom-compartment had little to no influence on the oscillation, which is mostly attributed to the membrane as it prevents turbulences and an increased influx of substrate into the central column. In Figure 4.4-24-b, the volume-flow of the central column was changed from 20 μL/min to 50 μL/min instead, and the oscillation times and velocities were tracked once more. Even though the differences are not striking, the higher flow-rate appeared to have changed the variance between the datapoints a little, as they are not spreading as much as they are in Figure 4.4-24-a. The average values on the other hand are virtually identical and did not seem to change much. Interestingly, a slight increase of the downward velocities was found while the variance decreased as well, even though the ascension-velocities were still identical. The combination of a flow-based oscillation device with the chemically driven microcapsule buoyancy made this concept very complex and difficult to analyse. While increasing the flow-rate of the central column seemed to have beneficial effects on the stability and quality of the oscillations, it is important to mind that the central flow also interacted with the oscillating capsules, which can and will manipulate the buoyant motion. One possible reason for the lower variance in Figure 4.4-24-b could be that the system reached its steady state quicker due to the higher flow-velocities, which would stabilise the oscillation. Furthermore, the methylene-blue studies and the simulations have shown that the central-flows dragged a certain amount of glucose from the top-phase into the column, which could increase at higher flow velocities. This could explain the higher downward-velocities of the capsules, as there would have been a higher glucose concentration present than in the 50 μL/min-case, which would increase the bubble-consumption speed and therefore the downward velocity. To properly understand the effect of the flow, more diffusion studies would be necessary under high flowrate conditions, to back up any assumptions at this stage.

In the experiments above, the focus was lying on small time-periods to analyse the patterns of single oscillation cycles. Figure 4.4-25 shifts that perspective to long-term oscillations, which enables the discussion of the stability of oscillations regarding the presented experimental flow-device. A protamine/DNA-microcapsule was prepared like in the previous experiment and the compartments of the oscillation column were filled with 0.1 M glucose and 30 mM H_2O_2. The microcapsule oscillated over a time of 600 minutes, during which it showed a very consistent trajectory without any major deviations. Only at the end of the oscillation experiment at ~600 min, the oscillation-frequency appeared slightly lower than at the beginning, which could indicate that the system is not stable for an indefinite amount of time. Other factors, that occurred during the experiment and were able to end the oscillation experiment prematurely, were interactions of the protamine/DNA-microcapsule with the glass-walls of the device in cases where the microcapsule had a slight lateral drift during the oscillations, micro-bubble formation inside the device or the tubing which interfered with the microcapsule or even stickiness of the microcapsule towards the dialysis membrane-barriers. Next, and to further discuss the relevancy of the flow-system for the stability of the oscillations, the same experiment was repeated under identical conditions, only this time all flows were stopped 100 minutes after the oscillation had started (Figure 4.4-26-a).

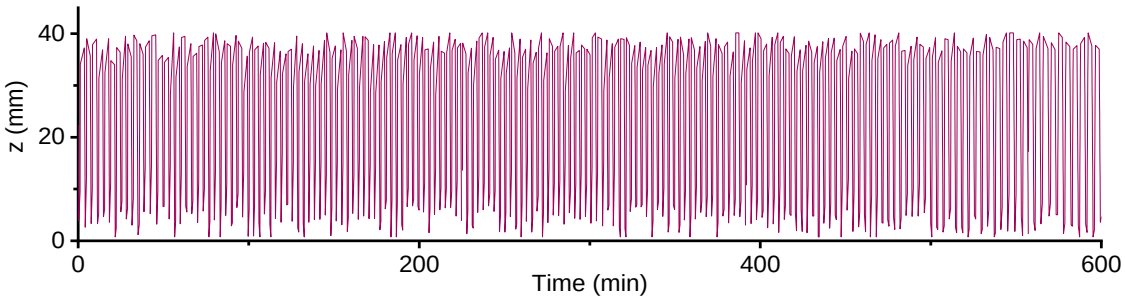

Figure 4.4-25: *Long-term oscillation of a single protamine/DNA-microcapsule. All flows of the device were set to 20 µL/min with 0.1 M glucose fed into the top- and 30 mM H_2O_2 in the bottom compartment. The oscillation was observed over a time-span of 600 minutes.*

Interestingly, the oscillation periods as well as the residence times in the top- and bottom phase stayed virtually the same for another 300-400 minutes, after which they started to rise almost exponentially from 2.6 min to up to 15 minutes. The diffusion studies from Figure 4.4-17 have shown that the substrates take a substantial amount of time to penetrate the oscillation volume, so it is not surprising that the oscillations maintained a certain amount of consistency for another while. When performing the same experiment once more, but cutting off the flows after 600 minutes instead, the results looked almost identical (Figure 4.4-26-b). Again, the oscillation periods appeared to rise after ~500 minutes of consistent oscillation and started to grow exponentially from 3.8 to 12 minutes. This time though, the increase happened while the flows were still running which now raises doubts about whether the flow system really maintains the stability of the oscillations and if it is relevant at all. What has been proven with the diffusion studies from Figure 4.4-17 though, is that the flows prevent an excessive penetration of the substrate into the oscillation column, so it appears difficult to dismiss the benefits of the applied flows altogether. Instead, it is necessary to find other sources of error that could cause the observed deterioration of oscillations independently from the established substrate interfaces and concentration gradients.

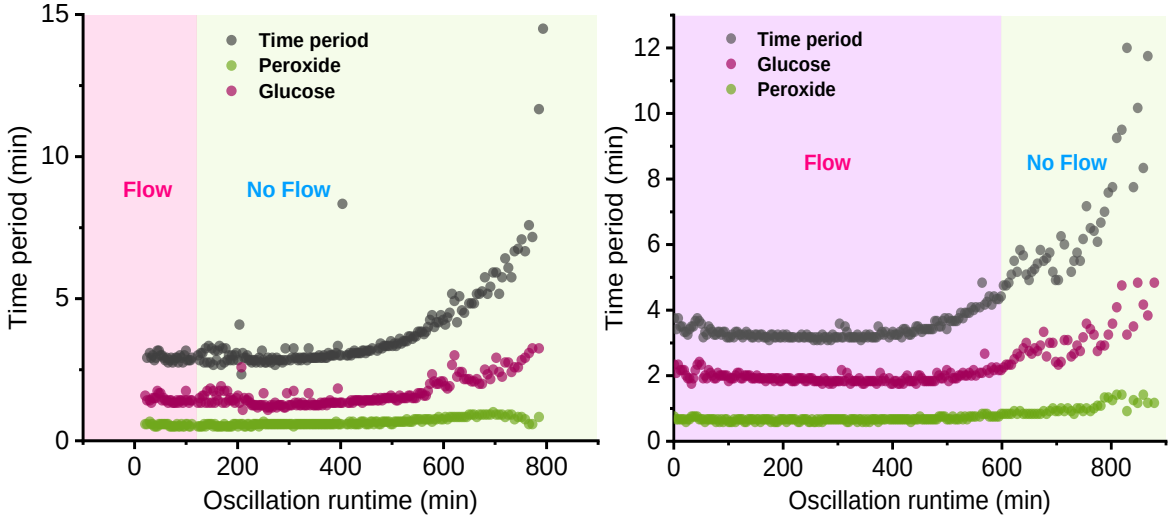

Figure 4.4-26: *Long-term oscillation of a single protamine/DNA-microcapsule. All flows of the device were set to 20 µL/min with 0.1 M glucose fed into the top- and 30 mM H_2O_2 in the bottom compartment. After 100 minutes (**a**) and after 600 minutes (**b**) all flows were stopped but the tracking continued. The plots show the oscillation period (**grey**), the residence time of the capsule in the glucose phase (**pink**) and in the H_2O_2-phase for each oscillation (**green**).*

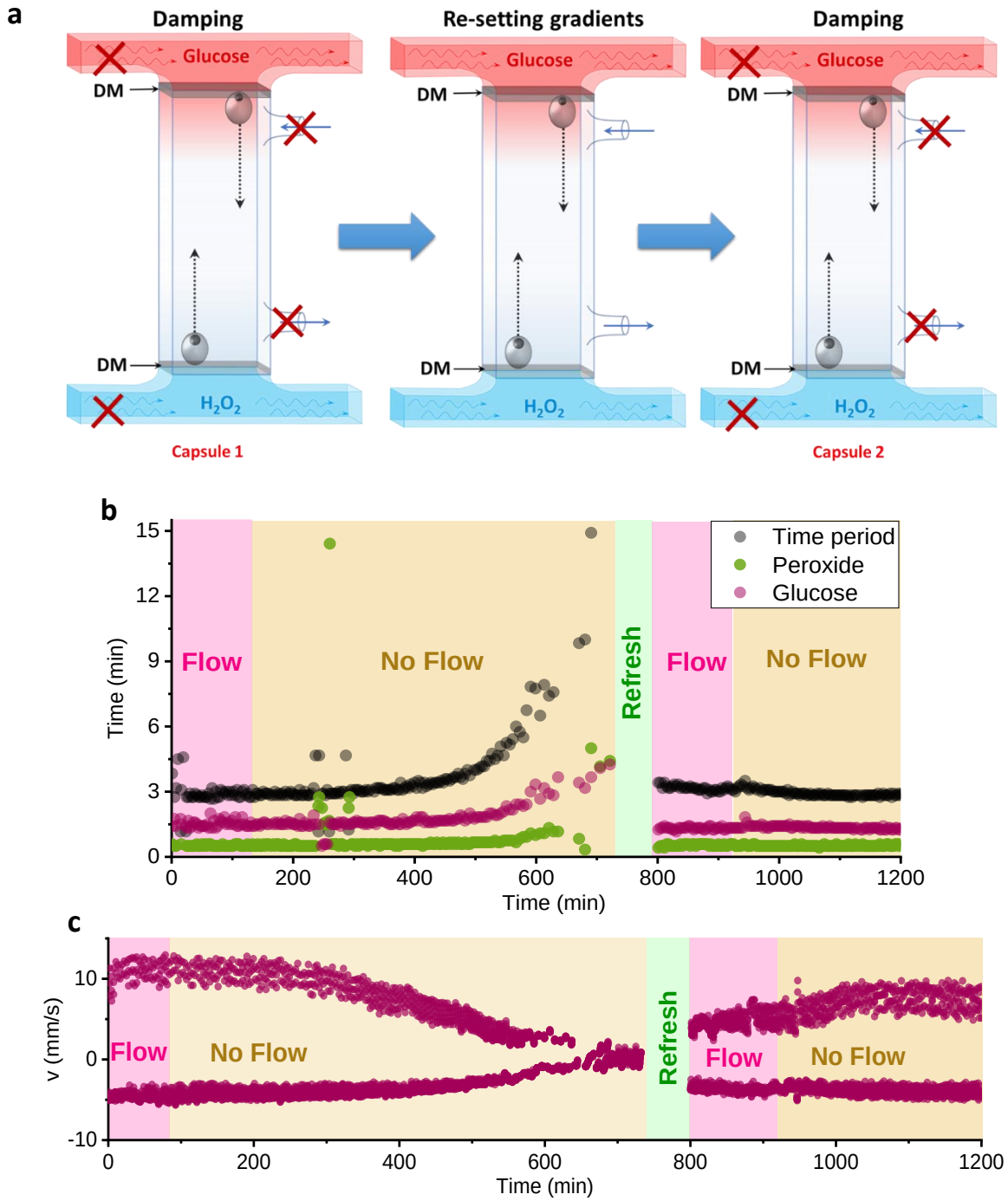

Figure 4.4-27: *Long-term oscillation of a single protamine/DNA-microcapsule.* ***a*** *All flows of the device were set to 20 µL/min with 0.1 M glucose fed into the top- and 30 mM H_2O_2 in the bottom compartment. After 120 minutes, all flows were stopped but the tracking continued. After 720 minutes, the capsule was removed from the device and the solutions inside refreshed by flushing all compartments with their respective solution. Afterwards, a fresh protamine/DNA-capsule was inserted into the oscillation column with a pre-nucleated oxygen bubble inside and the oscillation experiment continued.* ***b*** *Plot of the oscillation period (**black**), the residence time of the capsule in the glucose phase (**pink**) and in the H_2O_2-phase over time (**green**).* ***c*** *Plot of the vertical velocity of the protamine/DNA-microcapsule over time.*

One factor, that fits that description very well is the stability of the enzymes within protamine/DNA-microcapsules, or more specifically, the leakage of the enzymes in response to a changing chemical environment. While the current system runs purely on non-ionic components with glucose, H_2O_2, sucrose and water, there is gluconic acid which is being produced by GOx which could potentially

cause a similar enzyme leakage, like it was described before (See chapter 3 - Figure 3.4-27). To maintain the structure of this thesis though, the question of enzyme-leakage during oscillations will be discussed at a later point in part 4.4.5.

Finally, it was investigated whether the oscillation device can be reused after the first oscillation had finished (Figure 4.4-27). For this purpose, the protamine/DNA-microcapsule was removed after the first capsule had been oscillating for ~700 minutes within the oscillation device and without any flows applied. The device was then flushed with the respective solutions for 60 minutes without disassembling it or removing the solutions manually, after which a new protamine/DNA-microcapsule was introduced, and the oscillations were tracked once more. The velocity plots from Figure 4.4-27-c show that capsule 2, after resetting the concentration gradients, engaged in oscillations right away, even though the positive oscillation velocities were slightly lower (~5 mm/s) than during the first cycle. From 800 to 1100 minutes the velocities increased while the oscillation periods (Figure 4.4-27-b) decreased slightly from 3 min to ~2.8 min, after which the values stabilised. Once the flows were cut off a second time, the new capsule kept oscillating without showing any damping or change in velocities until up to 1200 minutes, even though it was expected that the capsule would dampen if the experiment was conducted for longer periods of time. This neither proves nor disproves enzyme leakage or enzyme fatigue during microcapsule oscillations, but it clearly shows a trend that appears in most if not all long-term microcapsule oscillation experiments. Figure 4.4-27 furthermore shows, that the concentration gradients within the oscillation device can be re-established by simply resetting the flow-system, even after prolonged inactivity.

4.4.4 Damped Oscillations

The experiments above have established the term and concept of long term “stable” or “sustained” oscillations, which needs to be distinguished from actual harmonic oscillators like they were described in the introduction. The reason why it would be inappropriate to use the term “harmonic” stems from the fact that the system is exposed to a subtle but constant damping, which becomes more and more obvious after about 200-300 minute of consistent oscillation (Figure 4.4-26). Instead, even the stable oscillations in this thesis would need a correcting term like stable-damped- or long-term damped oscillations. While the reason for the damping will be discussed later in this chapter, it is of great interest to gain control over the damping during the microcapsule’s oscillation. For one, it would enable more sophisticated motion patterns which have not been presented for protocells as of yet, and it would also present more insight into the interaction between the microcapsule, the enzymes and their environment.

Stable oscillations were designed by separating the fuelling substrates with an inert middle-layer and by constantly refreshing the substrate-gradients, which prevented the O_2-consumption and production from shifting to one of the two sides. To create damping though, it is necessary to make one of the antagonists gradually overpower the other. In all of the following experiments, the damping was generally investigated at the bottom of the device, or in other words, the shift towards a glucose oxidase dominated oxygen-consumption. A key step for the design of these novel, damped protocell oscillations was the change from a flow-based to a diffusion-based device. Instead of constantly refreshing the substrate concentrations and separating them spatially, no flows were applied, and the central phase was replaced with a consistent glucose-solution. This effectively changed the system in several ways: As soon as the experiment started, the H_2O_2-phase would start to diffuse into the glucose-bulk. While the capsule is oscillating, it would constantly be in contact with glucose, whereas the oxygen-production will decrease with every cycle, as the H_2O_2-concentration at the bottom compartment diluted progressively due to diffusion of the substrate (Figure 4.4-28-a). A 0.03 M glucose-solution was chosen for the bulk-phase within the column and the top compartment, and a

32 mM H_2O_2-solution was filled into the bottom compartment (Figure 4.4-28-c). In contrast to the oscillations from the previous experiments, the microcapsule would not oscillate the full distance between the two barriers right at the beginning (Figure 4.4-28-c). Instead, its amplitude increased steadily over a time of 100 minutes, which can be explained by the fact that H_2O_2 has just started to diffuse through the dialysis membrane and into the column, which provides the microcapsule with a steadily increasing H_2O_2 gradient. Interestingly, as soon as the capsule reached its maximum velocity (Figure 4.4-28-d), it started to slow down again. Even more so, once the oscillation passed the 200 minute mark, the oscillations became more and more irregular and stopped completely after about 350 minutes, at which point the capsule ended up on the top membrane from where it did not come back down. So, instead of observing an amplitude based damping, this setup achieved a frequency based damping instead, like the experiments from (Figure 4.4-25), even though the damping happened a lot sooner and more pronounced. Furthermore, the fact that the capsule ended up on the top side showed that the O_2-production dominated the consumption, and not the other way around as it was planned. The latter can be explained by the amount of H_2O_2 used for this experiment. Even though the concentration was low, the volume of the bottom compartment could hold up to 1.2 mL of H_2O_2 solution, which kept diffusing into the central column until the equilibrium shifted towards the O_2-production. Similarly, the deteriorating velocity can be explained by the progressing diffusion of H_2O_2 into the glucose bulk solution, which the capsule would experience earlier with every downward oscillation, thus slowing it down sooner and preventing it from penetrating deeper into the higher concentrations of the H_2O_2-layer. This effectively slowed down the upwards-velocities more than the downward-velocities as it is seen in Figure 4.4-28-d, but it decreased both velocities, nonetheless.

While diffusion-based damping of the frequency seems feasible, it was a little bit surprising that the oscillation would dampen after just 100 minutes compared to the previous experiments (Figure 4.4-27), which started to deteriorate after 400-500 minutes. So, it is necessary to address other potential reasons for this behaviour as well. One possible reason, which has been mentioned before is enzyme fatigue or leaking. One of the main differences between the sustained- and the damped oscillation experiments is the consistent glucose phase. In the latter case, glucose oxidase will be constantly active, which could promote leaking due to the sustained production of gluconic acid. Again, a thorough discussion will be presented later in this chapter in part 4.4.5.

Even though this design did not yield the expected results, it still offered a different approach to induce damped oscillations. To get a better understanding whether the damping can be controlled by changing the external parameters, the H_2O_2-concentration was decreased from 32 mM to 16 mM (Figure 4.4-28-e,f). Once the oscillation reached its maximum amplitude and velocity after ~100 minutes, it appeared much less stable in comparison to Figure 4.4-28-c as the time progressed. The velocities were generally lower with a maximum of about 5 mm/s, which is only half the speed from the case with 32 mM H_2O_2. They furthermore decreased a lot faster, and the oscillations stopped about 100 minutes earlier than in the previous experiment. To properly compare the results and highlight the effect of the damping, the oscillation periods for both 32 mM and 16 mM H_2O_2 were plotted (Figure 4.4-28-b). In general, the oscillation periods were about 0.3 minutes longer in case of 16 mM H_2O_2 and increased much earlier after just 200 minutes. They also went about 15 minutes higher than the longest oscillation period in case of 32 mM H_2O_2. Interestingly, with the lower H_2O_2 concentration, the capsule finished its oscillation on the bottom-barrier, which can be explained by the assumption that the capsule did not receive enough H_2O_2 to maintain the oscillation, ergo GOx was the dominant enzyme eventually.

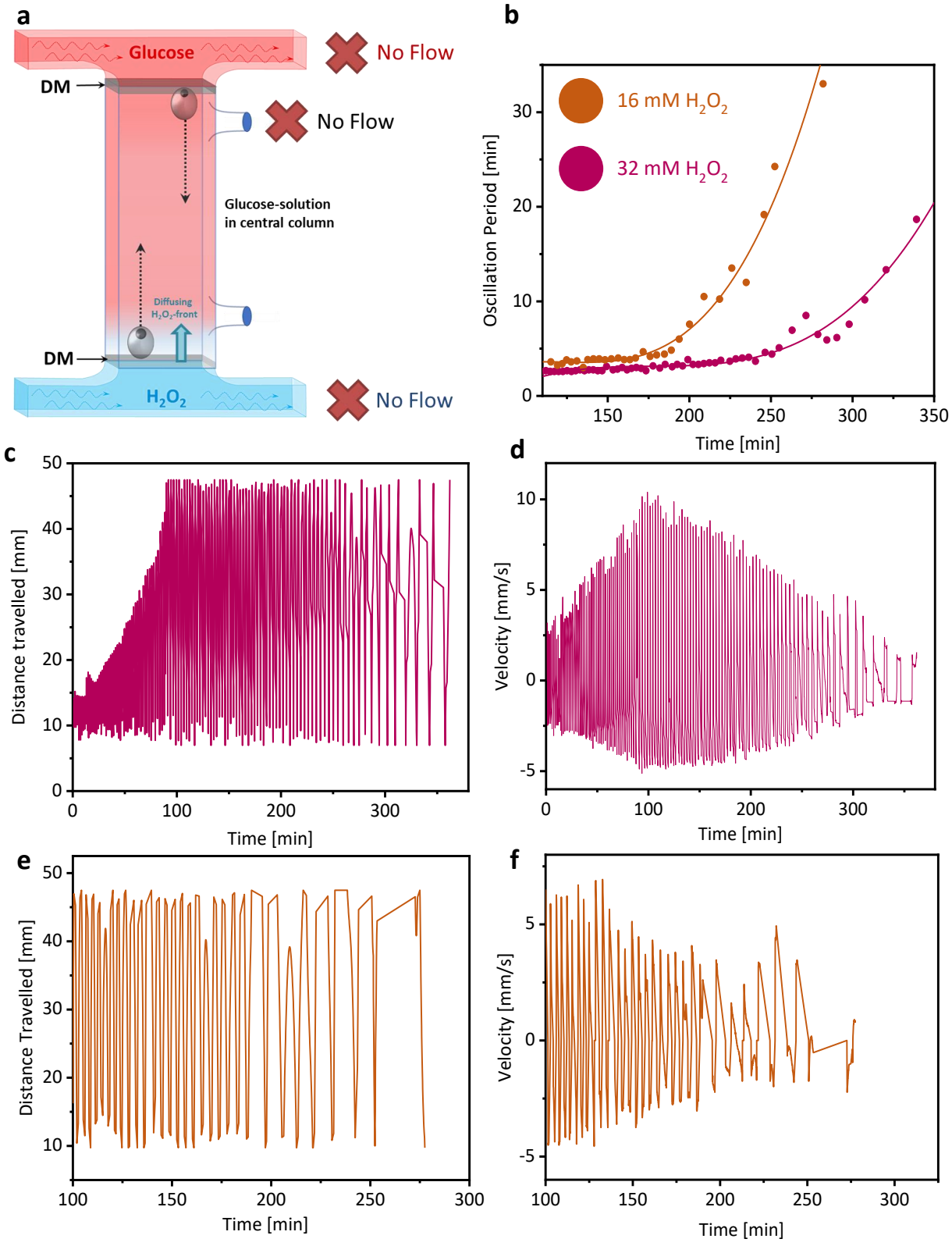

Figure 4.4-28: a *Illustration of the damping concept within the oscillation-device. The top and central-column were filled with glucose-solution, whereas the bottom-compartment contained a H_2O_2-solution. No flows were applied.* ***b*** *Oscillation periods extracted from the damped oscillations with 32 mM H_2O_2 (**red**) and with 16 mM H_2O_2 (**orange**).* ***c,e*** *Trajectory plot of the vertical displacement of a single oscillating protamine/DNA-microcapsule. The top and central column were filled with 0.03M glucose and the bottom compartment was filled with 32 mM H_2O_2 (**c**) or 16 mM H_2O_2 (**e**).* ***d,f*** *Velocity plots of the damped oscillations for 32 mM H_2O_2 (**d**) or 16 mM H_2O_2 (**f**) insider the bottom compartment..*

Reducing the H_2O_2-conentration even further to 8 mM lead only to a few oscillations or none at all, whereas increasing the concentration would often cause the capsule to spend long periods of time at the top-barrier, from where it would not re-descend. This can be explained by the observations from the previous chapter that protamine/DNA-capsules are very sticky and generally adhere to many different surfaces like the glass wall of the device but also the dialysis membrane that was used as a barrier for the oscillation. This did not seem to be an issue when the capsule only connected with the membrane briefly, but the longer the capsule resided against it, the higher the chances became that it would stick to it.

The oscillation device has proven to be reliable when it comes to long term stable oscillations, but it did not yield the envisioned damping results. As mentioned above, the main reason most likely stemmed from a too large volume of hydrogen peroxide, which still fuelled the oscillation for long periods of time. In Figure 4.4-29, a new device will be presented which was used to observe damped microcapsule oscillations. Instead of a custom made glass device, a commercially available optical cuvette (*Starna Scientific Ltd*, 29/SOG/5) was modified with a metal tube ($\varnothing_{Internal}$ = 0.7 mm), which was fitted right at the bottom of the inner compartment. Since this concept was supposed to be designed around much smaller volumes, the oscillation distance was further restricted by inserting a PTFE-membrane, which was wrapped around a yellow (10-200 µL) *Eppendorf*-pipette tip as a scaffold (Figure 4.4-29), which served as a smooth barrier for the capsule to oscillate against, while minimizing the risk of adhesion due to the material's non-sticking properties. In all the experiments to come, the system was assembled so that the distance between the bottom of the cuvette and the PTFE-membrane would span 8 mm. The tube enabled the attachment of a syringe-pump system to automate and control the injection of hydrogen peroxide into the cuvette. Previous studies were looking at similar systems without the convenience of a syringe pump and found that addition of the substrate by hand would cause unnecessary mixing, which reduced the reproducibility. Like in the experiment above, glucose-solution was used as the bulk-phase, which enabled a constant oxygen-depletion while the oxygen-producing H_2O_2-phase would slowly diffuse into the bulk medium, ultimately shifting the equilibrium more and more towards O_2-consumption.

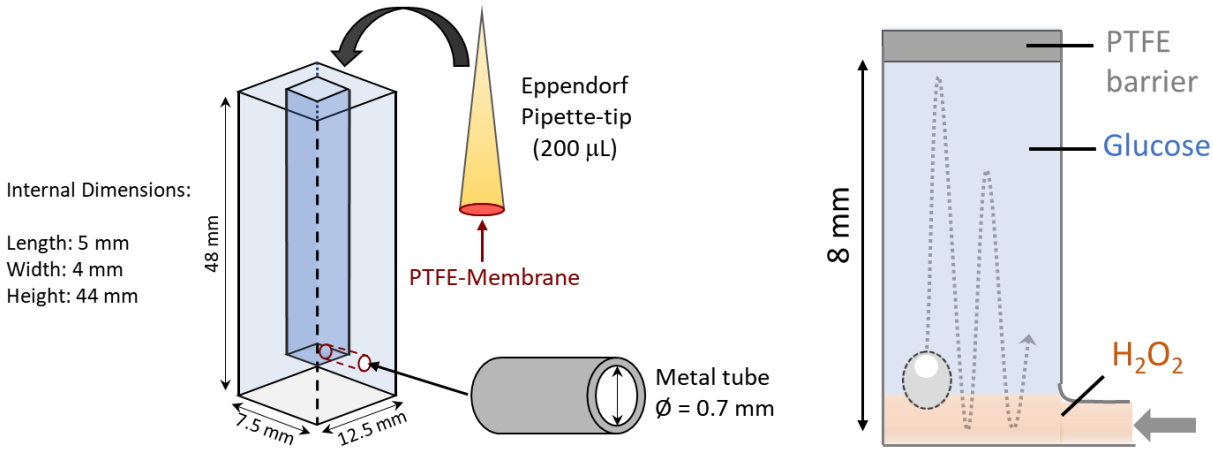

***Figure 4.4-29**: Illustration of the device used for damped protamine/DNA-microcapsule oscillations.*

Like for the previous device, it is necessary to understand the diffusion dynamics, since they will define the oscillation, and more importantly, the damping. Methylene blue has proven to be a reliable and easy to use dye to assess diffusion, which is why the same strategy was used for the damped-oscillation device. The images in Figure 4.4-30 show the diffusion of 7 µL methylene blue (5 mM, with 3 wt% sucrose) after injecting it at a velocity of 5 µL/min. The diffusion profile of Figure 4.4-30-a was

representative for most diffusion studies in this new device. The dye would start to diffuse evenly, but after about 120 minutes, it became evident, that the diffusion was a little bit quicker on the left side of the device. One reason could be the fact, that the methylene blue was injected on exactly the opposite side from where it did not settle evenly and formed a slight gradient. Another reason could be evaporation-effects at the top of the cuvette. To prevent any major evaporation or convections, the device was capped with a PDMS-lid or parafilm, even though the diffusion studies would not show any difference in the outcome.

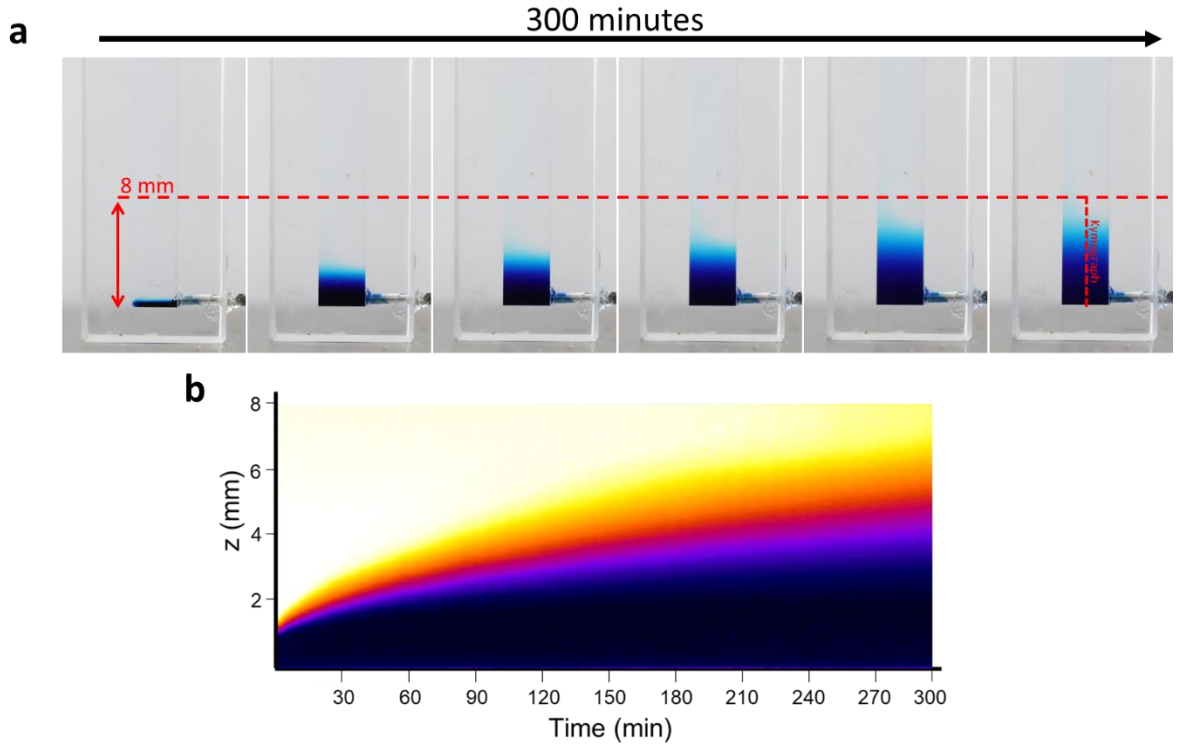

Figure 4.4-30: *Methylene blue diffusion studies for the damped oscillation device.* ***a*** *The column was filled with 1 mL glucose solution (0.1 M) before adding 7 µL of a 5 mM methylene blue solution (with 3 wt% sucrose) via a syringe pump and with a flow rate of 5 µL/min. The diffusion was then tracked via digital camera and pictures were taken every 2 minutes for 300 minutes altogether.* ***b*** *Kymograph line profile (dotted red line in* ***a****)*

To not unnecessarily complicate this experiment, the upper PTFE-barrier was left out, but Figure 4.4-30-a included a marker which indicates the exact distance where the tip with the PTFE-membrane in the upcoming experiments would be. Furthermore, to enable an easier assessment of the diffusion, a kymograph line profile was generated and superimposed with the time and the theoretical oscillation distance. This shows that even though the substrate would penetrate the oscillation volume, it would not do so for several hours, which gives a broad window to screen for optimal damping conditions and to observe short and longer lasting damped oscillations.

Just like for the stable oscillations, there are many parameters that can alter the oscillation pattern, amplitude, frequency and the general duration. So, it is important to keep as many of those variables static while only changing a select few. Parameters like the oscillation length, the injection flowrate and volume and also the concentration of functional components entrapped within the capsules will be kept constant. Instead, the substrate concentrations were varied between a defined set of conditions to gain a broad understanding about the effect on the damping and the oscillation. The glucose- and H_2O_2-concentration were altered between 100 mM, 80 mM, 60 mM glucose and 210 mM, 150 mM and 90 mM H_2O_2 respectfully, which resulted in 3X3 combinations of concentrations to

examine. To ensure a separation of the two phases, the H_2O_2-solution was mixed with 3 wt% sucrose. Since both phases were visually indistinguishable, the H_2O_2-phase was assumed to form a thin layer like it was observed for the methylene blue diffusion experiment. The capsule was always added to the device with a pre-nucleated oxygen bubble, and the experiment was started by addition of the substrate solution, once the capsule began to descend down from the PTFE-membrane. The results of each condition are summarized in Figure 4.4-31-a, showcased as vertical displacement plots.

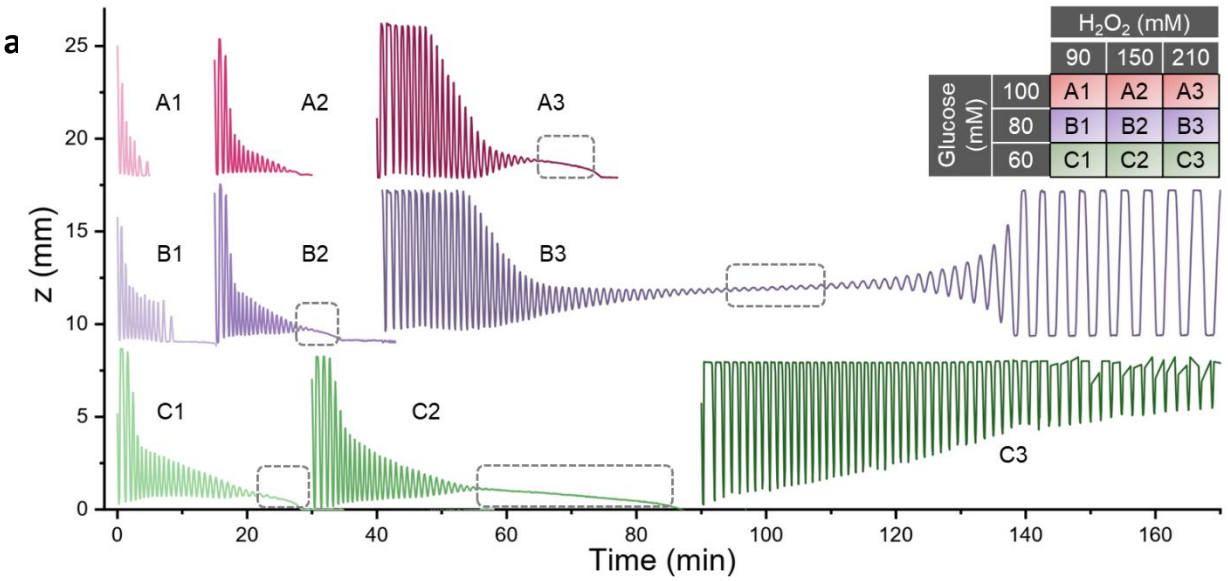

***Figure 4.4-31**: **a** Summarized results of the damped oscillation studies. Each graph shows the vertical displacement of a single protamine/DNA microcapsule at the respective substrate concentration, which are highlighted in the table. The oxygen-producing H_2O_2-layer was mixed with 3 wt% sucrose before injecting 7 µL into the glucose layer at 5 µL/min, which settled on the bottom of the cuvette. The oscillation was captured via digital camera and the capsule tracked digitally through a tracking plugin for the image analysis software "ImageJ". **b** Digital camera images of an oscillating protamine/DNA-microcapsule between the bottom of the device and the PTFE-membrane (8 mm distance). The injected hydrogen peroxide-phase is expected to be settled as a thin layer on the bottom of the cuvette-device.*

As it was envisioned for the previous damping experiments, here the capsule now engaged in oscillation which steadily decreased its oscillation amplitude until it stopped at the bottom of the device. Starting at the top left of Figure 4.4-31, condition A1 depicts the case with the lowest H_2O_2- and the highest glucose concentration (90 mM H_2O_2, 100 mM glucose), which means that the equilibrium is maximally shifted to the side of the oxygen consumption through GOx. As expected, it showed a very short lived oscillation of merely 5 minutes and with only 6 oscillations altogether. Each time the capsule would get in contact with the H_2O_2-phase, it produced a little less O_2 than in the previous cycle, thus causing the oscillation-damping. Substrate diffusion is most likely playing a crucial role in the damping process as it diluted the concentration of H_2O_2 on the bottom of the device.

Increasing the H_2O_2-conentration to 150 mM and 210 mM (Figure 4.4-31-A2, A3) therefore increased the duration and number of oscillations. To gather more data to compare the different damping conditions, Figure 4.4-32 calculates and plots the number of oscillations and the time it took for a full oscillation to come to a standstill. From A1 to A3, the number of oscillations increased from 6 to 24 (Figure 4.4-32-a), while the overall oscillation time went up to about 28 minutes (Figure 4.4-32-b). What is even more interesting is the change of the oscillation pattern. Whereas the capsule in A1 oscillated all the way to the bottom of the device, A2 and A3 showed a brief time period between 0-10 minutes, where the capsule would re-ascend before reaching the bottom barrier. At the same time, the capsule would also oscillate much further to the top side, even colliding with it for 4 minutes (Figure 4.4-31-A2) and 10 minutes (Figure 4.4-31-A3) respectively. Another interesting phenomenon can be seen at the end of the plot from Figure 4.4-31-A3. Even though the capsule oscillated from top to bottom initially, once the damping shows, it oscillated freely without touching any boundary between minute 15-25.

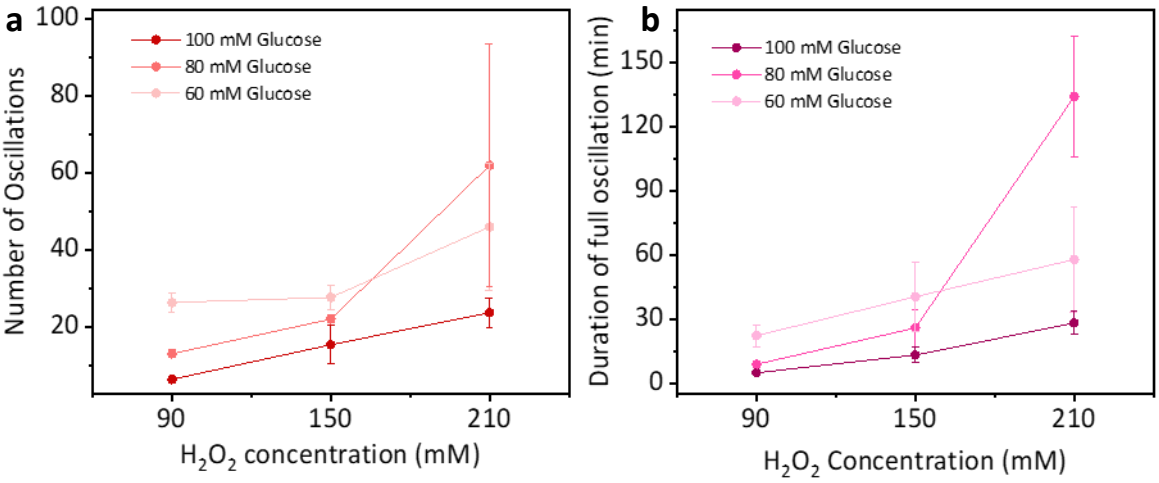

Figure 4.4-32: *Plots to compare the number of oscillations (**a**) and the duration of each full oscillation-experiment (**b**).*

The oscillation would then dampen up to a minimum, from where the capsule was suspended mid-solution, which can be seen between 25-35 minutes. The plot still indicates some small oscillations but it is difficult to tell, considering the experiment was tracked via digital camera images in intervals of 5 seconds, so it would lack the resolution to track very small or fast oscillations. Nonetheless, this is highly interesting, as the capsule and its enzymes approached a point of equilibrium, both chemically and spatially. The capsule has therefore found a location between the diffusing H_2O_2-front and the glucose bulk medium, where the enzymatic rates of GOx and catalase were almost identical. As the remaining H_2O_2 continued to diffuse upwards, the capsule slowly descended to the ground until catalase could not maintain the oxygen bubble anymore.

Decreasing the glucose concentration from 100 mM to 80 mM (Figure 4.4-31-B1) or 60 mM (Figure 4.4-31-C1) while maintaining the H_2O_2 concentration at 90 mM increased the number of oscillations and the general duration in similar fashion like it did for A2 to A3. At the same time, much longer free oscillations were observed like in the case of Figure 4.4-31-C1, where the capsule oscillated without colliding with either side for the full 30 minute length of its oscillation. Figure 4.4-31-C2, with 80 mM glucose and 150 mM H_2O_2 provided a unique case with a very long suspension-period. After ~25 minutes, the capsule barely showed any oscillations anymore, but stayed suspended for almost 30 minutes before it finally settled on the ground. The fact that the capsules in C1 and C2 were not

oscillating against the bottom-barrier anymore, but showed an upwards tendency with each cycle instead, gave a strong hint that catalase and the oxygen-production became more and more dominant. Figure 4.4-31-C3 represents the change from a GOx-dominated, to a catalase dominated oscillation, as the capsule would now oscillate and dampen towards the top-side. The oscillation lasted for ~83 minutes and would have most likely gone even longer, but the capsule came to close to the wall of the cuvette and got stuck between the PTFE-membrane/pipette tip and the glass wall. Since it is impossible to steer the capsule without causing any unwanted mixing effects after the H_2O_2 was injected, many experiments would end prematurely and needed to be repeated when the capsule got in contact with the wall, as it either got stuck or slowed down due to friction.

The statistical analysis from Figure 4.4-32 would predict that the conditions from C3 should produce the longest oscillation periods and the most overall oscillations, but B3 went way beyond that. The oscillation from Figure 4.4-31-B3 started off very similar to A3. The oscillation damped after about 15 minutes and reached its minimum after ~60 minutes. With all the previously discussed cases, it was expected that the oscillation would stop, and the capsule would descend after a short suspension-period. Instead, the capsule would continue to drift upwards while re-initiating its oscillation. After 100 minutes, the capsule had fully re-developed its oscillation amplitude from the bottom to the top barrier and it continued to do so up to 145 minutes after the start of the experiment. Even though the oscillation re-initiated, it is evident that the oscillation frequency went down when comparing the beginning to the end of the experiment. Figure 4.4-33 offers a comparative view on the development of the oscillation periods for the experiments from Figure 4.4-31. What can be taken from these plots is, that the oscillation periods increased faster, the longer the experiment went, which is especially evident for the cases B3 and C3. Another prominent feature of all longer lasting oscillations is an initial decrease of the oscillation periods, usually happening during the first half of the experiment. Like for many of the other experiments before, one of the most likely reasons to discuss is substrate diffusion. As H_2O_2 continues to disperse and dilute, the cell finds progressively less fuel, which slows down the oxygen-generation as well as the cell's motion. While this explains the late increase of the oscillation periods, it does not give many clues about the initial decrease. "Enzyme fatigue" is an important issue for microcapsule oscillations and will be discussed together with the bubble-growth studies in the next paragraph.

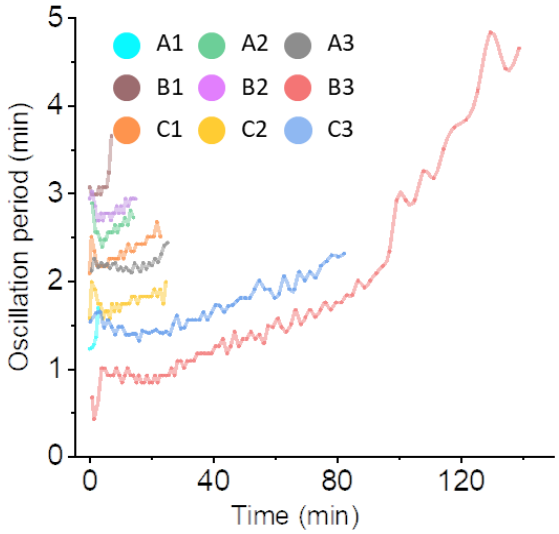

Figure 4.4-33: *Plotted oscillation periods for the damped oscillations from Figure 4.4-31. Each oscillation period is defined as the time it took for the protamine/DNA-microcapsule to finish one full oscillation. To improve the visualisation of the plots, each dataset was offset by a y-value of +0.3 min to the one below.*

The plots above have compared measurable parameters like the oscillation periods or the number of oscillation cycles, but they don't say much about the general oscillation pattern. There are many fine details that can be described during the damped oscillations which will be addressed and compared in Figure 4.4-34. A lot of these effects can be explained through the enzymatic interaction between GOx and catalase. If GOx is dominating the enzymatic equilibrium, the oscillation would primarily exhibit bottom-heavy oscillations (Figure 4.4-34-A1), whereas on the other side of the spectrum, the capsule would exclusively oscillate against the top barrier (Figure 4.4-34-C3). But it is in between these extremes where the oscillation patterns became interesting. Increasing the H_2O_2-concentration from A1 to A2, showed oscillations going all the way from end to end, and increasing the substrate concentration even further lead to free oscillations and the aforementioned suspension periods. Generally, the further the conditions benefitted catalase and the oxygen-production, the less the oscillation would connect with the bottom-barrier (Figure 4.4-34-A2), and the more free oscillations and longer hovering periods could be found (Figure 4.4-34-B2 and C2).

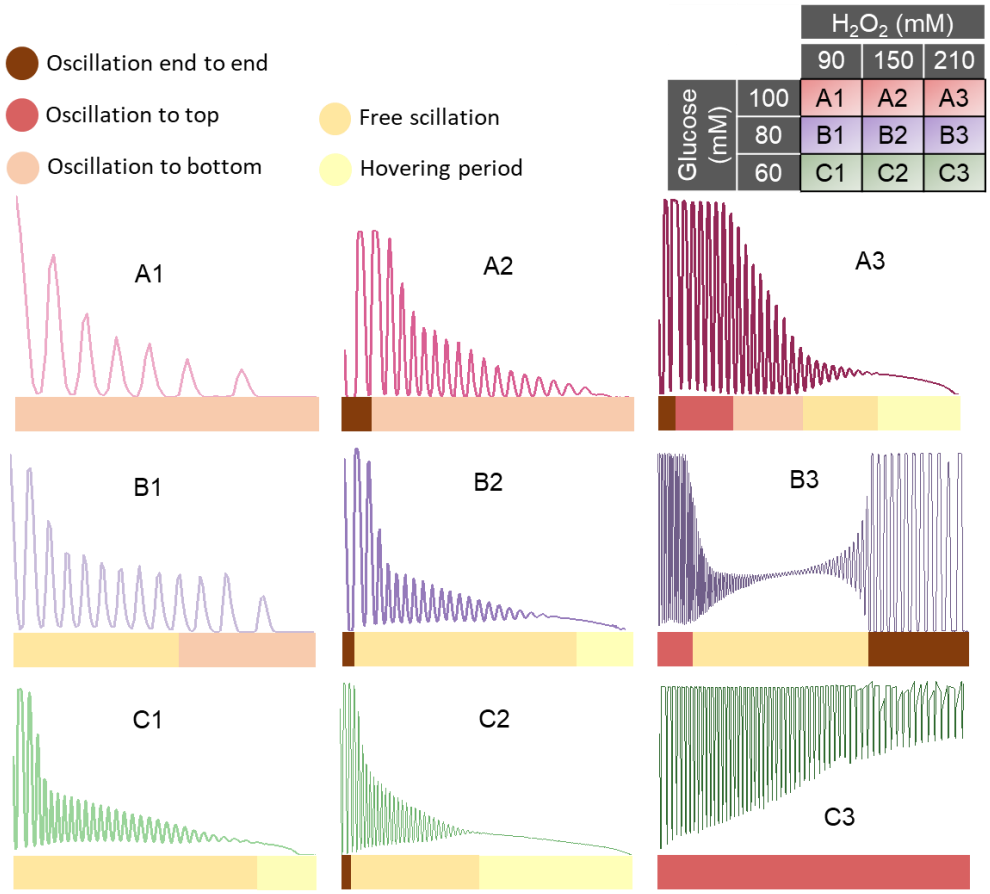

Figure 4.4-34: *Colour coding of distinct oscillation features in order to compare all 9 substrate conditions from Figure 4.4-31. The oscillation patterns were separated into 4 different categories: (**dark red**) Oscillations between both barriers, (**red**) capsules oscillating against the top barrier, (**light red**) capsules oscillating against the bottom barrier, (**orange**) free oscillations without collisions and (**yellow**) hovering periods during which the capsule is suspended within the solution without oscillating.*

These patterns seemed to develop more, when moving vertically between the different conditions, whereas the oscillations against the top barrier increased when moving from left to right (e.g. from A1 to A3). This can be explained by the fact, that an increase in the H_2O_2-concentration would lead to a larger overproduction of oxygen. Generally, the oxygen consumption took longer than the production, which means that the protamine/DNA-capsule will penetrate further into the top phase when increasing the H_2O_2-concentration. On the other hand, reducing the glucose-concentration does

not necessarily increase the oxygen-production rate, but it does decrease the oxygen-consumption. This directly decreases the velocity of the capsule's descent, which then penetrates less deep into the H_2O_2-layer and thus creating the presented oscillation patterns (e.g. from A2 over B2 to C2).

Another interesting question to ask is whether the capsule can re-engage in oscillation when adding more H_2O_2 once the oscillation has come to a halt. Figure 4.4-35 shows the oscillations of 3 different capsules which underwent a second (Figure 4.4-35-red and green) and even a third oscillation cycle (Figure 4.4-35-purple). In every case, the re-initiated oscillations showed a diminished amplitude, while oscillating at a slightly higher z-distance (Figure 4.4-35-red and purple), which is most likely being caused by the diffusion of the H_2O_2 from the first cycle. Lowering the amount of added H_2O_2 only boosted the capsule up for a single oscillation after which it slowly descended to the ground (Figure 4.4-35-green). Re-initiating the oscillation a third time by adding another 5 µL of H_2O_2 showed very similar results, as the capsule would only oscillate briefly before falling back down. All in all, manual re-initiation seems to be possible, but as the substrate diffused over time, the bi-phasic nature of the system deteriorates, which prevented the capsule from engaging into longer lasting oscillations.

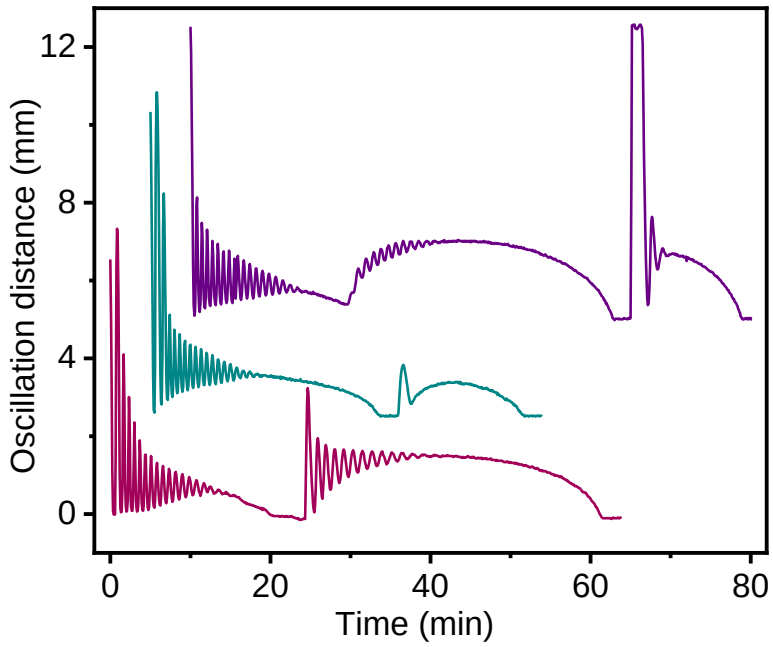

Figure 4.4-35: *Re-initiation of damped oscillations after the capsule came to a halt. The first oscillation was initiated with 210 mM H_2O_2 and the column was filled with 100 mM glucose. A second oscillation cycle was initiated by addition of 5 µL (**red**) or 3 µL (**green**) H_2O_2 (210 mM). In case of the **purple** curve, 5 µL H_2O_2 (210 mM) were added to restart a second and a third oscillation.*

While most oscillation plots show clear tendencies which can be explained by merely discussing the interactions between the enzymes, Figure 4.4-31-B3 still poses some important questions, which need to be addressed with further experimental data, before a solid statement can be made. The previous experiments were done on the assumption, that the diffusion of the injected H_2O_2 is the main contributor to the damping of the oscillation. In Figure 4.4-36, the plot from Figure 4.4-31-B3 was superimposed with the kymograph of the methylene-blue diffusion data from Figure 4.4-30.

As expected, the capsule penetrated into the superimposed H_2O_2-layer at the beginning of the oscillation. What is interesting though, is that the capsule aligned with the diffusing front just at its inversion point where the oscillation changed from an oxygen-depleting to a producing one (Figure

4.4-36). For a brief moment, the capsule would even rise parallel to the upwards diffusing front, as if it is oscillating just around the interface. Once the oscillation amplitude increased, the diffusing interface still seemed to be within the centre of the oscillation. With this information, it can be assumed that the capsule is indeed reacting to the interface of the H_2O_2 front by oscillating around it. Once the substrate is diluted enough and the oscillation has reached its minimum amplitude, the capsule will settle just around the interface. But this still does not explain the reason for the re-initiation. From a mere diffusion-related point of view, one of the most complicated parts of this system is the inclusion of sucrose to increase the density of the H_2O_2-solution. It is very difficult to simulate a diffusion based system made from 3 different components of different densities, especially when all three of them are visually indistinguishable. So, for now, there are only assumptions to be made to explain the correlation between the diffusion and the re-initiation of the oscillation. One possible scenario is that the H_2O_2 is released at different speeds, with one top layer quickly diffusing into the bulk which then caused the initial oscillation and damping. At the same time, another layer underneath diffuses at a much slower pace out of the dense sucrose-phase, which would not get in contact with the capsule until the point of inversion, where the capsule suddenly restarted its oscillation and increased its amplitude.

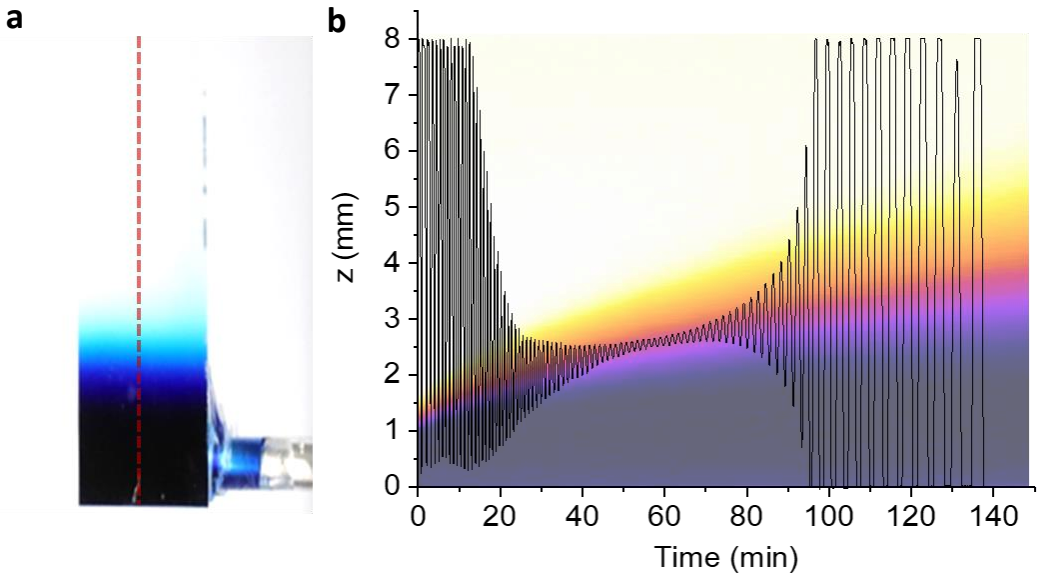

Figure 4.4-36: *Superimposition of the kymograph diffusion data from Figure 4.4-30 (**a**) and the plot B3 from Figure 4.4-31. The kymograph was coloured, and its contrast was increased through the "ImageJ – Lookup tables", to increase the contrast of the diffusing H_2O_2-interface (**b**).*

While the diffusion of H_2O_2 is an important factor and most likely contributes to the peculiar re-initiation from Figure 4.4-31-B3, this work requires more information to gather a proper understanding of both stable and instable damped oscillations. In part 4.4.5, the oxygen-bubble growth and depletion will be the focus of the investigation, to understand the dynamics regarding different substrate concentration mixtures. Furthermore, enzyme fatigue or leakage will be discussed and investigated experimentally and theoretically, to come to a conclusion on the matter of the presented re-initiation of oscillations.

4.4.5 Bubble volume studies and the discussion of "enzyme fatigue"

The previous studies were solely focused on the displacement of the oscillating microcapsule which can be seen as a secondary effect of the enzymatic cascade. The primary and much more relevant indicator of the enzymatic interaction is the size of the oxygen-bubble, which then directly correlates to the capsule's ascent or descent. The context of the previous statement can be visualised by going back to the oscillation-studies from the previous part, only this time, instead of the location of the capsule, the bubble-volume was tracked as well. Figure 4.4-37 shows two cases, one capsule oscillating under stable conditions, whereas the other one quickly dampens to a standstill.

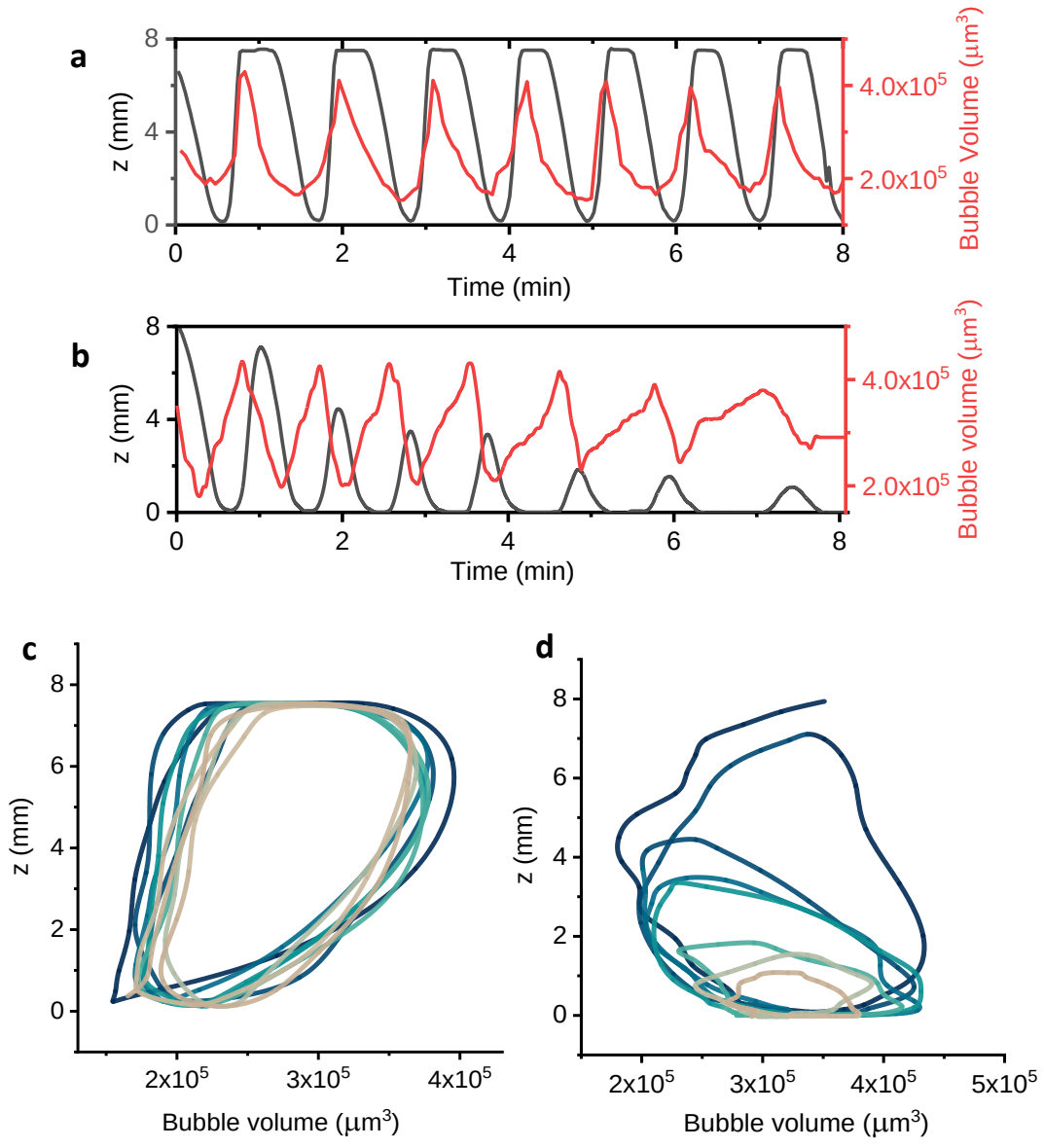

Figure 4.4-37: *Parallel tracking of the bubble volume and the displacement of a stably (**a**) and a damped oscillating protamine/DNA-microcapsule (**b**). Furthermore, the bubble-volume was plotted against the microcapsule-location for both the stable (**c**) and the damped oscillation (**d**).*

What stands out, is that in both cases the plotted lines of the bubble-volume and the capsule location appear to be slightly out of sync, with the bubble volume always changing before the capsule location. Like in a chain of command, the enzymes changed the bubble size, which then made the capsule go

up or down shortly after. This observation can be contributed to the viscous drag the capsule experiences inside the solution. In an ideal system without friction, buoyancy would pull the capsule up immediately, as soon as the bubble starts to grow, but with the laws of physics in place, it takes a little longer, before the capsule overcomes inertia. For this reason, the bubble-volume is a much stronger and more convenient indicator of the enzymatic interaction than the behaviour of the capsule itself. An interesting way of reassembling the datasets is by plotting the bubble volume against the location of the capsule, which changed the plot from an oscillation to a continuous spiral and which can be read to assess the stability of the oscillation. Figure 4.4-37-c shows a very stable loop with only minor variations, which depicts the stable oscillation from Figure 4.4-37-a. In case of the damped oscillation though, the loop diminishes both vertically and horizontally with every cycle until it breaks (Figure 4.4-37-d).

The experimental design from the previous part was ideal for very long and stable oscillations, but it left little room to study stable oscillations with different oscillation patterns, as the capsule would oscillate from end to end most of the times. Here, a different approach will be presented with a clear interface between a continuous oxygen producing bottom- and an oxygen consuming top-phase.

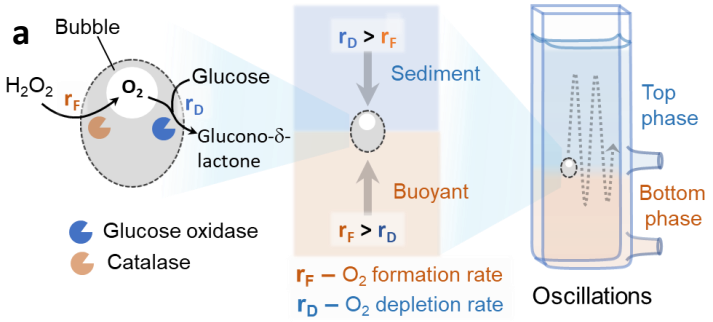

d

	Substrate	i	ii	iii	iv	v	vi
Top phase	Glucose (mM)	100	100	100	100	80	20
	H_2O_2 (mM)	0	0	0	0	6	0
Bottom phase	Glucose (mM)	0	20	40	80	40	0
	H_2O_2 (mM)	30	24	18	18	18	6

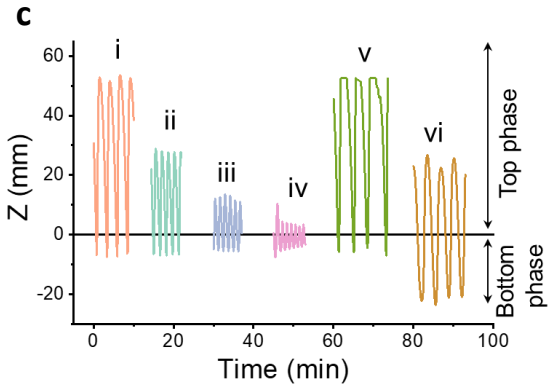

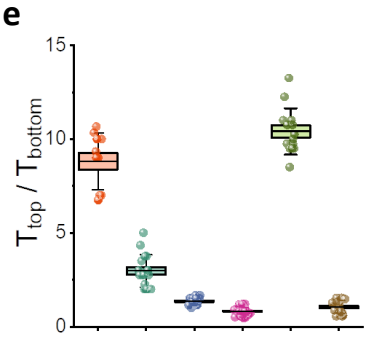

Figure 4.4-38: a *The graphic illustrates the control of overproduction and consumption of an oxygen-microbubble inside a protamine/DNA-microcapsule via the antagonistic interaction between entrapped glucose oxidase and catalase. The reaction rates of the two enzymes are controlled by spatial segregation of the respective substrates inside a vertical water column. By layering the oxygen-consuming glucose-phase (**blue**, top side) on top of an oxygen-producing hydrogen peroxide-phase (**red**, bottom side), the capsule is forced into an oscillatory motion pattern between the interface. Due to the spatial arrangement of the substrates, both driving forces, gravity and buoyancy, are alternatingly counteracted, which keeps the system out of equilibrium.* ***b*** *The image shows the glass column with the oxygen-consuming top-phase layered on top of the O_2-producing bottom phase. The interface was highlighted by adding 1 mM methylene blue to the bottom-phase.* ***c*** *The plots show the time-dependant vertical displacement of single protamine/DNA-microcapsules around a glucose- (bottom phase)/H_2O_2-interface (top phase). The respective concentrations of each phase are referenced in figure (**d**). The interface was plotted at z = 0 mm.* ***e*** *The box-plots show the calculated residence time-ratios T_{top}/T_{bottom} for the interface oscillations i-vi from fig. **c**.*

This concept enabled the investigation of conditions for both the top and the bottom-phase to assess whether they are suitable to promote microcapsule oscillation and also to investigate how the substrate concentration changes the oscillation pattern. While the latter is very interesting in regard to stable oscillations, the focus should lie on how the equilibrium between the O_2-production and consumption is influenced by the various substrate conditions. Experimentally, a 3% sucrose content in the bottom phase prevented the two solutions from mixing as they were gently layered on top of each other by utilising a syringe pump system attached to the tubes on the side of the glass-device (Figure 4.4-38-a). In order to produce different oscillation-patterns, the mixtures of glucose and H_2O_2 were adjusted for both phases according to the conditions in Figure 4.4-38-d.

Figure 4.4-38-c summarizes the oscillations under the concentration-conditions **i-vi**. Furthermore, the residence times in each phase were calculated and expressed as the residence time ratio T_{top}/T_{bottom} in Figure 4.4-38-e. Experiment **i** represents the closest case to the stable oscillation experiments from the previous part, with the top- and bottom-phase only containing one substrate respectively. Seen by the long oscillations towards the top phase, these conditions favour the oxygen-production with only very short residence times in the bottom phase. Since catalase and the oxygen-producing side were generally more responsive, the oxygen-production was progressively decreased in the bottom-phase from experiment **ii** to **iv** by either reducing the H_2O_2-concentration from 30 to 18 mM or increasing the glucose content from 0 to 80 mM. In return, this change drastically decreased the residence time in the top phase, while only slightly decreasing the time the capsule spent in the bottom phase. Parallelly the oscillation distance decreased from about 60 mm (**i**) over 35 mm (**ii**), 18 mm (**iii**) to 9 mm (**iv**) respectively. Interestingly, experiment **iv** showcased the most symmetrical oscillation around the interface, with the capsule almost travelling the same distance in both phases. Reducing the substrate concentrations to 20 mM glucose (top phase) and 6 mM H_2O_2 (bottom phase) in experiment **vi** produced very similar and symmetrical results, but with much longer oscillation distances (~ 40 mm).

The residence time ratio is a good and easy to read indicator to understand the dynamics between the enzymes during the oscillation. The higher the number, the more the system is shifted towards the oxygen-producing side, which can be seen for the experiments **i-iii**, but with the number approximating 1, the system would not only oscillate more symmetrically but it can also be assumed that the enzymatic rates of catalase and GOx will be very similar. Finally, experiment **v** shows an extreme case of oxygen-production, where the capsule still engaged in oscillation but would repetitively ascend to the air/liquid interface at the meniscus of the top phase, where the capsule resided for several minute before descending back down. On the one hand, these datasets offer some interesting insight into how the oscillation-length, or the amplitude, can be altered by changing the substrate concentrations around a clearly defined interface. On the other, they present distinct concentrations which are either oxygen-producing or consuming. The latter is a very important thing to understand, as it ultimately helps to predict whether a specific 2-phase system is suitable for microcapsule oscillation or not.

The following experiments aimed to understand whether a certain glucose/H_2O_2-micture is either causing oxygen-production or consumption within catalase- and GOx-containing protamine-microcapsules. To further highlight the equilibrium between O_2-production and consumption, the concentrations chosen for these experiments approximate the point at which one enzyme starts to overpower the other. To provide a high standard of reproducibility, the experiments were performed inside a 96-well plate with a defined volume of 100 µL of the respective substrate mixture. Furthermore, the O_2-bubble was generally pre-nucleated externally and then pre-incubated in a 0.1 M glucose-solution. The latter ensured, that all capsules entered the experiment inside the well-plate at

the same point in time, which was at the moment, the capsule started to descend within the glucose solution. The O_2-bubble inside the capsule was then tracked via microscope and later used to calculate the bubble-volume and its growth rates (Figure 4.4-39-c). Altogether, an array of 36 different concentration-combinations of hydrogen peroxide (0, 6, 12, 18, 24, 30 mM) and glucose (0, 20, 40, 60, 80, 100 mM) was investigated. The growth rate plots in Figure 4.4-39-d+e show that the oxygen-production rates are about 100 times higher than the consumption rates while working under much lower H_2O_2- than glucose concentrations, which correlates well with the statements made in previous experiments that catalase and the O_2-production are a lot more responsive and faster. The plots furthermore show that the bubble-growth rates did not increase linearly but rather exponentially or in a sigmoidal shape like it was the case for 30 mM H_2O_2 in Figure 4.4-39-e and for 0 mM glucose in Figure 4.4-39-d.

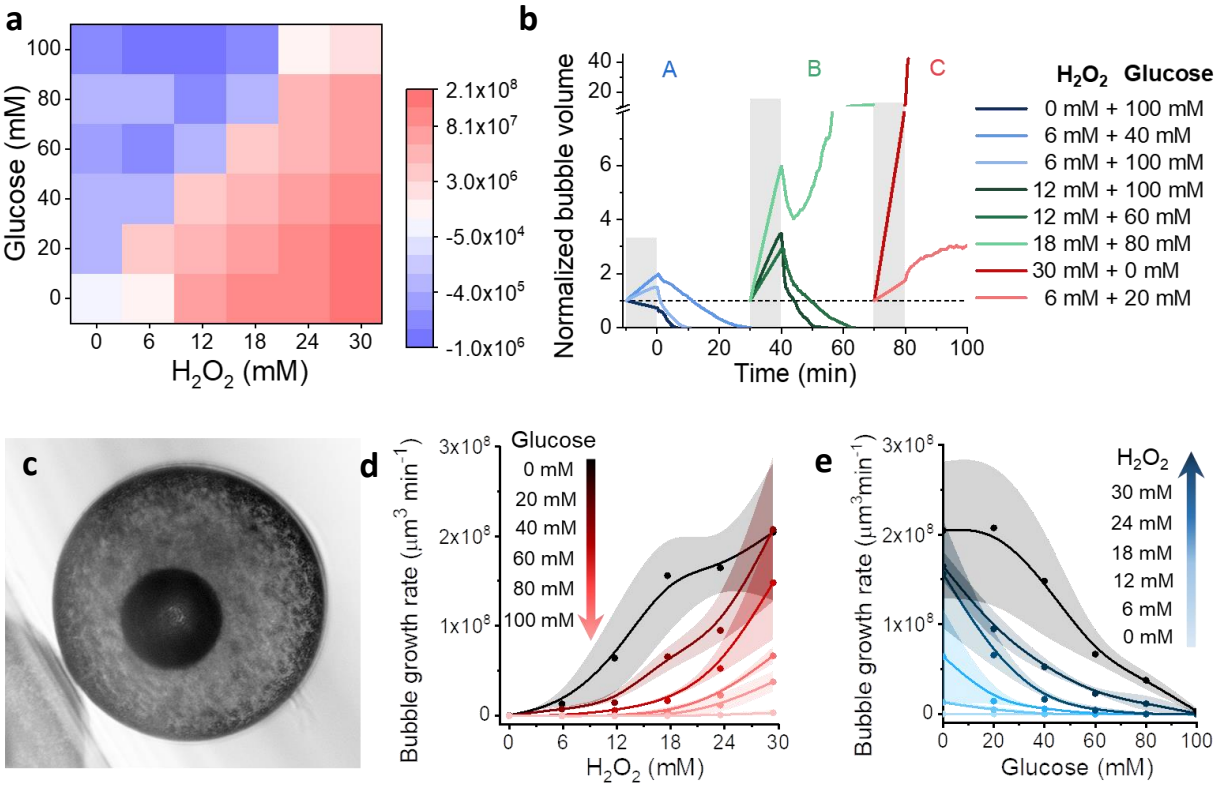

Figure 4.4-39: *Bubble growth studies performed inside a 96-well plate. The capsule was added to 100 µL of the respective glucose/H_2O_2-mixture according to* ***a*** *and the bubble volume was tracked microscopically.* ***a*** *The heatmap illustrates oxygen-producing and consuming conditions in various glucose (0, 20, 40, 60, 80, 100 mM) and H_2O_2-mixtures (0, 6, 12, 18, 24, 30 mM). Bubble growth is depicted in red, whereas bubble depletion is shown in blue.* ***b*** *The plot shows the time-dependant volume change of the oxygen-bubble inside a protamine/DNA-microcapsule.* ***c*** *Microscope image of a protamine/DNA-microcapsule with an internal oxygen bubble inside a 96-well plate.* ***d+e*** *Plotted growth rates associated with the concentrations of the heatmap in* ***a****. The growth rates were calculated by linear approximation of the tracked bubble-volume over a time period of 30 minutes.*

The growth rates were then plotted into a heat-map format, which was colour-coded according to the velocity of the growth-rate, with blue as the O_2-consumption-dominated- and red as the production-dominated medium. This is not only a very descriptive and accessible way to present data, but also enabled a simple visual assessment of the predominant state between the two enzymes. By spanning an imaginary diagonal from the bottom left to the top right, the graph can be divided into an oxygen-depleting and an oxygen-producing domain. The growth-rates in the oxygen-producing domain behaved mostly as predicted, with the velocities growing as the H_2O_2-concentration was increased,

while going down with an increase in glucose. The blue domain on the other hand did not exhibit so much regularity, as some cases showed lower oxygen-consumption rates even though they should have been higher (Figure 4.4-39-a, 80 mM glucose/6 mM H_2O_2) whereas others turned out to be oxygen-producing even though they were expected to be the opposite (100 mM glucose/24 mM H_2O_2). This could be explained due to the fact that the growth rates did not change linearly with the concentration as it was stated above. With this information, it was possible to locate the point of equilibrium somewhere between the two domains, right along the diagonal. Figure 4.4-39-b shows the bubble-growth plots for two extreme cases in each domain (0 mM H_2O_2/0.1 M glucose and 30 mM H_2O_2/0 M glucose) and for several combinations along the equilibrium diagonal. Many of those results came without much surprise, as the bubble would grow or shrink decreasingly fast, the closer the conditions moved towards the equilibrium diagonal. An interesting phenomenon, which could be observed for most datapoints in the blue domain close to the diagonal, was an initial increase in bubble size as soon as the capsule entered the substrate solution, after which the bubble began to shrink. Since no further studies have been done on enzyme responsiveness, there can only be assumptions at this point, but it seems likely that catalase reacts quicker than GOx, which caused a sudden spike in O_2-production, before GOx was able to achieve the same or higher reaction-rates. What stood out more than anything else was another domain and more specifically the condition with 18 mM H_2O_2 and 80 mM glucose. Whereas the surrounding datapoints (Figure 4.4-39-b: green plots) would also show an initial increase followed by a steady oxygen-depletion, here the bubble would grow first, shrink for ~10 minutes, but then start growing again until the end of the experiment. This is highly interesting and strongly resembled the aforementioned re-initiation of oscillation, which was documented in Figure 4.4-31-B3.

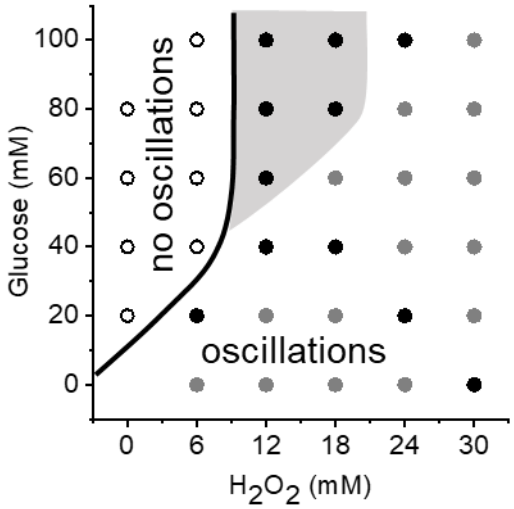

Figure 4.4-40: *This plot assesses the viability of 36 concentration-combinations of H_2O_2/glucose-mixtures for protamine/DNA-microcapsules to engage in oscillation. The respective combination of H_2O_2 and glucose-concentrations was mixed and used as the bottom phase, whereas 0.1 M glucose served as the top phase within the previously presented interface oscillation device (see Figure 4.4-38-a). All concentration-combinations which lead to oscillations are described with* ***black dots****, whereas the* ***hollow dots*** *refer to instances of no oscillation.* ***Grey dots*** *are theoretically expected oscillations, which have not yet been experimentally confirmed and the grey area outlines the datapoints which were expected to show oscillation but did not.*

In the following experiment, the various concentrations from Figure 4.4-39-a were used as the bottom phase in the previously presented interface oscillation device from Figure 4.4-38, in order to confirm whether the established oxygen-producing- and consuming conditions can be used in a microcapsule-oscillation experiment, to predict whether the capsule would oscillate or not. A 0.1 M glucose-solution was used as the top-phase and the results are displayed in a trinary heatmap (Figure 4.4-40), which

qualitatively assessed whether the capsule engaged in oscillation (black dots) or not (hollow dots). As the dataset did not require an investigation of every O_2-producing condition from the previous heatmap (Figure 4.4-39), the remaining ones were simply logically deducted and marked as hypothetic grey dots.

As oscillation can only happen when the bottom-phase is predominantly O_2-producing, it was expected that Figure 4.4-40 would be equally divided into two domains of oscillation and non-oscillation. Most datapoints were indeed coherent with the previous heat-map, except for 5 conditions (Figure 4.4-40-grey area), which turned out to facilitate oscillations, even though they were previously confirmed as O_2-depleting. Interestingly, this includes the same datapoint at 18 mM H_2O_2/80 mM Glucose, which exhibited the unique behaviour which was reported previously. To explain these unexpected oscillations, one has to go back to Figure 4.4-39-b where the capsules experienced an initial bubble-growth, before it started to shrink. The same phenomenon can be used to explain the oscillations. Once the capsule penetrated the bottom-phase, GOx took a little more time to react than catalase, which caused an immediate O_2-overproduction and the cell ascended before GOx had even reached its maximum enzymatic rate.

An important question that still needs to be addressed is the re-initiation of bubble growth or oscillation which have been reported over the past experiments. Chapter 3 has already discussed the effect of enzyme leakage from the cells when exposed to media with a high ionic strength like buffers. Indeed, neither glucose, nor sucrose or H_2O_2 is of ionic nature, but GOx produces gluconic acid, which is much more likely to cause enzyme leakage from the cells. Another possible scenario is an “enzyme fatigue” caused by prolonged activity or exposure to high concentrations of substrates. The following experiments will discuss these effects regarding the conditions used for protamine/DNA-microcapsule oscillation.

The oscillation re-initiation from Figure 4.4-31-B3 and the unexpected bubble growth from Figure 4.4-39-b all happened in a continuous glucose-bulk phase. For this reason, and since GOx is a lot easier to assess its enzymatic activity, this enzyme will be the focus on the following studies. Here, a custom-made continuous flow stirred reactor was designed to assess whether the enzymatic activity of GOx entrapped within protamine/DNA-microcapsules changed over time. For each experiment, 30 capsules were added to the reactor, through which a solution of HRP (2 U/mL), glucose (0.2 M) and ABTS (2,2'-azino-bis(3-ethylbenzothiazoline-6-sulfonic acid, 0.33 mg/mL) was pumped. On the other side, the CSTR was connected to a UV/VIS-spectrometer, measuring the absorbance of oxidised ABTS at 420 nm (Figure 4.4-41-a). Figure 4.4-41-b shows the time-dependant absorbance over a time-period of ~150 minutes. At t = 0, the flows were started and the enzymes began to interact with the injected substrate. Once the oxidised ABTS had reached the detector, the signal started to increase after 2 minutes and peaked after about 7 minutes. After ~10 minutes, the absorbance started to drop again and continued to do so in sigmoidal fashion up to a minimum after about 120 minutes. Effectively, the peak activity only lasted for about 10 minutes before the signal diminished to about 15% of the original intensity. While this does not answer the question of why the signal or the enzymatic activity decreases, it provides some important information on when the “fatigue” starts, which is about 10-15 minutes after the cell got in contact with the substrate. And indeed, there are some similarities between the GOx-activity-assay above and the 80 mM glucose/18 mM H_2O_2-sample from the bubble growth plots in Figure 4.4-39-b. In both cases, the activity of GOx seemed to start its decrease within a time frame of 10 to 20 minutes (Figure 4.4-42-a). Of course, one has to take into account that both experiments were very different in the way they were performed. The growing and shrinking bubble was a direct effect of the enzyme’s reaction and could be observed in real time, whereas the

spectrometric data came with a delay due to the flow/CSTR-system, which also contained 30 capsules instead of just one.

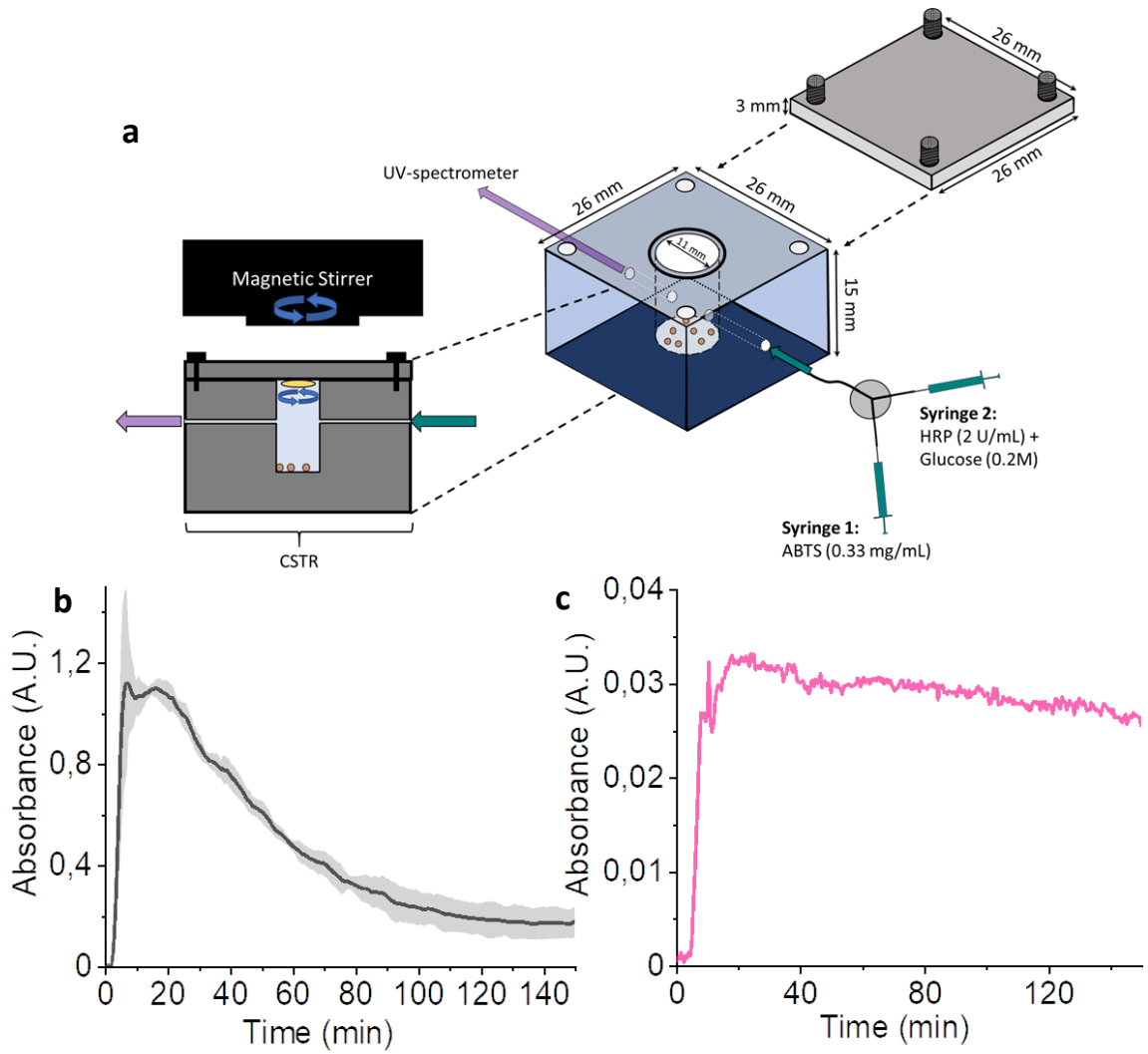

***Figure 4.4-41**: **a** „Enzyme fatigue"-assay with a custom-made continuous flow stirred reactor (CSTR, Volume V_{CSTR} = 855 µL, see Methods 4.3.23). 30 GOx and catalase containing protamine/DNA-microcapsules were added into the reactor chamber and sealed with a lid. HRP (2 U/mL), glucose (0.2 M) and ABTS (0.33 mg/mL) were injected into the reactor via syringe pumps at a flow rate of 0.25 mL/min, which refreshed the reactor-volume with a rate of F_{CSTR} = 0.29/min. The reactor was connected to a UV/VIS-spectrometer to read the absorbance of oxidised ATBS at a wavelength of 420 nm. **b** Plotted absorbance of oxidised ABTS and of a reference without ABTS (**c**).*

Furthermore, the change in bubble size is the product of both, GOx and catalase working against each other, which makes it impossible to directly compare the bubble size to the GOx activity. Nonetheless there seems to be a diminishing factor once the cells are in a continuous glucose environment. Now, this new information can be used to explain the re-initiation of oscillation from Figure 4.4-31-a-B3, which will be described in Figure 4.4-42-b. At the beginning, the capsule oscillated as expected by shifting from a stable oscillation to a progressive amplitude damping, which means that GOx is becoming the dominant enzyme at this stage. Once the oscillation reached its minimum after 40 minutes, the capsule retained a minimal oscillation for about 20-40 minutes, at which point GOx and catalase worked at almost identical rates. At the same time, GOx keeps losing more and more of its activity until the equilibrium between the two enzyme shifts to the other side and catalase becomes

the dominant enzyme. This moment can be marked at exactly 60 minutes of the plot in Figure 4.4-42-b. After that, GOx keeps losing activity whereas catalase produces more and more oxygen in relation to the consumption and the oscillation restarts.

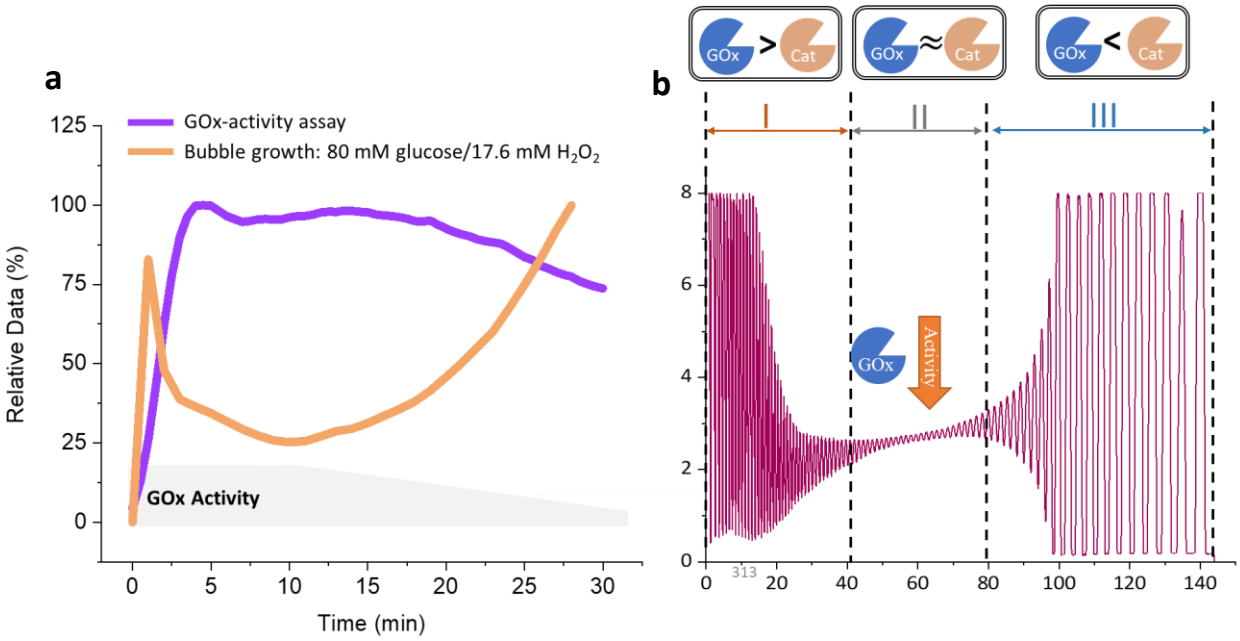

Figure 4.4-42: a *Superimposition of the bubble-growth plot from Figure 4.4-39-b (80 mM glucose/18 mM H_2O_2) with the GOx-activity assay from Figure 4.4-41, to investigate the decrease in GOx-activity over time.* ***b*** *Reassessment of the damped oscillation from Figure 4.4-31-a-B3 to explain the re-initiation of oscillation. The plot is divided into three sections to describe the effect of the decreasing GOx-activity on the oscillation.*

While logical, the explanation above still lacks further information. For one, the model is still solely based on the idea of "enzyme fatigue" which is a very vague term without a proper explanation on what happened to the enzyme or why it lost its activity. Furthermore, catalase was not included into the assumption of "enzyme fatigue". This made sense for the damped-oscillation experiment, as the capsule would only get in contact with H_2O_2 briefly during each oscillation, but not for the bubble growth-experiment, which worked with a continues glucose/H_2O_2-solution. One explanation, that could give a little more detail to "enzyme fatigue", would be oxidative damage from hydrogen peroxide. H_2O_2 is capable of oxidizing other chemical components due to its instable peroxide-bond and it seems feasible that it could also denature or damage GOx or even catalase over longer periods of time. In the following experiment, GOx- and catalase containing protamine/DNA-capsules were incubated in H_2O_2-solutions (19 mM and 6 mM H_2O_2) for up to 3 hours. To assess the damage on GOx, the enzyme's activity was again assessed through a coupled assay with HRP and ABTS. Furthermore, potential enzyme-leakage was investigated through fluorescent microscopy analysis by co-entrapping FITC-catalase and RITC-GOx.

The fluorescence-analysis showed a minor decrease between 18% for FITC-catalase (Figure 4.4-43-a) and 26% for RITC-GOx (Figure 4.4-43-b) after about 60 minutes. Leaving the capsules in the H_2O_2-solution for longer than 60 minutes did not seem to deteriorate the signal further. The colorimetric GOx-activity assay showed similar results (Figure 4.4-43-b). After 30 minutes, the cells appeared to have a slightly diminished activity, which did not seem to decrease much further for longer incubation times. The fluctuations between the remaining datapoints most likely stems from experimental errors, as there did not seem to be a logical trend between them. Furthermore, decreasing the H_2O_2-concentration to 6 mM did not change the outcome of the experiment in any meaningful way. So,

while this could be an indicator for oxidative damage of the enzymes, it appeared to be very minor and did not necessarily correlate with the observations from Figure 4.4-41.

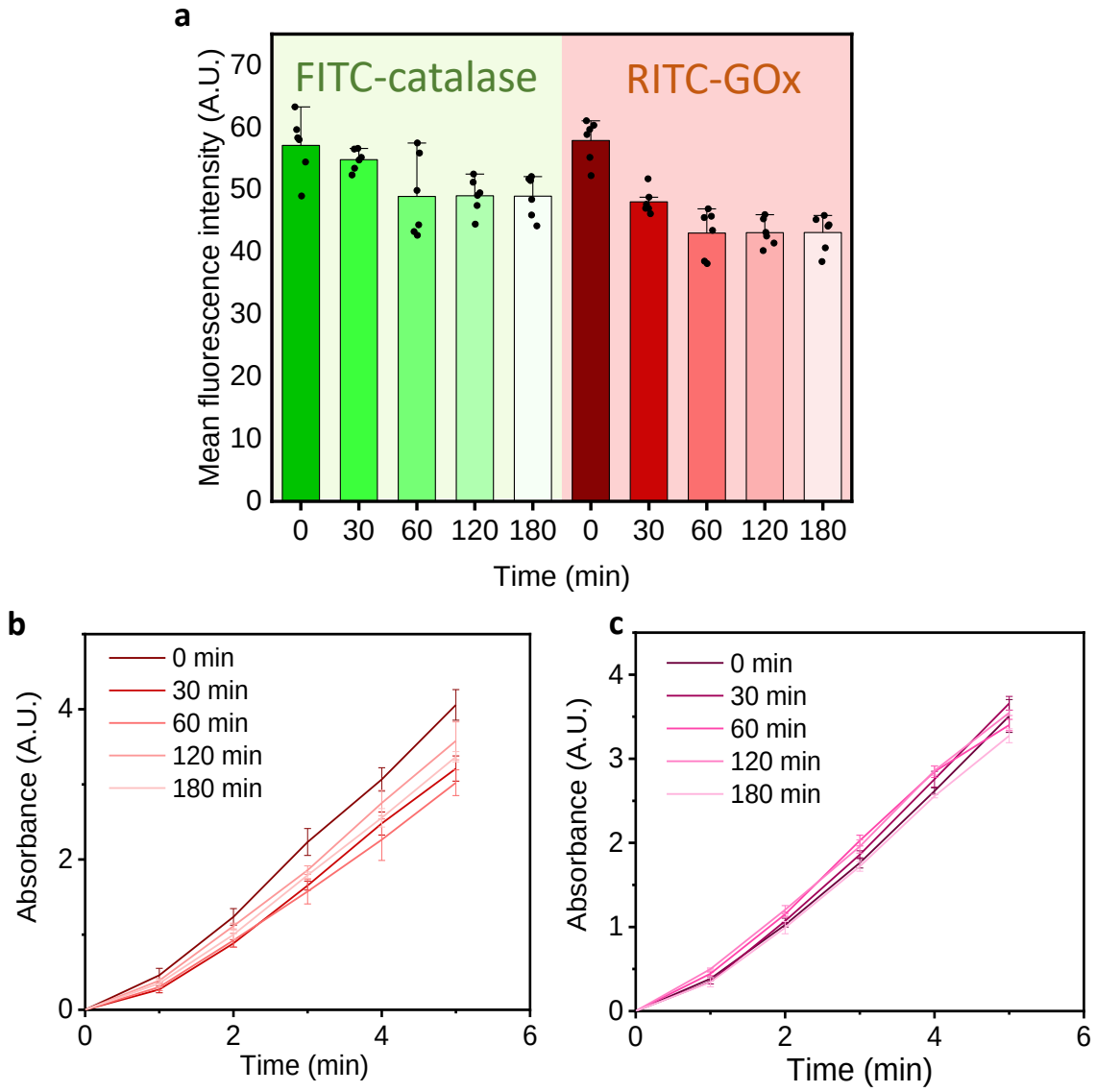

Figure 4.4-43: *Investigation of enzyme leakage or damage after incubation of protamine/DNA-microcapsules in H_2O_2-solution (19 mM).* ***a*** *The mean fluorescence intensity was determined for 6 capsules and plotted before and after incubation in H_2O_2 for FITC-catalase and RITC-GOx.* ***b*** *To assess the GOx-activity spectroscopically after H_2O_2-treatment, the capsules were mixed with ABTS (8.19 mM), HRP (8.3 U/mL) and Glucose (25 mM). Each measurement was done with two capsules and the absorbance was measured at 420 nm.* ***c*** *GOx-activity assay to understand the protective role of catalase. Cells were made identically but without entrapping catalase and FITC-catalase.*

Another important question is whether catalase provides any form of protection for co-entrapped enzymes like GOx. This time, cells were fabricated without entrapping catalase and FITC-catalase before incubating them in H_2O_2. As the results from Figure 4.4-43-c show, there is no distinguishable difference between the plotted curves, not even from 0 to 30 minutes, which further supports the assumption, that oxidative damage or enzyme leakage caused by H_2O_2 is a negligible error.

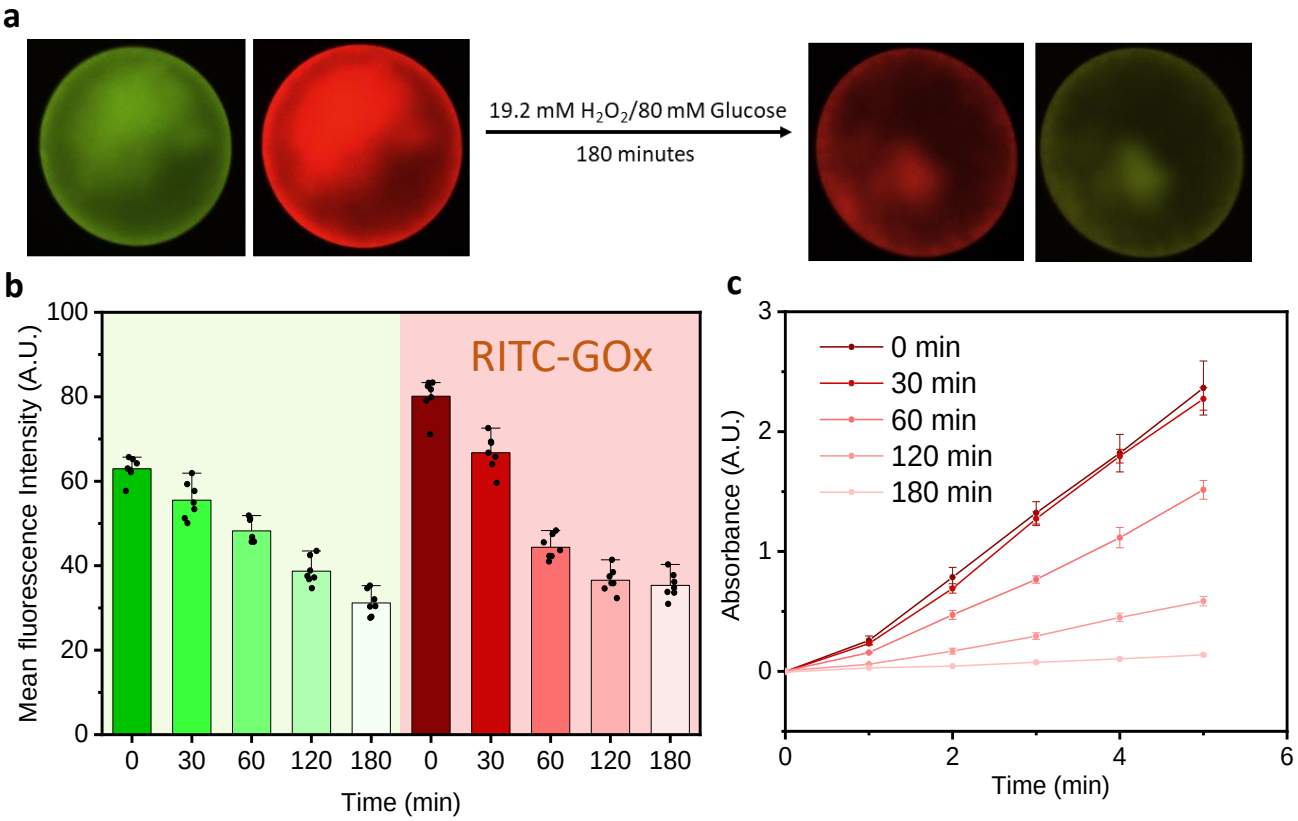

Figure 4.4-44: *Investigation of enzyme leakage from protamine/DNA-microcapsules in glucose solutions.* ***a*** *Fluorescence micrographs of capsules with FITC-catalase (**green**) and RITC-GOx (**red**) before and after incubation in 80 mM glucose/19 mM H_2O_2.* ***b*** *Bar-scatter-plots showing the mean fluorescence intensity of 7 capsules after distinct time-periods, coming from entrapped FITC-catalase and RITC-GOx.* ***c*** *UV/VIS-spectroscopy-data of the GOx-activity assay with ABTS and HRP, measured at 420 nm (ABTS (8.19 mM), HRP (8.3 U/mL) and Glucose (25 mM)).*

Next, Figure 4.4-44 utilises the same experimental techniques to investigate GOx and glucose as a potential cause for the deterioration of enzymatic activity on the cells. In reference to the bubble-growth studies above, a mixture of 80 mM glucose and 19 mM H_2O_2 was used to provoke enzyme leakage by incubating the cells for up to 180 minutes. Similar to the previous experiments, RITC-GOx and FITC-catalase were co-entrapped next to native catalase and glucose oxidase, in order to enable a microscopic analysis. Figure 4.4-44-b determined the mean fluorescence intensity of the cells after distinct time periods for both fluorophores. And indeed, this time the fluorescent signal continuously decreased, the longer the cells were left in the glucose/H_2O_2-solution. After 180 minutes, the signal-intensity was almost halved for both FITC-catalase and RITC-GOx (Figure 4.4-44-a+b) and the trend indicated that it would have decreased even further afterwards. The spectroscopic analysis of the GOx-reaction rate on the other hand not only showed a progressive decrease of the signal the longer the cell resided in the substrate-solution, after 180 minutes there was barely any measurable activity left (Figure 4.4-44-c). This is surprising, as the fluorescence-studies would imply a remaining activity of about 50%. Both datasets are not directly comparable though, even though they are supposed to investigate the same issue. Instead, they should be seen as supportive, rather than correlating information. The microscopic analysis relies on tagged enzymes, whereas the spectroscopic analysis assesses both RITC-GOx and native GOx, considering they are in an "active" state. This means, that the microscopic studies could visualise more "inactive" enzymes, which are still entrapped, and which would not show during the colorimetric analysis. Considering how established the HRP/GOx-cascade-reaction with ABTS is as a tool to assess GOx-reaction rates and the qualitative activity [106,107], and

since the effective enzymatic activity is the only relevant factor for the oscillation experiments, the spectroscopic dataset should contain more value than the microscopic studies. While it would be interesting to assess the supernatant as well, to prove that the enzymes are actually leaking off the capsules like it was shown in Figure 3.4-28, it was not feasible for this experiment, as H_2O_2 was already part of the solution the microcapsules were incubated in, which would give a positive feedback with HRP and ABTS no matter if GOx leaked off the cells or not. Either way, the datasets indicate that GOx and catalase are both deteriorating or leaking off the capsules when in contact with glucose for a prolonged period of time. The only reasonable explanation for this phenomenon is the produced gluconic acid from the reaction of GOx with glucose. Just like in the leakage experiments in chapter 3, the increasing ionic strength due to the released gluconic acid interferes with the electrostatic interactions between the enzymes and the cells until the enzymes desorb and diffuse out of the protamine/DNA-condensate. And indeed, it only took between 10-60 minutes to cause a relevant decrease in the GOx-reaction rate, which could very well be enough to shift the antagonistic equilibrium between catalase and GOx to the O_2-producing side during the oscillation of the protamine/DNA-microcapsule from Figure 4.4-31-a-B3. While more experiments will be needed to properly prove oscillation- or bubble-growth re-initiation, the leakage-studies should lay a good foundation to explain these phenomena.

4.5 Summary and Outlook

Chapter 4 utilised the fundamental research from chapter 3 to establish a rudimentary form of cell-motility via buoyancy in AMP/DNA- and protamine/DNA-microcapsules. The first half of this chapter focused on the introduction of microcapsule buoyancy via internal oxygen-bubble nucleation. Both capsule-types have shown to be able to entrap catalase and to produce internal oxygen-bubbles when immersed in a H_2O_2-environment. The buoyant ascent and the correlation between O_2-bubble nucleation and the catalase- and H_2O_2-concentration were analysed statistically to establish optimal working conditions to induce microcapsule buoyancy. The bubble inside the capsule not only changed the buoyancy dynamics, but also altered the capsule up to the point of irreversible damage once the membrane was not able to withstand the pressure of the growing O_2-bubble. The bubble growth was analysed microscopically for both cell types and the membrane stability was assessed by comparing the rupture points to the areal strain the capsules had to endure. These experiments, in combination with the previous stability studies from chapter 3, lead to the important conclusion, that protamine/DNA-capsules proved to be much more stable and reliable to work with than AMP-capsules, which lead to the decision to utilise protamine/DNA-capsules for all following studies.

To expand the concept even further, glucose oxidase was introduced as a chemical antagonist to catalase, which enabled the consumption of the O_2-bubble and forced the capsule to descend. By spatially separating the O_2-producing-(H_2O_2) from the O_2-depleting medium (glucose), the capsules were able to oscillate freely and independently. To ensure experimental reproducibility, a novel flow-device was designed. Its flow-properties were analysed through diffusion studies with methylene-blue, which helped to understand the complex flow- and diffusion dynamics of a multi-phase system. With this device, microcapsules were able to oscillate stably and without any external interaction for over 12 hours. The oscillations were then analysed by comparing different substrate concentrations, which resulted in an extensive amount of information about the general lengths of oscillations, oscillation periods and patterns.

More advanced oscillation patterns were then created in form of so called damped oscillations. The damping was either found in form of a damping of the oscillation periods, or in form of the oscillation distance. The former was realised within the stable oscillation device, whereas the latter could only be shown in a much smaller cuvette-device, which was modified for this purpose, and which was solely based on substrate diffusion. The investigation of these damped oscillations over many different substrate concentrations showed fascinating and unique oscillation patterns. One distinct case presented a damping followed by a re-initiation of oscillation, which was not reported in any other experiment. As this observation was initially hard to explain, it was investigated from three different perspectives: the H_2O_2-diffusion within the device, the bubble growth-dynamics and the stability of the enzymes on the cell. The former was simply realised by replacing the substrate with methylene blue, which enabled a visual representation of the substrate diffusion within the glucose solution.

To understand the bubble-growth dynamics, protamine/DNA-capsules were examined microscopically in a variety of different glucose/H_2O_2-concentration mixtures. From these datasets, the bubble growth rates were calculated, which enabled a distinction between O_2-producing- and O_2-consuming domains in form of a colour-coded heatmap. Interestingly, these studies resulted in another case, which showed a reversal of the growth-dynamics, where the bubble would initially deplete and then start growing again. Furthermore, by analysing the oscillation of microcapsules around a clearly defined substrate-interface within a column, it was possible to define a second heatmap, which depicted the conditions which enabled oscillation, and which did not.

Finally, the enzymatic stability was assessed through fluorescence microscopy and HRP/ABTS-assisted colorimetric assays. These studies confirmed, that H_2O_2 did neither lead to any oxidative damage to GOx nor did it cause any enzymes to leak off the cells. On the other hand, it provided sufficient proof, that the enzymatic conversion of glucose to gluconic acid interfered with the enzymes on the cells, which showed in form of substantial leakage into the surrounding medium. From the current point of view, this leakage was caused by the electrostatic interaction of gluconic acid with the enzymes or the material of the protamine/DNA-condensate. Nonetheless, there is still no experimental proof which could explain the exact mechanism why the enzymes are leaking off the cells. While this theory would explain the two cases of dynamics-reversal from the damped oscillation- and the bubble-growth studies, it is difficult to prove it during the actual oscillation- or bubble-growth experiment.

All in all, the experiments in this chapter provide an extensive amount of data to explain and analyse the underlying dynamics of microcapsule buoyancy and oscillations. To conclude this project logically in a 5th chapter, it is now necessary to utilise this novel oscillation-design in interesting applications. Due to the repetitive nature of oscillations, they could be used in form of transport processes, which focus on the uptake and release of a payload, or in form of chemical reactions, which the capsule performs after moving into an active environment.

4.6 Literature for chapter 4

1. van den Heuvel, M. G. L. & Dekker, C. Motor Proteins at Work for Nanotechnology. *Science* **317**, 333-336, doi:10.1126/science.1139570 (2007).
2. Thomas, N. A., Bardy, S. L. & Jarrell, K. F. The archaeal flagellum: a different kind of prokaryotic motility structure. *FEMS Microbiology Reviews* **25**, 147-174, doi:10.1111/j.1574-6976.2001.tb00575.x (2001).
3. Berg, H. C. The Rotary Motor of Bacterial Flagella. *Annual Review of Biochemistry* **72**, 19-54, doi:10.1146/annurev.biochem.72.121801.161737 (2003).
4. Nirody, J. A., Berry, R. M. & Oster, G. The Limiting Speed of the Bacterial Flagellar Motor. *Biophysical Journal* **111**, 557-564, doi:https://doi.org/10.1016/j.bpj.2016.07.003 (2016).
5. Wang, J. & Manesh, K. M. Motion Control at the Nanoscale. *Small* **6**, 338-345, doi:https://doi.org/10.1002/smll.200901746 (2010).
6. Loget, G. & Kuhn, A. Electric field-induced chemical locomotion of conducting objects. *Nature Communications* **2**, 535, doi:10.1038/ncomms1550 (2011).
7. Wang, W., Castro, L. A., Hoyos, M. & Mallouk, T. E. Autonomous Motion of Metallic Microrods Propelled by Ultrasound. *ACS Nano* **6**, 6122-6132, doi:10.1021/nn301312z (2012).
8. Wang, W. *et al.* Acoustic propulsion of nanorod motors inside living cells. *Angew Chem Int Ed Engl* **53**, 3201-3204, doi:10.1002/anie.201309629 (2014).
9. Dreyfus, R. *et al.* Microscopic artificial swimmers. *Nature* **437**, 862-865, doi:10.1038/nature04090 (2005).
10. Ghosh, A. & Fischer, P. Controlled Propulsion of Artificial Magnetic Nanostructured Propellers. *Nano Letters* **9**, 2243-2245, doi:10.1021/nl900186w (2009).
11. Hong, Y., Diaz, M., Córdova-Figueroa, U. M. & Sen, A. Light-Driven Titanium-Dioxide-Based Reversible Microfireworks and Micromotor/Micropump Systems. *Advanced Functional Materials* **20**, 1568-1576, doi:https://doi.org/10.1002/adfm.201000063 (2010).
12. Ibele, M., Mallouk, T. E. & Sen, A. Schooling Behavior of Light-Powered Autonomous Micromotors in Water. *Angewandte Chemie International Edition* **48**, 3308-3312, doi:https://doi.org/10.1002/anie.200804704 (2009).
13. Howse, J. R. *et al.* Self-Motile Colloidal Particles: From Directed Propulsion to Random Walk. *Physical Review Letters* **99**, 048102, doi:10.1103/PhysRevLett.99.048102 (2007).
14. Ismagilov, R. F., Schwartz, A., Bowden, N. & Whitesides, G. M. Autonomous Movement and Self-Assembly. *Angewandte Chemie International Edition* **41**, 652-654, doi:https://doi.org/10.1002/1521-3773(20020215)41:4<652::AID-ANIE652>3.0.CO;2-U (2002).
15. Pantarotto, D., Browne, W. R. & Feringa, B. L. Autonomous propulsion of carbon nanotubes powered by a multienzyme ensemble. *Chemical Communications*, 1533-1535, doi:10.1039/B715310D (2008).
16. Paxton, W. F. *et al.* Catalytic Nanomotors: Autonomous Movement of Striped Nanorods. *Journal of the American Chemical Society* **126**, 13424-13431, doi:10.1021/ja047697z (2004).
17. Schattling, P., Thingholm, B. & Städler, B. Enhanced Diffusion of Glucose-Fueled Janus Particles. *Chemistry of Materials* **27**, 7412-7418, doi:10.1021/acs.chemmater.5b03303 (2015).
18. Vicario, J. *et al.* Catalytic molecular motors: fuelling autonomous movement by a surface bound synthetic manganese catalase. *Chemical Communications*, 3936-3938, doi:10.1039/B505092H (2005).
19. Paxton, W. F., Sen, A. & Mallouk, T. E. Motility of Catalytic Nanoparticles through Self-Generated Forces. *Chemistry – A European Journal* **11**, 6462-6470, doi:https://doi.org/10.1002/chem.200500167 (2005).
20. Mei, Y. *et al.* Versatile Approach for Integrative and Functionalized Tubes by Strain Engineering of Nanomembranes on Polymers. *Advanced Materials* **20**, 4085-4090, doi:https://doi.org/10.1002/adma.200801589 (2008).

21. Sanchez, S. *et al.* The smallest man-made jet engine. *The Chemical Record* **11**, 367-370, doi:https://doi.org/10.1002/tcr.201100010 (2011).
22. Solovev, A. A. *et al.* Self-Propelled Nanotools. *ACS Nano* **6**, 1751-1756, doi:10.1021/nn204762w (2012).
23. Mei, Y., Huang, G. & Solovev, A. EB Ure na, I. Mönch, F. Ding, T. Reindl, RKY Fu, PK Chu, OG Schmidt. *Adv. Mater* **20**, 4085-4090 (2008).
24. Solovev, A. A., Mei, Y., Bermúdez Ureña, E., Huang, G. & Schmidt, O. G. Catalytic Microtubular Jet Engines Self-Propelled by Accumulated Gas Bubbles. *Small* **5**, 1688-1692, doi:https://doi.org/10.1002/smll.200900021 (2009).
25. Sanchez, S., Ananth, A. N., Fomin, V. M., Viehrig, M. & Schmidt, O. G. Superfast motion of catalytic microjet engines at physiological temperature. *Journal of the American Chemical Society* **133**, 14860-14863 (2011).
26. Sanchez, S., Solovev, A. A., Harazim, S. M. & Schmidt, O. G. Microbots swimming in the flowing streams of microfluidic channels. *Journal of the American Chemical Society* **133**, 701-703 (2011).
27. Soler, L., Martínez-Cisneros, C., Swiersy, A., Sánchez, S. & Schmidt, O. G. Thermal activation of catalytic microjets in blood samples using microfluidic chips. *Lab on a Chip* **13**, 4299-4303 (2013).
28. Fournier-Bidoz, S., Arsenault, A. C., Manners, I. & Ozin, G. A. Synthetic self-propelled nanorotors. *Chemical Communications*, 441-443, doi:10.1039/B414896G (2005).
29. Ozin, G. A., Manners, I., Fournier-Bidoz, S. & Arsenault, A. Dream Nanomachines. *Advanced Materials* **17**, 3011-3018, doi:https://doi.org/10.1002/adma.200501767 (2005).
30. Sánchez, S., Soler, L. & Katuri, J. Chemically Powered Micro- and Nanomotors. *Angewandte Chemie International Edition* **54**, 1414-1444, doi:https://doi.org/10.1002/anie.201406096 (2015).
31. Mirkovic, T., Zacharia, N. S., Scholes, G. D. & Ozin, G. A. Nanolocomotion—Catalytic Nanomotors and Nanorotors. *Small* **6**, 159-167, doi:https://doi.org/10.1002/smll.200901340 (2010).
32. Paxton, W. F., Sundararajan, S., Mallouk, T. E. & Sen, A. Chemical Locomotion. *Angewandte Chemie International Edition* **45**, 5420-5429, doi:https://doi.org/10.1002/anie.200600060 (2006).
33. Feynman, R. P., Leighton, R. B. & Sands, M. *The Feynman Lectures on Physics, Vol. II: The New Millennium Edition: Mainly Electromagnetism and Matter*. (Basic Books, 2011).
34. Freund, J. A. & Pöschel, T. *Stochastic Processes in Physics, Chemistry, and Biology*. (Springer Berlin Heidelberg, 2008).
35. Dhar, P. *et al.* Autonomously Moving Nanorods at a Viscous Interface. *Nano Letters* **6**, 66-72, doi:10.1021/nl052027s (2006).
36. Purcell, E. M. Life at low Reynolds number. *American Journal of Physics* **45**, 3-11, doi:10.1119/1.10903 (1977).
37. Elgeti, J., Winkler, R. G. & Gompper, G. Physics of microswimmers—single particle motion and collective behavior: a review. *Reports on Progress in Physics* **78**, 056601, doi:10.1088/0034-4885/78/5/056601 (2015).
38. Qiu, T. *et al.* Swimming by reciprocal motion at low Reynolds number. *Nature Communications* **5**, 5119, doi:10.1038/ncomms6119 (2014).
39. Lach, S., Yoon, S. M. & Grzybowski, B. A. Tactic, reactive, and functional droplets outside of equilibrium. *Chemical Society Reviews* **45**, 4766-4796, doi:10.1039/C6CS00242K (2016).
40. Lagzi, I., Soh, S., Wesson, P. J., Browne, K. P. & Grzybowski, B. A. Maze Solving by Chemotactic Droplets. *Journal of the American Chemical Society* **132**, 1198-1199, doi:10.1021/ja9076793 (2010).

41. Hanczyc, M. M., Toyota, T., Ikegami, T., Packard, N. & Sugawara, T. Fatty Acid Chemistry at the Oil−Water Interface: Self-Propelled Oil Droplets. *Journal of the American Chemical Society* **129**, 9386-9391, doi:10.1021/ja0706955 (2007).
42. Francis, W., Fay, C., Florea, L. & Diamond, D. Self-propelled chemotactic ionic liquid droplets. *Chemical Communications* **51**, 2342-2344, doi:10.1039/C4CC09214G (2015).
43. Ichimura, K., Oh, S.-K. & Nakagawa, M. Light-Driven Motion of Liquids on a Photoresponsive Surface. *Science* **288**, 1624-1626, doi:10.1126/science.288.5471.1624 (2000).
44. Florea, L. *et al.* Photo-Chemopropulsion – Light-Stimulated Movement of Microdroplets. *Advanced Materials* **26**, 7339-7345, doi:https://doi.org/10.1002/adma.201403007 (2014).
45. Sunamoto, J., Iwamoto, K., Akutagawa, M., Nagase, M. & Kondo, H. Rate control by restricting mobility of substrate in specific reaction field. Negative photochromism of water-soluble spiropyran in AOT reversed micelles. *Journal of the American Chemical Society* **104**, 4904-4907, doi:10.1021/ja00382a027 (1982).
46. Peng, F., Tu, Y., Men, Y., van Hest, J. C. M. & Wilson, D. A. Supramolecular Adaptive Nanomotors with Magnetotaxis Behavior. *Advanced Materials* **29**, 1604996, doi:https://doi.org/10.1002/adma.201604996 (2017).
47. Wilson, D. A., Nolte, R. J. M. & van Hest, J. C. M. Autonomous movement of platinum-loaded stomatocytes. *Nature Chemistry* **4**, 268-274, doi:10.1038/nchem.1281 (2012).
48. Peng, F., Tu, Y., van Hest, J. C. M. & Wilson, D. A. Self-Guided Supramolecular Cargo-Loaded Nanomotors with Chemotactic Behavior towards Cells. *Angewandte Chemie International Edition* **54**, 11662-11665, doi:https://doi.org/10.1002/anie.201504186 (2015).
49. Lu, A. X. *et al.* Catalytic Propulsion and Magnetic Steering of Soft, Patchy Microcapsules: Ability to Pick-Up and Drop-Off Microscale Cargo. *ACS Applied Materials & Interfaces* **8**, 15676-15683, doi:10.1021/acsami.6b01245 (2016).
50. Ma, X., Wang, X., Hahn, K. & Sánchez, S. Motion Control of Urea-Powered Biocompatible Hollow Microcapsules. *ACS Nano* **10**, 3597-3605, doi:10.1021/acsnano.5b08067 (2016).
51. Wu, Y., Lin, X., Wu, Z., Möhwald, H. & He, Q. Self-Propelled Polymer Multilayer Janus Capsules for Effective Drug Delivery and Light-Triggered Release. *ACS Applied Materials & Interfaces* **6**, 10476-10481, doi:10.1021/am502458h (2014).
52. Cao, S. *et al.* Cucurbit-Like Polymersomes with Aggregation-Induced Emission Properties Show Enzyme-Mediated Motility. *ACS Nano* **15**, 18270-18278, doi:10.1021/acsnano.1c07343 (2021).
53. Arqué, X. *et al.* Autonomous Treatment of Bacterial Infections in Vivo Using Antimicrobial Micro- and Nanomotors. *ACS Nano*, doi:10.1021/acsnano.1c11013 (2022).
54. Vilela, D. *et al.* Drug-Free Enzyme-Based Bactericidal Nanomotors against Pathogenic Bacteria. *ACS Applied Materials & Interfaces* **13**, 14964-14973, doi:10.1021/acsami.1c00986 (2021).
55. Xu, D. *et al.* Enzyme-Powered Liquid Metal Nanobots Endowed with Multiple Biomedical Functions. *ACS Nano* **15**, 11543-11554, doi:10.1021/acsnano.1c01573 (2021).
56. Llopis-Lorente, A. *et al.* Enzyme-Powered Gated Mesoporous Silica Nanomotors for On-Command Intracellular Payload Delivery. *ACS Nano* **13**, 12171-12183, doi:10.1021/acsnano.9b06706 (2019).
57. Xu, D. *et al.* Self-Propelled Micro/Nanomotors for On-Demand Biomedical Cargo Transportation. *Small* **16**, 1902464, doi:https://doi.org/10.1002/smll.201902464 (2020).
58. Hortelao, A. C. *et al.* Swarming behavior and in vivo monitoring of enzymatic nanomotors within the bladder. *Science Robotics* **6**, eabd2823, doi:doi:10.1126/scirobotics.abd2823 (2021).
59. Guix, M. *et al.* Biohybrid soft robots with self-stimulating skeletons. *Science Robotics* **6**, eabe7577, doi:doi:10.1126/scirobotics.abe7577 (2021).
60. Stanton, M. M., Simmchen, J., Ma, X., Miguel-López, A. & Sánchez, S. Biohybrid Janus Motors Driven by Escherichia coli. *Advanced Materials Interfaces* **3**, 1500505, doi:https://doi.org/10.1002/admi.201500505 (2016).

61. Mestre, R. *et al.* Improved performance of biohybrid muscle-based bio-bots doped with piezoelectric boron nitride nanotubes. *bioRxiv*, 2022.2003.2030.486204, doi:10.1101/2022.03.30.486204 (2022).
62. Song, S. *et al.* Engineering transient dynamics of artificial cells by stochastic distribution of enzymes. *Nature Communications* **12**, 6897, doi:10.1038/s41467-021-27229-0 (2021).
63. Rodríguez-Arco, L., Li, M. & Mann, S. Phagocytosis-inspired behaviour in synthetic protocell communities of compartmentalized colloidal objects. *Nature Materials* **16**, 857-863, doi:10.1038/nmat4916 (2017).
64. Buddingh', B. C., Elzinga, J. & van Hest, J. C. M. Intercellular communication between artificial cells by allosteric amplification of a molecular signal. *Nature Communications* **11**, 1652, doi:10.1038/s41467-020-15482-8 (2020).
65. Pfeifer, F. Distribution, formation and regulation of gas vesicles. *Nature Reviews Microbiology* **10**, 705-715, doi:10.1038/nrmicro2834 (2012).
66. Walsby, A. E. Gas vesicles. *Microbiological Reviews* **58**, 94-144 (1994).
67. Rodriguez-Arco, L., Kumar, B., Li, M., Patil, A. J. & Mann, S. Modulation of Higher-order Behaviour in Model Protocell Communities by Artificial Phagocytosis. *Angew Chem Int Ed Engl* **58**, 6333-6337, doi:10.1002/anie.201901469 (2019).
68. Bierman, J. & Kincanon, E. Reconsidering Archimedes' Principle. *The Physics Teacher* **41**, 340-344, doi:10.1119/1.1607804 (2003).
69. Halliday, D. *Fundamentals of Physics: EGrade Plus Stand-Alone Access*. (John Wiley & Sons, Incorporated, 2006).
70. PDB. *Catalase*, <https://pdb101.rcsb.org/motm/57> (2021).
71. Chelikani, P., Fita, I. & Loewen, P. C. Diversity of structures and properties among catalases. *Cellular and Molecular Life Sciences CMLS* **61**, 192-208, doi:10.1007/s00018-003-3206-5 (2004).
72. Murthy, M. R. N., Reid, T. J., Sicignano, A., Tanaka, N. & Rossmann, M. G. Structure of beef liver catalase. *Journal of Molecular Biology* **152**, 465-499, doi:https://doi.org/10.1016/0022-2836(81)90254-0 (1981).
73. Bucekova, M. *et al.* Honeybee glucose oxidase—its expression in honeybee workers and comparative analyses of its content and H2O2-mediated antibacterial activity in natural honeys. *Naturwissenschaften* **101**, 661-670, doi:10.1007/s00114-014-1205-z (2014).
74. Coulthard, C. E. *et al.* Notatin: an anti-bacterial glucose-aerodehydrogenase from Penicillium notatum Westling and Penicillium resticulosum sp. nov. *Biochemical Journal* **39**, 24-36, doi:10.1042/bj0390024 (1945).
75. Raba, J. & Mottola, H. A. Glucose Oxidase as an Analytical Reagent. *Critical Reviews in Analytical Chemistry* **25**, 1-42, doi:10.1080/10408349508050556 (1995).
76. PDB. *Glucose Oxidase*, <https://pdb101.rcsb.org/motm/77> (2021).
77. Duke, F. R., Weibel, M., Page, D. S., Bulgrin, V. G. & Luthy, J. Glucose oxidase mechanism. Enzyme activation by substrate. *Journal of the American Chemical Society* **91**, 3904-3909, doi:10.1021/ja01042a038 (1969).
78. Bright, H. J. & Porter, D. J. T. in *The Enzymes* Vol. 12 (ed Paul D. Boyer) 421-505 (Academic Press, 1975).
79. Tsuge, H., Natsuaki, O. & Ohashi, K. Purification, Properties, and Molecular Features of Glucose Oxidase from Aspergillus niger. *The Journal of Biochemistry* **78**, 835-843, doi:10.1093/oxfordjournals.jbchem.a130974 (1975).
80. Viswanathan, S. *et al.* in *Methods in Enzymology* Vol. 509 (ed Nejat Düzgüneş) 165-194 (Academic Press, 2012).
81. Fosset, M., Chappelet-Tordo, D. & Lazdunski, M. Intestinal alkaline phosphatase. Physical properties and quaternary structure. *Biochemistry* **13**, 1783-1788, doi:10.1021/bi00706a001 (1974).

82. NEUMANN, H. & LUSTIG, A. The Activation of Alkaline Phosphatase by Effector Molecules. *European Journal of Biochemistry* **109**, 475-480, doi:https://doi.org/10.1111/j.1432-1033.1980.tb04818.x (1980).
83. PDB. *REACTION MECHANISM OF ALKALINE PHOSPHATASE BASED ON CRYSTAL STRUCTURES. TWO METAL ION CATALYSIS*, <https://www.rcsb.org/structure/1ALK> (
84. Alam, S. N. *et al.* Intestinal Alkaline Phosphatase Prevents Antibiotic-Induced Susceptibility to Enteric Pathogens. *Annals of Surgery* **259**, 715-722, doi:10.1097/SLA.0b013e31828fae14 (2014).
85. Lallès, J.-P. Intestinal alkaline phosphatase: novel functions and protective effects. *Nutrition Reviews* **72**, 82-94, doi:10.1111/nure.12082 (2014).
86. Narisawa, S. *et al.* Accelerated fat absorption in intestinal alkaline phosphatase knockout mice. *Mol Cell Biol* **23**, 7525-7530, doi:10.1128/mcb.23.21.7525-7530.2003 (2003).
87. Reiss, I., Inderrieden, D. & Kruse, K. Bestimmung der knochenspezifischen alkalischen Phosphatase bei Störungen des Kalziumstoffwechsels im Kindesalter. *Monatsschrift Kinderheilkunde* **144**, 885-890, doi:10.1007/s001120050054 (1996).
88. Ghosh, S. S., Gehr, T. W. & Ghosh, S. Curcumin and chronic kidney disease (CKD): major mode of action through stimulating endogenous intestinal alkaline phosphatase. *Molecules* **19**, 20139-20156, doi:10.3390/molecules191220139 (2014).
89. Choi, B., Rempala, G. A. & Kim, J. K. Beyond the Michaelis-Menten equation: Accurate and efficient estimation of enzyme kinetic parameters. *Scientific Reports* **7**, 17018, doi:10.1038/s41598-017-17072-z (2017).
90. Johnson, K. A. & Goody, R. S. The Original Michaelis Constant: Translation of the 1913 Michaelis–Menten Paper. *Biochemistry* **50**, 8264-8269, doi:10.1021/bi201284u (2011).
91. Morin, D. *Oscillations*, <http://www.people.fas.harvard.edu/~djmorin/waves/oscillations.pdf> (
92. Ge, C. & Sutherland, S. Application of Experimental Modal Analysis to Determine Damping Properties for Stacked Corrugated Boxes. *Mathematical Problems in Engineering* **2013**, 651348, doi:10.1155/2013/651348 (2013).
93. Heitz, T., Giry, C., Richard, B. & Ragueneau, F. *How are the equivalent damping ratios modified by nonlinear engineering demand parameters*. (2017).
94. Ramamurti, V., Mithun, S., Prabhakar, N. & Sukumar, T. Experimental determination of damping ratios at higher modes for use in modal superposition. *Journal of Engineering and Technology Research* **4**, 114-128 (2012).
95. Kumar, B. V. V. S. P., Patil, A. J. & Mann, S. Enzyme-powered motility in buoyant organoclay/DNA protocells. *Nature Chemistry* **10**, 1154-1163, doi:10.1038/s41557-018-0119-3 (2018).
96. Bright, H. J. & Appleby, M. The pH dependence of the individual steps in the glucose oxidase reaction. *Journal of Biological Chemistry* **244**, 3625-3634 (1969).
97. Zia, M. A. *et al.* Thermal Characterization of Purified Glucose Oxidase from A Newly Isolated Aspergillus Niger UAF-1. *Journal of Clinical Biochemistry and Nutrition* **41**, 132-138, doi:10.3164/jcbn.2007018 (2007).
98. Patil, A. J. & Mann, S. Self-assembly of bio–inorganic nanohybrids using organoclay building blocks. *Journal of Materials Chemistry* **18**, 4605-4615, doi:10.1039/B805653F (2008).
99. Patil, A. J., Muthusamy, E. & Mann, S. Fabrication of functional protein–organoclay lamellar nanocomposites by biomolecule-induced assembly of exfoliated aminopropyl-functionalized magnesium phyllosilicates. *Journal of Materials Chemistry* **15**, 3838-3843, doi:10.1039/B504288G (2005).
100. Xing, w., Yin, G. & Zhang, J. *Rotating Electrode Methods and Oxygen Reduction Electrocatalysts*. (Elsevier Science, 2014).
101. (ILO), I. L. O. *International chemical safety card: ICSC 0865 - D-Glucose*, <https://www.ilo.org/dyn/icsc/showcard.display?p_version=2&p_card_id=0865> (

102. (ILO), I. L. O. *International chemical safety card: ICSC 1507 - Sucrose*, <http://www.inchem.org/documents/icsc/icsc/eics1507.htm > (
103. Darros-Barbosa, R., Balaban, M. O. & Teixeira, A. A. Temperature and Concentration Dependence of Density of Model Liquid Foods. *International Journal of Food Properties* **6**, 195-214, doi:10.1081/JFP-120017815 (2003).
104. Toledo, M. *Sucrose: concentration vs density*, <https://www.mt.com/gb/en/home/supportive_content/concentration-tables-ana/Sucrose_de_e.html> (2021).
105. Eloot, S. *Experimental and Numerical Modeling of Dialysis* Doctoral dissertation thesis, Ghent University, (2004-2005).
106. Yong, Y., Ouyang, P., Wu, J. & Liu, Z. A Diffusion-Reaction Model for One-Pot Synthesis of Chemicals with Enzyme Cascades. *ChemCatChem* **12**, 528-535, doi:https://doi.org/10.1002/cctc.201901161 (2020).
107. Zhang, Y., Tsitkov, S. & Hess, H. Proximity does not contribute to activity enhancement in the glucose oxidase–horseradish peroxidase cascade. *Nature Communications* **7**, 13982, doi:10.1038/ncomms13982 (2016).

Transport processes via protamine/DNA-microcapsule carriers

5.1 Abstract

Cargo- uptake and delivery by microscopic- or nanoscopic swimmers has developed into a highly complex but relevant topic in regard to drug delivery in modern medicine, environmental remediation, chemical sensing and as a general interest in the development of micro- or nanobots. The previous chapters have established the buoyancy based locomotion of giant protamine/DNA-microcapsules through the antagonistic interaction of entrapped catalase and glucose oxidase and by nucleation and maintenance of an encapsulated O_2 microbubble. As a next step, this concept will be expanded by exploiting the autonomous motility to perform a simple uptake, transport and release or a molecular payload. Polyoxometalate coacervate vesicles (PCVs) are used as cargo-containers to be picked up by the protamine/DNA-carrier. The functionality of protamine/DNA-microcapsules was increased by entrapping a third enzyme in urease, which induced the pH-dependant PCV-disintegration and release of the molecular cargo sequestered inside the PCVs. This presents a novel approach for programmable protocell-microbots, which can be used as a platform for communication between cell communities or chemical reaction networks.

5.2 Introduction

Human ingenuity has come up with a plethora of machines and devices that shape our everyday lives, but to this day there is still an undeniable fascination revolving around the idea of miniaturizing machines and robots to the micro- or nanoscale where they autonomously move and fulfil a designated task. Since the introduction to chapter 4 has already discussed the motility of micro- and nanomachines (MNMs) and some of the different ways to induce motion, this introduction will focus on the transportation of cargo. Cargo transportation is an important concept that plays a big role in the distribution of goods in our society, but also drives vital processes in nature and on the molecular scale. Nature has always been a paragon in this regard as it already provided popular examples on how micro/nanomachines (MNMs) and transport mechanisms can work. One of the most important transport phenomena in all living organisms is the regulation of concentrations within cells, to regulate the influx of important ions like Na^+, K^+, Ca^{2+}, Cl^-, amino acids, sugars and more. Here, one needs to distinguish between passive and active transport. The former is based on a concentration gradient, which transports the nutrients and ions through osmosis and diffusion. For molecular species which cannot naturally traverse the lipid bilayer of the membrane like glucose, specialised carrier proteins

can bind to the molecule and enable the passive transport through the membrane, which is called facilitated diffusion. Active diffusion on the other hand usually works against a concentration gradient and utilises energy in form of ATP to fuel specific pump-proteins like Na^+/K^+ ATPase, which transports sodium out, while simultaneously moving potassium into the cell. [1,2] The previous chapter has already described the motor function of myosin, dynein and kinesin, which move along the intracellular filament network made from actin and microtubules. These motors are capable of loading and transporting intracellular cargo like endo- and exosomes, melanosomes, mitochondria or ribonucleoparticles. [3] While these nanoscopic machines are highly interesting, they are also very complex and normally only function within their natural cell environment, which makes a synthetic replication a very difficult task. So instead of replicating biological MNMs, contemporary science utilises self-propelled micro- and nano swimmer concepts to function as cargo carriers for delivery. Popular MNMs usually revolve around inorganic or polymer-templates which were functionalised to facilitate motility and cargo uptake capabilities, like nano-wires [4-8], Janus-style micro- and nano spheres [9-12], micro- and nano-tubes [13-15] or polymerosome stomatocytes [16-18].

One field where these MNM-carriers play a significant role is the delivery of drugs, and even more specifically, in the field of cancer therapy, heart and vasculature diseases. [19] Whereas passive strategies normally rely on the diffusion of the drug, self-propelled MNM-drug carriers are able to move towards the area of interest on their own, or guided through an external stimulus. [20] He *et al*. designed polymer multilayer tubular nanomotors. The porous tubes were loaded with Pt-nanoparticles for O_2-bubble propulsion, iron-oxide particles for guidance via an external magnetic field and the antitumor-drug doxorubicin. [21] Once arrived at the target location, the release of the drug was triggered through disintegration of the carrier by sonication. Mhanna *et al.* designed artificial bacterial flagella which performed a corkscrew-like swimming motion in response to a rotating magnetic field to deliver calcein to mouse myoblasts. Here, the drug was loaded into liposomes, which were adsorbed onto the carriers and released through fusion or endocytosis, once the liposomes got in contact with the target cells. [22] Another interesting model was presented by Xu *et al.* who delivered DOX-hydrochloride through sperm-hybrid micromotors which were guided by a magnetic field. The drug loaded sperm was then released from the tetrapod microstructure, once it hit a cell cluster. [23] Mesoporous silica nanomotors in form of janus-style particles are another popular example of motile nanocarriers, which bind or adsorb their payloads within the mesopores and deliver them through sustained release [24], or after degradation of an egg-phosphatidylcholin surface bilayer once the carriers have reached the target cells. [25] He *et al.* furthermore presented polypeptide micro-rockets with an incorporated hydrogel containing drugs and other particles [11], and janus-style polymer microcapsules, which encapsulated the drug. [26] The release of the drug was triggered by a NIR-laser stimulus in both systems, which lead to a degradation of the compartment or the hydrogel. While drug delivery is most likely one of the most interesting applications of MNM-carriers, recent publications have also reported the transportation of other payloads like genes [27-30], proteins [31-34] and even colloid particles [19,35] and whole cells [36-39].

Another field, where MNMs are rising as valuable candidates is environmental remediation and the interaction with pollutants. Especially aqueous systems like oceans, lakes and rivers have experienced an increasing amount of pressure due to exposure to chemicals from our society, and there is an urgent need for new systems which can detect and remove the polluting compounds. Environmental sensing is one branch, where MNMs have already been applied with success, by exploiting the motility of nanomotors to detect chemical pollutants. Recent publications documented acceleration or deceleration of MNMs in the presence of silver ions [40,41] hydrazine [42] or other pollutants like heavy metals or pesticides, which can be used to test the water quality based on the velocity of the swimmers. [43] But mere sensing would not be enough, as the toxins and pollutants are often difficult

to remove from wastewater or even natural water resources. The development of new systems for the efficient remediation of our water sources is a highly relevant topic, and MNMs can play a vital role in this. One of the main tasks is to come up with a design that combines the motility of MNMs with materials that facilitate the controlled uptake and/or release of chemical pollutants. Guix *et al.* designed SAM-functionalised hydrophobic micro-swimmers for the purification of oil contaminated water through adsorption of the oil onto the swimmers. [44] Other groups focused on using molecularly imprinted polymers, which were integrated into micromotors and offered binding, transport and release of molecular toxins. [33,45,46] Instead of carrying the pollutants via the micromotors, the remediation can also be achieved through catalytical, or reactive material immobilised on or inside the MNMs. Sanchez *et al*. fabricated catalytical tubular micromotors which could degrade organic pollutants through Fenton oxidation reactions. [47,48] More recent studies have shown water-remediation systems based on inorganic micromotors for the removal of highly toxic pollutants like oil [49] or radioactive uranium. [50] Decontamination via adsorption of the pollutant to a removable scaffold is one of the most cost-efficient, effective and versatile approaches and there are many popular materials which can easily be exploited for aqueous detoxification like zeolites [51], activated carbon [52] or metal oxides [53], while using non-toxic fuels to maintain the motion of the micro/nanomotors. A simple, non-evasive substituent for harmful fuels like H_2O_2 was presented in form of IR-radiation, thus leading to motion via thermophoresis to remove harmful organic compounds like dyes. [54]

While MNMs motility has been a highly discussed topic, the combination of micromotors with the ability to take up and release cargo is where the real complications lie. Ideally, the binding of the payload to the carrier should be specific and efficient, followed by a controlled and triggered release once the carrier has transported the cargo to the desired location. In summary, some common uptake mechanisms are the encapsulation [11,18,25,26] of the cargo during the self-assembly of the carrier, liposome fusion to a mesoporous silica core [55,56], electrostatic binding or via selective antibodies [39], whereas release mechanism include light actuated alteration of the carrier [26] or breakage of the particle-shell [11], ultrasonic breaking [57,58] or pH-induced leakage and electrostatic desorption. [39,59,60] Many of these mechanisms change the carrier irreversibly or do not allow for a re-uptake of cargo, which prevents the carrier from undergoing multiple uptake- and release cycles or will not allow for a recycling of the carrier in general. Furthermore, many cargo/carrier concepts are based on inorganic materials and only work in the nanoscopic range. Recent protocellular research has come up with a vast repertoire of different microcompartments which enable facile entrapment of functional cargo [61-64], but may have not found their way into the field of micro/nanobots just yet.

This chapter will present a unique take on cargo uptake, transport and release with protamine/DNA-microcapsules as motile microcarriers. The concept of enzyme powered microcapsule motility via buoyancy has already been discussed in the previous chapters. This work will focus on establishing the cargo-system and the means of uptake, and release. As it was shown in chapter 3, protamine/DNA-microcapsules are not necessarily suitable for the encapsulation of small molecules while their high structural stability would not allow for a release of entrapped components through breaking. So instead of using protamine/DNA-capsules to carry the payload, a secondary carrier was chosen, which will then be carried by the protamine/DNA-capsule. Polyoxometalate coacervate vesicles (PCVs) are three-tiered membrane bound vesicles formed from polyDADMAC (PDDA)/ATP coacervates after stabilisation with sodium phosphotungstate (PTA) and were first described by D. Williams *et al.* in 2014 (Figure 5.2-1). [65] While the coacervate-microdroplets (Figure 5.2-1-A) are mere products of a liquid/liquid phase separation, the addition of PTA (Figure 5.2-1-C) changes their structure significantly. The microcompartments are bound by a semi-permeable membrane made from PTA/PDDA, with an ATP/PDDA coacervate phase underneath and an aqueous lumen in the centre

(Figure 5.2-1-B). In DLS-zeta potential scans, PCVs exhibited a slightly negative zeta potential of ~ -10 mV, from which one can assume that they contain a negative surface charge due to the PTA associated with the membrane. Furthermore, the PCVs showed good structural stability but started to disintegrate at high pH of above 12. What is most interesting for the sake of this chapter though, is the ability to readily sequester molecular cargo and even particles into the coacervate microdroplets which are then retained within the cell once the PCVs have formed. In this chapter, PCVs will be investigated as secondary cargo-carriers of a molecular payload, which will then be transported by the protamine/DNA-microcapsules. [65]

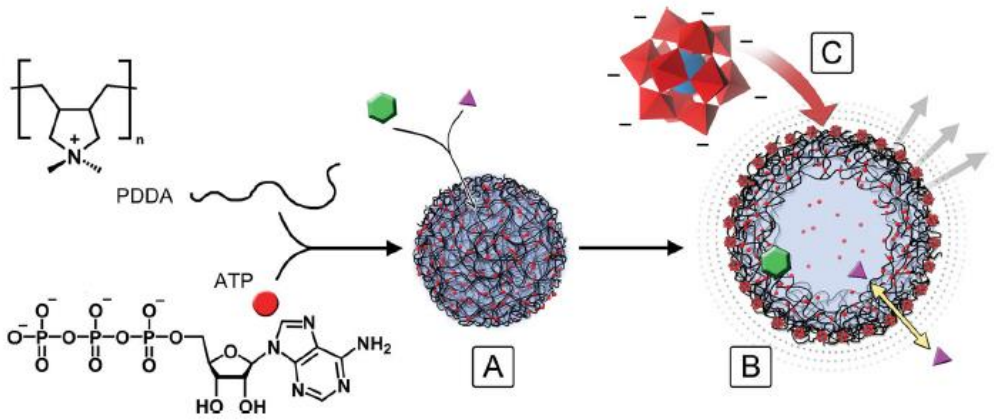

Figure 5.2-1: *Illustration of the assembly of polyoxometalate coacervate vesicles (PCVs). Coacervates droplets were formed through the liquid/liquid phase separation of polydiallyldimethylammonium chloride (PDDA) and adenosine triphosphate (ATP). Addition of phosphotungstate (**C**) then initiated membrane formation and the restructuration of the coacervate microdroplets (**A**) into a three-tiered micro-structure with a PTA/PDDA-membrane, a PDDA/ATP coacervate phase and an aqueous lumen (**B**).* [65]

In the work of D. Williams *et al.* PCVs have been described as very stable at high temperatures and even at high pH up to 12, after which they started to break.

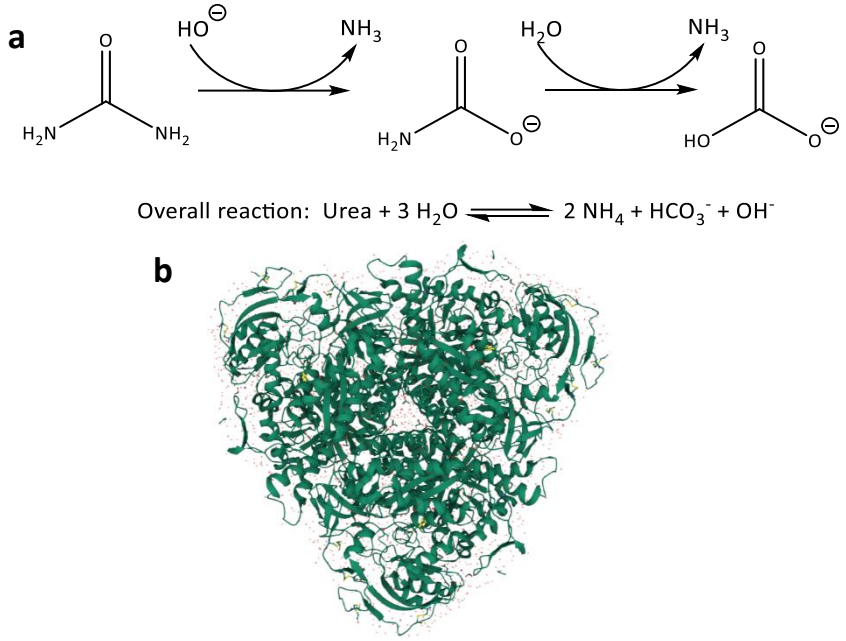

Figure 5.2-2: ***a*** *Catalytic steps and overall reaction of the conversion of urea to ammonia and carbonic acid.* [66] ***b*** *Crystal structure of urease.* [67]

Nonetheless, these studies were mainly done in di-water and without the addition of other salts. In this chapter, the cargo release will be showcased through a pH-triggered disintegration of the PCVs. The trigger mechanism was also implemented into the protamine/DNA-microcapsule carriers in form of entrapped urease enzymes. Urease is a nickel-containing metalloenzyme from the family of amidohydrolases and is usually found in bacteria, fungi, plants and some invertebrates and soil. Urease catalyses the conversion of urea to ammonia and carbonic acid. The catalytic steps involved in the reaction are described in Figure 5.2-2 according to Ciurli *et al*. [66]

While the products can be identified easily, the exact mechanism of the reaction is still not fully understood and there are many plausible theories, which have been proposed over the years. [68-70] Benini *et al.* proposed one of the more recent mechanisms (Figure 5.2-3), which nicely highlights the role of the two nickel-atoms and the surrounding amino acids for the reaction. The Nickel-atoms bind a bridging hydroxide, which acts as a nucleophile and as an acid while also coordinating urea through Ni(1) and Ni(2). Histidine and alanine-residues further stabilise the complex and the developing charges during the reaction. Specifically, His_{323} plays an important role, as it also facilitates the proton transfer onto one of the NH_2-groups, after which NH_4^+ and $H_2N\text{-}COO^-$ are being released.

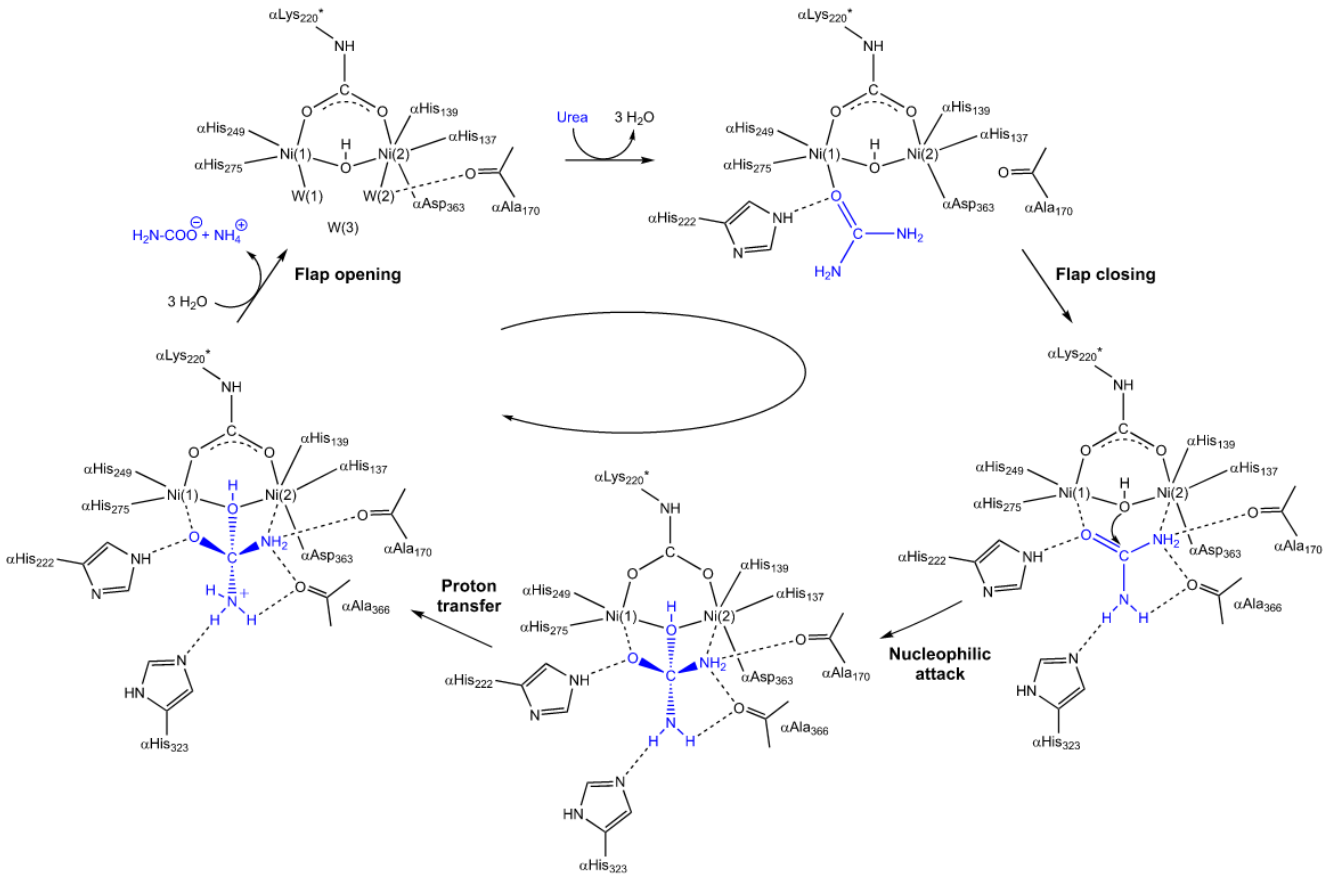

Figure 5.2-3: *Reaction mechanism of urease proposed by Beninin et al*.[71]

5.3 Methods

5.3.1 Transient reactivity of oscillating, enzyme-loaded protamine/DNA-microcapsules

This experiment once more utilised the cuvette-device which has already been presented in chapter 4 for the damped-oscillation experiments. The experimental device was prepared by mounting it to a metal stage, which held it in place and positioned it in front of a digital camera, which tracked the motion of the protamine/DNA-microcapsule. The cuvette was then filled with a non-reactive glucose-phase (0.08 M, 2 wt% sucrose), after which the remaining 300 μL at the top of the cuvette were filled by gently adding the reactive phase which contained the chromophore Ampliflu™ Red (Also called Amplex Red, 0.83 mM, 0.08 M glucose and 0 wt% sucrose). The H_2O_2-phase (160 mM, with 4 wt% sucrose) at the bottom of the device was added via a syringe pump at the following rate: 10 μL at 10 μL/min. To understand the diffusion within the device, both the reactive- and the bottom phase were dyed by mixing them with 3.2 mM methylene blue. The diffusion of the dyed phases was then tracked through camera imaging.

Protamine/DNA-microcapsules were fabricated according to the established protocol in 3.3.3 with 4 mg/mL DNA, 16.6 U/mg horseradish peroxidase, 19.8 kU/mL catalase, 2.9 kU/mL glucose oxidase and 20 mg/mL silica particles. To track the enzymatic oxidation of Ampliflu™ Red, the device was further fitted with a micro-spectroscope-probe (attached to an Ocean Optics Flame-S-VIS-NIR-ES), which was also mounted to the metal stage and positioned on the back of the cuvette, tracking the optical feed right in the centre of the reactive phase. A black sheet of cardboard was attached around the probe, to create a stronger contrast between the background and the protamine/DNA-microcapsule, which supported the camera-tracking once the oscillation started. The microcapsule was then prepared by pre-nucleating an O_2-microbubble inside the microcapsule before transferring it into a 0.1 M glucose-solution until it started to descend, after which the microcapsule was added to the oscillation device, at which point the camera tracking and the spectroscopic analysis began. Camera images were taken in 5s intervals, whereas spectroscopic readings were done in ~10s intervals.

5.3.2 Fabrication of PCVs

For the fabrication of PCVs, the stock solutions were generally prepared after the same protocol. 27.55 mg ATP was dissolved in 5 mL di water (10 mM) after which the pH was adjusted to 6.5 by addition of several droplets of 1 M NaOH. 78 μL PDDA (100-200 kDa) were dissolved in 10 mL di-water (~10 mM) and the pH set to 6.5 by adding several drops of 0.01 M NaOH. Finally, a solution of PTA was prepared by adding 64.4 mg phosphotungstate to 1 mL di-water (22 mM) and adjusting the pH to 6.5 by adding a few drops of 5 M NaOH and fine tuning the pH with 1 M NaOH.

Coacervates were fabricated by adding 500 μL of the PDDA-stock and 500 μL of the ATP stock-solutions into a 1.7 mL glass vial, fitted with a small stir bar. The solution was stirred at 1700 rpm for either 30s or 60s, depending on the demanded size of PCVs. As soon as both components were added, the mixture turned into a dull dispersion, confirming that the coacervates are forming. Once the stirring time was over, 100 μL of the PTA-stock solution were added and the dispersion was stirred for another 5-10 seconds. The PCVs were then transferred into a fresh vial and left to sediment for ~20 minutes, after which they were washed 2-3 times.

Functional components were sequestered into the PCVs by adding them during the coacervate formation. Small molecules like pyranine, TPPS, acriflavine were added in volumes of 25 μL (1 mM), whereas tagged enzymes like RITC-GOx, FITC-GOx, or RITC-HRP were added in volumes of 50 μL (1 mg/mL).

5.3.3 PCV-stability screening in different media and pH

To understand and assess the stability of PCVs, they were incubated in a variety of different media and at various pH. Generally, 50 μL of a PCV-dispersion were transferred into a 96-well plate and mixed with 200 μL of the solution of interest.

The following solutions and conditions were investigated: di-water (pH 5-12), HNa_2PO_4-buffer (50, 100, 500, 1000 mM and at pH 5-12), NaCl (50, 100, 500, 1000 mM at pH 10), Na_2SO_4 (50, 100, 500, 1000 mM at pH 10), MES (50, 100, 500, 1000 at pH 10) and urea (1, 10, 100, 1000 mM, pH 5-10).

5.3.4 Optimisation of PCV uptake by protamine/DNA-microcapsules

Depending on the experiment, the PCV uptake was performed in different ways, but the most common approach was by simply mixing protamine/DNA-microcapsules into a PCV-dispersion and making them adsorb onto the carriers. Generally, a single protamine/DNA-microcapsule was added into 1 mL of a PCV-dispersion and gently mixed for 1-5 minutes. The attachment usually happened right away, but longer mixing times significantly increased the loading of the PCVs onto the surface of the protamine/DNA-microcapsules. To improve the adhesion even more, protamine/DNA-capsules were mixed with a PCV-dispersion and left to sediment overnight.

To optimise the adhesion of PCVs to the protamine/DNA-capsules, the number of washing steps post fabrication were investigated. Protamine/DNA-capsules were washed 3-5 times, and PCVs were washed 1-3 times respectively with di-water, after which the adhesion of PCVs onto the protamine/DNA-capsules was discussed.

5.3.5 Microscopic analysis of PCV disintegration

PCVs were fabricated as described in 5.3.2 in two different sizes (30s and 60s stirring) and washed 3 times with di-water. 25 μL of the PCV-dispersion was then transferred into a 96-well plate and mixed with 100 μL HNa_2PO_4 (50 mM, pH 10), after which the disintegration of the PCVs was observed and recorded through an optical microscope (Leica DMI3000B).

5.3.6 PCV-disintegration induced by urease reaction

PCVs were fabricated as described in 5.3.2 in two different sizes (30s and 60s stirring) and washed 3 times with di-water. Similar to 5.3.5, 25 μL of the PCV-dispersion was transferred into a well of a 96-well plate and mixed with 1 M urea and 10 U/mL urease in either di-water or 50 mM HNa_2PO_4 at pH 7. The disintegration of the PCVs was observed via brightfield microscopy.

Alternatively, PCVs were fabricated with entrapped pyranine, which enabled the analysis of the disintegration through the fluorescence microscope.

5.3.7 pH-screening of urease containing protamine/DNA microcapsule

Protamine/DNA-microcapsules were fabricated according to the established protocol in (3.3.3), with 4 mg/mL DNA, 0.29 kU/mL urease, 19.8 kU/mL catalase, 2.9 kU/mL glucose oxidase and 20 mg/mL silica particles. In this experiment, 1 or 5 urease containing protamine/DNA-microcapsules were immersed in 200 μL urea (0.1 M, pH 7.0) to measure and plot the time dependant change of the pH caused by the catalytic conversion of urea by urease. The experiment was performed in a well-plate and with a pH-meter-probe reaching into the well close to the capsules (Figure 5.3-1). Alternatively, the pH-change of free urease in a urea solution was measured by immersing 10 U/mL urease in 0.1 M urea.

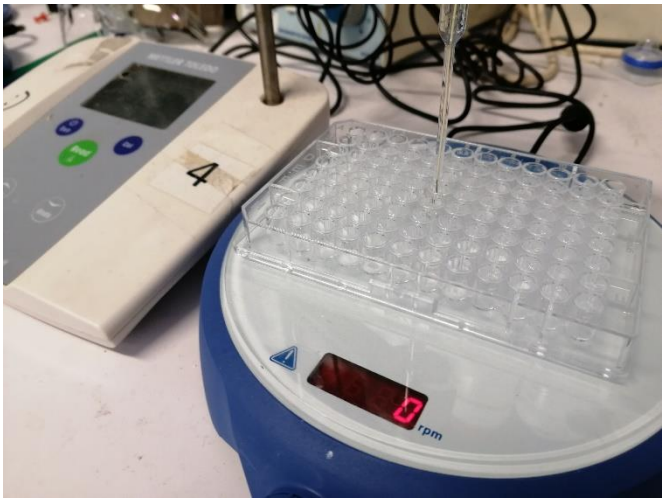

Figure 5.3-1: *Experimental setup of the pH-screening of urease containing protamine/DNA-microcapsules.*

5.3.8 Microscopic analysis of PCV-disintegration (adsorbed on urease containing protamine/DNA microcapsules)

Protamine/DNA-microcapsules were fabricated according to the established protocol (3.3.3), with 4 mg/mL DNA, 0.29 kU/mL urease, 19.8 kU/mL catalase, 2.9 kU/mL glucose oxidase and 20 mg/mL silica particles. PCVs were fabricated according to 5.3.2 with entrapped pyranine or RITC-GOx and attached to the capsules by mixing them for 20 minutes. The loaded protamine/DNA-capsule was then isolated from the PCV-dispersion by washing and transferred into a 96-well plate.

To start the disintegration of the of the PCVs, 1 or 5 loaded protamine/DNA-capsule were immersed in 200 µL urea (0.1 M, pH 7) and the process was observed under the fluorescence- and brightfield microscope.

5.3.9 Mimicking cellular defence strategies: destruction of PCVs via secretion through protamine/DNA-microcapsules

Protamine/DNA-microcapsules were fabricated according to the established protocol (3.3.3), with 4 mg/mL DNA, 0.29 kU/mL urease and 20 mg/mL silica particles. PCVs were fabricated according to 5.3.2 and with sequestered pyranine to make the PCVs appear under the fluorescence microscope.

For the experimental setup, a well of a 96-well plate was either filled with 100 µL of di-water (pH 7.0) or 50 mM HNa_2PO_4 (pH 7.0). 10 µL of a concentrated PCV dispersion were then added to the well, which should suffice to cover the ground of the well with the small vesicles. Finally, a single (or multiple) protamine/DNA-microcapsules were gently added on top of the PCV bed. Here, it was important to prevent any redispersion of the PCVs, as they would otherwise cover the capsule and potentially disturb the imaging later on. To start the experiment, 10 µL of a 1 M urea solution were gently added to the well. Again, it is important not to disperse too many PCVs, even though it is often hard to prevent as they easily lifted from the ground when adding new components to the well. Once the urea solution had been added, the well was observed under the optical/fluorescence microscope and the disintegration process was imaged.

5.3.10 Microscopic analysis and proof of concept of cargo transport, release and re-descent of the carrier.

Protamine/DNA-microcapsules were fabricated according to the established protocol (3.3.3), loaded with 4 mg/mL DNA, 0.29 kU/mL urease, 19.8 kU/mL catalase, 2.9 kU/mL glucose oxidase and 20 mg/mL

silica particles. A single capsule was loaded with PCVs and then transferred into a vial with di-water. Once the capsule had settled on the bottom of the vial, 5-10 μL of H_2O_2 (160 mM) were added with a pipette just above the capsule until a small O_2-microbubble has formed inside the capsule and it started to ascend. The capsule was transferred into a 96-well plate with 200 μL urea (0.1 M pH 7.0), which was positioned under a brightfield microscope to record the process. After 64 min, the solution was exchanged with 0.1 M glucose (pH 7.0) and the recording was continued until the O_2-bubble has been consumed by GOx and the capsule started to descend.

5.3.11 Enzyme leakage from protamine/DNA-microcapsules after urease activity

Protamine/DNA-microcapsules were fabricated similarly to 5.3.10.

For the quantitative analysis, the protamine/DNA-capsule was immersed in 100 μL of a 0.1 M urea solution (pH 7.0) for 90 minutes, after which the capsule was transferred out of the solution and washed 3-5 times. An optical cuvette was prepared by mixing ABTS (8.19 mM), HRP (8.3 U/mL) and glucose (25 mM) up to a volume of 1 mL. To increase the signal of the measurement, two capsules, which were separately incubated in urea solutions were combined and added to the optical cuvette, after which the cuvette was placed in the UV/VIS-spectrometer and the absorbance of the oxidised ABTS was measured at $\lambda_{Excitation,\ \mathbf{ABTS}}$ = 420 nm in 1 minute intervals for 5 minutes altogether.

Furthermore, a qualitative colorimetric analysis was done to understand whether the decrease of GOx-activity was caused by enzyme leakage. Here, a single protamine/DNA-capsule was incubated in 0.1 M urea like in the experiment above for 90 minutes. The supernatant was then separated from the capsule and the capsule was washed 3-5 times. The supernatant (100 μL) and the microcapsule (with 100 μL di-water) were then transferred into separate wells of a 96-well plate and mixed with 100 μL of a premixed solution of ABTS (8.19 mM), HRP (8.3 U/mL) and glucose (25 mM). A blank sample was also analysed of plain protamine/DNA-capsules which were not incubated in urea solution. After ~30 minutes, the wells were analysed and captured with a digital camera.

5.3.12 UV/VIS analysis of urease, glucose oxidase and catalase

To understand the absorption spectrum of the relevant enzymes for the uptake/transport and release experiment, urease, catalase and glucose oxidase were anlaysed with a UV/VIS spectrometer. The following concentrations were prepared for the analysis: 0.1 mg/mL glucose oxidase, 0.1 mg/mL urease and 0.5 mg/mL catalase.

5.3.13 Proof of concept: Spectrofluorometric analysis of the release of pyranine and RITC-HRP from PCVs loaded to a protamine/DNA-microcapsule

Protamine/DNA-microcapsules were fabricated similarly to 5.3.10. PCVs were fabricated according to 5.3.2 with entrapped pyranine or RITC-HRP and attached to the capsules by mixing them for 20 minutes. The loaded protamine/DNA-capsule was then isolated from the PCV-dispersion by washing and transferred into a 96-well plate.

The capsule was immersed in 100 μL of a 0.1 M urea solution (pH 7.0) for 1-2h, until all PCVs have been disintegrated which was confirmed via optical microscopy. Next, the microcapsule was removed from the volume and the supernatant was used to analyse the released cargo via a spectrofluorometer (FluoroMax-4P spectrofluorometer (*Horiba Scientific*)). Generally, each scan needed a sample volume of 5 μL and the cargo-release was tracked by measuring the cargo's specific emission wavelength: Pyranine: $\lambda_{Emission,\ Pyranine}$ = 515 nm, with $\lambda_{Excitation,\ Pyranine}$ = 450 nm, and RITC-HRP: $\lambda_{Emission,\ RITC\text{-}HRP}$ = 579 nm with $\lambda_{Excitation,\ RITC\text{-}HRP}$ = 544 nm.

5.3.14 Consecutive uptake, transport and release of cargo-PCVs via protamine/DNA-microcapsules

As a first step, an optical cuvette (*Starna Scientific Ltd*, 29/SOG/5, External dimensions: 48 mm (height) x 7.5 mm (width), x 12.5 mm (length) Internal dimensions: 44 mm (height) x 4 mm (width) x 5 mm (length)) was prepared for the experiment by cleaning it thoroughly with a KOH-basebath solution (0.8 M, with a ratio water: Isopropanol of 1 : 12) and then with di-water.

Next, the cuvette was filled with a 2% sucrose solution (pH 7.0, up to about 1-2 cm below the top of the cuvette) and 200 μL of a fresh PCV-dispersion, loaded with different cargo molecules (pyranine, RITC-HRP or HRP). The PCVs were left to sediment on the bottom of the cuvette. In the meantime, a freshly fabricated protamine/DNA-microcapsule with 4 mg/mL DNA, 0.29 kU/mL urease, 19.8 kU/mL catalase, 2.9 kU/mL glucose oxidase, 12 mg/mL silica particles and magnetic microparticles (5 mg/mL, *GE Healthcare-Lifesciences, Sera-Mag Carboxylate-modified magnetic Speedbeads, COOH-surface modified, 0.871 μm in diameter*) was added into a separate vial filled with di-water and gently mixed with about 5-10 μL H_2O_2 (160 mM) until a small O_2-microbubble nucleated inside the microcapsule. The microcapsule with the pre-nucleated O_2-bubble was then transferred into a separate 0.1 M glucose solution, where it was left until the capsule started to sediment, from where it was gently transferred into the cuvette. Once the microcapsule had sedimented on the ground, the remaining volume at the top of the column was filled with 0.1 M urea-solution (0 wt% sucrose, pH 7.0), which settled on top of the water column without mixing. At this point, the documentation of the experiment was started through a digital camera, which was positioned right in front of the cuvette (images taken in intervals of 5 s, videos were taken for faster parts of the experiment like the ascent or descent of the capsule). The microcapsule was then magnetically moved through the PCV-bed for ~10s to increase the loading efficacy before adding the H_2O_2-solution (160 mM, 4 wt% sucrose, 7 μL, 5 μL/min) through a small tube inlet, which was fixated right at the bottom of the cuvette, and which was connected to an external syringe-pump system. Once the capsule reached the urea-phase, 5 μL aliquots were taken in 20 minute intervals from the volume right around the microcapsule to analyse the release of the cargo spectroscopically with a FluoroMax-4P spectrofluorometer (*Horiba Scientific*). The emission was tracked for the following fluorophores: Pyranine was measured at $\lambda_{Emission,\ Pyranine}$ = 515 nm, with $\lambda_{Excitation,\ Pyranine}$ = 450 nm and RITC-HRP was measured at $\lambda_{Emission,\ RITC\text{-}HRP}$ = 579 nm with $\lambda_{Excitation,\ RITC\text{-}HRP}$ = 544 nm. After 120 minutes, the urea-phase was gently removed with a pipette and replaced with a glucose solution (0.1 M, pH 7.0), while taking care not to cause any mixing or turbulences. To assess the PCV-loading pre- and post-disintegration, the capsule was briefly transferred under an optical microscope and then returned into the oscillation column right at the beginning of the experiment and just before replacing the urea-phase with the glucose-phase. Once the capsule had sedimented again, the experiment was repeated without changing any of the solutions or the capsule itself. Alternatively, HRP was chosen as a third cargo-species, and the release was confirmed by mixing 10 μL aliquots (taken once after 80 minutes of incubation time in urea) with 100 μL of H_2O_2 (16 mM) and Ampliflu™ Red (0.5 mM), after which the fluorophore was tracked spectroscopically at $\lambda_{Emission,\ Amp.Red}$ = 588 nm with $\lambda_{Excitation,\ Amp.Red}$ = 571 nm.

5.4 Results and discussions

5.4.1 Transient reactivity of protamine/DNA-microcapsule oscillations

Before discussing the actual uptake, transport and release concept, and to span the connection from the previous chapter to this one, protamine/DNA-microcapsule oscillations will once more be presented, but this time in an improved and more application-based design. In this concept, the protamine/DNA-capsule was not simply oscillating between two phases, but instead performed a transient, enzymatically catalysed reaction as soon as it entered a third, reactive phase. While the experiment does not showcase any kind of transport, it presents a rudimentary form of communication between two different phases, which is mediated by the oscillating protamine/DNA-capsule. The general setup of the experiment is shown in Figure 5.4-1.

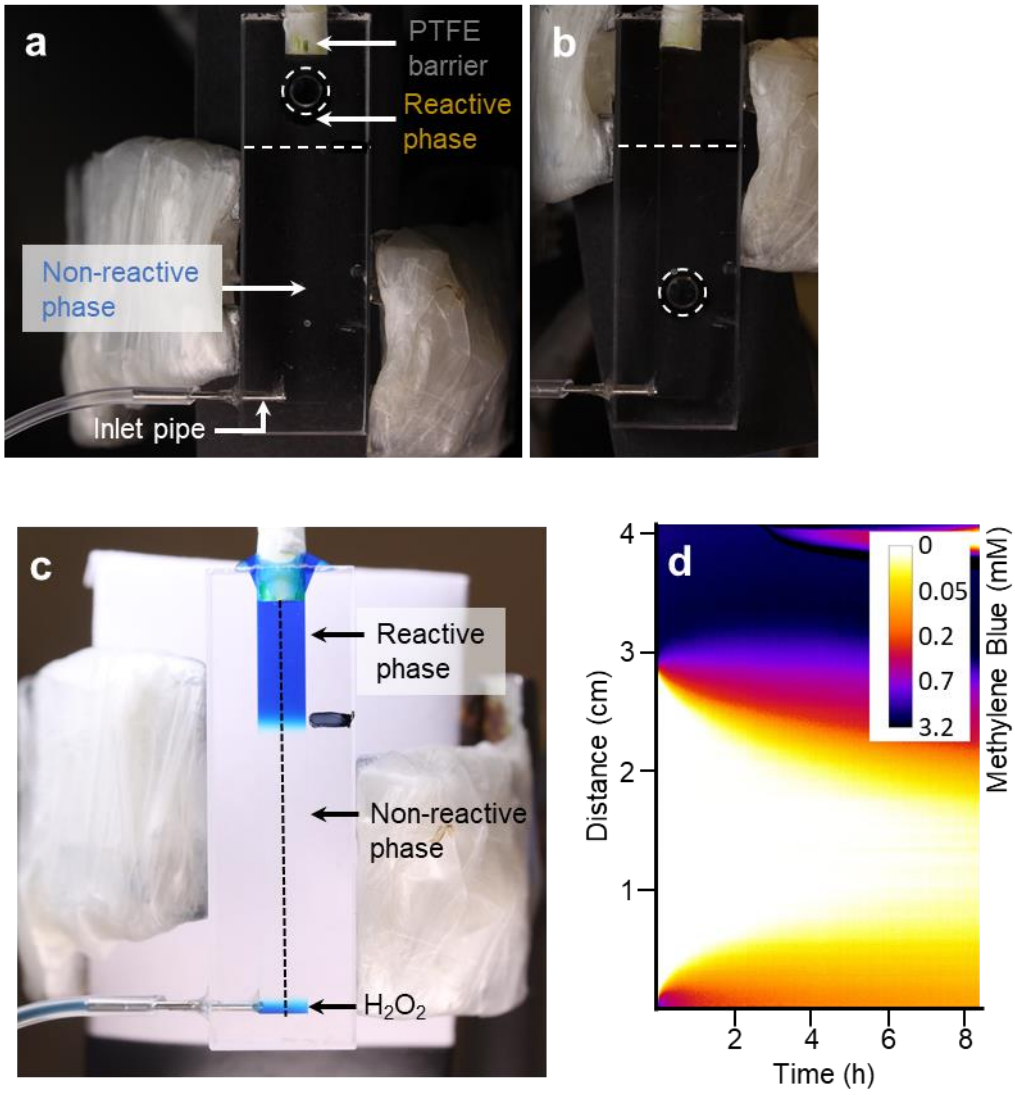

Figure 5.4-1: *Camera images of the experimental setup of the transient protamine/DNA-microcapsule reactivity experiment.* ***a-b*** *show the cuvette with the reactive phase above, indicated by the white line. The circular indicator shows the location of the UV/VIS-probe.* ***c*** *Methylene blue was used to indicate the locations of the three phases within the water-column.* ***d*** *shows a kymograph of the diffusion of methylene blue from the bottom- and the reactive phase into the non-reactive phase.*

Again, the cuvette device from the damped oscillation experiments in chapter 4 was used, as it provided very convenient dimensions to record both the motion of the capsule but also measure the

production of a chemical product within the reactive phase via an attached spectrometer probe. Furthermore, the attached inlet on the bottom of the cuvette allowed the addition of H_2O_2 via a syringe pump, which is less invasive and simplifies the assembly of the experimental device. Figure 5.4-1-c shows the assembled device with all three phases, the H_2O_2-phase (160 mM, with 4 wt% sucrose), the non-reactive glucose phase (0.08 M with 2 wt% sucrose) and the reactive phase, which had a volume of 300 µL and consisted of Ampliflu™ Red, (also called Amplex Red, 0.83 mM with 0.08M glucose). To showcase the density-induced phase separation and the establishment of smooth interfaces, the reactive phase and the H_2O_2-phase were dyed with 3.2 mM methylene blue. This setup furthermore allowed to assess the diffusion of the reactive phase and the H_2O_2-phase into the non-reactive phase over time, which is shown in the kymograph of Figure 5.4-1-d. The concentration was once again calculated from the calibration curve, which was presented in Figure 4.4-18. What this shows is, that the phases stay stable for quite a long time. The kymograph shows that the methylene blue does penetrate the central phase, but the concentration gradient is considerably low. For example, after 2 hours the reactive phase diffused about 0.8 mm into the central phase and diluted from 3.2 mM to about 0.2 – 0.01 mM. The actual experiment usually only ran for 40-60 minutes, which makes this setup quite stable and prevents any heavy dilution within the reactive phase which could distort the signal.

Just like ABTS in the previous experiments, Ampliflu™ Red is a chromophore that reacts with the enzyme HRP and produces a highly coloured red product, which can be excited at $\lambda_{Excitation\ Amplex\text{-}Red}$ = 571 nm, and which emits at $\lambda_{Emission\ Amplex\text{-}Red}$ = 588 nm. This raises the question why the chromophore was changed in the first place. Chapter 4 has discussed the concept of enzyme leakage from protamine/DNA-capsules and the same issue was found in ABTS-solutions. When using Amplex-red on the other hand, the enzymes were retained on the capsules and the leakage was minimal, which is why it was used for the transient reactivity experiments.

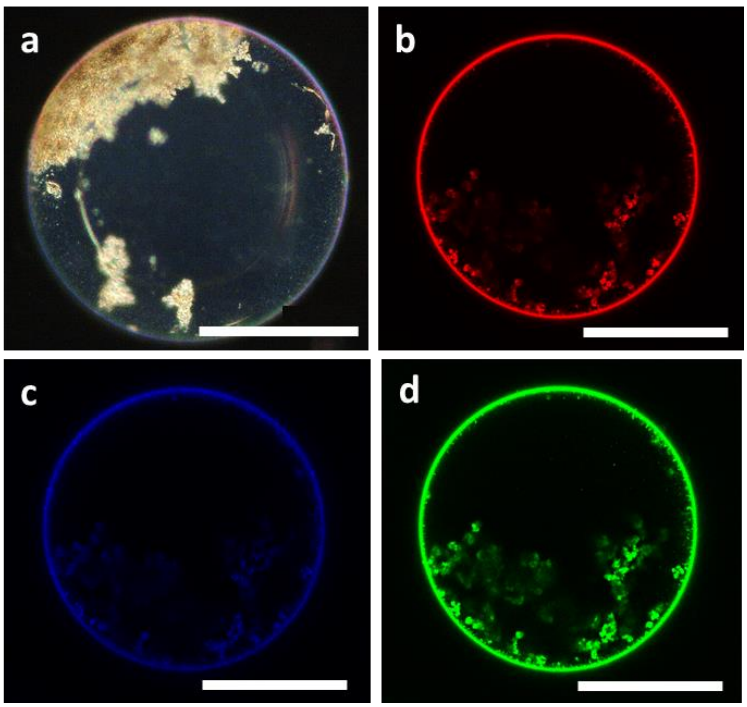

***Figure 5.4-2: a** A bright field image of a protamine/DNA-microcapsule containing RITC-GOx, FITC-catalase and Dylight-405-HRP. Corresponding confocal microscopy images showing presence of RITC-GOx (**b**), Dylight-405-HRP (**c**) and FITC-catalase (**d**). All scale bars: 200 µm.*

This means, that not only catalase and glucose oxidase are needed within the protamine/DNA-capsule, but also HRP as a third enzyme. Since the entrapment of three enzymes has not been proven yet, the following figure will show how RITC-GOx, FITC-catalase and Dylight-405-HRP are successfully found within the membrane of the protamine/DNA-capsule after 5 consecutive washing steps (Figure 5.4-2).

Finally, to assess the oxidation of Amplex-red within the reactive phase every time the capsule passes through, a micro-spectrometer-probe (attached to an *Ocean Optics Flame-S-VIS-NIR-ES)* was mounted to the apparatus. Figure 5.4-1-a and b show how the probe was either applied at the reactive phase, which was used to measure the oxidation of the Amplex-red, or within the non-reactive phase, which was done to read a blank-experiment and to show that there was no diffusion and/or background noise. The location of the UV/VIS-probe was indicated by a white circle.

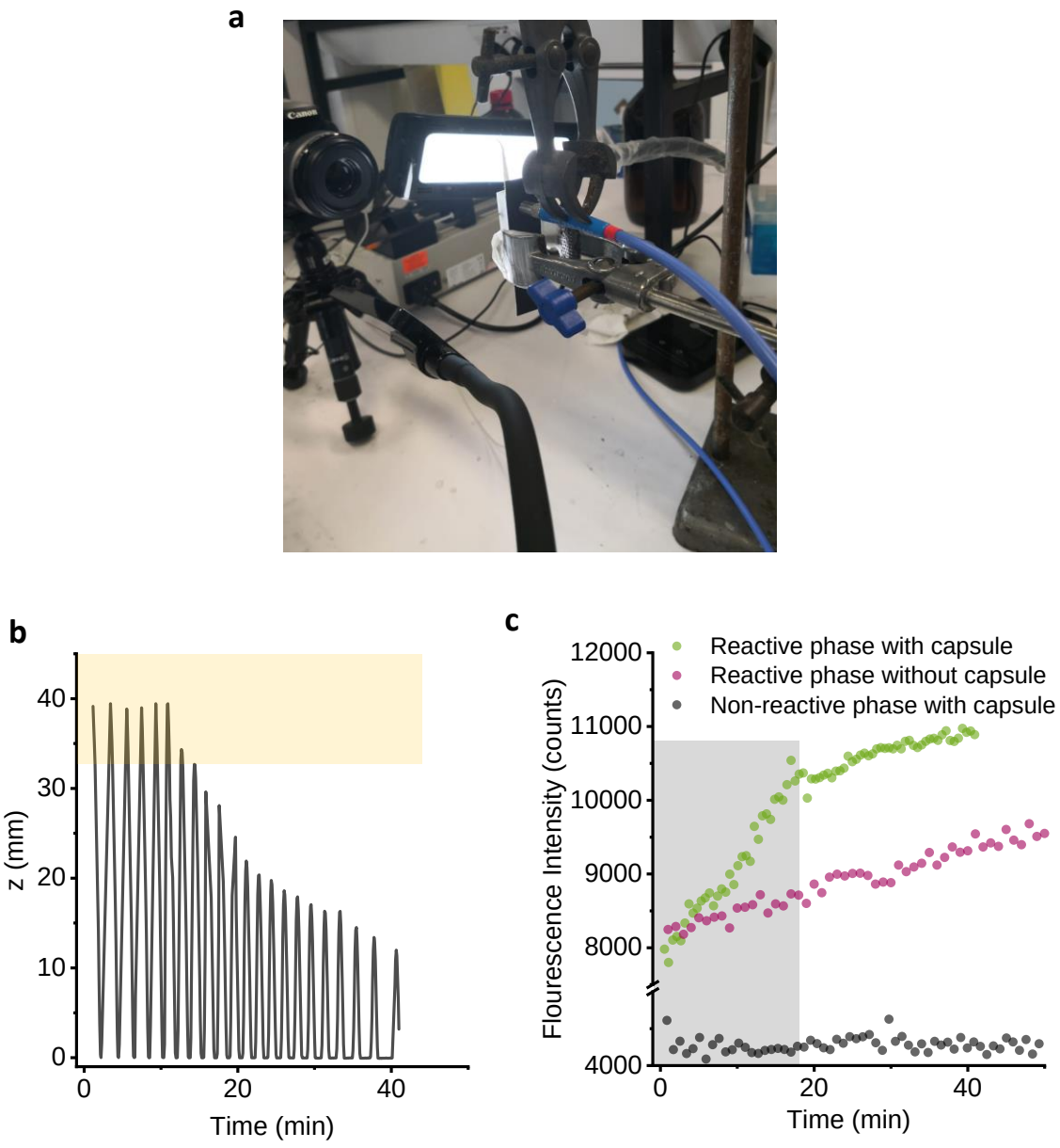

Figure 5.4-3: a *Photo of the experimental setup.* ***b*** *Tracked oscillation of a protamine/DNA-microcapsule between the reactive- and the non-reactive phase. The yellow box indicates the localisation of the reactive phase.* ***c*** *Fluorescence intensity count of the reactive phase at 588 nm, which was measured with a micro-UV/VIS spectrometer. The grey box indicates the time the protamine/DNA-capsule oscillated into the reactive phase.*

While the assembly of the device is complex, it was important to consistently start the experiment at the same time. Before adding the capsule to the device, an O_2-bubble was pre-nucleated and depleted externally just like in the experiments from chapter 4. As soon as the capsule entered the column, the top barrier was inserted into the device (a pipette tip, wrapped with a PTFE-membrane, see Chapter 4) and the H_2O_2-solution was added via syringe pump (7 μL at 5 μL/min). The capsule was then tracked via digital camera images in 5 s-intervals, which can be seen in Figure 5.4-3-b. The conditions of the oscillation were chosen so that the capsule's oscillation will eventually dampen, which makes it possible to see whether the capsule penetrating the reactive phase is indeed the reason for the increasing signal or not. The capsule was oscillating from end to end for about 11 minutes before it started to damp down. ~ 18 minutes into the experiment, the capsule would not penetrate the reactive phase anymore, after which it kept oscillating but noticeably started to slow down after 40 minutes, which was marked as the end of the experiment. Parallelly, the fluorescence intensity was tracked via the micro-spectrometer at 588 nm. The experimental setup included several lamps for the sake of tracking the capsule (Figure 5.4-3-a), and since the spectrometer-probe was applied at the back of the cuvette to prevent it from blocking the sight, it also captured the light of the lamps. While measuring the absorbance was also an option, it did not yield a good signal, which is why the photon count at 588 nm, which is effectively the fluorescence intensity, was measured. Figure 5.4-3-c shows three distinct datasets, the intensity measured within the non-reactive phase (Figure 5.4-3-c-black), the intensity in the reactive phase without (Figure 5.4-3-c-purple), and with an oscillating protamine/DNA-capsule (Figure 5.4-3-c-green). As expected, the datapoints of the non-reactive phase showed no increase of the signal, since there was no Amplex-red in this phase. This also shows that there was no measurable diffusion of oxidised Amplex-red from the reactive phase into the non-reactive phase within the time frame of 40 minutes. When measuring the fluorescence intensity without a capsule, it was surprising that the intensity slowly and steadily increased, even though there was no HRP present. This experiment shows that Amplex-red suffers from auto-oxidation, which causes the slow increase of the signal. Amplex-red is a highly sensitive chromophore and yields a very deep and intense coloration even at low concentrations, so every little auto-oxidation would be measurable. The reason for this can only be assumed. Amplex-red is usually kept in DMSO for storage inside a freezer, where it stays intact over long periods of time. So, the change of temperature, the transfer into an aqueous system and maybe even the addition of glucose could be responsible for the slow auto-oxidation, but this needs to be confirmed first. Finally, the fluorescence intensity was measured in the reactive phase with an oscillating protamine/DNA-microcapsule (Figure 5.4-3-c-green), which was already shown in Figure 5.4-3-b. During the first 18 minutes, the intensity increased linearly and at a much higher slope than afterwards. Furthermore, the slope > 18 min is very similar to the one of the dataset without the capsule (Figure 5.4-3-c-purple). This shows that the oscillating capsule was indeed triggering the oxidation of Amplex-red, and that the increase of the fluorescence intensity > 18 min was caused by the same auto-oxidation of Amplex-red which was discussed previously. Considering that the capsule is oscillating in and out of the reactive phase, one could expect a more "step-like" increase in the fluorescence-intensity, every time the capsule resides in the reactive phase. Then again, the background noise of the spectrometer, the diffusion of the chromophore and the short time periods between oscillations most likely prevent a clear distinguishment, even though the plot shows some slight plateaus within the first 18 minutes, which could be attributed to the times the capsule is descending out of the reactive phase. In summary, the experiment shows one example on how to increase the complexity of the protamine/DNA-capsule oscillation concept from chapter 4, by coupling the oscillation to a distinct chemical reaction in a localised area of the oscillation column.

5.4.2 Designing PCVs as cargo-containers of functional components for the uptake, transport and release via protamine/DNA-microcapsules

In the next part of the chapter, and to finally introduce the concept of cargo uptake, transport and release, it was necessary to gather a thorough understanding about the fabrication and the behaviour of PCVs. The foundation of PCV-fabrication is the formation of PDDA/ATP coacervates. While coacervates made from other components should also serve as a feasible platform for PCV-fabrication, this work solely revolves around the PCVs made from PDDA/ATP-coacervates, which was introduced by D. Williams *et al.* [65] Complex coacervation is highly dependent on the charge of the interacting compounds, which is experimentally defined by the pH and the concentration. Both PDDA and ATP were set to a pH of 6.5 and a concentration of 10 mM and DLS-zeta scans confirmed the expected positive and negative charge for PDDA and ATP respectively (Figure 5.4-4).

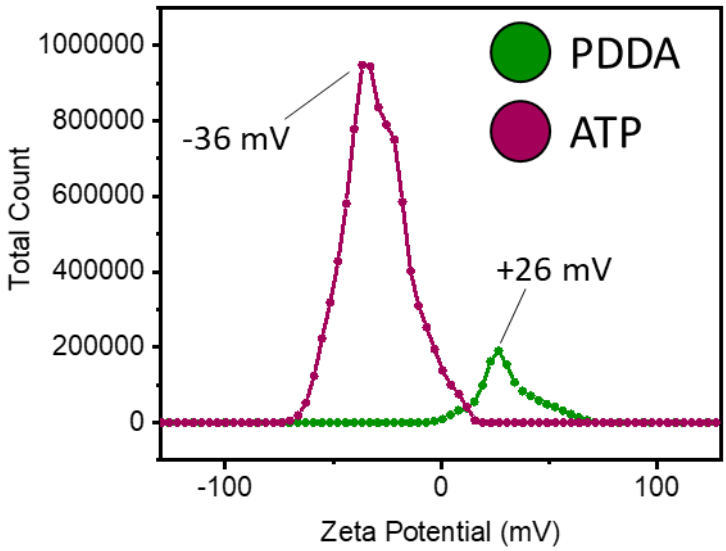

Figure 5.4-4: *DLS-zeta measurements of ATP (pH 6.5, 10 mM, -36 mV) and PDDA (pH 6.5, 10 mM, +26 mV).*

By simply mixing equimolar volumes of PDDA and ATP, the coacervates formed readily, which was indicated by the emergence of a visible turbidity (Figure 5.4-5-a). The size of the coacervates was heavily dependent on how long the coacervates were stirred for after mixing of the polyions. The reason for this lies in the coalescence of the coacervates. Once the coacervates get in contact with each other, they start to merge and form larger droplets. This can be observed when leaving the coacervate microdroplets for a longer period of time. After 1h, the former dull dispersion turned almost translucent, as the coacervates coalesced and formed 2 separate phases (Figure 5.4-5-b). While the stirring helps to form and disperse the coacervates, and later the PCVs, it does not prevent the coalescence. Instead, the longer the stirring time, the more chances the coacervates get to coalesce, which is why their sizes increased with the stirring time. Addition of PTA to the coacervates then initiated the transformation to the PCVs. While the coacervate dispersion appeared dull, it was more resembling of oil droplets in water, whereas the PCVs now appeared like a dispersion of solid colourless particles, which was comparable to a snow globe (Figure 5.4-6-a). Under the microscope the PCVs were highly spherical and, while not completely monodisperse in size, had a very uniform appearance (Figure 5.4-6-d). When stirring the coacervates for 30s, the resulting PCVs measured an average size of about 17 μm, when stirring them for 60s on the other hand, they turned out bigger

with an average size of 27 μm, while the smallest PCVs were as small as 4 μm and the largest as big as 60 μm (Figure 5.4-6-c).

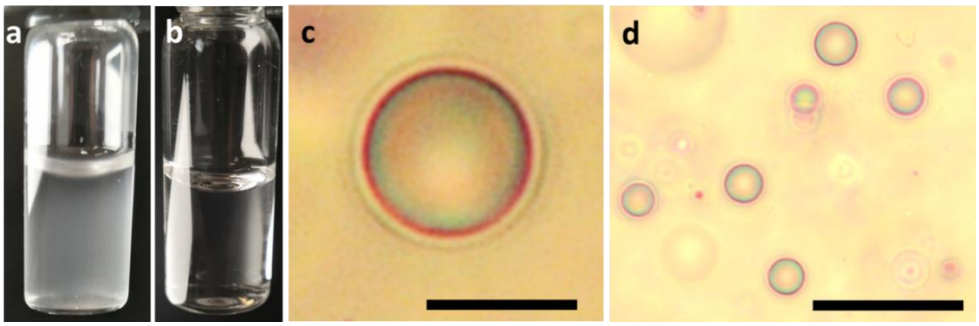

Figure 5.4-5: *Images of PDDA/ATP-coacervates. Camera image of fresh PDDA/ATP-coacervates inside a glass vial right after mixing of PDDA and ATP (**a**) and after letting them coalesce for 1 hour (**b**) and microscope images of a single (**c**, scale bar 30 μm) and multiple coacervates (**d**, scale bar 100 μm).*

When observing PCVs under phase contrast, their membrane appeared colourful and very pronounced, which can be attributed to the effect of birefringence, which is caused by materials with a high molecular organisation whose refractive index changes when experiencing light of different polarisations. [65,72] The birefringent domain is most likely found within the PTA/PDDA-membrane, due to the high organisation of the PTA. One of the most important properties of PCVs is the sequestration of functional molecules into the ATP/PDDA-coacervate phase. Small compounds like pyranine (Figure 5.4-6-f) or acriflavine can readily traverse the PTA/PDDA membrane and sequester into the coacervate layer, where they stay retained and did not leak in any substantial way.

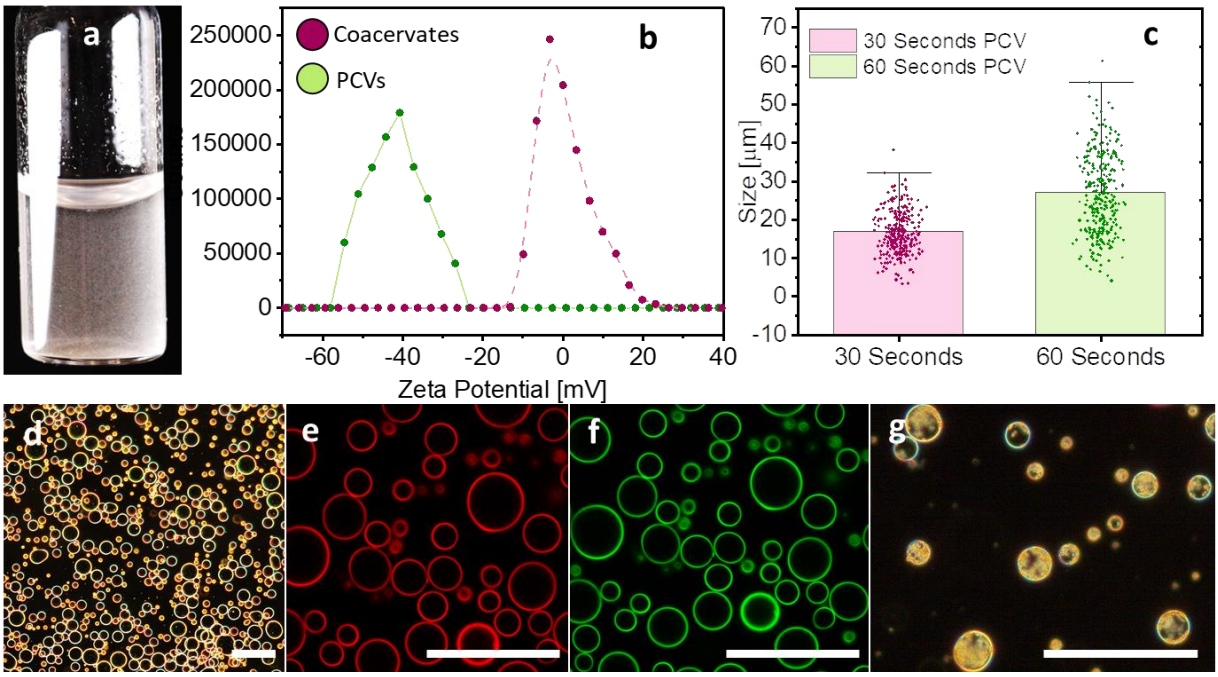

Figure 5.4-6: *Fabrication of PCVs. **a** Camera image of PCVs inside a vial right after the fabrication. **b** DLS-zeta-measurement of PCVs (green) and PDDA/ATP-coacervates. **c** Size-distribution of PCVs made from coacervates which were stirred for 30s or 60s. **d** Microscope image of PCVs. Image was taken with a phase-contrast filter to increase the contrast of the cells and the background. **e** Confocal microscopy image of PCVs with sequestered RITC-GOx (**e**), pyranine (**f**) and magnetic microparticles (**g**). All scale bars 100 μm.*

Larger molecules and proteins on the other hand like fluorescent tagged GOx (160 kDa, Figure 5.4-6-e), catalase (~232 kDa), horseradish peroxidase (40 kDa) or BSA (~ 66.5 kDa) did not pass through the membrane and had to be sequestered into the coacervates before the PTA/PDDA-shell was formed. As it can be seen in the confocal images of Figure 5.4-6-e-f, the fluorescent proteins are located close to the membrane and can be seen as a fluorescent ring, which confirms the hypothesis of D. Williams *et al*. that the PCVs are comprised of a multi-layered structure, with a distinct coacervate phase between the membrane and the lumen. Interestingly, particles like magnetic particles (Figure 5.4-6-g), fluorescent particles or silica particles could also be entrapped within the PCVs by simply sequestering them into the coacervates before PCV formation.

In this work, PCVs are supposed to act as both the carrier of a payload and as a cargo to be picked up at the same time. While protamine/DNA-microcapsules, the motile carrier, have shown to be very sticky and easily adsorb a multitude of compounds onto their membrane, it is still not sufficiently explained what type of interactions are responsible for the adhesiveness. Due to the abundance of arginine-residues of protamine, the previous assumption in chapter 3 saw electrostatic interactions as the most likely candidate for the general stickiness of the capsules. Following this concept, it would be very beneficial if PCVs were oppositely charged, which could increase the attraction between the two cell types and therefore the uptake probabilities substantially. Again, DLS-zeta potential scans were used to analyse the surface charge of PCVs and coacervates qualitatively. Coacervates exhibited a slight positive surface charge (+3.3 mV) when made from PDDA and ATP at pH 6.5 whereas PCVs turned out to be a lot more negatively charged and were measured to be -40 mV. In this work, PCVs were formed at molar ratios of ATP:PDDA:PTA of 1:1:0.4. Reducing the ratio to 1:1:0.1 and lower would not form consistent PCVs but rather a diffuse dispersion. This indicates that PTA is of utmost importance for the stabilisation of the microcompartments and that lower concentrations destabilise the vesicles due to insufficient crosslinking of the PTA/PDDA-membrane. Phosphotungstate is a heteropoly acid from the family of polyoxometalates (POMs) and comes in form of $[PW_{12}O_{40}]^{3-}$, which means it is not a small molecular species, but rather a cluster of 12 tungsten atoms, which are coordinated to oxygen and phosphate. The general term for a structure of this type is “Keggin structure” (Figure 5.4-7), which can be applied for many polyoxometalates. [73-76] Therefore, the negative zeta-potential should confirm, that the PTA-anion is mostly found on the surface, or the membrane, of the PCVs, which confirms the previously described results, and that PTA is exchanging ATP in coordination with PDDA.

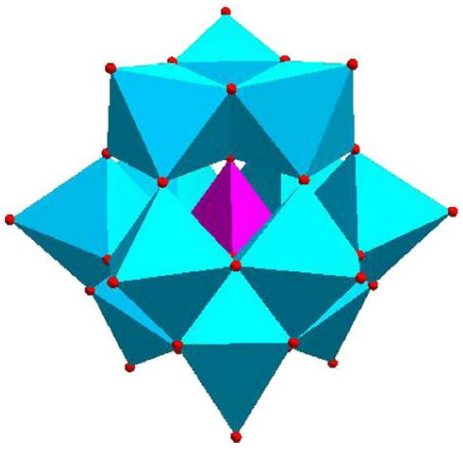

Figure 5.4-7: *Keggin structure of polyoxometalates.* [76]

And indeed, PCVs readily attached to the protamine/DNA-capsules and within a very short time frame. In a common experiment, a single or multiple protamine/DNA-microcapsules were immersed within a dispersion of PCVs in one of two ways, either by gently shaking and mixing them, or by letting them sediment onto the ground with the PCVs for a defined time. Using the latter method, the capsule was usually left to sediment overnight, which resulted in the highest amount of adsorbed PCVs. This can easily be explained by the fact that gravity increased the interaction between the carrier and the PCVs, whereas simple mixing like in the former method would only provide occasional collisions but not a guaranteed contact. Nonetheless and with either method, PCVs can be attached to the protamine/DNA-capsules in as little as a few seconds. Figure 5.4-8-b and Figure 5.4-8-c show a protamine/DNA-microcapsule with a uni-layer of PCVs attached to it. Even when using the above described large 60s-PCVs, the size difference between the two cells is still almost 10-fold, which makes PCVs so attractive as cargo or cargo-containers. This system becomes even more useful, as the PCVs would not detach once they are loaded onto the protamine/DNA-capsule. Neither rapid stirring, nor sonication or interaction with pipettes would detach the PCVs, which indicates some very strong interactions. Considering the assumption of electrostatic interactions, it was attempted to force the desorption of the PCVs by changing the ionic strength of the solution or by simply changing the pH.

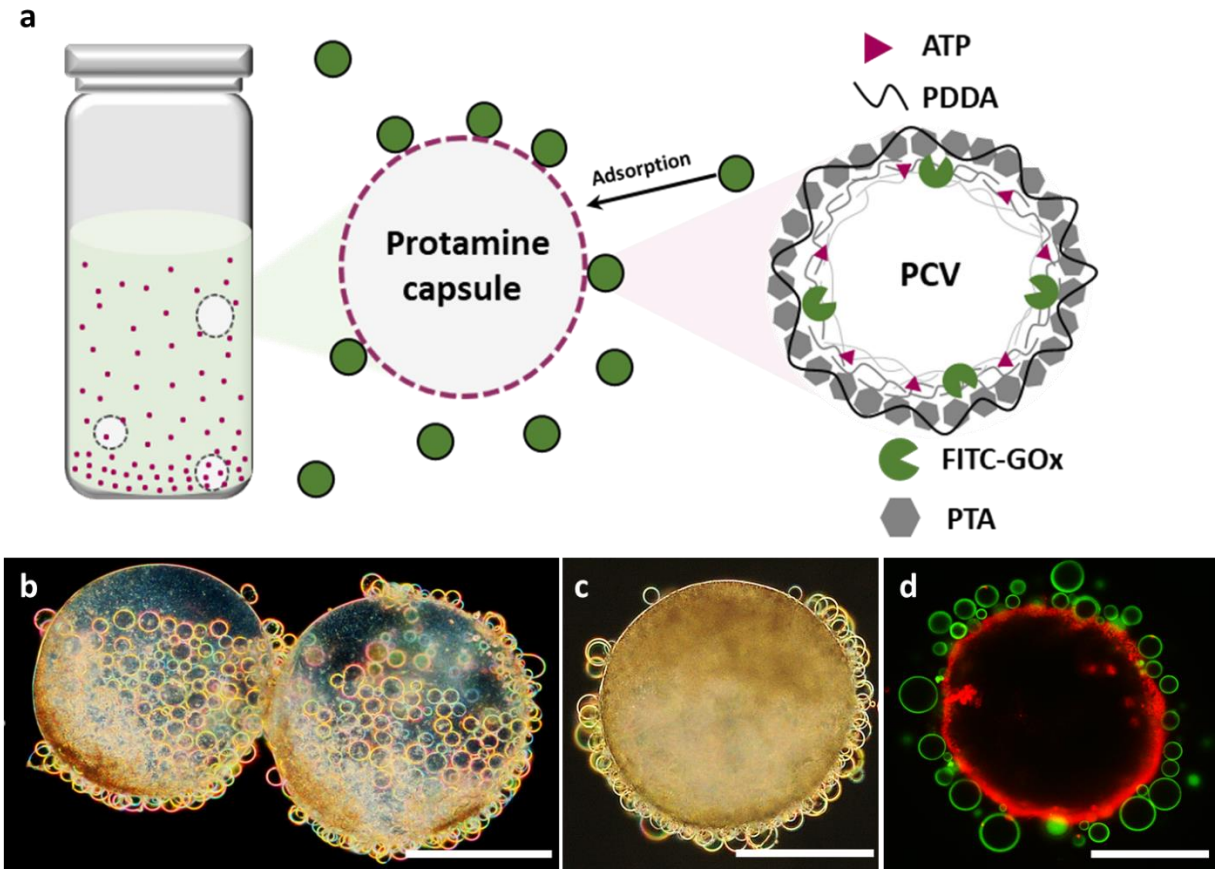

Figure 5.4-8: *Adsorption of PCVs onto protamine/DNA-microcarriers.* ***a*** *Schematic, describing the adsorption process.* ***b*** *Optical microscope image of PCVs attached to plain protamine/DNA capsules and* ***c*** *protamine/DNA-microcapsules with entrapped silica particles (10 mg/mL), catalase (19.8 kU/mL) and GOx (2.9 kU/mL).* ***d*** *Fluorescence microscope image of a protamine/DNA microcapsule stained with FITC-GOx and PCVs stained with pyranine. All scale bars: 200 µm*

Interestingly, none of the following conditions caused any observable desorption. The PCV-loaded protamine/DNA-microcapsules were immersed in sodium-phosphate buffer (pH 7, 50 mM, 100 mM), MES (pH 7, 50 mM, 100 mM), NaCl (pH 7, 50 mM, 100 mM) and di-water at various pH (3-9), yet none

of the changes lead to a release of the PCVs after stirring or sonication. To go even one step further, adsorption was still possible even in presence of 50 mM sodium phosphate (pH 3-8), which confirms that the pH or the surrounding ionic environment does not inhibit the binding of the PCVs. This could also debunk the theory that the adsorption is based on electrostatic interactions, even though it is still possible to assume that electrostatics, other non-defined interactions and soft-matter interactions are the reason for the strong adhesion. Just like histones in combination with DNA [77], protamine is a highly positively charged protein and exhibits very strong interactions with surfaces after forming the protamine/DNA-condensate. Either way, it is very complicated to define the exact type of interaction that leads to the PCV-uptake.

Another important task is the optimisation of the PCV-loading of the protamine/DNA-capsules. The method used to attach PCVs to the carrier capsules is highly dependent on the experiment which they are used for. Since this chapter aims to design an uptake and release concept though, the most relevant method for PCV uptake is the sedimentation of a protamine/DNA-capsule onto a bed of PCVs. Considering the sedimentation time, another assumption has to be made. To combine the previously described microcapsule oscillation and the novel uptake/release concept, it must be assumed that the protamine/DNA-carrier will only have a rather short amount of time to pick up the cargo, as it would otherwise be very difficult to control the oscillation. For this reason, the sedimentation times, or in other words the time the capsule resided on top of a PCV-bed to load the microcompartments onto its membrane, were set to a maximum of 2 minutes before the protamine/DNA-capsules with the attached PCVs were removed and washed. The number of washing steps on the other hand are another important parameter, as it defines the amount of excess protamine and DNA after the fabrication of protamine/DNA-capsules and the amount of PTA, PDDA and ATP after the fabrication of the PCVs. While the above studies did not show any interference of the adsorption efficacy with the ionic strength, these macro-ions can still change the uptake behaviour. In the following experiment, protamine/DNA-microcapsules and PCVs were washed 3-5 times and 1-3 times respectively to assess the adsorption efficacy. The experiment was performed in di-water and at pH 7 to prevent any other interactions with the cells (Figure 5.4-9). Here, a washing step is defined by the complete removal of the supernatant of sedimented cells or capsules and replacement with di-water. Generally, PCVs would not or only minimally adhere to the protamine/DNA-capsules if they have not been washed or only washed once (Figure 5.4-9). The same was found when using protamine/DNA-microcapsules which were only washed once or twice. Considering that protamine/DNA-microcapsules will be fabricated with entrapped enzymes which will be used in the later stages of this chapter, washing the capsules is a fundamentally important step to keep the enzymes active, which cannot be ensured if there's excess protamine and dsDNA in the solution. For this reason, washing protamine/DNA-capsules at least 3 times has been established as standard protocol. Washing the PCVs a second time on the other hand drastically increased the likeliness of sticking to the surface of the protamine/DNA-capsules and it appeared to improve the outcome even further when washing them a third time. Interestingly, it seemed like the number of adsorbed PCVs decreased with an increasing number of washing cycles for the protamine/DNA-capsules, even though they would still bind a sufficient number of PCVs to their surface. The reason for this behaviour can only be assumed, but the repetitive washing could change the chemical environment of the surface of the capsules, which then prevents the PCVs from sticking as much. Finally, washing either PCVs or protamine/DNA-capsules further did not change the outcome anymore.

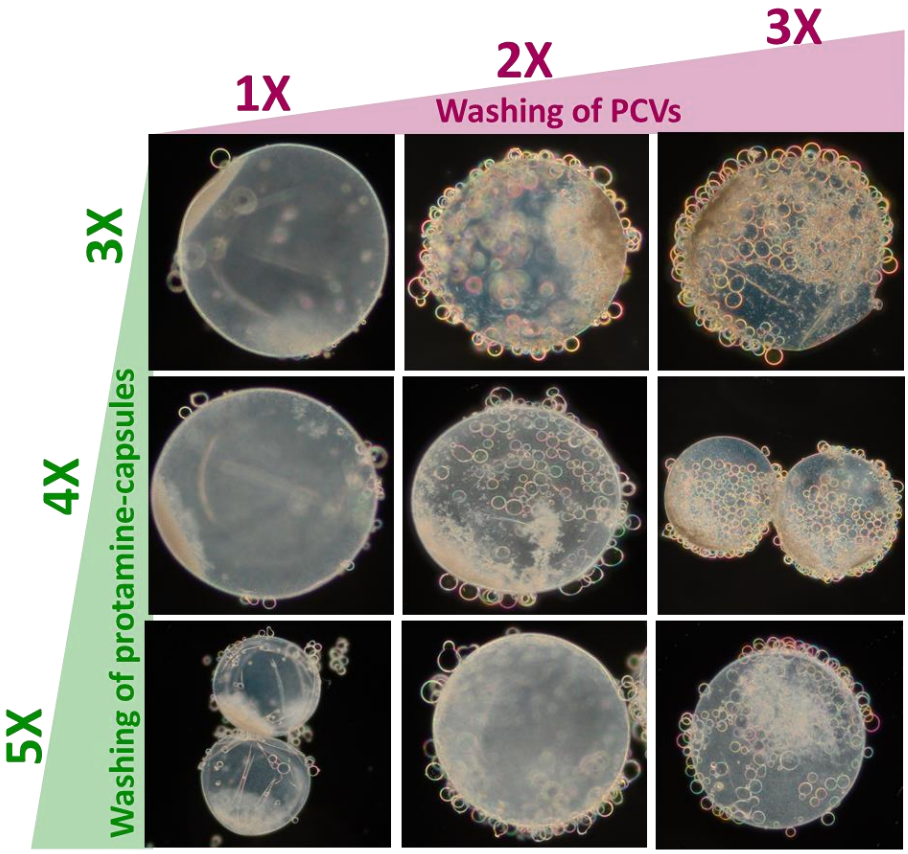

Figure 5.4-9: *Optimisation of PCV-uptake with protamine/DNA-microcapsules. The experiment was conducted in di-water at pH 7 and the protamine/DNA-microcapsules were sedimented onto a bed of PCVs for 2 minutes. Both PCVs and protamine/DNA-microcapsules were washed various amounts of times (1-3 times for PCVs and 3-5 times for protamine/DNA-capsules) before using them for the adsorption optimisation experiment.*

Another interesting and important thing to note is the general reproducibility of the PCV adsorption on protamine/DNA-capsules. While anchoring of PCVs on the surface of the protamine/DNA-microcapsules is facile, there are minor fluctuations in the number of adsorbed PCVs which are often hard to predict. One possible error source are the PTA, PDDA and ATP stock solutions. The results above from Figure 5.4-9 are generally reliable when produced within a short time frame of each other, but it seemed like they changed once the stock solutions are kept for a prolonged period of time. Another potential error could originate from the fabrication of the protamine/DNA-capsules. While, superficially, the capsules looked and behaved the same, the many variables of the protamine/DNA-capsule fabrication could lead to minor changes which then influence the adsorption of the PCVs.

With the PCV-desorption not being a valid concept, it is relevant to find an alternative way to release the cargo from the carriers. The studies from D. Williams *et al.* have shown that PCVs disintegrate when exposed to a pH greater than 12. To validate the concept and to confirm the previously reported results, PCVs were immersed in di-water at pH ranging from 5 to 12 for 1h, after which they were assessed via optical microscopy (Figure 5.4-10-purple). And indeed, the PCVs were stable and did not show any kind of damage at pH 5-9. When increasing the pH to 10 though, the PCVs appearance slowly deteriorated, which showed in form of a slight swelling and a loss of the colours around the membrane. Considering the colours most likely stemmed from the molecular organisation of the PTA/PDDA-complex, this could indicate that the high pH is now starting to affect it. This trend was then confirmed at pH 11 and higher, as the PCVs were completely disintegrated or dissolved, with no residues left behind. While this is an interesting find, as it shows that PCVs break slightly sooner than

literature has reported, it is not really a feasible concept for the release of cargo in relation to the established protamine/DNA-microcapsule oscillations, as the high pH would surely deactivate or even denature the enzymes. As an alternative, PCV stability was assessed in sodium phosphate buffer (50 mM) at pH 5-12 (Figure 5.4-10-green). The PCVs appeared to be stable at pH 5 to 7 but then already started to deteriorate at pH 8 and were completely disintegrated at pH 9 and above when immersed for 1 h.

These results are highly interesting as they now provide a much more convenient pH-range in which the cargo could be released through PCV-disintegration. Sadly, this does not answer why the PCVs break and disintegrate in the first place. One possible explanation is that the pH increase alters the charge of the poly-ions PTA, PDDA and ATP, which changes the interactions between them and weakens the structural integrity of the cell. There is very little scientific proof though to support or contradict this assumption. Another possible reason, which has a much more scientific foundation is the stability of PTA. In their own studies, Rhodes *et al*. investigated the stability of phosphotungstate at various pH and analysed the molecular decomposition.

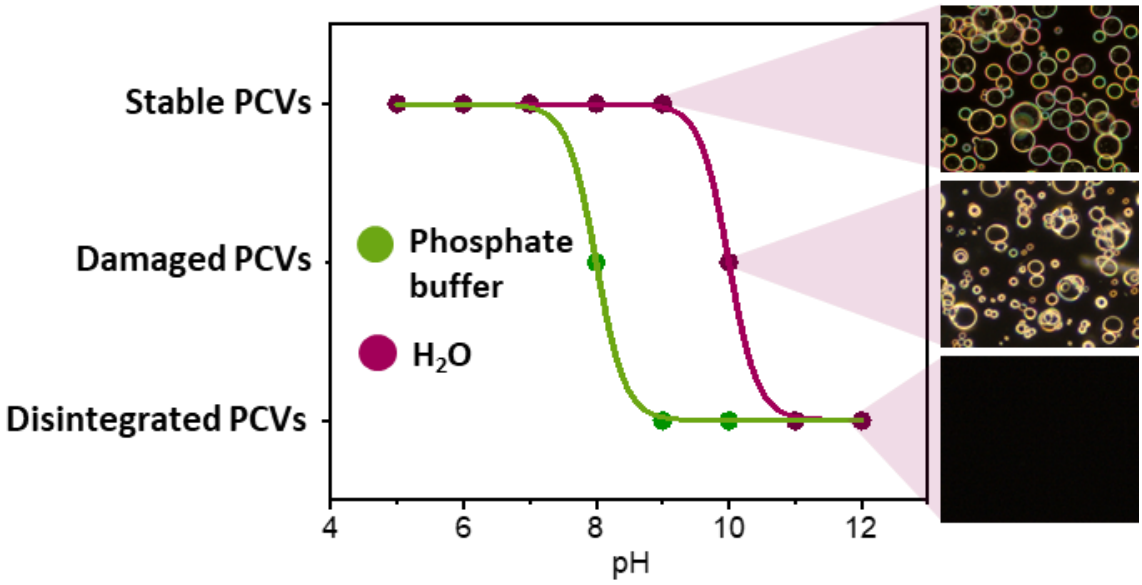

Figure 5.4-10: *PCV stability assay at various pH. The PCVs were immersed in di-water (**purple**) and sodium phosphate buffer (50 mM, **green**) at pH ranging from 5 to 12. The PCVs were observed under an optical microscope for 60 minutes and assessed according to their visual appearance as either "**stable"**, "**damaged"** or "**disintegrated"**.*

Here, they found that PTA does decompose as the pH increases and they defined the following states according to the pH that PTA was exposed to (Table 5.4-1). Above, PTA was described as a $[PW_{12}O_{40}]^{3-}$ complex, which is now put into perspective, as the polyoxometalate structure changes heavily depending on the surrounding pH. In fact, only at a very low pH of 1, the PTA structure was found to be predominantly $[PW_{12}O_{40}]^{3-}$ and started to change to dimers and other variations as the pH increases. What is most interesting though, is that PTA starts to decompose to its very basic components phosphate (PO_4^{3-}) and tungstate (WO_4^{2-}) once the pH surpassed 8. While one has to consider that PTA is locked inside the PDDA/PTA complex, which most likely prevents the decomposition to a degree, it certainly corelates well with the observed PCV decomposition at higher pH. [78]

Table 5.4-1: *PTA decomposition in relation to the pH.* [78]

pH	*PTA decomposition*
1	$[PW_{12}O_{40}]^{3-}$
2.2	$[PW_{12}O_{40}]^{3-}$, $[P_2W_{21}O_{71}]^{6-}$, $[PW_{11}O_{39}]^{7-}$
3.5	$[PW_{12}O_{40}]^{3-}$, $[P_2W_{21}O_{71}]^{6-}$, $[PW_{11}O_{39}]^{7-}$, $[P_2W_{18}O_{62}]^{6-}$ $[P_2W_{19}O_{67}]^{10-}$
5.4	$[P_2W_{21}O_{71}]^{6-}$, $[PW_{11}O_{39}]^{7-}$, $[P_2W_{18}O_{62}]^{6-}$
7.3	$[PW_9O_{34}]^{9-}$
8.3	PO_4^{3-}, WO_4^{2-}

This does not necessarily explain though, why the decomposition of the PCVs has accelerated so much when performing the experiment in sodium phosphate buffer. What seems most likely though, is that the ions of the buffered solution also interact with and weaken the PDDA/PTA-complex and the PDDA/ATP-coacervate phase and potentially also accelerate the decomposition of the PTA complex, which then results in an earlier PCV-disintegration.

To investigate the PCV-disintegration further, PCVs were immersed in other salt-solutions (NaCl, Na_2SO_4 HNa_2PO_4, MES and urea) at various concentrations (50 mM, 100 mM, 500 mM, 1M) at pH 9 (Table 5.4-2). What became clear fast was, that the sodium phosphate buffer indeed resulted in the quickest disintegration of the PCVs. Increasing the concentration only marginally changed the disintegration speed by a few minutes and the PCVs generally disintegrated within only 15 - 30 minutes. MES-buffer also enabled the PCV-disassembly at pH 9, even though the disintegration times were significantly longer, taking up to 2 hours at lower concentrations (500 mM – 50 mM) and ~ 1 hour at 1 M. Other salts like NaCl and Na_2SO_4 were predominantly ineffective as they neither damaged nor broke the PCVs. Only when using a substantially high concentration of 1 M, PCVs started to disintegrate in sodium sulfate over-night. These time periods are way too high though to enable any kind of triggered release in combination with the transport of the PCVs. Finally, urea was also chosen to assess the PCV-disintegration for the sake of the later parts of this chapter, in which urea will play an important role in combination with urease. What is important here, is that urea is not supposed to break the PCVs as it will only serve as substrate but should not interact with the PCVs. And indeed, the results have shown that urea does not damage or break the PCVs at pH 9, neither at high or low concentrations.

Table 5.4-2: *PCV disintegration in various buffers.*

Disintegration at pH = 9					
	NaCl	Na_2SO_4	HNa_2PO_4	MES	urea
1 M	✗	✓***	✓	✓*	✗
500 mM	✗	✗	✓	✓**	✗
100 mM	✗	✗	✓	✓**	✗
50 mM	✗	✗	✓	✓**	✗

* = 1 hour
** = 2 hours
*** = over night

Figure 5.4-11 shows the disintegration of PCVs of two different sizes (30s and 60s) in a 50 mM HNa_2PO_4 at pH 9, which was examined under the brightfield microscope. In both datasets, more PCVs are appearing within the first two images, which is due to more PCVs settling on the bottom of the well and therefore coming into focus of the microscope. The brightfield images show how the membrane weakened progressively, as the microcompartments first started to swell (~ 4 minutes) after which the membrane slowly disintegrated and vanished (8 minutes – 12 minutes). This is an interesting observation, as it shows that the membrane disintegration goes hand in hand with something that looks like an osmotic uptake of water from outside into the cell, which most likely further destabilised the structure. One question that arose during the experiment, was whether the PCVs just moved out of focus and the supposed disintegration was but a mere optical illusion, but thorough scanning through the well along the z-axis had proven that no PCVs were left inside the volume, which means that all cells have been disintegrated. Changing the size of the PCVs by altering the stirring times of the coacervates as it was described above did not change the outcome of the experiment in any way. In either case, the PCVs would break after merely 8 minutes and the process was virtually identical. Since the 60s variant was more convenient to work with and since there was no need to compare it much more to the smaller 30s PCVs, 60s PCVs were used in all further experiments.

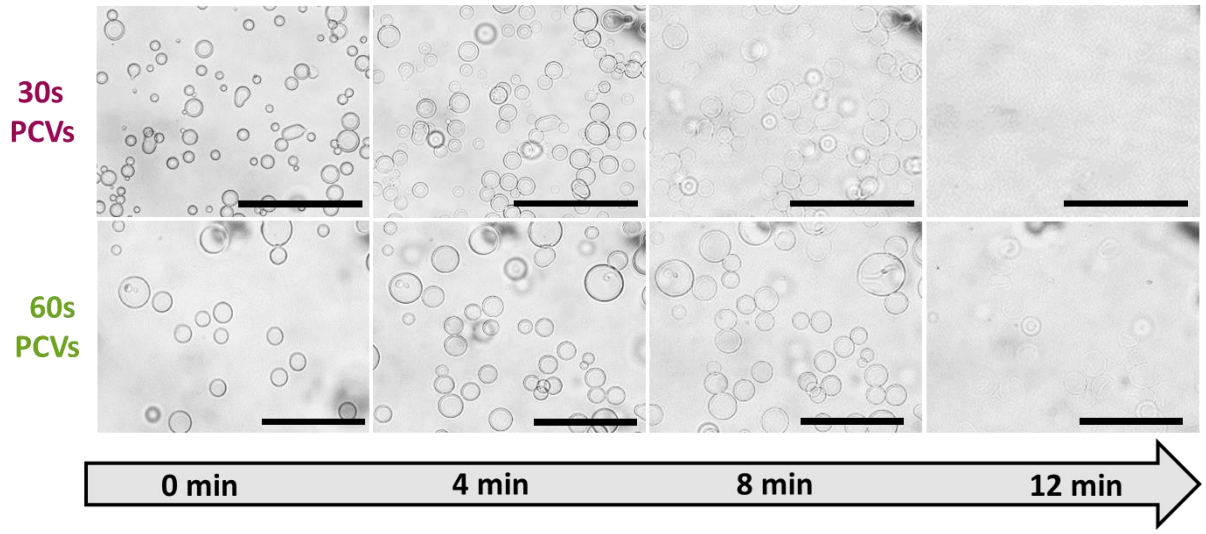

Figure 5.4-11: *Optical brightfield microscopy images of PCV-disintegration in 50 mM HNa_2PO_4 at pH 9. The size of the PCVs was altered by changing the stirring time of the previously formed coacervate droplets from 30s to 60s. The experiment was performed in a 96-well plate and with a volume of 200 µL. All scale bars: 200 µm.*

While utilising a buffer-salt to support PCV disintegration now is a valid concept, it still lacks depth and finesse as the protamine/DNA-microcapsules would still merely serve as the carrier but do not have any further purpose. So, instead of relying on a separate phase with a higher pH like it was shown above, the smarter concept would induce a pH change itself and therefore trigger the PCV-disintegration from the carrier. Enzyme-entrapment is an established concept for protamine/DNA-microcapsules and urease plays an important role in the regulation of the pH both in nature and in laboratory experiments. [79-81] For this reason, urease was entrapped within the protamine/DNA-microcapsules and just like for the other two enzymes, immersing the microcapsule in a urea solution would then theoretically trigger the urease reaction and therefore a local change of the pH and the disintegration of the PCVs (Figure 5.4-12-a).

To assess and confirm this hypothesis, protamine/DNA-microcapsules were fabricated with 19.8 kU/mL catalase, 2.9 kU/mL glucose oxidase and 0.29 kU/mL urease and immersed in 200 µL of a 0.1 M urea solution inside a 96-well plate. Since measuring the local pH at the protamine/DNA-membrane

is highly complicated, the pH was instead measured with a pH-meter probe within the overall volume but as close to the capsule(s) as possible (Figure 5.3-1). The pH-change was measured for a single capsule and for batches of 5 capsules and the surrounding solution was 0.1 M urea mixed with either 100 mM HNa_2PO_4-buffer (Figure 5.4-12-b) or di-water (Figure 5.4-12-c). The graph in Figure 5.4-12-b shows how the pH started to increase from the second the protamine/DNA-microcapsules were introduced into the urea/HNa_2PO_4-solution, even though the increase was a lot faster when adding 5 capsules. After roughly 20 minutes, the pH did not increase further in case of 5 microcapsules, which marked a pH of ~ 8.8. When using one capsule instead, the pH was still increasing but did not even surpass pH 8 after 20 minutes, which is fairly slow in comparison and could pose a problem considering a pH of 9 and higher seemed to be an important variable for PCV-disassembly. On the other hand, when doing the experiment without the addition of the phosphate buffer, the pH increase was substantially quicker. When adding 5 capsules, it took only about 5 minutes for the pH to surpass 9, after which it kept increasing, even though only at a diminished rate. A single protamine/DNA-capsule was now also capable of rising the pH up to a value of 8.8 after only 20 minutes, even though it also appeared to reach a plateau at this point (Figure 5.4-12-c). Sodium phosphate buffer has a buffering range from about 6 to 8, which explains the slower pH increase, especially in case of a single protamine/DNA-capsule in Figure 5.4-12-b. Furthermore, it also seemed like it prevented the pH from reaching 9 or going beyond that, as the measured pH plateaued at about 8.9 (Figure 5.4-12-b, for 5 capsules).

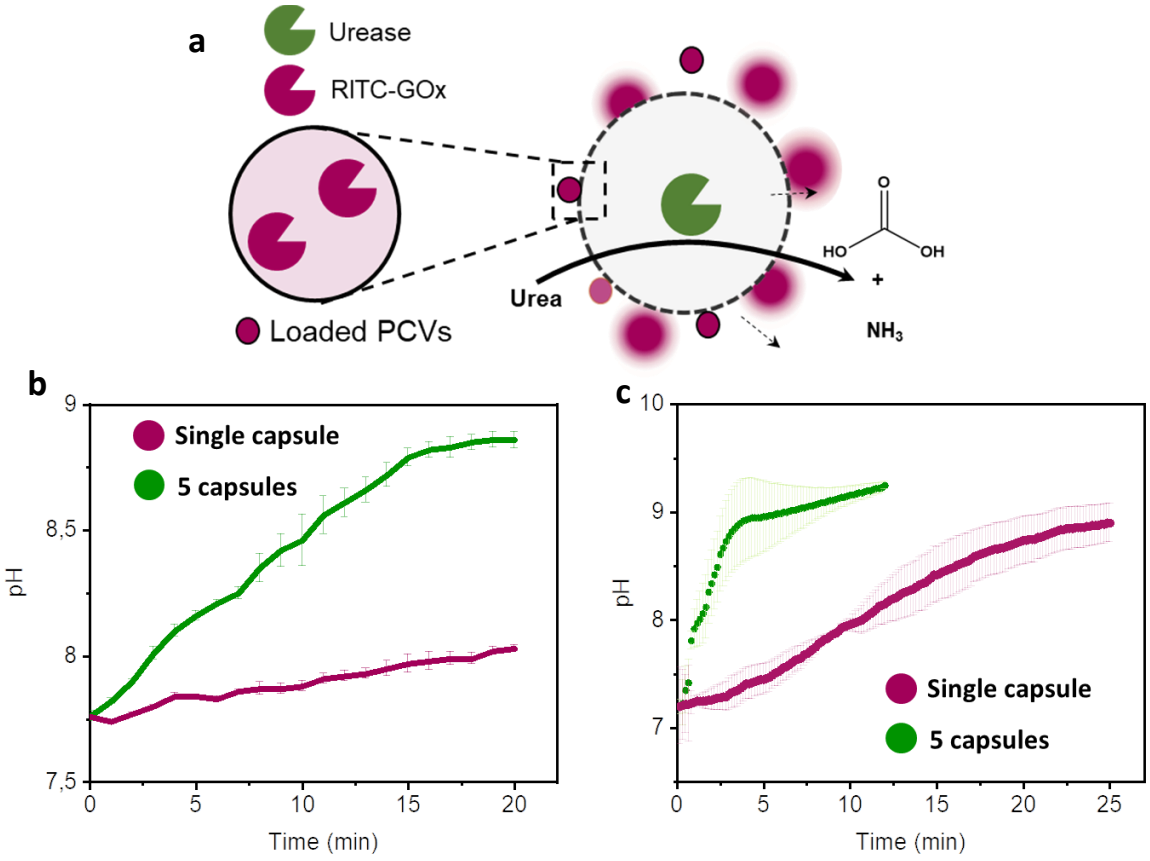

Figure 5.4-12: *pH-studies with protamine/DNA-microcapsules containing entrapped urease.* ***a*** *Illustration of protamine/DNA-microcapsules with entrapped urease and loaded with PCVs around the membrane. To visualise the PCV-disintegration, they were loaded with RITC-GOx. The conversion of urea through urease produces ammonia which raises the pH locally and in the surrounding solution. The pH was measured with a pH-meter for 1 (purple) and 5 (green) protamine/DNA-microcapsules in 100 mM HNa_2PO_4 + 0.1 M urea (**b**) or 0.1 M urea without any other buffering salts (**c**).*

The optimal urea-concentration for urease has been determined to be around 100-120 mM [82], yet it was interesting to see, if an increase in the urea concentration (1 M) could potentially accelerate the pH-increase and therefore the PCV-disintegration. The results in Figure 5.4-13 though show, that the difference is quite small. When using 5 capsules, the pH reached a value of 9 at about the same time as when using 0.1 M urea, but it increased a little further afterwards, up to a value of 9.25 after ~7 minutes. A similar shift was observable when using only 1 capsule, as the pH increased a little further up to a value of 9 after 25 minutes. To prevent any unwanted breaking or deterioration of the capsules and PCVs due to an unnecessarily high urea concentration, it was kept at 0.1 M for the rest of this chapter.

These results could now pose a few issues. When using a phosphate buffer to enable PCV-breakage, it seems very unlikely that entrapped urease in protamine/DNA-capsules will be able to rise the pH to 9 or higher, especially when only working with single capsules. On the other hand, the local pH-increase around the protamine/DNA-membrane and the attached PCVs could paint a different picture, which is not portrayed in the experiment above. Furthermore, the previous experiments (Figure 5.4-10) have ruled out di-water as the sole medium for PCV-disintegration, even though the pH-increase in a plain urea solution was very quick and reliable.

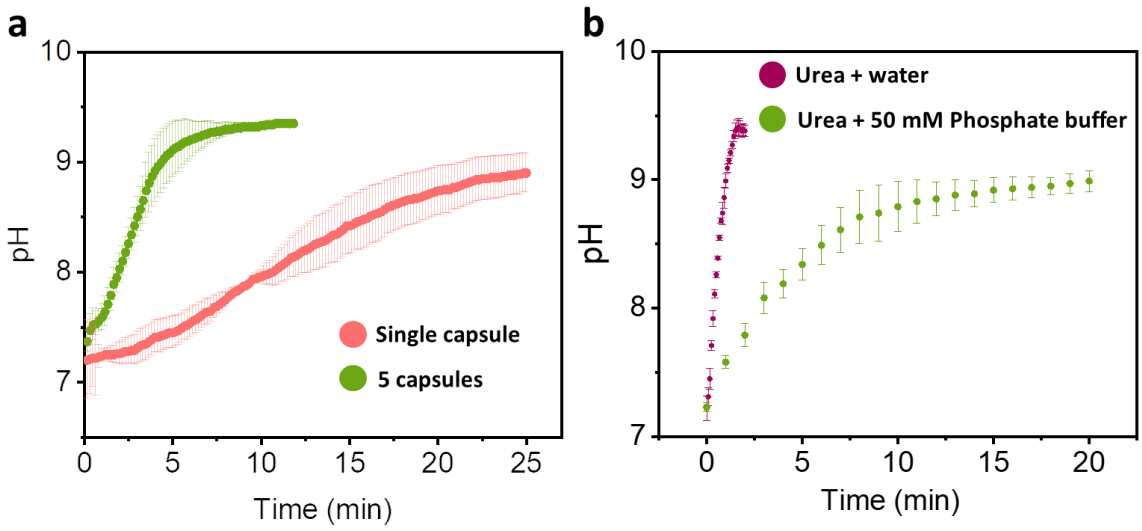

Figure 5.4-13: *Analysis of the pH-increase of (**a**) protamine/DNA-microcapsules in a 1 M urea solution and (**b**) pH increase of 10 U/mL of free urease mixed with 0.1 M urea.*

The next logical step is to test the urease/urea concept with the goal to disintegrate PCVs. In the following experiment, PCVs were once again dispersed inside a well of 96-well plate like in Figure 5.4-11, only this time they were immersed in a 0.1 M urea solution with 50 mM sodium phosphate at pH 7. The experiment was then started by addition of 10 U/mL urease, which initiated the rise of the pH (Figure 5.4-14). The optical microscopy images show how the PCVs start to disintegrate after 10 minutes. Once again, the PCVs start to swell before the membrane slowly disperses until all microcompartments have been dissolved after 35-40 minutes. While the results above showed how the complete disintegration took only 12 minutes in a 50 mM HNa_2PO_4-solution at pH 9, it is not surprising that it takes substantially longer for the PCVs to break when urease first needs to raise the pH. Nonetheless, Figure 5.4-14 proves that the same PCV disintegration can be achieved by using urease as the trigger, which opens a whole array of possibilities for potential release concepts.

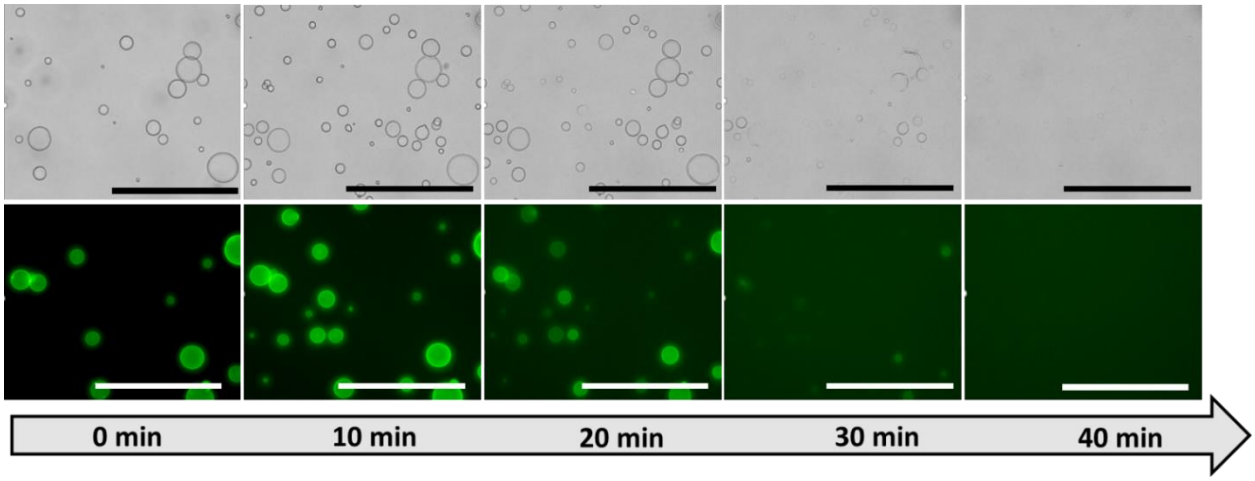

Figure 5.4-14: *Optical brightfield and fluorescence microscopy images of PCV-disintegration in 0.1 M urea and with 50 mM HNa_2PO_4 at pH 7.0. The experiment was performed in a 96-well plate with a volume of 200 µL and was started by addition of 10 U/mL urease.*

What is even more important though, is to show that sequestered and entrapped functional components can also be released. The fluorescence microscopy images from Figure 5.4-14 show a similar expansion and vanishing of the PCV-membrane, but they also visualise how the green fluorescent dye pyranine, which was sequestered into the PCVs beforehand, is slowly leaking out and into the surrounding medium after just 10 minutes, as the former black background starts to turn green. This furthermore shows, that PCVs do not need to be fully disintegrated for the sequestered cargo to be released, as the leakage appeared to start right when the vesicles began to swell. Performing the same experiment with green-fluorescent PCVs in water and without urea did not show any diffusion of the dye out of the PCVs, which proves that the leakage was induced by the PCV disintegration and in combination with urea and urease.

When repeating the same experiment without the buffer, the results were surprisingly similar (Figure 5.4-15). The PCVs started to swell after just 6 minutes and were mostly disintegrated after 24 minutes. It needs to be noted though, that not all PCVs disintegrated at the same speed, which is a common phenomenon, and which was observed in many experiments. This could be explained by the fact that PCVs slightly vary in size and maybe even membrane thickness, which then changes the time they need to break and dissolve. Nonetheless, the average disintegration time of ~20-25 minutes was confirmed over several experiments. This is highly interesting for several reasons. For one, the disintegration appeared to happen faster than in the previous experiment with the added sodium phosphate buffer. Considering the pH-increase is the main reason for the PCV breakage, it is to be expected that the buffer will slow the process down as it buffers the enzymatic production of the base. On the other hand, and what is even more surprising, the PCV disintegration happened in di-water and without the addition of any buffer, which was previously impossible at pH < 11 even with the addition of urea. Figure 5.4-13-b shows that the pH-increase of free, un-trapped urease is not substantially higher than the one of urease trapped within protamine/DNA-microcapsules, reaching a pH of ~9.5 and 9.0 when working with or without the addition of 50 mM sodium phosphate buffer respectively. So, if the PCV-disintegration was solely relying on a pH-increase, the urease/urea system should not suffice to break the vesicles. The only factor that changed from the previous studies in Table 5.4-2 and Figure 5.4-10 is the enzymatic reaction of urea with urease.

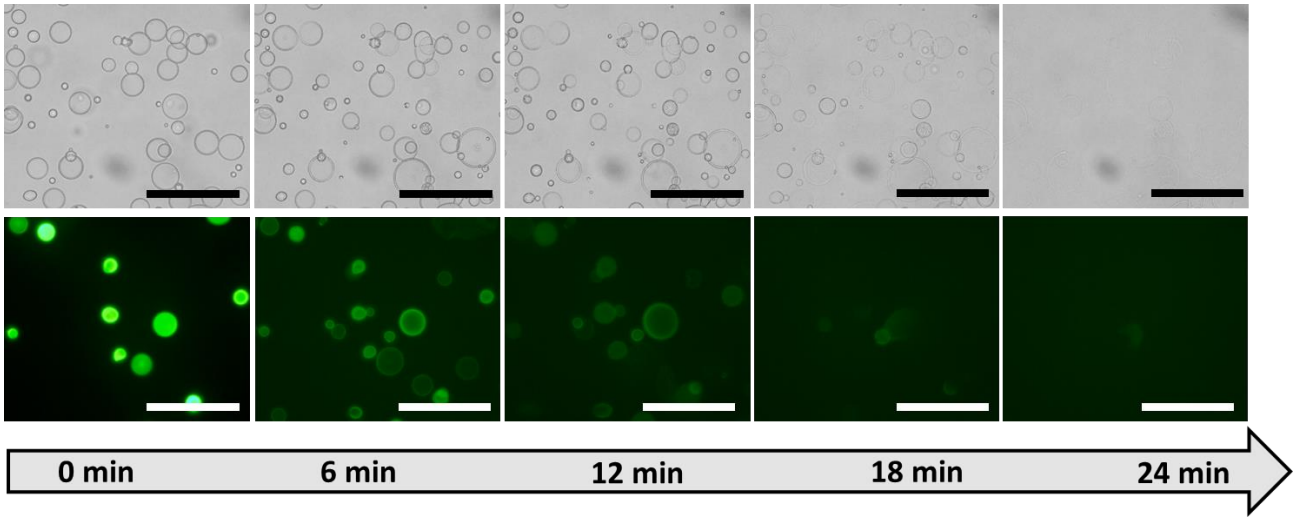

Figure 5.4-15: *Optical brightfield and fluorescence microscopy images of PCV-disintegration in 0.1 M urea at pH 7.0. The experiment was performed in a 96-well plate with a volume of 200 µL and was started by addition of 10 U/mL urease.*

When looking at the chemical equation of the reaction, the only products emerging from the conversion are ammonia and carbonic acid. While ammonia or more specifically NH_4^+-ions cause the pH to rise, it is the carbonic acid which could cause the PCVs to deteriorate just like in the case of sodium phosphate buffer (Figure 5.4-16).

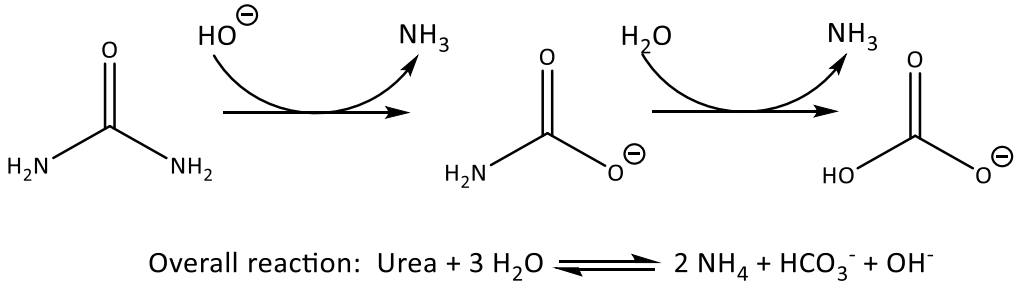

Figure 5.4-16: *Catalytic steps and overall reaction of the conversion of urea to ammonia and carbonic acid.* [66]

While the exact reason for the disintegration will be hard to pin down, the experiment shows that the urea/urease system is a valid option for the release of a payload from the PCVs and might even be preferential, since no other buffers will be needed. Nonetheless, the above experiment has only proven the disintegration of PCVs in a solution of urea and urease which does not represent the conditions which will potentially be used for the transport concept which envisioned protamine/DNA-capsules to contain the enzyme.

So, to establish this next step towards a working transport and release system, protamine/DNA-microcapsules were fabricated with 0.29 kU/mL urease, loaded with PCVs and then immersed in a 0.1 M urea solution at pH 7. In the first example, the urea solution also contained 50 mM HNa_2PO_4 to assess the relevancy of a buffer for future experiments. The optical micrographs of Figure 5.4-17 show the disintegration of the PCVs on the protamine/DNA-capsule in 30-minute intervals. After 30 minutes, the PCVs started to swell, just like in the experiments above and slowly faded away over the course of the following 90 minutes. After 120 minutes, many of the PCVs have vanished from the surface of the capsule, but there were still some which were clearly visible and did not disintegrate even though their appearance showed, that they were deteriorating. While the buffer most likely influences the disintegration as it buffers the rise of the pH, it does not necessarily explain why some

of the PCVs disintegrate as expected whereas others do not. The previous pH-studies indicated that the pH increase inside a buffered solution was very little, so one must assume that the local pH-increase along the membrane will be much more important than the overall increase inside the solution. So why do some PCVs deteriorate at such a slower pace than others? If the answer is not found in an uneven distribution of urease along the membrane, which is highly unlikely considering the previous studies of this thesis in chapter 3, the answer most likely is that these PCVs are either slightly more stable than others or that the PCVs did not get in contact with the products of the urea/urease reaction for some reason. While these results are not necessarily the same every time the experiment was repeated, there was a likelihood that some PCVs stayed intact even after a substantial incubation period.

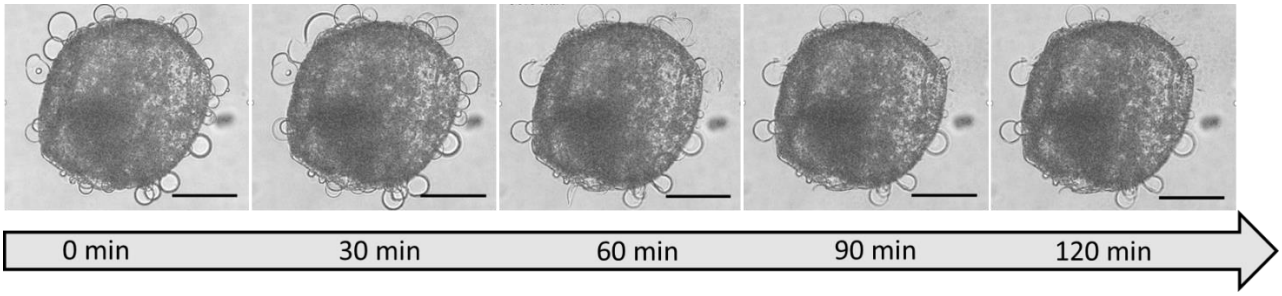

Figure 5.4-17: *Optical brightfield images of urease containing protamine/DNA-microcapsules (0.29 kU/mL urease) loaded with PCVs in a 0.1 M urea solution with 50 mM sodium phosphate (pH 7.0). The disintegration of the PCVs was tracked in 30 minute intervals.*

Next, the experiment was repeated in a 0.1 M urea solution and without adding any buffer (Figure 5.4-18). Once again, the PCVs started to swell after 30 minutes and continued to disintegrate. After 90 minutes most of the PCVs were disintegrated, even though there were a few PCVs which were still visible after 120 minutes just like in the previous case. Overall, though, the disintegration seemed to happen a lot quicker and much more reliable than with the buffered solution. To simulate the cargo delivery once more, RITC-GOx was chosen as the payload which was sequestered into the PCVs and appeared as a red fluorescence. The fluorescence microscopy images show how the PCVs disintegrate just like in the optical micrographs, while the payload was released into the surrounding medium. While the PCVs were barely visible after 90-120 minutes, there seemed to be a slight fluorescence left around the capsule, which could be due to RITC-GOx which was adsorbed onto the protamine/DNA-capsule after being release. To highlight the release of the entrapped RITC-GOx, the mean fluorescence of the whole capsule was tracked over the course of the experiment. The plotted data makes it easier to assess the exact time points during which the cargo can be expected. During the first 25 minutes the plotted curve seemed to be constant, after which it started to fall. After 50 minutes the cargo release started to visually decrease again and slowly approximated a minimum after ~150 minutes. That being said, after 90 minutes most of the cargo had already been released and the mean fluorescence is only tracking the released RITC-GOx in solution or the adsorbed RITC-GOx on the protamine/DNA-capsules. So, in a nutshell, the images and data above clearly show that the cargo-release with entrapped urease and without any buffers was superior, which also harmonised well with the previously discussed protamine/DNA-microcapsule oscillation, as using a buffered system would most likely change the enzymatic interactions of catalase and GOx.

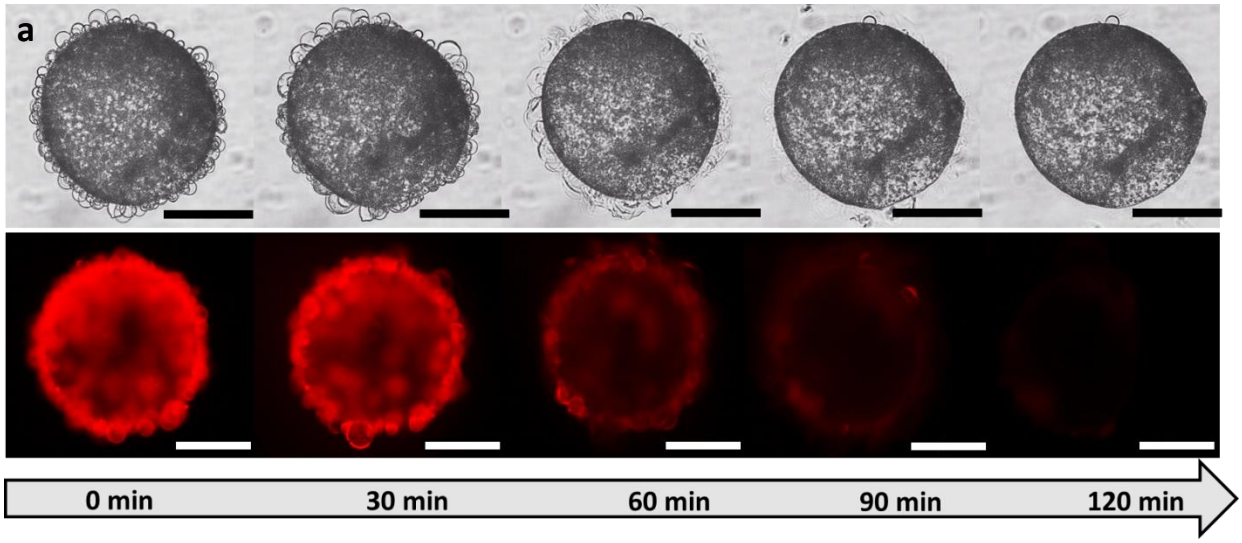

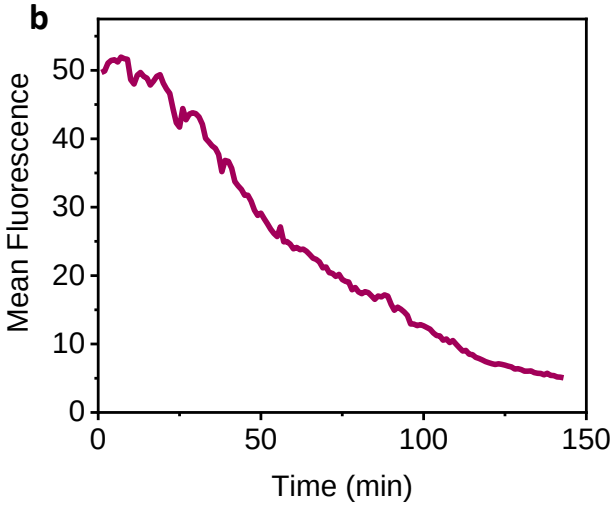

Figure 5.4-18: ***a*** *Fluorescence- and brightfield microscope images of urease-containing protamine/DNA-microcapsules (0.29 kU/mL urease) loaded with PCVs in a 0.1 M urea solution (pH 7.0). The disintegration of the PCVs was tracked in 30 minute intervals and the red fluorescence stemmed from the RITC-GOx cargo sequestered into the PCVs.* ***b*** *The mean fluorescence intensity of the PCV-covered protamine/DNA-capsules form* ***a*** *was plotted to support the visualisation of the release of the RITC-GOx cargo. The whole cell was used as the reference to track the mean fluorescence.*

Before coming to the actual transport, uptake and release experiments, the enzyme triggered disintegration of PCVs enables other interesting concepts, one of which should be described here. Many protocell-projects from the Mann group, as well as the work in this thesis, revolve around mimicking naturally occurring cellular or sub-cellular phenomena. So far, motility has been the focus of this thesis, which was presented over the past 3 chapters, but the novel concept of PCV-disintegration through enzyme-loaded protamine/DNA-microcapsules reminds of another important concept: cellular defence strategies. There is a vast number of different mechanisms that cells from organisms utilise to protect themselves and the organism from pathogens and parasites. The immune system of metazoans, ergo animal organisms, is probably one of the most popular and well-studied cases of defensive machinery. Here, immune cells are assigned which protect the organism from hostile intruders and guard the system from infection. [83-87] Cell compartmentalisation by itself serves as a defence mechanism, as pathogens must traverse these barriers to get inside of the cell. In response, the cells have established a variety of sensory machinery like pattern recognition receptors,

which send out an alarm signal to this host cell in case of an infection, which is then used to launch the appropriate response to eliminate the threat.[85,88] Many cells start their defensive strategies long before the pathogen reaches the system though. Here, the cell utilises chemorepellents which either deter or directly damage any dangerous microbe or pathogen. Example of such chemorepellents are H_2O_2 produced by the DUOX2 enzyme [89], the antimicrobial lectin RegIII-γ from some specialised epithelial Paneth cells, [90] and some cells and bacteria secret nitric oxide synthases (NOS) into their surroundings to defend themselves against other bacteria. [85,91,92]

The latter examples are very interesting as they resemble the way a protamine/DNA-capsule is destroying the surrounding PCVs. In the following experiments, PCVs will play the role of a pathogen which the host cell, the protamine/DNA-capsule, will encounter and therefore break to protect itself. Here, PCVs were laid out as a bed on the bottom of a 96-well plate onto which protamine/DNA microcapsules were added. The protamine/DNA-capsules were fabricated as usual but with only 0.28 kU/mL urease entrapped in them. Figure 5.4-19 shows two separate cases of single protamine/DNA-capsules on top of a bed of PCV- "pathogens".

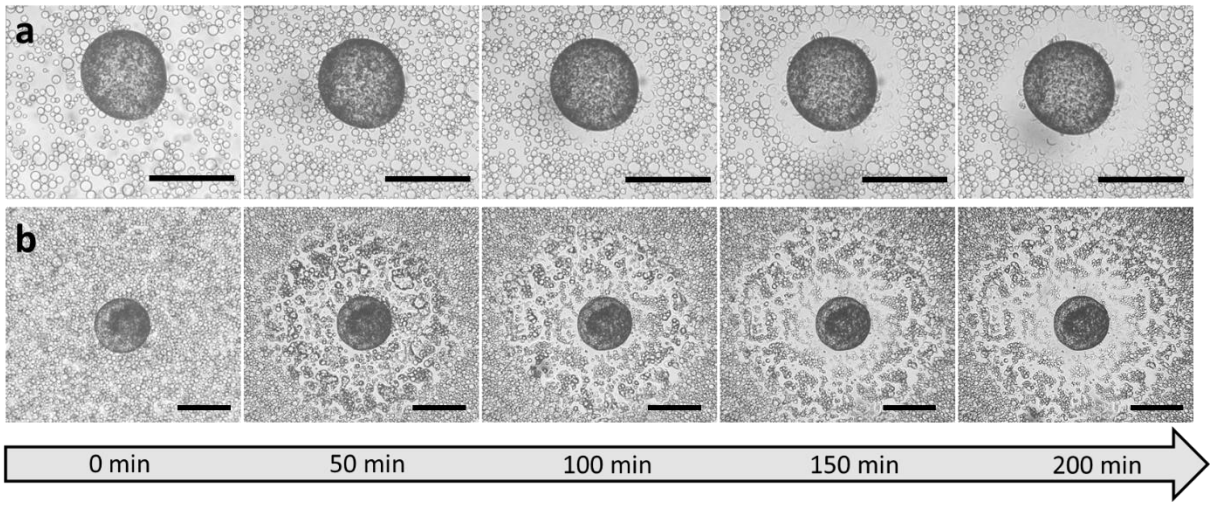

Figure 5.4-19: *Optical micrographs of a single protamine/DNA-microcapsule disintegrating surrounding PCVs in response to the addition of 10 μL of 1 M urea into a 100 μL dispersion of PCVs inside a 96 well plate. The capsule was immersed in either 50 mM HNa_2PO_4 (**a**) or in just di-water (**b**).*

The first image-set in Figure 5.4-19-a shows the capsule immersed in 50 mM HNa_2PO_4 (pH 7.0) and the experiment was started by addition of 10 μL urea (1 M). As soon as the capsule experienced the gradient of the injected urea, it engaged in its defensive strategy by secreting ammonia and carbonic acid through the reaction of urease and urea. During the first 50 minutes, there was no visible deterioration of the surrounding PCVs to be observed. Instead, smaller PCVs were still sedimenting from above the capsule, which were redispersed after adding the urea-solution. After 100 minutes, the PCVs around the capsule started to vanish which can be seen in form of a light halo around the capsule, which grew further as the PCVs continued to disintegrate. There are several interesting things to take away from this experiment. The fact that the PCVs are not only disintegrating around the capsule but instead, the area in which PCVs are destroyed is gradually expending with time indicates that the PCVs are indeed reacting to the secretion of the protamine/DNA-capsules. It also shows once again that, no matter if it is the pH increase, the production of ionic components or both, it is a localised effect that does not affect PCVs which are sufficiently far away from the capsule. The images from Figure 5.4-19-a furthermore show once more, that some PCVs on the surface of the capsule stay intact even after 200 minutes. Again, there is little data to support any assumption on why these PCVs

stay intact, especially since most of the surrounding PCVs have already been destroyed. When doing the same experiment without the HNa_2PO_4-buffer the results look slightly different (Figure 5.4-19-b). After 50 minutes, the PCVs around the capsule already appeared heavily deteriorated, whereas the cells in the first experiment were still intact. Again, this could be explained by the fact that the sodium phosphate buffer is having protective properties by preventing a fast rise in the pH. Continuing from there, the PCVs degraded further until most of them around the protamine/DNA-capsule were disintegrated. Nonetheless the disintegration pattern needs to be addressed, as the PCVs did not simply dissolve like in the previous experiment. Instead, the PCVs rather looked like they melted or almost like they turned back into the droplet character of the previously formed coacervates, as they also started to coalesce. Furthermore, there was no clear cut edge between the viable and the destroyed PCVs like in Figure 5.4-19-a. Instead, there were multiple areas: a small ring around the capsules where PCVs were mostly disintegrated, then a larger ring around that where PCVs were simply damaged, beyond which PCVs were generally intact. In Figure 5.4-20 the same experiment was repeated with fluorescent PCVs, which were fabricated with sequestered pyranine to further highlight the odd structure of the PCVs after urease activity. The left image shows the PCVs right at the start of the experiment whereas the right image depicts the state after 150 minutes. For one, it shows that even near the capsule, there are still fluorescent clusters of what looks like a foam or little droplets, even though their fluorescence has noticeably declined.

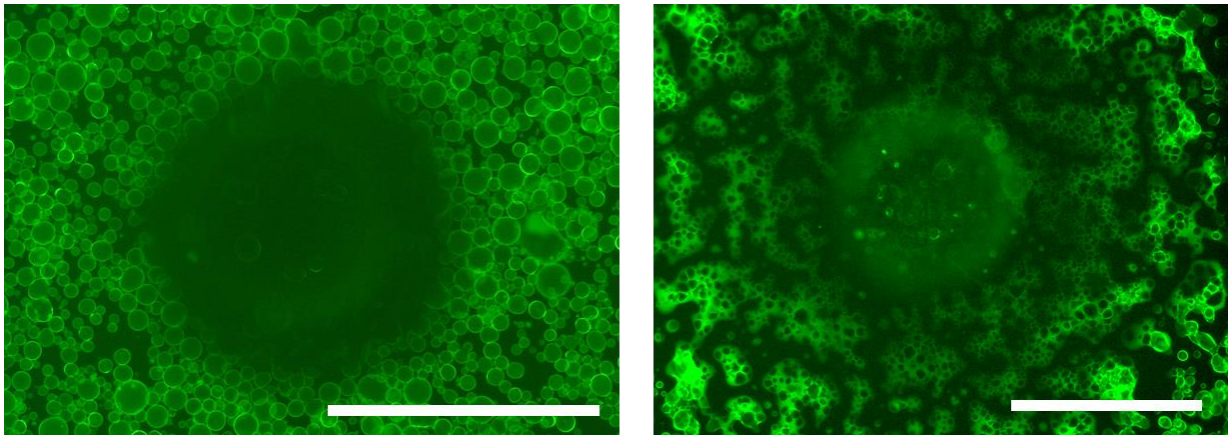

Figure 5.4-20: *Fluorescence microscopy images of PCVs surrounding a single protamine/DNA-microcapsule which contained entrapped urease (0.29 kU/mL). PCV disintegration was induced by addition of 10 µL of 1 M urea into 100 µL di-water inside a 96 well plate. Pyranine was sequestered into the PCVs during the fabrication to make them appear as green spheres under the fluorescence microscope.*

Nonetheless, the image highlights how many of these droplet-like structures start to coalesce and merge into each other, what would not be possible before the PCV-disintegration. Here, one could assume that the PCVs have indeed turned back into their coacervate-droplet character, and that only the PTA-containing membrane has been dissolved. This would be an interesting result, as there is no published literature on coacervate reformation from solid polyoxometalate coacervate vesicles. It would also furthermore support the theory that the coacervate phase is still present within the PCVs but is simply enclosed within the PTA/PDDA membrane.

The same experiment was then repeated with 3 protamine/DNA-capsules which were placed on a bed of PCVs. A 50 mM sodium phosphate buffer was used again as the medium, since it promoted a cleaner PCV disintegration than with di-water (Figure 5.4-21). For the first 20 minutes, there was no PCV disintegration visible, instead only more PCVs settled from the dispersion on the ground. After 40 minutes the PCVs around the capsules started to break and vanish and after 60 minutes, all PCVs in between the capsules were gone. After 80 minutes, most PCVs within the image were disintegrated

except for a few PCVs on the protamine/DNA-capsules, which were still intact even though all their surrounding has vanished. This experiment shows, that even though the capsules were spatially separated by a few hundred micrometres, their proximity did increase the disintegration process of the PCVs drastically. Whereas the previous experiment took about 100 minutes before the effect of the urease activity was visible (Figure 5.4-19-a), here it took only 20-40 minutes. And indeed, the images actually indicate that the proximity of the capsules is promoting the faster disintegration, considering the PCVs in between the capsules dissolved at a much quicker rate than the PCVs which were equally far away but not surrounded by capsules, e.g. the PCVs on the bottom left side of the 4th image. The experiment brings another image to mind, which is usually seen in practical biochemistry. Assuming the PCVs were bacterial colonies, the secretion of the protamine/DNA-capsules could be comparted to an antibiotic, which prevents the bacteria to grow around the cells. Either way, it is a nice reference to a naturally occurring phenomenon in organisms.

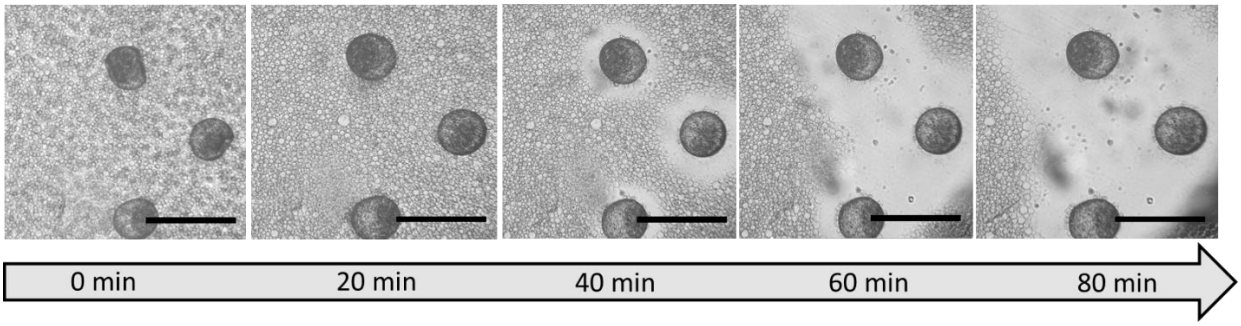

Figure 5.4-21: *Optical micrographs of protamine/DNA-microcapsules disintegrating surrounding PCVs in response to the addition of 10 μL of 0.1 M urea into a 100 μL dispersion of PCVs inside a 96 well plate.*

5.4.3 Uptake, transport and release

At this stage, all necessary steps have been established to set up a working cargo uptake, transport and release system, even though so far, all steps have only been observed disconnected from each other. So, what needs to be assessed next, is whether the enzymes which are needed to enable transport, and release can coexist next to each other, and if the system works if all steps are being performed in succession. The following experiment is designed as a proof of concept, which can then be used as a foundation for a real uptake, transport and release experiment. A protamine/DNA-microcapsule was fabricated with 19.8 kU/mL catalase, 0.29 kU/mL urease and 2.9 kU/mL glucose oxidase. The plain microcapsule (Figure 5.4-22) was then gently settled onto a bed of PCVs, which simulated the uptake of the cargo, after which 10 μL of a 160 mM H_2O_2-solution were gently added right above the capsule to nucleate an O_2-microbubble inside the capsule and make it ascend. The capsule was then transferred into a urea solution (0.1 M, pH 7.0) inside a 96-well plate and left for 90 minutes. The PCV-disassembly, ergo the cargo release, was observed through an optical brightfield microscope. Just like in the previous experiments, the PCVs began to swell after ~20-30 minutes and started to disintegrate progressively until most of them were gone after 90 minutes (Figure 5.4-22). As expected from previous experiments, there were still some PCV-residues on the microcapsule membrane which have not fully disintegrated, but the release of the cargo could be confirmed, nonetheless. Like it was described in chapter 4, the O_2-microbubble shrank even though no glucose was present yet, which is due to O_2 being slowly dissolved into the aqueous phase. This cannot be prevented and, considering the time frame of the experiment, should not cause any issues as GOx would still be necessary to initiate the re-descent by consuming the rest of the O_2-bubble. What stands out though, is that the O_2-consumption by GOx happened at a slower rate than for a fresh capsule with a newly nucleated O_2-bubble. It took about 30 until the bubble was small enough for the capsule to descend, which would normally only take about 10 minutes.

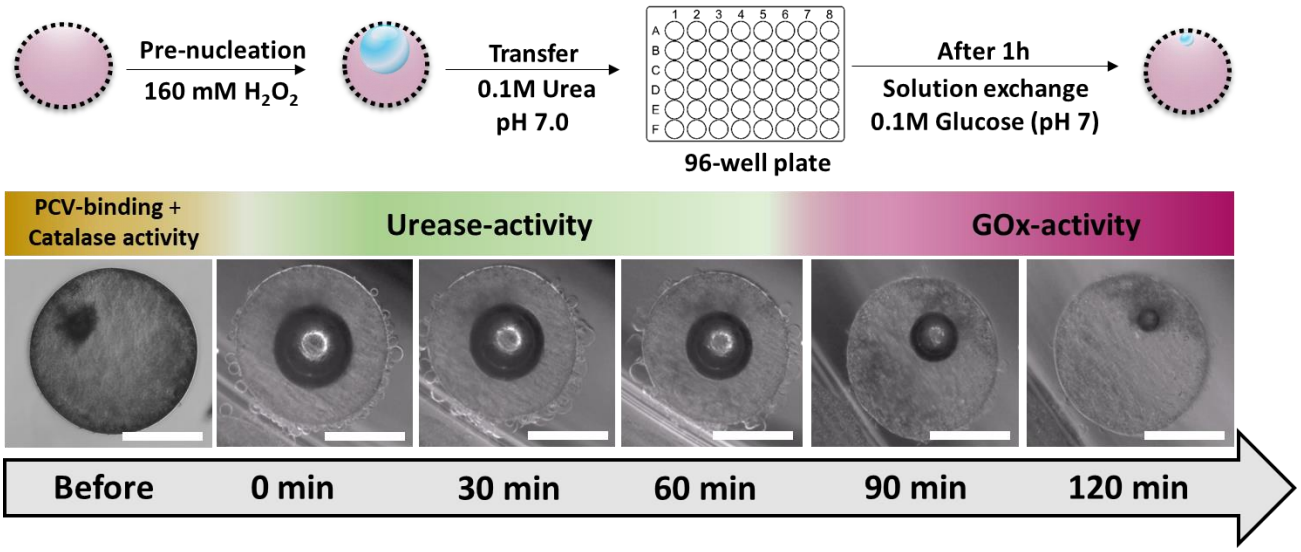

Figure 5.4-22: *Proof of concept for the transport and release of cargo within PCVs via protamine/DNA-microcarriers. Catalase (19.8 kU/mL), glucose oxidase (2.9 kU/mL) and urease (0.29 kU/mL) were entrapped within a single protamine/DNA-microcapsule and the capsule was successively exposed to H_2O_2, urea and glucose to simulate uptake, transport, release and re-descent inside a 96-well plate.*

This issue needs to be addressed in respect to the enzyme-leakage experiments from chapter 4. Again, one needs to assume that GOx leaks off the cells, only this time in response to urease being active. Once more, the decrease of the activity of GOx on the cells was assessed through a coupled enzymatic assay with HRP and the chromophore ABTS. Here, protamine/DNA-capsules were fabricated as in the previous experiment, with 19.8 kU/mL catalase, 2.9 kU/mL GOx and 0.28 kU/mL urease. Figure 5.4-23 shows the original activity of GOx-containing protamine/DNA-capsules and the activity after incubating them in 0.1 M urea for 90 minutes.

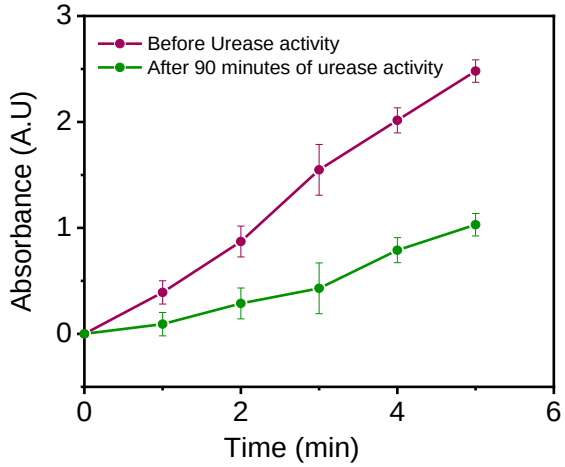

Figure 5.4-23: *Investigation of GOx leakage from protamine/DNA-microcapsules after incubation in 0.1 M urea solutions and in response to 90 minute urease activity. The cells were fabricated with 19.8 kU/mL catalase, 2.9 kU/mL GOx and 0.29 kU/mL urease. UV/VIS-spectroscopy-data was measured at 420 nm in form of a GOx-activity assay with ABTS and HRP.*

As expected from the experiment above, the capsule exhibited a reduced GOx activity within the HRP/ABTS assay, which diminished to almost 40% the original activity. This confirms that urease activity indeed decreased GOx activity, what it does not explain yet, is whether it is simply inhibiting

the enzyme, potentially through denaturation due to the increasing pH or the products of the enzymatic reaction, or if GOx is leaking from the cells, just like it was assumed for the enzyme fatigue in chapter 4.

To understand the latter the same simple enzymatic assay with ABTS and HRP can be used to examine the GOx content within the capsule and the supernatant, supposed it leaked off the cell. The urease-containing protamine/DNA-capsule was incubated in 0.1 M urea for 90 minutes, after which either the capsule (Figure 5.4-24-capsule before/after) or the supernatant (Figure 5.4-24-supernatant) were mixed with ABTS and HRP to assess the enzymatic activity. The depth of the produced colour of the oxidised ABTS was then used to qualitatively evaluate the enzyme-leakage. And indeed, as it can be seen in Figure 5.4-24, both the supernatant and the capsule after the incubation showed GOx activity. The lighter green colour of the supernatant implies that less GOx has leaked off the cell than what was still retained, but it proves that leakage is the driving factor for the GOx-activity deterioration. So, that leaves the question of what is causing the enzyme to leak off the cells. And it needs to be noted, that catalase and most likely even urease would also leak off the protamine/DNA-capsules to a similar degree. In the introduction to this chapter, it was described that urease produces both ammonia (NH_4^+) and carbonic acid (HCO_3^-). Here one can assume, that the produced ions interact with the adsorbed enzymes the same way that for example phosphate buffer or the enzymatic conversion of glucose via GOx from the capsule-membrane induce enzyme leakage. The previous leakage studies from chapter 4 (Figure 4.4-43 + Figure 4.4-44) have shown though, that the leakage effect is much stronger in a very small medium like a 96-well plate, and that it is most likely less pronounced in experiments where capsules oscillate in a larger volume like the oscillation columns. The same can most likely be expected for the urease-induced leakage, which should be reduced during the actual transport/release experiments, which will be done in a larger device. Nonetheless, enzyme leakage is, once again, an issue that needs to be addressed, as it will most likely negatively influence transport and release concept.

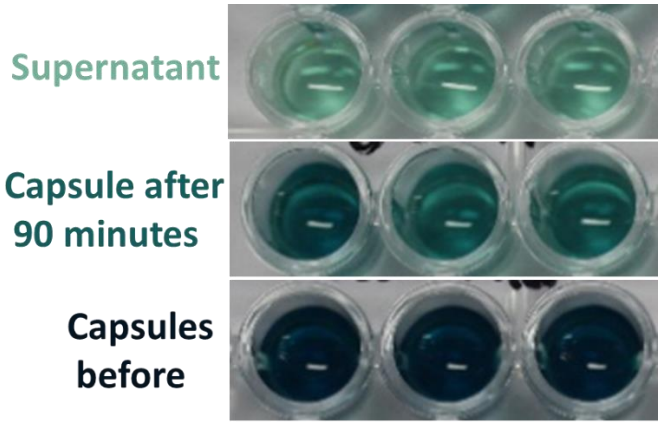

Figure 5.4-24: *GOx-leakage test by coupling it with the HRP/ABTS colorimetric assay. The assay was done by assessing the enzymatic activity of GOx on the protamine/DNA-microcapsule before the incubation period, and by doing the same experiment for the capsule or the supernatant after the incubation in 0.1 M urea for 90 minutes.*

The experiment from Figure 5.4-22 shows that the concept should work, the only thing that is left to do, is to design an experimental device, which allows the repetitive uptake, transport and release of the PCVs with only minor interference by the experimenter. Figure 5.4-25 illustrates the experimental setup of the following transport and release experiments. The oscillation column that was used is the same which has already been described in chapter 4 (Figure 4.3-6) for the damped oscillations. This device combines several convenient functions, most notably the bottom channel which allows the

addition of substrates like H_2O_2 through a controllable syringe pump and the fact that the device is open at the top, which allows the exchange of substrate solutions to change from cargo-release to, for instance, capsule descent. Furthermore, the whole system was based on a density gradient which was established through addition of certain amounts of sucrose to each phase. The column was first filled with di-water (2 wt% sucrose, pH 7.0), leaving about 300 μL at the top empty.

200 μL of a freshly prepared dispersion of PCVs sequestering pyranine as cargo was then added into the column and left to sediment on the bottom (Figure 5.4-25-b-d). The protamine/DNA-capsule carrier was once again fabricated with 19.8 kU/mL catalase, 2.9 kU/mL GOx and 0.28 kU/mL urease, 12 mg/mL silica particles, but also contained 5 mg/mL magnetic particles (Figure 5.4-25-f). While the particles are not relevant for the transport and release, they enable a quicker and easier uptake of the PCVs, as the experimenter can roll the capsule through the PCV-bed with an external magnet, which increased the chances of PCV-loading onto the capsule and furthermore improved the signal after the release, which is important due to the low concentrations of released cargo from the PCVs. Again, it was important to pre-nucleate the O_2-bubble inside the capsule externally and consuming it below the sedimentation-volume by adding it to an external glucose solution, before adding the capsule to the oscillation column. Once the capsule had settled, it was gently rolled through the PCV-bed with a magnet for several seconds, before adding the H_2O_2-solution (160 mM, pH 7.0, 4 wt% sucrose). Finally, the remaining volume at the top of the column was filled with about 200-300 μL of a urea solution (0.1 M, pH 7.0, 0 wt% sucrose), which settled on top of the 2% sucrose solution (Figure 5.4-25-e). The whole concept is described in Figure 5.4-25-a: The injection of the H_2O_2-phase induced the oxygen-production inside the protamine/DNA-capsule and its ascent. At the top of the column, it will reach the urea phase where the capsule will start disintegrating the PCVs and release the payload. Since released pyranine cannot be seen with the bare eye and using a large fluorescence microscope is not feasible for such an application, a spectrofluorometer was used instead by analysing small 5 μL aliquots (20 minute intervals) from the urea volume close to the capsule and measuring the presence of pyranine at $\lambda_{Emission,\ Pyranine} = 515$ nm, with $\lambda_{Excitation,\ Pyranine} = 450$ nm. After 120 minutes, the urea phase was gently extracted and replaced with a glucose solution (0.1 M, pH 7.0, 0 wt% sucrose) to initiate the O_2-bubble depletion and the capsule's descent.

Generally, the experimental setup is quite complex especially from an analytical perspective. Here, entities of very different size scales are combined in a single experiment which, ideally, should all be tracked and observed at the same time. The protamine/DNA-capsule carriers are the largest components and can be seen with the bare eye or a camera, while they move several centimetres in distance. At the same time the small PCVs are attached to the capsules which cannot be seen by eye and would need a microscope attached to the experimental contraption. And finally, the release of the molecular cargo needs to be measured, which can only be done via spectroscopy or fluorescence microscopy, considering the low concentrations which are sequestered inside the PCVs. For the reasons above, the final experiment applied three different means of analysis, a camera, which constantly tracked the movement of the protamine-microcapsule the same way it was done in chapter 4, a microscopic analysis of the capsule before and after PCV-disintegration, which was done by simply transferring the capsule under an optical microscope, and the spectrofluorometer-measurements via aliquots which tracked the release of the tagged cargo molecules.

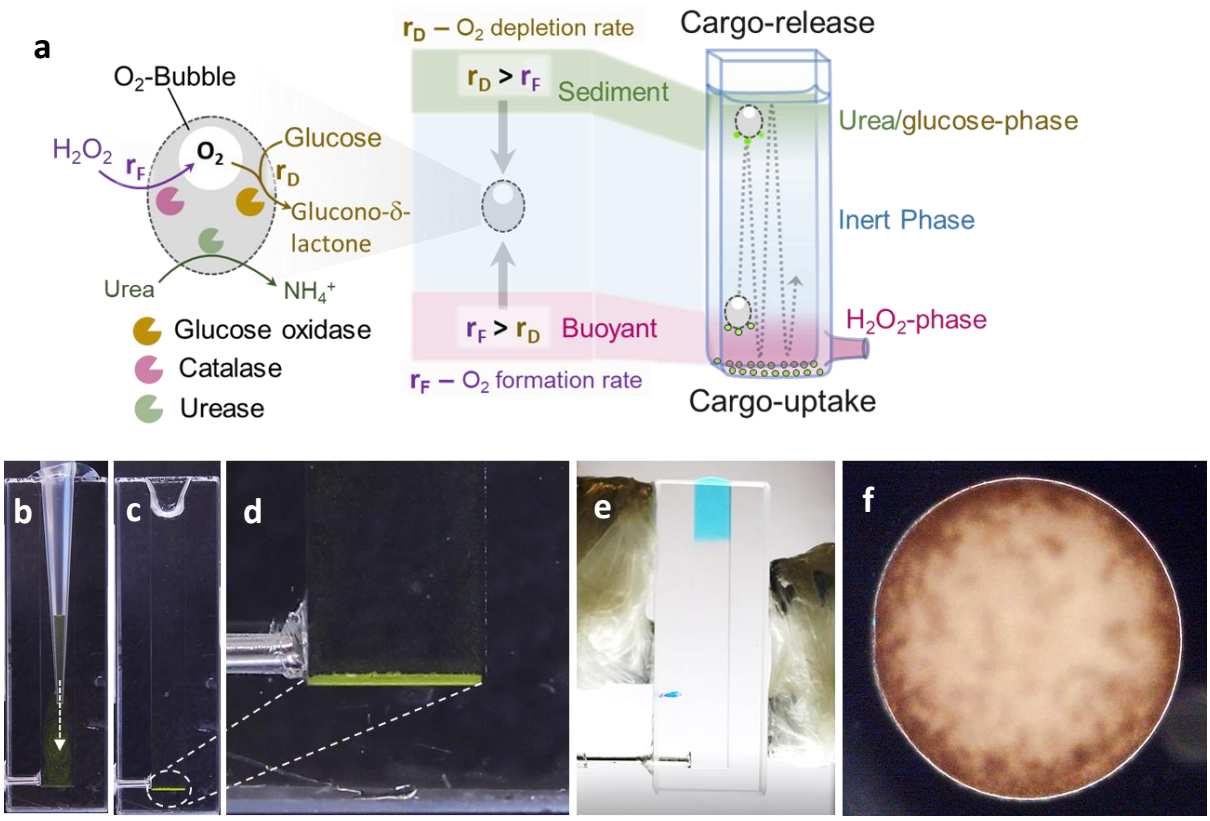

Figure 5.4-25: a *The graphic illustrates the enzymatic interactions inside protamine/DNA-microcapsules to facilitate motility and cargo release. The release of the sequestered pyranine cargo molecules was then tracked by taking 5 µL aliquots from the top-phase and measuring the emission of released pyranine at* $\lambda_{Emission,\ Pyranine}$ *= 515 nm. Once the cargo has been released, the urea phase will be exchanged with glucose, which induces* O_2*-consumption and the eventual capsule descent.* ***b-e*** *Camera images showing the setup of the oscillation device by sedimenting the PCVs and forming a clean interface between the top-phase and the water column below. Methylene blue (5 mM) was added to the top-phase to highlight the interface (**e**).* ***f*** *Microscope image of a protamine/DNA-microcapsule with entrapped 0.87 µm magnetic microspheres.*

Throughout the work with PCVs, many different fluorophores were sequestered, yet none of them was as efficiently entrapped as pyranine. It yielded one of the strongest fluorescent signals and even dyed the PCVs in a fluorescent green colour (Figure 5.4-25-b-d), which visually proved the entrapment of pyranine inside the microcompartments. Before working on the transport concept, it was necessary to establish whether protamine/DNA-capsules loaded with pyranine-containing PCVs would produce a measurable signal. For this purpose, three protamine/DNA-microcapsules were coated with pyranine-containing PCVs, which are shown in Figure 5.4-26-d. All three microcapsules exhibited a consistent monolayer of PCVs, even though the loading of PCVs was increasing from capsule 1 to capsule 3 (Figure 5.4-26-d). The microcapsules were then incubated in 100 µL urea (0.1 M) inside separate wells of a 96-well plate for 2 hours during which pyranine was released into the 100 µL volume. Similar to the final transport concept, 5 µL aliquots were taken from the supernatant to assess the cargo release via spectrofluorometer (Figure 5.4-26-c). As expected from the amount of loaded PCVs seen on the microscope images, the emission-signal increased from capsule 1 (Average Peak: 102493.34 A.U.) to almost 3.7 times the intensity (Capsule 3), with an average peak intensity of 368306.67 A.U. While this proves that the pyranine-release can be traced spectroscopically, it does not quantify the actual amount of released pyranine from the capsules.

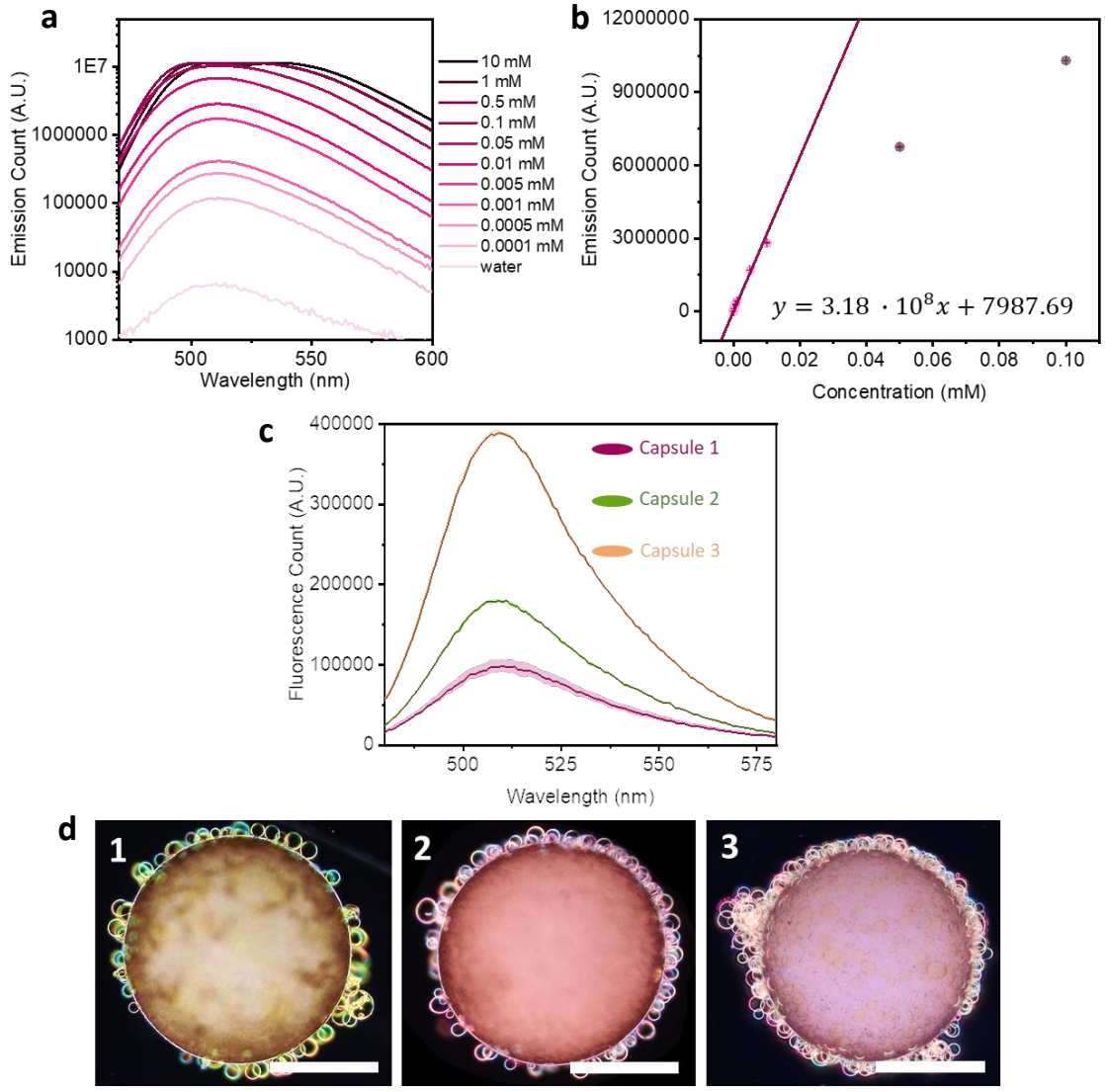

Figure 5.4-26: *Assessment of pyranine as cargo for the transport and release-concept.* ***a*** *Calibration of the spectrofluorometer against the emission of various pyranine concentrations (10, 1, 0.5, 0.1, 0.05, 0.01, 0.005, 0.001, 0.0005, 0.0001 mM, and water) after excitation at* $\lambda_{Excitation,\ Pyranine}$ *= 450 nm.* ***b*** *Calibration via linear regression. The pink datapoints were included into the linear regression whereas the grey points were excluded* ***c*** *Emission signal of released pyranine from 3 different protamine/DNA-capsules (****d****) after 120 min of incubation in 0.1 M urea. All scale bars: 200 µm.*

Table 5.4-3: *Measured emission and calculated amounts of released pyranine from single protamine/DNA-microcapsules.*

Experiment No°	Average Pyranine Emission Peak [A.U.]	Average amount of released Pyranine [µM]	Average amount of released Pyranine [ng]
1	102493.34	0.29	15.58
2	170466.67	0.51	26.79
3	368306.67	1.13	59.42

To increase the quality of the analysis, the emission signal was calibrated against several pyranine concentrations (10, 1, 0.5, 0.1, 0.05, 0.01, 0.005, 0.001, 0.0005, 0.0001 mM and water), which can be seen in (Figure 5.4-26-a+b). Even at concentrations of 0.0001 mM the spectrofluorometer is still able

to measure a very distinguishable signal, which shows just how sensitive the fluorophore really is. As a reference, a 0.1 M urea solution without any microcapsules or pyranine-containing PCVs was analysed, which showed, that there was a very low baseline-emission even without pyranine present. The signal could be an artifact from the excitation peak, which is fairly close at $\lambda_{Excitation,\ Pyranine}$ = 450 nm, nonetheless it is sufficiently low and does not overlap with the calibration or the measured intensities from the released pyranine (Figure 5.4-26-c). The actual amounts of released pyranine from single microcapsules were then summarized in Table 5.4-3, which increased from 15.58 ng to 59.42 ng between capsule 1 to 3. While the error of each datapoint for the calibration is not very large, it needs to be addressed that the calibration has its limits due to the fact that the emission does not drop back to 0 when there was no pyranine present. Instead, the intercept of the linear regression lies at about 5800 A.U., which would be the sensitivity limit for the determination of the pyranine concentration. Considering that the released pyranine produced a signal about 20 times higher than the baseline though, the calibration should suffice for any of the experiments to come.

Finally, all pieces were in place to prepare the actual uptake and release experiment according to the previously described method. Figure 5.4-27-b shows camera images which depict the relevant steps of the experiment: the insertion of the capsule into the oscillation column and its descent to the bottom **(I + II)**, the addition of urea **(III)**, the cargo uptake **(IV)**, the catalase induced ascent **(V)**, the cargo release **(VI)**, the addition of glucose and the GOx-mediated descent **(VII + VIII)**. Here, it was crucial that both the protamine/DNA-microcapsule and the PCVs were freshly fabricated on the day of the experiment. Protamine/DNA-capsules tended to become stickier the longer they were being stored. While this was beneficial for the uptake of PCVs it was not really necessary as protamine/DNA-capsules were already sticking readily to the smaller PCVs, but they also started to stick to the glass walls of the device, which would cause the experiment to fail. The PCVs on the other hand seemed to become less likely to stick to the protamine/DNA-capsules the more time went on. Furthermore, O_2-bubble nucleation seemed to increase externally along the PCV-layer, which would also result in failure, either because the capsule would not ascent, or because the bubble would contaminate the oscillation column. Even though enzyme leakage was expected to cause an issue, especially regarding GOx-activity, the experiments here were not showing a considerable increase in the time it took to deplete the O_2-bubble. This could be explained by the long period of time the capsule was residing within the urea-layer (120 minutes), which already caused a substantial O_2-depletion since the gas simply dissolved into the surrounding solution, as it was shown in chapter 4 (Figure 4.4-14). The microscope image of the capsule after the release also confirms this theory, considering the dark outline of the bubble inside the capsule has shrunken considerably. Once the capsule was engaged in the PCV-disintegration within the urea phase, ergo the cargo release, aliquots were taken to measure the released pyranine. The measured results are shown in Figure 5.4-27-a in form of an overlay of emission spectra which were taken in 20 minute intervals. The microscope images of the protamine capsule during the first cycle show that the uptake was successful and that the capsule was covered in a dense monolayer of PCVs (Figure 5.4-27-a-1st cycle-left image). Previous studies had established the assumption that PCVs start to break after roughly 30-40 minutes, even though this was a mere visual interpretation through fluorescence- and brightfield microscopy. The spectrofluorometer-data shows that the release of the cargo actually starts much earlier during the first 20 minutes, even though it further increased between 20 and 60 minutes. After 60 minutes, the released concentration reached a maximum at ~ 0.28 mM, after which it started to decrease again. Indeed, the practice of taking aliquots via pipette was prone to error, yet the concentration decrease seemed to happen reliably after 60-80 minutes. This could be a hint that all pyranine has been released and is now diffusing away from the capsule into the bulk medium, hence reducing the concentration around the cell. Nonetheless, a more accurate explanation is still pending. The brightfield image of the capsule

after the release clearly shows, that the majority of the PCVs have been disintegrated and only one remained visible on the image (Figure 5.4-27-a-1st cycle-right image).

Once the first cycle had finished, the same steps were repeated, thus forcing the capsule into a second and, later, a third cycle of uptake, transport and release (Figure 5.4-27-a).

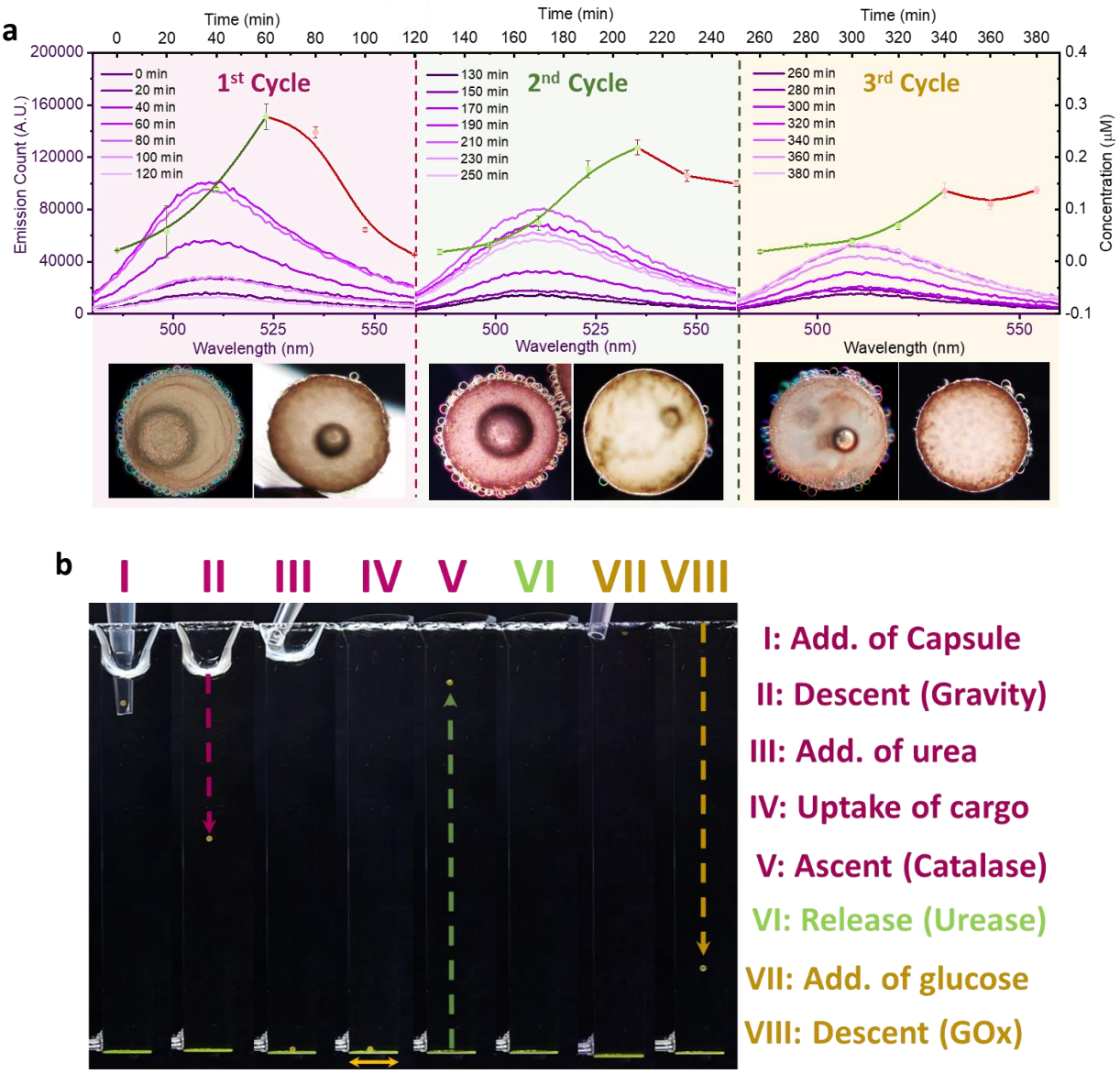

Figure 5.4-27: *Uptake, transport and release of PCV-cargo by protamine/DNA-microcapsules.* ***a*** *Measured fluorescence emission in 5 µL aliquots, which were taken in 20 minute intervals and over a time of 2 hours. Each cycle is comprised of uptake, ascent, release and descent and was performed without resetting the system. Below each plot, the images depict the protamine/DNA-microcapsule right after the uptake (**left image**) and the release (**right image**) during each cycle.* ***b*** *Camera image sequence, showing the relevant steps during the uptake, transport and release experiment.*

The loading of the capsule seemed to decrease during the second cycle and even more during the third, while also showing more and more deformations on the surface (Figure 5.4-27-a-2nd and 3rd cycle). Generally, the capsule is exposed to a lot of stress due to the changing chemical environment but also due to the constant change of pH, which causes the capsule to deform slightly as it is shown in the images after the release of the cargo. It must be mentioned though, that the microcapsule usually regained most of its former structure once it had redescended, which can be seen in the images

before the release (Figure 5.4-27-a-1st – 3rd cycle, left images). Furthermore, the disintegration of the PCVs most likely adsorbed even more molecular components onto the protamine/DNA-capsule, which then either caused enzymes to leak off, or maybe also prevented PCVs from adsorbing to the capsule the same way they would to a freshly fabricated one. Also, the column became more and more contaminated with disintegrated PCVs, products of the enzymatic reactions of GOx and urease and H_2O_2. Most of these components were removed when exchanging the urea and glucose solutions, but it will be hard to prevent a contamination 100%, as the column was not reset for each cycle.

So, considering the lower PCV-load during the second cycle, it was expected that the signal of the released pyranine would not reach the same intensity as during the first. It took about 20 minutes longer before the onset of the increase became visible and the emission peak was also reached 20 minutes later at about 0.22 mM, which is roughly 0.06 mM lower than the released amount of pyranine during the first cycle. Again, the concentration started to decrease 20 minutes after reaching the emission peak, which shows the consistency of this phenomenon. The microcapsule still exhibited a few unbroken PCVs on its membrane after the disintegration, yet most of the PCVs were vanished from its surface. Finally, the capsule performed a third cycle and now clearly showed a reduced amount of adsorbed PCVs. While the signal increased slightly during the first 40 minutes, it took ~60 minutes before it rose relevantly, reaching its peak at 0.13 mM, which is substantially lower than the previous cycles. Once more, the concentration decreased after reaching the peak, but only marginally and without a comparable drop like in the first cycle. The capsule furthermore exhibited more unbroken PCVs, which would correlate well with the increasing time of the cargo-release. This could indicate, that either the urease activity is decreasing due to leakage or enzyme deactivation, or that the PCVs take a lot longer to break than in the first cycle.

Pyranine is a fairly small fluorophore and should be able to diffuse readily through the membrane of the PCVs, when solely looking at its molecular size. The studies of D. Williams *et al.* [65] have shown that pyranine would not leak from the PCVs, nonetheless it is important to establish a relevant negative-experiment to prove the same statement for the transport and release concept. So, in order to understand whether pyranine would leak from the loaded PCVs in the urea phase, the same experimental setup as in Figure 5.4-25 and Figure 5.4-27 was prepared, but without any entrapped urease inside the protamine/DNA-capsules. This way, a potential leakage of pyranine can be assessed in relation to the chemical environment in the urea phase and in proximity to the other 2 enzymes, but without disintegrating any of the PCVs at the same time. Figure 5.4-28-b shows a loaded protamine/DNA-microcapsule with a very dense monolayer of pyranine-containing PCVs, which, under the previous circumstances, would create a definitive and measurable emission signal. But instead, due to the lack of urease, the emission signal showed no substantial increase beyond some minor fluctuations and its baseline peak. Even after 120 minutes, it was virtually identical, which offers a strong argument against pyranine leakage without the disintegrating effect of urease.

Even though the experiment has shown to be complicated from an experimental point of view with several roadblocks along the way, the results which were presented over the previous figures have proven, that it is possible to establish a working uptake, transport and release system with protamine/DNA-microcapsules as the motile carrier. From this point onward, the main goal will be to increase the complexity of the cargo-transport system further until the microcapsules are capable of performing not just simple transport/release-mechanisms, but more sophisticated functions in combination with chemical reactions. Before this can be realised though, it is necessary to test the limits of this system and to understand what other components can be used as cargo to eventually increase the functionality and complexity.

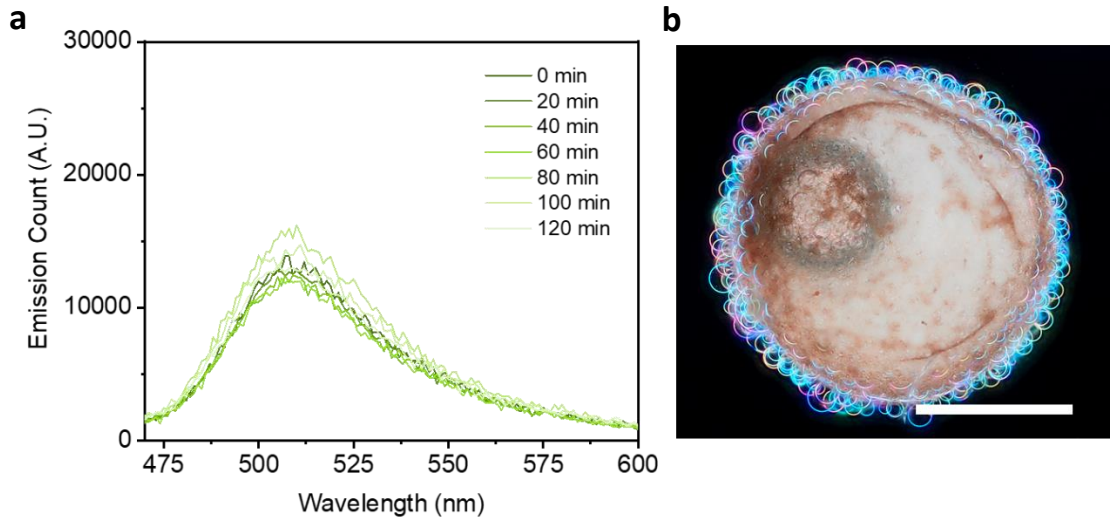

Figure 5.4-28: *Control experiment for the uptake, transport and release of pyranine-loaded PCVs via protamine/DNA-microcapsules:* ***a*** *spectrofluorometer scans after 0, 20, 40, 60, 80, 100 and 120 minutes, once the capsule had entered the 0.1 M urea phase.* ***b*** *optical micrograph of the PCV-loaded protamine/DNA-capsules. Scale bar: 200 µm.*

In the following experiment, RITC-HRP was used as the cargo-molecule instead of pyranine. While the feedback will be merely fluorescent like in the first experiment, the entrapment and release of enzymes serves as the next step to more functionality. The reason RITC was chosen as a fluorescent tag for the payload was to minimise the error when measuring the cargo-release with the UV/VIS-spectrometer. Figure 5.4-29 shows the UV/VIS-absorbance spectra of all three enzymes, catalase, urease and glucose oxidase. Considering the enzyme leakage, which was described and assumed above, it could be possible that other leaked enzymes like native GOx, catalase or urease absorb at similar wavelengths and interfere with the measurement, even though it seems very unlikely that the leaked enzymes will exhibit such a strong absorbance, that they could be tracked within an emission spectrum via aliquots.

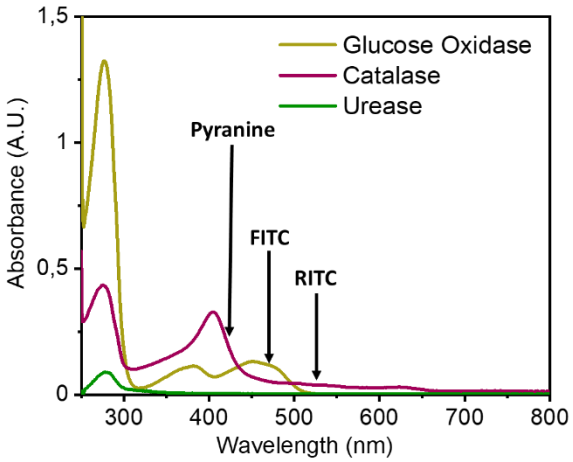

Figure 5.4-29: *UV/VIS-spectra of glucose oxidase, catalase and urease.*

The spectra show, that only RITC absorbs at a wavelength which is not already occupied by absorption peaks from the enzymes, which is why RITC was chosen as a fluorescent tag for the payload. First, RITC-HRP was established as a working fluorophore by entrapping it within the PCVs and releasing it

from a loaded protamine microcapsule just like it was done in Figure 5.4-26 for pyranine. (Figure 5.4-30)

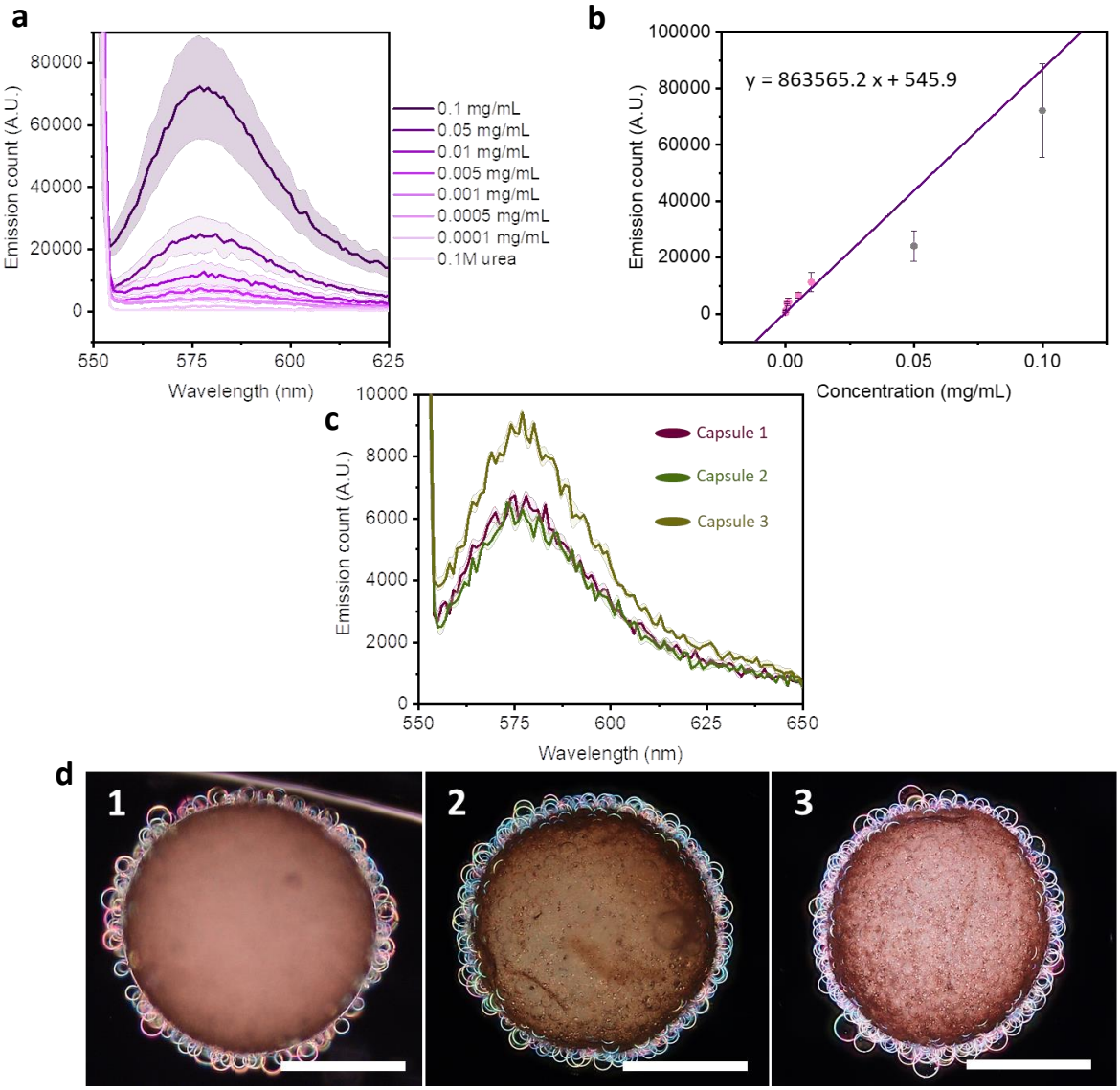

Figure 5.4-30: *Assessment of RITC-HRP as cargo for the transport and release-concept.* ***a*** *Calibration of the spectrofluorometer against various RITC-HRP concentrations (0.1, 0.05, 0.01, 0.005, 0.001, 0.0005, 0.0001 mM, and 0.1 M urea).* ***b*** *Calibration via linear regression. The pink datapoints were included into the linear regression whereas the grey points were excluded* ***c*** *Emission signal of released RITC-HRP from 3 different protamine/DNA-capsules (**d**) after 120 min of incubation in 0.1 M urea. All scale bars: 200 µm.*

Table 5.4-4: *Measured emission and calculated averaged amounts of released RITC-HRP from single protamine/DNA-capsules*

Capsule No°	Average RITC-HRP emission peak [A.U.]	Average released RITC-HRP per capsule [µg/mL]	Average approximated amount of released RITC-HRP per capsule [nM/mL]	Average amount of RITC-HRP released per capsule [µg]
1	6253.33	6.60	0.16	0.66
2	5956.67	6.26	0.15	0.62
3	8746.66	9.49	0.23	0.95

To calibrate the concentration of RITC-HRP to the spectrofluorometer signal, various concentrations of RITC-HRP (0.1, 0.05, 0.01, 0.005, 0.001, 0.0005, 0.0001 and 0.1 M urea without any RITC-HRP) were analysed by exciting the fluorophore at $\lambda_{Excitation,\ RITC\text{-}HRP}$ = 544 nm and measuring the fluorescence at $\lambda_{Emission,\ RITC\text{-}HRP}$ = 579 nm. Like in the previous experiment, 3 separate protamine-microcapsules were prepared by covering them with RITC-HRP containing PCVs. Figure 5.4-30-d shows how all three capsules exhibited a very dense monolayer of PCVs with comparable distributions. Each capsule was then immersed in 0.1 M urea (pH 7) for 120 min after which 5 μL samples were taken to assess the fluorescence of the released RITC-HRP (Figure 5.4-30-c). In all three cases, the released RITC-HRP was measurable at 579 nm, even though capsule 3 showed a slightly higher fluorescence intensity. By using the calibration from Figure 5.4-30-b, the amounts of released RITC-HRP were determined and summarized in Table 5.4-4. Interestingly, the calculated amounts of released RITC-HRP (0.65 μg - 0.95 μg) are substantially higher than the released pyranine in the previous experiment, even though pyranine exhibited an almost 30 times higher fluorescence response ($6985.55_{Avg.}$ (RITC-HRP) vs $213755.60_{Avg.}$ (pyranine)). One obvious thing to consider is the molecular mass of the tagged horseradish peroxidase, which is a lot higher than the one of pyranine. Table 5.4-4 shows the concentrations which were measured after the release by approximating the molecular mass of RITC-HRP to about 40 kDa. [93] This clearly shows that the average released concentration of pyranine is about 3000 times higher than the released concentrations of RITC-HRP. Other factors which most likely changed the release behaviour are the general fluorescence which can be yielded from each fluorophore and the amount which was actually entrapped inside the coacervate phase of the PCVs. Considering the much larger size of HRP compared to pyranine, it seems reasonable that the entrapped HRP-concentration was substantially lower.

Just like in Figure 5.4-27, RITC-HRP-containing PCVs were used as cargo for the uptake-, transport- and release-concept. Figure 5.4-31-a shows 2 successive cycles after which the experiment was terminated. The images of the capsule before and after the release show that the release must have been successful, as almost no PCVs were remaining on the capsule after the first release, and only a few residues were left after the second (Figure 5.4-31-a). The PCV-loading was generally higher during the first cycle, whereas the second showed a much decreased number of PCVs on the capsule membrane. Once again, samples were taken in form of 5 μL aliquots over a time period of 120 minutes and in 20 minute intervals. The spectrofluorometer plots of Figure 5.4-31-a show the progressive release of RITC-HRP. Considering the lower concentrations and the lower measured emission counts, the error of the plots is generally higher than in the pyranine experiments, keeping in mind that the spectrofluorometer is working a lot closer to its detection limits. Nonetheless, the release of RITC-HRP was detected, reaching a maximum of ~ 6.7 μg/mL after 60 minutes (Figure 5.4-31-a-1st cycle), which aligns well with the release-experiments from Figure 5.4-27. Past 60 minutes, the fluorescence started to decrease, which again can be explained by diffusion after all the cargo had been released. The second cycle showed an overall decreased fluorescence signal which peaked between 60-80 minutes (Figure 5.4-31-a-2nd cycle, 4.2 μg/mL). This could be linked to the PCV-loading of the second cycle which appeared to be lower than during the first, or to a decrease in the release efficacy, considering the capsule appeared to have a few unbroken PCVs on its membrane (See Figure 5.4-31-a). Again, a blank experiment was performed without entrapped urease, to prove that no leakage of RITC-HRP was observed.

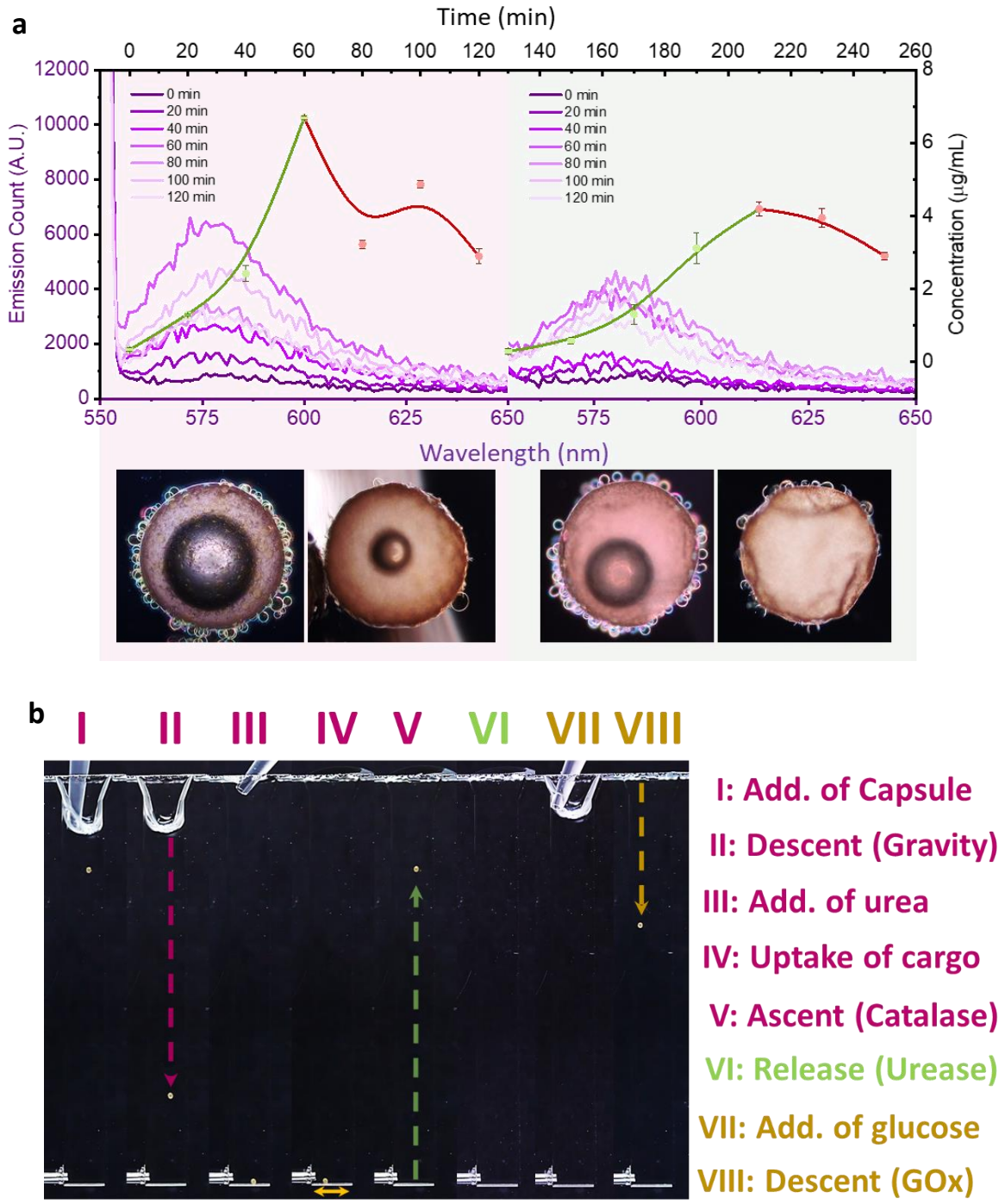

Figure 5.4-31: *Uptake, transport and release of PCV-cargo (RITC-HRP) by protamine/DNA-microcapsules.* ***a*** *Measured fluorescence emission ($\lambda_{Emission,\ RITC\text{-}HRP}$ = 579 nm) in 5 µL aliquots, which were taken in 20 minute intervals and over a time of 2 hours. Each cycle is comprised of uptake, ascent, release and descent and was performed without resetting the system. Below each plot, the images depict the protamine/DNA-capsule right after the uptake (**left image**) and the release (**right image**) during each cycle.* ***b*** *Camera image sequence, showing the relevant steps during the uptake, transport and release experiment.*

The experiment was performed exactly like the previous transport attempts and Figure 5.4-32 shows the measured fluorescent emission over a time period of 120 minutes in the urea phase. Here, no increase of fluorescence was observed, which is consistent with the previous results and the reports from D. Williams *et. al.* [65] in regard to the retention of enzymes inside PCVs and the potential leakage.

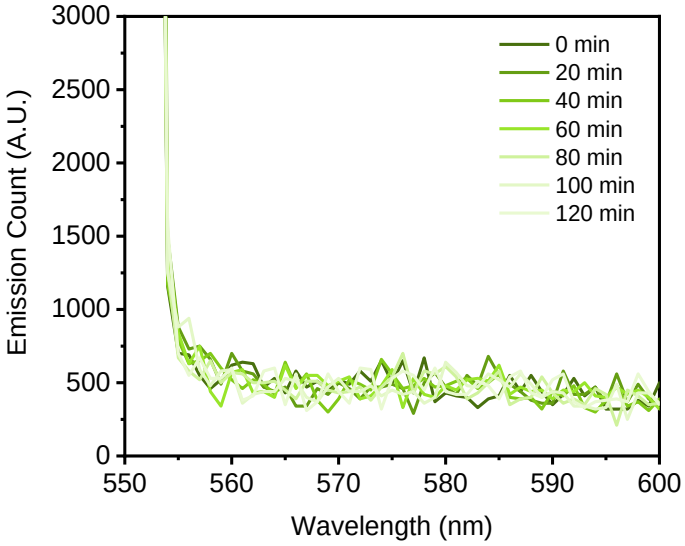

Figure 5.4-32: *Blank experiment to test for RITC-HRP leakage from the PCVs in the absence of urease.*

This proves that even larger cargo like enzymes can be transported and released by using protamine/DNA-microcapsule carriers. Since HRP was tagged with RITC, it most likely lost a lot of its native reactivity which makes this design unsuitable for coupling an actual chemical reaction to the release. Instead, the following experiment will examine the transport and release of untagged HRP. The enzyme has been used extensively throughout this thesis due to its unique catalytic capabilities, especially in combination with fluorescent substrates. Unfortunately, adding the substrate into the top-phase of the oscillation is not a suitable design choice, as the small substrates would simply diffuse into the PCVs and react with the entrapped enzyme, without the need for a release-mechanism. Instead, the enzymatic reaction was performed externally by taking samples () once the PCV-disintegration was finished after 80 minutes. The samples were mixed with the fluorescent substrate Ampliflu™ Red (0.5 mM, $\lambda_{Excitation,\ Amp.Red}$ = 571 nm, $\lambda_{Excitation,\ Amp.Red}$ = 588 nm) and H_2O_2 (16 mM), which started the enzymatic oxidation of Ampliflu™ Red. The production of the fluorophore was then tracked via spectrofluorometer over 4 minutes (24s per scan, 10 scans). The rest of the experimental procedure was kept virtually identical to the previous experiments, except that only one cycle was investigated. Figure 5.4-33-green shows that the released HRP was indeed still active and started to oxidise the fluorophore as soon as the enzyme was added to the substrate solution. The same experiment was repeated with capsules that did not contain any urease, which should stop the release of HRP. Interestingly, once the aliquot was added to the substrate solution, the signal was still showing an increase, even though at a much lesser rate. The experiments from the beginning of this chapter in Figure 5.4-3 have already discussed the phenomenon of auto-oxidation of Ampliflu™ Red, even when no enzyme was present. This could explain the observations here, even though it remains to be questioned, whether HRP not simply leaked off the cells while the capsule remained in the urea phase. While HRP should not be capable of diffusing through the PCVs, one could assume that surface adsorbed HRP could indeed desorb and be taken up with the aliquot. This seems less likely though, as the amount of released HRP is already very low and complicated to analyse, so it appears questionable if a few desorbed molecules from the PCV-surface could indeed cause such a signal. In comparison, the released HRP-signal (Figure 5.4-33-green) shows a faster rate of increase than the negative sample and proves that the released enzymes are still intact and active.

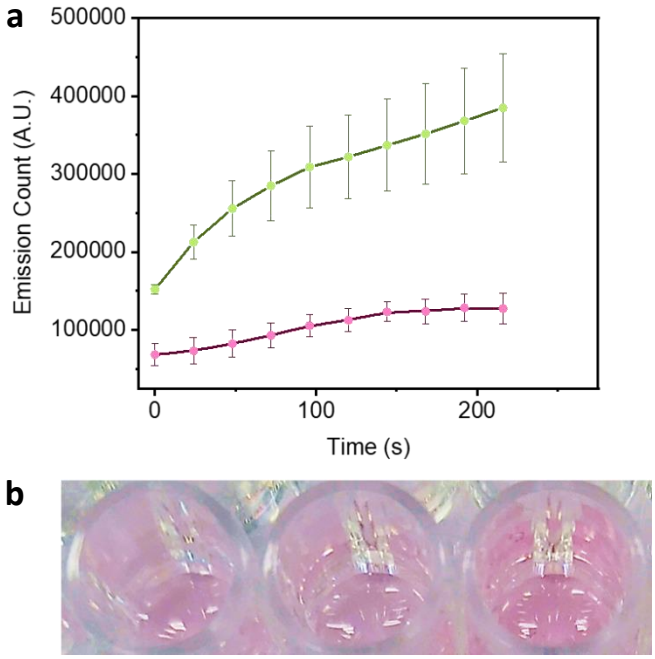

Figure 5.4-33: *Enzymatic assay of released HRP. Ampliflu™ Red was used as the fluorophore, which was tracked at $\lambda_{Excitation,\ Amp.Red}$ = 571 nm, $\lambda_{Emission,\ Amp.Red}$ = 588 nm. The cargo was transported into a 0.1 M urea phase, where the release was triggered by entrapped urease over a time period of 80 minutes.* ***a*** *The plots show the increase in fluorescence from Ampliflu™ Red, which is progressively oxidised by HRP. The green plot depicts three transport-experiments with a single capsule, whereas the pink plot served as a negative, with the capsule not containing any urease. For each measurement, a 10 µL aliquot was taken after the release and mixed with 100 µL Ampliflu™ Red (0.5 mM) and H_2O_2 (16 mM). Emission spectra were taken in 24s intervals over a time period of 216 seconds.*

The camera images furthermore show a visual representation of the enzymatic reaction, as the substrate solution turned slightly red after the enzyme was incubated inside the solution for 12 hours. While the time seems excessive, it was necessary to actually observe a visual coloration, considering the low amounts of released HRP from each transport experiment.

While the results above show a very promising start into the concept of transport and release of molecular cargo via protamine/DNA-microcapsules, they are only the first step and merely prove that the concept is legitimate. From here on, it is necessary to gradually increase the complexity of the system, with the goal of designing a way of communication between protocells and separate chemical environments, or even between different protocell-populations. This obviously demands a high amount of coordination and an even more sophisticated design, nonetheless, the first steps have been laid out.

5.5 Summary and Outlook

Nature is full of fascinating phenomena and behaviours which we can learn a lot from. Protocellular research offers a wide array of tools to approach nature from a synthetic-, or bottom-up approach. This not only allows us to really focus and design cells in a highly specific manner, but we can also try to mimic aspects of nature, which are usually intertwined in a vast and complex network of different functionalities and materials, which makes an experimental approach otherwise almost impossible. This final experimental chapter serves as the logical conclusion to the previous two chapters. Here, the previously developed and established motility of protamine/DNA-microcapsules was exploited to design a rudimentary and repeatable cargo uptake, transport and release system.

In the first part, the protamine/DNA-microcapsule oscillation concept from chapter 4 was introduced once more by coupling the oscillations to a rudimentary and localised transient chemical reaction. HRP was introduced as a third enzyme inside protamine/DNA-capsules next to catalase and glucose oxidase, which catalysed the oxidation of the highly sensitive chromophore Amplex-red. A density-promoted separation of three distinct phases was used to distinguish between an oxygen-producing bottom phase, a central glucose phase and a reactive top phase, containing Amplex-red. By tracking the damped oscillation of the capsule with a camera while measuring the fluorescence intensity of the oxidised Amplex-red through a UV/VIS-probe, the oscillation was directly correlated with the increasing spectroscopic signal, for as long as the capsule oscillated into the reactive phase. As a next step it would be highly interesting to increase the complexity even further by using protamine/DNA-microcapsule oscillations to facilitate communication between the bottom and the top phase, or maybe even separate cell communities.

Protamine/DNA-microcapsules, despite their stickiness and tendency for adsorption, turned out to be highly unspecific in the way they bind to other cell entities, objects or molecules. This made it necessary to find a cargo, that can both be attached to- and released from the carrier capsules on demand and without destroying the carrier in the process. In the next part of this chapter, polyoxometalate coacervate vesicles (PCVs) were investigated and established as the cargo-container of choice. The term cargo-container was used, as PCVs were utilised as disposable container for the actual molecular cargo to be released and as the container, which will be picked up by the protamine/DNA-capsule-carrier at the same time. The fabrication of PCVs was established and described according to the original research from D. Williams *et al.*. [65] The PCVs were thoroughly assessed microscopically by describing their shape, size, appearance, and unique sequestration capabilities and through DLS-zeta potential measurements. The latter gave some important clues on the charge-state of the polymers used to fabricate the PCVs, the coacervate precursor and the PCVs themselves, which was then used later to make assumptions on the interactions between PCVs and protamine/DNA-capsules.

The uptake of the PCVs by protamine/DNA-capsules was shown to happen readily and improved by optimising the fabrication-protocols, or more specifically, the washing steps for each cell system. With the uptake of the PCVs being established, the release of the cargo sequestered into the PCVs was investigated first, but it was shown that neither a change of pH or ionic strength of the surrounding solution, nor mechanical stimuli resulted in a detachment of the PCVs, as the interactions between the two cell types were too strong. Instead, the focus was shifted towards breaking the PCVs and releasing a sequestered cargo from inside the vesicles. The PCV-breakage or PCV-disintegration, as it was called throughout this chapter, was shown to happen in relation to an increase of pH in combination with an increase of ionic strength in the vicinity of the PCVs. While the exact mechanism has not been established, PCV-disintegration was investigated in various pH in both di-water and sodium phosphate-buffer. Furthermore, PCVs were exposed to a variety of other salt-solutions (MES,

Na_2SO_4, NaCl) even though the optimal conditions for PCV-disassembly were found to be in a 50 mM sodium phosphate at pH 9-10. Here it would be highly interesting to further investigate the exact reason on why and how PCVs break and how the ions of the buffers and the increased pH cause the disintegration.

In order to make the system more sophisticated, the PCV-disintegration was connected to a trigger, which was embedded inside the protamine/DNA-capsules. Urease was entrapped next to glucose oxidase and catalase, and it was established that the three enzymes can coexist within the capsules. Since the pH is an important parameter, it was assessed how much and how quickly a single urease containing protamine/DNA-capsule can affect the surrounding pH, while also outlining the optimal urea concentrations. It was then shown that PCVs indeed disintegrated in response to urease activity, which was then also proven for entrapped urease inside protamine/DNA-microcapsules with free PCVs and PCVs loaded onto a protamine/DNA-capsule. Furthermore, when sequestering a fluorescent cargo like RITC-GOx or pyranine, the release of the cargo was shown through fluorescence microscopy.

Finally, all steps of uptake, transport and release were combined in preparation for the planned cargo transport and release experiment. It was shown that all 3 necessary steps can be done in succession, even though enzyme leakage due to a change of ionic strength within the capsule's vicinity was once again discussed, as GOx-activity decreased after prolonged urease-reaction with urea. Pyranine and RITC-HRP were chosen as suitable cargo due to their strong fluorescent signal, which was used to track the release via spectrofluorometer, which appeared to be the most valuable method for the experiment. Here, the successive uptake, transport and release of PCVs mediated by protamine/DNA-microcapsule carriers was shown over 3 transportation cycles without resetting the system. Lastly, PCVs were loaded with native HRP, to showcase the release of an active enzymatic compound. While this system has been shown to work, there are still many aspects which can be improved on. First, it would be interesting to release other cargo like e.g. micro- or nanoparticles or functional molecules which trigger another reaction pathway once they have been released. The latter point is especially important and would be the next logical conclusion for the transport and release concept, as it would enable the communication between chemical networks like different cell-populations and it would add just another layer of complexity. Protamine/DNA-capsules are very sticky and easy to load with potential cargo, but they offer very little opportunity for detachment. Here, it would be interesting to find a potential cargo which can both be attached and detached on demand and without breaking it, which would make the whole process a lot quicker and more convenient to work with. Alternatively, it would be interesting to see if a different motile capsule/cell system could provide more convenience for the uptake/release of cargo, but this would take a lot more effort to design.

5.6 Literature for chapter 5

1. Lodish, H. F. *et al. Molecular Cell Biology*. (W.H. Freeman, 2000).
2. Voet, D., Voet, J. G. & Pratt, C. W. *Fundamentals of Biochemistry: Life at the Molecular Level*. (Wiley, 2016).
3. Titus, M. A. Myosin-driven intracellular transport. *Cold Spring Harbor perspectives in biology* **10**, a021972 (2018).
4. Fattah, Z. *et al.* Straightforward single-step generation of microswimmers by bipolar electrochemistry. *Electrochimica Acta* **56**, 10562-10566, doi:https://doi.org/10.1016/j.electacta.2011.01.048 (2011).
5. Fournier-Bidoz, S., Arsenault, A. C., Manners, I. & Ozin, G. A. Synthetic self-propelled nanorotors. *Chemical Communications*, 441-443, doi:10.1039/B414896G (2005).
6. Mirkovic, T., Zacharia, N. S., Scholes, G. D. & Ozin, G. A. Fuel for Thought: Chemically Powered Nanomotors Out-Swim Nature's Flagellated Bacteria. *ACS Nano* **4**, 1782-1789, doi:10.1021/nn100669h (2010).
7. Paxton, W. F. *et al.* Catalytic Nanomotors: Autonomous Movement of Striped Nanorods. *Journal of the American Chemical Society* **126**, 13424-13431, doi:10.1021/ja047697z (2004).
8. Possin, G. E. A Method for Forming Very Small Diameter Wires. *Review of Scientific Instruments* **41**, 772-774, doi:10.1063/1.1684640 (1970).
9. Baraban, L. *et al.* Catalytic Janus Motors on Microfluidic Chip: Deterministic Motion for Targeted Cargo Delivery. *ACS Nano* **6**, 3383-3389, doi:10.1021/nn300413p (2012).
10. Gao, W. *et al.* Seawater-driven magnesium based Janus micromotors for environmental remediation. *Nanoscale* **5**, 4696-4700, doi:10.1039/C3NR01458D (2013).
11. Wu, Y., Lin, X., Wu, Z., Möhwald, H. & He, Q. Self-Propelled Polymer Multilayer Janus Capsules for Effective Drug Delivery and Light-Triggered Release. *ACS Applied Materials & Interfaces* **6**, 10476-10481, doi:10.1021/am502458h (2014).
12. Baraban, L. *et al.* Control over Janus micromotors by the strength of a magnetic field. *Nanoscale* **5**, 1332-1336, doi:10.1039/C2NR32662K (2013).
13. Mei, Y., Solovev, A. A., Sanchez, S. & Schmidt, O. G. Rolled-up nanotech on polymers: from basic perception to self-propelled catalytic microengines. *Chemical Society Reviews* **40**, 2109-2119, doi:10.1039/C0CS00078G (2011).
14. Solovev, A. A., Mei, Y., Bermúdez Ureña, E., Huang, G. & Schmidt, O. G. Catalytic Microtubular Jet Engines Self-Propelled by Accumulated Gas Bubbles. *Small* **5**, 1688-1692, doi:https://doi.org/10.1002/smll.200900021 (2009).
15. Solovev, A. A., Sanchez, S., Pumera, M., Mei, Y. F. & Schmidt, O. G. Magnetic Control of Tubular Catalytic Microbots for the Transport, Assembly, and Delivery of Micro-objects. *Advanced Functional Materials* **20**, 2430-2435, doi:https://doi.org/10.1002/adfm.200902376 (2010).
16. Abdelmohsen, L. K. E. A. *et al.* Dynamic Loading and Unloading of Proteins in Polymeric Stomatocytes: Formation of an Enzyme-Loaded Supramolecular Nanomotor. *ACS Nano* **10**, 2652-2660, doi:10.1021/acsnano.5b07689 (2016).
17. Peng, F., Tu, Y., van Hest, J. C. M. & Wilson, D. A. Self-Guided Supramolecular Cargo-Loaded Nanomotors with Chemotactic Behavior towards Cells. *Angewandte Chemie International Edition* **54**, 11662-11665, doi:https://doi.org/10.1002/anie.201504186 (2015).
18. Wilson, D. A., Nolte, R. J. M. & van Hest, J. C. M. Autonomous movement of platinum-loaded stomatocytes. *Nature Chemistry* **4**, 268-274, doi:10.1038/nchem.1281 (2012).
19. Peng, F., Tu, Y. & Wilson, D. A. Micro/nanomotors towards in vivo application: cell, tissue and biofluid. *Chemical Society Reviews* **46**, 5289-5310, doi:10.1039/C6CS00885B (2017).
20. Xu, D. *et al.* Self-Propelled Micro/Nanomotors for On-Demand Biomedical Cargo Transportation. *Small* **16**, 1902464, doi:https://doi.org/10.1002/smll.201902464 (2020).
21. Wu, Z. *et al.* Self-propelled polymer-based multilayer nanorockets for transportation and drug release. *Angewandte Chemie International Edition* **52**, 7000-7003 (2013).

22. Mhanna, R. *et al.* Artificial Bacterial Flagella for Remote-Controlled Targeted Single-Cell Drug Delivery. *Small* **10**, 1953-1957, doi:https://doi.org/10.1002/smll.201303538 (2014).
23. Xu, H. *et al.* Sperm-Hybrid Micromotor for Targeted Drug Delivery. *ACS Nano* **12**, 327-337, doi:10.1021/acsnano.7b06398 (2018).
24. Ma, X., Hahn, K. & Sanchez, S. Catalytic Mesoporous Janus Nanomotors for Active Cargo Delivery. *Journal of the American Chemical Society* **137**, 4976-4979, doi:10.1021/jacs.5b02700 (2015).
25. Xuan, M., Shao, J., Lin, X., Dai, L. & He, Q. Self-Propelled Janus Mesoporous Silica Nanomotors with Sub-100 nm Diameters for Drug Encapsulation and Delivery. *ChemPhysChem* **15**, 2255-2260, doi:https://doi.org/10.1002/cphc.201402111 (2014).
26. Wu, Z., Lin, X., Zou, X., Sun, J. & He, Q. Biodegradable Protein-Based Rockets for Drug Transportation and Light-Triggered Release. *ACS Applied Materials & Interfaces* **7**, 250-255, doi:10.1021/am507680u (2015).
27. Esteban-Fernández de Ávila, B. *et al.* Acoustically Propelled Nanomotors for Intracellular siRNA Delivery. *ACS Nano* **10**, 4997-5005, doi:10.1021/acsnano.6b01415 (2016).
28. Kagan, D. *et al.* Functionalized Micromachines for Selective and Rapid Isolation of Nucleic Acid Targets from Complex Samples. *Nano Letters* **11**, 2083-2087, doi:10.1021/nl2005687 (2011).
29. Qiu, F. *et al.* Magnetic Helical Microswimmers Functionalized with Lipoplexes for Targeted Gene Delivery. *Advanced Functional Materials* **25**, 1666-1671, doi:https://doi.org/10.1002/adfm.201403891 (2015).
30. Xu, X. *et al.* Precision-Guided Nanospears for Targeted and High-Throughput Intracellular Gene Delivery. *ACS Nano* **12**, 4503-4511, doi:10.1021/acsnano.8b00763 (2018).
31. Esteban-Fernández de Ávila, B. *et al.* Nanomotor-Enabled pH-Responsive Intracellular Delivery of Caspase-3: Toward Rapid Cell Apoptosis. *ACS Nano* **11**, 5367-5374, doi:10.1021/acsnano.7b01926 (2017).
32. Hansen-Bruhn, M. *et al.* Active Intracellular Delivery of a Cas9/sgRNA Complex Using Ultrasound-Propelled Nanomotors. *Angewandte Chemie International Edition* **57**, 2657-2661, doi:https://doi.org/10.1002/anie.201713082 (2018).
33. Orozco, J. *et al.* Molecularly Imprinted Polymer-Based Catalytic Micromotors for Selective Protein Transport. *Journal of the American Chemical Society* **135**, 5336-5339, doi:10.1021/ja4018545 (2013).
34. Uygun, M. *et al.* Ultrasound-propelled nanowire motors enhance asparaginase enzymatic activity against cancer cells. *Nanoscale* **9**, 18423-18429, doi:10.1039/C7NR07396H (2017).
35. Gao, W. *et al.* Cargo-Towing Fuel-Free Magnetic Nanoswimmers for Targeted Drug Delivery. *Small* **8**, 460-467, doi:https://doi.org/10.1002/smll.201101909 (2012).
36. Kim, S. *et al.* Fabrication and Characterization of Magnetic Microrobots for Three-Dimensional Cell Culture and Targeted Transportation. *Advanced Materials* **25**, 5863-5868, doi:https://doi.org/10.1002/adma.201301484 (2013).
37. Lin, Z. *et al.* Magnetically Actuated Peanut Colloid Motors for Cell Manipulation and Patterning. *ACS Nano* **12**, 2539-2545, doi:10.1021/acsnano.7b08344 (2018).
38. Medina-Sánchez, M., Schwarz, L., Meyer, A. K., Hebenstreit, F. & Schmidt, O. G. Cellular Cargo Delivery: Toward Assisted Fertilization by Sperm-Carrying Micromotors. *Nano Letters* **16**, 555-561, doi:10.1021/acs.nanolett.5b04221 (2016).
39. Garcia-Gradilla, V. *et al.* Functionalized Ultrasound-Propelled Magnetically Guided Nanomotors: Toward Practical Biomedical Applications. *ACS Nano* **7**, 9232-9240, doi:10.1021/nn403851v (2013).
40. Kagan, D. *et al.* Chemical Sensing Based on Catalytic Nanomotors: Motion-Based Detection of Trace Silver. *Journal of the American Chemical Society* **131**, 12082-12083, doi:10.1021/ja905142q (2009).
41. Wu, J. *et al.* Motion-based DNA detection using catalytic nanomotors. *Nature Communications* **1**, 36, doi:10.1038/ncomms1035 (2010).

42. Gao, W., Pei, A., Dong, R. & Wang, J. Catalytic Iridium-Based Janus Micromotors Powered by Ultralow Levels of Chemical Fuels. *Journal of the American Chemical Society* **136**, 2276-2279, doi:10.1021/ja413002e (2014).
43. Orozco, J. *et al.* Artificial Enzyme-Powered Microfish for Water-Quality Testing. *ACS Nano* **7**, 818-824, doi:10.1021/nn305372n (2013).
44. Guix, M. *et al.* Superhydrophobic Alkanethiol-Coated Microsubmarines for Effective Removal of Oil. *ACS Nano* **6**, 4445-4451, doi:10.1021/nn301175b (2012).
45. Huang, C. & Shen, X. Janus molecularly imprinted polymer particles. *Chemical Communications* **50**, 2646-2649, doi:10.1039/C3CC49586H (2014).
46. Masqué, N., Marcé, R. M., Borrull, F., Cormack, P. A. G. & Sherrington, D. C. Synthesis and Evaluation of a Molecularly Imprinted Polymer for Selective On-Line Solid-Phase Extraction of 4-Nitrophenol from Environmental Water. *Analytical Chemistry* **72**, 4122-4126, doi:10.1021/ac0000628 (2000).
47. Soler, L., Magdanz, V., Fomin, V. M., Sanchez, S. & Schmidt, O. G. Self-Propelled Micromotors for Cleaning Polluted Water. *ACS Nano* **7**, 9611-9620, doi:10.1021/nn405075d (2013).
48. Gao, W. & Wang, J. The Environmental Impact of Micro/Nanomachines: A Review. *ACS Nano* **8**, 3170-3180, doi:10.1021/nn500077a (2014).
49. Mou, F. *et al.* Magnetically modulated pot-like MnFe2O4 micromotors: nanoparticle assembly fabrication and their capability for direct oil removal. *Advanced Functional Materials* **25**, 6173-6181 (2015).
50. Ying, Y., Pourrahimi, A. M., Sofer, Z., Matějková, S. & Pumera, M. Radioactive Uranium Preconcentration via Self-Propelled Autonomous Microrobots Based on Metal–Organic Frameworks. *ACS Nano* **13**, 11477-11487, doi:10.1021/acsnano.9b04960 (2019).
51. Ning, P., Bart, H.-J., Li, B., Lu, X. & Zhang, Y. Phosphate removal from wastewater by model-La(III) zeolite adsorbents. *Journal of Environmental Sciences* **20**, 670-674, doi:https://doi.org/10.1016/S1001-0742(08)62111-7 (2008).
52. Dillon, A. C. & Heben, M. J. Hydrogen storage using carbon adsorbents: past, present and future. *Applied Physics A* **72**, 133-142, doi:10.1007/s003390100788 (2001).
53. Kumar, K. Y., Muralidhara, H. B., Nayaka, Y. A., Balasubramanyam, J. & Hanumanthappa, H. Low-cost synthesis of metal oxide nanoparticles and their application in adsorption of commercial dye and heavy metal ion in aqueous solution. *Powder Technology* **246**, 125-136, doi:https://doi.org/10.1016/j.powtec.2013.05.017 (2013).
54. Zhao, Y., Wang, D., Luan, Y. & Du, X. NIR-light propelled bowl-like mesoporous polydopamine@UiO-66 metal−organic framework nanomotors for enhanced removal of organic contaminant. *Materials Today Sustainability* **18**, 100129, doi:https://doi.org/10.1016/j.mtsust.2022.100129 (2022).
55. Butler, K. S. *et al.* Protocells: Modular Mesoporous Silica Nanoparticle-Supported Lipid Bilayers for Drug Delivery. *Small* **12**, 2173-2185, doi:https://doi.org/10.1002/smll.201502119 (2016).
56. Dengler, E. C. *et al.* Mesoporous silica-supported lipid bilayers (protocells) for DNA cargo delivery to the spinal cord. *Journal of Controlled Release* **168**, 209-224, doi:https://doi.org/10.1016/j.jconrel.2013.03.009 (2013).
57. Skirtach, A. G. *et al.* Ultrasound stimulated release and catalysis using polyelectrolyte multilayer capsules. *Journal of Materials Chemistry* **17**, 1050-1054, doi:10.1039/B609934C (2007).
58. Wu, Z. *et al.* Self-Propelled Polymer-Based Multilayer Nanorockets for Transportation and Drug Release. *Angewandte Chemie International Edition* **52**, 7000-7003, doi:https://doi.org/10.1002/anie.201301643 (2013).
59. Ganta, S., Devalapally, H., Shahiwala, A. & Amiji, M. A review of stimuli-responsive nanocarriers for drug and gene delivery. *Journal of Controlled Release* **126**, 187-204, doi:https://doi.org/10.1016/j.jconrel.2007.12.017 (2008).

60. Li, J. *et al.* Micromotors Spontaneously Neutralize Gastric Acid for pH-Responsive Payload Release. *Angewandte Chemie International Edition* **56**, 2156-2161, doi:https://doi.org/10.1002/anie.201611774 (2017).
61. Axthelm, F. *et al.* Antioxidant Nanoreactor Based on Superoxide Dismutase Encapsulated in Superoxide-Permeable Vesicles. *The Journal of Physical Chemistry B* **112**, 8211-8217, doi:10.1021/jp803032w (2008).
62. Huang, X. *et al.* Interfacial assembly of protein–polymer nano-conjugates into stimulus-responsive biomimetic protocells. *Nature Communications* **4**, 2239, doi:10.1038/ncomms3239 (2013).
63. Koga, S., Williams, D. S., Perriman, A. W. & Mann, S. Peptide–nucleotide microdroplets as a step towards a membrane-free protocell model. *Nature Chemistry* **3**, 720-724, doi:10.1038/nchem.1110 (2011).
64. Li, M., Green, D. C., Anderson, J. L. R., Binks, B. P. & Mann, S. In vitro gene expression and enzyme catalysis in bio-inorganic protocells. *Chemical Science* **2**, 1739-1745, doi:10.1039/C1SC00183C (2011).
65. Williams, D. S., Patil, A. J. & Mann, S. Spontaneous Structuration in Coacervate-Based Protocells by Polyoxometalate-Mediated Membrane Assembly. *Small* **10**, 1830-1840, doi:https://doi.org/10.1002/smll.201303654 (2014).
66. Mazzei, L., Musiani, F. & Ciurli, S. The structure-based reaction mechanism of urease, a nickel dependent enzyme: tale of a long debate. *JBIC Journal of Biological Inorganic Chemistry* **25**, 829-845, doi:10.1007/s00775-020-01808-w (2020).
67. A. Begum, S. B., M. I. Choudhary, C. Betzel. *Crystallographic structure analysis of urease from Jack bean (Canavalia ensiformis) at 1.49 A Resolution*, <https://www.rcsb.org/structure/4gy7> (1995).
68. Dixon, N. E., Riddles, P. W., Gazzola, C., Blakeley, R. L. & Zerner, B. Jack bean urease (EC 3.5.1.5). V. On the mechanism of action of urease on urea, formamide, acetamide, N-methylurea, and related compounds. *Canadian Journal of Biochemistry* **58**, 1335-1344, doi:10.1139/o80-181 %M 6788353 (1980).
69. Karplus, P. A., Pearson, M. A. & Hausinger, R. P. 70 Years of Crystalline Urease: What Have We Learned? *Accounts of Chemical Research* **30**, 330-337, doi:10.1021/ar960022j (1997).
70. Zambelli, B., Musiani, F., Benini, S. & Ciurli, S. Chemistry of Ni2+ in Urease: Sensing, Trafficking, and Catalysis. *Accounts of Chemical Research* **44**, 520-530, doi:10.1021/ar200041k (2011).
71. Benini, S. *et al.* A new proposal for urease mechanism based on the crystal structures of the native and inhibited enzyme from Bacillus pasteurii: why urea hydrolysis costs two nickels. *Structure* **7**, 205-216, doi:https://doi.org/10.1016/S0969-2126(99)80026-4 (1999).
72. Wu, S.-T., Efron, U. & Hess, L. D. Birefringence measurements of liquid crystals. *Applied optics* **23**, 3911-3915 (1984).
73. Cotton, F. A., Wilkinson, G. & Geoffrey, W. *Advanced Inorganic Chemistry: A Comprehensive Text*. (Interscience Publishers, 1972).
74. Dias, J. A., Dias, S. C. L., Caliman, E., Bartis, J. & Francesconi, L. in *Inorganic Syntheses: Volume 36* 210-217 (2014).
75. Keggin, J. F. Structure of the Molecule of 12-Phosphotungstic Acid. *Nature* **131**, 908-909, doi:10.1038/131908b0 (1933).
76. Mansir, N., Taufiq-Yap, Y. H., Rashid, U. & Lokman, I. M. Investigation of heterogeneous solid acid catalyst performance on low grade feedstocks for biodiesel production: A review. *Energy Conversion and Management* **141**, 171-182, doi:https://doi.org/10.1016/j.enconman.2016.07.037 (2017).
77. Lavelle, C., Victor, J.-M. & Zlatanova, J. Chromatin fiber dynamics under tension and torsion. *International journal of molecular sciences* **11**, 1557-1579 (2010).

78. Zhu, Z., Tain, R. & Rhodes, C. A study of the decomposition behaviour of 12-tungstophosphate heteropolyacid in solution. *Canadian Journal of Chemistry* **81**, 1044-1050, doi:10.1139/v03-129 (2003).
79. Deng, H.-H. *et al.* pH-Sensitive gold nanoclusters: preparation and analytical applications for urea, urease, and urease inhibitor detection. *Chemical Communications* **51**, 7847-7850, doi:10.1039/C5CC00702J (2015).
80. Mascini, M. & Guilbault, G. G. Urease coupled ammonia electrode for urea determination in blood serum. *Analytical Chemistry* **49**, 795-798, doi:10.1021/ac50014a031 (1977).
81. Sidebotham, R. L., Worku, M. L., Karim, Q. N., Dhir, N. K. & Baron, J. H. How Helicobacter pylori urease may affect external pH and influence growth and motility in the mucus environment: evidence from in-vitro studies. *European Journal of Gastroenterology & Hepatology* **15**, 395-401 (2003).
82. El-Hefnawy, M. E., Sakran, M., Ismail, A. I. & Aboelfetoh, E. F. Extraction, purification, kinetic and thermodynamic properties of urease from germinating Pisum Sativum L. seeds. *BMC Biochemistry* **15**, 15, doi:10.1186/1471-2091-15-15 (2014).
83. Beutler, B. *et al.* GENETIC ANALYSIS OF HOST RESISTANCE: Toll-Like Receptor Signaling and Immunity at Large. *Annual Review of Immunology* **24**, 353-389, doi:10.1146/annurev.immunol.24.021605.090552 (2006).
84. Kim, B.-H., Shenoy, Avinash R., Kumar, P., Bradfield, Clinton J. & MacMicking, John D. IFN-Inducible GTPases in Host Cell Defense. *Cell Host & Microbe* **12**, 432-444, doi:10.1016/j.chom.2012.09.007 (2012).
85. MacMicking, J. D. Interferon-inducible effector mechanisms in cell-autonomous immunity. *Nature Reviews Immunology* **12**, 367-382, doi:10.1038/nri3210 (2012).
86. Randow, F., MacMicking, J. D. & James, L. C. Cellular Self-Defense: How Cell-Autonomous Immunity Protects Against Pathogens. *Science* **340**, 701-706, doi:10.1126/science.1233028 (2013).
87. Randow, F. & Münz, C. Autophagy in the regulation of pathogen replication and adaptive immunity. *Trends in Immunology* **33**, 475-487, doi:10.1016/j.it.2012.06.003 (2012).
88. Kagan, Jonathan C. Signaling Organelles of the Innate Immune System. *Cell* **151**, 1168-1178, doi:10.1016/j.cell.2012.11.011 (2012).
89. Botteaux, A., Hoste, C., Dumont, J. E., Van Sande, J. & Allaoui, A. Potential role of Noxes in the protection of mucosae: H2O2 as abacterial repellent. *Microbes and Infection* **11**, 537-544, doi:https://doi.org/10.1016/j.micinf.2009.02.009 (2009).
90. Vaishnava, S. *et al.* The Antibacterial Lectin RegIIIγ Promotes the Spatial Segregation of Microbiota and Host in the Intestine. *Science* **334**, 255-258, doi:10.1126/science.1209791 (2011).
91. Gusarov, I., Shatalin, K., Starodubtseva, M. & Nudler, E. Endogenous Nitric Oxide Protects Bacteria Against a Wide Spectrum of Antibiotics. *Science* **325**, 1380-1384, doi:10.1126/science.1175439 (2009).
92. McGettigan, J. *et al.* Insect renal tubules constitute a cell-autonomous immune system that protects the organism against bacterial infection. *Insect Biochemistry and Molecular Biology* **35**, 741-754, doi:https://doi.org/10.1016/j.ibmb.2005.02.017 (2005).
93. Ribatti, D. in *Milestones in Immunology* (ed Domenico Ribatti) 37-46 (Academic Press, 2017).

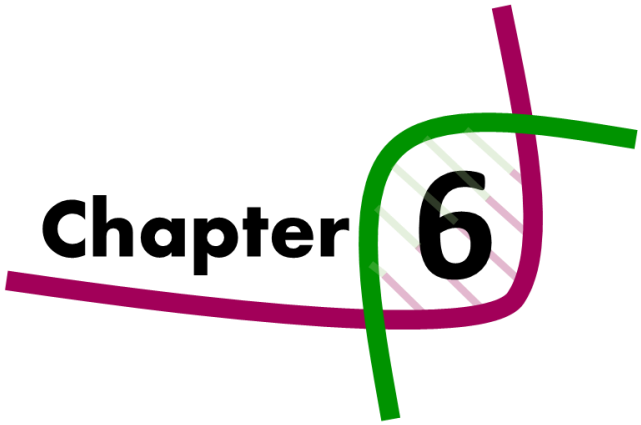

Future work

6.1 Photo-control of protamine/DNA-microcapsule motility

The core theme of this project was to modify the enzymes glucose oxidase and/or catalase with a so called “photo-switch”, which is capable of isomerizing after being irradiated with light of a specific wavelength. In theory and when bound close to the active site of the enzyme, the isomerisation would then change the interaction between the enzyme and its substrate, thus decreasing or increasing the enzymatic rate. This is a very non-invasive way of changing the enzymatic activity, which would normally only be possible via concentration or temperature changes. In regard to the oscillation-experiments from chapter 4, this concept would allow the control of the microcapsule oscillation depending on the light that is being used. One could change the oscillation pattern or simply start and stop the oscillation by changing the wavelength of the light, which would be a novel pathway of controlling microcapsule oscillations.

Spiropyrans (SP) are photo switches, with a molecular structure which consists of an indolin-species on the left and a benzopyran on the right, which are connected through a spiro-carbon junction. The closed-ring structure is called spiropyran and can, upon interaction with ultraviolet light (~ 355 nm) change its structure to the open-ring photoisomer, the merocyanine (MC) form. One of the many key benefits of spiropyrans and what makes them so unique are the vastly different properties between the two photo isomers. For one, due to the charge-separation, MC exhibits a vastly different dipole-moment compared to SP. Secondly, MC not only changes in structure but also in size, where SP occupies less volume than MC. Furthermore, MC absorbs strongly around 550 nm, making it appear dark blue, whereas SP is mostly colourless. At the same time, they also show different emission-behaviour with SP not exhibiting strong emission at all and MC showing a strong emission band around $\lambda_{Emission}$ = 650 nm. Lastly, MC is more basic than SP and can be protonated to MCH^+. Experimentally, the pK_a of MCH^+ has been determined to be around 2.25, which can be explained by looking at the stabilisation of the phenoxide anion, due to the electronic conjugation within the molecule but also because of the electron-withdrawing effects of the NO_2-group. [1-3]

Although spiropyrans are mainly advertised as photoswitches, the isomerisation can be triggered reversibly by a variety of stimuli. This includes a change of solvents (Solvatochromism), pH (Acidochromism), metal ions, redox potential (Electrochromism), temperature (Thermochromism) and mechanical force (Mechanochromism). The isomerisation itself is a first-order process [4] and is illustrated in Figure 6.1-1. Irradiation of SP with UV-light leads to the cleavage of the C_{Spiro}-O bond, which results in a cis-form of MC. [5] The ring-opening can happen either as a 6π-electro-cyclic ring

opening (Figure 6.1-1-right) or as heterolytic C-O-bond cleavage (Figure 6.1-1-left), leading to either the quinoidal (Figure 6.1-1 (4)) or the zwitterionic-form (Figure 6.1-1 (3)). Rotation around the C-C bonds eventually forms the more stable *trans*-MC. The reverse isomerisation from MC to SP happens spontaneously and can be accelerated by VIS-light, following first-order kinetics. [6] Depending on the stabilising effects from polar environments, the transition from SP to MC can also happen spontaneously in the dark, whereas it will need visible light activation to reform SP. In this case SP is the metastable state which is referred to as negative photochromism [7]

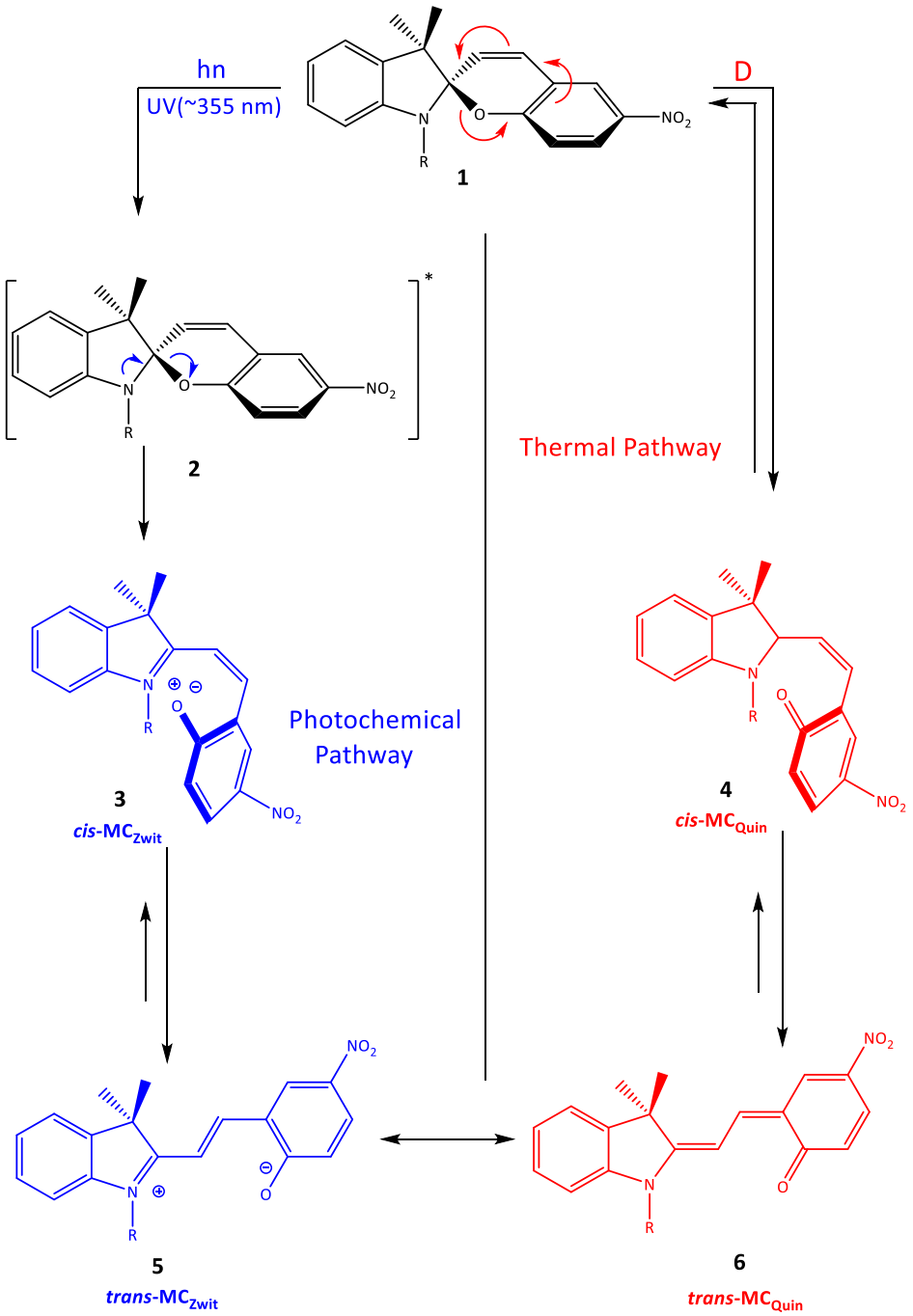

Figure 6.1-1: *Mechanism of isomerisation between spiropyran and merocyanine. (**blue**) photochemical pathway, (**red**) thermal pathway.* [4-6]

Considering the properties shown above, spiropyrans find numerous applications in research, technological- and medical applications. [8] Depending on the rest "R" on the indoline-group, SP can be coupled to a variety of materials and molecules to enhance or alter their function. Coupling-studies of SP to polymers improved polymer solubility [9,10], they showcased photocontrol of polymeric microchannels [11,12], altered the mechanical properties of polymers [13] or even showed complexation-behaviour of SP-modified polymers to metal ions. [14] Another interesting application is the coupling of SP to biopolymers such as enzymes or DNA. Here, studies showed the photocontrol of polypeptide conformation [15], the reversible change of enzymatic activity of various enzymes [16-20], the photocontrol of DNA-hybridisation and protein folding [21,22] or the photocontrol of transport through nanopores [23]

As presented in the literature quoted above, it is possible to modify and control the activity of enzymes by coupling of SP into the polypeptide structure. Although there is no clear answer to why the activity changes, there are several factors that come into consideration. Like explained above, SP and MC exhibit rather different chemical and physiochemical properties and isomerisation changes the hydrophobicity, the size, the dipole-moment and the acidity. Depending on where in the enzymatic structure the dye is coupled to, one can expect distortion of the molecular structure, a change in accessibility of substrates into the active site and eventually a change in activity during the conversion of the substrate. Looking at the studies in literature, a broad spectrum of results for different enzymes was found. One of the earliest experiments, the modification of α-Amylase yielded a reduction of ~18-36% in activity [17] when exposed to visible light, while β-Amylase changed by up to 87%. [16] Other enzymes like glucose oxidase (GOx) decreased in activity by ~40% [24] under UV-light, whereas HRP showed a decrease of as much as 92% when exposed to visible light. [20] Not only does the modification of enzymes change the activity by different amounts, it is also hard to predict which wavelength of light will be activating and which one will be deactivating.

To covalently couple SP to biopolymers like enzymes, it needs a functional group that is suitable for a mild and quick coupling reaction. One of the most convenient pathways is the coupling via EDC/NHS-chemistry, which targets primary amines and couples them to carboxylated molecules. Since primary amines and COOH-groups would otherwise not react with each other, it is necessary to reduce the activation energy for the reaction, which is done by EDC and NHS. The carbodiimide EDC will first form the active ester (Figure 6.1-2 (3)), which could already react with the primary amine. However, they tend to hydrolyse quickly in contact with water, which increases even more at higher pH (pH >8). In order to stabilise the intermediate, it is common practise to add sulfo-NHS, which can form a second sulfo-NHS-ester intermediate (Figure 6.1-2 (5)) which can ultimately react with the primary amine of the target to form the coupled product (Figure 6.1-2 (7)). [25]

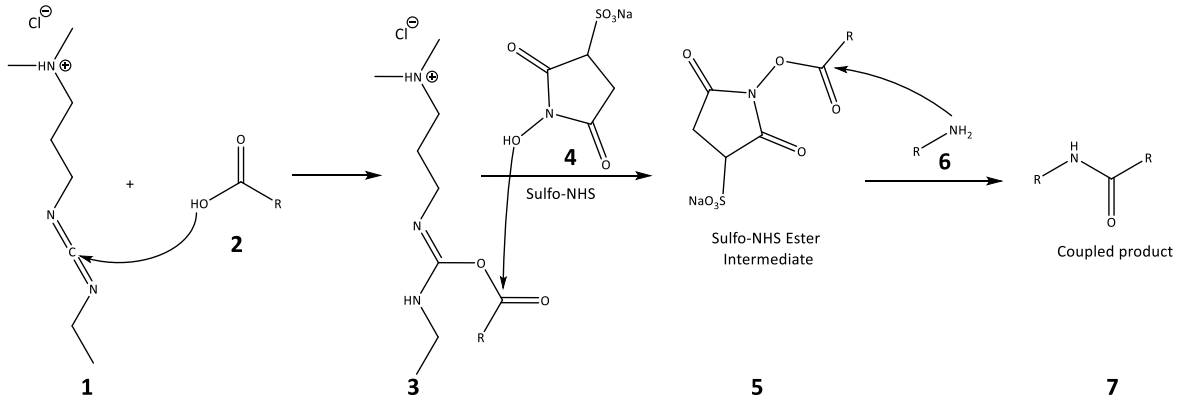

Figure 6.1-2: *EDC/NHS coupling.* [25]

To make SP accessible for EDC/NHS-chemistry, it is necessary to attach the COOH-functionality. According to the literature above, the most popular position for such a modification is the N-atom of the indoline-group. The experiments from this report were working with a propionic-acid substituent (SP-COOH) as seen in Figure 6.1-3. The coupling-targets are the primary amines of the enzymes, which usually can be found as Lysine-residues. Since the number of primary amines varies from enzyme to enzyme, the amount of coupled SP-COOH can vary and therefore yield different changes in activity.

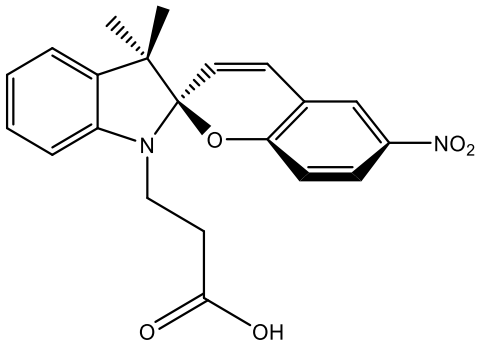

Figure 6.1-3: *SP-COOH for EDC/NHS-coupling experiments.*

The project was originally designed to be a major part of this thesis but did not come to fruition for several reasons. In the following part, the current state of the work will be outlined and what caused the project to stagnate. SP-COOH was synthesised over a 2 step synthesis and characterised successfully. Apart from exhibiting the correct signals in both IR- and NMR-spectroscopy, it also showed the characteristic photochromism in different solvents.

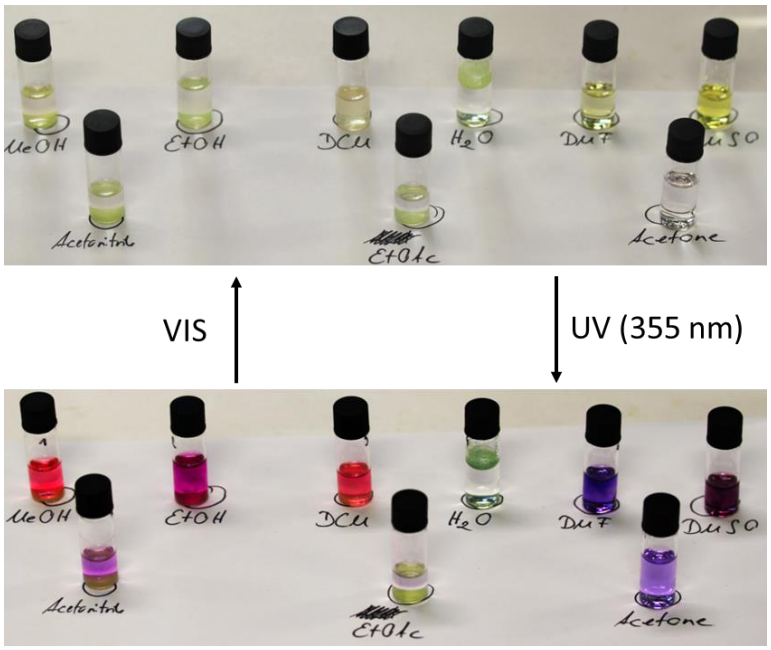

Figure 6.1-4: *Photochromism of SP-COOH in different solvents*

SP-COOH was then covalently coupled into GOx and HRP, as these two enzymes have already been mentioned in literature previous to this work. The coupling was done via a simple EDC/NHS-chemsitry protocol and appeared successful, as both enzymes exhibited a new absorbant peak when analysed via UV/VIS spectroscopy.

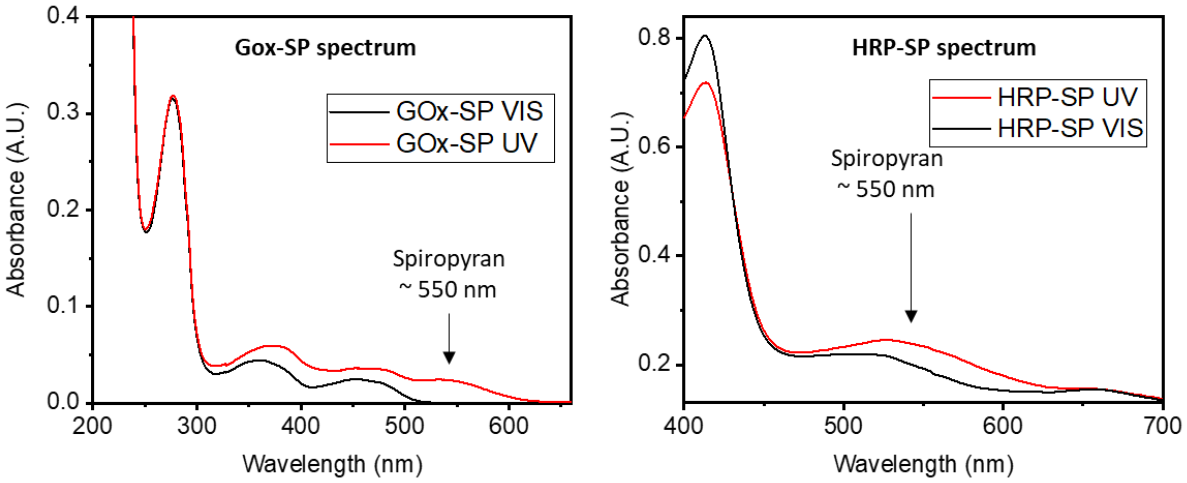

Figure 6.1-5: *UV/VIS-spectra of GOx-SP and HRP-SP.*

Like in many other experiments in this thesis, a coupled enzymatic assay with GOx, HRP and ABTS was used to assess how the modification of the enzymes with SP-COOH has changed their activity when either shining UV-light or visible light onto the enzymes. In an ideal scenario, one would expect something like it is described in Figure 6.1-6, which aligns with the results from the papers, which have introduced this concept previously. [20,24] In case of GOx-SP, visible light increased the enzymatic rate whereas UV-light decreased it, which was reversed for HRP-SP. These results would have been optimal, if they were reproducible. In fact, the experimental setup for the confirmational "switch" via light while simultaneously measuring the enzymatic activity posed a lot of questions and problems.

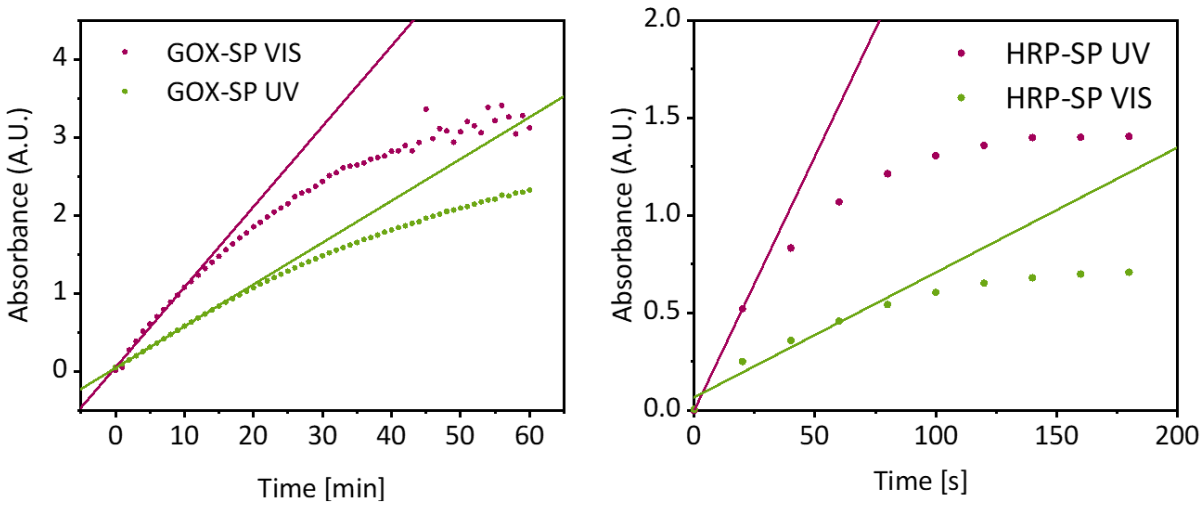

Figure 6.1-6: *Enzymatic activity assay of GOx-SP and HRP-SP. Coupling reaction was terminated after 20 minutes. Before the measurement, the enzyme GOx-SP (0.00025 mg/mL) or HRP-SP (60 U/mL) was pre-illuminated with either VIS or UV-light (355 nm) for 20 minutes, and then mixed with ABTS (16 mM), Glucose (1 mM), and HRP (0.001 mg/mL). The mixture was furthermore illuminated with the same light source inside the UV/VIS spectrometer using a solvent-probe (light-conducting glass rod) and the lamp was turned off between each measurement. Measurements were taken every minute for up to 60 minutes. The plots show the data points for both the UV- and the VIS-experiment. The activity-change was determined by comparing the linear approximations of the first 10-15 minutes of both graphs.*

For one, none of the subsequent experiments with GOx-SP and HRP-SP were successful in a way, that they showed any measurable change in activity, no matter if the enzyme was irradiated with UV-light or visible light. The experiment was optimised by adapting experimental procedures for the SP-modification from numerous papers, focusing on NHS/EDC- or DCC-chemistry yet without success. The way the modified enzymes were illuminated was changed between a constant illumination within the UV/VIS-spectrometer, a constant illumination outside of the UV/VIS-spectrometer and a defined illumination time before the experiment, after which the samples were kept in the dark. Neither approach led to any substantial results, but it brought up another important issue, which is the denaturation of enzymes in response to UV-illumination. Even at very low UV-intensities the enzymatic activity deteriorated irreversibly when illuminating the modified enzymes to ensure they were switched to the open merocyanine form. Regarding the published literature, this posed many questions which, up to this day, could not be answered, considering all experimental steps from the literature were followed.

As time was the limiting factor that prevented this project from going forward, it is necessary to look ahead to see what can still be done. Considering the microcapsule-oscillation concept from this thesis relies so heavily on enzymatic interaction, it keeps being a fascinating idea to modify the enzymes with a chemical compound which can reversibly alter the enzymatic rate of reaction. Spiropyrans are only one candidate which was investigated, mostly because previous studies have already looked into this idea and because these molecules are generally well understood. The only molecular species investigated was SP-COOH, due to the simplicity of modifying enzymes due to the COOH-moiety, but there is a vast repertoire of other spiropyran variants which could also serve as valid candidates for the modification of enzymes. Despite all the benefits of SP-COOH, it still lacked an important feature, which is a good solubility in water. In all experiments, SP-COOH had to be pre-dissolved in ethanol before it could be transferred into water. This usually only allowed for low SP-COOH-concentrations of <1 mg/mL, which made the modification of enzymes or even polymers more complicated. Here, it would be helpful to design an SP-COOH species with a higher water solubility, which could make the coupling to bio- or macromolecules more efficient. Finally, it needs to be addressed whether UV-light can indeed function to change the activity of modified enzymes. Here it would be necessary to use even weaker UV-lamps, which could trigger the photo-switch without destabilising the enzyme. If not, it would be necessary to design or re-conceptualise the approach towards other photoswitches which do not need UV-light for their isomerisation. Otherwise, there are many other photo-switches which have been discussed over the years and which could be used instead of SP-COOH.

6.2 Protamine/DNA-microcapsule tissues

With protocells only being singular entities, the next logical step in many protocellular research projects is to form networks or tissues of protocells. While protamine/DNA-microcapsules have shown that surface modification is a rather difficult task to perform, their stickiness is a property that can be used to make them adhere not only to other objects like particles, walls or other cells like PCVs, but that they can also adhere to each other, considering they are put under enough pressure.

In a dispersion and under standard gravity, protamine/DNA-capsules would simply settle on the ground but mostly would not stick to each other, and even if they do, simple re-dispersion would break the agglomerates apart. When placed in a centrifuge though, the centrifugal force that the capsules experience was enough to make them irreversibly stick to each other. The tissues in Figure 6.2-1 show that they are comprised of intact protamine/DNA-capsules which have not been broken in the process of the centrifugation. Considering the conical shape of an *Eppendorf*-vial which was used for the centrifugation, the cells within the tissue were not distributed evenly, but rather in a gaussian distribution, which means that there are more capsules adhered to the centre of the tissue, than to

the sides. Figure 6.2-1-c furthermore investigated catalase containing protamine-capsules which also formed intact protamine-capsule tissues. These tissues were capable of floating upwards when immersed in a H_2O_2-phase, even though the buoyancy was more random and chaotic than the buoyancy of single capsules. Instead of internal nucleation, the O_2-bubbles nucleated on the surface of the tissue which caused the tissue to tumble in all directions. This would be an interesting concept, to fabricate buoyant microcapsule tissues which are capable of nucleating bubbles inside the capsules with a homogenous distribution over all capsules. This would turn the inert microcapsule tissues into something like a micro-raft, which would be capable of floating up and down just like the single microcapsules. With a little more control over the fabrication, one could also design rafts with a heterogenous distribution of O_2-producing (ergo catalase containing) microcapsules and O_2-consuming (GOx-containing) capsules.

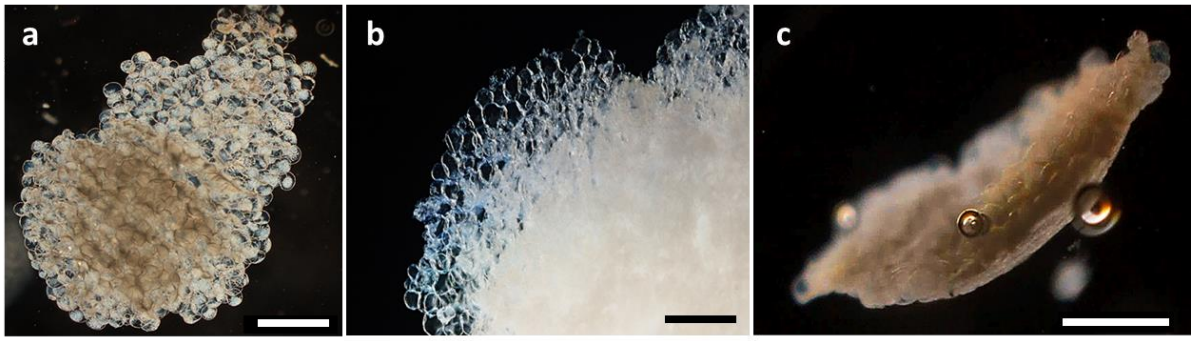

Figure 6.2-1: *Protamine/DNA-microcapsule tissues, prepared from centrifugation in a standard Eppendorf vial. The tissues formed after 5 minutes at 3000 rpm (**a-c**). It was also possible to use protamine/DNA-capsule with entrapped catalase (19.8 kU/mL). The bubbles around the tissue resulted from immersion in a H_2O_2-solution, as the tissue floated upwards and tumbled due to the production and nucleation of O_2. Scale bars: 1 mm (a+b), 100 μm (c).*

A core issue of the way these protamine-capsule tissues are fabricated is the fact that a centrifuge is needed, which implies many different steps like the usage of centrifuge vials. Considering that the centrifuge has an angled axis, it is very difficult to produce completely homogenously distributed tissues. One way to achieve this, was by re-shaping the bottom of the vial in a way, that the surface the capsule will be pushed towards via the centrifugal force is orthogonal to the vector of the centrifugal force. This was done by using PDMS to form a small mould, which allowed the capsules to settle in an even and homogenous way (Figure 6.2-2).

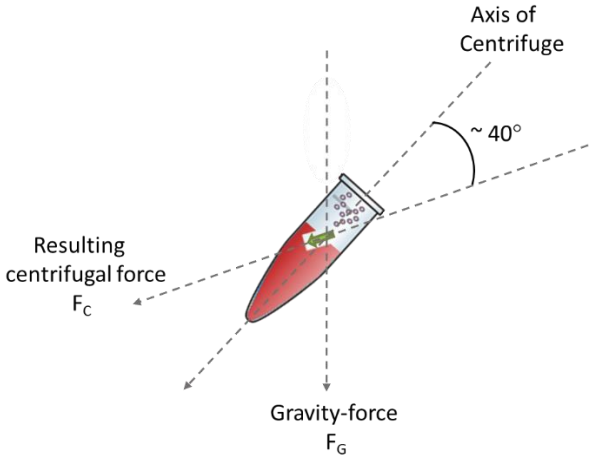

Figure 6.2-2: *Directions of forces within the centrifuge and inside PDMS-filled Eppendorf vials during the fabrication of protamine/DNA-microcapsule tissues.*

By shaping the mould in various geometries, this allowed to also shape the resulting tissues in whatever way imaginable. Figure 6.2-3 shows several microcapsule tissues with two distinct shapes. In the first example the PDMS-mould was shaped in form of a diamond, which is then imprinted in the protamine-capsule tissue (Figure 6.2-3-a+b). The tissue's shape follows the shape of the mould with only a few capsules protruding from it. Nonetheless the tissues were stable and did not fall apart even when exposing it to mechanical stress. The same was done with a circular shape, which produced very nicely shaped circular protocell-tissues (Figure 6.2-3-c-e). Here, it was also shown that the size of the protamine-capsules can be varied as well, leading to protamine-capsule tissues with regularly sized protamine-capsules (~300 μm in diameter per capsule, Figure 6.2-3-c), large protamine-capsules (~600 μm in diameter per capsule, Figure 6.2-3-d) and small protamine capsules (~150 μm in diameter per capsule, Figure 6.2-3-e).

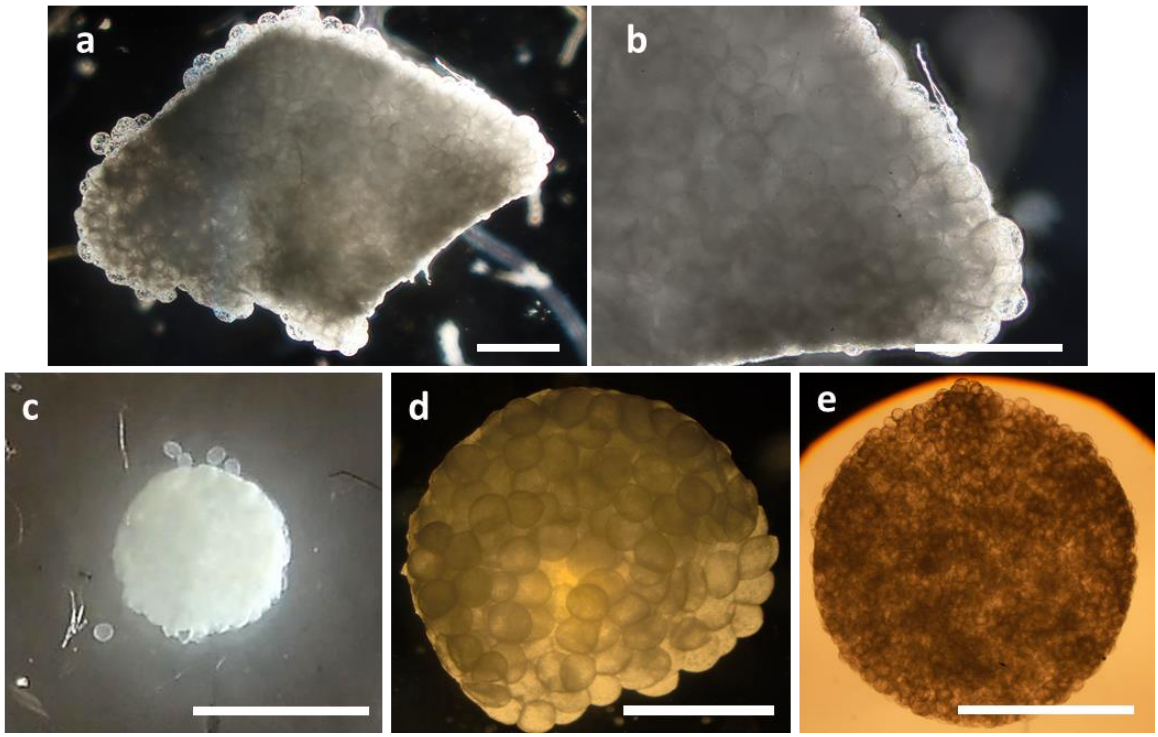

Figure 6.2-3: *Shaped protamine/DNA-microcapsule tissues.* ***a+b*** *diamond shaped protamine-capsule tissue,* ***c+e*** *circular shaped microcapsule tissue with regular sized microcapsules (~300 μm in diameter per capsule,* ***c****), large microcapsules (~600 μm in diameter per capsule,* ***d****) and small microcapsules (~150 μm in diameter per capsule,* ***e****).*

All in all, the concept seems promising but comes with several issues which have not been overcome to this date. The fabrication of the cell-tissues is most likely the biggest issue. While the tissues look stable and in good shape, using a centrifuge is highly inconvenient. Not only does it require a lot of preparation for the fabrication, the detachment of the fabricated tissue from the PDMS mould can be very complicated and often leads to broken tissues as it would stick to the mould. Furthermore, it has not been confirmed yet, if the capsules were indeed intact after the process or if they have collapsed in any way, which would directly lead to the question whether a raft-concept with internal O_2-bubble nucleation is indeed feasible. What would be a more chemical and convenient way to fabricate protamine-capsule microtissues would be to chemically link the capsules to each other. Brief attempts with EDC/NHS chemistry or other amine-coupling agents like glutaraldehyde were done, but so far, no alternative pathway was found to actually produce protamine-capsule tissues without the use of

mechanical force. Either way, it is an interesting project which could be picked up in the future for the fabrication of functional and motile protamine-capsule microtissues.

6.3 Literature for chapter 6

1. García, A. A. *et al.* Photon-Controlled Phase Partitioning of Spiropyrans. *The Journal of Physical Chemistry A* **104**, 6103-6107, doi:10.1021/jp0003757 (2000).
2. Hall, R. A., Thistlethwaite, P. J., Grieser, F., Kimizuka, N. & Kunitake, T. Acid-base equilibria of merocyanine air-water monolayers. *Langmuir* **10**, 3743-3748 (1994).
3. Sumaru, K., Kameda, M., Kanamori, T. & Shinbo, T. Characteristic phase transition of aqueous solution of poly (N-isopropylacrylamide) functionalized with spirobenzopyran. *Macromolecules* **37**, 4949-4955 (2004).
4. Görner, H. Photochromism of nitrospiropyrans: effects of structure, solvent and temperature. *Physical Chemistry Chemical Physics* **3**, 416-423, doi:10.1039/B007708I (2001).
5. Krysanov, S. A. & Alfimov, M. V. Ultrafast formation of transients in spiropyran photochromism. *Chemical Physics Letters* **91**, 77-80, doi:https://doi.org/10.1016/0009-2614(82)87037-1 (1982).
6. Whelan, J. *et al.* Photochemical and thermal spiropyran (SP)-merocyanine (MC) interconversion: a dichotomy in dependence on viscosity. *Physical Chemistry Chemical Physics* **14**, 13684-13691, doi:10.1039/C2CP42259J (2012).
7. Zhou, J. *et al.* Detailed investigation on a negative photochromic spiropyran. *Journal of Photochemistry and Photobiology A: Chemistry* **90**, 117-123 (1995).
8. Klajn, R. Spiropyran-based dynamic materials. *Chemical Society Reviews* **43**, 148-184 (2014).
9. Irie, M., Menju, A. & Hayashi, K. Photoresponsive polymers. Reversible solution viscosity change of poly (methyl methacrylate) having spirobenzopyran side groups. *Macromolecules* **12**, 1176-1180 (1979).
10. Irie, M., Menju, A., Hayashi, K. & Smets, G. Reversible viscosity change of photochromic spirobenzopyran copolymer solutions. *Journal of Polymer Science: Polymer Letters Edition* **17**, 29-31 (1979).
11. Ivanov, A., Eremeev, N., Wahlund, P.-O., Galaev, I. Y. & Mattiasson, B. Photosensitive copolymer of N-isopropylacrylamide and methacryloyl derivative of spyrobenzopyran. *Polymer* **43**, 3819-3823 (2002).
12. Sumaru, K., Kameda, M., Kanamori, T. & Shinbo, T. Reversible and efficient proton dissociation of spirobenzopyran-functionalized poly (N-isopropylacrylamide) in aqueous solution triggered by light irradiation and temporary temperature rise. *Macromolecules* **37**, 7854-7856 (2004).
13. Smets, G. Photochemical reactions in polymeric systems. *Pure and Applied Chemistry* **42**, 509-526 (1975).
14. Suzuki, T., Kato, T. & Shinozaki, H. Photo-reversible Pb2+-complexation of thermosensitive poly(N-isopropyl acrylamide-co-spiropyran acrylate) in water. *Chemical Communications*, 2036-2037, doi:10.1039/B407342H (2004).
15. Montagnoli, G., Pieroni, O. & Suzuki, S. Control of peptide chain conformation by photoisomerising chromophores: Enzymes and model compounds. *Polymer Photochemistry* **3**, 279-294, doi:https://doi.org/10.1016/0144-2880(83)90036-2 (1983).
16. Aizawa, M., Namba, K. & Suzuki, S. Light-induced enzyme activity changes associated with the photoisomerization of bound spiropyran. *Archives of biochemistry and biophysics* **182**, 305-310 (1977).
17. Karube, I., Nakamoto, Y., Namba, K. & Suzuki, S. Photocontrol of urease-collagen membrane activity. *Biochimica et biophysica acta* **429**, 975-981 (1976).
18. Namba, K. & Suzuki, S. PHOTO-CONTROL OF ENZYME ACTIVITY WITH A PHOTOCHROMIC SPIROPYRAN COMPOUND—MODIFICATION OF α-AMYLASE WITH SPIROPYRAN COMPOUND—. *Chemistry Letters* **4**, 947-950 (1975).
19. Sakata, T., Yan, Y. & Marriott, G. Optical switching of dipolar interactions on proteins. *Proceedings of the National Academy of Sciences* **102**, 4759-4764 (2005).

20. Weston, D., Kirkham, J. & Cullen, D. Photo-modulation of horseradish peroxidase activity via covalent attachment of carboxylated-spiropyran dyes. *Biochimica et Biophysica Acta (BBA)-General Subjects* **1428**, 463-467 (1999).
21. Asanuma, H. *et al.* Spiropyran as a regulator of DNA hybridization with reversed switching mode to that of azobenzene. *Chemistry letters* **30**, 108-109 (2001).
22. Hirakura, T., Nomura, Y., Aoyama, Y. & Akiyoshi, K. Photoresponsive nanogels formed by the self-assembly of spiropyrane-bearing pullulan that act as artificial molecular chaperones. *Biomacromolecules* **5**, 1804-1809 (2004).
23. Koçer, A., Walko, M., Meijberg, W. & Feringa, B. L. A light-actuated nanovalve derived from a channel protein. *Science* **309**, 755-758 (2005).
24. Katz, E., Willner, B. & Willner, I. Light-controlled electron transfer reactions at photoisomerizable monolayer electrodes by means of electrostatic interactions: active interfaces for the amperometric transduction of recorded optical signals. *Biosensors and Bioelectronics* **12**, 703-719, doi:https://doi.org/10.1016/S0956-5663(97)00038-9 (1997).
25. Hermanson, G. (Academic Press (Elsevier), 2008).